Phenomenology of leptogenesis: From cosmological phase transitions to new mechanisms and experimental probes

Dissertation submitted for the award of the title
"Doctor of Natural Sciences"
to the Faculty of Physics, Mathematics and Computer Science of
Johannes Gutenberg University Mainz

Martin Aria Mojahed
born in Stavanger, Norway

Mainz, June 17, 2025

Date of submission: 17.06.2025
Date of defense: 19.09.2025

Til Mor og Baba

Be name khodaye ranginkaman

Abstract

This thesis addresses several aspects of leptogenesis, a theoretical paradigm that attempts to resolve two prominent open questions in high-energy phenomenology: the origin of neutrino masses and the observed baryon asymmetry of the universe (BAU).

The thesis is structured into three parts, with the first part focusing on first-order phase transitions (FOPTs) and cosmic strings (CSs) within the context of gauged $U(1)_{B-L}$ extensions of the Standard Model (SM). Initially, we re-examine the FOPT and gravitational-wave (GW) production in the classically conformal $U(1)_{B-L}$ model, identifying regions of parameter space that provide optimal conditions for bubble-assisted leptogenesis. Subsequently, we investigate the production of right-handed neutrinos (RHNs) from CSs and assess the magnitude of the $B-L$ asymmetry that they may source.

The second part of this thesis is dedicated to the recently proposed wash-in leptogenesis (WILG) mechanism, which does not require any CP violation in the RHN sector. Specifically, we derive a lower bound on the mass of the lightest RHN by requiring WILG to successfully account for the observed BAU. Moreover, we introduce a novel ultraviolet mechanism for WILG based on non-minimal gravitational interactions.

In the final part of this thesis, we present novel strategies to search for new physics (NP) in rare Kaon and B-meson decays, focusing on the channels $K \to \pi + \not{E}$, $B \to K(K^*) + \not{E}$, and $B \to X_s + \not{E}$. We demonstrate that careful measurements of the kinematic distributions of missing energy can serve as a powerful tool to distinguish between the effective operators contributing to NP. Particular attention is devoted to lepton-number-violating (LNV) NP, and how observing LNV NP in rare meson decays could put leptogenesis under tension.

List of publications

This thesis is based on the publications and preprints listed below, with the author's contributions highlighted. Authors are listed alphabetically in high-energy phenomenology and theory.

[1] A. J Buras, J. Harz and M. A. Mojahed, *Disentangling new physics in $K \to \pi\nu\bar{\nu}$ and $B \to K\,(K^*)\,\nu\bar{\nu}$ observables* JHEP 10 (2024) 087, [2405.06742]: Building on some initial work and a draft by AJB and JH, MAM expanded the analysis in several directions, performed all calculations presented in the paper (both analytical and numerical), and wrote a complete paper draft, which was subsequently refined to produce the final paper.

[2] M. A. Mojahed, K. Schmitz and X. Xu *Gravitational charge production* , Phys. Rev. D. (2025) **111** 055005, [2409.10605]: MAM initiated the project by presenting the idea and preliminary notes to KS. All authors contributed significantly to the project, with MAM contributing to numerical and analytical calculations and to writing the final paper.

[3] M. A. Mojahed, K. Schmitz, and D. Wilken, *A lower bound on the right-handed neutrino mass from wash-in leptogenesis*, [2501.07634]: This project formed the basis of DWs masters thesis, and was initiated and supervised by KS. All numerical calculations were carried out by both MAM and DW. Analytical calculations were carried out and checked by all authors. The manuscript was written by KS.

[4] J. Harz, and M. A. Mojahed, *Probing the first-order phase transition in the classically conformal $B - L$ model* (To appear soon): Project building on research conducted by Florian Heger during his master-thesis project at TUM, supervised by JH, Kåre Fridell, and Chandan Hati. MAM extended, refined, and expanded upon this work, performed all calculations (both numerical and analytical), and wrote a complete paper draft.

[5] K. Fridell, J. Harz, C. Hati and M.A. Mojahed *Non-thermal leptogenesis with cosmic strings*, (To appear soon): Project building on research conducted by Florian Heger during his master-thesis project at TUM, supervised by KF, JH, and CH. MAM critically reexamined existing treatments of non-thermal leptogenesis from cosmic strings. All derivations and calculations (both numerical and analytical) were carried out by MAM. Some numerical explorations and cross checks were carried out by KF in the initial stages of the project. MAM wrote a first draft, with one subsection by KF.

In addition, the following works were published during the author's Ph.D., but not discussed further in this thesis:

[6] N. Bernal, J. Harz, M. A. Mojahed and Y. Xu, *Graviton- and Inflaton-mediated Dark Matter Production after Large Field Polynomial Inflation*, Phys. Rev. D. (2025) **111**, 043517, [2406.19447].

[7] M. A. Mojahed and T. Brauner, *Nonrelativistic effective field theories with enhanced symmetries and soft behavior*, JHEP 03 (2022) 086, [2201.01393].

Contents

Prologue

CHAPTER I

Beyond the Standard Model puzzles

Embarking on a career as a high-energy physics (hep) phenomenologist in 2025 is a dual-edged endeavor, marked by both great privilege and considerable challenge. On one hand, it is a privilege to build upon the foundational work of the physics giants of the previous century. On the other hand, it is a struggle to extend beyond their remarkably successful theories.

The early 20th century witnessed a revolutionary transformation in physics with the advent of quantum mechanics and relativity. Building upon this foundation, the latter half of the 20th century established two foundational frameworks that underlie modern high-energy physics phenomenology:

1. The Standard Model (SM) of particle physics [8–10], a relativistic quantum field theory (QFT) that encapsulates our current understanding of the universe's fundamental constituents and their interactions via three of the four known fundamental forces, excluding gravity.
2. The Lambda-Cold Dark Matter (ΛCDM) model [11–18] – the Standard Model of cosmology – explains the universe's large-scale structure and evolution from the Big Bang to the present day. Notably, ΛCDM postulates the existence of two forms of energy not accounted for by the SM: cold dark matter and dark energy.

The SM has been rigorously tested through an extensive experimental program, exemplified by the remarkable agreement between theoretical predictions and experimental measurements of the electron's magnetic moment, currently precise to one part in 10^{14} [19,20]. The last major success of the SM was the discovery of the Higgs boson at ATLAS [21] and CMS [22] in 2012. Determining parameters of the SM to ever higher precision and searching for discrepancies between the SM and experimental data remains an important program in present-day phenomenology. Meanwhile, the ΛCDM model is supported by the observed abundance of light elements, the observed anisotropies in the cosmic microwave background (CMB), the observed large-scale structure of our universe, and the accelerating expansion of the universe [18].

The unprecedented success of the SM and ΛCDM has left sparse clues about where specifically the hep community should go from here in their search for new physics (NP). Two of the most compelling clues we are left with are the experimental evidence for neutrino masses, which are massless in the SM, and the magnitude of the matter-antimatter asymmetry of our observable universe. Leptogenesis [23] is a popular paradigm that addresses these puzzles by extending the SM with at least two right-handed neutrinos (RHNs), which facilitate neutrino mass generation and dynamically produce a baryon asymmetry in the early universe. This thesis is devoted to exploring various aspects of leptogenesis, including theoretical models, new mechanisms, and opportunities to probe leptogenesis at future experiments.

Testing leptogenesis experimentally is a significant challenge. Many leptogenesis realizations involve heavy RHNs far beyond the reach of particle colliders, which we will loosely refer to as high-scale leptogenesis. While building bigger and better colliders has been a pathway to discoveries of NP in previous decades, it is not feasible to use current collider technology to reach energy scales relevant for high-scale leptogenesis. If we want to investigate high-scale leptogenesis or other phenomena involving very high mass scales, we better search for alternative and complementary probes. This has lead many high-energy phenomenologists to consider cosmology and astronomy as laboratories for NP. A particularly promising avenue is gravitational waves (GWs), which have received significant attention since LIGO and Virgo's first direct observation in 2015, originating from the merger of two black holes [24]. The GW background in the present universe will be mapped out across a wide range of frequencies and amplitudes by a combination of proposed and running GW observatories and pulsar timing arrays (PTAs). The resulting power spectrum may encode signals from primordial sources present in the early universe, and thereby present a window to the universe around the time of the Big Bang. In fact, PTAs may already have made the first detection of a GW signal of primordial origin [25–29]. Finally, GW experiments also provide the possibility to probe theories at energies beyond the reach of colliders, test theories of secluded dark sectors, and potentially exclude classes of theories that predict large GW backgrounds.

Several phenomena in the early universe can generate detectable GW backgrounds, and we will focus on sources associated with phase transitions (PTs). A cosmological first-order phase transition (FOPT) is a PT in the early universe leading to the formation of bubbles of the new phase and the release of latent heat. As bubbles collide they source GWs, which may be observable at future GW observatories. A second prediction in many beyond the SM (BSM) extensions that feature new phase transitions is the formation of topological defects. Topological defects are non-trivial field configurations, arising from symmetry-breaking phase transitions as a result of different regions of space adopting distinct vacuum states. Examples are cosmic strings, domain walls, and monopoles. Importantly, topological defects present another potential source of GWs. In the first part of this thesis, we study aspects of certain BSM extensions featuring a FOPT and the formation of cosmic strings. The overarching aim is to explore potential interplay between leptogenesis and GW sources, and opportunities to probe high-scale leptogenesis with gravitational waves.

In the second part of the thesis, we will shift our focus from probing leptogenesis to exploring some recent theoretical developments. Here, we will explore the so-called wash-in leptogenesis (WILG) framework, where RHNs only need to satisfy two of Sakharov's three conditions [30] for dynamically generating the baryon-asymmetry of the universe (BAU). This should be contrasted with standard leptogenesis scenarios, where the RHNs are required to satisfy all three of Sakharov's conditions [30]. Ultimately, relaxing the role of RHNs in satisfying Sakharov's conditions comes at the price of having to introduce a nonminimal cosmological background to provide suitable initial conditions for WILG to act on. In Chapter VI, we explore a new mechanism to generate suitable initial conditions for WILG during inflationary reheating via non-minimal gravitational interactions. In Chapter VII, we proceed to determine how light the lightest RHN can be while still accounting for the BAU via WILG.

Finally, observing lepton-number violation (LNV) would have profound implications for neutrino physics and leptogenesis, potentially indicating a Majorana nature of neutrinos and constraining high-scale leptogenesis. The primary focus of the third part of the thesis is to consider rare meson decays as a laboratory to search for LNV, and provide strategies to disentangle LNV from other types of NP in these systems. A more concise outline of the thesis will be provided at the end of this chapter.

I.1 Open problems

Next, we list some of the longstanding open problems in contemporary hep phenomenology that are left unanswered by the SM, ΛCDM, and cosmic inflation, and point out connections to the research presented in this thesis.

- **Dark energy:** Approximately 68% of the energy density of the universe today is made up of dark energy, required to explain the observed accelerated expansion of the universe. What is the nature of dark energy, and how does it arise? [31]
- **Hubble tension:** The value of the Hubble constant H_0 inferred from early-universe observations using the ΛCDM model yields $H_0 \approx 67.4\,\mathrm{km/s/Mpc}$. The value obtained from late-universe, local measurements, yields $H_0 \approx 73.0\,\mathrm{km/s/Mpc}$. The discrepancy exceeds 5σ, and suggests either unrecognized systematic errors in one or both measurements, or a need for NP beyond ΛCDM that modifies the early or late-time expansion history of the universe [32].
- **Dark matter:** The origin and nature of dark matter (DM) remains one of the most pressing open problems in particle physics and cosmology. Astrophysical and cosmological observations — from galactic rotation curves and gravitational lensing to cosmic microwave background anisotropies and large-scale structure — indicate that approximately 27% of the energy density of the universe is composed of non-luminous, non-baryonic dark matter. The allowed mass range for dark matter famously spans roughly 80 orders of magnitude, and in a worst-case scenario, dark matter may only interact gravitationally with the SM. Understanding the origin and properties of dark matter is a central challenge at the intersection of high-energy particle phenomenology, cosmology, and astrophysics. A detailed and modern account of dark matter, from its evidence to theories and detection, can be found in [33].

  In Chapter IX we will encounter particles that could make up part of the dark matter abundance.
- **The cosmological constant problem:** "The mother of all naturalness problems". The cosmological constant problem [34] can be phrased as the uber-sensitivity of the vacuum energy to the details of ultraviolet (UV) physics of which we are ignorant [35].
- **Inflation:** Cosmic inflation is a paradigm that postulates a quasi-exponential expansion of space prior to the hot Big Bang phase. Its original motivations were to remove unwanted cosmological relics such as monopoles and resolve fine-tuning issues of pre-inflationary hot Big Bang models, such as the horizon and the flatness problems [36–39]. In its simplest realizations, the period of inflation is driven by a scalar field, the inflaton, which is slowly rolling down its potential. The inflationary paradigm provides a natural mechanism for generating primordial density perturbations through quantum fluctuations of the inflaton [40–42]. These fluctuations seed the large-scale structure of the universe and leave imprints in the CMB, consistent with current observations [43]. Despite its successes, inflation remains theoretically incomplete, and some open problems are: What initiates inflation? How generic are the initial conditions that allow a sufficiently long inflationary phase? What is the microphysical origin of the inflaton field and its potential? What are the details of the reheating phase of the universe following the end of inflation?

Chapter VI is the only part of this thesis where we will have to specify an inflationary scenario. In the remaining chapters, we implicitly assume a period of inflation followed by a reheating period ending with a reheating temperature that is sufficiently high to validate our treatment.

- **Unification of gravity and QFT:** So far, no framework that unifies QFT and gravity has produced experimentally confirmed predictions. Achieving a consistent quantum theory of gravity would complete the unification of all known interactions and shed light on puzzles such as the hierarchy and cosmological-constant problems.
- **Grand unification:** The SM gauge group may be embedded into a single symmetry such as $SU(5)$ or $SO(10)$, which would unify the observed forces (excluding gravity) [44–47]. Is this idea realized in nature, and if so, how?

  In Chapter IV, we will consider an extension of the SM that was originally motivated to arise as part of a grand unified theory.
- **The electroweak hierarchy problem:** First, if the SM is all there is, then there is no electroweak (EW) hierarchy problem since the Higgs mass is an input and not calculable. In some sense, the EW hierarchy problem amounts to a concern that an extension of the SM, in which the Higgs boson mass is calculable, should not be highly fine-tuned. To illustrate this point, it is instructive to consider the SM as an effective field theory valid up to a cutoff Λ and computing one-loop corrections from SM fields to the Higgs mass, one obtains a quadratic contribution in Λ of the form,

$$\Delta m_H^2 \;=\; \frac{\Lambda^2}{16\pi^2}\left(-6\,y_t^2+\frac{9}{4}g^2+\frac{3}{4}g'^2+6\lambda\right), \tag{I.1}$$

  see e.g. Ref. [48] and references therein. In the SM alone, the Higgs mass is just a free parameter that needs to be fixed by measurement, and a suitable renormalization procedure absorbs the divergent contribution above. In an extension of the SM with additional physical scales, the divergence in Eq. (I.1) is replaced by finite, calculable contributions. In this context, Eq. (I.1) should be understood as the statement that the Higgs mass is sensitive to UV physics, and the EW hierarchy problem is a naturalness problem.
- **Strong CP problem:** This is a third naturalness problem concerning the smallness of charge-parity (CP) violation in the strong sector of the SM: In principle, the QCD Lagrangian contains a term of the form,

$$\mathcal{L}_{\rm QCD} \supset -\theta\frac{\alpha_s}{8\pi}G^a_{\mu\nu}\tilde{G}^{a\mu\nu}. \tag{I.2}$$

  The physical CP parameter $\bar{\theta}=\theta+\arg\,\det(M_q)$, where M_q is the quark-mass matrix, enters low-energy hadronic observables, which currently constrain $\bar{\theta}\lesssim 10^{-10}$ [49]. The smallness of this parameter is known as the strong CP problem.
- **Vacuum stability of our universe:** Around the time of the Higgs boson was discovered [21,22], there was a surge of interest in the stability of its potential [50–53]. Evidence for metastability was put forward, although the immediate consequence for our existence is limited, as the tunnel rate is many orders of magnitude larger than the age of the universe [53]. Current uncertainties in SM parameters do not permit a conclusive exclusion or confirmation of the stability of the SM vacuum [54].

  In Chapter III, we will encounter arguments that are based on vacuum-stability considerations.

Two other open problems, of great relevance to this thesis, are the origin of **neutrino masses** and the **baryon asymmetry of the universe**, which we elaborate on in the following.

I.1.1 Neutrino masses

A variety of experiments have established flavor oscillations among the SM neutrino species [55–62], which provides direct evidence for mass splitting between the three neutrino species. However, neutrinos are massless in the SM. Unlike all other SM fermions, they cannot acquire Dirac masses, due to the absence of RHNs, N_R, in the SM. A Majorana mass term for SM neutrinos, ν_L,

$$-\frac{1}{2}m_{ij}\overline{\nu}_{L_i}\nu^c_{L_j} + \text{h.c.} \tag{I.3}$$

is forbidden by SM gauge invariance. Here $\nu^c_L = C\nu^*_L$, where C is the charge-conjugation operator. Note, however, that the term in Eq. (I.3) is allowed in the broken phase of the SM, as the neutrino is electrically neutral.

Hence, to incorporate neutrino masses in the SM, we are faced with two options:[1]

1. Extend the SM to allow for a Dirac mass term.
2. Extend the SM to allow for the generation of a Majorana mass term.

Option 1 is achieved by introducing three RHNs[2], which are singlets under the SM gauge group, and extend the SM Lagrangian by

$$\mathcal{L}_{\text{Dirac}} = \overline{N}_{R_i} i\partial\!\!\!/ N_{R_i} - (Y_\nu)_{ij}\overline{L}_i\widetilde{H}N_{R_j} + \text{h.c.}\,, \tag{I.4}$$

where L is a SM lepton doublet, H the SM Higgs doublet, $\widetilde{H} \equiv i\sigma_2 H^*$, and Y_ν is a 3×3 Yukawa matrix. After electroweak symmetry breaking (EWSB), the Yukawa interactions in Eq. (I.4) generate neutrino masses in a manner analogous to those of other leptons and quarks.

Next, we turn to option 2, which will be the scenario considered in this thesis. A key observation is that Majorana masses violate total lepton number, L,[3] by two units while Dirac masses preserve total lepton number.[4] Hence, to realize Majorana masses, we need a (gauge-invariant) SM extension that leads to LNV and generates Eq. (I.3) in the broken phase of the SM. In the language of effective field theory (EFT), this means searching for SM gauge-invariant $\Delta L = 2$ higher-dimensional operators (whose origin can be attributed to NP operating above the electroweak scale). Notably, this bottom-up perspective on Majorana masses permits a unified perspective on tree-level seesaw [63–73] and radiative (Majorana) mass models [74].

Interestingly, the lowest-dimension effective operator one can write down using the SM field content and SM gauge symmetry is directly related to Majorana neutrino mass,

$$\mathcal{O}_5 = \frac{C_{ij}}{\Lambda}\left(\overline{L^c_i}\widetilde{H}^*\right)\left(\widetilde{H}^\dagger L_j\right) + \text{h.c.} \tag{I.5}$$

[1] Strictly speaking, there is a third option: Extending the SM to allow for both a Dirac and a Majorana mass term.

[2] As current neutrino data is consistent with the lightest SM neutrino being massless, one is strictly speaking only required to introduce two RHNs. However, in this thesis we will consider the case of three RHNs.

[3] Not to be confused with a SM-lepton doublet, which we also denote by L. From here on, the meaning of L should be clear from the context it appears in.

[4] Hence, to avoid a Majorana mass term from entering Eq. (I.4), lepton-number conservation is typically assumed in Dirac-mass models.

where C_{ij} denote Wilson coefficients (WCs) and Λ is a (heavy) mass scale. Eq. (I.5) is known as the "Weinberg operator" [75]. Upon EWSB, this operator generates Majorana neutrino masses,

$$m_{ij} = \frac{C_{ij}}{\Lambda} v_h^2 \sim \frac{v_h^2}{\Lambda}, \tag{I.6}$$

where v_h denotes the Higgs vacuum-expectation value (vev). Eq. (I.6) is the celebrated seesaw formula, which achieves a large suppression of neutrino masses with respect to the weak scale, v_h, by invoking heavy NP at a scale $\Lambda \gg v_h$. For higher-dimensional generalizations of the Weinberg operator, and Majorana-neutrino masses from other $\Delta L = 2$ effective operators, see Ref. [74] and references therein.

From a model-building perspective, the next question would be "What kind of renormalizable models can generate the Weinberg operator?" The simplest answer(s) to this question, where the operator is obtained by integrating out a single heavy field at tree level, are the celebrated type-I seesaw [63–67], type-II seesaw [68–72], and type-III seesaw mechanisms [73]. In this thesis, we will consider type-I seesaw where three heavy SM gauge singlet fermions – RHNs – couple to $\overline{L}\widetilde{H}$, with the following Lagrangian

$$\mathcal{L}_{\text{Seesaw}} = \overline{N}_{R_i} i\partial\!\!\!/ N_{R_i} - (Y_\nu)_{ij}\overline{L}_i\widetilde{H}N_{R_j} - \frac{1}{2}M_{ij}\overline{N}_{R_i}N^c_{R_j} + \text{h.c.} \tag{I.7}$$

After EWSB, the second and third terms give the following mass contributions

$$\mathcal{L}_{\text{mass}} = -\overline{\nu_{L_i}}(m_D)_{ij}N_{R_j} - \frac{1}{2}M_{ij}\overline{N^c_{R_i}}N_{R_j} + \text{h.c.} \tag{I.8}$$

Introducing a 3+3-component vector of spinors, $\Psi = \begin{pmatrix} \nu_L \\ N^c_R \end{pmatrix}$, we can write the mass terms in matrix notation,

$$\mathcal{L}_{\text{mass}} = -\frac{1}{2}\overline{\Psi^c}\begin{pmatrix} 0 & m_D \\ m_D^T & M \end{pmatrix}\Psi + \text{h.c.} \tag{I.9}$$

In the limit $M \gg m_D$, the diagonalization of this matrix gives three light neutrino mass eigenstates (mostly ν_L) with Majorana mass matrix,

$$m_\nu^{\text{light}} \approx m_D M^{-1} m_D^T, \tag{I.10}$$

and three heavy (mostly N_R) mass eigenstates with Majorana mass matrix

$$m_\nu^{\text{heavy}} \approx M. \tag{I.11}$$

Details about the seesaw mechanisms can be found in [76], and details about neutrino masses and more can be found in [18].

I.1.2 Baryon asymmetry of the universe

Next, we turn to the matter-antimatter puzzle. The observable universe seems to contain almost exclusively matter and nearly no antimatter. Indeed, from direct experience, it is clear that our solar system does not contain a significant amount of antimatter. Moreover, if the observable universe was a patchwork made out of regions strongly dominated by either matter or antimatter, then annihilation processes along the boundaries separating the matter-dominated regions from the antimatter dominated regions would result in characteristic gamma ray signals. The absence of such signals has made it possible to constrain the local abundance of antimatter up to very large length scales [77]. The possibility of macroscopic objects, such as antistars, or stellar systems made out of antimatter have also not been observed [78, 79]. Finally, it has been shown that if matter and antimatter are present in equal amounts on cosmological scales, then the matter region we belong to has to cover virtually the entire visible universe [80]. More elaborate arguments about the observational evidence for a matter-antimatter asymmetry in the universe can be found in Ref. [81].

The preceding arguments suggest the following relation in the observable universe,

$$\eta_B \equiv \frac{n_B}{n_\gamma}\bigg|_{T_0} = \frac{n_B - n_{\bar{B}}}{n_\gamma}\bigg|_{T_0}, \tag{I.12}$$

where n_γ, n_B, $n_{\bar{B}}$, and T_0 denote the present day number densities of photons, baryons, antibaryons, and the temperature of the cosmic-microwave background (CMB). The parameter η_B can be determined in two independent ways. The first method is via big-bang nucleosynthesis (BBN), the theory that predicts the abundances of the light element isotopes D, ^{3}He, ^{4}He, and ^{7}Li. In the context of the SM + ΛCDM, η_B is the only unknown parameter that enters the prediction of primordial abundances of light nuclei. The BBN predictions can be compared with observational determinations of the abundances of the light elements, in particular the abundance of Deuterium [82]. Consistency between theoretical BBN predictions and observations leads to [18, 83],

$$\eta_B^{\mathrm{BBN}} = (6.05 \pm 0.25) \cdot 10^{-10}. \tag{I.13}$$

The second method to determine η_B is by measuring the power spectrum of (the tiny) temperature fluctuations in the CMB [84]. Temperature fluctuations in the CMB arose from acoustic oscillations of the baryon-photon fluid in the early universe, driven by the gravitational potential wells formed by inhomogeneities in the dark matter distribution. The acoustic oscillations are sensitive to η_B as it affects the primordial plasmas equation of state. The impact of η_B is primarily reflected in the relative amplitude of odd and even peaks in the power spectrum. Since the CMB is a relic from the time of recombination, when the temperature of the universe was six orders of magnitude lower than at the time of BBN, and the physics that produces the acoustic peaks in the power spectrum is very different from BBN, this is a truly independent determination of η_B. The current value inferred from the CMB reads [85]

$$\eta_B^{\mathrm{CMB}} = (6.12 \pm 0.04) \cdot 10^{-10}. \tag{I.14}$$

An important prediction of ΛCDM is that the baryon-to-photon ratio remains unchanged between the time of BBN and recombination. The impressive agreement between Eq. (I.13) and Eq. (I.14) is therefore a great triumph for ΛCDM and a strong indication that one can rely on observational determinations of the BAU.

Having established the value of η_B in our universe, it is natural to ask if it is low or high. On the one hand, baryonic matter only constitutes roughly 5% of the energy density of the universe, while dark matter and dark energy constitute roughly 95%. On the other hand, it is instructive to note that in a locally-baryon symmetric universe, baryons and anti-baryons would remain in thermal equilibrium down to $T \sim 20$ MeV where the number of baryons and antibaryons would freeze out (FO) to $n_B/n_\gamma = n_{\bar{B}}/n_\gamma \sim 10^{-19}$, a result known as the "annihilation catastrophe" [86]. Compared to this number, the observed value for η_B is impressively large, and suggests that the universe should have been baryon-antibaryon asymmetric at $T = \mathcal{O}(100)$ MeV. This leads us to the question of how such an asymmetry could come to be.

One may assume that the asymmetry between matter and antimatter was present from the very beginning, and make it an initial condition for the Big Bang. However, this viewpoint is challenged by the cosmic inflation paradigm. Any pre-existing matter-antimatter asymmetry prior to cosmic inflation would have been diluted and negligible at the time of inflationary reheating. Hence, if one accepts the cosmic-inflation hypothesis, it is not possible to account for the observed BAU by stating that it was simply an initial condition at the beginning of everything. Instead, the baryon-asymmetry must be generated dynamically by *baryogenesis* in the post-inflationary universe. In this context, the puzzle "why is there more matter than antimatter in the universe?" can be sharpened to "what is the baryogenesis mechanism that generated the BAU?"

Sakharov's conditions

Successful baryogenesis requires three conditions, as first formulated by Sakharov in 1967 [30]:

1. Baryon number (B) violation: A state with $B = 0$ cannot evolve into a state with $B \neq 0$ in the absence of baryon-number violation.
2. C and CP violation: If C or CP invariance holds, then for every process that generates a matter-antimatter asymmetry there is an equally probable C or CP conjugate process that generates an asymmetry with the opposite sign.
3. Departure from thermal equilibrium: A state in thermal equilibrium enjoys time-translation invariance, implying that the expectation values of all observables, including B, are constant.

These three conditions can be proved using statistical and quantum mechanics as follows [81]. Let the universe be described by a density matrix ρ. The von Neumann equation governs the time evolution of ρ in the Schrödinger picture

$$i\frac{d\rho(t)}{dt} = [H, \rho(t)], \tag{I.15}$$

where H denotes the Hamiltonian. Let $\hat{B}$ denote the baryon number operator, such that the baryon number is given by $B(t) = \mathrm{Tr}\left[\hat{B}\rho(t)\right]$. If B and H commute, such that baryon number is a symmetry of the system, then the von Neumann equation gives

$$\frac{dB(t)}{dt} = -i\,\mathrm{Tr}[B[H, \rho(t)]] = 0, \tag{I.16}$$

which proves the first condition. To prove the second condition, consider an arbitrary discrete operator X that commutes with the Hamiltonian and anticommutes with B.[5] Using the von Neumann equation, we compute,

$$\frac{d}{dt}[X, \rho(t)] = [X, \frac{d\rho}{dt}] = -i[X, [H, \rho]] = -i[H, [X, \rho(t)]]. \tag{I.17}$$

As a consequence, if $\rho(t_0)$ is symmetric under X at initial time t_0, $[X, \rho(t_0)] = 0$, then Eq. (I.17) ensures that ρ is symmetric under X at all times. To prove the third condition, assume a system in thermal equilibrium described by

$$\rho = \frac{1}{Z}e^{-H/T}, \qquad Z = \mathrm{Tr}\left\{e^{-H/T}\right\}, \tag{I.18}$$

[5]Under these conditions, X could be C, CP, or a generalized notion of these operators.

and that the Hamiltonian is symmetric under CPT-transformations. These assumptions lead to

$$\mathrm{Tr}\{B\rho\} = \mathrm{Tr}\big\{B(CPT)^{-1}(CPT)\rho\big\} = \mathrm{Tr}\big\{(CPT)B(CPT)^{-1}\rho\big\} = -\,\mathrm{Tr}\{B\rho\}, \qquad \text{(I.19)}$$

where we in the last step used $(CPT)B(CPT)^{-1} = -B$. This proves Sakharov's third condition.

Right-handed neutrino decays and the BAU

In the past decades, there have been many great proposals for baryogenesis mechanisms. They will not be done any justice in this thesis, and the interested reader is referred to e.g. Refs. [87, 88] and references therein for further reading. The focus of this thesis is leptogenesis [23], which is a leading baryogenesis paradigm that extends the SM by adding two or more RHNs. As RHNs can explain the smallness of the observed neutrino mass scale via the type-I seesaw mechanism, leptogenesis provides an economic framework that addresses two of the major open BSM puzzles at the same time.

Leptogenesis, like any baryogenesis mechanism, must satisfy Sakharov's three conditions. Standard leptogenesis realizations achieve this as follows: The Yukawa coupling Y_ν in Eq. (I.7) provides a source of CP violation (Sakharov's second condition). The rate of the CP-violating Yukawa interactions can be slow enough to ensure departure from thermal equilibrium (Sakharov's third condition). The Majorana masses of the RHNs break lepton number, and the ($B+L$-violating) SM (weak) sphaleron processes [89] partially convert the lepton asymmetry into a baryon asymmetry above or at the electroweak scale (Sakharov's first condition). Further details about specific leptogenesis mechanisms of direct relevance to this thesis will be given in Chapters II and V.

I.2 Structure and outline of thesis

This thesis is divided into three parts. Each part begins with a chapter that provides a theoretical foundation for the work presented in the subsequent chapters of the respective part. In Chapter II, we introduce the four-dimensional effective potential at one loop, and review aspects of GW production from FOPTs that will be of direct relevance to our study in Chapter III. Selected elements of cosmic strings and thermal leptogenesis (TLG) are also provided. In Chapter III, we consider various aspects of the FOPT in the classically-conformal $B-L$ model [90]. We also explore opportunities to probe parameter space consistent with leptogenesis using gravitational waves. The results will appear in a publication Ref. [4]. In Chapter IV, we consider cosmic strings from $B-L$ breaking as a non-thermal source for leptogenesis and compare asymmetry production sourced by cosmic strings with thermal asymmetry production. In Chapter V, we initiate the second part of the thesis by reviewing aspects of WILG and gravitational baryogenesis. This provides a suitable starting point for our discussion of a new gravitational charge-production mechanism in Chapter VI, which led to the publication [2]. In Chapter V, we investigate how light the lightest RHN can be while remaining compatible with successful WILG, which led to the publication [3]. Chapter VIII provides an introduction to the last part of the thesis by covering selected aspects of semi-leptonic decays, lepton-number violation, and reviewing how observing LNV in rare meson decays can put leptogenesis under tension. In Chapter IX, we present strategies to disentangle NP in rare semileptonic Kaon and B decays, with special emphasis on LNV NP, using effective field theory. This led to the publication [1]. Final conclusions are given in Chapter X.

Part I

Breaking gauged $U(1)_{B-L}$ in the early universe

CHAPTER II

Theoretical background

A phase transition generally refers to a qualitative change in the macroscopic state or phase of a system as a control parameter such as temperature, pressure, or an external field is varied. It describes how a system reorganizes itself from one phase into a new phase with distinct physical properties. Some examples, of varying degrees of sophistication, include water freezing or boiling, (de)magnetization of a ferromagnet, emergence of superfluidity/ superconductivity, transition from quark-gluon plasma to hadronic matter, and exotic condensed-matter systems exhibiting a change in topological invariant(s). We will be concerned with thermodynamic phase transitions, which can be defined as a line in the (T, μ)-plane (where T is temperature and μ is chemical potential) across which the grand canonical free energy density $f(T, \mu)$ is non-analytic [91]. In particular, if the n-th order derivative of f with respect to some thermodynamic variable is discontinuous, there is a n'th order phase transition. If no non-analyticity occurs, but there is still a rapid change in physical behavior, then one has a crossover transition.

In this thesis, we will only be interested in phase transitions associated with the spontaneous breaking of a (continuous) symmetry. For such phase transitions, one can by construction always assign a so-called order parameter. The latter is defined as a quantity that transforms non-trivially under the broken symmetry, has a non-vanishing expectation value in the broken phase and a vanishing expectation value in the symmetric phase.

The theory of phase transitions associated with spontaneously broken symmetries plays an important role in the evolution of the early universe. In the context of pure SM physics, and assuming that the maximal temperature of the early universe exceeded 160 GeV [92], it is believed that the universe initially evolved in a state with electroweak symmetry. As the temperature dropped to roughly 160 GeV, the universe underwent electroweak symmetry breaking characterized by the order parameter $\langle HH^\dagger \rangle$. As the temperature of the hot universe dropped further to roughly 150 MeV [93, 94], the (approximate) chiral symmetry was broken, signaled by a non-vanishing expectation value of the quark condensate $\langle \bar{q}q \rangle$. The current consensus of the hep community is that both of these transitions were of order infinity (crossovers) within the SM [94–97]. However, in some extensions of the SM, either one or both of these transitions can become first order (e.g. [98–103] and references therein). From a theoretical point of view, it has long been appreciated that a first-order electroweak phase transition could have interesting implications for baryogenesis [89, 104, 105]. From an observational point of view, it has long been appreciated that cosmological FOPTs can give rise to out-of-equilibrium dynamics that can source gravitational waves [106], which can be searched for at current and planned GW experiments. Our focus will be on phase transitions associated with the breaking of a symmetry in BSM theories. Namely, in Chapter III, we will consider FOPTs associated with a broken gauged (continuous) $B-L$ symmetry in the context of a specific BSM model realization.

Another interesting consequence of symmetry–breaking phase transitions is the formation of topological defects, as explained in the following. For a generic symmetry-breaking pattern

$$G \longrightarrow H, \tag{II.1}$$

where G denotes the initial full symmetry and H denotes the unbroken symmetry, the set of degenerate vacua is described by the manifold

$$\mathcal{M} = G/H. \tag{II.2}$$

The system undergoes spontaneous symmetry breaking when the order-parameter field ϕ acquires a non-zero vacuum expectation value by selecting a specific point on the vacuum manifold $\mathcal{M}$. If $\mathcal{M}$ possesses non-trivial topology, i.e. if at least one homotopy group satisfies

$$\pi_i(\mathcal{M}) \neq 0 \quad \text{for some } i, \tag{II.3}$$

then certain field configurations cannot be continuously deformed to the trivial vacuum and are therefore stable. These field configurations are known as topological defects. The correspondence is

$$\begin{aligned}
\pi_0(\mathcal{M}) \neq 0 &\quad \Rightarrow \text{domain walls},\\
\pi_1(\mathcal{M}) \neq 0 &\quad \Rightarrow \text{cosmic strings},\\
\pi_2(\mathcal{M}) \neq 0 &\quad \Rightarrow \text{monopoles},\\
\pi_3(\mathcal{M}) \neq 0 &\quad \Rightarrow \text{textures},
\end{aligned}$$

see for example Ref. [107] for details. The Kibble mechanism [108] explains how topological defects form during a cosmological phase transition. Causally disconnected regions of the universe choose independent vacuum values (i.e. different values for the order parameter), and when these regions come into contact, defects form at their boundaries. In the SM, the relevant homotopy groups are trivial, so no stable defects survive. However, many extensions of the SM, including those considered in the next two chapters, predict $\pi_1(\mathcal{M}) \neq 0$, leading to stable cosmic strings. Cosmic strings can lead to observational effects, including gravitational waves that could potentially be probed at future experiments if the mass scale associated with the symmetry breaking is high enough.

The rest of this chapter is organized as follows. In Section II.1, we introduce the quantum effective potential and how to calculate it to one loop, including thermal corrections. The section is mostly included for pedagogical reasons and can safely be skimmed through by an experienced reader. In Section II.2, we introduce several FOPT parameters, how to compute them from the effective potential, and how they can be used to determine the stochastic gravitational-wave background (SGWB) from the FOPT. This section will be of direct relevance for large parts of Chapter III. Section II.3 summarizes aspects of cosmic strings that will be used in the following two chapters. In Section II.4, we collect some useful results from TLG that will be applied in Chapter IV.

II.1 Effective potential

In theories exhibiting spontaneous symmetry breaking, it is imperative to determine the vev, $\langle\phi\rangle$, of a quantum field ϕ,[1] to track how the system evolves from one phase to

[1]Though ϕ could in general be a product of elementary fields, we will for simplicity assume that it is an elementary field.

another. At the classical level, $\langle\phi\rangle$ is obtained by minimizing the energy associated with its potential, $V(\phi)$, providing a simple geometric picture of $\langle\phi\rangle$ as the minimum of V. The corresponding object in the full quantum theory, whose minimum give the exact value of $\langle\phi\rangle$, is the effective potential.

To quantitatively discuss the effective potential formalism, it is sufficient to consider the QFT of a scalar field ϕ with classical action $S(\phi)$ in the presence of an external source J. The generating functional reads,

$$Z[J] = \int \mathcal{D}\phi e^{i[S(\phi)+\int d^4x J(x)\phi(x)]} \equiv e^{iW[J]}, \tag{II.4}$$

where $W[J]$ is the generator of connected Greens functions. The classical field, $\phi_c \equiv \langle\phi\rangle$, is defined as

$$\phi_c \equiv \frac{\delta W[J]}{\delta J(x)}, \tag{II.5}$$

and the generating functional of 1PI Green's functions, i.e. the effective action, is given by the functional Legendre transform

$$\Gamma[\phi_c] = W[J] - \int d^4x J(x)\phi_c(x). \tag{II.6}$$

It follows from Eq. (II.6) that

$$\frac{\delta\Gamma[\phi_c]}{\delta\phi_c(x)} = -J(x) \implies \left.\frac{\delta\Gamma[\phi_c]}{\delta\phi_c(x)}\right|_{J=0} = 0. \tag{II.7}$$

The stationary condition in Eq. (II.7) is analogous to the stationary condition of the classical action, $\frac{\delta S}{\delta\phi} = 0$, which yields classical field equations. Hence, Eq. (II.7) can be considered as the equation of motion (EoM) of the field ϕ_c, which takes quantum effects into account [109].[2] From the effective action, one can define the effective potential, $V_{\text{eff}}(\phi_c)$, as,

$$\Gamma[\phi_c] = -\int d^4x V_{\text{eff}}(\phi_c). \tag{II.8}$$

Assuming that translational invariance is unbroken, then ϕ_c is constant and combining Eqs.(II.7) and (II.8) immediately gives

$$\left.\frac{\partial V_{\text{eff}}}{\partial\phi_c}\right|_{J=0} = 0. \tag{II.9}$$

The effective potential has an important interpretation in terms of energy density [110, 111]: $V_{\text{eff}}(\phi_c)$ is the minimum of the expectation value of the energy density for all states constrained by the condition that the scalar field ϕ has expectation value ϕ_c. Consequently, in the absence of external currents, the vacuum state of the theory will evolve to a state in which the effective potential is minimized (and not only stationary, as was required by Eq. (II.9)) [109].

[2] In fact, the interpretation of $\Gamma[\phi_c]$ as an effective action is further justified by the fact that $W[J]$ can be calculated as a sum of connected tree graphs, with vertices and propagators calculated as if the action was $\Gamma[\phi_c]$ instead of $S[\phi]$, see e.g. Ref [109] for a textbook discussion.

II.1.1 Calculating the effective potential

The remainder of this section will focus on the foundation for calculating the effective potential. For completeness, we first consider the foundation of the original calculation by Coleman and Weinberg [112], before we proceed with a functional calculation to motivate a master formula for V_{eff} to one-loop in a general QFT with fields of spin $s \leq 1$.

Foundation of the original Coleman-Weinberg method

The effective action can be functionally expanded as,

$$\Gamma[\phi_c] = \sum_{n=0}^{\infty} \frac{1}{n!} \int d^4x_1 ... d^4x_n \phi_c(x_1)...\phi_c(x_n)\Gamma^{(n)}(x_1, ..., x_n), \tag{II.10}$$

where $\Gamma^{(n)}$ are the one-particle irreducible (1PI) Green functions.[3] The Fourier transformed quantities read,

$$\Gamma^{(n)}(x_1, ..., x_n) = \int \prod_{i=1}^{n} \left[\frac{d^4p_i}{(2\pi)^4} e^{ip_i x_i} \right] (2\pi)^4 \delta^4(p_1 + ... + p_n)\Gamma^{(n)}(p), \tag{II.11}$$

$$\widetilde{\phi}(p) = \int d^4x e^{-ipx} \phi_c(x), \tag{II.12}$$

which upon insertion into Eq. (II.10) yields,

$$\Gamma[\phi_c] = \sum_{n=0}^{\infty} \frac{1}{n!} \int \prod_{i=1}^{n} \left[\frac{d^4p_i}{(2\pi)^4} \widetilde{\phi}(-p_i) \right] (2\pi)^4 \delta^4(p_1 + ... + p_n)\Gamma^{(n)}(p_1, ..., p_n). \tag{II.13}$$

Assuming translational invariance, Eq. (II.12) reduces to $\widetilde{\phi}(p) = (2\pi)^4 \phi_c \delta^4(p)$. Plugging this result into Eq. (II.13), using $\int d^4x = (2\pi)^4\delta^4(0)$, and recalling the definition in Eq. (II.8), we arrive at

$$V_{\text{eff}}[\phi_c] = -\sum_{n=0}^{\infty} \frac{1}{n!} \phi_c^n \Gamma^{(n)}(p_i = 0). \tag{II.14}$$

Hence, we have demonstrated that V_{eff} is given by the sum of all 1PI Greens functions with zero external momenta. Eq. (II.14) states that to calculate the effective potential to a given loop order, one has to appropriately sum all 1PI graphs with n external ϕ legs carrying zero external momenta to that given loop order. This was the method originally used by Coleman and Weinberg in their seminal paper [112]. For pedagogical examples of how to calculate V_{eff} using this method, see e.g. [114]. A drawback of this method is that it requires combinatorial considerations (from summing and evaluating loop diagrams) that become highly cumbersome beyond one loop.

Functional-integral method

In this thesis, we will consider the effective potential to one loop. One can then quite straightforwardly compute the effective potential using functional methods, as initially developed by Jackiw [115], as an alternative to carrying out the infinite sum in Eq. (II.14). Since most theses and pedagogical reviews encountered by the author that compute the

[3] For a pedagogical proof of this, see e.g. [113].

effective potential to one loop use the method by Coleman and Weinberg [112], we decided to present the functional-integral approach. We will first consider the scalar field theory in Eq. (II.4), following the textbook discussion in Ref. [113], before we sketch how the calculation generalizes to QFTs of the type that we will eventually be interested in.

The Lagrangian of the scalar field can be split into a renormalized part $\mathcal{L}_R$ and a part containing the counterterms,

$$\mathcal{L} = \mathcal{L}_R + \delta\mathcal{L}. \tag{II.15}$$

We can split the source as $J(x) = J_R(x) + \delta J$, with $J_R(x)$ defined by

$$\left.\frac{\delta\mathcal{L}_R}{\delta\phi}\right|_{\phi=\phi_c} + J_R(x) = 0. \tag{II.16}$$

With these definitions in place, Eq. (II.4) can be written as,

$$e^{iW[J]} = \int \mathcal{D}\phi\, e^{i\int d^4x(\mathcal{L}_R[\phi]+J_R\phi)} e^{i\int d^4x(\delta\mathcal{L}[\phi]+\delta J\phi)}. \tag{II.17}$$

Writing ϕ as the classical field plus a quantum fluctuation, $\phi = \phi_c + \widetilde{\phi}$, one can write the first exponent in the equation above as

$$\begin{aligned}\int d^4x\,(\mathcal{L}_R + J_R\phi) = \int d^4x\,(\mathcal{L}_R[\phi_c] + J_R\phi_c) + \int d^4x\widetilde{\phi}(x)\left(\left.\frac{\delta\mathcal{L}_R}{\delta\phi}\right|_{\phi=\phi_c} + J_R(x)\right)\\ + \frac{1}{2}\int d^4x d^4y \widetilde{\phi}(x)\widetilde{\phi}(y)\left.\frac{\delta^2\mathcal{L}_R}{\delta\phi(x)\delta\phi(y)}\right|_{\phi=\phi_c} + \ldots\end{aligned} \tag{II.18}$$

where higher-order terms have been neglected as they give rise to higher-order corrections [113]. The integrand in the second exponent in Eq. (II.17) can be written as

$$(\delta\mathcal{L}[\phi_c] + \delta J\phi_c) + \left(\delta\mathcal{L}[\phi_c + \widetilde{\phi}] - \delta\mathcal{L}[\phi_c] + \delta J\widetilde{\phi}\right). \tag{II.19}$$

Here, it is consistent to neglect the second term on the right-hand side, as it gives contributions that can be included in the terms neglected in Eq. (II.18). Combining Eqs. (II.17), (II.18), and (II.19), we then obtain

$$\begin{aligned}e^{iW[J]} &= e^{i\int d^4x(\mathcal{L}_R[\phi_c]+\delta\mathcal{L}[\phi_c]+J\phi_c)}\int \mathcal{D}\widetilde{\phi} e^{\frac{i}{2}\int d^4x d^4y\widetilde{\phi}(x)\frac{\delta^2\mathcal{L}_R}{\delta\phi(x)\delta\phi(y)}\widetilde{\phi}(y)} + \ldots\\ &= e^{i\int d^4x(\mathcal{L}_R[\phi_c]+\delta\mathcal{L}[\phi_c]+J\phi_c)}\left[\det\left(-\frac{\delta^2\mathcal{L}_R}{\delta\phi\delta\phi}\right)\right]^{-1/2} + \ldots,\end{aligned} \tag{II.20}$$

where we in the second step performed a standard bosonic Gaussian integral and ignored an overall (unphysical) normalization constant. From this result and the definition in Eq. (II.6) it immediately follows that

$$\Gamma[\phi_c] = \int d^4x\,(\mathcal{L}_R[\phi_c] + \delta\mathcal{L}[\phi_c]) + \frac{i}{2}\log\det\left(-\frac{\delta^2\mathcal{L}_R}{\delta\phi\delta\phi}\right). \tag{II.21}$$

Upon using the following identity for a generic operator M,

$$\log\det M(x-y) = \int d^4x \int \frac{d^4p}{(2\pi)^4}\,\mathrm{tr}\log M(p), \tag{II.22}$$

and the definition of the effective potential in Eq. (II.8), one arrives at

$$V_{\text{eff}}[\phi_c] = -\mathcal{L}_R[\phi_c] - \delta\mathcal{L}[\phi_c] - \frac{i}{2}\int \frac{d^4p}{(2\pi)^4}\,\mathrm{Tr}\log\left(-\frac{\delta^2\mathcal{L}_R(p)}{\delta\phi\delta\phi}\right). \tag{II.23}$$

In a theory of a relativistic scalar field, the quadratic contribution is of the generic form

$$\left(-\frac{\delta^2\mathcal{L}_R}{\delta\phi\delta\phi}\right) = \delta^4(x-y)(\partial^2 + m^2(\phi_c)) \tag{II.24}$$

which gives a one-loop effective potential of the following form

$$V_{\text{eff}}[\phi_c] = -V_R[\phi_c] - \delta V[\phi_c] - \frac{i}{2}\int \frac{d^4p}{(2\pi)^4}\,\mathrm{Tr}\log\left(-p^2 + m^2(\phi_c)\right). \tag{II.25}$$

Here, V_R denotes the tree-level potential in renormalized perturbation theory, and δV denotes the counterterms arising from the tree-level potential.

It is not difficult to generalize the discussion above to a theory encompassing gauge fields and fermions coupling to the scalar field ϕ. Since only Abelian gauge fields will be of direct relevance to our work, we will stick to the Abelian case, thereby avoiding complications related to ghosts. Specifically, let us consider a theory of a complex scalar field $\phi \equiv \frac{1}{\sqrt{2}}(\phi_1 + i\phi_2)$, where ϕ_i are real, which is charged under a gauged $U(1)$ symmetry. We also include n_f fermions, $\{\psi_f\}$, an Abelian gauge field, A_μ, and n_s additional scalars $\{s_s\}$ that are uncharged under the gauged $U(1)$. The generating functional for such a theory takes the form

$$\begin{aligned} Z[J] = e^{iW[J]} &= \int \mathcal{D}\phi \prod_{f=1}^{n} \mathcal{D}\bar{\psi}_f\mathcal{D}\psi_f \prod_{s=1}^{n} \mathcal{D}s_s\mathcal{D}A e^{i\int d^4x(\mathcal{L}_R + J_R\phi)} e^{i\int d^4x(\delta\mathcal{L}+\delta J\phi)} \\ &= \int \mathcal{D}\phi \prod_{f=1}^{n} \mathcal{D}\bar{\psi}_f\mathcal{D}\psi_f \prod_{s=1}^{n} \mathcal{D}s_s\mathcal{D}A e^{iS[\phi,s,\psi,A,J]} \end{aligned} \tag{II.26}$$

and the most general renormalizable Lagrangian in R_ξ gauge (see e.g. [113]) takes the schematic form

$$\begin{aligned} \mathcal{L}_R = &-\frac{1}{4}F_{\mu\nu}^2 - \frac{1}{2\xi}(\partial^\mu A_\mu)^2 + |D_\mu\phi|^2 + \sum_{s=1}^{n}\frac{1}{2}\partial_\mu s_s\partial^\mu s_s - V(\phi,s) \\ &+ \sum_{f=1}^{n_f}\bar{\psi}_f(i\not{D} - m_f(\phi))\psi. \end{aligned} \tag{II.27}$$

To evaluate the effective potential to one loop, we first need to perform a background-field expansion similar to Eq. (II.18), neglecting terms of cubic and higher order in quantum fluctuations of ϕ, as in Eq. (II.20). The result takes the following form,

$$\begin{aligned} S[\phi,s,\psi,A,J] = &\int d^4x\, d^4y \left[-\frac{1}{2}A_\mu(x)i\Delta^{-1}_{\mu\nu}(\phi_c;x-y)A_\nu(y) - \frac{1}{2}\tilde{\phi}_a(x)iD^{-1}_{ab}(\phi_c;x-y)\tilde{\phi}_b(y)\right] \\ &+ \int d^4x\, d^4y \left[-\frac{1}{2}s_a(x)iS^{-1}_{ab}(\phi_c;x-y)s_b(y) - \bar{\psi}_a(x)iM^{-1}_{ab}(\phi_c;x-y)\psi_b(y)\right] \\ &+ \int d^4x e A_\mu(x)\epsilon_{ab}\phi_c^a\partial_\mu\phi^b(x) - \int d^4x\left[V(\phi_c,s=0) + \delta V(\phi_c,s=0) - J\phi_c\right], \end{aligned} \tag{II.28}$$

where the exact form of the operators Δ^{-1}, D^{-1}, S^{-1}, M^{-1}, can be determined from Eq. (II.27). We are now in a position to highlight two points: First, in the Landau gauge, $\partial_\mu A^\mu = 0$ with $\xi = 0$, the kinetic-mixing terms between A and ϕ_i in the third line of Eq. (II.28) vanish upon integration by parts. This simplifies the 1-loop calculation significantly, and is one reason for why calculations of V_{eff} are often carried out with this choice of gauge, as will be done by us from this point. The second point is that by comparing Eq. (II.26) and (II.28), we see that we are only left with a handful of Gaussian integrals. Hence, by repeating the steps leading to Eq. (II.23), we obtain

$$\begin{aligned} V_{\text{eff}}[\phi_c] = V_R[\phi_c, s=0] + \delta V[\phi_c, s=0] - \frac{i}{2}\int \frac{d^4p}{(2\pi)^4}\operatorname{Tr}\log\left(-i\Delta^{-1}(\phi_c;p)\right) \\ - \frac{i}{2}\int \frac{d^4p}{(2\pi)^4}\operatorname{Tr}\log\left(-iD^{-1}(\phi_c;p)\right) - \frac{i}{2}\int \frac{d^4p}{(2\pi)^4}\operatorname{Tr}\log\left(-iS^{-1}(\phi_c;p)\right) \\ + i\int \frac{d^4p}{(2\pi)^4}\operatorname{Tr}\log\left(-iM^{-1}(\phi_c;p)\right), \end{aligned} \tag{II.29}$$

where the relative difference of (-2) in the fermionic coefficient stems from the difference in bosonic and fermionic Gaussian integrals. This result can be written as,

$$V_{\text{eff}}[\phi_c] = V_0[\phi_c] + V_1[\phi_c], \tag{II.30}$$

$$V_0[\phi_c] = V_R[\phi_c, s=0], \tag{II.31}$$

$$\begin{aligned} V_1[\phi_c] = \delta V[\phi_c, s=0] - \frac{i(d-1)}{2}\int \frac{d^dp}{(2\pi)^d}\operatorname{Tr}\log\left(-p^2 + m_A^2(\phi_c)\right) \\ - \frac{i}{2}\sum_{a=1}^{2}\int \frac{d^dp}{(2\pi)^d}\operatorname{Tr}\log\left(-p^2 + m_{\phi_a}^2(\phi_c)\right) - \frac{i}{2}\sum_{j=1}^{n_s}\int \frac{d^dp}{(2\pi)^d}\operatorname{Tr}\log\left(-p^2 + m_{s_j}^2(\phi_c)\right) \\ + i\sum_{j=1}^{n_f} N_j \int \frac{d^dp}{(2\pi)^d}\operatorname{Tr}\log\left(-p^2 + m_{f_j}^2(\phi_c)\right), \end{aligned} \tag{II.32}$$

where $m(\phi_c)$ denotes background-field dependent masses, N_j denotes the number of degrees of freedom (DoF) of the j'th fermion ($N_j = 4\,(2)$ for Dirac (Majorana)), and $d-1 = 3$. From this form of the one-loop potential, one can straightforwardly derive the well-known formulas for V_1 collected below.

II.1.2 Zero-temperature contribution

Carrying out the integrals in Eq. (II.32) in dimensional regularization, and imposing the $\overline{\text{MS}}$ renormalization scheme to fix δV [116], one obtains the standard result [112]

$$V_{\text{eff}}^{\overline{\text{MS}},\,\text{Landau}}[\phi_c, T=0] = V_0[\phi_c] + V_1[\phi_c], \tag{II.33}$$

$$V_0[\phi_c] = V_R[\phi_c, s=0], \tag{II.34}$$

$$V_1[\phi_c] = \frac{1}{64\pi^2}\sum_i (-1)^{2s_i}(1+2s_i)m_i^4(\phi)\left[\log\frac{m_i^2(\phi_c)}{\mu^2} - C_i\right], \tag{II.35}$$

where the sum runs over all real scalar, Weyl fermion, and vector boson DoFs. s_i denotes the spin of the i'th field, and $C_i = 3/2$ for scalars and fermions and $5/6$ for gauge bosons. In Landau gauge, all three degrees of freedom of each massive vector boson and the one DoF of each Goldstone scalar must be counted [117].

Renormalization-group improved effective potential

Next, we discuss the renormalization-group (RG) improved effective potential. Let α_c denote (an appropriate normalization of) the most dominant coupling entering Eq. (II.35). For the perturbative result in Eq. (II.35) to be reliable, the combination $\alpha_c \log\left(\frac{\phi_c^2}{\mu^2}\right)$, must be small.[4] Since the renormalization scale μ is arbitrary, one can always choose it such that $\alpha_c \log\left(\frac{\phi_c^2}{\mu^2}\right)$ is small for a given ϕ_c. However, if one is interested in the effective potential across a range in field space from ϕ_1 to ϕ_2, then $\alpha_c \log\left(\frac{\phi_1}{\phi_2}\right)$ has to be small for reliable results. In our applications, we will consider large regions in field space, where this condition is doomed to fail. One then has to consider the so-called RG improved effective potential, which is reliable for any field values as long as α_c remains small. The defining equation of the RGE improved effective potential follows from the statement that V_{eff} cannot depend on the arbitrary choice of μ,

$$\frac{dV_{\text{eff}}}{d\mu} = 0 \implies \left(\mu\frac{\partial}{\partial\mu} + \beta(g_i)\frac{\partial}{\partial g_i} - \gamma\phi\frac{\partial}{\partial\phi_c}\right)V_{\text{eff}} = 0, \tag{II.36}$$

where $\beta(g_i)$ denotes the beta function associated with the coupling g_i, and γ denotes the anomalous dimension of ϕ. In the next chapter, we will verify that upon performing the following promotions in the potential Eq. (II.33), the RGE in Eq. (II.36) will be satisfied to one loop: $\phi_c^2 \to Z_\phi \phi_c^2$ (where Z_ϕ denotes the one-loop wave-function renormalization), introducing $t = \log\left(\frac{\mu(\phi_c)}{M}\right)$ where $\mu(\phi_c) = \phi_c$ and M is a fixed mass scale, and promoting couplings λ to running couplings $\lambda(t)$.

II.1.3 Finite-temperature contributions

Thermal effects play an important role in cosmological phase transitions in the hot early universe [118–121]. Operationally, using the imaginary-time formalism one obtains the leading thermal corrections to V_{eff} as follows (see e.g. [91, 122] for details). Wick rotate the integrals in Eq. (II.29), replace four momenta as follows, $p_\mu \to (i\omega_n, \vec{k})$, where $\vec{k}$ denotes the usual three-momentum and ω_n are the Matsubara frequencies [123]

$$\omega_n = \begin{cases} 2n\pi T, & \text{for bosons} \\ (2n+1)\pi T, & \text{for fermions} \end{cases} \tag{II.37}$$

and replace integrals over p^0 with sums over Matsubara modes

$$\int \frac{dp^0}{2\pi} \to T \sum_{n=-\infty}^{\infty} . \tag{II.38}$$

The resulting equation for the one-loop corrections to the effective potential becomes,

$$\Delta V_1(\phi_c, T) = \frac{T}{2}\sum_i (-1)^{2s_i}(1+2s_i) \sum_{n=-\infty}^{\infty} \int \frac{d^3k}{(2\pi)^3} \log[k^2 + \omega_n^2 + m_i^2(\phi_c)] \\ + \delta V[\phi_c, s=0], \tag{II.39}$$

[4] Here we are implicitly ignoring the possibility of a dimensionful coupling, m^2, that could shift the relation to $\alpha_c \log\left(\frac{m^2(\phi_c)+m^2}{\mu^2}\right)$, since there will be no couplings with (classical) scaling dimension different from zero in the classically conformal model considered in the next chapter of this thesis.

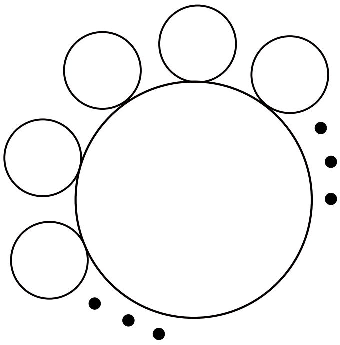

Figure II.1: Illustration showing a diagram of Daisy type.

in the notation described below Eq. (II.35). This equation can be recast as the temperature-independent Coleman–Weinberg potential in Eq. (II.35) plus the following thermal correction [120],

$$V_T^{\text{Landau}} = \frac{T^4}{2\pi^2}\left[\sum_{i,\ \text{bosons}}(2s_i+1)J_B\left(\frac{m_i^2(\phi_c)}{T^2}\right) - \sum_{i,\ \text{fermions}}(2s_i+1)J_F\left(\frac{m_i^2(\phi_c)}{T^2}\right)\right], \tag{II.40}$$

where

$$J_B(y^2) = \int_0^\infty dk\, k^2 \log\left[1 - e^{-\sqrt{k^2+y^2}}\right], \tag{II.41}$$

$$J_F(y^2) = \int_0^\infty dk\, k^2 \log\left[1 + e^{-\sqrt{k^2+y^2}}\right]. \tag{II.42}$$

Daisy resummation

It is well known that finite-temperature perturbation theory breaks down at high temperatures [119,120,124,125]. When the temperature T becomes large compared to a bosonic mass scale, it effectively leads to a temperature enhancement of an associated coupling of the form $\lambda \to \lambda\frac{T}{m}$, which spoils the perturbative expansion when $T \gg m$. The problem manifests itself when considering daisy (ring) diagrams shown in Fig. II.1 for the case of a $\lambda\phi^4$ interaction. Let the inner loop be the i'th Matsubara mode of the field, then the contribution from a diagram with $N-1$ petals goes schematically as[5]

$$T\lambda^{N+1}\left[\int \frac{d^3p}{(2\pi)^3}\frac{1}{(p^2+m_{T_i}^2)^N}\right]\left[\sum\!\!\!\!\!\!\int_Q \frac{1}{Q^2}\right]^N \sim T\lambda m_{T_i}^3\left(\frac{T^2\lambda}{m_{T_i}^2}\right)^N, \tag{II.43}$$

where Q denotes momenta in a petal, and we have defined $m_{T_i}^2 = m^2 + \omega_i^2$. For modes with $|i| > 0$, one has $m_{T_i}^2 \gtrsim (2\pi T)^2$, and higher-order corrections with $N \gtrsim 2$ are parametrically suppressed by λ^N.[6] However, for the bosonic zero mode, we see that higher-order perturbative corrections do not scale as λ but rather as $\frac{\lambda T^2}{m^2}$, which breaks perturbation theory for $T \gg m$ and is even (IR) divergent in the limit $m \to 0$.

The simplest method to deal with this breakdown of perturbation theory is to resum the leading infrared-divergent contributions in a process known as daisy resummation [127,128]. To perform the resummation, one first calculates the thermal corrections

[5] An overview of sumintegrals can be found e.g. in Appendix A in [126].

[6] The same is true for all fermionic modes.

to the bosonic zero modes. In particular, one resums the one-loop thermal self-energy corrections $\Pi_i(T)$, commonly known as thermal masses, to the bosonic propagators at high temperature and vanishing external momentum, which corresponds to the infrared (IR) limit. Then, the bosonic contributions to the effective potential are updated by replacing $m_i^2(\phi_c) \to m_i^2(\phi_c) + \Pi_i(T)$ for bosonic zero modes of scalar fields and longitudinal modes of vector fields.[7] This leads to the following modification of the effective potential in Eq. (II.39)

$$\Delta V_1^{\text{resum}}(\phi_c, T) = \Delta V_1(\phi_c, T) + \frac{T}{12} \sum_b \int \frac{d^3k}{(2\pi)^3} \left[\log[k^2 + (m_b^2 + \Pi_b)] - \log[k^2 + (m_b^2)] \right], \tag{II.44}$$

where the sum runs over scalar fields and longitudinal modes of vector bosons. The result can be conveniently written as [128]

$$\Delta V_1^{\text{resum}}(\phi_c, T) = \Delta V_1(\phi_c, T) + V_{\text{Daisy}}, \tag{II.45}$$

$$V_{\text{Daisy}} = -\frac{T}{12} \sum_b \left[(m_b^2 + \Pi_b)^{3/2} - m_b^3 \right]. \tag{II.46}$$

In summary, the full one-loop effective potential that we will make use of can be written as

$$V_{\text{eff}}(\phi, T) = V_{T=0} + V_{\text{T}} + V_{\text{Daisy}}, \tag{II.47}$$

where $V_{T=0}$ can be determined from Eqs. (II.35) and (II.36), V_{T} from Eq. (II.40), and V_{Daisy} from Eq. (II.46).

II.2 First-order phase transition and gravitational waves

In the high–temperature limit, the effective potential is dominated by V_T, whose leading contribution scales as $\phi_c^2 T^2$, ensuring a global minimum at $\phi_c = 0$ and thus symmetry restoration for sufficiently high temperatures. Consequently, theories exhibiting spontaneous symmetry breaking may have undergone a symmetry-breaking PT after the hot Big Bang, if the maximal temperature in the early universe was sufficiently high for the symmetry to be restored [129].

As the temperature drops, the emergence of a new global minimum, $\phi_c \neq 0$, can proceed in two qualitatively different ways. In a FOPT, a local minimum separated from the true minimum at $\phi_c = 0$ by a potential barrier emerges. This situation is illustrated in the left panel of Fig. II.2. At the critical temperature, T_c, the two minima become degenerate. At lower temperatures, $\phi_c = 0$ is reduced to a local minimum, implying a discontinuity in the position of the global minimum of V_{eff} as a function of temperature at T_c. The transition of the field from the local minimum at $\phi_c = 0$ to the global minimum proceeds through either quantum tunneling or thermal fluctuations. This should be contrasted with a higher-order phase transition, where the global minimum evolves continuously from $\phi_c = 0$ to $\phi_c \neq 0$ as a function of temperature, as illustrated to the right in Fig. II.2.

In the remainder of this section, we focus on FOPTs, presenting the transition rate and relevant thermodynamic quantities that characterize their associated GW production in the early universe.

[7] Transverse modes do not acquire a thermal mass and are therefore not resumed in the Daisy procedure. In fact, transverse modes of non-abelian gauge fields cause IR issues at higher order in perturbation theory: the so-called Linde problem [124].

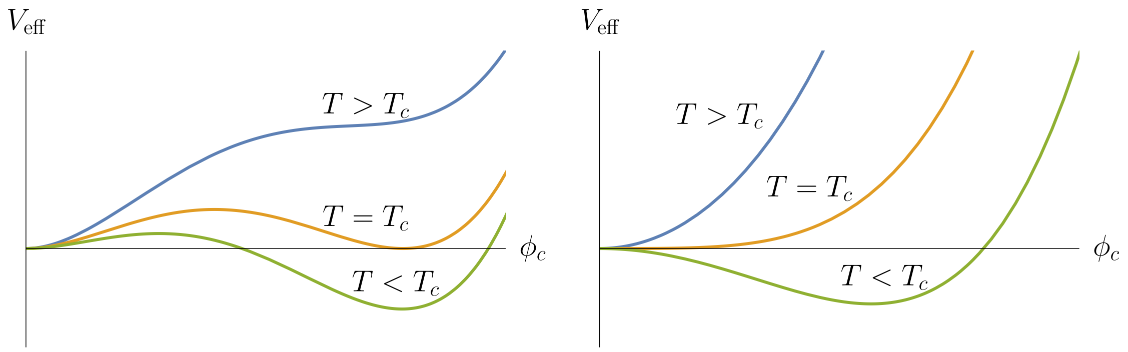

Figure II.2: Qualitative illustration of how the effective potential changes as a function of temperature for a FOPT (left) and a higher-order PT (right).

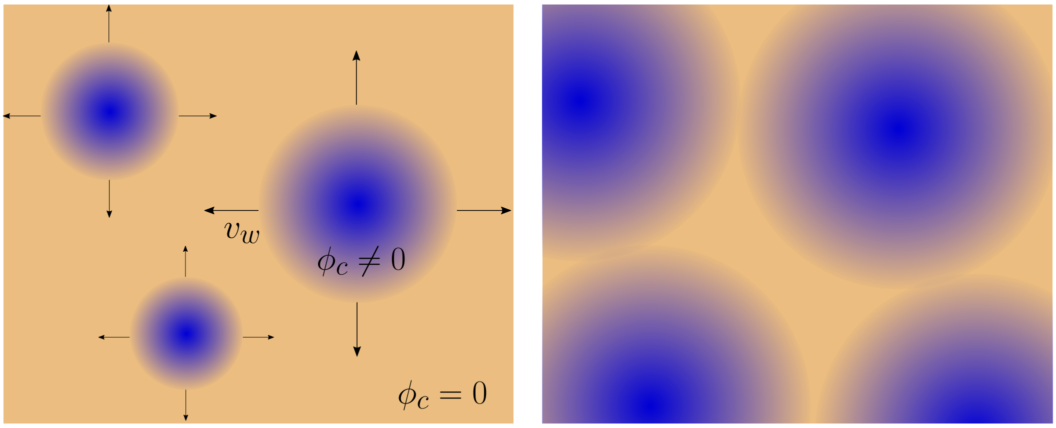

Figure II.3: Left: Illustration showing bubbles of true vacuum nucleating and expanding in a sea of false vacuum. Right: Illustration of the universe around the time of percolation.

II.2.1 Formation of bubbles

As the universe cools down, the field localized in the false vacuum has to transition to the true vacuum. True vacuum nucleates at localized positions in spacetime, as quantum or thermal fluctuations drive the field through or above the potential barrier, respectively. This leads to the formation of extended bubbles in space, which contain the energetically favored ground state.

The nucleation rate per unit volume due to quantum fluctuations and thermal fluctuations can be obtained using semiclassical methods, and the result reads [130–133]

$$\Gamma_n \sim \begin{cases} R_0^{-4}\left(\frac{S_{E,4}}{2\pi}\right)^2 e^{-S_{E,4}}, & \text{for quantum tunneling,} \\ T^4\left(\frac{S_{E,3}}{2\pi T}\right)^{3/2} e^{-S_{E,3}/T}, & \text{for thermal fluctuations.} \end{cases} \tag{II.48}$$

Here R_0 denotes the initial radius of the nucleated bubble, and $S_{E,d}$ the d-dimensional Euclidean action

$$S_{E,d} = \Omega_d \int_0^\infty dr \left[\frac{1}{2}\left(\frac{d\phi_b}{dr}\right)^2 + V_{\text{eff}}(\phi_b)\right], \tag{II.49}$$

where Ω_d is the d-dimensional solid angle, and $d = 4\,(3)$ for vacuum decay via quantum tunneling (thermal fluctuations). The $O(d)$ symmetric bounce field configuration, ϕ_b, is the solution to the following equation of motion,

$$\frac{d^2\phi_b}{dr^2} + \frac{d-1}{r}\frac{d\phi_b}{dr} = \frac{dV_{\text{eff}}}{d\phi_b}, \tag{II.50}$$

with boundary conditions,[8]

$$\phi_b(r \to \infty) = 0, \qquad \left.\frac{d\phi_b}{dr}\right|_{r=0} = 0, \tag{II.51}$$

ensuring finite action and regularity, respectively. From here on, we will only consider bubble-nucleation from thermal fluctuations, as this will provide the dominant contribution in later applications, and we will denote the Euclidean bounce action by S_3. The latter will be calculated numerically using the `FindBounce` package [134].

With the nucleation rate at hand, it is useful to introduce characteristic temperature scales associated with different stages of the FOPT. The nucleation temperature T_n, which characterizes the onset of bubble nulceation, is commonly defined as

$$\Gamma_n(T_n) = H^4(T_n), \tag{II.52}$$

which corresponds to the emergence of approximately one bubble per horizon. Here H denotes the Hubble parameter, given by

$$H^2 = \frac{\rho}{3M_{\text{P}}^2}, \tag{II.53}$$

where M_{P} is the reduced Planck mass and ρ is the energy-density of the universe. For our purposes, the energy-density can be decomposed into a sum of radiation energy-density ρ_R, vacuum energy-density ρ_V, and additional (unspecified) energy-density ρ_A

$$\rho = \rho_R + \rho_V + \rho_A, \qquad \rho_R = \frac{\pi^2}{30}g_*(T)T^4, \qquad \rho_V = \Delta V_{\text{eff}}. \tag{II.54}$$

Here $g_*(T)$ denotes the number of thermal relativistic degrees of freedom at temperature T, and ΔV_{eff} denotes the potential difference between the true and the false vacuum. The nucleation temperature is lower than the critical temperature, and the separation between T_n and T_c is referred to as supercooling, with strong supercooling corresponding to $T_n \ll T_c$.

The nucleation temperature does not provide a reliable measure of the completion of the phase transition. To this end, the percolation temperature T_* is introduced as described in the following. The probability, $P(T)$, that a point remains in the unstable vacuum while the universe undergoes adiabatic expansion is given by [135, 136]

$$P(T) = e^{-I(T)}, \tag{II.55}$$

$$I(T) = \frac{4\pi}{3}\int_T^{T_c} \frac{dT'\Gamma(T')v_w^3}{(T')^4 H(T')}\left(\int_T^{T'}\frac{d\widetilde{T}}{H(\widetilde{T})}\right)^3, \tag{II.56}$$

where v_w denotes the wall velocity of the expanding bubble. Although nucleation is a stochastic process, a large connected cluster is highly likely to form at a critical threshold of the true vacuum fraction, known as the percolation threshold, see [137] and references

[8]Here, we assume that the false vacuum corresponds to $\phi_b = 0$. More generally, if the false vacuum is located at ϕ_b^f, then the first condition below becomes $\phi_b(r \to \infty) = \phi_b^f$.

therein for details. The temperature measure of the percolation threshold in cosmological phase transitions is commonly defined as [138]

$$I(T_*) = 0.34, \tag{II.57}$$

which corresponds to $P(T_*) \approx 0.7$. However, the probability measure in Eq. (II.55) can be a misleading measure of progress for the phase transition if the universe is dominated by vacuum energy [139, 140], in which case the false vacuum is inflating and the percolation criterion in Eq. (II.57) is insufficient to guarantee a successful completion of the phase transition. This observation motivates the following necessary condition to guarantee successful completion of the phase transition: In addition to the requirement in Eq. (II.57), the physical volume of the false vacuum should decrease around the time of percolation. This statement translates into the following relation [141]

$$3 + T\frac{dI}{dT} < 0. \tag{II.58}$$

Once Eq. (II.58) is satisfied, the fraction of physical space remaining in the false vacuum decreases, and the transition should complete successfully.

II.2.2 Characteristic parameters

In addition to the temperature scales introduced above, several additional characteristic parameters are required to characterize a cosmological FOPT and the associated GW production. These parameters are discussed in the next two subsections.

The strength of the FOPT, α, is commonly parametrized by the energy density released in the transition (latent heat) normalized to the radiation-energy density at the time of the transition,

$$\alpha \equiv \frac{1}{\rho_R}\left(\Delta V - \frac{T}{4}\frac{\partial \Delta V(T)}{\partial T}\right)\Bigg|_{T_*}. \tag{II.59}$$

As reviewed below, the GW amplitude depends on the size of α.

A second key parameter is the duration of the transition, controlled by how steeply the bounce action S_3/T falls near the nucleation temperature T_n. If S_3/T decreases rapidly, the dimensionless ratio, Γ/H^4, can become much greater than one shortly after nucleation, leading to many bubbles per Hubble volume and a fast completion. A shallow slope in S_3/T yields the opposite behavior. The time scale is conventionally characterised by[9]

$$\frac{\beta}{H} \approx T_* \frac{d}{dT}\frac{S_3}{T}\Bigg|_{T_*}. \tag{II.60}$$

Equivalently, the duration of the FOPT can be parametrized by the average bubble radius R_* at the time of percolation [141, 142],

$$R_* = \left[v_w^3 T_* \int_{T_*}^{T_c} \frac{T_*^2}{(T')^2}\frac{dT'}{(T')^2}\frac{\Gamma(T')}{H(T')}e^{-I(T')}\right]^{-1/3}. \tag{II.61}$$

[9]This expression is obtained by defining $\beta \equiv \frac{\partial_t \Gamma}{\Gamma}$, which leads to $\frac{\beta}{H} = \frac{1}{H}\frac{d\log\Gamma}{dt} = \frac{d\log\Gamma}{d\log a} \approx -T\frac{d\log\Gamma}{dT} \approx T\frac{d}{dT}\frac{S_3}{T}$, where one assumes an adiabatically expanding universe, i.e. $a^3 s(T) = \text{constant}$, and the last step neglects the temperature-dependence of the prefactor in Eq. (II.48).

The two scales in Eq. (II.60) and (II.61) are related by $\beta = \frac{\mathrm{Max}[v_w, c_s]\eta}{R_*}$, where $c_s = 1/\sqrt{3}$ is the sound speed in the plasma [141, 142], and a standard choice for the proportionality factor is $\eta = (8\pi)^{1/3}$ [143], while simulations have shown $\eta \approx 5$ for strongly supercooled transitions [144].[10]

Next, let us consider a nucleated bubble. If the region inside the bubble where $\frac{d\phi_c}{dr}$ deviates significantly from zero is much smaller than the bubble size, then the bubble is said to have a thin wall. However, even if the initial bubble profile does not exhibit a thin wall shortly after nucleation, it is possible to associate a thin-wall radius R_0 to it as follows,

$$V_{\text{thin-wall}} = \frac{4\pi}{3}\left[V_{\text{eff}}(0, T_n) - V_{\text{eff}}(\phi_{\text{in}}(r=0), T_n)\right] R_0^3. \tag{II.62}$$

R_0 is determined by requiring that $V_{\text{thin-wall}}$ equals the potential energy of the physical bubble,

$$V_{\text{initial}} = 4\pi \int r^2\, dr\, V_{\text{eff}}(\phi_{\text{in}}(r), T_n). \tag{II.63}$$

In Ref. [145], it was demonstrated that utilizing R_0 as an input variable enables an analytic approximation of the wall energy E_{wall}, i.e. the energy stored in the bubble wall of the expanding bubble, that is in good agreement with results obtained by simulating the expanding bubble.

The expansion of the bubble is driven by ΔV_{eff}. Meanwhile, the thermal plasma surrounding the bubble exerts friction on it, resulting in a total pressure difference across the wall given by

$$\Delta P = \Delta V_{\text{eff}} - P_{1\to 1} - P_{1\to N}. \tag{II.64}$$

Here

$$P_{1\to 1} \approx \sum_i \frac{c_i k_i}{24} M_i^2 T_*^2, \tag{II.65}$$

is the LO pressure contribution corresponding to friction from particles that gain mass in the transition [146]. The sum in Eq. (II.65) runs over all particles i that gain mass in the phase transition, $c_i = 1\,(1/2)$ for bosons (fermions), and k_i denote the (massive) DoFs of species i. The second (NLO) contribution in Eq. (II.64) accounts for transition radiation at the wall. Different studies have obtained different results for the scaling of $P_{1\to N}$ with the Lorentz factor of the bubble wall γ [147–150]. We will adapt the result of Ref. [147], where $P_{1\to N}$ scales as γ^2, which presents the most conservative estimate.[11] By setting $\Delta P = 0$, one obtains the equilibrium value for γ,

$$\gamma_{\text{eq}} \approx \sqrt{\frac{\Delta V_{\text{eff}} - P_{1\to 1}}{P_{1\to N}/\gamma^2}}. \tag{II.66}$$

[10] This is the first and last time we mention β in this thesis, and we will only work with the quantity R_* defined in Eq. (II.61) from here on.

[11] Following Ref. [147], there has been growing consensus that the NLO pressure scale with γ^1 up to logarithmic corrections [148, 149], see also the very recent paper [151], and it would be interesting to revisit our results using $P_{1\to N} \sim \gamma$ in the future. We expect that setting $P_{\text{NLO}} \sim \gamma$ will lead to larger values for γ_{eq}, which is defined via the relation $\Delta V_{\text{eff}} = P_{1\to 1} + P_{\text{NLO}}(\gamma_{\text{eq}})$, and that this will increase the region of parameter space where the transition is of runaway nature and where the GW production is primarily sourced by bubble collisions (with $\kappa_{\text{col}} \approx 1$, see Eq. (II.68) below).

At the (average) time of bubble collisions, γ takes the following value [145]

$$\gamma_* = \mathrm{Min}[\widetilde{\gamma}_*, \gamma_{\rm eq}], \qquad \widetilde{\gamma}_* = \frac{2R_*}{3R_0}. \tag{II.67}$$

Here $\widetilde{\gamma}_* < \gamma_{\rm eq}$ corresponds to a runaway transition, meaning that bubbles keep accelerating until the time of collision. For $\widetilde{\gamma}_* > \gamma_{\rm eq}$ bubbles reach a terminal velocity before colliding. Using these parameters, the bubble collisions efficiency factor, $\kappa_{\rm col}$, can be expressed as [152]

$$\kappa_{\rm col} = \frac{E_{\rm wall}}{E_V} = \begin{cases} \left[1 - \frac{1}{3}\frac{\widetilde{\gamma}_*^2}{\gamma_{\rm eq}^2}\right]\left(1 - \frac{\alpha_\infty}{\alpha_n}\right) & \widetilde{\gamma}_* < \gamma_{\rm eq}, \\ \frac{2\gamma_{\rm eq}}{3\widetilde{\gamma}_*}\left[1 - \frac{\alpha_\infty}{\alpha_n}\right] & \widetilde{\gamma}_* > \gamma_{\rm eq}, \end{cases} \tag{II.68}$$

where

$$E_V = \frac{4\pi R_*^3 \Delta V(T_*)}{3}, \qquad \alpha_\infty = \frac{P_{1\to 1}}{\rho_R(T_*)}. \tag{II.69}$$

As we will see below, the bubble-efficiency factor determines the relative importance of bubble collisions as a GW source.

Next, we briefly comment on the bubble-wall velocity, v_w. For strongly supercooled FOPTs, it is safe to assume that the bubbles approach the speed of light. In scenarios without strong supercooling, bubbles may acquire a subluminal terminal velocity. Determining the bubble-wall velocity in such a case is nontrivial and beyond the scope of our work.[12] Instead, we will assume that the bubble wall velocity satisfies $v_w \approx 1$. This requires $\alpha > \alpha_\infty$ [145], and we will therefore restrain our analysis to parts of parameter space where this condition is satisfied. However, we note that a crude estimate of v_w can be obtained by adapting the Chapman-Jouget velocity [154],

$$v_w(\alpha) = \frac{\sqrt{1/3} + \sqrt{\alpha^2 + 2\alpha/3}}{1+\alpha}. \tag{II.70}$$

In our analysis, we verify compatibility between the two diagnostics of when v_w significantly deviates from 1.

II.2.3 Gravitational wave spectra and detection

Next, we will consider GW production associated with FOPTs. Due to the weakness of gravity, GWs propagate freely from their time of production until today. Therefore, they offer a clean probe of the process(es) that sourced them, and can be used to probe energy scales far beyond the reach of particle colliders, as explained in Chapter I. Below, we will review how the characteristic parameters introduced above can be used to parametrize GW production from a FOPT, focusing on aspects of direct relevance to our study. The interested reader is referred to [155] and references therein for more on cosmological backgrounds of GWs.

We consider three sources through which the nucleated bubbles can source GWs; bubble collisions, sound waves, and turbulence in the thermal plasma. For $\widetilde{\gamma}_* < \gamma_{\rm eq}$, a large fraction of the vacuum energy is used to accelerate the bubble walls, making bubble collisions the dominant source of GWs. In the opposite regime, $\widetilde{\gamma}_* > \gamma_{\rm eq}$, a terminal

[12] We note that a new package for calculating the wall velocity recently became available, which might make determining v_w accurately more feasible in future studies [153].

velocity is reached, and the fraction of the total released energy going into the bubble wall decreases rapidly. The dominant energy fraction is then transferred into kinetic and thermal energy of the surrounding plasma, making plasma contributions the dominant GW source.

Following Ref. [152], we employ results from many-bubble simulations in the thin-wall approximation to estimate the GW spectrum sourced by bubble collisions in supercooled transitions. The quantity of interest is $\Omega_{\rm GW}(f) \equiv \frac{1}{\rho_c}\frac{d\rho_{\rm GW}}{d\log f}$, where $\rho_{\rm GW}$ is the energy density of GWs, ρ_c is the critical energy-density of the universe, and f denotes GW frequency. The template takes the form [156],

$$\Omega_{\rm col,*}(f) = 2.3\cdot 10^{-3}(R_*H_*)^2\left(\frac{\kappa_{\rm col}\alpha}{1+\alpha}\right)^2\left[1+\left(\frac{f}{f_d}\right)^{-1.61}\right]\left(\frac{f}{f_{\rm col}}\right)^{2.54} \times\left[1+1.13\left(\frac{f}{f_{\rm col}}\right)^{2.08}\right]^{-2.30}, \tag{II.71}$$

Here H_* denotes the Hubble rate at percolation, f_d is given by

$$f_d = 0.044R_*^{-1}, \tag{II.72}$$

and the peak frequency reads

$$f_{\rm col} = 0.28R_*^{-1}. \tag{II.73}$$

Propagation of sound waves is sourced by the remaining fraction of the released vacuum energy, $(E_V - E_{\rm wall})/E_V$. There is a characteristic time scale associated with the so-called sound-wave period

$$\tau_{\rm sw} = \min\left[\frac{1}{H_*}, \frac{R_*}{U_f}\right], \tag{II.74}$$

after which the plasma enters a non-linear regime where GWs are sourced by turbulence. Here, U_f denotes the root-mean-square fluid velocity, which can be estimates as [157],

$$U_f^2 \approx \frac{3}{4}\frac{\alpha_{\rm eff}}{1+\alpha_{\rm eff}}\kappa_{\rm sw}, \tag{II.75}$$

where $\kappa_{\rm sw}$ is the efficiency factor for GW production from sound waves [158],

$$\kappa_{\rm sw} = \frac{\alpha_{\rm eff}}{\alpha}\frac{\alpha_{\rm eff}}{0.73+0.083\sqrt{\alpha_{\rm eff}}+\alpha_{\rm eff}}, \qquad \alpha_{\rm eff} = \alpha(1-\kappa_{\rm col}). \tag{II.76}$$

An upper limit on the energy transfer into GWs from the plasma was obtained in [145], by assuming that the energy left in the plasma motion at time $\tau_{\rm sw}$ is transferred to turbulence without heat loss to the plasma. The spectrum of GWs sourced by sound waves and turbulence then take the following form [145],

$$\Omega_{\rm sw,*}(f) = 0.384(\tau_{\rm sw}H_*)(R_*H_*)\left(\frac{\kappa_{\rm sw}\alpha}{1+\alpha}\right)^2\left(\frac{f}{f_{\rm sw}}\right)^3\left[1+\frac{3}{4}\left(\frac{f}{f_{\rm sw}}\right)^2\right]^{-7/2}, \tag{II.77}$$

$$\Omega_{\rm turb,*}(f) = 6.85(R_*H_*)(1-\tau_{\rm sw}H_*)\left(\frac{\kappa_{\rm sw}\alpha}{1+\alpha}\right)^{3/2}\frac{\left(\frac{f}{f_{\rm turb}}\right)^3\left[1+\left(\frac{f}{f_{\rm turb}}\right)\right]^{-11/3}}{1+8\pi f/H_*}, \tag{II.78}$$

respectively. By inspecting the expressions above, one can see that if non-linearities do not develop in the plasma within a Hubble time, then the GW production from turbulence vanishes. Finally, for $v_w \approx 1$, the peak frequencies for GWs sourced by sound waves and turbulence read [145, 152],

$$f_{\rm sw} \approx 8R_*^{-1}, \tag{II.79}$$

$$f_{\rm turb} \approx 9.1R_*^{-1}, \tag{II.80}$$

respectively.

Finally, let us mention that the GW templates presented above were state-of-the art at the time when we initiated our calculations. Later, other templates have been suggested, see for example Ref. [159] and references therein. This, however, does not invalidate our general approach and our conclusions.

Redshift and detection

To compare the predicted GW signal with present-day observations, we must account for the redshift from production to today. Relevant results are reviewed below, including the possibility of an intermediate matter-dominated era driven by the symmetry-breaking scalar ϕ [152, 160].

Following the completion of the FOPT, the matter energy density ρ_ϕ and radiation energy density ρ_R can be tracked via the following Boltzmann equations,

$$aH\frac{d\rho_R}{da} + 4H\rho_R = \Gamma_\phi\rho_\phi, \tag{II.81}$$

$$aH\frac{d\rho_\phi}{da} + 3H\rho_\phi = -\Gamma_\phi\rho_\phi, \tag{II.82}$$

where

$$H^2 = \frac{\rho_R + \rho_\phi}{3M_P^2}, \tag{II.83}$$

and Γ_ϕ denotes the decay rate of the symmetry-breaking scalar field ϕ. Here, M_P denotes the reduced Planck mass. The equations are solved from the time of percolation, where the initial conditions read [152]

$$\rho_{\phi*} = 3M_P^2H_*^2\kappa_{\rm col}\frac{\alpha}{1+\alpha}, \tag{II.84}$$

$$\rho_{R*} = 3M_P^2H_*^2(1-\kappa_{\rm col})\frac{\alpha}{1+\alpha}. \tag{II.85}$$

As can be seen from the equations above, a significant intermediate period of matter domination can be realized if Γ_ϕ is small and the bubble-collision efficiency factor is non-negligible.

Finally, by introducing an additional characteristic parameter, a_x, parametrizing when ρ_R becomes negligible to ρ_ϕ , the GW abundance observed today can be expressed as [152],

$$\Omega_{\rm GW,0}(f) = \begin{cases} \left(\frac{a_*}{a_0}\right)^4\left(\frac{H_*}{H_0}\right)^2\Omega_{\rm GW,*}\left(\frac{a_0}{a_*}f_*\right), & \text{for} \quad f > f_* \\ \left(\frac{a_f}{a_0}\right)^4\left(\frac{H_f}{H_0}\right)^2\Omega_{\rm GW,*}\left(\frac{a_0}{a_*}f_*\right)\left(\frac{f}{f_*}\right)^3, & \text{for} \quad f < f_*, \end{cases} \tag{II.86}$$

where,

$$2\pi f = a_fH_f, \qquad 2\pi f_* = a_*H_*, \tag{II.87}$$

and

$$\left(\frac{a}{a_0}\right)^4\left(\frac{H}{H_0}\right)^2 = 1.67\cdot 10^{-5}h^{-2}\left(\frac{100}{g_{\rm eff}(T_x)}\right)^{1/3}\left(\frac{a}{a_x}\right)^4\left(\frac{H}{H_x}\right)^2, \tag{II.88}$$

$$\frac{a_0}{a_*} = 1.3\times 10^{15}\left(\frac{T_x}{100\text{GeV}}\right)\left(\frac{g_{\rm eff}(T_x)}{100}\right)^{1/3}\frac{a_x}{a_*}. \tag{II.89}$$

Here, the subscript "x" denotes that the quantity is evaluated at $a = a_x$. We will use $\frac{\rho_\phi(a_x)}{\rho_R(a_x)} = 0.1$ in our calculations.

Finally, to quantify the observability of the resulting GW signal in Eq. (II.86), we will compute the signal-to-noise ratio (SNR) for selected detectors using

$$\text{SNR} = \sqrt{\mathcal{T}\int_{f_{\rm min}}^{f_{\rm max}} df\left(\frac{\Omega_{\rm GW,0}h^2}{\Omega_{\rm sens}h^2}\right)^2}. \tag{II.90}$$

Here $\mathcal{T}$ denotes the duration of collecting data for the considered experiment. The term in the denominator, $\Omega_{\rm sens}h^2$, denotes the noise curve of the relevant detector, which we take from [161]. In our study, we consider (projected sensitivity for) the following experiments: LISA [162], BBO and DECIGO [163,164], aLIGO + aVirgo + Kagra [165–167], ET [168], and CE [169,170].

Final comments

There are various sources of theoretical uncertainty entering the calculations presented so far. For the sake of transparency, we point out some of the uncertainties that will not be considered in our work, referring the interested reader to [137,171,172] and references therein for further details and estimates of the impact that the various sources have. We calculate the effective potential in Landau gauge, however, the effective potential is not gauge invariant away from the minimum. The effective potential has higher-order μ-dependence. Higher-order thermal effects can be important, and new calculation approaches are being explored, see e.g. [173–175]. As is customary, we model all bubbles to be of similar size at the time of percolation, rather than as a distribution [176].

In Chapter III, we will, however, consider the impact of using different schemes for Daisy resummation, previously neglected thermal mass contributions, and differences in using the full one-loop RGE improved effective potential and selected simpler approximations.

II.3 Cosmic strings

The next topic that we will review is cosmic strings. In Chapters III and IV, we explore BSM scenarios that extend the SM gauge group by a $U(1)_{B-L}$ symmetry and examine the cosmological consequences of its spontaneous breaking in the early universe. A generic prediction of these models is the formation of a network of cosmic strings.[13] The following section provides an overview of key cosmic-string properties relevant to our subsequent analysis, including a brief summary of the evolution of string networks, and their energy-loss mechanisms (gravitational radiation and particle emission). Details can be found in [107,177].

[13]If the spontaneously broken symmetry is global instead of gauged, then global strings can form, see e.g. [107] for details.

Example

The canonical example of a local cosmic string arises from the Abelian Higgs (AH) model, where the field configuration of a static, straight local cosmic string aligned along the z-axis is cylindrically symmetric and takes the form [178, 179]

$$\phi(r) = e^{in\theta} f(r), \tag{II.91}$$

$$A = -\frac{n\alpha(r)}{er}\hat{\theta}, \tag{II.92}$$

in cylindrical coordinates. Here n denotes the winding number of the string, which counts the number of times the phase of the complex scalar field wraps around the vacuum manifold when traversing in a closed loop around the string. The functions $f(r)$ and $\alpha(r)$ are determined by substituting Eqs. (II.91) and (II.92) into the Euler-Lagrange equations for ϕ and A. Explicit solutions to these equations are not known, but can be obtained numerically. However, finite energy per unit length and regularity of the string at the origin dictates,

$$f(r) \to 1, \quad \alpha(r) \to 1, \quad r \to \infty, \tag{II.93}$$

$$f(0) = \alpha(0) = 0, \tag{II.94}$$

respectively. The tension of the string, μ, is roughly set by the vev of the symmetry-breaking field

$$\mu \sim \langle|\phi|\rangle^2 \tag{II.95}$$

and the string width is set by m_ϕ^{-1} [107].

Formation and evolution

We now consider the formation and evolution of cosmic string networks, providing a broad overview and deferring technical discussions to Chapter IV. Recall from the introduction to this chapter, that a suitable topology of the vacuum manifold ($\pi_1(\mathcal{M}) \neq 0$) quite generally implies the existence of cosmic strings in the early universe through the Kibble mechanism [108]. At formation, the network of strings consists of long strings (making up the majority) and loops. Shortly after formation, the network may evolve through a transient friction epoch where interactions with the thermal plasma damp the string motion. The thermal friction is commonly parametrized by the following effective length scale [107, 180]

$$l_{\text{fric}} \equiv \frac{\mu}{\beta_{\text{fric}} T^3}. \tag{II.96}$$

Here β_{fric} encodes the interactions between the string and the plasma, and can be $\mathcal{O}(1)$ for Aharonov-Bohm interactions between the string and plasma particles [181]. Thermal friction is important at high temperatures until $2H \gtrsim l_{\text{fric}}^{-1}$. At lower temperatures, the following two effects compete about the string evolution:

1. Stretching by Hubble expansion, which can lead the network to dominate the energy density of the universe.
2. Fragmentation of the string network into loops that decay away.

In particular, loops are formed when string segments cross, which can happen through self intersection or strings colliding. After a loop is created, it starts to decay by emitting gravitational and/ or particle radiation. The two competing effects (1. and 2. above) drive the network to an attractor solution, in which the charactersitic length scales describing the network scale with cosmic time (c.f. [182–186] for pioneering work and also [187–190]).

In the following, we will consider properties of cosmic string loops. The energy density transferred into loops per unit time can be obtained by considering the energy loss from the network required to maintain scaling, and the result reads [107, 191, 192],

$$\left.\frac{d\rho}{dt_i}\right|_{\text{loop}} = \frac{\sqrt{2}\mu C_{\text{eff}}(t_i)}{t_i^3}, \tag{II.97}$$

where C_{eff} parametrizes the loop-formation efficiency. The number density of loops of type α produced per unit volume and time can then be expressed as

$$\frac{dn_\alpha}{dt_i} = \frac{F_\alpha}{\gamma_\alpha \mu l_\alpha(t_i)} \left.\frac{d\rho}{dt_i}\right|_{\text{loop}} = \frac{F_\alpha \sqrt{2} C_{\text{eff}}}{\gamma_\alpha l_\alpha(t_i) t_i^3}, \tag{II.98}$$

where γ_α and F_α denote the Lorentz factor and the fraction of energy that goes into loops of type α with initial length $l_\alpha(t_i) = \alpha t_i$, respectively. Based on the findings of large Nambu-Goto numerical simulations [190, 193] we will employ a picture where loops are produced in two categories; big and small [191, 192].

- For big loops, we set $F_\alpha \approx 0.1$, $\gamma_\alpha \approx \sqrt{2}$, and $\alpha = 0.1$.
- For small loops, we set $F_\alpha \approx 0.9$, $\gamma_\alpha \approx 50$, and $\alpha \approx \Gamma G\mu$

The loops shrink by emitting gravitational and particle radiation. When the loop length becomes comparable to the string width, the loop inevitably overlaps with itself, which makes it annihilate into a burst of constituent particles. In particular, at early times when

$$t \lesssim \frac{w}{\Gamma G\mu}, \tag{II.99}$$

we will assume that the energy which would have gone into small loops with length shorter than their width is converted directly to particle radiation instead. In the following, we review how loops shrink by emitting gravitational and particle radiation.

Loop decay

Gravitational radiation: The power of GW emission from a loop is independent of its length, and reads [107]

$$P_{\text{GW}} = \Gamma G\mu^2, \tag{II.100}$$

where G denotes Newton's constant and Γ is the GW emission efficiency factor, which we set to $\Gamma \approx 50$ [194].

Particle radiation: The role of particle radiation as an energy-loss mechanism for loops has been subject to debate for many years. Different lattice simulations of Abelian Higgs strings have found that particle radiation provides the dominant energy-loss mechanism for all loops [195–199], a subdominant mechanism for all loops [200, 201], and dominant energy-loss mechanism for loops shorter than a characteristic length scale that depends on its small-scale structure [202]. In our study of non-thermal leptogenesis via particle-production from cosmic strings in Chapter IV, we will employ the following two descriptions of particle radiation from loops:

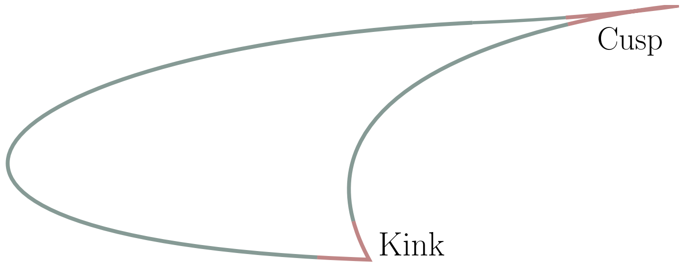

Figure II.4: Illustration of a loop featuring a cusp and a kink.

1. Following the proposal in Ref [203], which is based on simulations in [202], we treat particle-emission as the dominant energy-loss mechanism for small loops and GW emission as the dominant channel for big loops. The relevant formulae for loop decay in this treatment are summarized below.
2. We treat the conversion from loops to particle radiation as instantaneous. This should be understood as an upper limit on the energy loss from loops to particle radiation. The energy-density per unit time going into particle radiation is then set by Eq. (II.97), and the loops have no time to emit GWs.

Loop evolution and GW spectrum from loops

In treatment 1. described above, particle decay is the dominant energy-loss contribution for $l > l_*$, where l_* denotes a critical loop length. Following [192], we model shrinking loops by assuming that while $l > l_*$, they shrink by emitting gravitational radiation only, while for $l < l_*$, they decay by emitting massive radiation and no gravitational radiation. The critical size l_* depends on the small-scale structure of the strings, and manifests itself as a cutoff for the GW spectra at high frequency, which could be a target for future ultrahigh-frequency GW detectors [204].

A kink is a discontinuity in the tangent vector of the string, c.f. Fig. II.4, and typically occur when a loop is formed. In the case where kinks are prevalent on strings, the critical size has been estimated up to an $\mathcal{O}(1)$ factor as [203]

$$l_*^{(k)} \sim \frac{w}{\Gamma G\mu}, \tag{II.101}$$

where w denotes the width of the string. We model the loop evolution in this case as [192, 203]

$$\frac{dl}{dt} \approx \begin{cases} -\Gamma G\mu, & l > l_*^{(k)}, \\ -\frac{w}{l}, & l < l_*^{(k)}. \end{cases} \tag{II.102}$$

Cusps are transient string configurations that can be thought of as a sharp fold of a part of the loop, c.f. Fig. II.4. The critical length for loops whose small-scale structure is dominated by cusps is [203]

$$l_*^{(c)} \sim \frac{w}{(\Gamma G\mu)^2}. \tag{II.103}$$

The loop evolution is in this case modeled as

$$\frac{dl}{dt} \approx \begin{cases} -\Gamma G\mu, & l > l_*^{(c)}, \\ -\sqrt{\frac{w}{l}}, & l < l_*^{(c)}. \end{cases} \tag{II.104}$$

Interestingly, the gravitational radiation emitted by strings throughout the cosmic history could be probed at future GW experiments. The GW spectra generated using loop-description 1. above are shown in Fig. II.5 for different values of the symmetry breaking scale, as indicated by the numbers in the plot. Within this framework, cosmic strings associated with breaking scales $\langle \phi \rangle \gtrsim 10^{14}$ GeV are excluded by NANOGrav, as seen from the figure, and breaking scales covering many orders of magnitude can be tested at future experiments. Furthermore, non-standard cosmological histories can leave an imprint or deviation from flatness in the spectrum, making GWs from cosmic strings an intriguing window to probe the pre-BBN era in many BSM models, see e.g. [191, 205–208].

Fig. II.5 was obtained using the formulae presented in Ref. [192], which are omitted here for brevity. Importantly, it involves summing over all contributions from loops produced after the friction-dominated epoch ended, $t_{\rm fric}$, and that were longer than l_* at formation. However, we note that in their treatment, they did not account for the impact that particle radiation has on the evolution of loops that were initially longer than l_*. While this is not important for loops with initial lengths $l_i \gg l_*$,[14] it might be important to reliably predict the GW spectra in the vicinity around the high-frequency cut-off discussed next.[15]

The constraints imposed by requiring that only loops created after $t_{\rm fric}$ and loops with initial lengths above l_* contribute to the GW spectra can be translated into characteristic cut-off frequencies, after which the spectra are expected to fall off, see e.g. [192, 204] for details. For loops dominated by cusps, the result reads, [204]

$$f_{\rm GW}^{\rm cusp} = 62.3\,{\rm kHz}\sqrt{\frac{1}{\beta_c}}\left(\frac{G\mu}{10^{-11}}\right)^{3/4}, \tag{II.105}$$

where $\beta_c = N_c \lambda^{-1/4}$. Here, λ denotes the quartic coupling of the complex scalar field and N_c the number of cusps, which is expected to be two in each oscillation [209]. Eq. (II.105) with $\beta_c = 2$ is illustrated by the gray dashed curve in Fig. II.5. The constraints from $l_*^{(k)}$ and $t_{\rm fric}$ typically fall outside the frequency range shown in Fig. II.5, and are therefore not discussed further. However, it should be noted that the cut-off associated with thermal friction/ particle radiation provides an interesting case to probe with a combination of regular and ultrahigh frequency gravitational wave detectors, as the former could probe the symmetry-breaking scale and the latter might probe the high-frequency fall off [204].

Bounds on $G\mu$

Finally, we discuss current upper bounds on the string tension. The absence of cosmic string signatures in the CMB yields [210–212],

$$G\mu \lesssim \text{few} \times 10^{-7}. \tag{II.106}$$

This constraint is obtained by considering the effect of long (network) cosmic strings on the CMB and is therefore not affected by assumptions on e.g., loop distributions. A discussion of other constraints can be found in Appendix A in Ref. [192].

An analysis performed by the NANOGRAV collaboration [26], following the 15 year data set release [25], obtained the following constraint,

$$G\mu \lesssim 10^{-10}, \tag{II.107}$$

[14]This can be understood from Eq. (115) in [192], and that the particle cut-off would only impact the high-frequency tail of such loops.

[15]The author thanks Peera Simakachorn for discussions about this point.

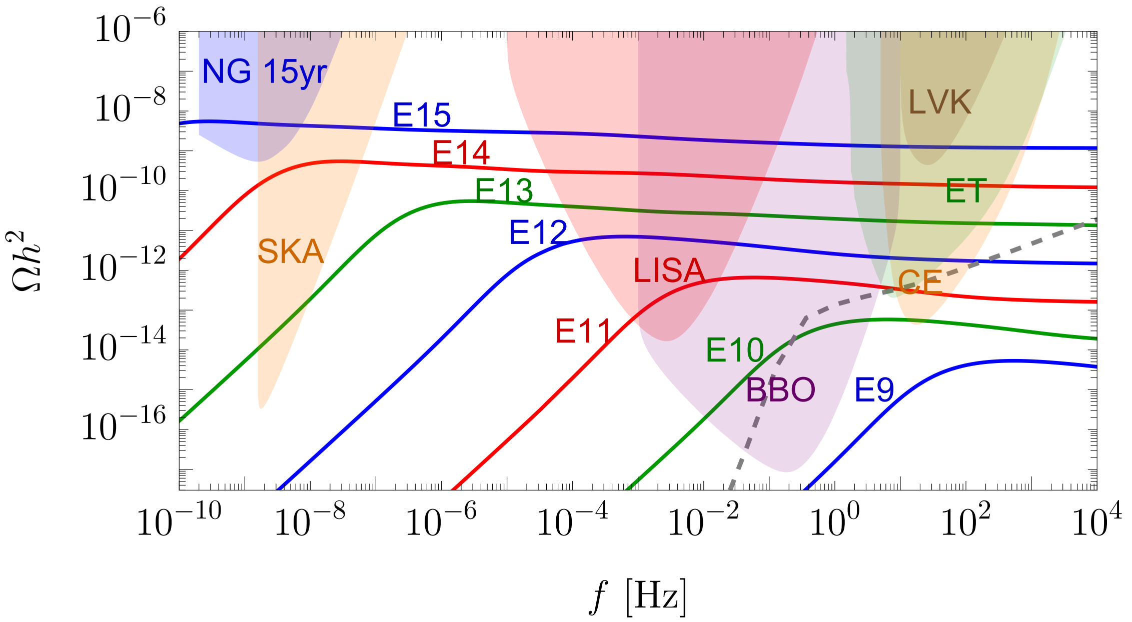

Figure II.5: Illustration of GW spectra from cosmic string loops obtained using the treatment in Ref. [192].

using a Nambu-Goto description of cosmic strings, see also Refs. [213–215] for some earlier related work and bounds. The bound in Eq. (II.107) corresponds to $\langle\phi\rangle \lesssim 10^{14}$ GeV. However, it has been pointed out that further information about the fraction of long-lived loops in a cosmic string network is required for reliable constraints on μ [216], and that the GW background from a local string network is much weaker than that obtained in a pure Nambu-Goto description [199]. As an extreme case, if all energy from cosmic-string loops is emitted via particle radiation without any GW production, then Eq. (II.106) provides the strongest model-indepedent bound on the string tension, corresponding to $v_\phi \lesssim \text{few} \times 10^{15}$ GeV.

II.4 Thermal leptogenesis in a nutshell

In the final section of this chapter, we turn from phase-transition phenomena to aspects of TLG that will be of direct relevance for the following two chapters. This section also serves as a foundation for understanding how the non-standard leptogenesis mechanism considered in the second part of this thesis differs from standard TLG.

As discussed in Chapter I, leptogenesis [23] is a prominent paradigm for generating the BAU by introducing two or more RHNs to the SM. We will review key aspects of standard TLG with a hierarchical RHN mass structure.[16] In TLG, the lightest RHN is thermally produced and generates a lepton asymmetry through out-of-equilibrium CP-violating decays [23, 223–226]. The resulting lepton asymmetry is then partially converted into the BAU by SM (weak) sphaleron processes, which violate $B + L$ [89].

The Boltzmann equations governing TLG in the SM augmented by at least two RHNs

[16] We adopt the one-flavor approximation, implicitly summing over lepton flavors in the final state, as in Eq. (II.111). This description is valid for $T \gtrsim 10^{12}$ GeV when no SM processes are efficient enough to probe the flavor composition of charged-lepton states. For a discussion of flavor effects in leptogenesis, see Refs. [217–222].

take the following form [225],

$$\frac{dY_{N_1}}{dz} = -(D+S)(Y_{N_1} - Y_{N_1}^{\mathrm{eq}}), \tag{II.108}$$

$$\frac{dY_{B-L}}{dz} = -\epsilon_1 D(Y_{N_1} - Y_{N_1}^{\mathrm{eq}}) - WY_{B-L}, \tag{II.109}$$

in a radiation-dominated universe. Here,

$$z \equiv M_{N_1}/T, \qquad Y \equiv \frac{n}{s}, \tag{II.110}$$

where T denotes the temperature of the thermal plasma, and n and s denote number density and entropy density, respectively. ϵ_1 denotes the CP-asymmetry parameter in N_1 decays,

$$\epsilon_1 \equiv \frac{\Gamma(N_1 \to LH) - \Gamma(N_1 \to \bar{L}H^\dagger)}{\Gamma(N_1 \to LH) + \Gamma(N_1 \to \bar{L}H^\dagger)}, \tag{II.111}$$

where L here denotes a sum over the SM lepton doublets, and H is the SM Higgs boson. D parametrizes decays/ inverse decays of N_1 and S parametrizes $\Delta L = 1$ scatterings involving one external RHN. W parametrizes LNV interactions, and the last term on the right-hand side of Eq. (II.109) is known as the "washout term", as it erases generated $B-L$ asymmetry.

Formally, the resulting $B-L$ asymmetry is given by [225],

$$Y_{B-L}(z) = Y_{B-L}(z_i)e^{-\int_{z_i}^{z} dz' W(z')} + \epsilon_1 \int_{z_i}^{z} dz' \frac{D}{D+S}\frac{dY_{N_1}}{dz'} e^{-\int_{z'}^{z} dz'' W(z'')}. \tag{II.112}$$

It is clear that an initial $B-L$ asymmetry present at an early instance, z_i, can be severely diminished by washout processes, as seen from the first term on the r.h.s. of Eq. (II.112). If RHNs are thermalized at early times, the majority of the $B-L$ generation takes place at $T \sim M_{N_1}$ where the equilibrium-distribution of N_1 changes rapidly. This asymmetry is partially erased by washout contributions encoded by the exponential function in the second term on the r.h.s. of Eq. (II.112). In Chapter IV, we will consider the possibility of creating RHNs non-thermally at $T \ll M_{N_1}$, where W is typically much weaker than for $T \sim M_{N_1}$. The benefit of such an approach is manifest; less of the produced asymmetry is destroyed by washout effects.

Thermal leptogenesis is commonly divided into two regimes characterized by the magnitude of an effective neutrino mass parameter [227],

$$\widetilde{m}_1 \equiv \frac{(Y_\nu^\dagger Y_\nu)_{11} v_h^2}{M_{N_1}}, \tag{II.113}$$

where Y_ν denotes the Dirac Yukawa coupling. This should be compared to the so-called equilibrium neutrino mass [225],

$$m_* \approx 1.07 \cdot 10^{-3}\,\mathrm{eV}. \tag{II.114}$$

The cases,

$$\widetilde{m}_1 > m_*, \qquad \widetilde{m}_1 < m_*, \tag{II.115}$$

are referred to as strong washout regime and weak washout regime, respectively. Light neutrino masses in the range $\mathcal{O}(0.01-0.1)$ eV point to the strong washout regime, see e.g. Ref. [228] and references therein for details. In the strong washout regime, any initial asymmetry present at early times becomes insignificant for the prediction of Y_{B-L} at late times, which takes the universal form [225],

$$Y_{B-L} = \epsilon_1 \bar{\kappa}_f(\widetilde{m}_1,\, M_{N_1}\bar{m}^2), \tag{II.116}$$

with

$$\bar{\kappa}_f(\widetilde{m}_1,\, M_{N_1}\bar{m}^2) = \kappa_f(\widetilde{m}_1)\exp\left\{-\frac{\omega}{z_B}\left(\frac{M_{N_1}}{10^{10}\text{ GeV}}\right)\left(\frac{\bar{m}}{\text{eV}}\right)^2\right\}, \tag{II.117}$$

where $\omega \approx 0.186$ and

$$z_B = \frac{2m_*}{\widetilde{m}_1\kappa_f(\widetilde{m}_1)}. \tag{II.118}$$

Here, $\kappa_f(\widetilde{m}_1)$ encodes washout from inverse decays, which dominate for $M_{N_1} \ll 10^{14}$ GeV,

$$\kappa_f(\widetilde{m}_1) = (2\pm 1)\cdot 10^{-2}\left(\frac{0.01\,\text{eV}}{\widetilde{m}_1}\right)^{1.1\pm 0.1}. \tag{II.119}$$

The second factor in Eq. (II.117), which encodes washout from $\Delta L = 2$ processes, depends on the absolute neutrino mass scale $\bar{m} = \sqrt{m_1^2+m_2^2+m_3^2}$ and M_{N_1}. Specifically, the $\Delta L = 2$ processes are $HL \leftrightarrow H^\dagger \bar{L}$ and $HH \leftrightarrow \bar{L}\bar{L}$ with heavy (off-shell) RHNs in the s-channel and t-channel, respectively.

Finally, it noteworthy that the absolute neutrino mass scale is severely constrained by Planck: $m_1 + m_2 + m_3 < 0.12$ eV (95% C.L.) [17].[17] Combining this with best-fit values for neutrino-mass splittings (see e.g. [18, 230]), we obtain

$$0.05\,\text{eV} \lesssim \bar{m} \lesssim 0.07\,\text{eV}\,(\textbf{NH}), \qquad 0.07\,\text{eV} \lesssim \bar{m} \lesssim 0.08\,\text{eV}\,(\textbf{IH}), \tag{II.120}$$

for normal hierarchy (NH) and inverted hierarchy (IH), respectively.[18]

$\Delta L = 2$ washout

As indicated in Eq. (II.117), the washout from $\Delta L = 2$ processes may become disastrous for sufficiently high M_{N_1}. Writing $\widetilde{m}_1 = K m_*$ with $K \gtrsim 1$,[19] Eq. (II.117) can be written as

$$\bar{\kappa}_f(\widetilde{m}_1,\, M_{N_1}\bar{m}^2) \approx \frac{0.23}{K^{1.1}}\exp\left\{-\frac{1}{K^{0.1}}\left(\frac{\bar{m}}{0.05\,\text{eV}}\right)^2\left(\frac{M_{N_1}}{1.8\cdot 10^{14}\,\text{GeV}}\right)\right\}, \tag{II.121}$$

where we have used the central values in Eq. (II.119). The strong washout factor makes it challenging to realize successful leptogenesis for $M_{N_1} \gtrsim 10^{15}$ GeV. We will refer to RHNs in this mass range as "heavy RHNs" below. Significant efforts have been made to rescue high-scale leptogenesis with heavy RHNs by adding non-thermal sources of RHN production, see e.g. [231] and references in [232] for concrete examples. The common idea behind these proposals is to source RHNs at $z \gg 1$, when the effect of washout is less

[17] The quoted result could be viewed as conservative, as DESI 2024 has obtained slightly more stringent bounds [229].

[18] Definitions of NH and IH along with details about neutrino mass splittings can be found in Ref. [18].

[19] Here K is the well-know decay parameter $K = \frac{\Gamma_{\text{r.f.}}}{H(M_{N_1})}$ where $\Gamma_{\text{r.f.}}$ denotes the decay rate of N_1 at zero temperature [86].

severe, and a larger fraction of the generated asymmetry survives. For future reference, we list the contribution to W from $\Delta L = 2$ processes, which is given by [225]

$$W_{\Delta L=2} \approx \frac{\omega}{z^2}\left(\frac{M_{N_1}}{10^{10}\ \mathrm{GeV}}\right)\left(\frac{\bar{m}}{\mathrm{eV}}\right)^2, \tag{II.122}$$

at low temperatures. The contribution to W from inverse decays reads [225],

$$W_{\mathrm{ID}}(z) \approx \frac{1}{4}Kz^2\sqrt{1+\frac{\pi}{2}z}e^{-z}. \tag{II.123}$$

Davidson-Ibarra bound

Finally, we comment on the role of the CP-asymmetry parameter ϵ_1 in generating an asymmetry. From Eqs. (II.109) and (II.116), it is evident that generating a specific amount of $B-L$ asymmetry through RHN decay imposes a lower bound on ϵ_1. Within the type-I seesaw framework, the maximum attainable value of ϵ_1 is given by [233, 234]

$$\epsilon_1^{\mathrm{max}} = \frac{3}{8\pi}\frac{M_{N_1}m_{\mathrm{atm}}}{v_h^2} \approx 10^{-6}\left(\frac{M_{N_1}}{10^{10}\ \mathrm{GeV}}\right), \tag{II.124}$$

where m_{atm} denotes the atmospheric neutrino-mass parameter. Eq. (II.124) in conjunction with the requirement to reproduce the observed BAU leads to the famous Davidson-Ibarra bound $M_1 \gtrsim 10^9$ GeV in thermal leptogenesis, where the exact lower limit depends on initial conditions [234].

In closing, we mention that there exist leptogenesis mechanisms that are compatible with RHN masses below the Davidson-Ibarra bound. In resonant leptogenesis [235–238], the bound is circumvented by requiring a quasi-degenerate RHN mass spectrum (i.e. a small mass splitting between the two lightest RHNs), which leads to a resonant enhancement of the CP-asymmetry parameter. In ARS-type leptogenesis [239], the asymmetry is not generated via decays but CP-violating oscillations of GeV-scale RHNs instead, see also [240, 241].

CHAPTER III

First-order phase transition in the classically conformal $B - L$ model

This chapter and the next explore BSM scenarios that extend the SM gauge group by an additional $U(1)_{B-L}$ symmetry. In this chapter, we focus on a specific model realization, while the subsequent chapter adopts a more general approach. We begin by briefly motivating our investigation in the context of the open questions discussed in Section I.1, commenting on how our work extends previous studies, and outlining the structure of the chapter.

III.1 Motivation in a nutshell

One approach to addressing the theoretical limitations of the SM is to extend its gauge group. A minimal extension involves adding a $U(1)_X$ gauge group. In the next two chapters, we focus on $X = B - L$, a choice that is anomaly-free in the presence of three right-handed neutrinos. Gauged $U(1)_{B-L}$ extensions of the SM possess several appealing features, including:

- The three RHNs, which are required by the consistency of the theory, can explain the lightness of the observed neutrino masses through the Type-I seesaw mechanism [63–67]. The spontaneous breaking of $U(1)_{B-L}$ gives mass to the RHNs, and all masses in the theory are then generated by the spontaneous breaking of local symmetries as in the SM.
- The presence of right-handed neutrinos allows for addressing the observed BAU through leptogenesis [23].
- While not the focus of our study, we note that one of the RHNs can serve as a dark matter candidate if it is charged under a stabilizing Z_2 symmetry, as discussed in Refs. [242, 243]. Alternatively, dark matter can be accommodated by introducing additional fields.
- Gauged $U(1)_{B-L}$ appears in many GUTs, which provide an elegant framework for understanding fundamental forces.

In this chapter, we will consider the so-called minimal classically conformal $U(1)_{B-L}$ (CCBL) model [90, 242–248]. Some attractive features of classically conformal models of relevance for this thesis are:

- Classical conformal[1] (CC) invariance generically results in flat scalar potentials with

[1] In the following, we use the terms "classically conformal" and "classically scale invariant" interchangeably since they are equivalent in four-dimensional unitary and renormalizable field theories [249, 250].

thermally induced potential barriers, permitting suitable conditions for large supercooling and huge latent heat release from a FOPT, which can result in strong GW signals [137,140,145,173,251–271]. Classical scale invariance is therefore a paradigm that can be experimentally tested at GW observatories in the future, and can hence be probed at mass scales far beyond those accessible at colliders.

- In CC models, all mass scales are generated dynamically via quantum mechanical effects. In particular, this leads to a calculable origin for the electroweak scale in extensions of the SM.
- Without dimensionful parameters, the theory has fewer free parameters at the classical level, which leads to increased predictive power.

In conclusion, by extending the SM gauge group by $U(1)_{B-L}$ and imposing classical scale invariance, we gain a predictive framework suitable for addressing several open BSM questions. In this framework, the spontaneous breaking of the $U(1)_{B-L}$ symmetry can lead to a large SGWB from the associated FOPT [145, 152, 256, 258, 272–275], which can be probed at future GW observatories, e.g. [25,162–170,276–284]. This makes understanding phase-transition dynamics in CCBL an interesting leading-order question, due to its observational consequences. An interesting next-to-leading-order question is what one might hope to learn about open BSM questions (such as the origin of the BAU) from the observation of a SGWB at future experiments, see e.g. [259, 264, 265, 268, 269, 274, 285–293] for related ideas. This chapter addresses both of these questions, with a particular focus on the mass-scale of RHNs and conditions for successful leptogenesis.

The rest of this chapter is organized as follows. Below, we briefly comment on how our study can be understood in relation to some previous studies of the CCBL model. In Section III.2, we first introduce the classically conformal $U(1)_{B-L}$ model, the effective potential, and comment on an IR breakdown in perturbation theory. We proceed to investigate various aspects of the FOPT, including supercooling below the QCD scale, and present results for various thermodynamic quantities including comparisons between different calculation methods. In Section III.3, we discuss the SGWB produced as a result of the first-order phase transition. This includes an updated treatment of the lifetime of the symmetry-breaking field, which has important consequences for the observed SGWB. Numerical results in Section III.2 and Section III.3 are valid in the limit where RHN masses can be treated as light (compared to the mass of the new Z' gauge boson). In Section III.4, the impact of heavy RHNs is treated. There, we provide a scan over model parameters where favorable conditions for bubble-assisted leptogenesis (BALG) [264, 286, 291, 294–296] are satisfied. Section III.5 discusses the combined SGWB from cosmic strings and bubble dynamics. We conclude in Section III.6. Additional details about renormalization group equations (RGEs) and the effective potential are included in Appendix A and B, respectively. This chapter is based on the work in [4], and the results presented here, including all plots, significant equations, and lines of argument were first reported in that paper.

Brief literature context

Sections III.2 and III.3 can be viewed as a refinement and extension of the influential papers [152, 258] on the phenomenology of the FOPT and GW production in the CCBL model. Notably, we extend beyond the parameter space considered there, improve the calculation of the effective potential, and show how an improved treatment of the lifetime of the symmetry-breaking field has a large impact on the resulting GW spectra in significant regions of parameter space. We also discuss the nature of the PT for supercooling below the QCD scale, finding agreement with another recent study [297]. Section III.4, considers the impact of heavy RHNs on the phase transition and GW production, which was not explored in [152,258]. Following recent developments on leptogenesis assisted by bubble dynamics [264,286,291,294–296], we point out that efficient BALG points to near-critical masses of RHNs (c.f. the text around Eq. (III.30) for a precise definition). We then map out parameter space with favorable conditions for BALG in the CCBL, going beyond the study of BALG in CCBL in Ref. [264], by including the effect of heavy RHNs in the effective potential (which we show is an important effect). Finally, in Section. III.5 we demonstrate that a characteristic GW signal featuring significant overlapping contributions from both cosmic strings and FOPT dynamics can be detected at upcoming GW observatories. While the idea of identifying unique GW signatures arising from the superposition of different sources is not new, concrete examples have so far (to the best of our knowledge) been limited to models involving at least two distinct symmetry-breaking scales, see for example [298–300].

III.2 Phase transition and QCD-induced effects

In addition to the SM particle content, the CCBL model introduces a $B-L$ vector boson Z', a SM-neutral $U(1)_{B-L}$-breaking complex scalar field $\Phi = \frac{1}{\sqrt{2}}(\phi + i\chi)$, and three RHNs N_i. Leptons, quarks, and Φ carry $B-L$ charge -1, $+1/3$, and -2, respectively. The tree-level scalar potential of the theory reads

$$V = \lambda_\phi(\Phi^\dagger\Phi)^2 + \lambda_H(H^\dagger H)^2 + \lambda_p(\Phi^\dagger\Phi)(H^\dagger H), \tag{III.1}$$

where H denotes the SM Higgs doublet. The absence of dimensionful parameters in the scalar potential is a result of imposing classical scale invariance. The RHNs interact via an extended Yukawa sector

$$\mathcal{L}_N = -Y_N^i \Phi \overline{N_i^c} N_i - Y_D^{ij} \overline{L_i} \widetilde{H} N_j + \text{h.c.}. \tag{III.2}$$

Without loss of generality, we have assumed Y_N to be diagonal. When Φ acquires a nonzero vev, this term dynamically generates Majorana masses. The second term on the r.h.s. of Eq. (IV.1) is the standard Yukawa interaction that generates Dirac masses upon electroweak (EW) symmetry breaking. Finally, there is kinetic mixing between the $U(1)_Y$ and $U(1)_{B-L}$ gauge fields, which is generally produced by quantum corrections even if set to zero at a certain scale. Upon diagonalizing the kinetic-mixing term, the covariant derivative takes the following form

$$D_\mu = \partial_\mu + i g_Y q_Y B_\mu + i(\widetilde{g} q_Y + g_{B-L} q_{B-L}) B'_\mu + ..., \tag{III.3}$$

where the contributions from $SU(3)_c \times SU(2)_L$ are the same as in the SM and therefore omitted for brevity. Here g_i, q_i, and B_i denote gauge couplings, gauge charges, and gauge fields, respectively, and $\widetilde{g}$ parametrizes the kinetic mixing. We will assume throughout this chapter that $\langle\phi\rangle \equiv v_{B-L} \gg \langle h \rangle \equiv v_h$. It is then a good approximation to identify B' with Z' and B with the SM hypercharge gauge field [301].

III.2.1 Effective potential

The 4D effective potential in this model can be calculated following the methods outlined in Section. II.1, and written in the following form[2]

$$V_{\text{eff}}(\phi, T) = V_{T=0} + V_{\text{T}}(\phi, T) + V_{\text{Daisy}}(\phi, T) + V_{\text{QCD}}. \tag{III.4}$$

[2] From here on, we will no longer denote the background field by ϕ_c but merely as ϕ for notational simplicity.

Here, $V_{T=0}$ is the RGE-improved effective potential in Landau gauge at zero temperature. $V_{\rm T}$ is the standard one-loop finite-temperature contribution, and $V_{\rm Daisy}$ denotes the contribution from Daisy resummation. The final term, $V_{\rm QCD}$, encodes QCD effects that are triggered if supercooling persists to temperatures below the QCD scale, and which affect Φ via the portal coupling in Eq. (III.1). Finally, in Eq. (III.4) we have implicitly assumed that the initial $B-L$ phase transition can be studied by setting $v_h = 0$ and only consider dependence on ϕ.[3] This assumption is commonly used when $\langle\phi\rangle \equiv v_{B-L} \gg \langle h\rangle \equiv v_h$ and was scrutinized in the context of a classically conformal model with extended gauge sector in [262]. There, it was shown that reducing the scalar potential to the direction of the new symmetry-breaking scalar is a reliable approximation.

In the following, we summarize the expressions for each of the contributions in Eq. (III.4). Starting with $V_{T=0}$, we note that for classically conformal models, it can be formally written in the following form [90, 112, 302, 303]

$$V_{T=0} = \frac{\lambda(t)}{4} G^4(t)\phi^4, \qquad G(t) = \exp\left\{-\int_0^t dt'\, \gamma[\lambda(t')]\right\}, \tag{III.5}$$

where $t = \log(\mu/\mu_0)$, with μ the RG scale and μ_0 an arbitrary reference scale, λ parametrizing a set of couplings, and γ denoting the anomalous dimension of the field ϕ. A variety of approximations of Eq. (III.5) have been employed in the literature. One widely used approximation, which was introduced in the seminal paper [90] and employed in many subsequent studies of GW-production in CCBL, improves the tree-level potential by including a running coupling and the wavefunction renormalization factor. We review how this construction works in Appendix B, and proceed by describing the result used by us.

The one-loop RGE improved zero-temperature contribution to $V_{\rm eff}$ in Landau gauge and the $\overline{\rm MS}$ renormalization scheme reads

$$V_{T=0}\left(\sqrt{Z_\phi(t)}\phi,\, t\right) = V_{\rm tree}\left(\sqrt{Z_\phi(t)}\phi,\, t\right) + V_{\rm CW}\left(\sqrt{Z_\phi(t)}\phi,\, t\right), \tag{III.6}$$

with

$$V_{\rm tree}(\phi,\, t) = \frac{\lambda_\phi(t)}{4}\phi^4, \tag{III.7}$$

$$\begin{aligned} V_{\rm CW}(\phi,\, t) = {} & \frac{\lambda_p^2\phi^4}{64\pi^2}\left[\log\frac{\lambda_p\phi^2}{2\mu^2} - \frac{3}{2}\right] + \frac{9\lambda_\phi^2\phi^4}{64\pi^2}\left[\log\frac{3\lambda_\phi\phi^2}{\mu^2} - \frac{3}{2}\right] + \frac{48 g_{B-L}^4\phi^4}{64\pi^2}\left[\log\frac{4g_{B-L}^2\phi^2}{\mu^2} - \frac{5}{6}\right] \\ & + \frac{\lambda_\phi^2\phi^4}{64\pi^2}\left[\log\frac{\lambda_\phi\phi^2}{\mu^2} - \frac{3}{2}\right] - \sum_{i=1}^{3}\frac{8Y_{N_i}^4\phi^4}{64\pi^2}\left[\log\frac{2Y_{N_i}^2\phi^2}{\mu^2} - \frac{3}{2}\right], \end{aligned} \tag{III.8}$$

where the wave-function renormalization is given by $Z_\phi(t) = \exp\left\{-2\int_0^t \gamma(t')\, dt'\right\}$ and the anomalous dimension γ reads [304],

$$\gamma = \frac{1}{16\pi^2}\left[2\sum_i (Y_{N_i})^2 - 12 g_{B-L}^2\right]. \tag{III.9}$$

Here $t \equiv \log\frac{\mu(\phi,T)}{v_{B-L}}$, as introduced in Section II.1, which is fixed as $\mu(\phi,\, T) = {\rm Max}[\phi,\, \pi T]$, following Ref. [173]. All couplings in Eq. (III.8) are evolved using the 1-loop RGEs listed

[3] For temperatures below the QCD scale, however, we set v_h to a nonzero value as described later in this section.

in Appendix A, although we have suppressed the explicit t dependence of couplings in Eq. (III.8) for the sake of readability. One can readily verify that this result for $V_{T=0}$ satisfies the RGE in Eq. (II.36) to one loop,

$$\mu \frac{dV_{T=0}}{d\mu} = \left(\beta_{\lambda_\phi} \frac{\partial}{\partial \lambda_\phi} - \gamma \phi \frac{\partial}{\partial \phi} \right) V_{\text{tree}} + \mu \frac{\partial V_{\text{CW}}}{\partial \mu} = 0, \tag{III.10}$$

with γ given in Eq. (III.9) and β_{λ_ϕ} in Eq. (A.9).

One can freely fix the minimum of Eq. (III.6) to be located at a given value $\phi = v_{B-L}$, by imposing

$$\left. \frac{dV_{T=0}}{d\phi} \right|_{v_{B-L}} = 0. \tag{III.11}$$

This constraint equation leads to a boundary condition for $\lambda_\phi(t)$ at $t = 0$,

$$\begin{aligned} &\lambda_\phi(0) + \frac{1}{32\pi^2} \left[\lambda_p^2(0) + 10\lambda_\phi^2(0) + 48 g_{B-L}^4(0) - 8 \sum_{i=1}^{3} Y_{N_i}^4(0) \right] + \frac{\lambda_p^2(0)}{16\pi^2} \left[\log\left(\frac{\lambda_p(0)}{2} \right) - \frac{3}{2} \right] \\ &+ \frac{9\lambda_\phi^2(0)}{16\pi^2} \left[\log\left(3\lambda_\phi(0)\right) - \frac{3}{2} \right] + \frac{48 g_{B-L}^4(0)}{16\pi^2} \left[\log\left(4 g_{B-L}^2(0)\right) - \frac{5}{6} \right] + \frac{\lambda_\phi^2(0)}{16\pi^2} \left[\log\left(\lambda_\phi(0)\right) - \frac{3}{2} \right] \\ &- \sum_{i=1}^{3} \frac{8 Y_{N_i}^4(0)}{16\pi^2} \left[\log\left(2 Y_{N_i}^2(0)\right) - \frac{3}{2} \right] \approx 0, \end{aligned} \tag{III.12}$$

where we used Eq. (III.9) and Eq. (A.9). The equation simplifies to

$$\lambda_\phi(0) \approx \frac{g_{B-L}^4(0)}{\pi^2} \left[1 - 3\log\left(4 g_{B-L}^2(0)\right) \right] - \frac{1}{2\pi^2} \sum_{i=1}^{3} Y_{N_i}^4(0) \left[1 - \log\left(2 Y_{N_i}^2(0)\right) \right], \tag{III.13}$$

after neglecting contributions from scalars, which are subleading [265]. In the limit where the right-handed neutrinos are much lighter than the Z', Eq. (III.13) reduces to a relation of the form $\lambda_\phi \sim g_{B-L}^4$. Relations of this type between the scalar coupling and the fourth power of the gauge coupling are characteristic to Coleman-Weinberg models, ensuring that 1-loop and tree-level contributions to $V_{T=0}$ are comparable in size such that radiative symmetry breaking is indeed possible, c.f. Eqs. (III.7) and (III.8). The depth of the potential at the minimum is obtained by plugging Eq. (III.13) into (III.6)-(III.8),

$$V_{T=0}^{\min} \approx -\frac{v_{B-L}^4}{16\pi^2} \left[6 g_{B-L}^4(0) - \sum_{i=1}^{3} Y_{N_i}^4(0) \right]. \tag{III.14}$$

In particular, for fixed v_{B-L} and Y_{N_i}, increasing g_{B-L} leads to a deeper potential. We will comment more on the impact of Y_{N_i} on the potential in Section III.4.

The scalar mass, m_ϕ, is given by the double derivative of $V_{T=0}$ evaluated at v_{B-L}. The result reads,

$$\begin{aligned} m_\phi^2 = \left. \frac{d^2 V_{T=0}}{d\phi^2} \right|_{\phi = v_{B-L}} &\approx -4\lambda_\phi(0) v_{B-L}^2 - \frac{\lambda_p^2(0) v_{B-L}^2}{4\pi^2} \left[\log\left(\frac{\lambda_p(0)}{2} \right) - \frac{3}{2} \right] \\ &- \frac{9\lambda_\phi^2(0) v_{B-L}^2}{16\pi^2} \left[\log\left(3\lambda_\phi(0)\right) - \frac{3}{2} \right] - \frac{48 g_{B-L}^4(0) v_{B-L}^2}{4\pi^2} \left[\log\left(4 g_{B-L}^2(0)\right) - \frac{5}{6} \right] \end{aligned}$$

$$
\begin{aligned}
&- \frac{\lambda_\phi^2(0) v_{B-L}^2}{4\pi^2}\left[\log\left(\lambda_\phi(0)\right) - \frac{3}{2}\right] + \sum_{i=1}^{3} \frac{8 Y_{N_i}^4(0) v_{B-L}^2}{4\pi^2}\left[\log\left(2Y_{N_i}^2(0)\right) - \frac{3}{2}\right] \\
&\approx \frac{v_{B-L}^2}{\pi^2}\left[6 g_{B-L}^4 - \sum_{i=1}^{3} Y_{N_i}^4(0)\right]. \qquad \text{(III.15)}
\end{aligned}
$$

By inspecting the result, it is seen that for $\left(\sum_{i=1}^{3} Y_{N_i}^4\right) > 6g_{B-L}^4$ the scalar mass is tachyonic and the potential does not have a stable minimum at $\phi = v_{B-L}$. This implies that a mass hierarchy $M_{Z'} \gtrsim M_{N_i}$ is a requirement to ensure vacuum stability. [4]

Finally, to evaluate the various couplings entering V_{eff}, we simultaneously solve all the RGE equations for the couplings listed in Eqs. (A.1)-(A.10). The boundary conditions for SM couplings are set at the Z pole, $t = \log \frac{m_Z}{v_{B-L}}$, to match their measured values [305]. The boundary condition for λ_ϕ is determined by Eq. (III.13), while the remaining BSM couplings are fixed as follows

$$\widetilde{g}(0) = -0.5, \qquad \text{(III.16)}$$

$$\lambda_p\left(\log \frac{m_Z}{v_{B-L}}\right) = \mu_h \frac{v_{h,\text{SM}}^2}{v_{B-L}^2}, \qquad \text{(III.17)}$$

$$Y_{N_i}(0) = \frac{M_{N_i}}{\sqrt{2} v_{B-L}}, \qquad \text{(III.18)}$$

$$g_{B-L}(0) = \frac{M_{Z'}}{2 v_{B-L}}, \qquad \text{(III.19)}$$

where μ_h denotes the coefficient of the quadratic term in the SM Higgs potential and $v_{h,\text{SM}} \approx 246$ GeV. Note that Eq. (III.17) ensures that the SM Higgs potential is produced dynamically through $B-L$ breaking. We ignore Y_D in the following, as it has negligible effects on the phase-transition dynamics. The choice $\widetilde{g} = -0.5$ is made following [152, 258], motivated by the observation that it can ensure EW vacuum stability to the Planck scale [258]. We are then left with the following free parameters: the breaking scale v_{B-L}, the heavy gauge-boson mass $M_{Z'}$, and the three RHN masses M_{N_i}. For simplicity, we will set $M_{N_1} = M_{N_2} = M_{N_3} \equiv M_N$ in the following.

Finite temperature corrections

The leading thermal correction to the effective potential follows directly from Eqs. (II.40) and (III.1)-(III.3),

$$
\begin{aligned}
V_T(\phi, T, t) = &\sum_{i=1}^{3} \frac{(-2)T^4}{2\pi^2} J_F\left(\frac{M_{N_i}^2(\phi)}{T^2}\right) + \frac{4T^4}{2\pi^2} J_B\left(\frac{m_{h_i}^2(\phi)}{T^2}\right) + \frac{T^4}{2\pi^2} J_B\left(\frac{m_w^2(\phi)}{T^2}\right) \\
&+ \frac{3T^4}{2\pi^2} J_B\left(\frac{M_{Z'}^2(\phi)}{T^2}\right) + \frac{T^4}{2\pi^2} J_B\left(\frac{m_\chi^2(\phi)}{T^2}\right), \qquad \text{(III.20)}
\end{aligned}
$$

where we have introduced $\overline{\text{MS}}$ field-dependent masses

$$m_{h_i}^2(\phi) \equiv \frac{\lambda_p \phi^2}{2}, \qquad m_w^2(\phi) \equiv 3\lambda_\phi \phi^2, \qquad m_\chi^2(\phi) \equiv \lambda_\phi \phi^2, \qquad \text{(III.21)}$$

[4] Equivalently, the same conclusion can be drawn as follows: The equation for the minimum of the potential, Eq. (B.3), together with the RG evolution of λ_ϕ governed by Eq. (A.9) imply that $\phi = v_{B-L}$ is turned into a maximum instead of a minimum if $\left(\sum_{i=1}^{3} Y_{N_i}^4\right) > 6g_{B-L}^4$. The scalar coupling λ_ϕ then runs to negative values at higher scales rendering the potential unbounded from below.

$$M_{Z'}(\phi) \equiv 2g_{B-L}\phi, \qquad M_i(\phi) \equiv Y_N^i \phi\sqrt{2}. \tag{III.22}$$

For $M_{N_i} \ll M_{Z'}$, the thermal contribution in Eq. (III.20) is typically dominated by the gauge boson. This statement can be motivated as follows. The CW relation $\lambda_\phi \sim g_{B-L}^4$ implies that g_{B-L} is larger than λ_ϕ for $g_{B-L} < 1$, which is the regime considered by us. The portal coupling scales as $\lambda_p \sim \frac{v_h^2}{v_{B-L}^2}$ at the EW scale, c.f. Eq. (III.17), and although RGE effects generically increase its value at higher scales, it generally remains much smaller than g_{B-L}. Meanwhile, if M_{N_i} and $M_{Z'}$ are comparable, then RHNs and Z' have comparable impact on the thermal potential. We will consider this scenario and the associated PT dynamics in Section III.4.1.

The Daisy-resummed contribution to the effective potential follows directly from Eq. (II.46),

$$\begin{aligned} V_{\text{Daisy}}(\phi, T, t) = &-\frac{4T}{12\pi}\left[(m_{h_i}^2(\phi)+\Pi_{h_i})^{\frac{3}{2}} - m_{h_i}^3(\phi)\right] - \frac{T}{12\pi}\left[(m_w^2(\phi)+\Pi_\phi)^{\frac{3}{2}} - m_w^3(\phi)\right] \\ &- \frac{T}{12\pi}\left[(m_\chi^2(\phi)+\Pi_\chi)^{\frac{3}{2}} - m_\chi^3(\phi)\right] - \frac{T}{12\pi}\left[(M_{Z'}^2(\phi)+\Pi_{Z'})^{\frac{3}{2}} - M_{Z'}^3(\phi)\right], \end{aligned} \tag{III.23}$$

The thermal masses are calculated following [306],

$$\Pi_{h_i} = \frac{T^2}{4}\left[\frac{\lambda_p}{3} + \frac{g^2+\widetilde{g}^2}{4} + y_t^2 + 2\lambda_H + \frac{3g_2^2+g^2}{4}\right], \tag{III.24}$$

$$\Pi_\phi = \Pi_\chi = \frac{T^2}{6}\left[\lambda_p + 2\lambda_\phi + 6g_{B-L}^2 + \sum_{i=1}^{3}\left(Y_M^i\right)^2\right], \tag{III.25}$$

$$\Pi_{Z'} = T^2\left[4g_{B-L}^2 + \frac{8}{3}g_{B-L}\widetilde{g} + \frac{11}{6}\widetilde{g}^2\right], \tag{III.26}$$

where y_t is the top-yukawa coupling, g is the SM hypercharge gauge coupling, and g_2 is the $SU(2)_L$ gauge coupling. As consistency checks, we have verified that the last three terms in Eq. (III.24) are in agreement with the known SM result. The result in Eq. (III.25) can also be obtained by substituting the high-temperature expansions in Eqs. (II.41) and (II.42) into Eq. (III.20) and then evaluate the double-derivative w.r.t. ϕ, which yields the same result. Finally, the result in Eq. (III.26) is consistent with the general result for mass corrections of longitudinal Abelian gauge bosons with associated gauge coupling g [307],

$$\Pi_{U(1)} = g^2T^2\left[\frac{1}{6}\sum_s Q_s^2 + \frac{1}{12}\sum_f Q_f^2\right], \tag{III.27}$$

where the sums run over all scalar (s) and fermionic (f) DOFs with charge Q_s and Q_f, respectively, under the $U(1)$ gauge symmetry. To the best of our knowledge, the last two terms in (III.26) were either neglected or missed in analyses of CCBL before our study Ref. [4]. The impact of these terms on the phase-transition dynamics is discussed in Section III.2.5.

QCD effects

Classically conformal models can realize extreme supercooling, where the universe undergoes a period of thermal inflation as a result of its energy budget being dominated by ΔV_{eff}. If the period of thermal inflation proceeds over a significant number of e-folds, the temperature of the thermal plasma may drop to the QCD scale, triggering chiral symmetry breaking (χSB). Once quark condensates form, classical scale invariance is broken. The formation of the top chiral condensate induces a linear term in the SM Higgs potential through the SM quark-Yukawa sector, which generates a nonzero vev for the SM Higgs $\langle h\rangle \equiv v_{\rm QCD} = \mathcal{O}(0.1\ \text{GeV})$ [228, 266, 297, 308–313]. As a result, the portal coupling in Eq. (III.1) generates a quadratic contribution to the effective potential along the ϕ-direction, which can be modeled as [309, 310]

$$V_{\rm QCD}\left(\sqrt{Z_\phi}\phi,\, T,\, t\right) = \frac{\lambda_p(t) v_{\rm QCD}^2 Z_\phi \phi^2}{4}\Theta(T_{\rm QCD}-T). \tag{III.28}$$

Here Θ denotes the Heaviside step function, and we take $v_{\rm QCD} = T_{\rm QCD} = 0.1$ GeV in our analysis [258].

Some final comments about Eq. (III.28) are in order. First, both the strong gauge coupling and the top yukawa coupling become nonperturbative at $\mu \sim \Lambda_{\rm QCD}$, resulting in the breakdown of the coupled system of 1-loop RGEs and perturbative predictability. A proper treatment of this issue would either require a fully nonperturbative calculation or matching to a low-energy EFT of QCD, both of which are beyond the scope of this work. Instead, we will stop evolving the couplings in the nonperturbative region $\mu \lesssim \Lambda_{\rm QCD}$ and use their values slightly above $\Lambda_{\rm QCD}$. A second point is that the value of $v_{\rm QCD}$ employed in Eq. (III.28) should be understood as a rough approximation. A more accurate treatment would again require nonperturbative methods, for example lattice QCD calculations, as the formation of the quark condensate is governed by strongly-coupled dynamics.

III.2.2 IR breakdown of perturbation theory

Before we proceed to study FOPT dynamics in this model, it is interesting to note the following feature: Perturbation theory breaks down in the IR for CCBL. This observation was, to the best of our knowledge, first made in [303], but subsequently overlooked in many phenomenological studies. The quartic coupling λ_ϕ, whose value is fixed at $\mu = v_{B-L}$ via Eq. (III.13), evolves according to the one-loop renormalization group equation (RGE):

$$16\pi^2\frac{d\lambda_\phi}{dt} = 16\left(6g_{B-L}^4 - \sum_i Y_{N_i}^4\right) + 8\lambda_\phi\left(-6g_{B-L}^2 + \sum_i Y_{N_i}^2\right) + 20\lambda_\phi^2 + 2\lambda_p^2, \tag{III.29}$$

and runs to large negative values in the IR, reaching a singular point at $\Lambda_{\rm IR}$. The value of the IR pole, $\Lambda_{\rm IR}$, increases with larger g_{B-L} (while keeping other couplings fixed), but can be lowered by decreasing $-6g_{B-L}^4 + \sum_i Y_{N_i}^4$, effectively approaching the region where the potential becomes unbounded from below (cf. Eq. (III.15)). This motivates the definition

$$M_N^{\rm cr.} \equiv \frac{M_{Z'}}{2^{1/4}}, \tag{III.30}$$

representing the value of M_N where $(-6g_{B-L}^4 + \sum_i Y_{N_i}^4) = 0$ for three degenerate right-handed neutrinos. In Fig. III.1, the region below each curve (corresponding to different values of M_N as indicated in the figure) indicates where $|\lambda_\phi| < 4\pi$ down to the QCD scale. Larger $M_{Z'}$ values require smaller maximal g_{B-L} to compensate for running over extended scales. The figure also demonstrates that as M_N approaches $M_N^{\rm cr.}$, the perturbativity issue becomes less severe, as evident from the first term in Eq. (III.29).

The behavior of λ_ϕ falls into three distinct categories:

1. λ_ϕ remains perturbative down to $\mu = \Lambda_{\rm QCD}$, where the theory is rendered nonperturbative by the IR behavior of QCD.

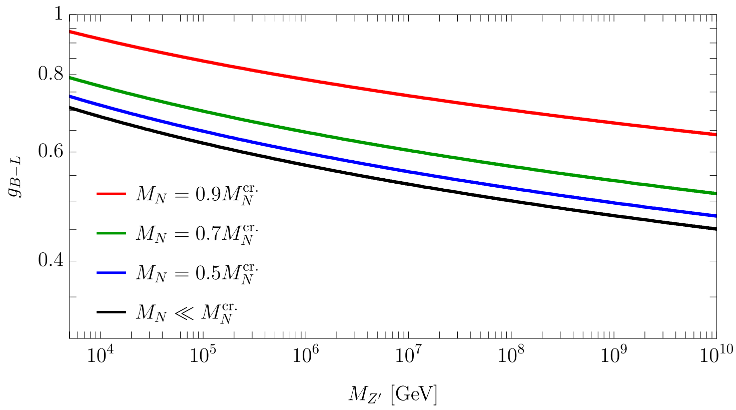

Figure III.1: The curves show where in parameter space the perturbativity of λ_ϕ breaks down at the QCD scale, for different choices of M_N as indicated by the labels. Perturbativity breaks down before (after) the QCD scale above (below) the curves [4].

2. λ_ϕ becomes nonperturbative at a scale $T_* > \mu > \Lambda_{\text{QCD}}$. The calculation of the phase transition, where $\mu = \text{Max}[\phi, \pi T]$, remains under perturbative control.
3. λ_ϕ becomes nonperturbative at a scale $m_\phi > \mu > T_*$, rendering a breakdown of the perturbative 1-loop treatment of the phase transition dynamics.

As discussed in Section III.4.2 in the context of BALG and its associated gravitational wave signatures, understanding regimes where perturbativity breaks down above Λ_{QCD} can be phenomenologically relevant.

III.2.3 Phase transition

With the effective potential in hand, we are equipped to investigate the first-order phase transition by computing the relevant quantities outlined in Section II.2.1. Our analysis extends previous studies in two key respects. First, we explore a broader region of parameter space, and second, we provide a more detailed discussion of QCD-induced transitions [152]. In particular, we consider $B - L$ breaking scales up to 10^{10} GeV and chart the parameter region where QCD effects may catalyze the transition.

However, as noted in the preceding section, a precise treatment of QCD-induced effects would require a nonperturbative analysis. Consequently, our numerical results in the regime $T_* < T_{\text{QCD}}$ should be regarded as qualitative. Still, we highlight several robust features of this regime that can be understood without detailed knowledge of strong dynamics.

Unless otherwise specified, we will assume $M_N \ll M_{Z'}$ throughout, deferring the discussion of $M_N \sim M_{Z'}$ to Section III.4.

III.2.4 The phase transition below and above T_{QCD}

To provide an overview of the various regimes of the model, we start by pointing out Fig. III.2. A detailed discussion of how the figure was obtained is deferred to later in this section where the behavior of R_* and R_0 are considered. The orange region is where QCD effects catalyze the first-order phase transition. In terms of the gauge coupling g_{B-L}, the region covers $0.01 \lesssim g_{B-L} \lesssim 0.3$. In terms of $M_{Z'}$, the region extends to $M_{Z'} \approx 1.5 \cdot 10^8$ GeV. For heavier Z', QCD-effects are insufficient to catalyze an escape from extreme supercooling, and dynamics beyond bubbles would be required, as e.g. outlined in [314],

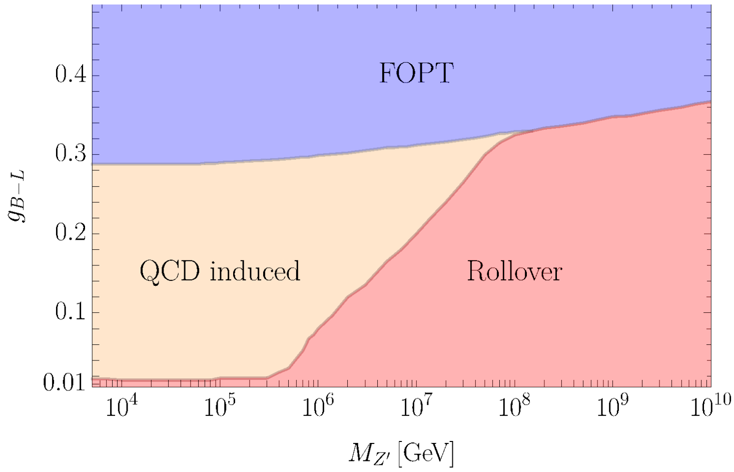

Figure III.2: Overview of parameter space showing where the phase transition is expected to be of first order and complete successfully above (below) the QCD temperature in blue (orange), and where it is expected to be a rollover (orange) [4].

which we will not discuss further. The region where a FOPT takes place above $T_{\rm QCD}$ is shown in blue. Finally, the region in red shows where the transition is expected to be a so-called rollover [297]. Unlike a FOPT, where the field transitions over the barrier due to thermal fluctuations, a rollover occurs when the field rolls down the potential due to classical equations of motion. This happens if the field remains in the false vacuum until the barrier vanishes, and then relaxes to the global minimum.

In the following, we will consider QCD effects on the phase transition. It has been well understood that the QCD-induced contribution in Eq. (III.28) to the effective potential efficiently counteracts the thermal barrier and drives the bounce action S_3/T to zero [4, 258]. We will consider two qualitative features arising at $T \lesssim T_{\rm QCD}$ as a consequence of this characteristic behavior [4]:

(i) When determining R_*, the calculation can become highly sensitive to small uncertainties in T_*. This can lead to large uncertainties in the prediction of the resulting GW spectrum.

(ii) The time scale governing the QCD-induced exit from supercooling can be so short that the phase transition effectively shifts from a first-order transition to a rollover [297]. We provide a perspective on how to capture this change in dynamics by comparing the characteristic bubble radii at the times of percolation and production.

To illustrate point (i), consider the impact of varying the gauge coupling g_{B-L} for a fixed value of $M_{Z'}$. A reduction in g_{B-L} leads to an increase in the bounce action S_3/T, which suppresses the transition rate. This trend is shown in Fig. III.3 for $M_{Z'} = 5 \cdot 10^7$ GeV and gauge couplings $g_{B-L} = 0.3$ (blue), $g_{B-L} = 0.32$ (red), $g_{B-L} = 0.34$ (green). In the case of $g_{B-L} = 0.34$, Eq. (II.57) is satisfied well above the QCD scale. In contrast, for smaller couplings, the transition rate is more suppressed. Thus, for $g_{B-L} = 0.3$ and $g_{B-L} = 0.32$, the percolation condition is only met after the QCD-induced drop in S_3/T.

For the presented benchmark points, the condition in Eq. (II.58) is not met at T_* but only at lower temperatures. On each curve in Fig. III.3, the two points indicate different key temperatures: the rightmost point marks where Eq. (II.57) is satisfied, while the leftmost point shows the first occurrence of when the percolation criterion defined in Eq. (II.58) is met. Because there is a nonzero gap between these two points, uncertainty arises in pinpointing the exact temperature at which the phase transition completes. This uncertainty becomes significant since the magnitude of the bounce action can change dramatically over the interval between the two points—as illustrated by the red benchmark point—leading to a correspondingly large uncertainty in the calculation of R_* in Eq. (II.61). Specifically, the integrand on the right-hand side of Eq. (II.61) is exponentially sensitive to a decrease in S_3/T through $\Gamma(T)$, whereas its sensitivity to changes in $I(T)$ is limited by Eq. (II.58), and the Hubble parameter is approximately constant. For the red benchmark point, the calculation yields $R_*H_* \approx 6$ when T_* is determined by the rightmost point and $R_*H_* \approx 0.1$ when determined by the leftmost point. In comparison, for the blue benchmark point, the corresponding values are $R_*H_* \approx 0.04$ and $R_*H_* \approx 0.03$, respectively.

The third panel in Fig. III.3 shows how the uncertainties in R_* translates into uncertainties in the resulting GW spectra, which are computed as described in Section II.2.1. The criterion in Eq. (II.58) is satisfied for the solid curves and not satisfied for the dashed ones. As shown, even a slight uncertainty in T_* for the red benchmark point results in uncertainties spanning many orders of magnitude in the GW spectra. For reference, the spectrum corresponding to $R_*H_* = 1$ is included as the red dotted curve. In contrast, for the blue benchmark point the effect is less pronounced, leading only to $\mathcal{O}(1)$ uncertainties in both the peak amplitude and the frequency.

Keeping $M_{Z'}$ fixed and reducing the value of g_{B-L} in the regime where $T_* < T_{\rm QCD}$, results in a bounce action that decreases very sharply around the temperature $T_{\rm roll}$ — the temperature at which S_3/T approaches zero — while reaching extremely high values for temperatures just above $T_{\rm roll}$. Consequently, the transition rate remains negligibly small except within a very narrow temperature window, during which S_3/T rapidly falls from very high values to zero. This behavior is illustrated in Fig. III.4 for $M_{Z'} = 10^5$ GeV, with $g_{B-L} = 0.2$ (green), $g_{B-L} = 0.1$ (red), $g_{B-L} = 0.03$ (blue), where the dots mark the respective percolation temperatures. As observed in the figure, for sufficiently small values of g_{B-L}, S_3/T begins to resemble a step function. A similar observation was made in Ref. [297], where the authors argue that for small enough gauge couplings one enters a regime in which thermal transitioning is too inefficient to convert the entire false vacuum (which initially fills the universe) before S_3/T vanishes. In this scenario, if bubble nucleation becomes ineffective, the scalar field remains in the false vacuum until the thermal barrier between the two vacua disappears, allowing it to roll down to the true vacuum configuration.

Physically, reducing the gauge coupling while keeping $M_{Z'}$ fixed makes the first-order phase transition (FOPT) occur more quickly. Equivalently, many bubbles are nucleated within a single Hubble volume in a short time interval, resulting in smaller average bubble radii at the time of percolation. In the regime where $T_* < T_{\rm QCD}$, lowering g_{B-L} leads to reduced values of both R_*H_* and R_*/R_0, where R_0 is a measure of the average bubble size at the time of nucleation, c.f. the discussion around Eq. (II.62). If the ratio R_*/R_0 becomes of order one, then the first-order phase transition description ceases to be valid. We therefore use R_*/R_0 as a measure to determine the region of parameter space where the transition shifts from being first order to a rollover.

We have now assembled all the necessary ingredients to discuss how Fig. III.2 was obtained. By employing $R_*/R_0 < 10$ as a measure of when the FOPT description breaks down, we obtained the boundary to the red region in Fig. III.2. For comparison, the values of $(R_*H_*,\, R_*/R_0)$ for the benchmark points shown in Fig. III.4 are $(3 \cdot 10^{-5},\, 10^2)$ (blue), $(4 \cdot 10^{-4}, 2 \cdot 10^3)$ (red), $(5 \cdot 10^{-3}, 2 \cdot 10^4)$ (green). The boundary between the blue and the orange regions in Fig III.2 was obtained by requiring that both Eq. (II.57) and (II.58) be

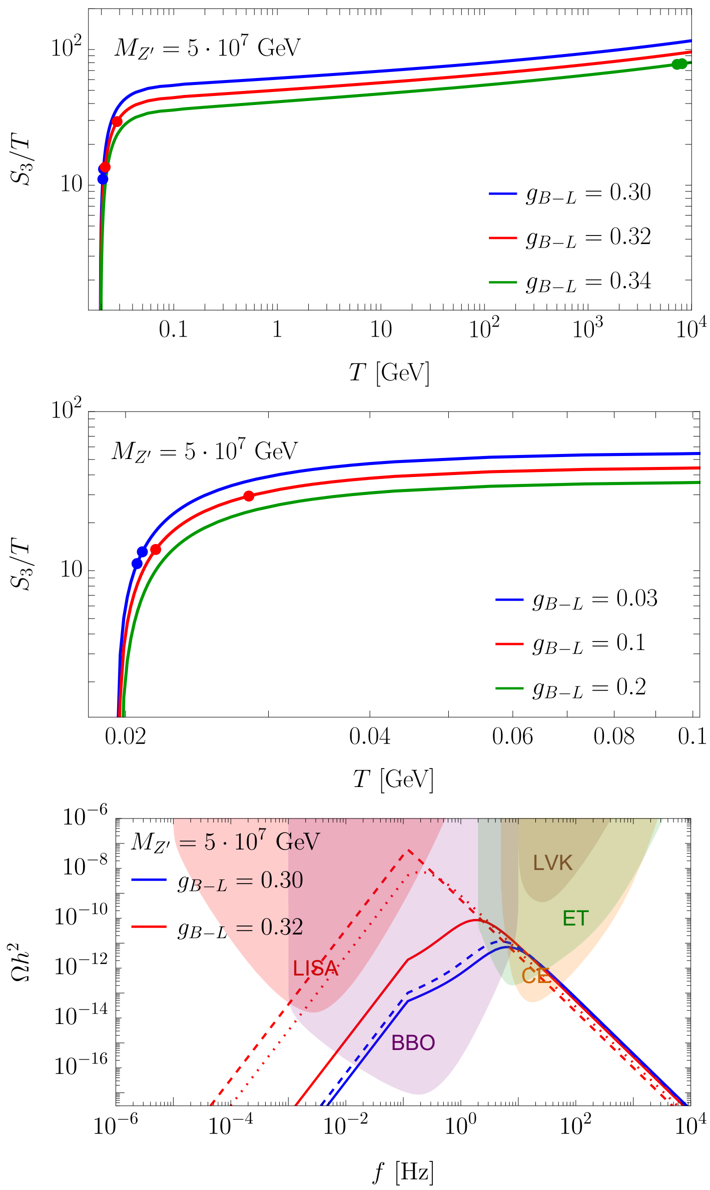

Figure III.3: Top: Evolution of the bounce action S_3/T for $M_{Z'} = 5 \cdot 10^7$ GeV and $g_{B-L} = 0.3$ (blue), $g_{B-L} = 0.32$ (red), $g_{B-L} = 0.34$ (green). The significant change and eventual vanishing of S_3/T for $T < T_{\rm QCD}$ is induced by the QCD-contribution in Eq. (III.28). The pair of dots indicate the temperature at which Eq. (II.57) is satisfied and at which Eq. (II.58) is first satisfied. Middle: A zoom-in view of the top panel in the region $T < T_{\rm QCD}$. Bottom: GW spectra corresponding to the pairs of points shown in the first two panels. The criterion in Eq. (II.58) is (un)satisfied for solid (dashed) spectra. For reference, we have included the red-dashed spectra corresponding to $R_* H_* = 1$, see text for details [4].

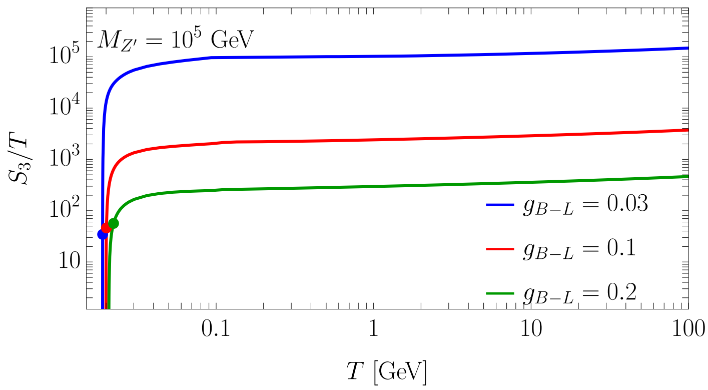

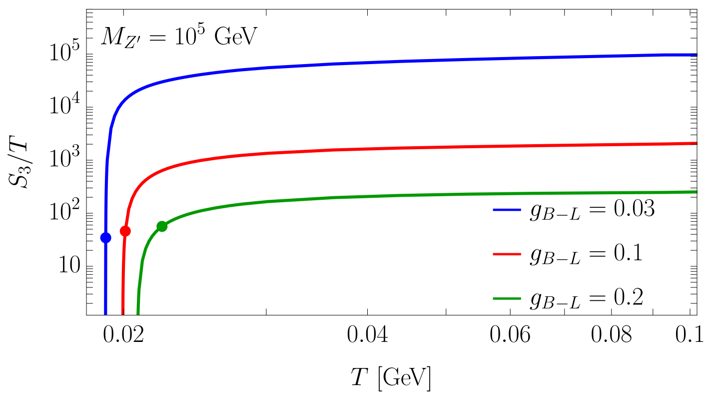

Figure III.4: Top: Evolution of the bounce action S_3/T for $M_{Z'} = 10^5$ GeV and $g_{B-L} = 0.03$ (blue), $g_{B-L} = 0.1$ (red), $g_{B-L} = 0.2$ (green). The dots indicate the percolation temperature. Bottom: A zoom-in view of the left panel in the region $T < T_{\rm QCD}$ [4].

satisfied above $T_{\rm QCD}$ in the blue region.

QCD-induced FOPT: Simplified arguments and parametric understanding

So far, our analysis of QCD effects on the first-order phase transition (FOPT) has been entirely numerical. In the following, we provide simple analytical estimates and illustrative numerical examples to elucidate how QCD dynamics affect the transition rate Γ, to sharpen our understanding of QCD's impact and limitations as a catalyst of FOPTs.

We begin with Fig. III.5, which depicts $\Gamma(T)/H^4(T)$ as a function of temperature. The upper panel corresponds to $M_{Z'} = 10^5$ GeV, and the lower panel to $M_{Z'} = 10^9$ GeV. In the upper panel, QCD dynamics enhances the nucleation rate per Hubble volume and Hubble time, $\Gamma(T)/H^4(T)$, by many orders of magnitude above unity before the rollover temperature is reached (i.e., the termination point of each curve). For low values of the gauge coupling—as illustrated by the orange, green, and blue curves—the nucleation rate remains extremely suppressed up until just moments before the potential barrier vanishes. This behavior implies that the FOPT occurs over a very short time scale. Moreover, the effect becomes progressively more pronounced by reducing g_{B-L} further and further.

In contrast, the lower panel—which shows $\Gamma(T)/H^4(T)$ for $M_{Z'} = 10^9$ GeV and selected values of g_{B-L}—reveals that QCD effects are insufficient to enhance $\Gamma(T)/H^4(T)$ above unity for $M_{Z'} = 10^9$. In this case, either bubble nucleation catalyzes the transition at temperatures several orders of magnitude above $T_{\rm QCD}$ (as seen in the red and orange curves) or the transition cannot complete via bubble nucleation at all (as indicated by the green and blue curves).

To gain simple parametric intuition about how QCD effects influence the nucleation rate, consider the regime where the temperature approaches $T_{\rm roll}$ from above. In this limit, the nucleation rate behaves parametrically as

$$\left.\frac{\Gamma}{H^4}\right|_{T\approx T_{\rm roll}^+} \sim \frac{T_{\rm roll}^4}{H^4}, \tag{III.31}$$

with

$$H^4 \approx \frac{(\Delta V)^2}{9M_P^4}, \qquad \Delta V \approx \frac{3M_{Z'}^4}{128\pi^2}, \tag{III.32}$$

where we have used Eqs. (III.14) and (II.48). Combining these expressions and setting $T_{\rm roll} = \mathcal{O}\,(0.01\text{ GeV})$, one obtains the parametric estimate

$$\left.\frac{\Gamma}{H^4}\right|_{T\approx T_{\rm roll}^+} \sim \left(\frac{M_P \cdot 1\text{ GeV}}{M_{Z'}^2}\right)^4. \tag{III.33}$$

In particular, setting $M_{Z'} = 10^5$ GeV yields an estimate that agrees qualitatively with the value observed in the upper panel in Fig. III.5. It also suggests that QCD effects are insufficient to provide nucleation rate of order unity for $M_{Z'} \gtrsim 10^9$ GeV, which is consistent with the behavior shown in the lower panel in Fig. III.5.

It is crucial to note that $\Gamma(T)/H^4(T) \gtrsim 1$ is a necessary but not sufficient condition for the phase transition to complete. The orange region in Fig. III.2, representing FOPT completion below $T_{\rm QCD}$, is determined by requiring that also Eqs. (II.57) and (II.58) should be satisfied. Eq. (II.58) provides a considerably stronger constraint than simply requiring a unit nucleation rate, thus imposing a more stringent upper bound on $M_{Z'}$ for QCD-induced FOPT completion. Therefore, Eq. (III.33) approaching unity should be interpreted as a qualitative, rather than precise, upper bound on $M_{Z'}$. The full numerical analysis underlying Fig. III.2, which incorporates the constraints from Eqs. (II.57) and (II.58), reveals an upper bound on $M_{Z'}$ that is nearly an order of magnitude lower than the simple estimate based on $\Gamma(T)/H^4(T) \sim 1$.

Thermodynamic quantities across parameter space

Next, we extend the scope of our discussion from focusing on aspects of QCD-induced FOPTs to include regions of parameter space where $T_* > T_{\rm QCD}$. To this end, numerical results of thermodynamic quantities in the $M_{Z'} - g_{B-L}$ plane will be shown.

Figure III.6 displays the following quantities: T_* (top left), the ratio T_*/T_n (top middle), the FOPT strength α (top right), the ratio α/α_∞ (bottom left), and the bubble collisions efficiency factor $\kappa_{\rm col}$ (bottom right) over large regions of parameter space. In the top left panel, one observes that reducing the gauge coupling at fixed $M_{Z'}$ leads to lower percolation temperatures. The top middle panel demonstrates that in the QCD-induced regime, the nucleation temperature T_n is very close to the percolation temperature T_*, whereas in scenarios where supercooling ends slightly above $T_{\rm QCD}$, these temperatures may differ by a factor of a few. This confirms the common lore that T_n is not always an accurate indicator for the completion of a strongly supercooled FOPT [137]. The top right panel reveals that the FOPT is strongest in the QCD-induced regime, in agreement with the findings of [152]. The lower left panel in Fig. III.6 displays the ratio $\alpha > \alpha_\infty$ across the $M_{Z'} - g_{B-L}$ plane, showing that the ratio becomes approximately one on the boundary to

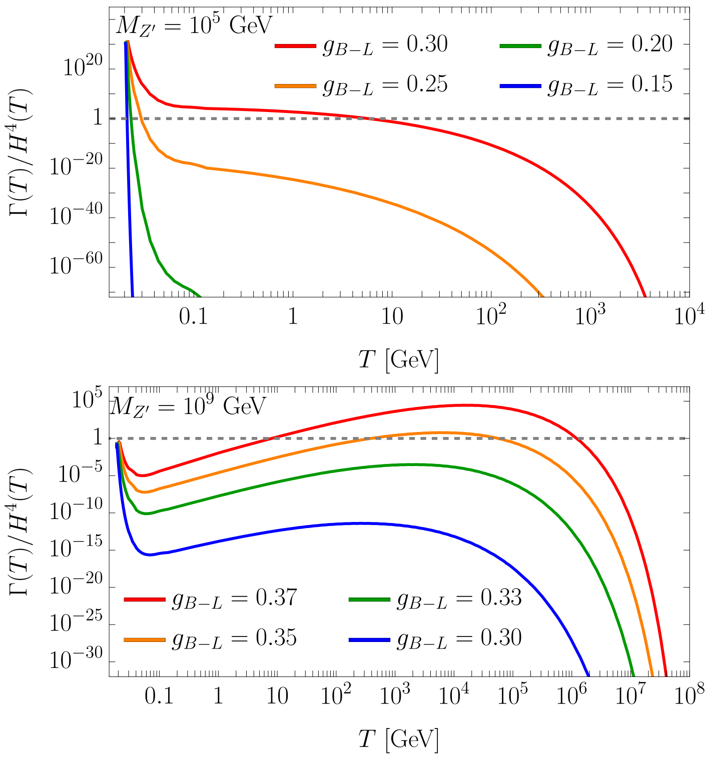

Figure III.5: Bubble-nucleation rate Γ/H^4 for various choices of gauge couplings and $M_{Z'} = 10^5$ GeV ($M_{Z'} = 10^9$ GeV) shown in the upper (lower) panel. The dashed gray line shows $\Gamma/H^4 = 1$, which indicates the nucleation temperature, see text for details [4].

the upper gray region. As mentioned in Section. (II.2.1), we use $\alpha \approx \alpha_\infty$ as a diagnostic to determine the region where the assumption $v_w \approx 1$ is expected to break down. Finally, as discussed in Section II.2.1, when $\widetilde{\gamma}_* < \gamma_{\rm eq}$, a large fraction of the vacuum energy is used to accelerate the bubble walls, making bubble collisions the dominant source of gravitational waves. The region of parameter space where this condition is satisfied corresponds to the red area in the left panel of Fig. III.6. Once a terminal velocity is reached, corresponding to $\widetilde{\gamma}_* > \gamma_{\rm eq}$, the fraction of the total released energy going into the bubble wall decreases rapidly and instead goes predominantly into kinetic and thermal energy in the plasma. In this regime, plasma contributions become the primary source of gravitational waves.

Figure III.7 presents contours of the quantities $R_* H_*$ (left panel) and R_*/R_0 (right panel) across the $M_{Z'} - g_{B-L}$ plane. The left panel illustrates that $R_* H_*$ reaches its maximum when supercooling terminates near the QCD phase transition, as highlighted by the red band in the center. Moving downward in the plot, QCD dynamics cause $R_* H_*$ to decrease, while moving upward leads to smaller values due to reduced supercooling. The right panel shows that when the phase transition is triggered by QCD effects, the ratio R_*/R_0 undergoes a dramatic change, signaling that QCD dynamics is significantly accelerating the phase transition.

III.2.5 Sensitivity to running couplings and thermal masses

As mentioned in Section III.2, our treatment of the effective potential differs from that of some previous works on phase-transition dynamics in the classically conformal $B-L$ model [152, 258, 264]. The following discussion examines the sensitivity of the percolation

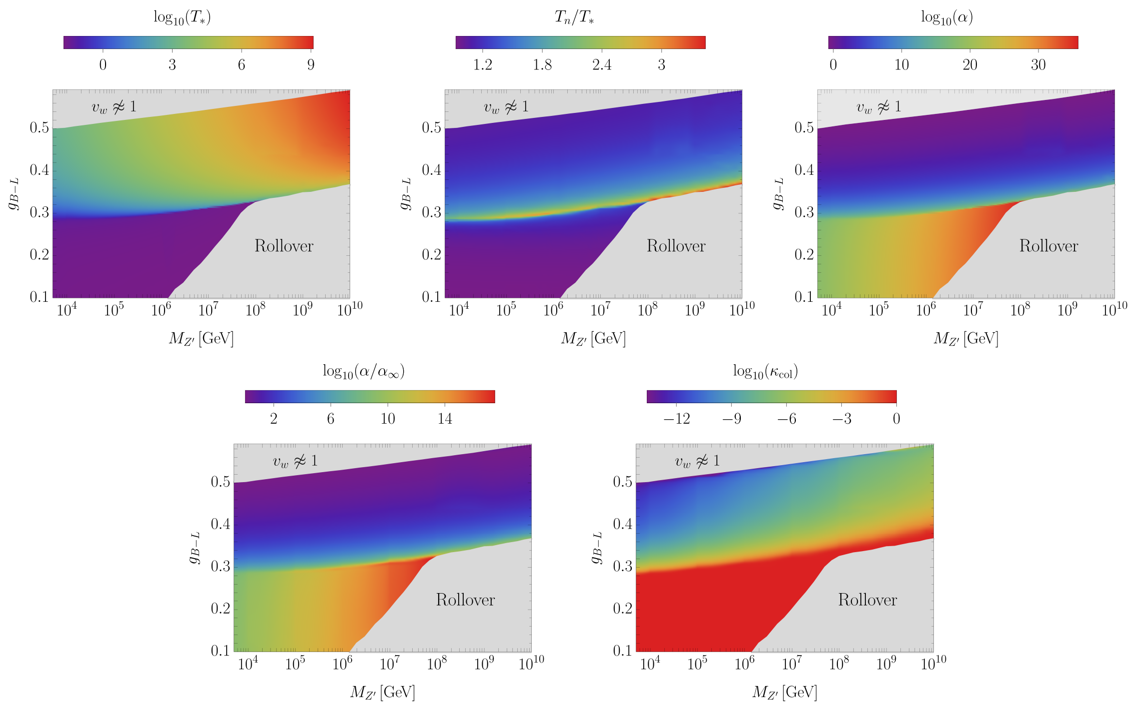

Figure III.6: $M_{Z'} - g_{B-L}$ planes showing T_* (top left), T_*/T_n (top middle), α (top right), α/α_∞ (bottom left), and $\kappa_{\rm col}$ (bottom right). The upper gray region shows where our assumption $v_w \approx 1$ becomes questionable, and the lower-gray region where the transition is expected to turn into a crossover [4].

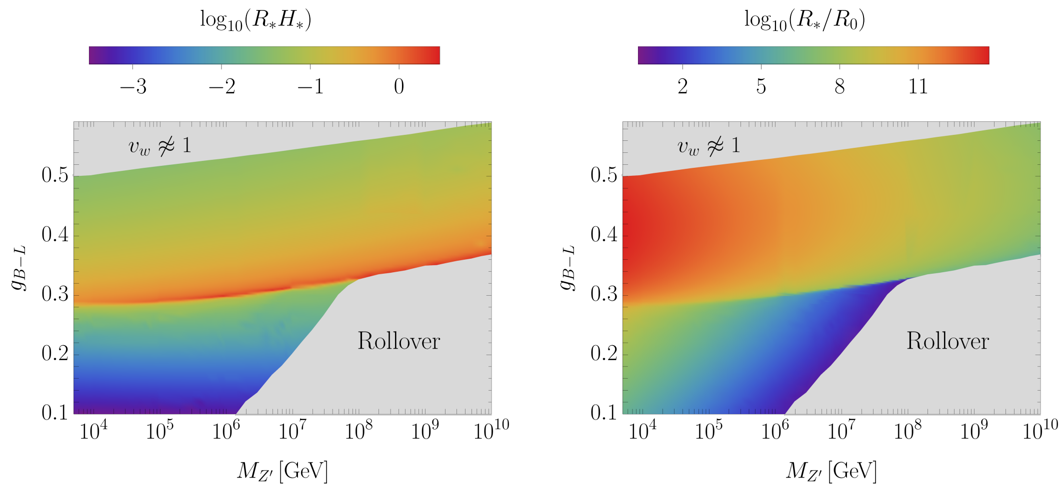

Figure III.7: $M_{Z'} - g_{B-L}$ planes showing R_*H_* (left) and R_*/R_0 (right). The gray regions are explained in Fig. III.6 [4].

temperature and the onset of a QCD-triggered transition to the specifics of the effective potential description and calculation. We will also analyze the resulting impact on the transition strength α and the characteristic bubble size $R_* H_*$.

For clarity, we consider four distinct approaches to calculating the effective potential [4]:

- **Scenario 1 (S1):** This scenario, adopted throughout this chapter, utilizes the effective potential presented in Section III.2.1 with the zero-temperature potential given by Eq. (III.6). All couplings run and are evaluated at the renormalization scale $\mu = \text{Max}[\phi, \pi T]$, as advocated in, e.g., Ref [173].
- **Scenario 2 (S2):** Here, only the couplings within the $T = 0$ part of the effective potential run. The couplings contributing to the finite-temperature corrections are held fixed. This scenario allows us to isolate the impact of running couplings within the finite-temperature contributions.
- **Scenario 3 (S3):** This scenario treats the effective potential following the approach of Refs. [152, 258]:

$$V_{\text{eff}} = \frac{\lambda_\phi(t)}{4}\phi^4 + \frac{T^4}{2\pi^2}\sum_j k_j J_T\left(m_j(\phi)^2 + \Pi_j(T)\right) + \frac{\lambda_p(t) v_{\text{QCD}}^2 \phi^2}{4}\Theta\left(T_{\text{QCD}} - T\right), \tag{III.34}$$

where the sum runs over the RHNs, the $B-L$ gauge boson, ϕ and χ.[5] The following expressions for the thermal masses are used [152, 258],

$$\Pi_\phi = \Pi_\chi = \frac{T^2}{6}\left[2\lambda_\phi + 6g_{B-L}^2 + \sum_{i=1}^{3}\left(Y_M^i\right)^2\right], \qquad \Pi_{Z'} = 4g_{B-L}^2 T^2, \tag{III.35}$$

which should be contrasted with the thermal masses in Eqs. (III.24)-(III.26) employed in S1 and S2. Only the couplings λ_ϕ and λ_p run, and they are evaluated at the scale set by the scalar field $\mu = \phi$.
- **Scenario 4 (S4):** This scenario builds upon S3 by incorporating corrections to the Z' thermal mass due to nonzero $\widetilde{g}$,

$$\Pi_{Z'} = T^2\left[4g_{B-L}^2 + \frac{8}{3}g_{B-L}\widetilde{g} + \frac{11}{6}\widetilde{g}^2\right]. \tag{III.36}$$

This allows us to assess the impact of this corrected thermal mass. As argued earlier, we set $\widetilde{g} = -0.5$ in this work following the suggestion in [152, 258]. By comparing (III.35) and (III.36) one can see that the thermal barrier is weakened in S4 compared to S3 when $g_{B-L} > \frac{11}{32}$.

Figure III.8 shows the percolation temperature T_* (top left), the phase transition strength α (top right), and the characteristic bubble size $R_* H_*$ (bottom) for the four effective potential scenarios described above. We fix $M_{Z'} = 10^5$ GeV and $M_N = 10^3$ GeV, while varying g_{B-L}. S1 is shown in black, S2 in blue, S3 in red, and S4 in green.

The upper left panel in Fig. III.8 shows that the different effective potentials yield substantially distinct predictions for the percolation temperature T_*, with solid curves indicating the minimum temperature at which both Eqs. (II.57) and (II.58) are satisfied, and dashed curves representing temperatures where only Eq. (II.57) is met. Notably, all

[5] It should be noted that the thermal corrections here are treated in the so-called Parwani procedure [127] in contrast to the Arnold-Espinosa treatment [128] employed in Eq. (III.4).

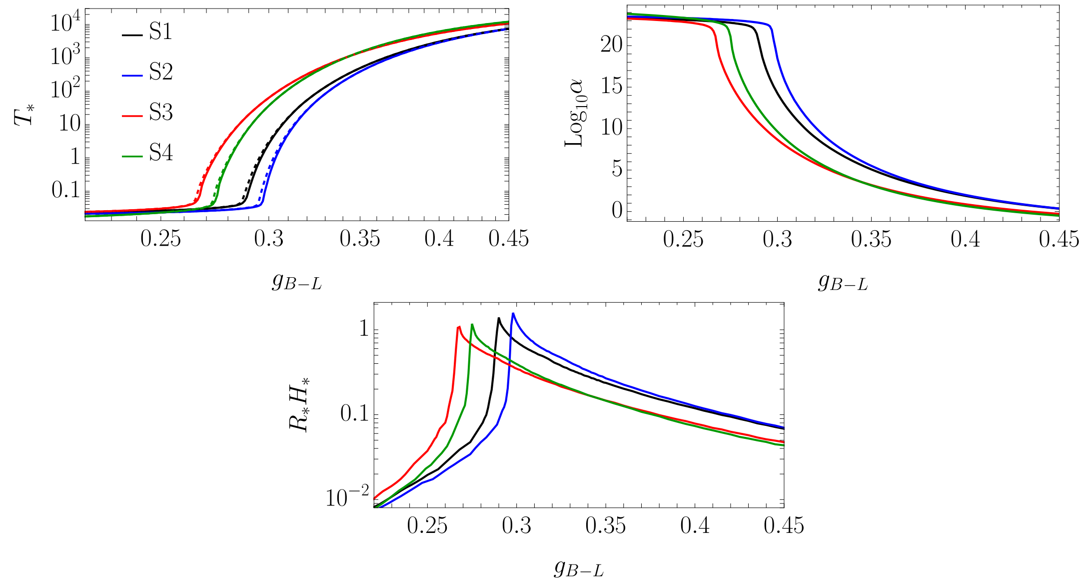

Figure III.8: Comparison of T_* (upper left), α (upper right) and R_*H_* (lower) corresponding to the four different effective potentials described in the text. S1 is shown in black, S2 in blue, S3 in red, S4 in green [4].

scenarios exhibit a common feature: an inherent uncertainty in determining T_* when supercooling terminates slightly above $T_{\rm QCD}$. The upper right and lower panels demonstrate significant differences in the phase transition strength α and the characteristic bubble size R_*H_* among the four scenarios. Although the curves exhibit qualitatively similar behavior, they are shifted relative to each other, as a consequence of the differences in T_* between the scenarios.

The discrepancies in T_*, α, and R_*H_* have a profound impact on the predicted gravitational wave (GW) spectra, as illustrated in Fig. III.9. The figure presents the GW spectra for $g_{B-L} = 0.28$ (left panel) and $g_{B-L} = 0.4$ (right panel),[6] with a prominent discrepancy between the red and green spectra in the left panel. This discrepancy arises from the distinct dominant sources of GWs: bubble collisions for the green spectrum and sound waves for the red spectrum. Here, the green curve's slight double-peak structure is attributed to its primary sourcing by bubble collisions, accompanied by a significantly smaller yet non-negligible sound-wave contribution. In both panels, there is a clear difference between S1 & S2 and S3 & S4. Ultimately, Figs. III.8 and III.9 underscore how differences in the determination of the effective potential can lead to significantly different predictions for observables.

III.3 Gravitational waves

The following section examines the gravitational wave (GW) spectrum produced by the first-order phase transition (FOPT). We demonstrate that, contrary to previous claims in the literature, achieving a significant period of intermediate matter domination in this model requires substantial fine-tuning. This section considers the regime where $M_N \ll M_{Z'}$, while the case of comparable masses ($M_N \sim M_{Z'}$) is analyzed in Section III.4.

To illustrate gravitational wave signatures in this model, we present selected spectra

[6]The sensitivity curves for various experiments are taken from Ref. [161].

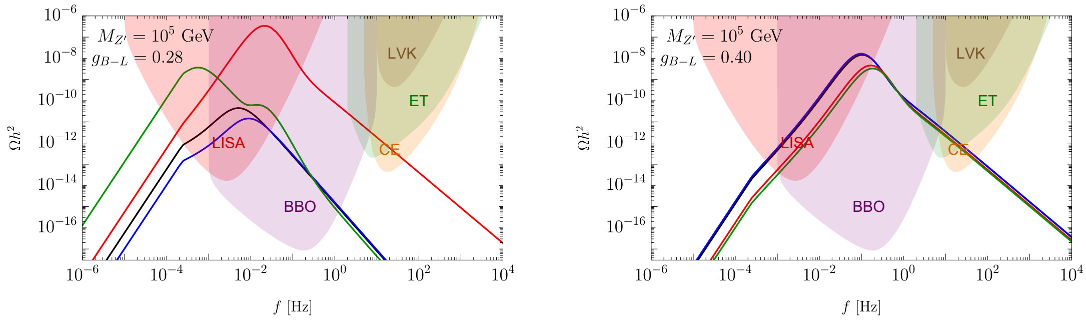

Figure III.9: Gravitational wave spectra corresponding to the four different scenarios with the same color-coding as in Fig. III.8 for $g_{B-L} = 0.28$ (left) and $g_{B-L} = 0.4$ (right) [4].

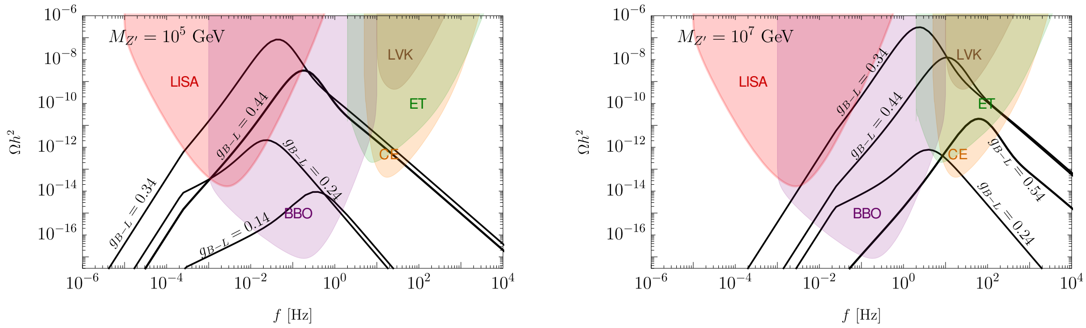

Figure III.10: Illustration of resulting gravitational wave spectrum for $M_{Z'} = 10^5$ GeV (left panel) and $M_{Z'} = 10^7$ GeV (right panel) for different choices of g_{B-L} as indicated in the figure [4].

in Fig. III.10. The left panel shows results for $M_{Z'} = 10^5$ GeV, while the right panel corresponds to $M_{Z'} = 10^7$ GeV, each displaying spectra for various values of the gauge coupling g_{B-L} as indicated in the figure. For smaller gauge couplings ($g_{B-L} = 0.14$ and 0.24), the gravitational wave signal is dominated by bubble collisions, whereas for larger couplings ($g_{B-L} = 0.34$, 0.44, and 0.54), plasma contributions become the primary source. Note that this is consistent with our discussion of $\kappa_{\rm col}$ in the previous section. In the panel to the left, $g_{B-L} = 0.54$ is not shown since it is in the region where $v_w \approx 1$ becomes questionable, while in the panel to the right, $g_{B-L} = 0.14$ is not shown since it is in the "rollover" regime, c.f. Fig. III.2. Finally, the shift in higher peak frequencies for higher values of v_{B-L}, is a direct consequence of the increasing value of H_* from larger energy budgets. This can be understood (parametrically) by recalling the following dependencies $R_* \sim H_*^{-1}$ and $f_{\rm peak} \sim R_*^{-1}$ presented from Section II.2.1.

A comprehensive overview of the peak amplitude $\Omega_{\rm peak}$ and the corresponding peak frequency $f_{\rm peak}$ is illustrated in the left and right panels of Fig. III.11, respectively. The highest peak amplitudes are achieved by maximizing supercooling while ensuring that the bubble walls reach a terminal velocity before colliding, allowing plasma sources to be the primary contributors to the gravitational wave (GW) spectra. In the left panel, the region below the red area indicates that bubble collisions are the dominant source of GW contributions. The narrow yellow band around $g_{B-L} \sim 0.3$ corresponds to percolation temperatures above $T_{\rm QCD}$, as shown in the left panel of Fig. III.6. For fixed $M_{Z'}$, the minimum peak frequency occurs in the region where bubble collisions dominate the GW contribution and $T_* > T_{\rm QCD}$. Reduced supercooling leads to smaller R_*, as depicted in Fig. III.7, resulting in higher peak frequencies, with $f_{\rm peak} \sim R_*^{-1}$. When $T_* < T_{\rm QCD}$,

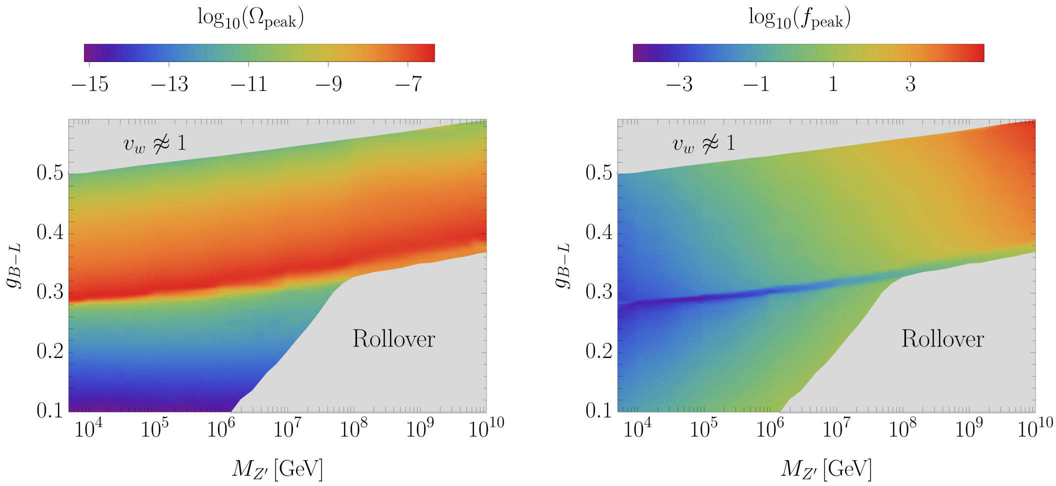

Figure III.11: $M_{Z'} - g_{B-L}$ planes showing $\Omega_{\rm peak}$ (left) and $f_{\rm peak}$ (right). The gray regions are explained in Fig. III.6 [4].

QCD effects accelerate the transition, leading to smaller R_* and consequently higher peak frequencies.

While, Fig. III.11 presents a comprehensive overview of the GW spectra associated with bubble dynamics in this model, it is not of immediate phenomenological use. To fully assess the observability of the SGWB generated in this model, we calculate the signal-to-noise ratio (SNR) for selected detectors using the formula presented in Eq. (II.90) with $\mathcal{T} = 4$ years. In Fig. III.12, we show the results for LISA (top left) [162], BBO (top middle) [163,164], DECIGO (top right), aLIGO + aVirgo + Kagra (bottom left) [165–167], ET (bottom middle) [168], and CE (bottom left) [169,170]. LISA can probe a significant part of the parameter space for $M_{Z'} \lesssim 10^6$ GeV. CE and ET are quite complementary to LISA, as they can probe large portions of parameter space for $M_{Z'} \gtrsim 10^5$ GeV. Advanced Ligo-Virgo-Kagra will also be able to probe some parameter space outside LISA's reach. Finally, BBO and DECIGO will be able to probe most of the parameter space considered here, apart from the upper right corner– corresponding to heavy Z' and large gauge couplings– and a small region in the lower part of our parameter space. Altogether, Fig. III.12 highlights the testability of the CCBL model at future GW observatories, and which parts of parameter space can be excluded or lead to a breakthrough discovery.

Impact of the lifetime of ϕ

Next, we consider how the symmetry-breaking field ϕ may impact the GW spectra. It is well known that GWs can be used as a powerful probe of the lifetime of ϕ. In particular, if ϕ is long-lived, it can temporarily dominate the energy density of the universe in a matter-like phase, thereby affecting both the amplitude and spectral shape of the resulting gravitational wave signal. This possibility has been explored in several works, see e.g. [152, 192, 315–318]. In the following, we revisit the estimation of the lifetime of ϕ, arguing that previous treatments of this model have been too simplistic.

We begin by reviewing a simple estimate for the decay rate Γ_ϕ used in previous studies, which suggests that an intermediate matter-dominated era emerges after the phase transition in large regions of parameter space for $M_{Z'} \gg 2 \cdot 10^5$ GeV. However, when including decays of the form $\phi \to NN$ and renormalization group (RG) running effects, we argue that realizing such a phase requires significantly more fine-tuning than indicated by the

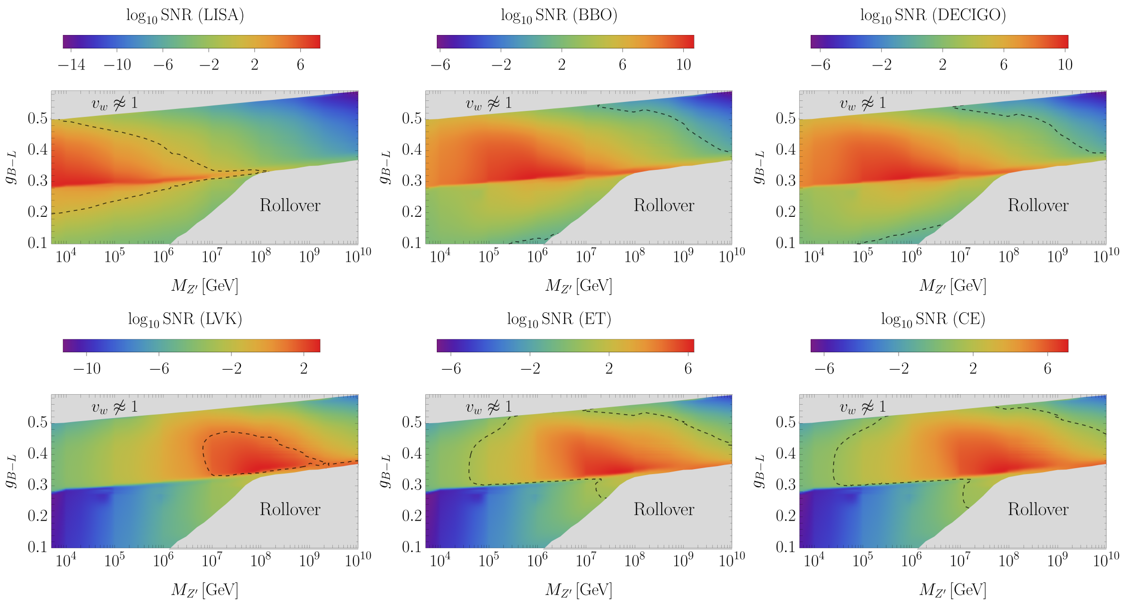

Figure III.12: $M_{Z'}-g_{B-L}$ planes showing $\log_{10}$ SNR for LISA (top left), BBO (top middle), DECIGO (top right), LVK (bottom left), ET (bottom middle), CE (bottom right). The contour corresponding to SNR= 10 is shown by black-dashed curves [4].

naive approximation.

In particular, the detailed study of gravitational wave spectra in the CCBL model presented in Ref. [152] considered only a single decay mode, $\phi \to hh$, and adopted the approximate decay rate

$$\Gamma_\phi \approx 2.5 \times 10^7 g_{B-L} \left(\frac{M_{Z'}}{\text{GeV}}\right)^{-3}. \tag{III.37}$$

This decay rate directly impacts the evolution of the universe's energy density, as can be seen from the Boltzmann equations (II.81)–(II.82). Based on Eq. (III.37), Ref. [152] concluded that a significant matter-dominated epoch may arise for $M_{Z'} \gg 2 \cdot 10^5$ GeV, assuming strong phase transitions with $\alpha \gg 1$. This impacted the peak amplitude of the GW spectra as follows: increasing the symmetry-breaking scale, while keeping g_{B-L} fixed, lead to increasingly suppressed peak amplitudes for $M_{Z'} \gg 2 \cdot 10^5$ GeV [152].[7]

A more accurate treatment of the scalar decay rate must account for both additional decay channels and radiative corrections to the $\phi \to hh$ process. In particular, RG running significantly affects the portal coupling λ_p, which governs the rate of $\phi \to hh$ decays. The one-loop RG equation for λ_p is given by:

$$\begin{aligned} 16\pi^2 \frac{d\lambda_p}{dt} = &\left(-\frac{3}{2} g^2 - \frac{9}{2} g_2^2 - 24 g_{B-L}^2 - \frac{3}{2} \tilde{g}^2 + 4 \sum_i Y_{N_i}^2 + 6 Y_t^2 + 12 \lambda_h + 8 \lambda_\phi \right) \lambda_p \\ &+ 12 g_{B-L}^2 \tilde{g}^2 + 4 \lambda_p^2. \end{aligned} \tag{III.38}$$

To trigger a first-order phase transition (FOPT), a sizable g_{B-L} is generally required, as established in Fig. III.2. Recall also that sizeable $\tilde{g}^2$ is motivated to resolve the SM

[7] It is worth noting that the description employed so far is somewhat idealized: the effective equation of state (EoS) ω during the intermediate phase before ϕ decays is not exactly zero (as in pure matter domination), but instead lies between that of radiation and matter, as pointed out to us by Yann Gouttenoire. This subtlety does not affect our following discussion.

instability and perturbativity of the model [258]. Even if $\widetilde{g}$ is zero at some scale, it will generically evolve to nonzero values at both higher and lower scales due to its RG evolution governed by:

$$16\pi^2 \frac{d\widetilde{g}}{dt} = \left(\frac{41}{3}g^2 + 12g_{B-L}^2\right)\widetilde{g} + \frac{32}{3}\widetilde{g}^2 g_{B-L} + \frac{32}{3}g^2 g_{B-L} + \frac{41}{6}\widetilde{g}^3. \tag{III.39}$$

As a consequence, although λ_p must remain small at the electroweak scale to reproduce the observed Higgs potential, RG running typically drives it to significantly larger values at higher scales, c.f. the first term on the second line of Eq. (III.38). Consequently, the obtained value of $\Gamma_{\phi\to hh}$ is generically orders of magnitude larger than the result in Eq. (III.37) when λ_p is evaluated at $\mu = m_\phi \gg m_{Z^0}$. This has an important consequence: The predicted duration of the matter-dominated epoch typically becomes negligible if $\Gamma_{\phi\to hh}$ is evaluated at $\mu = m_\phi \gg m_{Z^0}$. Since the process under consideration is ϕ decays (with ϕ oscillating around the minimum of its potential located at $\phi = v_{B-L}$), we advocate evaluating $\lambda_p(\mu = m_\phi)$ when computing $\Gamma_{\phi\to hh}$, which we do in the following. Finally, we note that varying μ by a factor few around $\mu = v_h$ generates large relative corrections to the decay width, signaling large theoretical uncertainty if one would calculate Γ_ϕ using $\lambda_p(\mu = v_h)$.

Even if the decay channel $\phi \to hh$ would be suppressed, the presence of a right-handed neutrino with mass $M_N < m_\phi/2$ opens up a new decay channel that is independent of the value of λ_p, and which can significantly impact the duration of the matter-like era. The total decay rate, taking all possible channels into account, reads[8]

$$\Gamma = \Gamma(\phi \to hh) + \Gamma(\phi \to NN) + \Gamma\left(\phi \to \bar{f}_{\rm SM} f_{\rm SM}\right) + \Gamma_{\phi\to VV}, \tag{III.40}$$

$$\Gamma(\phi \to hh) = \frac{v_{B-L}^2 \lambda_p^2}{32\pi m_\phi}\sqrt{1 - 4\frac{m_h^2}{m_\phi^2}}, \tag{III.41}$$

$$\Gamma(\phi \to NN) = \frac{g_{BL}^2}{4\pi} m_\phi \sum_{i=1}^{3} \frac{m_{N_i}^2}{M_{Z'}^2}\left(1 - 4\frac{m_{N_i}^2}{m_\phi^2}\right)^{3/2}, \tag{III.42}$$

$$\Gamma\left(\phi \to \bar{f}_{\rm SM} f_{\rm SM}\right) = \frac{m_\phi \sin^2\theta}{16\pi v_h^2}\sum_f m_f^2 \left(1 - \frac{4m_f^2}{m_\phi^2}\right)^{3/2}, \tag{III.43}$$

$$\Gamma_{\phi\to VV} = \frac{C_V m_\phi^3 \sin^2\theta}{16\pi v_h^2}\sqrt{1 - \frac{4m_V^2}{m_\phi^2}}\left(1 - \frac{4m_V^2}{m_\phi^2} + \frac{12m_V^4}{m_\phi^4}\right), \tag{III.44}$$

where $C_V = 1(2)$ for $V = Z^0\,(W^\pm)$ and the scalar mixing is defined by $\sin 2\theta = \frac{2v_h v_\phi \lambda_p}{m_\phi^2 - m_h^2}$ [268]. Since three RHNs are required in this model to ensure vanishing gauge anomalies, we stress that it is mandatory to consider ϕ decays to RHNs. Consequently, even if λ_p were small enough to suppress all other decay modes, on-shell decays into RH neutrinos can still efficiently deplete the ϕ energy density. A simple criterion for the kinematic accessibility of this decay can be obtained straightforwardly from Eq. (III.15), which implies that $m_\phi > M_N$ requires $g_{B-L} \gg \frac{M_N}{M_{Z'}}$.

In summary, accounting for both $\phi \to NN$ decays and the RG evolution of λ_p significantly alters the predicted duration of any intermediate ϕ-dominated era. Our analysis shows that such a phase requires substantially more fine-tuning than previously

[8] ϕ is always lighter than Z' in the classically-conformal $U(1)_{B-L}$ model, so on-shell decays of ϕ into $Z'Z'$ are kinematically forbidden.

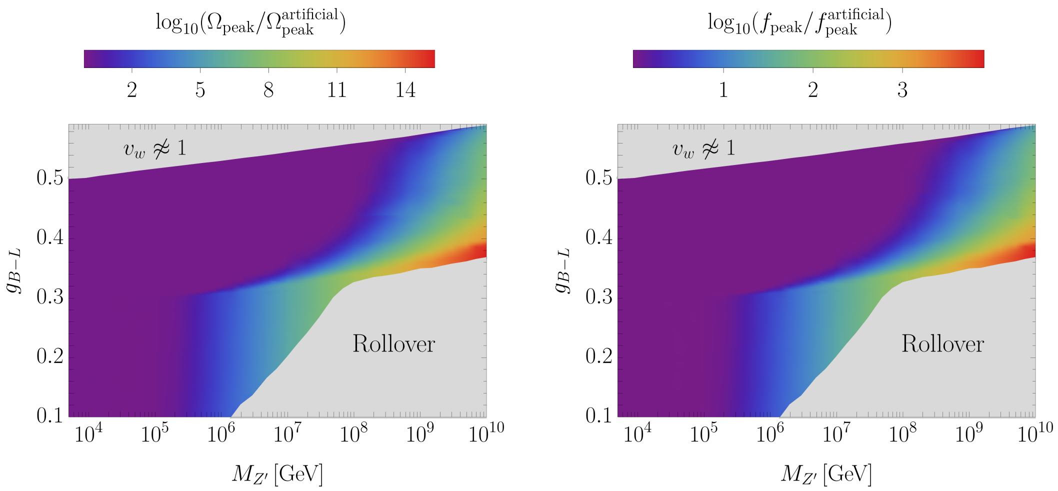

Figure III.13: $M_{Z'} - g_{B-L}$ planes showing $\Omega_{\text{peak}}/\Omega_{\text{peak}}^{\text{artificial}}$ (left) and $f_{\text{peak}}/f_{\text{peak}}^{\text{artificial}}$ (right). The gray regions are explained in Fig. III.6 [4].

suggested [152]. In Fig. III.13, we display the ratios $\Omega_{\text{peak}}/\Omega^{\text{artificial}}$peak (left) and $f$peak$/f^{\text{artificial}}$peak (right), where the "artificial" quantities are computed using the approximate decay rate in Eq. (III.37). These results reveal a qualitative shift in the predicted gravitational wave spectra across large regions of parameter space for $M_{Z'} > 2 \cdot 10^5$ GeV, particularly in scenarios with extreme supercooling where ϕ dominates the energy budget at percolation. We emphasize that when using the full decay rate in Eq. (III.40) in conjunction with the running couplings described in Eqs. (III.16)–(III.19), the intermediate ϕ-dominated era becomes entirely negligible across the parameter space.

III.4 Right-handed neutrino masses and leptogenesis

So far, we have considered the regime $M_N \ll M_{Z'}$, or equivalently, $M_N \ll M_N^{\text{cr.}}$. The purpose of the following section is to analyze how heavier right-handed neutrinos affect the FOPT and the resulting GW spectra. We will then identify regions of parameter space that are particularly suited for BALG, and investigate prospects for probing the relevant parameter space at GW experiments in the future.

III.4.1 Direct impact of right-handed neutrino masses

The right-handed neutrinos couple to the symmetry-breaking scalar field via the Yukawa coupling in Eq. (IV.1). Consequently, their masses explicitly enter the Coleman-Weinberg potential in Eq. (III.8), affecting both the phase-transition dynamics and the resulting production of gravitational waves. To gain insight into exactly how heavy RHNs affect the FOPT, we utilize the high-temperature expansion of the thermal functions in Eq. (III.20) [91],

$$J_B(x) \to \frac{\pi^2}{12}x - \frac{\pi}{6}x^{\frac{3}{2}} + \mathcal{O}\left(x^2 \log(x)\right), \tag{III.45}$$

$$J_F(x) \to -\frac{\pi^2}{24}x + \mathcal{O}\left(x^2 \log(x)\right), \tag{III.46}$$

where we have ignored $J_{B,F}(0)$ as only field-dependent terms are relevant to the following argument. Within this high-temperature approximation, the temperature-dependent part of the effective potential can be written on the following form,

$$V_T + V_{\text{Daisy}} = A(\phi)T^2 - B(T,\phi)T + ..., \tag{III.47}$$

with

$$A(\phi) = \frac{1}{24}\left[4m^2_{h_i}(\phi) + m^2_w(\phi) + m^2_\chi(\phi) + 3M^2_{Z'}(\phi) + \sum_{i=1}^{3} M^2_{N_i}(\phi)\right], \tag{III.48}$$

$$B(T,\phi) = \frac{1}{12\pi}\left[4(m^2_{h_i}(\phi)+\Pi_{h_i})^{\frac{3}{2}} + (m^2_w(\phi)+\Pi_\phi)^{\frac{3}{2}} + (m^2_\chi(\phi)+\Pi_\chi)^{\frac{3}{2}} + (M^2_{Z'}(\phi)+\Pi_{Z'})^{\frac{3}{2}}\right]. \tag{III.49}$$

From Eqs. (III.47) and (III.48), it immediately follows that RHNs enhance the thermal barrier separating the metastable (false) vacuum from the true vacuum. This effect is illustrated in the left panel in Fig. III.14, where the solid black curve corresponds to light RHNs, while the dashed and dotted curves represent scenarios with progressively heavier RHNs.

As the RHN Yukawa couplings increase, the potential becomes shallower around the true minimum, which can be inferred from Eq. (B.2). This behavior is shown to the right in Fig. III.14, using the same benchmark parameters as in the panel to the left. It is important to note that raising the RHN mass beyond $M_N \gtrsim M_{Z'}$ renders the scalar mass m^2_ϕ in Eq. (III.15) tachyonic, destabilizing the potential and making it unbounded from below. Therefore, we restrict our analysis to the physically viable regime $M_N \lesssim M_{Z'}$. Within this range for M_N, increasing the RHN Yukawa couplings has two key effects: it raises the thermal barrier and simultaneously lowers the depth of the true vacuum, leading to enhanced supercooling. In the benchmark scenario shown in Fig. III.14, the percolation temperature decreases significantly—from $T_* \approx 2750$ GeV for $M_N \ll M_N^{\text{cr.}}$ to $T_* \approx 1260$ GeV and $T_* \approx 11$ GeV for $M_N = 0.5$ and $0.8, M_N^{\text{cr.}}$, respectively.

The analytic considerations above indicate that for RHNs to significantly impact the gravitational wave (GW) spectrum, their mass M_N must be large enough to appreciably modify the effective potential without rendering it unstable. Our numerical analysis confirms this expectation: varying M_N while keeping $M_{Z'}$ and g_{B-L} fixed has little effect on the resulting GW spectra, except when M_N approaches the critical value in Eq. (III.30), beyond which the effective potential becomes unbounded from below. This behavior is illustrated in the lower panel in Fig. III.14, which shows the GW spectra corresponding to the benchmark scenarios discussed previously. This representative example demonstrates that RHNs have a noticeable impact on the GW signal only for $M_N \gtrsim 0.5, M_N^{\text{cr.}}$.

Finally, we note that while the direct influence of RHN masses on the GW spectrum is negligible for masses significantly below $M_N^{\text{cr.}}$, there exist scenarios where gravitational wave observations could indirectly constrain the RHN mass scale. For instance, detecting a GW signal that exhibits signatures of a matter-dominated epoch would suggest a long-lived scalar ϕ, thereby placing bounds on the RHN Yukawa couplings and the kinetic mixing parameter $\widetilde{g}$. Combined with an estimate of the $U(1)B-L$ breaking scale $vB-L$ inferred from the GW spectrum, this could provide valuable, albeit circumstantial, information about the RHN mass scale [317].

III.4.2 Probing bubble-assisted leptogenesis

So far, we have demonstrated that RHNs can only significantly impact FOPT if their masses are very close to the critical value $M_N^{\text{cr.}}$. Intriguingly, such heavy RHNs are motivated by a recently proposed mechanism for low-scale leptogenesis known as bubble-assisted leptogenesis [264, 286, 291]. This mechanism has been thoroughly studied within

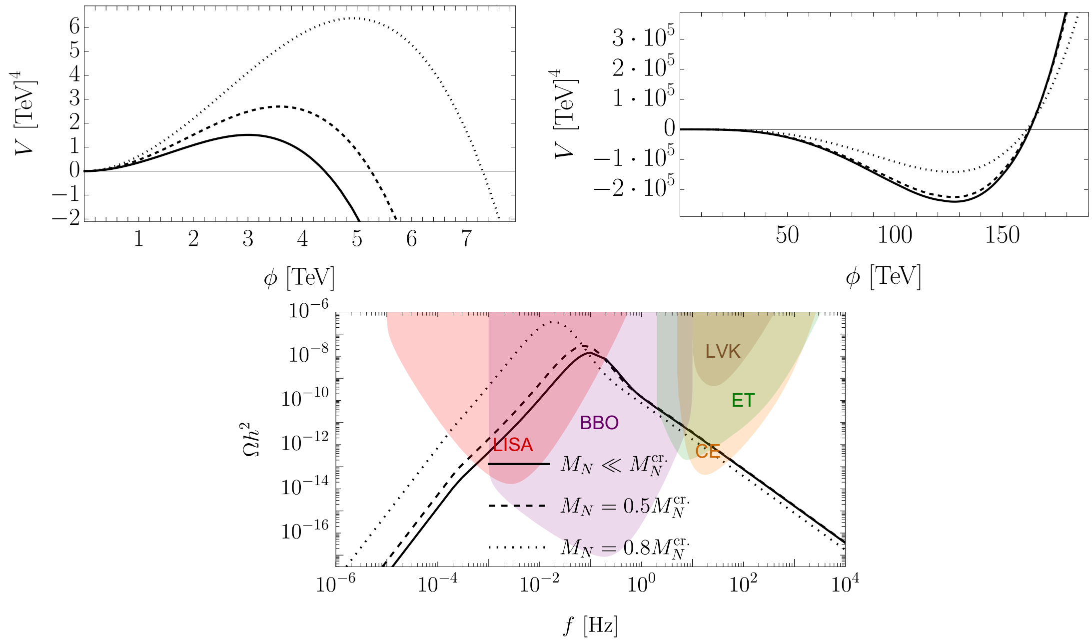

Figure III.14: Top: Illustration of V_{eff} for $g_{B-L} = 0.4$, $M_{Z'} = 10^5$ GeV, $M_N \ll M_N^{\text{c.r.}}$ (black), $M_N = 0.5 M_N^{\text{cr.}}$ (black dashed), and $M_N = 0.8 M_N^{\text{cr.}}$ (black dotted). The temperature is fixed to $T = 2750$ GeV, which corresponds to the percolation temperature for $M_N \ll M_N^{\text{cr.}}$. Bottom: Gravitational wave production associated with the three different benchmark points [4].

the framework of the CCBL model in [291], and the novel aspect of our work is the recognition that the RHN masses which enable efficient BALG are so close to $M_N^{\text{cr.}}$ that they substantially modify the dynamics of the phase transition. This should be contrasted with the standard treatment of this model, where $M_N \ll M_N^{\text{cr.}}$ is assumed when calculating the effective potential. In the following section, we map out the region of parameter space where conditions for BALG are favorable and examine the associated GW production from the FOPT.

Background and analytic arguments

BALG is intimately connected to the broader concept of mass-gain mechanisms for baryogenesis [294–296]. The underlying principle of this mechanism involves leveraging bubble dynamics as a means to drive the RHNs out of thermal equilibrium. As bubbles nucleate

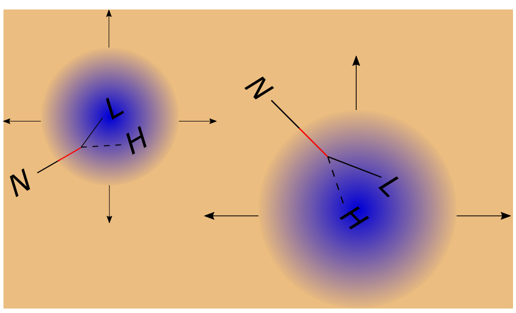

Figure III.15: Schematic illustration of BALG during bubble expansion.

and expand, RHNs from the surrounding plasma can penetrate the bubble walls (provided the wall velocities are sufficiently high) and acquire a mass (via the nonzero scalar vev). The RHNs inside the bubble subsequently decay, generating a non-zero lepton asymmetry as illustrated schematically in Fig. III.15. If T_n is significantly lower than M_N, then washout from inverse decays will be Boltzmann suppressed during the asymmetry generation, which provides an advantage over conventional thermal leptogenesis, c.f. Eq. (II.109). However, following the completion of the FOPT is a period of reheating, during which additional washout effects can occur. Furthermore, the baryon asymmetry produced during the FOPT is diluted by a factor proportional to $(T_n/T_{\rm rh})^3 = (1+\alpha_n)^{-3/4}$,where $\alpha_n = \frac{\Delta V}{\rho_R(T_n)}$, due to entropy injection from reheating. The successful application of this mechanism therefore requires a delicate balance between a strong FOPT and a sufficiently low reheating temperature to mitigate strong washout and dilution effects.

For the sake of completeness, let us mention that the technical analysis necessary to determine the final baryon asymmetry generated within the bubble-assisted mechanism can be systematically broken down into three steps, as outlined in Ref. [291]. Firstly, one must compute the wall velocity of the expanding bubbles, which is essential for quantifying the number of RHNs that enter the bubbles. Secondly, the Boltzmann equations for the $B-L$ asymmetry Y_{B-L} and the RHN density Y_N inside the bubbles must be solved, starting at $T = T_n$, while incorporating all relevant washout terms. Finally, the results for Y_{B-L} and Y_N obtained in the second step must be combined with an additional dilution factor $(T_n/T_{\rm rh})^3$ and used when solving the Boltzmann equations a second time, starting at $T = T_{\rm rh}$.

Ref. [291] established that BALG in the context of CCBL can provide an enhancement of the baryon asymmetry of the universe over conventional TLG, independently of the CP-asymmetry parameter ϵ_1, for $M_N \gtrsim 10^7$ GeV. This does not preclude the possibility of successful BALG at lower masses ($M_N \lesssim 10^7$ GeV), though such scenarios would likely require a stronger resonant enhancement of ϵ_1 than in conventional (resonant) leptogenesis. Ref. [291] further established that BALG can be more efficient than TLG if the reheating temperature is sufficiently low, specifically for $T_{\rm rh}/M_N \lesssim 1/7$, as washout processes become sufficiently ineffective. However, for $T_{\rm rh}/M_N \lesssim 1/11$, the resulting supercooling becomes too severe, with strong dilution of the baryon asymmetry due to the smallness of the ratio $(T_n/T_{\rm rh})^3$. In terms of α_n, they found that a viable enhancement over TLG is achievable for $1 \lesssim \alpha_n \lesssim 100$. In the following, we demonstrate that the parameter region favorable for BALG – identified in Ref. [291] —- corresponds to RHN masses that are very close to their critical value.

After the completion of the phase transition, the scalar field ϕ decays and reheats the universe. In the mass range of interest, the decay channel $\phi \to NN$ is kinematically forbidden, and reheating proceeds predominantly via $\phi \to hh$. We have verified numerically that ϕ decays rapidly. For the sake of analytic understanding, we also compare the decay rate of this process with the Hubble expansion rate,

$$\frac{\Gamma_{\phi\to hh}}{H} \sim \left(\frac{\lambda_p}{10^{-4}}\right)^2 \left(\frac{v_{B-L}}{10^9\ \text{GeV}}\right) \left(\frac{10^9\ \text{GeV}}{T}\right)^2 \left(\frac{10}{\sqrt{g_*(T)}}\right) \left(\frac{0.1}{\sqrt{\lambda_\phi(0)}}\right), \tag{III.50}$$

which provides intuition on how large λ_p must be for given v_{B-L} and T_*.

Since ϕ decays rapidly after the FOPT, it is justified to treat the reheating as instantaneous so the reheating temperature $T_{\rm rh}$ can be obtained from simple energy conservation

$$T_{\rm rh} \approx \left(T_*^4 + \frac{30}{\pi^2 g_*}\Delta V\right)^{1/4}, \tag{III.51}$$

where the difference in potential energy is well approximated by

$$\Delta V = \frac{-\lambda_\phi(0)v_{B-L}^4}{4}, \qquad -\lambda_\phi(0) \approx \frac{1}{4\pi^2}\left(6g_{B-L}^4 - \sum_{i=1}^{3} Y_{N_i}^4\right). \tag{III.52}$$

For $T_{\rm rh}/M_N \approx 1/11$, one has $T_{\rm rh}^4 \gg T_n^4$ [291], such that the second term on the r.h.s. of Eq. (III.51) dominates and we obtain

$$T_{\rm rh} \approx 0.09\left(M_{Z'}^4 - 2M_N^4\right)^{1/4}. \tag{III.53}$$

From Eq. (III.53), one can verify that $T_{\rm rh}/M_N \approx 1/11$ yields $M_N \approx 0.6 \times M_{Z'}$, or equivalently [4]

$$M_N \approx 0.7 M_N^{\rm cr.}. \tag{III.54}$$

In the opposite limit, where $T_{\rm rh}/M_N \approx 1/7$, one has $T_{\rm rh}/T_n \approx 1 + \mathcal{O}(0.1)$ and $T_n/M_N \gtrsim 0.12$ [291], which upon using Eq. III.51 yields $M_N \lesssim 0.9 M_N^{\rm cr.}$ [4].

To summarize, we have shown that within the CCBL model, the parameter region where BALG is most efficient corresponds to right-handed neutrino masses in the range $0.7M_N^{\rm cr.} \lesssim M_N \lesssim 0.9M_N^{\rm cr.}$. In this regime, the RHNs are sufficiently heavy to substantially influence the dynamics of the FOPT and, consequently, the resulting GW spectrum, invalidating the commonly used approximation $M_N \ll M_N^{\rm cr.}$. In the following, we provide an overview of the key thermodynamic quantities relevant for BALG and the associated gravitational wave production within this promising region of parameter space.

As a final remark, we note that Ref. [264] considered BALG in the minimal classically conformal $U(1)_{B-L}$ model in the resonant regime. It was pointed out in Ref [291] that their estimate for the final baryon asymmetry is too optimistic, due to the ignorance of washout effects from RHN annihilation. During our study, we also found that the benchmark scenario in Ref. [264], which was chosen on the premise that it would avoid washout from inverse decays, does suffer from additional washout from IDs. Altogether, this should clarify that there is a sizeable suppression in the generated baryon symmetry compared to the estimate presented in Ref. [264].

Parameter space

In Fig. III.16, we present the $M_N - g_{B-L}$ parameter planes, illustrating the behavior of T_* (first row), α_n (second row), $(T_{\rm rh}/T_n)^3$ (third row), and $\Omega_{\rm peak}$ (fourth row). The mass of the Z' boson is fixed to 10^8 GeV in the left column and 10^9 GeV in the right column. In the shaded gray region at the bottom of each plot, conditions are unfavorable for BALG. Here, α_n grows by several orders of magnitude, and its values have been omitted for visual clarity.

The vertical axes in the above-mentioned figures take on significantly larger values than the vertical axes of the $M_N - g_{B-L}$ planes shown earlier in this chapter. The reason is that larger RHN masses enhance the thermal barrier in the effective potential, requiring an increased g_{B-L} to maintain the same percolation temperature. Importantly, despite the large values of g_{B-L} and $M_{Z'}$, the FOPT calculation remains within the perturbative regime at the relevant temperature scales. This is because heavy RHNs soften the IR behavior of the running quartic coupling λ_ϕ, as discussed in Section III.2.2. However, when compared with Fig. III.1, it becomes evident that in substantial regions of the parameter space explored here, perturbativity breaks down at scales above the QCD transition temperature and we are in regime 2 discussed below Eq. (III.30).

The first row in Fig. III.16 displays T_*, which lies roughly within the range $10^{-2} \lesssim T_*/M_{Z'} \lesssim 10^{-1}$. From the second and third rows, we see that the optimal conditions for BALG – namely $\alpha = \mathcal{O}(1)$ and $(T_{\rm rh}/T_n)^3 = \mathcal{O}(1)$ – are realized in a sizeable region of parameter space close to where $v_w \not\approx 1$. The fourth row shows the corresponding gravitational wave amplitudes Ωh^2, which is primarily in the range $\Omega h^2 = \mathcal{O}(10^{-9} - 10^{-10})$, within the region most favorable for BALG. In contrast, in the lower regions of the parameter space, which are less optimal for BALG, Ωh^2 can increase to $\mathcal{O}(10^{-7} - 10^{-8})$.

In Fig. III.17, we show $\log_{10}$SNR for BBO (left), LVK (middle), and ET (right), with $M_{Z'}$ fixed to 10^8 GeV (10^9 GeV) in the top (bottom) row.[9] Both BBO and ET can probe large regions of the considered parameter space for $M_{Z'} = 10^8$ GeV. Also LVK will be able to probe some of the considered parameter space for $M_{Z'} = 10^8$ GeV. However, when the mass scale is increased to $M_{Z'} = 10^9$ GeV, the GW spectra fall outside the reach of LVK for the parameters considered here. Meanwhile, BBO and ET can probe roughly half of the considered parameter space, although the parameters providing the most optimal conditions for BALG fall slightly outside their experimental sensitivity.

The results presented in Fig. III.17 demonstrate that significant portions of the parameter space where conditions for BALG are favorable can be probed by several proposed GW experiments in the future. Thus, in the context of CCBL, upcoming GW experiments provide an exciting opportunity to test a leptogenesis mechanism where the mass scale associated with the RHNs lies far outside the reach of colliders [264, 286, 291].

Comment: Leptogenesis assisted by scalar decays

For completeness, we briefly comment on the non-viability of scalar-decay-assisted leptogenesis in the minimal CCBL model. As previously noted, the decay channel $\phi \to NN$ is inevitable for RHN masses satisfying $m_\phi > 2M_N > 0$, from the consistency of the model. Hence, the scalar ϕ can act as a nonthermal source for leptogenesis [319–322] in the sense that RHNs are among its decay products. Decays into RHNs can have a significant impact on the final $B-L$ asymmetry if they occur (numerously) at temperatures much lower than the RHN mass, $T \ll M_N$, where washout processes are inefficient. However, realizing this scenario requires the hierarchy $T_{\rm rh} \ll M_N < \frac{1}{2}m_\phi$, which is not achievable within the minimal CCBL setup: As readily seen from Eqs. (III.15) and (III.53), this condition cannot be satisfied simultaneously, thereby rendering scalar-decay-assisted leptogenesis ineffective in this model.

III.5 A SGWB from cosmic strings and bubbles

Up to this point, our discussion of gravitational wave sources has been restricted to bubbles of true vacuum and their associated dynamics. We now broaden our scope to include cosmic strings: Since $\pi_1(U(1)) \neq 0$, a network of cosmic strings is expected to form in this model, as discussed in Chapter II. The string network evolves toward the linear scaling regime, sustained through the production of cosmic string loops, which lose energy via particle and gravitational radiation, as outlined in Section II.3. In the following, we consider the SGWB sourced by cosmic strings under the assumptions laid out in Section II.3. As shown in Fig. II.5, this background could be detectable by BBO for the highest symmetry-breaking scales considered here, i.e. $v_{B-L} \sim 10^{10}$GeV. Consequently, it may be possible to probe a characteristic GW signal featuring significant overlapping contributions from

[9] We do not find good observational prospects for LISA, meaning SNR is small within the entire considered region of parameter space, and therefore do not discuss it further.

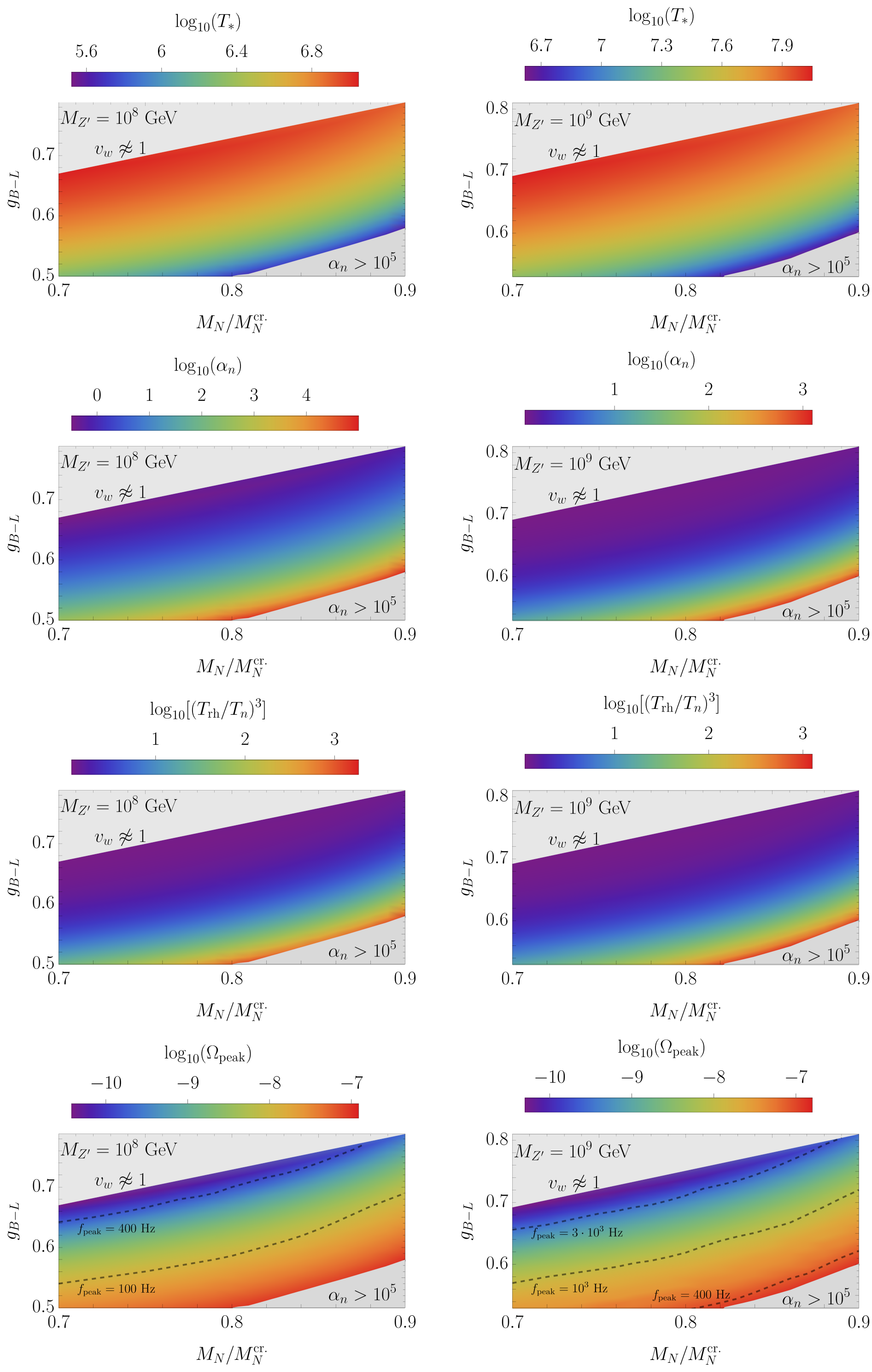

Figure III.16: $M_N - g_{B-L}$ planes showing T_* (first row), α_n (second row), $(T_{\rm rh}/T_n)^3$, and $\Omega_{\rm peak}$. $M_{Z'}$ is fixed to 10^8 GeV (10^9 GeV) in the left (right) column. In the lower gray region, α_n increases by many orders of magnitude and is omitted for readability. Notice that the y-axis is different in the left and right column [4].

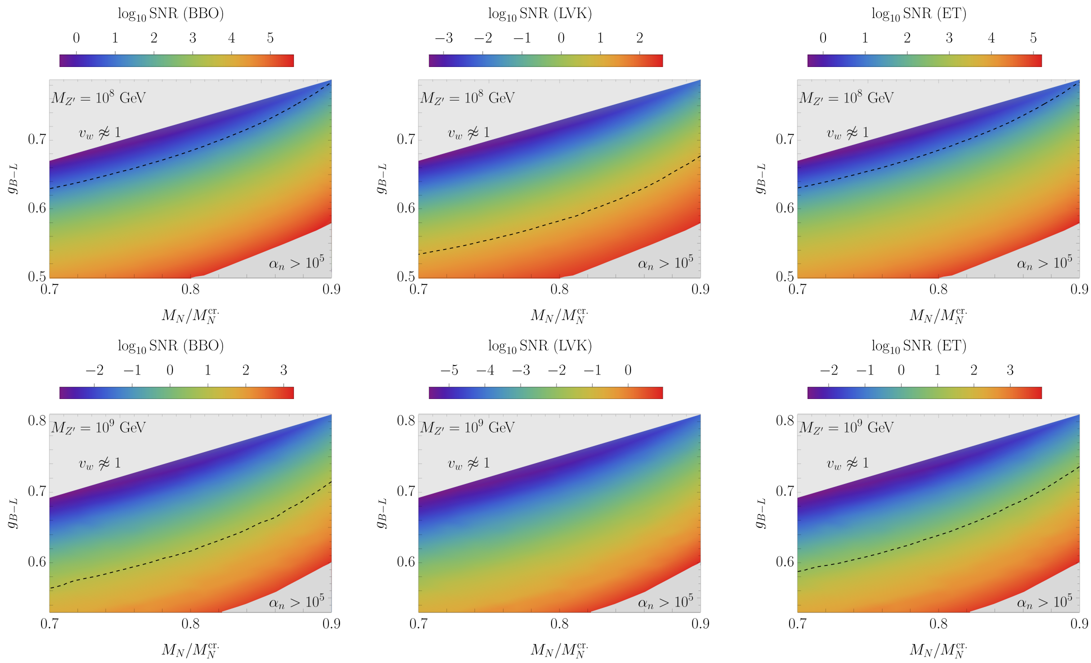

Figure III.17: $M_{Z'} - g_{B-L}$ planes showing $\log_{10}$ SNR for BBO (left), LVK (middle), and ET (right). $M_{Z'}$ is fixed to 10^8 GeV (10^9 GeV) in the top (bottom) row [4].

both cosmic strings and FOPT dynamics. While the idea of identifying unique GW signatures arising from the superposition of different sources is not new, concrete examples have so far (to the best of our knowledge) been limited to models involving at least two distinct symmetry-breaking scales (see, e.g., [298–300]). The aim of the following section is to demonstrate that, within the CCBL model, a distinctive GW signal can emerge even from a single symmetry-breaking event.

To the right in Fig. III.18, we show the stochastic gravitational wave spectra generated by cosmic strings for symmetry-breaking scales $v_{B-L} = 10^9$GeV (red), $v_{B-L} = 4\times10^9$ GeV (green), and $v_{B-L} = 10^{10}$GeV (blue). These results illustrate that GWs sourced by cosmic strings could be detectable by BBO for $v_{B-L} \gtrsim 10^9$GeV. The gray dashed line indicates the expected cut-off frequency for string loops dominated by cusp structures, discussed in Section II.3. In the right panel of Fig. III.18, we show the GW spectra from cosmic strings (black curve) and from FOPT dynamics (colored curves) with the symmetry-breaking scale fixed to $v_{B-L} = 10^{10}$GeV, and different values for the gauge coupling g_{B-L} as indicated in the figure. The blue and red spectra are predominantly sourced by bubble collisions, with the red spectrum exhibiting a double-peak structure due to a significant contribution from plasma sources. In contrast, the green and purple spectra are primarily sourced by plasma effects. Increasing g_{B-L} shifts the spectra toward higher frequencies, eventually pushing them beyond the sensitivity reach of the experiments considered here. As evident from the figure, BBO and ET could potentially detect signals exhibiting overlapping contributions from cosmic strings and bubble collisions for $v_{B-L} \simeq 10^{10}$ GeV within the CCBL model.

III.6 Conclusions

Extending the SM gauge group by $U(1)_{B-L}$ provides an interesting route to address questions about the origin of neutrino masses, the origin of the BAU, and the nature of DM.

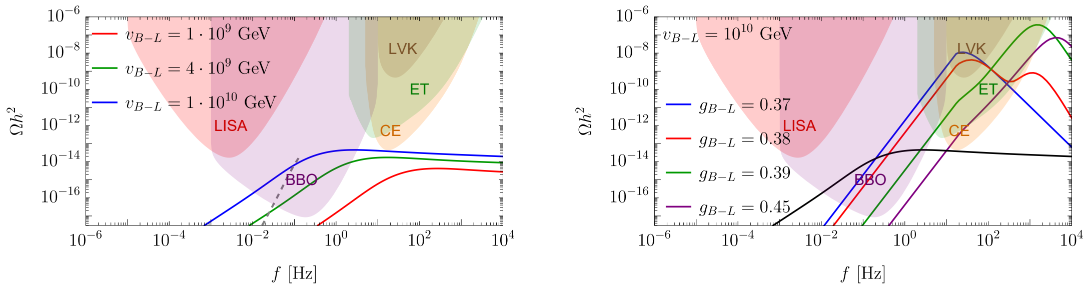

Figure III.18: Left: SGW spectra from cosmic strings for breaking scale $v_{B-L} = 10^9$ GeV (red), $v_{B-L} = 4 \cdot 10^9$ GeV (green), $v_{B-L} = 10^{10}$ GeV (blue). Right: SGWs sourced by cosmic strings (black curve) and FOPT dynamics (colored curves) for fixed $v_{B-L} = 10^{10}$ GeV. The value of the gauge coupling is $g_{B-L} = 0.37$ (blue), $g_{B-L} = 0.38$ (red), $g_{B-L} = 0.39$ (green), and $g_{B-L} = 0.45$ (purple) [4].

In this chapter, we considered a minimal $B-L$ model exhibiting classical scale invariance. The model dynamically generates RHN masses and the EW scale, and can address the baryon asymmetry of the universe through BALG. The primary focus of this chapter, however, has been the strongly first-order phase transition associated with $B-L$ breaking, which occurs over a significant portion of the parameter space, and the resulting gravitational wave background.

In Section III.2.4, we examined how QCD dynamics influence the phase transition in regimes where supercooling drives the plasma temperature below the QCD scale. We showed that the explicit breaking of scale invariance induced by QCD accelerates the phase transition, resulting in smaller bubble radii at the time of percolation. By requiring that the bubble radii at percolation significantly exceed those at the time of nucleation, we carved out the region of parameter space where QCD effects can catalyze a first-order phase transition (FOPT). The region is illustrated in Fig. III.2, which summarizes the phase-transition dynamics across a broad range of the model's parameter space. We also emphasized that small uncertainties in the percolation temperature for a QCD-induced FOPT can lead to large variations in the resulting gravitational-wave (GW) spectrum, as shown in Fig.III.3. Our findings motivate dedicated non-perturbative studies of QCD-triggered FOPTs, particularly since this regime is (partly) accessible to upcoming GW experiments.

Following the FOPT there is an intermediate phase of reheating, during which the scalar field ϕ may temporarily dominate the energy budget of the universe, which could leave a characteristic feature in the GW spectrum. Accounting for RG evolution of couplings and for $\phi \to NN$ decays, we argued that the duration of the intermediate ϕ-dominated phase is negligible without fine tuning. This should be contrasted with previous findings [152], where an extended ϕ-domination phase was predicted across sizable regions of parameter space. We demonstrated that predictions for the peak amplitude and frequency of the GW spectrum are significantly affected by the calculation of the lifetime of ϕ, as shown in Fig. III.13, with deviations between our and previous results reaching several orders of magnitude. Consequently, our updated signal-to-noise ratio (SNR) predictions (Fig. III.12) suggest more optimistic detection prospects in large portions of parameter space, improving upon previous results [152].

Theoretical consistency of the CCBL model requires the presence of three RHNs. In fact, the RHNs play an important role in generating light neutrino masses through type-I seesaw and the BAU through leptogenesis in this model. However, RHNs are often neglected in the calculation of V_{eff}. This is justified in the limit where $M_N \ll M_{Z'}$. In contrast, if $M_N \sim M_{Z'}$, then the RHNs can have a significant impact on the effective potential and consequently the FOPT dynamics and GW production. In fact, favorable conditions for leptogenesis via bubble assistance point to heavy RHNs comparable to $M_{Z'}$ [291]. Motivated by this observation, we mapped out the parameter space where conditions for BALG are optimal, demonstrating that the mechanism can be probed significantly by upcoming GW experiments, c.f. Figs. III.16 and III.17. In particular, we identified the mechanism as a target for both the Einstein Telescope and BBO for M_N in the promising mass range of $10^8 - 10^9$ GeV.

Finally, as established in Chapter II, the formation of a cosmic string network is a generic prediction in theories featuring spontaneous breaking of a $U(1)$ symmetry in the early universe. In this chapter, we considered the GW signal sourced by loops of cosmic strings. Notably, we demonstrated that for a symmetry-breaking scale of $v_{B-L} \sim 10^{10}$ GeV, the resulting SGWB exhibits a distinctive spectral shape with non-negligible overlapping contributions from both cosmic strings and FOPT dynamics. As illustrated in Fig. III.18 for a number of parameter points, the combined spectrum lies within the reach of upcoming GW experiments. While the concept of multi-component GW signals is not new, to our knowledge this is the first explicit realization of overlapping contributions from cosmic strings and a FOPT originating from the same symmetry-breaking event. Fig. III.18 thus serves as a concrete proof-of-principle for such a signal within an established BSM model.

A Renormalization-group equations

Below, we list the 1-loop RGE's for the couplings in the theory [301, 304, 323],

$$16\pi^2 \frac{dg}{dt} = \frac{41}{6} g^3, \tag{A.1}$$

$$16\pi^2 \frac{dg_2}{dt} = -\frac{19}{6} g_2^3, \tag{A.2}$$

$$16\pi^2 \frac{dg_3}{dt} = -7 g_3^3, \tag{A.3}$$

$$16\pi^2 \frac{dg_{B-L}}{dt} = \frac{32}{3}\widetilde{g} g_{B-L}^2 + \frac{41}{6}\widetilde{g}^2 g_{B-L} + 12 g_{B-L}^3, \tag{A.4}$$

$$16\pi^2 \frac{d\widetilde{g}}{dt} = \left(\frac{41}{3} g^2 + 12 g_{B-L}^2\right)\widetilde{g} + \frac{32}{3}\widetilde{g}^2 g_{B-L} + \frac{32}{3} g^2 g_{B-L} + \frac{41}{6}\widetilde{g}^3, \tag{A.5}$$

$$\begin{aligned}16\pi^2 \frac{dY_t}{dt} =& \left(\frac{5}{3} g_{B-L}\widetilde{g} - \frac{17}{12} g^2 - \frac{9}{4} g_2^2 - 8 g_3^2 - \frac{2}{3} g_{B-L}^2 - \frac{5}{3} g_{B-L}\widetilde{g} - \frac{17}{12}\widetilde{g}^2\right) Y_t \\ &+ \frac{9}{2} Y_t^3,\end{aligned} \tag{A.6}$$

$$16\pi^2 \frac{dY_{N_i}}{dt} = Y_{N_i}\left[4Y_{N_i}^2 - 6 g_{B-L}^2 + 2\sum_j Y_{N_j}^2\right], \qquad (i = 1, 2, 3) \tag{A.7}$$

$$\begin{aligned}16\pi^2 \frac{d\lambda_H}{dt} =& \frac{3}{8} g^4 + \frac{3}{4} g^2 g_2^2 + \frac{9}{8} g_2^4 + \frac{3}{4} g^2 \widetilde{g}^2 + \frac{3}{4} g_2^2 \widetilde{g}^2 + \frac{3}{8}\widetilde{g}^4 - 6 Y_t^4 \\ &+ \left(-3g^2 - 9g_2^2 - 3\widetilde{g}^2 + 12 Y_t^2\right)\lambda_h + 24\lambda_h^2 + \lambda_p^2,\end{aligned} \tag{A.8}$$

$$16\pi^2 \frac{d\lambda_\phi}{dt} = 96 g_{B-L}^4 - 16\sum_i Y_{N_i}^4 + 8\lambda_\phi\left(-6 g_{B-L}^2 + \sum_i Y_{N_i}^2\right) + 20\lambda_\phi^2 + 2\lambda_p^2, \tag{A.9}$$

$$16\pi^2 \frac{d\lambda_p}{dt} = \left(-\frac{3}{2}g^2 - \frac{9}{2}g_2^2 - 24g_{B-L}^2 - \frac{3}{2}\widetilde{g}^2 + 4\sum_i Y_{N_i}^2 + 6Y_t^2 + 12\lambda_h + 8\lambda_\phi \right) \lambda_p$$
$$+ 12g_{B-L}^2\widetilde{g}^2 + 4\lambda_p^2. \tag{A.10}$$

Here g, g_2, and g_3 denote the SM hypercharge, weak, and strong gauge couplings, respectively. Y_t denotes the top Yukawa, and the remaining couplings are defined in Section III.2.

B Approximation of the effective potential

In the following, we review the approximation of $V_{T=0}$ introduced in [90], and used in many subsequent studies of this model,

$$V_{T=0}\left(\sqrt{Z_\phi(t)}\phi,\, \mu\right) = \frac{\lambda_\phi(t)}{4} Z_\phi^2(t)\phi^4, \tag{B.1}$$

with $Z_\phi(t)$ and γ given in Section III.2.1. Fixing the minimum of the potential at $\phi = v_{B-L}$, implies the following boundary condition for $\lambda_\phi(t)$,

$$\left.\frac{d\lambda_\phi}{dt}\right|_{t=0} + 4\lambda_\phi(0)\left[1-\gamma(0)\right] = 4\lambda_\phi(0) + \frac{1}{8\pi^2}\left[\lambda_p^2(0) + 10\lambda_\phi^2(0) + 48g_{B-L}^4(0) - 8\sum_{i=1}^{3} Y_{N_i}^4(0)\right]$$
$$\approx 4\lambda_\phi(0) + \frac{1}{\pi^2}\left[6g_{B-L}^4(0) - \sum_{i=1}^{3} Y_{N_i}^4(0)\right] = 0, \tag{B.2}$$

where in going to the second line we neglected loop contributions from scalars, which are subleading [265]. For $M_N \ll M_{Z'}$, Eq. (B.2) reduces to $\lambda_\phi(0) \approx -\frac{3}{2\pi^2}g_{B-L}^4(0)$, manifesting the characteristic relationship between λ_ϕ and g_{B-L}^4 in Coleman-Weinberg models. Plugging Eq. (B.2) into (B.1), we obtain

$$V_{T=0}^{\min} \approx -\frac{v_{B-L}^4}{16\pi^2}\left[6g_{B-L}^4(0) - \sum_{i=1}^{3} Y_{N_i}^4(0)\right], \tag{B.3}$$

in agreement with Eq. (B.3). The mass of ϕ is obtained straightforwardly from Eq. (B.1), and the result reads [90]

$$m_\phi^2 = \left.\frac{d^2V_{T=0}}{d\phi^2}\right|_{\phi=v_{B-L}} \approx \frac{v_{B-L}^2}{8\pi^2}\left[\lambda_p^2 + 10\lambda_\phi^2 + 48g_{B-L}^4 - 8\sum_{i=1}^{3} Y_{N_i}^4\right]_{t=0} = -4\lambda_\phi(0)v_{B-L}^2$$
$$\approx \frac{v_{B-L}^2}{\pi^2}\left[6g_{B-L}^4 - \sum_{i=1}^{3} Y_{N_i}^4(0)\right], \tag{B.4}$$

which is in agreement with Eq. (III.15).

CHAPTER IV

Cosmic strings as a non-thermal source for leptogenesis

IV.1 Introduction

In this chapter, we will continue our study of gauged $U(1)_{B-L}$ models, and consider breaking scales up to 10^{15} GeV. In contrast to the previous chapter, where we considered a specific model and its gravitational wave signatures, we will take a more general approach here and only require that (gauged) $B-L$ is spontaneously broken in the hot early universe and that RHNs have the following Yukawa interactions,

$$\mathcal{L}_N = -Y_N^i \Phi \overline{N_i^c} N_i - Y_D^{ij} \overline{L_i} \widetilde{H} N_j + \text{h.c.}\,. \tag{IV.1}$$

The first term dynamically generates Majorana masses when Φ acquires a vev while the second term generates Dirac masses upon electroweak (EW) symmetry breaking.

By adapting a generalist approach without specifying the scalar sector of the theory, we will not have much to say about the nature of the $B-L$ phase transition, which could be of first or higher order. However, a generic prediction in the class of models under study is the formation of a network of cosmic strings (CS), as reviewed in Chapter II. For sufficiently high breaking scales, the GW production from loops of cosmic strings could be probed at upcoming experiments, c.f. Fig. II.5, which makes these models interesting from an observational point of view. Additionally, loops of cosmic string can also decay via particle radiation, as discussed in Section II.3, and with the scalar-breaking field Φ coupling directly to the RHN as in Eq. (IV.1), loop decays could result in significant non-thermal production of RHNs. In particular, the lepton asymmetry generated by RHNs sourced at $T \ll M_N$ would be protected from large wash-out effects.

The question that we will pursue in this chapter is whether or not the non-thermal production of RHNs from cosmic string loops can have a significant impact on leptogenesis, see Refs. [324–334] for related earlier work in this direction. This is an interesting question not only from a theoretical point of view, but also because it could provide a link between observable gravitational waves and high-scale leptogenesis with mass scales far beyond the reach of particle colliders. From a practical point of view, however, it is clear that a quantitative analysis of $B-L$ asymmetry from loops of cosmic string will inherently suffer from large sources of uncertainty. The latter includes particle-production efficiency from strings, evolution of cosmic strings before reaching the linear scaling regime, how energetic particles emitted from loops are, and more.

This chapter aims to systematically study particle production rates from cosmic strings and use the results to estimate the maximum impact that cosmic strings can have as a non-thermal source for leptogenesis. In particular, we will show that the $B-L$ asymmetry resulting from RHN-production from linearly scaling cosmic strings in a radiation-dominated universe is a negligible effect, contrary to previous claims in the literature.

The chapter is structured as follows: We start with a brief historical note, to put our work into context. In Section IV.2, we present classical Boltzmann equations for leptogenesis in the presence of cosmic strings, leaving some technical details to Appendix A. The resulting Boltzmann equation for RHNs involve a source term from cosmic-string loops. In Section IV.3, we provide analytical expressions for this term for various classes of loops and for different epochs in the cosmic string evolution, leaving detailed derivations to Appendix B. In particular, using the velocity-dependent one-scale (VOS) model [335–338], which is an analytical framework to model the evolution of the long-string network, we include a detailed treatment of strings during the friction-dominated epoch. In Section IV.4, we determine the impact of non-thermally sourced RHNs from cosmic strings on leptogenesis before summarizing our results and providing an outlook in Section IV.5. It will be assumed throughout this chapter that the $B-L$ symmetry is broken when the universe was radiation dominated.[1] A brief discussion of the case of non-thermal breaking of $U(1)_{B-L}$ is included at the end of the chapter.

Brief historical context

Cosmic strings in a $U(1)_{B-L}$ model where RHNs receive their mass via spontaneous symmetry breaking, as in Eq. (IV.1), may host localized right-handed-neutrino bound states, making them current carrying cosmic strings (CCCS). In particular, by setting $\Phi = 0$ in Eq. (IV.1) and the winding number of Φ to n, it is possible to show that there exists n RHN zero-mode solutions to the Dirac equation in the (straight) cosmic string background [339, 340]. Zero-modes move along the straight string at the speed of light, and turn the string into a superconducting wire or a superconducting string as pointed out by Witten four decades ago [341]. It should be noted that the string is not superconducting in the usual electromagnetic sense, but under $U(1)_{B-L}$. At the microscopic level, CCCS may be generated through capture of RHNs by cosmic strings with simultaneous emission of a $U(1)_{B-L}$ gauge boson [342] or a Φ field [343]. Cosmic-string loops are also expected to have bound-state solutions, albeit with nonvanishing effective masses.[2]

The observation that RHNs can be trapped as transverse zero modes in the core of the strings, motivated the original proposal of non-thermal leptogenesis via cosmic strings [329]: As cosmic string loops decay, they release the neutrinos trapped in the core. The released neutrinos acquire a heavy Majorana mass and decay to produce a lepton asymmetry. This idea was subsequently considered in Refs. [331–333] in a cosmological history where $T \gtrsim M_{N_1}$, and in Ref. [334] in the context of (supersymmetric) hybrid inflation. The physical picture presented in these papers was that loops of string decay by emitting gravitational radiation until their lengths become comparable to their width, after which they annihilate and emit $\mathcal{O}(1)$ RHNs. These papers concluded that non-thermally produced RHNs from cosmic strings could provide the dominant contribution to the BAU for $v_\phi \gtrsim 10^{11-13}$ GeV.

The current chapter aims to revisit the expectation that cosmic strings associated with sufficiently high v_ϕ can have a significant impact on leptogenesis in light of updated pre-

[1] We expect the results of our analysis to also be reliable if the symmetry is broken at the end of inflationary reheating shortly before the universe becomes radiation dominated.

[2] In the absence of cusps and small scale structure on the loop, one expects a picture derived on the assumption of exact zero modes to still hold for cosmic strings with radius much larger than the width of the string [344].

dictions for particle-production rates and a careful evaluation of string evolution. In particular, we will incorporate that RHNs may be emitted by loops while they shrink, in addition to being emitted in the final collapse.

Finally, we will model the evolution of the long-string network and loops using results and frameworks developed for non-superconducting strings, leaving a more detailed analysis for future work. Some recent generalizations of the VOS model [335–337] to facilitate semi-analytical modeling of dynamics of CCCS networks and various applications of it can be found in [345–349]. For recent field-theory simulations of the evolution of a current-carrying network of strings, see [350], and also [351] for related recent developments.

IV.2 Boltzmann equations

In the following, we set up classical Boltzmann equations incorporating RHN-production from cosmic-string loops. This framework will be used in Section IV.4 to calculate the contribution from non-thermally sourced RHNs to the BAU.

A complication in writing down the Boltzmann equations is that the momentum-distribution of the non-thermally produced RHNs can be sensitive to the details of the particle emission from loops. After being emitted into the thermal plasma, the RHNs may attain kinetic equilibrium through number-conserving scatterings with other particles in the plasma. However, for $T \ll M_N$, all scattering rates are expected to be suppressed compared to the Hubble expansion, and the emitted RHNs may not reach kinetic equilibrium. In principle, non-equilibration of RHNs does not pose a problem if the Boltzmann equations are analyzed at the level of phase-space distribution functions. However, in the context of the present study, we prefer to work with integrated Boltzmann equations, which become more complicated if the assumption of kinetic equilibrium breaks down. In the following, we will therefore present equations valid in two different regimes:

- For $T \gtrsim M_{N_1}$, we assume a thermal population of RHNs generated through interaction in the thermal bath and possibly CS-sourced RHNs. The RHNs are assumed to be in kinetic equilibrium and subject to the standard integrated Boltzmann equation from TLG with the addition of a source term associated with cosmic-string loops.
- For $T \ll M_{N_1}$, we no longer assume the RHNs to be in kinetic equilibrium. Here, we derive an integrated Boltzmann equation under a certain assumption (to be specified) about the momentum distribution of RHNs inherited from CS decay, see Ref. [322] for a similar approach in a different context.[3]

We work in the one-flavor approximation,[4] use Maxwell-Boltzmann statistics, and ignore the effects of Fermi blocking and stimulated emission.

IV.2.1 Boltzmann equations describing the first period

For $T \gtrsim M_{N_1}$, the Boltzmann equations take the following form,[5]

$$\frac{\partial Y_{N_1}}{\partial z} = -2S_{2N}\left(Y_{N_1}^2 - (Y_{N_1}^{\mathrm{eq}})^2\right) - (D+S)\left(Y_{N_1} - Y_{N_1}^{\mathrm{eq}}\right) + \frac{1}{s(z)H(z)\cdot z}\frac{\partial n_{N_1}^{\mathrm{cs}}}{\partial t}, \tag{IV.2}$$

$$\frac{\partial Y_{B-L}}{\partial z} = -\epsilon_1 D\left(Y_{N_1} - Y_{N_1}^{\mathrm{eq}}\right) - WY_{B-L}. \tag{IV.3}$$

[3] There are also more sophisticated methodologies available to deal with kinetic decoupling in the context of Boltzmann equations, see e.g. Refs. [352, 353].

[4] As pointed out, this is the correct description for $T \gtrsim 10^{12}$ GeV, which is the regime of primary interest in this chapter.

[5] See e.g. [224, 225] for details about D, S, and W, and [354] for details about S_{2N}.

Here, $H(z)$ denotes the Hubble parameter, $z = M_{N_1}/T$, ϵ_1 is the CP-asymmetry in N_1 decays, and $Y = n/s$, where s denotes entropy density. D accounts for decays and inverse decays, S for $\Delta L = 1$ scatterings involving one external N_1, and W for washout processes. The first term on the r.h.s. of Eq. (IV.2) accounts for the processes $NN \leftrightarrow f\bar{f}, Z'Z', Z'\phi, \phi\phi$ [354]. The last term on the r.h.s. of Eq. (IV.2) accounts for RHN production from loops of cosmic string, where $\frac{\partial n_{N_1}^{\rm cs}}{\partial t}$ denotes the RHNs production rate from CS loops.

IV.2.2 Boltzmann equations describing the second regime

Next, we present evolution equations for Y_{B-L} and Y_{N_1} for $z \gg 1$, including the possibility of breakdown of kinetic equilibrium. Some details about their derivations have been included in Appendix A.

The Boltzmann equation for RHNs at $z \gg 1$ takes the approximate form,

$$\frac{\partial Y_N}{\partial z} \approx \frac{Kz}{\gamma_N}(Y_N^{\rm eq} - Y_N) + \frac{1}{s(z)H(z)\cdot z}\frac{\partial n_N^{\rm c.s.}}{\partial t}, \tag{IV.4}$$

where γ_N denotes the Lorentz factor of RHNs emitted from cosmic loops, and K is the standard decay parameter [86]

$$K = \frac{\Gamma_{\rm r.f.}}{H(M)}, \tag{IV.5}$$

and $\Gamma_{\rm r.f.}$ denotes the zero-temperature decay width of N_1. The limit of kinetic equilibrium can be recovered (approximately) by setting $\gamma_N = 1$. The Boltzmann equation for $B - L$ takes the form,

$$\frac{\partial Y_{B-L}}{\partial z} \approx -\epsilon_1 \frac{Kz}{\gamma_N}\left(Y_N - Y_N^{\rm eq}\right) - Y_{B-L}\left[W_{\rm ID} + 2W_{\Delta L=2}^{\rm sub}\right], \tag{IV.6}$$

when accounting for washout contributions from inverse decays and $\Delta L = 2$ scatterings.

IV.2.3 Estimate of $B - L$ generation for $z \gg 1$

As a preparation for the leptogenesis analysis for scaling cosmic strings, it will be useful to derive an analytical upper limit on the baryon asymmetry produced for $z \gg 1$. First, for $z \gg 1$, we can neglect $Y_{N_1}^{\rm eq}$. As a second simplification, we will neglect washout contributions. This will allow us to obtain an analytical upper limit on the generated $B - L$ asymmetry. With these simplifications, the Boltzmann equations above reduce to,

$$\frac{\partial Y_{N_1}}{\partial z} \approx -K'zY_{N_1} + \frac{1}{s(z)H(z)\cdot z}\frac{\partial n_N^{\rm c.s.}}{\partial t}, \tag{IV.7}$$

$$\frac{\partial Y_{B-L}}{\partial z} \approx -\epsilon_1 K'zY_{N_1}, \tag{IV.8}$$

where we defined

$$K' \equiv \frac{K}{\gamma_N}. \tag{IV.9}$$

Note that in the limit $\frac{\partial n_N^{\rm c.s.}}{\partial t} = 0$, the $B - L$ asymmetry takes the expected form,

$$Y_{B-L}(z) = Y_{B-L}(z_0) - \epsilon_1 \int_{z_0}^{z} \frac{\partial Y_{N_1}(z')}{\partial z'} dz', \quad z_0 \gg 1. \tag{IV.10}$$

Below, we will find that the source term for scaling cosmic strings in a radiation-dominated universe can be written on the following form,

$$\frac{1}{s(z)H(z)\cdot z}\frac{\partial n_N^{\text{c.s.}}}{\partial t} = Cz^{-n}, \qquad n \geq 2, \tag{IV.11}$$

where C is a constant. Substituting this parametrization into Eq. (IV.7), one can readily verify that the set of Boltzmann equations (IV.7)-(IV.8) has the following general solution

$$Y_{N_1}(z) = e^{-\frac{1}{2}K'z^2}\left[Y_{N_1}(z_0)\, e^{\frac{1}{2}K'z_0^2} + C\int_{z_0}^{z} x^{-n} e^{\frac{1}{2}K'x^2}\, dx\right], \tag{IV.12}$$

$$\begin{aligned} Y_{B-L}(z) &= Y_{B-L}(z_0) - \epsilon_1 Y_{N_1}(z_0)\left(1 - e^{-\frac{1}{2}K'(z^2-z_0^2)}\right) \\ &\quad - \epsilon_1 C\int_{z_0}^{z} x^{-n}\left(1 - e^{-\frac{1}{2}K'(z^2-x^2)}\right) dx. \end{aligned} \tag{IV.13}$$

It immediately follows that the generated asymmetry is bounded from above as follows,

$$\begin{aligned} |Y_{B-L}(z) - Y_{B-L}(z_0)| &\leq \epsilon\left[Y_{N_1}(z_0) + \frac{C}{n-1}\left(z_0^{1-n} - z^{1-n}\right)\right] \\ &\leq \epsilon\left(Y_{N_1}(z_0) + \frac{C}{(n-1)z_0^{n-1}}\right). \end{aligned} \tag{IV.14}$$

Note that this inequality turns into an equality if one sets $Y_{B-L}(z) - Y_{B-L}(z_0) = \epsilon_1 \int_{z_0}^{z} \frac{1}{s(z)H(z)\cdot z}\frac{\partial n_N^{\text{c.s.}}}{\partial t}$ as was done in Refs. [331, 334].

We obtained Eq. (IV.14) by considering $z, z_0 \gg 1$ where contributions from scatterings involving one RHN are negligible compared to decays, Y_N^{eq} is vanishingly small, and assuming washout effects are suppressed. By introducing a phenomenological parameter $\kappa_w(z)$, we can recast our result for the generated asymmetry as,

$$|Y_{B-L}(z) - Y_{B-L}(z_0)| = \kappa_w(z)\epsilon_1\left[Y_{N_1}(z_0) + \frac{C}{(n-1)}\left(\frac{1}{z_0^{n-1}} - \frac{1}{z^{n-1}}\right)\right], \qquad \kappa_w(z) \leq 1, \tag{IV.15}$$

where $\kappa_w(z)$ encodes the effect of $K'z^2 < \infty$ and washout effects that we have ignored in our analytical treatment. Asymptotically, when both washout effects and RHN injection are negligible, we expect $\kappa_w(z \to \infty)$ to become a constant.

Finally, the baryon asymmetry generated as a result of loop decays takes the form,

$$|Y_B(z \gg z_0) - Y_B(z_0)| \approx C_{\text{sph}}\left(\kappa_w(z)\epsilon_1 Y_{N_1}(z_0) + \epsilon_1\, \kappa_{\text{w}}(z)\frac{C}{n-1}\frac{1}{(z_0)^{n-1}}\right), \tag{IV.16}$$

where C_{sph} is the sphaleron-conversion factor [355]. Ignoring a potential initial N_1 abundance at z_0, which will be accounted for in more complete calculations presented in the second part of Section IV.4, the result reduces to

$$|Y_B(z) - Y_B(z_0)| \approx C_{\text{sph}}\epsilon_1\, \kappa_{\text{w}}(z)\frac{C}{n-1}\frac{1}{(z_0)^{n-1}}. \tag{IV.17}$$

For this contribution to account for the observed BAU, $Y_B \approx 8.7 \cdot 10^{-11}$, the constant C must satisfy

$$C \approx \frac{Y_B(n-1)(z_0)^{n-1}}{C_{\text{sph}}\epsilon_1\kappa_w(z)} \gtrsim \frac{2.7(n-1)(z_0)^{n-1}}{\kappa_w(z)}\left(\frac{10^6\ \text{GeV}}{M_{N_1}}\right)$$

$$\gtrsim 2.7\,(n-1)(z_0)^{n-1}\left(\frac{10^6\ \mathrm{GeV}}{M_{N_1}}\right), \tag{IV.18}$$

where we used the bound in Eq. (II.124) in the second step, and $\kappa_w(z) \leq 1$ in the last step. We will return to this result in Section IV.4.

IV.3 Non-thermal right-handed-neutrino production rate

In the following, we will derive analytical expressions for the source term $\frac{\partial n_N^{\mathrm{c.s.}}}{\partial t}$ entering the Boltzmann equation for Y_{N_1}, using the methodology reviewed in Section II.3. We first consider contributions during the linear-scaling regime, where the string behavior is best understood. We then proceed with a critical examination of potential contributions during the friction-dominated epoch. Ultimately, the results derived in the linear-scaling regime will be of limited interest to leptogenesis. Nonetheless, we provide detailed derivations of the results in Appendix B, hoping that they may prove useful in other contexts.

The number of loops produced per unit time during linear scaling, and the power emitted via particle radiation can be determined from the equations presented in Section II.3. The picture is more subtle in the friction-dominated epoch, where we will rely on the VOS model to analyze the behavior of the long-string network and loops. After the particle-emission rates from cosmic-string loops have been estimated, the next problem amounts to determining the fraction of emitted particles that are RHNs or decay to RHNs. Abelian Higgs simulations do not offer insight to the number of RHNs produced, as the only quanta in the AH model are Φ and A_μ. We will handle the uncertainty in number of produced RHNs by introducing a phenomenological parameter $0 \leq f_N \leq 1$, which we define as the power emitted from loops into RHNs normalized by the total power emitted from loops into particle radiation.

IV.3.1 Particle emission from loops produced during linear scaling

Strings experience a significant friction force due to elastic scatterings with particles in the plasma for a period after formation, as explained in Section II.3. The friction force per unit length in the rest frame of a string moving with velocity $\boldsymbol{v}$ through a plasma with temperature T is given by [180]

$$\boldsymbol{F} = -\frac{\mu \boldsymbol{v}}{l_f\sqrt{1-\boldsymbol{v}^2}}, \tag{IV.19}$$

where l_f is the so-called friction length scale. The most prominent contribution to $\boldsymbol{F}$ arises from Aharonov-Bohm (AB) scattering of $U(1)_{B-L}$ charged particles off the string [181]. Intuitively, this effect arises as cosmic string solutions are cylindrical field-configurations carrying magnetic flux Φ_B determined by $n = \frac{q_\phi}{2\pi}\oint_\gamma \vec{A}\cdot d\vec{l} = \frac{q_\phi}{2\pi}\Phi_B$, which is confined within a diameter roughly given by the Compton wavelength of the $B-L$ gauge field [107]. In this sense, the string constitutes a nearly-idealized solenoid giving rise to Aharonov-Bohm scattering effects. The friction length scale associated with the Aharonov-Bohm force takes the following form,

$$l_f = \frac{\mu}{\beta T^3}, \tag{IV.20}$$

where the drag-coefficient is given by [180]

$$\beta = 2\pi^{-2}\zeta(3)\sum_i g_i \sin^2(\pi\nu_i). \tag{IV.21}$$

The sum runs over all thermalized and relativistic particle species in the plasma with mass $m \ll T$. Here g_i is the number of relativistic degrees of freedom multiplied by 1 (3/4) for bosons (fermions) and ν_i is the AB phase, meaning that when a particle with $B-L$ charge q_i is transported on a closed path around the string its wavefunction picks up a phase $2\pi\nu_i = 2\pi\left(\frac{q_i}{q_\phi}\right)$, where $q_\phi = 2$. Notably, all SM particles and RHNs contribute to damping the $U(1)_{B-L}$ string, with the contribution from SM species given by $\beta_{\rm SM} = \frac{27\zeta(3)}{\pi^2}$.

The friction force in Eq. (IV.19) significantly damps the string's motion initially, and smoothens out kinks and cusps on a string, reducing the efficiency of radiation channels during the friction-dominated era [356]. The duration of the friction-dominated epoch can be estimated using the VOS model, which provides a notion of *friction time*. The latter is typically defined as the instance when damping due to the frictional force becomes comparable to damping due to the expansion of the universe [335],

$$2H(t_{\rm fric}) = \frac{\beta[T(t_{\rm fric})]^3}{\mu}. \tag{IV.22}$$

For a radiation dominated universe, the temperature corresponding to the latter can be estimated as

$$T_{\rm fric} = \frac{2\pi}{3\beta}\sqrt{\frac{g_*}{10}}\frac{\mu}{M_P} \approx \frac{2\pi}{3\beta}\sqrt{\frac{g_*}{10}}\left(\frac{v_\phi}{M_P}\right)v_\phi, \tag{IV.23}$$

where we in the last step used Eq. (II.95). If we assume that the network formation time t_F is the cosmic time when the energy scale of the universe is equal to the string tension [192], and that the universe is radiation dominated at the time, then the corresponding formation-temperature is given by

$$T_F \approx \left(\frac{30}{\pi^2 g_*}\right)^{1/4} v_\phi. \tag{IV.24}$$

Parametrically, we see that the two temperature scales in Eq. (IV.23) and (IV.24) are separated by v_ϕ/M_P, implying that lowering v_ϕ increases the duration of the friction-dominated epoch. As a first approximation, which we will return to later in detail, it is possible to assume that the network reaches scaling behavior at $t = t_{\rm fric}$. The results presented in the following for particle production from loops produced during linear scaling are then only valid for $t_i > t_{\rm fric}$, where t_i denotes the time when a loop is produced.

We find that the rate of RHN injection from loops of cosmic strings can be expressed on the following form,

$$\frac{dn^{\rm cs}_{N_1}}{dt} = \frac{\sqrt{2}f_N\mu F_\alpha C_{\rm eff}(t_i)}{\gamma_\alpha E_N}\frac{A}{t^k}, \tag{IV.25}$$

for each combination of loop size and energy-loss mechanism considered here, c.f. Appendix B for details. The parameters A and $k > 0$ encode the specifics of the loops and energy-loss mechanism considered and will be given on a case-by-case basis below, $E_N = \gamma_N M_{N_1}$ denotes the average energy of the produced RHNs, and μ, F_α, γ_α, $C_{\rm eff}$ were introduced in Section II.3. We also provide (approximate) relations between t_i and t, which can be used to assess when the expressions satisfy the validity condition $t_i > t_{\rm fric}$.

Small cusp-dominated loops: For small cusp-dominated loops, we obtain a contribution from collapsing loops and direct particle radiation from strings when the would-be-size of the loop is smaller than its width

$$A = 1, \qquad k = 3, \quad t = t_i, \qquad\qquad \text{for} \quad \frac{\omega}{\Gamma G\mu} \gtrsim t, \tag{IV.26}$$

$$A \approx \frac{\omega}{\Gamma G\mu}, \quad k=4, \quad t \approx t_i + \frac{2}{3\sqrt{w}}(\Gamma G\mu t_i)^{3/2}, \quad \text{for} \quad \frac{\omega}{(\Gamma G\mu)^3} \gtrsim t \gtrsim \frac{\omega}{\Gamma G\mu}, \tag{IV.27}$$

The contribution from cusp-evaporations read,

$$A = N_c, \quad k=3, \quad t \approx t_i, \quad \text{for} \quad \frac{\omega}{(\Gamma G\mu)^3} \gtrsim t \gtrsim \frac{\omega}{\Gamma G\mu}, \tag{IV.28}$$

where $N_c \sim 2$ is the average number of cusp annihilations per period [209].
Big cusp-dominated loops: The contribution from collapsing loops reads,

$$A = \alpha_l^{3/2} w^{1/6}, \quad k=19/6, \quad t = t_i + \frac{2}{3}\frac{1}{w^{1/2}}(\alpha t_i)^{3/2}, \quad \text{for} \quad \frac{\omega}{(\Gamma G\mu)^3} \gtrsim t \gtrsim \frac{\omega}{\alpha_l^3}, \tag{IV.29}$$

and from cusp evaporations,

$$A \approx \frac{N_c \alpha_l^{1/2}}{w^{1/6}}, \quad k=17/3, \quad t \approx \frac{(\alpha_l t_i)^{3/2}}{w^{1/2}}, \quad \text{for} \quad \frac{\omega}{(\Gamma G\mu)^3} \gtrsim t \gtrsim \frac{\omega}{\alpha_l^3}. \tag{IV.30}$$

Small kink-dominated loops: The contribution from collapsing loops reads,

$$A = 1, \qquad k=3, \quad t = t_i, \qquad \text{for} \quad \frac{\omega}{\Gamma G\mu} \gtrsim t, \tag{IV.31}$$

$$A \approx \frac{\omega}{\Gamma G\mu}, \quad k=4, \quad t \approx t_i + \frac{(\alpha_l t_i)^{3/2}}{w^{1/2}}, \quad \text{for} \quad \frac{\omega}{(\Gamma G\mu)^2} \gtrsim t \gtrsim \frac{\omega}{\Gamma G\mu}, \tag{IV.32}$$

and from kink-kink collisions,

$$A \approx \frac{N_{kk}}{w\mu^{1/2}}, \quad k=3, \quad \text{for} \quad \frac{\omega}{(\Gamma G\mu)^2} \gtrsim t \gtrsim \frac{\omega}{\Gamma G\mu}, \tag{IV.33}$$

where N_{kk} is the average number of kink-kink collisions per oscillation.
Big kink-dominated loops: The contribution from collapsing loops reads,

$$A = \alpha_l^{3/2} w^{1/4}, \quad k=11/4, \quad t \approx t_i + \frac{(\alpha_l t_i)^2}{2w}, \quad \text{for} \quad \frac{\omega}{(\Gamma G\mu)^2} \gtrsim t \gtrsim \frac{\omega}{\alpha_l^2}, \tag{IV.34}$$

and from kink-kink collisions,

$$A \approx \frac{N_{kk}\alpha_l^{1/2}}{\mu^{1/2}w^{5/6}}, \quad k=11/4, \quad t \approx \frac{(\alpha_l t_i)^2}{2w}, \quad \text{for} \quad \frac{\omega}{(\Gamma G\mu)^2} \gtrsim t \gtrsim \frac{\omega}{\alpha_l^2}. \tag{IV.35}$$

Only GW radiation: We also consider loops that shrink by emitting gravitational radiation and only emit particles in their final collapse. The contribution from small loops reads,

$$A = 1, \qquad k=3, \quad \text{for} \quad \frac{\omega}{\Gamma G\mu} \gtrsim t, \tag{IV.36}$$

$$A \approx \frac{2^{5/2}\omega}{\Gamma G\mu}, \quad k=4, \quad \text{for} \quad t \gtrsim \frac{\omega}{\Gamma G\mu}, \tag{IV.37}$$

and the contribution from big loops reads,

$$A = \frac{\alpha_l^{3/2} w}{(\Gamma G\mu)^{5/2}}, \quad k=4, \quad t \gtrsim \frac{w}{\Gamma G\mu}. \tag{IV.38}$$

Instantaneous particle emission: In light of recent AH simulations [199], see also [357], we also consider a maximal RHN production rate from strings, where the full energy-loss rate from long strings to loops is converted instantaneously to particle radiation. The purpose is to assess the potential impact of cosmic strings on leptogenesis in a maximally optimistic scenario, providing a benchmark estimate that can inform future studies once a consensus on particle production from loops is fully established within the community. The result reads,

$$A = 1, \quad k = 3, \quad t = t_i. \tag{IV.39}$$

For future reference, we also include the full expression in this case,

$$\frac{dn_N}{dt} \approx f_N \frac{\sqrt{2}\mu C_{\text{eff}}(t)}{\gamma_N M_{N_1} t^3}. \tag{IV.40}$$

IV.3.2 Going beyond the linear scaling regime

Next, we want to consider the contribution to the BAU from loops produced in the friction-dominated epoch. This is complicated by several sources of uncertainty:

- The role of particle production in cosmic-string loop decays is a topic of debate, as discussed in Section II.3. Abelian-Higgs simulations by different groups yield qualitatively different results for particle production rates, with existing studies focusing on the linear scaling regime where friction is negligible. To our knowledge, there are currently no quantitative predictions for the efficiency of particle production from cosmic strings during the friction-dominated epoch derived from numerical simulations. Consequently, any quantitative assessment of particle-production efficiency for $z \lesssim z_{\text{fric}}$ is subject to significant uncertainty.
- Prior to the onset of the linear scaling regime, the characteristic properties of the cosmic string network evolve dynamically. A widely adopted framework for modeling this evolution is the VOS model [335–337] mentioned several times in this chapter, in which the average string velocity and the characteristic network length-scale are treated as dynamical variables. This approach provides a quantitative description that captures the complete evolution of the string network following its formation [338]. We will employ the VOS model to analyze energy loss from the long-string network to loops during the friction-dominated epoch.

VOS model

In the following, we summarize the VOS formulae that are of direct relevance to us and refer the interested reader to Refs. [107, 335, 336, 338] for further details about the formalism. The energy-loss rate from the long-string network to loops is given by

$$\left(\frac{d\rho_\infty}{dt_i}\right)_{\text{to loops}} = \frac{\widetilde{c} v_\infty \mu}{L^3(t_i)}. \tag{IV.41}$$

Here $\widetilde{c}$ denotes the loop-chopping efficiency, v_∞ the average root-mean-square velocity of string-segments of the long strings, and L the single length scale entering the framework. L can be interpreted as the average distance between strings or a correlation length [338], and $\widetilde{c}$ is the only free parameter of the model and has to be determined from e.g. simulations. Abelian Higgs [358, 359] and Nambu-Goto [337] simulations suggest the following (constant) values,

$$\textbf{AH}: \ \widetilde{c} = 0.57 \pm 0.04, \qquad \textbf{NG}: \ \widetilde{c} = 0.23 \pm 0.04, \tag{IV.42}$$

respectively. We stress that the values for $\widetilde{c}$ are obtained for strings in the linear scaling regime, and that in principle, the value of $\widetilde{c}$ could be modified in the friction-dominated epoch. This provides an important source of uncertainty in VOS modeling of the friction-dominated epoch, which deserves attention in future studies.

By identifying $L_i = \xi(t_i)t_i$, where ξ is a time-dependent parameter, the expression above can be rewritten to the form given in Eq. (II.97),

$$\left(\frac{d\rho_\infty}{dt_i}\right)_{\text{to loops}} = \frac{\sqrt{2}\mu C_{\text{eff}}(t_i)}{t_i^3}, \qquad \text{with} \quad C_{\text{eff}}(t_i) = \frac{\widetilde{c}v_\infty}{\sqrt{2}\xi^3}. \tag{IV.43}$$

For a given value or parametrization of $\widetilde{c}$, the efficiency parameter C_{eff} can be determined by solving the VOS equations for the long-string network [335, 336],

$$\frac{dL}{dt} = HL(1+v_\infty^2) + \frac{Lv_\infty^2}{2l_f} + \frac{\widetilde{c}v_\infty}{2}, \tag{IV.44}$$

$$\frac{dv_\infty}{dt} = (1-v_\infty^2)\left[\frac{k(v_\infty)}{L} - v_\infty\left(2H + \frac{1}{l_f}\right)\right], \tag{IV.45}$$

where l_f was defined in Eq. (IV.20) and $k(v_\infty)$ is a phenomenological function that has been fitted by simulations [337],

$$k(v) = \frac{2\sqrt{2}}{\pi}(1-v^2)(1+2\sqrt{2}v^3)\frac{1-8v^6}{1+8v^6}. \tag{IV.46}$$

In the linear-scaling regime, ξ and v_∞ become constant yielding a time-indepedent value for C_{eff}.

Solution to VOS equations

To solve the VOS equations (IV.44)-(IV.45), we first rewrite them in terms of the dimensionless quantities ξ, v_∞, and $z = M_{N_1}/T$,[6]

$$\frac{d\xi}{dz} = \frac{\widetilde{c}v_\infty}{z} + \frac{\xi}{z}\left[-1 + v_\infty^2 + \frac{v_\infty^2\beta}{2z}\sqrt{\frac{90}{\pi^2 g_*}}\left(\frac{M_{N_1}M_P}{\mu^2}\right)\right], \tag{IV.47}$$

$$\frac{dv_\infty}{dz} = \left(\frac{1-v_\infty^2}{z}\right)\left[\frac{2k(v_\infty)}{\xi} - 2v_\infty - \frac{v_\infty\beta}{z}\sqrt{\frac{90}{\pi^2 g_*}}\left(\frac{M_{N_1}M_P}{\mu}\right)\right]. \tag{IV.48}$$

Numerical example solutions are displayed in Fig. IV.1 for $v_\phi = 10^{14}$ GeV and $M_{N_1} = 10^{14}$ GeV (top) and $M_{N_1} = 10^{10}$ GeV (bottom) where ξ is shown to the left, v_∞ in the middle, and the rate of energy loss from the long-string network to loops given in Eq. (IV.41) to the right. The gray dashed line shows the value of z_{fric} obtained from Eq. (IV.23). Note that the values on the horizontal axes differ in the two lowest rows compared to the first two rows for v_∞ and $\frac{d\rho_\infty}{dt_i}$. Some comments are in order:

- The long-string network relaxes to the linear scaling regime (ξ = constant) after z_{fric}. Recall that in the analytical calculations above, we assumed that the string network reached scaling instantaneously at $z = z_{\text{fric}}$. We see that this is not an accurate approximation. In fact, scaling is reached significantly after the end of friction domination $z_s \gg z_{\text{fric}}$.
- The initial evolution of the correlation-length parameter, ξ, is sensitive to initial conditions, and subsequently flows to an attractor solution that is independent of initial conditions (c.f. the left column of Fig. IV.1).

[6] In particular, we use $\frac{d}{dt} = zH\frac{d}{dz}$, $t = \frac{1}{2H}$, and $\frac{d\xi}{dt} = \frac{1}{t}\frac{dL}{dt} - \frac{L}{t^2}$.

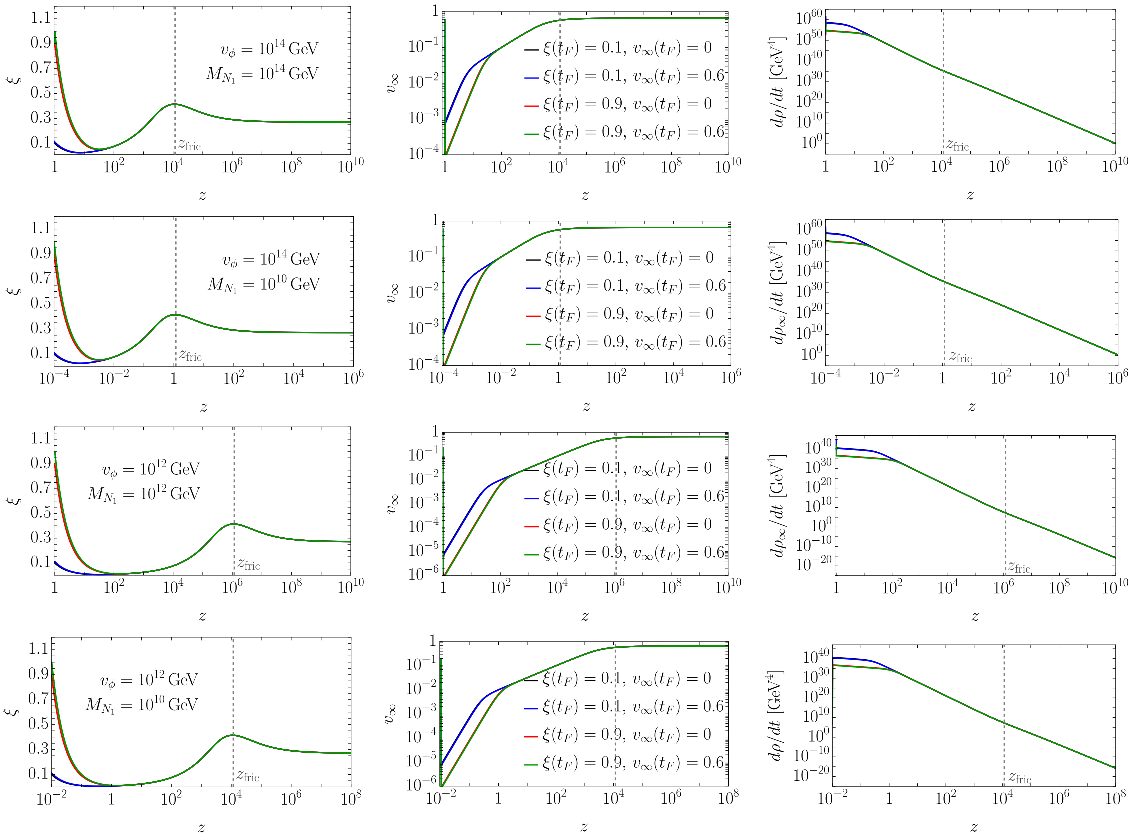

Figure IV.1: Example solutions for ξ (first column), v_∞ (second column), and $\frac{d\rho_\infty}{dt_i}$ (third column). The value of v_ϕ and M_{N_1} is the same in each row (as indicated in the first figure of each row). The different colored curves correspond to different initial conditions for ξ and v_∞ at $t \approx t_F$, as indicated in the labels in the second column.

- The long-string average root-mean-square (rms) velocity, v_∞, is initially suppressed by the thermal plasma, making the string motion non-relativistic, independently of initial conditions (c.f. the middle column in Fig. IV.1). The string motion gradually becomes relativistic, and for $z \gg z_{\rm fric}$ it asymptotes to the scaling value given implicitly by $v_\infty = \sqrt{\frac{k(v_\infty)}{k(v_\infty)+\widetilde{c}}}$ [192].

- The fact that v_∞ is time dependent could imply that the average boost factor γ_α of loops of type α also exhibits a strong time dependence. This could have implications for their production rate.

- All results are obtained assuming that $\widetilde{c} = 0.23$ from the time of formation. Altering this assumption could lead to drastically different results.

- We find that the results for $(v_\phi/\text{GeV},\, M_{N_1}/\text{GeV}) = (10^a,\, 10^{a-c})$, $c > 0$, are similar to the results for $(v_\phi/\text{GeV},\, M_{N_1}/\text{GeV}) = (10^a,\, 10^a)$ upon rescaling the z-axis by a factor 10^{-c}.

- Using Eq. (IV.43), we find $C_{\rm eff} = 5.4$ in the linear scaling regime, in agreement with Ref. [192].

VOS for loops

Next, we consider loop evolution in VOS. As stated above, there are no recent simulations to guide our understanding of particle production from loops during the friction-dominated epoch. However, it is understood that the efficiency of radiation energy loss from loops is sensitive to the rms velocity of loops v_l: The rate of energy loss from loops to gravitational radiation scales with the sixth power of v_l,

$$\left(\frac{dl}{dt}\right)_{\rm GW} = -\Gamma G\mu \left(2v_l^2\right)^3 , \tag{IV.49}$$

where the factor $\left(2v_l^2\right)^3$ is typically omitted as the loops are expected to satisfy $v_l = 1/\sqrt{2}$ in the linear scaling regime [336]. Similarly, radiation-loss due to particle production is expected to be sensitive to v_l, as an efficient damping force (induced by the thermal plasma) is expected to smooth out small-scale structure that could source particle radiation. For this reason, we will use relativistic v_l as a means to diagnose at which point in the cosmic evolution particle production from loops may become significant.

VOS equations for a loop of cosmic string with length l and rms-velocity v_l can be formulated as [336]

$$\frac{dl}{dt} = (1-2v_l^2)Hl - \frac{lv_l^2}{l_f} - \left(\frac{dl}{dt}\right)_{\rm Rad} , \tag{IV.50}$$

$$\frac{dv_l}{dt} = (1-v_l^2)\left[\frac{2\pi k(v_l)}{l} - v_l\left(2H + \frac{1}{l_f}\right)\right] , \tag{IV.51}$$

where

$$\left(\frac{dl}{dt}\right)_{\rm Rad} = \left(\frac{dl}{dt}\right)_{\rm GW} + \left(\frac{dl}{dt}\right)_{\rm P.R.} . \tag{IV.52}$$

The first term on the r.h.s. of Eq. (IV.52) is given in Eq. (IV.49), and the second term denotes energy loss due to particle radiation. It is clear from Eq. (IV.51) that as loops shrink, their motion becomes more relativistic.

Solution of VOS for loops

To solve the loop VOS equations (IV.50)-(IV.51), we find it useful to define a dimensionless quantity $\zeta(t) \equiv l(t)/w$,[7] and rewrite the equations as

$$\frac{d\zeta}{dz} = \frac{\zeta}{z}\left[(1-2v_l^2) - \left(\frac{\beta v_l^2}{z}\right)\sqrt{\frac{90}{\pi^2 g_*}}\left(\frac{M_{N_1}M_P}{\mu}\right)\right] - v_l^6\left(\frac{\Gamma z}{\pi^2}\right)\sqrt{\frac{90}{g_*}}\frac{\mu w^{-1}}{M_P M_{N_1}^2}, \tag{IV.53}$$

$$\frac{dv_l}{dz} = \left(\frac{1-v_l^2}{z}\right)\left[\frac{2\pi z^2 k(v_l)}{\zeta}\sqrt{\frac{90}{\pi^2 g_*}}\left(\frac{M_P w^{-1}}{M_{N_1}^2}\right) - 2v_l - \frac{\beta v_l}{z}\sqrt{\frac{90}{\pi^2 g_*}}\left(\frac{M_P M_{N_1}}{\mu}\right)\right], \tag{IV.54}$$

where we used $G = \frac{1}{8\pi M_P^2}$ and conservatively set the impact of particle production on the loop evolution to zero.[8] For concreteness, we will set $\sqrt{\mu} = w^{-1} = v_\phi$ in the following. The initial size of big and small loops discussed in Section II.3 read

$$\zeta_0(z) = \frac{\alpha z^2}{2}\sqrt{\frac{90}{\pi^2 g_*}}\frac{w^{-1}M_P}{M_N^2}, \qquad \zeta_0(z) = \frac{\Gamma z^2}{16\pi}\sqrt{\frac{90}{\pi^2 g_*}}\frac{\mu w^{-1}}{M_P M_N^2}, \tag{IV.55}$$

[7] Note that $\zeta(t) \sim 1$ signals the final collapse of the loop.

[8] This is a conservative estimate, as further energy loss via radiation would lead to v_l becoming relativistic sooner.

respectively. Solving $\zeta_0 > 1$ for z gives the range in z for which the long strings produce the associated loop type rather than direct emission of particle radiation,

$$z > \text{Max}\left[z_F,\ \sqrt{\frac{2}{\alpha}\sqrt{\frac{\pi^2 g_*}{90}}\frac{M_N^2}{M_P w^{-1}}}\right], \tag{IV.56}$$

$$z > \text{Max}\left[z_F,\ \sqrt{\frac{16\pi}{\Gamma}\sqrt{\frac{\pi^2 g_*}{90}}\frac{M_P M_N^2}{\mu w^{-1}}}\right], \tag{IV.57}$$

where the first (second) result is for big (small) loops and z_F denotes the formation temperature.

Small loops: We have numerically solved Eq. (IV.53) for small loops for different values of v_ϕ in the range $10^{10} \lesssim v_\phi/\text{GeV} \lesssim 10^{15}$ and $z_F \lesssim z_i \lesssim 10^4$ with initial condition $v_l = 0$ at loop formation z_i. In all cases, we find that $v_l \to 1/\sqrt{2}$ practically instantaneously. Based on this observation, we conclude that particle production from small loops during the friction-dominated epoch could be efficient.

Big loops: We have also solved Eq. (IV.53) for big loops. In this case, we find that loops produced at $z_i \sim z_F$ remain nonrelativistic until the last moments before they decay. For increasing $z_i \gg z_F$, the loops gradually become relativistic as they shrink, with loops associated with higher breaking scales being relativistic for a longer period of their lifespan compared to loops associated with lower breaking scales. This is illustrated in Fig. IV.2, where $\zeta(z)$ is shown in the first column and $v_l(z)$ in the second column for $(v_\phi/\text{GeV},\ M_{N_1}/\text{GeV}) = (10^{14},\ 10^{14})$ and $(10^{12},\ 10^{12})$ in black and blue, respectively. Rows $1-2$ correspond to $z_i = 1$, rows $3-4$ to $z_i = 10$, rows $5-6$ to $z_i = 100$, and rows $7-8$ to $z = 10^3$. We find that the results for $(v_\phi/\text{GeV},\ M_{N_1}/\text{GeV}) = (10^a,\ 10^{a-c})$, $c > 0$, are similar to the results for $(v_\phi/\text{GeV},\ M_{N_1}/\text{GeV}) = (10^a,\ 10^a)$ upon rescaling the z-axis by a factor 10^{-c}.

For $(v_\phi/\text{GeV},\ M_{N_1}/\text{GeV}) = (10^{14},\ 10^{14})$, we observe that big loops become relativistic soon after creation for $z_i \gtrsim 100$. The corresponding statement for $(v_\phi/\text{GeV},\ M_{N_1}/\text{GeV}) = (10^{12},\ 10^{12})$ requires $z_i \gtrsim 10^4$. Interestingly, as seen from the second row in Fig. IV.2, loops can undergo a stretching phase for sufficiently low z_i and sufficiently low v_ϕ. The reason is that the Hubble expansion becomes more important than shrinking effects, which indeed vanish in the limit $v_l \to 0$.

Particle production

In the following, we adopt an optimistic benchmark scenario for particle production, and analyze it within the VOS framework outlined above. While the VOS framework can accommodate more sophisticated scenarios, including non-monochromatic loop production and time-dependent particle-production efficiencies, the lack of detailed simulations of string networks and loops in the friction-dominated epoch necessitates simplifying assumptions. We defer further explorations to future work, when simulations can inform the choice of input parameters.

Analogeous to Eq. (IV.40), we consider a scenario where the energy lost by the string network is converted to particle radiation instantaneously. The resulting RHN production takes the form,

$$\frac{dn_N^{\text{c.s.}}}{dt} = f_N\left(\frac{\widetilde{c}(t)v_\infty(t)}{\gamma_N(t)\xi^3(t)}\right)\frac{\mu}{M_{N_1}t^3}, \tag{IV.58}$$

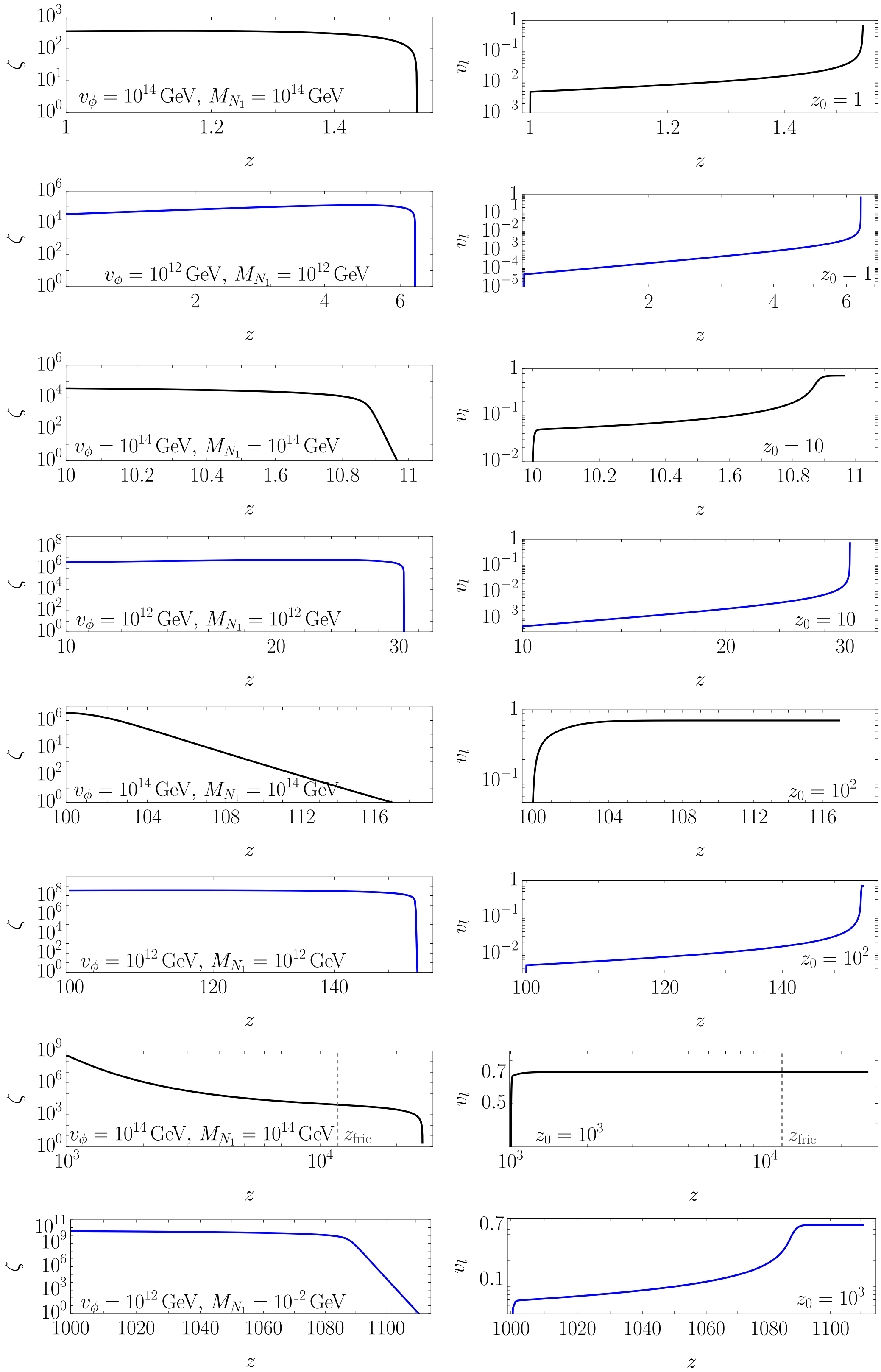

Figure IV.2: $\zeta(z)$ (first column) and $v_l(z)$ (second column) for $(v_\phi/\mathrm{GeV},\, M_{N_1}/\mathrm{GeV}) = (10^{14},\, 10^{14})$ and $(10^{12},\, 10^{12})$ in black and blue, respectively. Rows $1-2$ correspond to $z_i = 1$, rows $3-4$ to $z_i = 10$, rows $5-6$ to $z_i = 100$, and rows $7-8$ to $z = 10^3$.

where we have indicated that the loop-chopping efficiency, $\widetilde{c}$, and the average Lorentz boost of the emitted RHNs, γ_N, could be time dependent.

This scenario yields similar conclusions to assuming that energy is primarily lost to small loops of initial length $l_i(t) \sim \Gamma G\mu t$. For sufficiently early times, we have, $l_i < w$, and the string network effectively produces particle radiation. For $l_i \sim w$, loops annihilate shortly after formation, so for $l_i \lesssim w$, the two descriptions are similar. Since the energy-loss rate of the long-string network is suppressed at later times (cf. Eq. (IV.41)), contributions from $l_i \gg w$, where the difference between instantaneous particle radiation and small-loop production becomes significant, are typically negligible.

IV.4 Leptogenesis

In the following, we will consider how RHN production from cosmic strings may impact leptogenesis. We will first obtain analytical upper limits on the asymmetry generated by cosmic-string sourced RHNs during linear scaling, using the expressions for $\frac{dn_N^{\mathrm{c.s}}}{dt}$ derived in Section IV.3.1. To convert the latter to a form suitable for a standard leptogenesis analysis in a radiation-dominated universe, we use the standard relation[9]

$$t = \frac{1}{2H} \approx \frac{1}{2}\sqrt{\frac{\pi^2 g_*}{90}}\frac{T^2}{M_P}. \tag{IV.59}$$

We then provide a detailed discussion of asymmetry production during the friction-dominated phase, focusing on a maximally optimistic scenario for particle-production efficiency.

IV.4.1 Asymmetry production during the linear scaling regime

As a first step, it is useful to check if particle production from a linearly scaling network during the second regime discussed in Section IV.2 can account for the BAU. We will do this by computing the coefficient C introduced around Eq. (IV.11), and check the bound in Eq. (IV.18) for producing the BAU during linear scaling with maximal CP violation and no washout. Let us consider the RHN injection for instantaneous particle production derived in Eq. (IV.40), which takes the following form

$$\frac{1}{zsH}\frac{dn_N}{dt} \approx Cz^{-2}, \qquad C = \frac{2\sqrt{2}f_N C_{\mathrm{eff}}}{\gamma_N}\left(\frac{g_*}{g_{*s}}\right)\left(\frac{v_\phi}{M_P}\right)^2, \tag{IV.60}$$

where we used Eq. (II.95). Equating this with Eq. (IV.18), using Eq. (IV.23) and setting $z_0 = z_{\mathrm{fric}}$ and $C_{\mathrm{eff}} = 5.4$, we obtain that for the BAU to be created in said regime in the limit of vanishing washout and ϵ_1 saturating the upper bound in Eq. (II.124), M_{N_1} must satisfy

$$\frac{M_{N_1}}{\mathrm{GeV}} > 2\cdot 10^{16}\frac{1}{f_N}\left(\frac{10^{15}}{v_\phi}\right)^3\left(\frac{M_{N_1}}{v_\phi}\right)\left(\frac{g_{*s}}{g_*}\right)\left(\frac{\gamma_N}{10}\right)\sqrt{\frac{106.75}{g_*}}. \tag{IV.61}$$

This formula assumes that the string network reaches scaling instantaneously at $z = z_{\mathrm{fric}}$, which is an overly optimistic assumption, c.f. the discussion in Section IV.3.2 and in particular Fig. IV.1. Correcting for this by setting $z_0 > z_{\mathrm{fric}}$ would lead to an even stronger bound on M_{N_1}.

[9] See for example Ref. [360].

For the symmetry to be broken in the radiation-dominated post-inflationary universe, we require $M_P/v_\phi \gtrsim 10^3$. More precisely: Planck [17] places an upper bound on the Hubble parameter during inflation, $H_{\rm inf} \lesssim 6 \times 10^{13}$ GeV, derived from limits on the tensor-to-scalar ratio. If reheating is instantaneous, the Hubble parameter at the onset of the radiation-dominated era satisfies $H_{\rm rd} \lesssim H_{\rm inf}$, giving a maximal reheating temperature $T_{\rm rh}^{\rm max} \lesssim 6 \cdot 10^{15}$ GeV. Non-instantaneous reheating can only strengthen this bound as energy is redshifted away. Assuming the $U(1)_{B-L}$ symmetry is thermally restored after inflation, it can only break once the universe cools below the scale v_ϕ, which requires $v_\phi \lesssim T_{\rm rh}^{\rm max}$. This implies $M_P/v_\phi \gtrsim 10^3$, under the assumption of thermal symmetry restoration.

Finally, we remind the reader that $0 \leq f_N \leq 1$ and that the value of the boost factor γ_N is uncertain. Large simulation have shown that small loops are produced with a boost factor $\gamma_s \gtrsim 10$ [190, 193]. Since the rest-mass of a small loop with effective radius $R \gtrsim w$ is given by $2\pi\mu R$, which is larger than v_ϕ, we expect the RHNs produced in our instantaneous particle production picture to satisfy $\gamma_N \gtrsim \gamma_s \gtrsim 10$. Putting all of this together, and requiring $M_{N_1} \lesssim v_\phi$ for perturbative Yukawa couplings, we see that the non-thermal production of RHNs during scaling, cannot account for the full BAU. To summarize, we reached this conclusion by making the following assumptions:

- All the energy injected into loops during the linear scaling regime is immediately transferred into RHNs. Changing this assumption can only lead to a lower value for the asymmetry.
- The CP-asymmetry parameter is maximal, i.e. ϵ_1 saturates the upper bound in Eq. (II.124). Changing this assumption can only lead to a lower value for the asymmetry.
- We neglect all washout. Changing this assumption can only lead to a lower value for the asymmetry.
- We used $z_0 = z_{\rm fric}$, which is unrealistic. In fact, $z_0 \gg z_{\rm fric}$, implying that we significantly overestimate the resulting asymmetry production during linear scaling in the calculation above.
- We assumed that the symmetry is broken in a post-inflationary universe, such that the string network is not diluted away by cosmic inflation, which requires $M_P/v_\phi \gtrsim 10^3$.

Note that we did not have to compare the asymmetry production sourced by linearly scaling strings with the standard thermal LG contribution to (robustly) conclude that the former does not play an important role in explaining the observed BAU.

Comparison with literature [331, 333]: Our conclusion conflicts with previous work [331, 333], which suggested that RHN production from cosmic strings could lead to overproduction of baryon asymmetry. In their studies, the dominant production mechanism was through the final collapse of small loops that shrink by emitting gravitational radiation. In our notation, their result takes the following form up to an $\mathcal{O}(1)$ factor,

$$\frac{dn_{N_1}^{\rm c.s.}}{dt} \sim f_N \frac{1}{(\Gamma G\mu)t^4}. \tag{IV.62}$$

This is comparable to Eq. (IV.37), which leads to a similar parametric result upon identifying $\mu \sim v_\phi^2$, $w \sim v_\phi^{-1}$, $E_N \sim v_\phi$.

In Ref. [331], it was argued that the asymmetry produced from RHNs emitted from loops can be estimated as,

$$Y_{B-L} \approx \epsilon_1 \int \frac{1}{s} \frac{dn_{N_1}^{\text{c.s.}}}{dt} dt. \tag{IV.63}$$

Our Eq. (IV.13) is a refinement of this relation. Upon inserting Eq. (IV.62) into Eq. (IV.13), and using the time-temperature relation (IV.59), we obtain[10]

$$\begin{aligned} Y_{B-L} &\approx \kappa_w\, \epsilon_1\, 2.8 \cdot 10^{-5} \left(\frac{50}{\Gamma}\right) \sqrt{\frac{g_*}{106.75}} \left(\frac{g_*}{g_{*s}}\right) \left(\frac{M_{N_1}}{v_\phi}\right)^3 \left(\frac{v_\phi}{10^{13}\,\text{GeV}}\right)^2 \frac{1}{(\sqrt{2}z_s)^3} \\ &\lesssim \kappa_w\, 2.8 \cdot 10^{-8} \left(\frac{50}{\Gamma}\right) \sqrt{\frac{g_*}{106.75}} \left(\frac{g_*}{g_{*s}}\right) \left(\frac{M_{N_1}}{v_\phi}\right)^4 \left(\frac{v_\phi}{10^{13}\,\text{GeV}}\right)^3 \frac{1}{(\sqrt{2}z_0)^3}, \end{aligned} \tag{IV.64}$$

where we in the second line used Eq. (II.124). Upon choosing $M_{N_1} \sim v_\phi$, and setting $\kappa_w \approx 1$ and $z_0 \sim 1$,[11] one could naively conclude that it is possible to overproduce baryon asymmetry from loops associated with $B-L$ breaking well below the GUT scale if washout effects are weak, consistent with the findings in Ref. [331,333]. However, in Refs. [331,333] the authors assume that the string network is in the linear scaling regime. As reviewed in Section IV.3.2, the string network is not expected to reach linear scaling until the temperature has dropped well below the value in Eq. (IV.23), which implies

$$z_0 \gg z_{\text{fric}} \approx 0.5 \left(\frac{M_P}{v_\phi}\right) \left(\frac{M_{N_1}}{v_\phi}\right). \tag{IV.65}$$

Inserting this into Eq. (IV.64) we obtain

$$\begin{aligned} Y_{B-L} &\ll \kappa_w\, 7.8 \cdot 10^{-6} \left(\frac{50}{\Gamma}\right) \sqrt{\frac{g_*}{106.75}} \left(\frac{g_*}{g_{*s}}\right) \left(\frac{M_{N_1}}{v_\phi}\right) \left(\frac{v_\phi}{10^{13}\,\text{GeV}}\right)^3 \left(\frac{v_\phi}{M_P}\right)^3 \\ &\sim 5 \cdot 10^{-12} \kappa_w \left(\frac{50}{\Gamma}\right) \sqrt{\frac{g_*}{106.75}} \left(\frac{g_*}{g_{*s}}\right) \left(\frac{M_{N_1}}{v_\phi}\right) \left(\frac{v_\phi}{10^{15}\,\text{GeV}}\right)^6. \end{aligned} \tag{IV.66}$$

This result shows that, in the limit of vanishing washout and maximum value for ϵ_1, particle-production during linear scaling can still not account for the full BAU for $v_\phi \lesssim 10^{15}$ GeV. In conclusion, we have shown that the optimistic results in Ref. [331, 333], are inconsistent: Although the authors work under the assumption of linearly scaling strings, their calculation includes contributions at $z \ll z_{\text{fric}}$, which provides the dominant contribution to the baryon asymmetry.

IV.4.2 Asymmetry production during friction domination

The above calculations show that leptogenesis sourced by cosmic strings in the linear scaling regime does not provide a viable explanation of the origin of the BAU. The next step is to consider the contribution to the BAU from loops produced in the friction-dominated epoch. Large uncertainties in decay mechanisms, string evolution, loop evolution, and initial conditions for the string network plague the calculation of the lepton asymmetry. The accuracy gained by performing a full-fledged numerical analysis of Boltzmann equations would be drowned in these uncertainties. For this reason, we will generalize the treatment of Boltzmann equations in Section IV.2.3 to obtain analytical estimates of the $B-L$ asymmetry. First, we summarize the remaining assumptions that our numerical examples will follow:

[10] The factor of $\sqrt{2}$ accompanying z_s follows from the relation $t \approx 2t_i$ in Eq. (IV.37).

[11] Note that Eq. (IV.13) was derived under the assumption $z_0 \gg 1$, so $z_0 \sim 1$ is strictly speaking well outside the regime of validity of the equation.

- The source term for RHN-injection from cosmic strings is parametrized as follows

$$\frac{1}{s(z)H(z)\cdot z}\frac{\partial n_N^{\text{c.s.}}}{\partial t} = C(z)z^{-n}, \qquad n \geq 2, \tag{IV.67}$$

where we now allow C to have a $z-$dependence. We will specialize to the optimistic scenario described around Eq. (IV.58), for which the source term takes the following form,

$$\frac{1}{zsH}\frac{dn_N}{dt} = 2f_N\frac{\widetilde{c}(z)v_\infty(z)}{\gamma_N(z)z^2\xi^3(z)}\left(\frac{g_*}{g_{*s}}\right)\frac{\mu}{M_P^2} \equiv C(z)z^{-2}, \tag{IV.68}$$

with

$$C(z) = 2f_N\frac{\widetilde{c}(z)v_\infty(z)}{\gamma_N(z)\xi^3(z)}\left(\frac{g_*}{g_{*s}}\right)\frac{\mu}{M_P^2}. \tag{IV.69}$$

- In our numerical examples, we will consider the case $v_\phi = M_{N_1}$. In principle, one could have $M_{N_1} \lesssim v_\phi$ while retaining perturbative RHN Yukawa couplings. Since the energy-loss rate from long strings decrease with time, fixing $M_{N_1} \gg v_\phi$ would result in the bulk of non-thermal RHN production taking place when washout effects are highly efficient, resulting in a suppressed final asymmetry compared to the case of heavier RHNs.
- We will primarily focus on the region $z \gg 1$, where the long-string evolution is less sensitive to initial conditions for $v_\phi = M_{N_1}$, c.f. Fig. IV.1. This is also motivated by the observation that the contribution from CS to Y_{N_1} is negligible for $z = \mathcal{O}(1)$ as we demonstrate in the following.

For $z = \mathcal{O}(1)$, the RHN yield is described by Eq. (IV.2). For simplicity, we ignore the S_{2N} term in the following, which depends on several BSM parameters, and the resulting equation reads

$$\frac{\partial Y_{N_1}}{\partial z} = -\left(D+S\right)\left(Y_{N_1} - Y_{N_1}^{\text{eq}}\right) + \frac{1}{s(z)H(z)\cdot z}\frac{\partial n_{N_1}^{\text{cs}}}{\partial t}, \tag{IV.70}$$

where Ref. [225] is used to obtain an expression for the scattering term S. We solve Eq. (IV.2) numerically for $M_{N_1} = v_\phi = 10^{15}$ GeV and $K = 10$ with initial conditions $\xi(z=1) = 0.1$ and $v_\infty(z=1) = 0$. Note that the result is insensitive to the choice of $v_\infty(z=1)$ and increasing $\xi(z=1)$ leads to a lower production-rate of N_1, c.f. Fig. IV.1. The result is shown in Fig. IV.3. In the upper panel, we show Y_{N_1} obtained when the source term in Eq. (IV.70) is included (green), Y_{N_1} obtained when the source term in Eq. (IV.70) is zero (red), and $Y_{N_1}^{\text{eq}}$ (blue). To assess the impact of the source term, we consider

$$\frac{(Y_{N_1}^{\text{full}} - Y_{N_1}^{\text{eq}}) - (Y_{N_1}^{\text{no source}} - Y_{N_1}^{\text{eq}})}{Y_{N_1}^{\text{no source}} - Y_{N_1}^{\text{eq}}} = \frac{Y_{N_1}^{\text{full}} - Y_{N_1}^{\text{no source}}}{Y_{N_1}^{\text{no source}} - Y_{N_1}^{\text{eq}}}, \tag{IV.71}$$

where $Y_{N_1}^{\text{full}}$ ($Y_{N_1}^{\text{no source}}$) denotes the solution to Eq. (IV.70) with (without) the source term. We find that Eq. (IV.71) is below 1% for $z \lesssim 8$ and below 10% for $z \lesssim 12$. This indicates that the source term has a negligible impact (at most $\mathcal{O}(1\%)$) on the asymmetry production for $z = \mathcal{O}(1)$. Meanwhile, for $z = \mathcal{O}(10)$, the cosmic-string source term has a dramatic impact on the Y_{N_1} abundance. We consider this regime next.

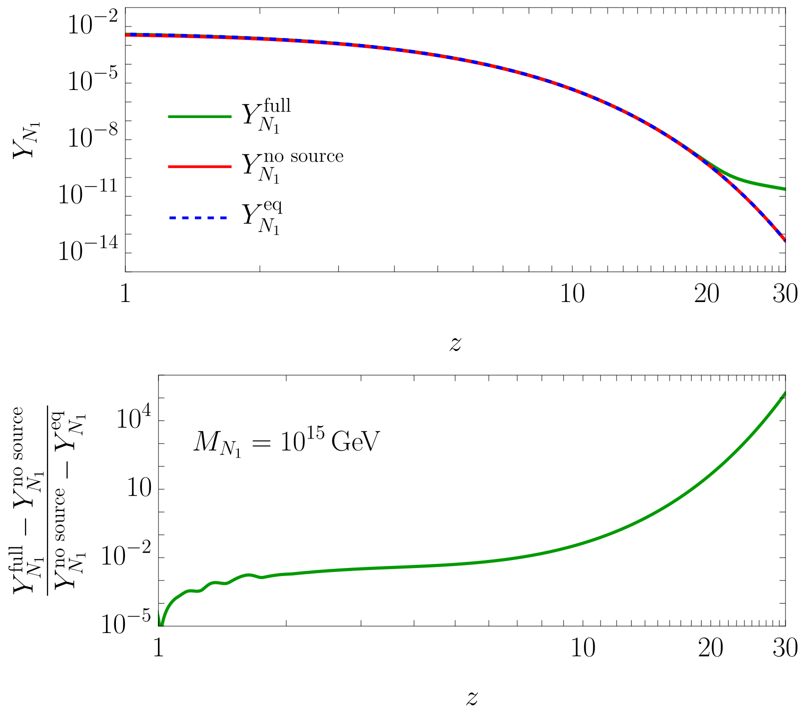

Figure IV.3: Upper panel: Y_{N_1} obtained when the source term in Eq. (IV.70) is included (green), Y_{N_1} obtained when the source term in Eq. (IV.70) is zero (red), and $Y_{N_1}^{\rm eq}$ (blue). Lower panel: Numerical evaluation of Eq. (IV.71). See text for details.

For $z \gg 1$, where $Y_{N_1}^{\rm eq}$ is small compared to Y_{N_1}, the equations (IV.4)-(IV.6) are applicable, which we reproduce here in a suitable form,

$$\frac{\partial Y_N}{\partial z} \approx -K' z Y_N + \frac{1}{s(z)H(z)\cdot z}\frac{\partial n_N^{\rm c.s.}}{\partial t}, \tag{IV.72}$$

$$\frac{\partial Y_{B-L}}{\partial z} \approx -\epsilon_1 K' z Y_N - Y_{B-L} W. \tag{IV.73}$$

For the parametrization in Eq. (IV.67), the general solutions for $z \geq z_0 \gg 1$ read

$$Y_{N_1}(z) = e^{-\frac{1}{2}K'z^2}\left[Y_{N_1}(z_0)\, e^{\frac{1}{2}K'z_0^2} + \int_{z_0}^{z} C(x)\, x^{-n} e^{\frac{1}{2}K'x^2}\, dx\right], \tag{IV.74}$$

$$\begin{aligned} Y_{B-L}(z) = {}& Y_{B-L}(z_0)\, e^{-\int_{z_0}^{z} W(u)\,du} \\ & - \epsilon_1 Y_{N_1}(z_0)\cdot K' e^{\frac{1}{2}K'z_0^2}\int_{z_0}^{z} y\, e^{-\int_y^z W(u)\,du}\, e^{-\frac{1}{2}K'y^2}\, dy \\ & - \epsilon_1 K' \int_{z_0}^{z} y\, e^{-\int_y^z W(u)\,du}\, e^{-\frac{1}{2}K'y^2}\left(\int_{z_0}^{y} C(x) x^{-n}\, e^{\frac{1}{2}K'x^2}\, dx\right) dy. \end{aligned} \tag{IV.75}$$

Note that this solution explicitly encodes the effect of washout effects, W, and is valid for any choice of $C(z)$ in Eq. (IV.67) although we specialize to the parametrization in Eq. (IV.69).

In Fig. IV.4, we show the result for Y_{N_1} (green curve) as a function of z, for $v_\phi = M_{N_1} = 10^{15}$ GeV and $z > 20$. We have fixed, $f_N = \gamma_N = 1$, i.e., assuming all energy is converted to non-relativistic RHNs. The decay parameter is fixed to $K = 10$, and increasing its value leads to a decrease in Y_{N_1}. We have included the photon yield Y_γ (black dashed) and the

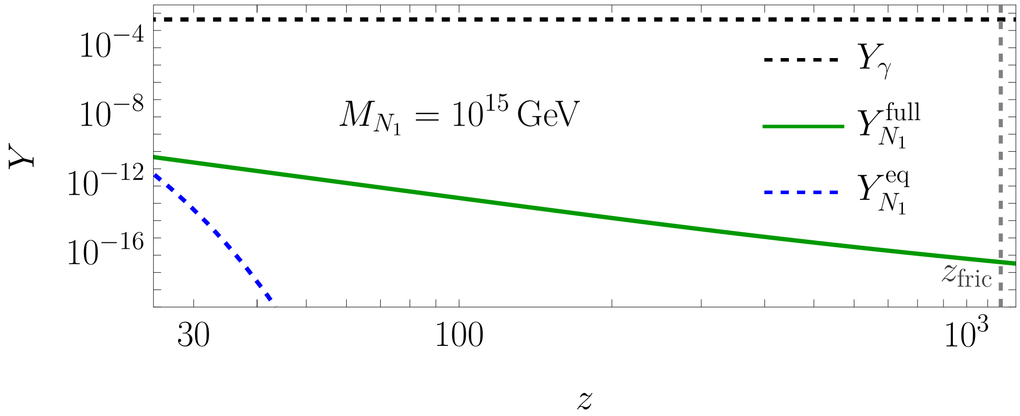

Figure IV.4: Y_{N_1} (red), $Y_{N_1}^{\rm eq}$ (blue), and Y_γ (black) as a function of z starting from where Y_{N_1} is insensitive to initial conditions for the long-string network for $v_\phi = M_{N_1} = 10^{15}$ GeV, $f_N = \gamma_N = 1$, and $K = 10$. Increasing K while keeping other parameters fixed leads to a decrease in Y_{N_1}.

RHN-equilibrium yield $Y_{N_1}^{\rm eq}$ (blue dashed) for reference. The vertical gray line to the far right in the plot marks the end of the friction-dominated epoch. As can be seen, the RHN yield during the friction-dominated epoch can be many orders of magnitude higher than the corresponding value at $z \approx z_{\rm fric}$.

We now have all the ingredients to numerically evaluate the asymmetry generated from non-thermally sourced RHNs in the regime $z \gg 1$. This contribution should be compared with the thermally produced abundance, given in Eq. (II.116), and reproduced here for convenience,

$$Y_{B-L}^{\rm th}(z \to \infty) = \epsilon_1 \bar{\kappa}_f. \tag{IV.76}$$

It is convenient to normalize the asymmetry generated from non-thermally sourced RHNs at $z > z_0$ by Eq. (IV.76), to make the dependence on ϵ_1 drop out, and using Eq. (IV.75) we obtain

$$\frac{\left(Y_{B-L}(z) - Y_{B-L}(z_0)\, e^{-\int_{z_0}^{z} W(u)\,du}\right)}{Y_{B-L}^{\rm th}(z \to \infty)} = -\frac{Y_{N_1}(z_0)}{\bar{\kappa}_f} K' e^{\frac{1}{2}K' z_0^2} \int_{z_0}^{z} y\, e^{-\int_y^z W(u)\,du}\, e^{-\frac{1}{2}K' y^2}\, dy$$
$$-\frac{K'}{\bar{\kappa}_f} \int_{z_0}^{z} y\, e^{-\int_y^z W(u)\,du}\, e^{-\frac{1}{2}K' y^2} \left(\int_{z_0}^{y} C(x) x^{-n}\, e^{\frac{1}{2}K' x^2}\, dx \right) dy. \tag{IV.77}$$

If the expression above is $\mathcal{O}(1)$ or larger in the limit $z \to \infty$, it would signal that cosmic strings could play an important role in generating the BAU.

Using $W = W_{\Delta L=2} + W_{\rm ID}$, c.f. Eqs. (II.122)-(II.123) for explicit expressions, $K = 10$, $z_0 = 20$, and the maximal values $f_N = \gamma_N = 1$, we show Eq. (IV.77) as a function of z in Fig. IV.5 for $v_\phi = M_{N_1} = 10^{15}$ GeV (green) and $v_\phi = M_{N_1} = 10^{14}$ GeV (red). The solid curves correspond to $\bar{m} = 0.05$ eV, and the dashed curves to $\bar{m} = 0.07$ eV. The results indicate that RHNs sourced by cosmic strings at $z \gg 1$ have a negligible impact on the final asymmetry. We find that varying z_0 from 15 to 30 leads to a final result for the asymmetry that differs from the ones shown by factor of 1.05 to 0.8 (3.8 to 0.44) for $M_{N_1} = 10^{15}$ GeV ($M_{N_1} = 10^{14}$ GeV). The comparatively larger variation for $M_{N_1} = 10^{14}$ GeV is attributed to less efficient washout, and $v_\infty(z)$ and $\xi(z)$ being more sensitive to z in this regime.

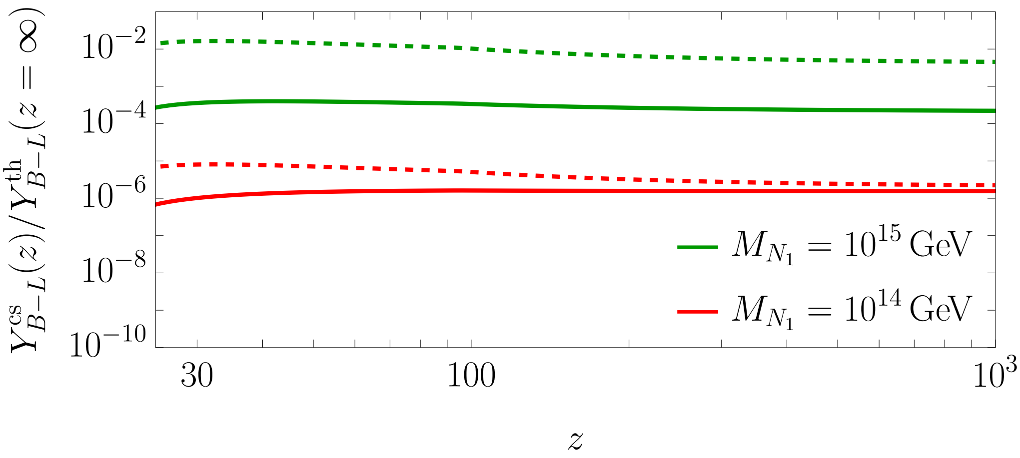

Figure IV.5: Asymmetry yield generated by cosmic strings at $z \gg 1$ as a function of z, normalized by $Y^{\rm th}_{B-L}(z=\infty)$ for $v_\phi = M_{N_1} = 10^{15}$ GeV (green) and $v_\phi = M_{N_1} = 10^{14}$ GeV (red). The solid curves correspond to $\bar{m} = 0.05$ eV, and the dashed curves to $\bar{m} = 0.07$ eV.

In summary, we have shown that even for highly optimistic parameters for RHN-production from cosmic strings, the latter can at most provide $\mathcal{O}(1\%)$ corrections to the final baryon asymmetry for $M_{N_1} \lesssim 10^{15}$ GeV and $v_\phi \lesssim 10^{15}$ GeV.

IV.5 Summary and outlook

In this chapter, we considered if RHN production from cosmic strings arising from spontaneously broken gauged $U(1)_{B-L}$ can play an important role in leptogenesis. We focused on the scenario where $B - L$ is broken in the post-inflationary universe after (or near the end of) inflationary reheating. In this scenario, the universe is radiation-dominated, and one can solve a coupled set of two Boltzmann equations for Y_{N_1} and Y_{B-L} as a function of temperature.

There are large uncertainties associated with particle-production rates from local cosmic strings, which lead to large uncertainties in the predictions of the baryon asymmetry generated from CS-sourced RHNs. To gauge the potential importance of CS for LG, we included predictions based on maximally optimistic assumptions on the efficiency of RHN production from strings. Furthermore, the discussion was divided into two parts:

1. Contribution from RHNs produced during the linear scaling regime.
2. Contribution from RHNs produced during the friction-dominated epoch.

We first considered the first point and demonstrated that, contrary to previous claims in the literature, RHN production in the linear-scaling regime has a negligible impact on the BAU. Along the way, we presented analytic expressions for particle-production rates for cosmic strings with different small-scale structure, which we hope to be useful in contexts beyond the present study.

Next, we considered the second point above using the VOS framework to model the evolution of long strings and loops during the initial friction-dominated epoch. We showed that the RHN-production rate can be much larger during this epoch compared to the linear scaling regime, and correspondingly, larger contributions to the BAU may be generated. However, for breaking scales $v_\phi \lesssim 10^{15}$ GeV, which are required to be consistent with

CMB constraints on the string tension, c.f. Eq. (II.106), we found that the contribution to the BAU from strings is very small compared to the standard TLG contribution, even for maximally optimistic choices of string parameters.

As new knowledge about cosmic-string evolution and particle production is developed in the future, we hope that our study may serve as a useful benchmark for studies addressing possible connections between cosmic strings and leptogenesis. In closing, we provide an outlook of scenarios that may be promising for future studies.

Outlook

In this chapter, we assumed that $U(1)_{B-L}$ is broken after the end of inflationary reheating. This allowed us to conduct a study that does not depend on specifics of an inflationary scenario, and to compare the string contribution with the standard thermal contribution. In the future, it would be interesting to understand if there are viable scenarios where $U(1)_{B-L}$ is broken non-thermally, allowing a hierarchy $v_\phi \gg T_{\rm rh}$, where $T_{\rm rh}$ denotes the inflationary reheating temperature, such that the thermal production of RHNs is suppressed. This would bypass one of the main obstructions encountered in this chapter, namely that the asymmetry from thermally produced RHNs dominates over the asymmetry produced by CS sourced RHNs. In the absence of other non-thermal sources of RHNs, cosmic strings could then provide the most important source for leptogenesis.

In the context of (supersymmetric) hybrid inflation models [361–363] featuring a $U(1)_{B-L}$ symmetry, $B-L$ can be broken at the end of inflation. It has been suggested that the spontaneous breaking of $U(1)_{B-L}$ to end hybrid inflation can generate the initial conditions of the hot early universe [364–366]. In this context, heavy neutrinos are produced non-thermally through inflationary (p)reheating dynamics, and their subsequent decay can account for the BAU [366]. In particular, the reheating temperature may be much smaller than M_{N_1}, such that the contribution to the BAU from thermally produced RHNs is negligible and washout effects are highly suppressed [334]. It could be interesting to understand if there is experimentally allowed parameter space associated with hybrid inflation realizations with spontaneously broken $U(1)_{B-L}$ where (p)reheating dynamics cannot account for the BAU, while cosmic strings can.

More generally, it would be interesting to understand if there are viable model realizations where $U(1)_{B-L}$ is broken in a post-inflationary universe where the maximum temperature is much lower than v_ϕ and M_{N_1} and the initial abundance of cosmic strings is not highly diluted. We leave such explorations for future work.

A Integrated Boltzmann equations without kinetic equilibrium

A detailed account of classical Boltzmann equations for leptogenesis without the assumption of kinetic equilibrium can be found in Ref. [367], which we follow below. We begin at the level of phase-space distributions f_{N_1} and $f_{\Delta L}$, for N_1 and the lepton asymmetry, respectively,

$$\frac{\partial f_N}{\partial t} - |\vec{p}_N| H \frac{\partial f_N}{\partial |\vec{p}_N|} = C_{S_{2N}}[f_N] + C_{D_N}[f_N] + C_{S_N}[f_N] + \text{CS}, \tag{A.1}$$

$$\frac{\partial f_{\Delta L}}{\partial t} - |\vec{p}_{\Delta L}| H \frac{\partial f_{\Delta L}}{\partial |\vec{p}_{\Delta L}|} = C_{D_{\Delta L}}[f_{\Delta L}] + C_{S_{\Delta L}}[f_{\Delta L}] + \text{CS}, \tag{A.2}$$

where by definition

$$g_N \int \frac{d^3p}{(2\pi)^3} \mathrm{CS} \equiv \frac{\partial n_N^{\text{c.s.}}}{\partial t}, \tag{A.3}$$

and $C_{S_{2N}}$, $C_{D/\Delta L}$, and $C_{S/\Delta L}$ denote collision terms involving two external RHNs, decays/ inverse decays, and other scatterings, respectively. Transforming to dimensionless coordinates $z = M/T$ and $y_i = |\vec{p}_i|/T$ we obtain

$$\frac{\partial f_N}{\partial z} = \frac{1}{H(z) \cdot z} \left(C_{S_{2N}}[f_N(y,z)] + C_{D_N}[f_N(y,z)] + C_{S_N}[f_N(y,z)] + \mathrm{CS} \right), \tag{A.4}$$

$$\frac{\partial f_{\Delta L}}{\partial z} = \frac{1}{H(z) \cdot z} \left(C_{D_{\Delta L}}[f_{\Delta L}(y,z)] + C_{S_{\Delta L}}[f_{\Delta L}(y,z)] \right). \tag{A.5}$$

In the limit $z \gg 1$, the r.h.s. of Eq. (A.4) is dominated by C_{D_N} [225], and we can therefore safely neglect $C_{S_{2N}}$ and C_{S_N}, which simplifies the Boltzmann equation for N_1 significantly. In evaluating the washout contribution in Eq. (A.5), we include the effects of decays/ inverse decays and $\Delta L = 2$ scatterings, which importantly are not Boltzmann suppressed for $z \gg 1$. Under these assumptions, the Boltzmann equation governing the RHNs can be written as

$$\frac{\partial f_N}{\partial z} = \frac{\Gamma_{\text{r.f.}} M}{z H(z) E_N} \left(f_N^{\text{eq}} - f_N \right) + \frac{1}{H(z) \cdot z} (\mathrm{CS}), \tag{A.6}$$

where $\Gamma_{\text{r.f.}}$ denotes the decay width of the RHN in its rest frame at zero temperature.

The RHN population in the regime under consideration is sourced by cosmic-loop decays, which determines the initial momentum distribution of RHNs. In the following, we assume that their distribution is sharply peaked around $E_N = \gamma_N M_{N_1}$, where γ_N parametrizes how boosted the emitted RHNs are. Under this assumption, we can then treat the factor E_N in Eq. (A.6) as a constant and integrate both sides over $g_N \int \frac{d^3p}{(2\pi)^3}$, which upon using Eq. (A.6) gives

$$\frac{\partial Y_N}{\partial z} = \frac{\Gamma_{\text{r.f.}}}{z H(z)} \frac{1}{\gamma_N} (Y_N^{\text{eq}} - Y_N) + \frac{1}{s(z) H(z) \cdot z} \frac{\partial n_N^{\text{c.s.}}}{\partial t}. \tag{A.7}$$

It is instructive to compare the first term on the r.h.s. with the contribution from decays/ inverse decays in the standard result, Eq. (IV.2), in the limit $z \gg 1$. There, the said term takes the form $D \approx \frac{\Gamma_{\text{r.f.}}}{z H(z)}$, see e.g. Ref. [225], and we see that Eq. (A.7) has an additional suppression factor of $\frac{1}{\gamma_N}$. Similarly, by following Section 3 in Ref. [367] and Appendix A in Ref. [224], we obtain

$$\frac{\partial Y_{\Delta L}}{\partial z} = \epsilon_1 \frac{\Gamma_{\text{r.f.}}}{z H(z)} \frac{1}{\gamma_N} \left(Y_N - Y_N^{\text{eq}} \right) - Y_{\Delta L} \left[W_{\text{ID}} + 2 W_{\Delta L = 2}^{\text{sub}} \right], \tag{A.8}$$

with

$$W_{\text{ID}} = \frac{1}{4} K z^3 K_1(z) = \frac{1}{2} D \frac{N_N^{\text{eq}}}{N_l^{\text{eq}}} = \frac{\gamma_D}{2 n_L^{\text{eq}}}, \qquad W_{\Delta L = 2}^{\text{sub}} = \frac{\gamma_N^{\text{sub}}}{n_L^{\text{eq}}}, \tag{A.9}$$

where explicit expressions for γ_D and γ_N^{sub} can be found in Ref. [224]. The form of these Boltzmann equations is in agreement with the results in Ref. [322].

B Derivations of particle-production rates during linear scaling regime

In this appendix, we provide detailed derivations of analytic expressions for RHN injection from different types of cosmic-string loops in the linear scaling regime.[12]

Particle emission from small cuspy loops

In the following, we consider particle emission from small cuspy loops. The critical length l_c of a cuspy loop, defined in Eq. (II.103), is a measure of when energy loss via GW emission becomes more important than energy loss via particle production. Once the length of the loop is smaller than the critical length, particle decay becomes the dominant energy-loss contribution. We have verified that the following inequality is satisfied for the time scales relevant to our leptogenesis analysis,

$$\Gamma G\mu t \lesssim l_c. \tag{B.1}$$

Consequently, we can neglect energy loss due to GW emission and use the following formula to estimate how loops evolve in time [203]

$$\frac{dl}{dt} = -\sqrt{\frac{w}{l}}. \tag{B.2}$$

Final collapse

The number of small loops collapsing per unit time and volume at time $t > \frac{w}{\Gamma G\mu}$ equals the number of loops created inside a volume $\left(\frac{a(t_i)}{a(t)}\right)^3$ at an earlier time t_i. A relation between t and t_i is obtained by integrating Eq. (B.2) and setting $l(t) \approx 0$,

$$t = t_i + \frac{2}{3\sqrt{w}}(\Gamma G\mu t_i)^{3/2}. \tag{B.3}$$

The production rate of small loops inside a unit volume at time t_i can be read out from Eq. (II.98)

$$\frac{dn}{dt_i} = \frac{F_s\sqrt{2}C_{\text{eff}}(t_i)}{\gamma_s(\Gamma G\mu)t_i^4}, \tag{B.4}$$

so the number of small loops collapsing per unit volume at time t is

$$\dot{n}^{\text{col}-\text{small}}(t) \approx \frac{F_s\sqrt{2}C_{\text{eff}}(t_i)}{\gamma_s(\Gamma G\mu)t_i^4}\left(\frac{a(t_i)}{a(t)}\right)^3. \tag{B.5}$$

All loops created at the same time collapse at the same time so there is no need to integrate over loop distributions to obtain the total number of loops collapsing at a given time [369]. The injection rate of RHNs per unit volume from small loops collapsing at a time t can then be estimated as,

$$\dot{n}_N^{\text{col}-\text{small}}(t) \approx f_N \begin{cases} \frac{\mu F_s\sqrt{2}C_{\text{eff}}(t_i)}{\gamma_s t^3 E_N} & t = t_i, & \text{if } t \lesssim \frac{w}{\Gamma G\mu}, \\ \frac{F_s\sqrt{2}C_{\text{eff}}(t_i)}{\gamma_s(\Gamma G\mu)t_i^4}\left(\frac{a(t_i)}{a(t)}\right)^3 \frac{\mu w}{E_N}, & t = t_i + \frac{2}{3\sqrt{w}}(\Gamma G\mu t_i)^{3/2}, & \text{if } t \gtrsim \frac{w}{\Gamma G\mu}. \end{cases} \tag{B.6}$$

[12] See Section 6.4 in Ref. [368] and references therein for earlier related analysis.

The fraction of scale factors can be rewritten in terms of time in the usual way,

$$\left(\frac{a(t_i)}{a(t)}\right)^3 = \left(\frac{t_i}{t}\right)^p, \qquad p = \frac{2}{1+\omega} \tag{B.7}$$

where ω denotes the equation-of-state of the universe. For the time-scales relevant to our leptogenesis discussion, Eq. (B.6) can be further simplified to

$$\dot{n}_N^{\mathrm{col-small}}(t) \approx f_N \frac{\mu F_s \sqrt{2} C_{\mathrm{eff}}(t_i)}{\gamma_s E_N} \times \begin{cases} \frac{1}{t^3} & \text{if } t \lesssim \frac{w}{\Gamma G\mu}, \\ \frac{w}{(\Gamma G\mu) t^4}, & \text{if } \frac{w}{(\Gamma G\mu)^3} \gtrsim t \gtrsim \frac{w}{\Gamma G\mu}. \end{cases} \tag{B.8}$$

Cusp evaporation

Cuspy loops also emit particle radiation through cusp evaporation. In the vicinity of a cusp, string segments overlap, c.f. Fig. II.4, and the corresponding portions of the string can decay into massive radiation. The typical length of an overlapping segment has been estimated to be of size $\sqrt{wl}$ [370]. Hence, we model the energy going into massive particles emitted per cusp evaporation to be of order $\mu\sqrt{wl}$ with corresponding radiated power [192]

$$P_{\mathrm{cusp}}^{\mathrm{part}} = N_c \mu \sqrt{\frac{w}{l(t)}}, \tag{B.9}$$

where $N_c \sim 2$ is the average number of cusp annihilations per period [209]. The corresponding average number of RHNs radiated per unit time from a shrinking loop of length $l(t) < l_c$ at time t is estimated as

$$\frac{dN_N^{\mathrm{cusp}}}{dt} = f_N \frac{N_c \mu \sqrt{w}}{\sqrt{l(t)} E_N}. \tag{B.10}$$

The number density of loops with length l at time t is related to the number density of loops produced at an earlier instant t_i,

$$\frac{dn(t)}{dl} = \left[\frac{a(t_i)}{a(t)}\right]^3 \frac{dn(t_i)}{dt_i} \frac{dt_i}{dl}, \tag{B.11}$$

where the loop-length evolution equation in Eq. (B.2) dictates,

$$l(t)^{3/2} = l_i^{3/2}(t_i) + \frac{3\sqrt{w}}{2}(t_i - t), \qquad \frac{dt_i}{dl} = \frac{\sqrt{l(t)}}{\sqrt{w} + (\Gamma G\mu)^{3/2}\sqrt{t_i}}. \tag{B.12}$$

Substituting (II.98) and (B.12) into (B.11), and folding Eqs. (B.11) with (B.10) we obtain the following expression for the number density of RHNs emitted from cusps on small loops at times $t > \frac{w}{\Gamma G\mu}$,

$$\dot{n}_N^{\mathrm{cusp-small}}(t) \sim f_N \int_w^{(\Gamma G\mu t)} dl \left[\frac{a(t_i)}{a(t)}\right]^3 \frac{F_s \sqrt{2} C_{\mathrm{eff}}(t_i)}{\gamma_s (\Gamma G\mu) t_i^4} \left(\frac{1}{\sqrt{w} + (\Gamma G\mu)^{3/2}\sqrt{t_i}}\right) \frac{N_c \mu \sqrt{w}}{E_N}. \tag{B.13}$$

It is clear that the integral receives the largest contributions from the smallest loops, i.e. loops created at the earliest possible time $t_i(t)$. Loops with size $l(t) \sim w$ satisfy,

$$t = t_i + \frac{2(\Gamma G\mu t_i)^{3/2}}{3\sqrt{w}} - \frac{2}{3}w, \tag{B.14}$$

so we can employ the following approximation,

$$\begin{cases} t_i \approx t, & \text{if } \frac{w}{(\Gamma G\mu)^3} \gtrsim t > \frac{w}{\Gamma G\mu}, \\ t_i \approx \frac{(\sqrt{w}t)^{2/3}}{\Gamma G\mu}, & \text{if } t > \frac{w}{(\Gamma G\mu)^3}. \end{cases} \tag{B.15}$$

For $t \lesssim \frac{w}{(\Gamma G\mu)^3}$, we approximate the integral in Eq. (B.13) by the value of the integrand evaluated at $t_i = t$, multiplied by the length of the full integration domain. For completeness, we also provide an analytic estimate valid for larger t, that is of less relevance to our leptogenesis analysis. Here, we use Eq. (B.2) to find that a good parametric estimate for the length of loops born an $\mathcal{O}(1)$ number later than t_i is $l(t) \approx (\sqrt{w}t_i)^{2/3}$. Multiplying the integrand evaluated at $t_i = \frac{(\sqrt{w}t)^{2/3}}{\Gamma G\mu}$ with this length scale yields a parametric estimate of the integral at times $t > \frac{w}{(\Gamma G\mu)^3}$. The final result is summarized in the following expression

$$\dot{n}_N^{\text{cusp}-\text{small}}(t) \approx f_N \frac{F_s \sqrt{2} C_{\text{eff}} N_c \mu \sqrt{w}}{\gamma_s E_N} \begin{cases} 0, & \text{if } \frac{w}{\Gamma G\mu} > t, \\ \frac{1}{w^{1/2} t^3}, & \text{if } \frac{w}{(\Gamma G\mu)^3} \gtrsim t \gtrsim \frac{w}{\Gamma G\mu}, \\ \frac{(\Gamma G\mu)^{\frac{4}{3}-p}}{w^{\left(\frac{17}{18}-\frac{p}{3}\right)}} \frac{1}{t^{\left(\frac{23}{9}+\frac{p}{3}\right)}}, & \text{if } t_{\text{EWSB}} > t \gtrsim \frac{w}{(\Gamma G\mu)^3}. \end{cases} \tag{B.16}$$

We have verified numerically that these analytical estimates are in good agreement with the full integral representation in Eq. (B.13).

Particle emission from big cuspy loops

Next, we consider particle emission from small cuspy loops. Big loops are produced with a length comparable to the size of the cosmic horizon,

$$l = \alpha_l t, \qquad \alpha_l \approx 0.1. \tag{B.17}$$

After a critical cosmic time t_c given by

$$t_c = \frac{l_c}{\alpha_l} = \frac{w}{\alpha_l (\Gamma G\mu)^2}, \tag{B.18}$$

newly created big loops initially shrink mainly by emitting gravitational radiation. After shrinking to a parametric lengthscale $l(t) \lesssim l_c$, particle production becomes the dominant energy-loss channel and the shrinking rate accelerates until annihilation.

Final collapse

Loops with sizes comparable to l_c or larger will only be produced after a time t_c given by Eq. (B.18), and the lifetime τ of such loops are,

$$\tau \gtrsim \frac{l_c^{3/2}}{\sqrt{w}} = \frac{w}{(\Gamma G\mu)^3}. \tag{B.19}$$

We find that collapse of loops with initial size $l \gtrsim l_c$ are irrelevant in the context of leptogenesis, and are therefore discarded. For loops with an initial size smaller than l_c, i.e. the loops considered below, shrinking is dictated by particle emission.

The annihilation rate of big loops per unit volume at time t is equal to the number of loops created inside a volume $\left(\frac{a(t_i)}{a(t)}\right)^3$ at time t_i obtained from Eq. (B.2),

$$t = t_i + \frac{2}{3} \frac{1}{\sqrt{w}} (\alpha t_i)^{3/2}. \tag{B.20}$$

The number of RHNs decaying per unit volume and time from big loops collapsing at a time t is then,

$$\dot{n}_N^{\rm collapse-big}(t) \approx f_N \frac{\mu w F_s C_{\rm eff}(t_i)}{E_X \alpha_l t_i^4} \left(\frac{a(t_i)}{a(t)}\right)^3. \tag{B.21}$$

For loops created at $t_i \gtrsim \frac{w}{\alpha_l^3}$, Eq. (B.20) reduces to $t \approx \frac{2}{3}\frac{(\alpha_l t_i)^{3/2}}{\sqrt{w}}$,[13] and we obtain,

$$\dot{n}_N^{\rm collapse-big}(t) \approx f_N \frac{\mu F_s C_{\rm eff}(t_i)}{E_N} \frac{\alpha_l^{3-p}}{w^{\frac{1-p}{3}} t^{\frac{8+p}{3}}}, \qquad \frac{w}{(\Gamma G\mu)^3} > t \gtrsim \frac{w}{\alpha_l^3}. \tag{B.22}$$

Cusp evaporation

Following the steps outlined for small cuspy loops and taking into account that large loops can become so sizeable that also energy loss via gravitational radiation can become dominant we use the following estimate,

$$l(t) \approx \left[(\alpha_l t_i)^{3/2} - \frac{3\sqrt{w}}{2}(t-t_i)\right]^{2/3} - \Gamma G\mu(t-t_i), \tag{B.23}$$

$$\frac{dt_i}{dl} \approx \frac{\sqrt{l(t)+\Gamma G\mu(t-t_i)}}{(\Gamma G\mu)\sqrt{l(t)+\Gamma G\mu(t-t_i)} + \alpha_l\sqrt{l_i} + \sqrt{w}}, \tag{B.24}$$

and obtain,

$$\dot{n}_N^{\rm cusp-big}(t) \approx f_N \int_w^{\alpha_l t} dl \frac{1}{t^p} \frac{F_s C_{\rm eff}(t_i)}{\alpha_l t_i^{4-p}} \frac{dt_i}{dl} \frac{N_c \mu\sqrt{w}}{\sqrt{l(t)} E_N}, \qquad t > \frac{w}{\alpha_l}. \tag{B.25}$$

The integrand is proportional to,

$$\frac{1}{t^p}\frac{1}{t_i^{4-p}}\frac{dt_i}{dl}\frac{1}{\sqrt{l(t)}} = \frac{1}{t^p}\frac{1}{t_i^{4-p}}\left(\frac{1}{\Gamma G\mu\sqrt{l(t)} + \frac{\alpha_l\sqrt{l_i}+\sqrt{w}}{\sqrt{1+\Gamma G\mu(t-t_i)/l(t)}}}\right), \tag{B.26}$$

so the integral receives its dominant contribution from loops that are close to collapsing.[14] This is to be expected, as the loop-production efficiency decreases with time and the energy-loss efficiency from particle radiation increases with decreasing loop size. Loops produced around $t_i \approx \frac{1}{\alpha_l}(\sqrt{w}t)^{2/3}$ have length $l(t) \approx w$,[15] and loops produced at $n \times t_i(t)$, $n > 1$, have length $l(t) \equiv l_n$ with

$$l_n^{3/2} \approx (n^{3/2}-1)(\alpha_l t_i)^{3/2}, \tag{B.27}$$

assuming that $\alpha_l\sqrt{\alpha_l t_i} > \sqrt{w}$. As an approximation, we can therefore estimate the value of the integral by the characteristic length scale $(\alpha_l t_i)$ multiplied by the integrand evaluated at $t_i = \frac{1}{\alpha_l}(\sqrt{w}t)^{2/3}$ and $l(t) = (\sqrt{w}t)^{2/3}$. The result reads,

$$\dot{n}_N^{\rm cusp-big}(t) \approx f_N \frac{F_s C_{\rm eff}(t_i) N_c \mu}{E_N} \frac{\alpha_l^{2-p}}{w^{\frac{2-p}{3}}} \frac{1}{t^{\frac{7+p}{3}}}, \qquad \frac{w}{(\Gamma G\mu)^3} \gtrsim t \gtrsim \frac{w}{\alpha_l^3}. \tag{B.28}$$

[13]The regime where $t_i \lesssim \frac{w}{\alpha_l^3}$ typically ends before the friction-time, and is hence irrelevant.

[14]In this case, the term inside the parenthesis in Eq. (B.26) reduces to $\frac{\sqrt{1+\Gamma G\mu(t-t_i)/l(t)}}{\alpha_l\sqrt{l_i}}$.

[15]This is strictly speaking only true while particle production is the dominant energy-loss contribution, i.e. while $t_i \lesssim \frac{w}{\alpha_l(\Gamma G\mu)^2}$, which turns out to be well within the interesting regime for our leptogenesis analysis.

Numerically, we find that this estimate is in agreement with the full evaluation of Eq. (B.26) up to $\mathcal{O}(1)$ factors.

The calculations above for big loops are only reliable as long as the loops collapsing at time t were also created during the linear-scaling regime.[16] The loop-production rate $\frac{dn}{dt_i}$, assumptions about loop sizes at formation, and the effectiveness of energy-loss mechanisms are all made under the assumption $t_i > t_{\rm fric}$. Hence, Eq. (B.28) is expected to break down at times $t \sim t_{\rm fric}$, and should not be used for $t_i < t_{\rm fric}$, with t_i given by Eq. (B.20).

Particle emission from kink-dominated loops

For loops with kinks, a parametric expectation of the critical length scale l_k at which gravitational radiation becomes the dominant decay channel is [202, 203],

$$l_k \approx \frac{w}{\Gamma G\mu}, \tag{B.29}$$

and the length-evolution is dictated by

$$\frac{dl}{dt} \approx \begin{cases} -\Gamma G\mu, & l \gg l_k, \\ -\frac{w}{l}, & l \ll l_k. \end{cases} \tag{B.30}$$

The derivation of particle emission from kink-dominated loops is carried out similarly as the cusp-dominated loops. Below, we summarize the results.

Particle emission from small kinky loops

First, we consider particle emission from small kinky loops. If such loops are created at times t_i satisfying,

$$t_i < \frac{w}{(\Gamma G\mu)^2}, \tag{B.31}$$

they shrink predominantly due to particle decay. This condition is satisfied in the regime relevant for our leptogenesis analysis. Following the steps from Eq. (B.3)-(B.8), we obtain a similar result for the collapse of small kink-dominated loops

$$\dot{n}_N^{\rm col-small}(t) \approx f_N \frac{\mu F_s \sqrt{2} C_{\rm eff}(t_i)}{\gamma_s E_N} \times \begin{cases} \frac{1}{t^3} & \text{if } t \leq \frac{w}{\Gamma G\mu}, \\ \frac{w}{(\Gamma G\mu)t^4}, & \text{if } \frac{w}{(\Gamma G\mu)^2} \geq t \gtrsim \frac{w}{\Gamma G\mu}. \end{cases} \tag{B.32}$$

For small kink-dominated loops, the analogous relations to Eq. (B.11) read

$$l^2(t) = l_i^2(t_i) - 2w(t - t_i), \qquad \frac{dt_i}{dl} = \frac{l(t)}{(\Gamma G\mu)^2 t_i + w}, \tag{B.33}$$

and using [203]

$$P_{\rm kink} \approx \frac{N_{kk}\mu^{1/2}}{l}, \tag{B.34}$$

where N_{kk} denotes the average number of kink-kink collisions per oscillation, the average rate of RHNs emitted reads

$$\frac{dN_N^{\rm kink}}{dt} = f_N \frac{N_{kk}\sqrt{\mu}}{l E_N}. \tag{B.35}$$

[16] Notice that this is not an issue for small loops, as they decay on sufficiently short timescales that t and t_i are comparable.

The particle production rate is then straightforwardly obtained as,

$$\dot{n}_N^{\text{kink-small}}(t) \sim f_N \int_w^{(\Gamma G\mu t)} dl \left[\frac{a(t_i)}{a(t)}\right]^3 \frac{F_s\sqrt{2}C_{\text{eff}}(t_i)}{\gamma_s(\Gamma G\mu)t_i^4}\left(\frac{1}{w+(\Gamma G\mu)^2 t_i}\right)\frac{N_{kk}\mu^{1/2}}{E_N}. \quad \text{(B.36)}$$

Employing similar approximations as those leading to Eq. (B.16), we arrive at

$$\dot{n}_N^{\text{kink-small}}(t) \approx f_N \frac{F_s\sqrt{2}C_{\text{eff}}N_{kk}\sqrt{\mu}}{\gamma_s w E_N}\begin{cases} 0, & \text{if } \frac{w}{\Gamma G\mu} > t, \\ \frac{1}{t^3}, & \text{if } \frac{w}{(\Gamma G\mu)^2} \gtrsim t > \frac{w}{\Gamma G\mu}. \end{cases} \quad \text{(B.37)}$$

Particle emission from big kinky loops

For a big kinky loop, we obtain the following relation between the time of formation t_i and the time of collapse t

$$2wt = t_i(\alpha_l^2 t_i + 2w) \approx (\alpha_l t_i)^2, \quad \text{(B.38)}$$

assuming $l_i \gtrsim w/\alpha_l$ in the last step. The collapse rate for big kink-dominated loops then yields the following RHN injection,

$$\dot{n}_N^{\text{collapse-big}}(t) \approx f_N \frac{\mu F_s C_{\text{eff}}(t_i)}{E_N}\frac{\alpha_l^{3-p}}{w^{1-p/2}t^{2+p/2}}, \qquad \frac{w}{(\Gamma G\mu)^2} \gtrsim t \gtrsim \frac{w}{\alpha_l^2}. \quad \text{(B.39)}$$

RHN radiation from kink-collisions at early times, before gravitational radiation plays a significant role, takes the form

$$\dot{n}_N^{\text{kink-big}}(t) \approx f_N \int_w^{\alpha_l t} dl \frac{1}{t^p}\frac{F_s C_{\text{eff}}(t_i)}{\alpha_l t_i^{4-p}}\frac{dt_i}{dl}\frac{N_{kk}\mu^{1/2}}{l(t)E_N}, \qquad t > \frac{w}{\alpha_l}, \quad \text{(B.40)}$$

with

$$l(t) \approx \sqrt{l_i^2(t_i) - 2w(t-t_i)}, \qquad \frac{dt_i}{dl} \approx \frac{l(t)}{\alpha_l^2 t_i + w}. \quad \text{(B.41)}$$

For $l_i \gtrsim w/\alpha_l$, the smallest loops present at time t satisfy the relation $t_i \approx \frac{\sqrt{2wt}}{\alpha_l}$. Loops created at later times, nt_i with $n = \mathcal{O}(1)$, have lengths $l(t) \approx \sqrt{(n^2-1)}\alpha_l t_i$. Hence, we estimate the value of the integral by the value of the integrand evaluated at $t_i = \frac{\sqrt{2wt}}{\alpha_l}$ multiplied by the characteristic length scale $\alpha_l t_i$. The result reads,

$$\dot{n}_N^{\text{kink-big}}(t) \approx f_N \frac{F_s C_{\text{eff}}N_{kk}\sqrt{\mu}}{E_N}\frac{\alpha_l^{2-p}}{w^{2-p/2}t^{2+p/2}}, \qquad \frac{w}{(\Gamma G\mu)^2} \gtrsim t \gtrsim \frac{w}{\alpha_l^2}. \quad \text{(B.42)}$$

We stress that the validity of these formulae rely on the loops being produced at times $t_i < t_{\text{fric}}$.

Particle production from loops shrinking due to GW emission

Here we present the particle production rates for loops that shrink dominantly due to gravitational radiation. Such loops have longer lifetimes than the loops considered above and only emit particles in their final collapse. The contribution from small loops reads,

$$\dot{n}_N^{\text{col-small}}(t) \approx f_N \begin{cases} \frac{\mu F_s\sqrt{2}C_{\text{eff}}(t_i)}{\gamma_s t^3 E_N}, & t = t_i, \quad \text{if } t_i \lesssim \frac{w}{\Gamma G\mu}, \\ \frac{F_s\sqrt{2}C_{\text{eff}}(t_i)2^{4-p}\mu w}{E_N\gamma_s(\Gamma G\mu)t^4}, & t \approx 2t_i, \quad \text{if } t_i \gtrsim \frac{w}{\Gamma G\mu}. \end{cases} \quad \text{(B.43)}$$

This result is in parametric agreement with the estimate employed in Refs. [331, 333]. The contribution from big loops takes the following form on time scales relevant for our analysis,

$$\dot{n}_N^{\text{col}-\text{big}}(t) \approx f_N \frac{F_s C_{\text{eff}}(t_i)\alpha_l^{3-p}\mu w}{E_N(\Gamma G\mu)^{4-p}t^4}, \qquad t \approx \frac{\alpha_l t_i}{\Gamma G\mu}, \qquad \text{if } t \gtrsim \frac{w}{\Gamma G\mu}. \tag{B.44}$$

This rate is only valid for big loops created after the friction-dominated epoch has ended, i.e. $t \gtrsim \frac{\alpha_l t_{\text{fric}}}{\Gamma G\mu}$.

Particle production from loops assuming instantaneous particle emission

In light of recent AH simulations [199], see also [357], we also consider a maximal RHN production rate from strings, assuming that the full energy-budget of loops is transformed to particle radiation instantaneously. This analysis aims to assess the potential impact of cosmic strings on leptogenesis in a maximally optimistic scenario, providing a benchmark estimate that can inform future studies once a consensus on particle production from loops is fully established within the community.

In the limit where the energy loss from long strings due to loop formation [107,191,192],

$$\left.\frac{d\rho}{dt_i}\right|_{\text{loop}} = \frac{\sqrt{2}\mu C_{\text{eff}}(t_i)}{t_i^3}, \tag{B.45}$$

is instantaneously transferred into RHNs with an average Lorentz factor γ_N, we obtain

$$\frac{dn_N}{dt} \approx f_N \frac{\sqrt{2}\mu C_{\text{eff}}(t)}{\gamma_N M_{N_1} t^3}. \tag{B.46}$$

Part II

Wash-in leptogenesis & chargegenesis

CHAPTER V

Background and motivation

In the first part of this thesis, we considered type-I seesaw BSM extensions and leptogenesis scenarios where the three Sakharov conditions for baryogenesis are satisfied within the RHN sector. Specifically, $B-L$ violation and CP violation occurred through RHN interactions. In a type-I seesaw extension, $B-L$ violation is inherent due to the Majorana nature of RHNs, whereas the requirement of CP violation in the RHN sector can be relaxed. In this part of the thesis, we investigate the WILG paradigm [371], which liberates the RHN sector from the necessity of sufficient CP violation.

Rather than assuming adequate CP violation within the RHN sector, WILG assumes a non-minimal cosmological background with primordial charge asymmetries generated by CP-violating dynamics at high energies, which we term "chargegenesis". The RHNs then act as spectators that redistribute these primordial charge asymmetries in a $B-L$-violating manner. The crucial point is that RHN interactions generically drive the plasma towards a $B-L$-violating state, even if $B-L=0$ initially.

In this part of the thesis, we examine both WILG and chargegenesis. In Chapter VI, we discuss a chargegenesis mechanism based on non-minimal gravitational interactions, which can generate suitable initial conditions required by WILG. In Chapter VII, we adopt a bottom-up perspective on WILG, agnostic to the UV mechanism that produced the initial conditions. There, we address the question, "what is the lower-bound on the lightest RHN mass when requiring that the BAU can be generated via WILG?". The rest of this chapter is organized as follows. In Section V.1, we review some basic aspects of WILG, focusing primarily on the temperature regime relevant to our study in Chapter VII. We end Section V.1 with a brief comparison of WILG with some related (and unrelated) leptogenesis frameworks. In Section V.2, we review basic aspects of gravitational baryogenesis, which is closely related to the chargegenesis mechanism considered by us in Chapter VI. We also contextualize our work by commenting on some previous extensions of gravitational baryogenesis, and close with derivations of two results of significant importance to our analysis.

V.1 Wash-in leptogenesis

The underlying philosophy of WILG is to treat RHNs on a similar footing as weak sphalerons. As explained in Ref. [372], the theoretical discovery of the weak sphalerons forty years ago called for a new analysis of the chemical transport in the SM plasma. Now, the experimental discovery of neutrino oscillations could arguably be used to call for another revision. Namely, when the type-I seesaw paradigm is used to explain neutrino masses, it is essential to incorporate RHN interactions into the chemical transport dynamics of the early universe plasma. Just as weak sphalerons wash in a baryon asymmetry in the standard leptogenesis framework, RHNs can wash in a $B - L$ asymmetry.

An integral ingredient in WILG is primordial charge asymmetries (or primordial charge densities). In this context, charge densities describe the differences in number densities between fermions and antifermions, $q_i = n_i - \bar{n}_i$. Charge densities can also be expressed in terms of the chemical potentials μ_i of the corresponding fermion species as, $q_i = g_i \mu_i T^2/6$ [226], where g_i denotes the multiplicity of species i. No choice of q_i in the SM is conserved at temperatures slightly above the EWPT, due to weak and strong sphalerons and Yukawa interactions. However, at higher temperatures – corresponding to earlier times after the hot Big Bang – some (linear combinations of) q_i become approximately conserved as the rate(s) of the interaction(s) that would violate them are insignificant compared to the Hubble expansion. Heuristically, a charge-violating interaction Γ_q scales as $\Gamma_q \sim T$ while $H \sim T^2/M_P$. As such, at higher temperatures, the number of conserved global charges in the SM increases. Depending on the temperature scale at which the $B - L$ asymmetry is washed in by RHNs, there can be up to eleven suitable (linearly independent) choices of global charges that can be employed in WILG,

$$\begin{aligned} &q_e, \quad q_{2B_1 - B_2 - B_3}, \quad q_{u-d}, \quad q_{d-s}, \quad q_{B_1 - B_2}, \\ &q_\mu, \quad q_{u-c}, \quad q_\tau, \quad q_{d-b}, \quad q_B, \quad q_u. \end{aligned} \tag{V.1}$$

see Ref. [371] and in particular the supplement material for details and definitions. The chargegenesis mechanism only needs to create one or a few among these global charges at high temperatures, while RHNs (with a mass scale that is potentially much lower than the energy scale associated with chargegenesis) will automatically ensure the generation of $B - L \neq 0$ even if the chargegenesis mechanism conserves $B - L$.

As the temperature in the thermal plasma drops, the last remaining global charge to be eliminated by SM interactions is the asymmetry between right-handed electrons and left-handed positrons, q_e. Consequently, as long as the temperature scale of WILG exceeds the equilibration temperature of the electron Yukawa interaction, $T_e \approx 85$ TeV [373], it is always possible to achieve successful WILG assuming a non-zero primordial electron charge generated by chargegenesis, $q_e^{\mathrm{ini}} \neq 0$. As we will be particularly interested in WILG around the equilibration temperature of the electron Yukawa interaction, we will specialize the remaining discussion to the temperature range $T \lesssim 10^6$ GeV, where q_e is the only approximately conserved global SM charge. Detailed discussions of WILG for general temperatures can be found in Refs. [371, 372].

To make progress, we need to express the 16 SM chemical potentials,[1]

$$\mu_i, \quad \text{with} \quad i = e, \mu, \tau, L_e, L_\mu, L_\tau, u, c, t, d, s, b, Q_1, Q_2, Q_3, H, \tag{V.2}$$

in terms of the chemical potentials that are (approximately) conserved by SM interactions, namely $\bar{\mu}_e$ and $\bar{\mu}_{\Delta_\alpha}$, where $\Delta_\alpha \equiv B/3 - L_\alpha$ and α denotes a lepton flavor. Following Ref. [371], we define conserved chemical potentials $\bar{\mu}_C$ as $q_C = \bar{\mu}_C T^2/6$, which absorb the multiplicity factor. Relations between chemical potentials imposed by interactions in the thermal plasma are obtained by writing down 16 linear equations that relate the chemical potentials of processes in thermal equilibrium and constrain chemical potentials

[1] Here, we do not include the three RHN chemical potentials μ_{N_i}. A clear justification for this can be found in Ref. [372]. Although μ_{N_i} could, in principle, be nonzero at high temperatures, it is driven to zero when M_{N_i} becomes non-negligible. At the time of wash-in LG, $T \sim M_{N_i}$, one can safely work with $\mu_{N_i} = 0$, and all effects of μ_{N_i} at higher temperatures will have been reverted and hence are irrelevant for the outcome of WILG.

associated with conserved charges [355]. For example, above T_e, one has the constraint equation $\mu_e = \bar{\mu}_e = \text{const}$, and below the equilibration temperature of weak sphalerons, one has $\mu_{L_e} + \mu_{L_\mu} + \mu_{L_\tau} + 3(\mu_{Q_1} + \mu_{Q_2} + \mu_{Q_3}) = 0$. Following the procedure outlined in Refs. [371, 372] (see also [355]), the 16 relations can be written in matrix form as

$$\begin{pmatrix} \mu_e \\ \mu_\mu \\ \mu_\tau \\ \mu_{L_e} \\ \mu_{L_\mu} \\ \mu_{L_\tau} \\ \mu_u \\ \mu_c \\ \mu_t \\ \mu_d \\ \mu_s \\ \mu_b \\ \mu_{Q_1} \\ \mu_{Q_2} \\ \mu_{Q_3} \\ \mu_H \end{pmatrix} = \begin{pmatrix} 1 & 0 & 0 & 0 \\ 7/481 & 1/13 & -29/111 & 8/111 \\ 7/481 & 1/13 & 8/111 & -29/111 \\ -415/962 & -11/26 & 2/37 & 2/37 \\ 59/962 & 1/26 & -35/111 & 2/111 \\ 59/962 & 1/26 & 2/111 & -35/111 \\ 3/37 & 0 & -1/37 & -1/37 \\ 3/37 & 0 & -1/37 & -1/37 \\ 3/37 & 0 & -1/37 & -1/37 \\ -6/481 & 1/13 & 3/37 & 3/37 \\ -6/481 & 1/13 & 3/37 & 3/37 \\ -6/481 & 1/13 & 3/37 & 3/37 \\ 33/962 & 1/26 & 1/37 & 1/37 \\ 33/962 & 1/26 & 1/37 & 1/37 \\ 33/962 & 1/26 & 1/37 & 1/37 \\ 45/962 & -1/26 & -2/37 & -2/37 \end{pmatrix} \begin{pmatrix} \bar{\mu}_e \\ \bar{\mu}_{\Delta e} \\ \bar{\mu}_{\Delta\mu} \\ \bar{\mu}_{\Delta\tau} \end{pmatrix}. \tag{V.3}$$

It is trivial to check that the equation above yields $\mu_{B/3-L} = \bar{\mu}_{\Delta e} + \bar{\mu}_{\Delta\mu} + \bar{\mu}_{\Delta\tau}$. Hence, if the chargegenesis mechanism did not generate an asymmetry in $B/3 - L$, then $q_{B/3-L}$ remains zero in the thermal plasma, as expected.

The discussion so far makes no reference to RHNs. For concreteness, we will consider hierarchical RHN masses with the lightest RHN having mass $M_1 \sim 10^5 - 10^6$ GeV and the other RHNs heavier than 10^6 GeV, so we only need to focus on N_1. In this regime, the dominant processes involving N_1 are decays (Ds) and inverse decays (IDs). At $T \sim M_1$, if Ds/IDs are efficient, then $\mu_H + \mu_{L_\alpha} = \mu_{N_1} = 0$, which is dubbed the "strong wash-in regime". Combining the strong wash-in condition with Eq. (V.3) gives rise to three additional relations among chemical potentials

$$\begin{pmatrix} \mu_{L_e} + \mu_H \\ \mu_{L_\mu} + \mu_H \\ \mu_{L_\tau} + \mu_H \end{pmatrix} = \begin{pmatrix} -5/13 \\ 4/37 \\ 4/37 \end{pmatrix} \bar{\mu}_e - \begin{pmatrix} 6/13 & 0 & 0 \\ 0 & 41/111 & 4/111 \\ 0 & 4/111 & 41/111 \end{pmatrix} \begin{pmatrix} \bar{\mu}_{\Delta_e} \\ \bar{\mu}_{\Delta_\mu} \\ \bar{\mu}_{\Delta_\tau} \end{pmatrix} = \begin{pmatrix} 0 \\ 0 \\ 0 \end{pmatrix}. \tag{V.4}$$

The second term on the right-hand side is a standard contribution in flavored-leptogenesis [217, 219–222, 374], accounting for spectator processes in the thermal bath [375–377]. Meanwhile, the first term on the right-hand side is the relevant term for WILG.

It should now be clear that the RHN interactions are driving the plasma to a state with nonzero $B - L$ charge, i.e. "washing in Δ_α", where the resulting asymmetry can be determined by solving the matrix equation above, which yields

$$\begin{pmatrix} \bar{\mu}_{\Delta_e} \\ \bar{\mu}_{\Delta_\mu} \\ \bar{\mu}_{\Delta_\tau} \end{pmatrix} = \begin{pmatrix} -5/6 \\ 4/15 \\ 4/15 \end{pmatrix} \bar{\mu}_e \implies q_{B-L}^{\text{win}} = -\frac{3}{10} q_e, \tag{V.5}$$

where q_{B-L}^{win} denotes the asymmetry produced via WILG. The intuition behind this result is [378]: The Yukawa interactions between N_1, L_α, and H can wash-out the lepton asymmetries stored in L_α but not the lepton asymmetry stored in right-handed electrons. This results in a nonzero total lepton asymmetry, even for initial conditions where $B - L = L = 0$.

Let us summarize some important points about this result and the underlying assumptions, which will be important for our study. The following discussion is based on Ref. [372], where additional details and further points can be found.

- The result in Eq. (V.5) is independent of the CP violation in the RHN sector. In fact, the asymmetry generated from WILG can be viewed as a contribution on top of the TLG contribution, such that [371]

$$\left.\frac{q_B}{s}\right|_{\text{today}} = C_{\text{sph}} \left.\frac{q_{B-L}^{\text{th}} + q_{B-L}^{\text{win}}}{s}\right|_{T_{B-L}}, \tag{V.6}$$

  where T_{B-L} denotes the temperature at which RHN interactions become inefficient, q_{B-L}^{th} is the contribution from TLG, and C_{sph} is the sphaleron conversion factor [355].
- The derivation of Eq. (V.5) relies on the assumption that RHN interactions are sufficiently efficient to enforce the conditions $\mu_H + \mu_{L_\alpha} = \mu_{N_1} = 0$. In a more general treatment, one must determine the wash-in contribution by solving the Boltzmann equations for the three charges q_{Δ_α} [237, 238],

$$-\left(\partial_t + 3H\right) q_{\Delta_\alpha} = \varepsilon_{1\alpha} \Gamma_1 \left(n_{N_1} - n_{N_1}^{\text{eq}}\right) - \sum_\beta \gamma_{\alpha\beta}^{\text{w}} \frac{\mu_{\ell_\beta} + \mu_\phi}{T} \tag{V.7}$$

  where the first term on the r.h.s. is the standard source term for q_{Δ_α} in thermal LG and the second term is a washout contribution in standard LG, c.f. [3,371] for details. Since the BEqs are linear in q_{Δ_α}, one can split them into a thermal contribution and a wash-in contribution, where the latter takes the form [371],

$$(\partial_t + 3H) q_{\Delta\alpha}^{\text{win}} = \sum_\beta \frac{6\gamma_{\alpha\beta}^{\text{w}}}{T^3} \left(q_\beta^0 - \sum_\sigma C_{\beta\sigma} q_{\Delta\sigma}^{\text{win}}\right). \tag{V.8}$$

  These equations were solved in Ref. [371] and the results obtained in Eq. (V.5) exhibit excellent agreement with the exact solutions when the RHN decay parameters satisfy $K_{i\alpha} = \Gamma_{i\alpha}(T = 0)/H(T = M_1) \gg 1$ [371]. Recall from the discussion in Section II.4 that this condition corresponds to the strong-washout regime in TLG and, analogously, defines the regime where RHNs efficiently wash in the $B - L$ asymmetry in WILG.

- Finally, the derivation above is based on the assumption that q_e remains (approximately) constant, a condition that is justified when $T_{B-L} \gtrsim T_e$. Under this assumption, the original study, Ref. [371], concluded that WILG can occur at temperatures as low as $T \approx 100$ TeV.

In the next chapter, we will go beyond the assumptions in the second and third points above by numerically solving a coupled system of Boltzmann equations for q_{Δ_α} and q_e. This will allow us to improve the previous estimate $T \gtrsim 100$ TeV of the temperature range in which WILG can take place. We will achieve this by numerically solving the three Boltzmann equations for Δ_α coupled to a Boltzmann equation for q_e in the temperature regime $T \sim T_e$. Naively, one could expect that by increasing the initial asymmetry in q_e^{ini} it would be possible to push the limits of WILG further and further. However, in our treatment, the allowed q_e^{ini} range will be bounded from above by requiring that SM chiral plasma instability (CPI) [379–385] is not triggered by q_e^{ini}. If the initial asymmetry in right-handed electrons is too large, then an efficient SM chiral plasma instability will be triggered and convert the chiral charge stored in q_e into helical hypermagnetic fields. The helicity stored in these fields subsequently triggers a significant overproduction of baryon asymmetry [386] through the mechanism of baryogenesis via helicity decay [387–395] at the time of the electroweak phase transition. A detailed treatment of CPI is beyond the scope of this thesis, and we refer to the references above for further details. Here, we simply quote the upper bound on q_e^{ini} to avoid triggering an efficient CPI: The initial chemical potential associated with right-handed electrons, $\bar{\mu}_e^{\mathrm{ini}}$ (which is related to q_e^{ini} via $q_e^{\mathrm{ini}} = \frac{\bar{\mu}_e^{\mathrm{ini}}}{6} T^2$) must satisfy [373]

$$\left.\frac{\bar{\mu}_e}{T}\right|_{\mathrm{ini}} \lesssim 9.6 \times 10^{-4}\,. \tag{V.9}$$

For completeness, we note that the CPI bound is typically given in terms of the chiral chemical potential associated with $U(1)_Y$, $\mu_{Y,5} \equiv \sum_i \epsilon_i g_i Y_i^2 \mu_i$, where the sum runs over SM fermion species where $\epsilon_i = \pm 1$ for right/ left-handed fields and Y_i denotes the hypercharge of species i. It follows from Eq. (V.3) that before the onset of WILG in the temperature regime of interest, we have $\mu_{Y,5} = \frac{711}{481}\,\bar{\mu}_e$ [372, 386] (see e.g. Table 1 in Ref. [372] for an overview of values for ϵ_i, g_i, and Y_i).

Related ideas

Before concluding our discussion of WILG, we highlight that the framework builds on earlier baryogenesis proposals. Below, we contextualize WILG within the broader landscape of baryogenesis mechanisms by discussing its connections to and distinctions from other prominent baryogenesis paradigms.

e_R asymmetry without RHNs [396]: A historically relevant question was posed in Ref. [396]: Can the BAU be generated solely through a primordial asymmetry in e_R, assuming no $B-L$ violation? Their setup corresponds to the one considered above, but without RHNs. The authors of Ref. [396] recognized that any primordially generated e_R asymmetry would decouple from weak sphalerons for temperatures above T_e, estimated at the time to be around 1 TeV. This temperature is not far from the sphaleron decoupling temperature, which motivated the question of whether e_R could be converted into e_L rapidly enough for weak sphalerons to transform them into antiquarks, thereby erasing the BAU.[2] Their conclusion was negative, highlighting the necessity of $B-L$

[2]Indeed, Eq. (V.3) confirms that if some e_R asymmetry survives until after sphaleron FO, a net baryon

violation to generate a BAU from primordial SM charge asymmetries with total $B-L=0$.

e_R asymmetry with B/L violation [397,398]: The baryogenesis idea closest to WILG was realized over 30 years ago in Refs. [397,398], shortly after Ref. [396]. The authors of Refs. [397,398] demonstrated that a primordial asymmetry with $B-L=0$ and nonzero q_e could generate the BAU in the presence of higher-dimensional operators that violate L and/or B and whose interactions fall out of equilibrium above T_e.[3] WILG builds upon this observation, but utilizes RHNs for $B-L$ violation instead of higher-dimensional operators. Thus, wash-in leptogenesis can be seen as a reconciliation of the findings in Refs. [397,398] with the type-I seesaw paradigm, where $B-L$ violation is inherently achieved through RHNs rather than higher-dimensional operators as originally envisioned [397, 398]. Notably, the experimental confirmation of neutrino oscillations [55,57,58,60–62] occurred years after the publication of Refs. [396–398], strengthening the case for RHNs between the time of those publications and the development of WILG.

Hiding away asymmetry: Another observation made in Ref. [396] was that, starting with $B-L=0$ but nonzero q_{Δ_α}, LNV interactions could generate the BAU from primordial lepton-flavor asymmetries q_{Δ_α} if the LNV interactions involving one or more (but not all) generations were out of equilibrium until sphaleron FO. I refer to scenarios where $B-L=0$ in the sum of all sectors, but $B-L$ can be nonzero in some sectors, ultimately leading to the BAU as "hiding scenarios." For example, the scenario in Ref. [396] qualifies as a hiding scenario, since $B-L=0$ when all flavors are considered, but $B-L\neq 0$ individually in the different flavors. Hiding scenarios have been a popular approach to mechanisms that simultaneously address the baryon asymmetry and dark matter density,[4] see, e.g., Refs. [399–401] and references therein for some early ideas. In contrast, WILG is not a hiding scenario, as it can work for a chargegenesis that yields initial conditions where $B-L=0$ in all sectors/species. A $B-L$ asymmetry is only washed in when the RHNS enter (or are close to) thermal equilibrium.

Neutrinogenesis [402]: Neutrinogenesis is a well-known hiding mechanism involving right-handed neutrinos RHNs. It can be viewed as a logical extension of the idea presented in Ref. [396], where hiding an asymmetry in right-handed electrons was considered. Specifically, Ref. [402] proposed that if fermions carrying B or L with sufficiently small Yukawa couplings existed, $(B+L)$ could be hidden in right-handed particles until long after the electroweak phase transition. The authors of Ref. [402] suggested extending the SM with a purely Dirac mass structure for neutrinos and generating an asymmetry in RHNs balanced by an equal and opposite asymmetry in the SM lepton sector, resulting in a vanishing total lepton number. This approach differs from WILG for the same reasons given in the previous paragraph.

asymmetry remains, as evident from the expressions for μ_L and μ_B:

$$\mu_L = \mu_e + \mu_\mu + \mu_\tau + 2(\mu_{L_e} + \mu_{L_\mu} + \mu_{L_\tau}) = \frac{1}{481}\left[-259\bar{\mu}_{\Delta_e} - 325(\bar{\mu}_{\Delta_\mu} + \bar{\mu}_{\Delta_\tau}) + 198\bar{\mu}_e\right],$$

$$\mu_B = \mu_u + \mu_c + \mu_t + \mu_d + \mu_s + \mu_b + 2(\mu_{Q_1} + \mu_{Q_2} + \mu_{Q_3}) = \frac{6}{481}\left[37\mu_{\Delta_e} + 26\left(\bar{\mu}_{\Delta_\mu} + \bar{\mu}_{\Delta\tau}\right) + 33\bar{\mu}_e\right].$$

[3] At the time, a primordial e_R asymmetry was motivated as follows: "Regenerating the baryon asymmetry from an e_R asymmetry is generic, in the sense that it is natural for decaying GUT gauge bosons or supersymmetric condensates to produce as large an excess of e_R's as of any other particle." [397]

[4] This is typically achieved by generalizing the notion of, e.g., baryon number to a dark sector or mediators between the visible and dark sectors.

V.2 Gravitational baryogenesis

In the following section, we will briefly review aspects of gravitational baryogenesis [403], which will be useful for the study in the next chapter. As a first step, it is instructive to consider the main idea underlying spontaneous baryogenesis [404–406],[5] and how gravitational baryogenesis can be viewed as an extension of the spontaneous-baryogenesis paradigm.

Spontaneous baryogenesis

At the end of Chapter I, we reviewed Sakharov's three conditions for baryogenesis. The proof of the out-of-equilibrium condition, relied on CPT invariance. The idea of spontaneous baryogenesis is to bypass the condition of a departure from thermal equilibrium by invoking (transient) spontaneous breaking of the CPT symmetry, which shifts the energy spectra of baryons relative to that of antibaryons. If baryon-number-violating interactions are present, then a non-vanishing baryon asymmetry could be generated even in thermal equilibrium.

A canonical realization of spontaneous baryogenesis involves a real scalar field ϕ coupled to the baryon current j^μ_B as follows,

$$\frac{\partial_\mu \phi}{M} j^\mu_B, \tag{V.10}$$

where M denotes a model-dependent mass scale. Assuming that the scalar field is homogeneous,[6] the interaction above reduces to

$$\frac{\dot{\phi}}{M} j^0_B \equiv \sum_i \mu_i n_i. \tag{V.11}$$

If $\dot{\phi}$ can be treated as a classical background, then CPT symmetry is spontaneously broken.[7] Recall that j^0_i is simply the difference in the number density between particles and antiparticles in species i, $j^0_i = n_i - \bar{n}_i$, and that $j^0_B = \sum_i B_i j^0_i$ where B_i is the baryon-number of species i. As suggested in Eq. (V.11), the (normalized) background-motion of the scalar field, $\frac{\dot{\phi}}{M}$, can be viewed as an effective chemical potential that shifts the baryon and anti-baryon energy spectra relative to each other [404]. Hence, if B-violating interactions are efficient while $\dot{\phi} \neq 0$, the number-density of baryons will follow a distribution with effective chemical potential μ_B. When the B-violating interactions decouple at a temperature T_D, the baryon number density becomes frozen to the value it attained during decoupling and a net asymmetry remains,

$$\frac{n_B(T_D)}{s(T_D)} \approx \frac{1}{s(T_D)} \frac{\mu_B T_D^2}{6} = \frac{1}{s(T_D)} \sum_i B_i \frac{g_i \kappa_i \dot{\phi} T_D^2}{6M}, \tag{V.12}$$

where

$$\kappa_i = \begin{cases} 1 & \text{for fermions,} \\ 2 & \text{for bosons.} \end{cases} \tag{V.13}$$

[5]See e.g. Refs. [405–411] for some early concrete implementations in particle-physics models and Ref. [412] for a discussion of cosmological aspects of spontaneous baryogenesis.

[6]This assumption is compatible with the hypothesis that the universe underwent a period of inflation prior to the hot big bang.

[7]We stress that the term $\frac{\partial_\mu \phi}{M} j^\mu_B$ does not violate CPT, as it should be for any interaction derivable from a relativistic field theory.

Gravitational baryogenesis and chargegenesis

Gravitational baryogenesis is based on the same set of ideas as spontaneous baryogenesis, but uses the time evolution of the cosmological background itself as a source of CPT violation rather than a time-varying spatially homogeneous scalar field. Specifically, an interaction of the following form is assumed [403]

$$S \supset \frac{1}{M_*^2} \int d^4x \sqrt{-g}\, (\partial_\mu \mathcal{R})\, j_B^\mu, \tag{V.14}$$

where $\mathcal{R}$ denotes the Ricci scalar curvature, g is the determinant of the metric, and M_* is a cut-off scale. This interaction is CP violating but respects CPT. However, in an expanding universe, where $\dot{\mathcal{R}} \neq 0$, this interaction spontaneously breaks CPT and shifts the baryon and anti-baryon energy spectra relative to each other, resulting in an effective chemical potential of the form

$$\mu_B^{\text{eff}} = \frac{\dot{\mathcal{R}}}{M_*^2}. \tag{V.15}$$

The resulting baryon-asymmetry can then be estimated the same way as above,

$$\frac{n_B(T_D)}{s(T_D)} \approx \frac{1}{s(T_D)} \sum_i B_i \frac{g_i \kappa_i \dot{\mathcal{R}} T_D^2}{6 M_*^2}, \tag{V.16}$$

where T_D again denotes the decoupling temperature of baryon-number-violating interactions.

As seen from Eqs. (V.15)-(V.16), $\dot{\mathcal{R}}$ takes center stage in this mechanism. In an FLRW universe, it can be expressed as[8]

$$\dot{\mathcal{R}} = \frac{3}{M_P^2} \rho \dot{\omega} + \frac{\sqrt{3}}{M_P^3} (1+\omega)(1-3\omega) \rho^{3/2}, \tag{V.17}$$

where ω denotes the EoS of the universe. Since Eq. (V.17) will be an important result for us, we review its derivation at the end of this chapter.

Equation (V.17) shows that the gravitationally induced effective chemical potential in Eq. (V.15) vanishes when $\omega = -1$ or $\omega = 1/3$. This indicates that during epochs dominated by radiation or vacuum energy, such as the standard cosmological history following inflationary reheating or inflation itself, respectively, the effective chemical potential is significantly suppressed. The suppression of $\dot{\mathcal{R}}$ in a radiation-dominated universe can be mitigated by enhancing the trace anomaly of the energy-momentum tensor. This may for instance be achieved by introducing numerous new particles charged under a novel $SU(N)$ gauge group into the thermal plasma, as initially proposed in Ref. [403]. Alternatively, substituting $\mathcal{R}$ with a scalar function $f(\mathcal{R})$ in Eq. (V.14) offers another viable approach [414, 415]. Furthermore, various modified gravity theories have been explored in subsequent studies to overcome suppression of $\dot{\mathcal{R}}$ [416–425].

In the next chapter, we will consider a straightforward framework to circumvent the significant suppression of $\dot{\mathcal{R}}$ by leveraging the oscillations of the inflaton field ϕ during the reheating stage after inflation [426–429]. Following a period of slow-roll inflation driven by ϕ rolling down its potential $V(\phi)$, ϕ begins to oscillate around the potential minimum. For

[8] Note that the first term below was not considered in the original reference [403], but included in some later works [413].

a monomial potential approximation around the minimum, $V(\phi) \approx \phi^p$, the EoS parameter is given by $\omega \approx (p-2)/(p+2)$ [430], which generally deviates from $1/3$ or -1. As we will demonstrate, this makes the gravitational chargegenesis mechanism compatible with high-scale inflationary scenarios without requiring modifications to gravity or the addition of new particle species to the thermal plasma.

In the context of WILG, the gravitational-baryogenesis framework described above can be relaxed [2]. In particular, the gravitational interaction can be generalized to the form

$$S \supset \frac{1}{M_*^2} \int d^4x \sqrt{-g}\, J_A^\mu \partial_\mu \mathcal{R}, \tag{V.18}$$

where A represents any SM global charge conserved at high temperatures, suitable for WILG (c.f. the discussion around Eq. (V.1)). The effective chemical potential,

$$\mu_A^{\text{eff}} = \frac{\dot{\mathcal{R}}}{M_*^2}. \tag{V.19}$$

induces non-zero chemical potentials μ_i for particle species i carrying A charge. These particles may also carry other global charges. If an interaction in the plasma violates one of these charges, say C, the bias introduced by $\mu_i \propto \mu_A^{\text{eff}}$ generates a non-zero equilibrium charge asymmetry q_C^{eq}. The precise relation between q_C^{eq} and μ_A^{eff} has been worked out in previous literature and can be found in Eq. (2.31) in Ref. [431]. Although that equation applies to spontaneous baryogenesis with an axion, a, it can be readily applied to our scenario upon substituting $\dot{a}/f \to \dot{\mathcal{R}}/M_*^2$.

The chargegenesis mechanism relies on a non-minimal gravitational interaction of the form in Eq. (V.18), which begs the question: How could such an interaction arise? Originally, it was envisioned to arise from quantum gravity [403]. Subsequent studies revealed that an effective interaction of the form (V.18) is a natural consequence of high-scale CP violation in curved spacetime, potentially resulting in a cutoff scale $M_* \ll M_P$ [432–435]. In fact, a theory of gravitational leptogenesis has already been constructed, where A is identified with lepton number [432–438]. In that context, the interaction in Eq. (V.18) arises dynamically at two loops in the type-I seesaw mechanism when the seesaw Lagrangian is minimally coupled to gravity, due to CP violation in the right-handed neutrino RHN Yukawa sector. Combining this with LNV from RHNs yields a novel leptogenesis contribution. We highlight that the charges A and C associated with the current in Eq. (V.18) and the violated charge, respectively, need not be identical. This relaxes the assumptions required for successful baryogenesis via chargegenesis, and liberates the RHN sector from CP violation constraints, as RHNs only need to wash in a non-zero $B-L$ asymmetry.

Derivation of two useful results

Derivation of Eq. (V.17): We derive Eq. (V.17) by contracting Einstein's equation[9]

$$\mathcal{R}_{\mu\nu} = 8\pi G(T_{\mu\nu} - \frac{1}{2} T g_{\mu\nu}) \tag{V.20}$$

with the inverse metric $g^{\mu\nu}$, yielding

$$g^{\mu\nu}\mathcal{R}_{\mu\nu} \equiv \mathcal{R} = -8\pi G T^\mu_\mu = -8\pi G(1-3\omega)\rho. \tag{V.21}$$

[9]Details about Einsteins equation and Friedmann-Lemaitre-Robertson-Walker (FLRW) geometry can be found in any textbook on general relativity and cosmology, see e.g. Refs. [439, 440].

In Eq. (V.20), T denotes the trace of the energy-momentum (EM) tensor (not to be confused with temperature), and in Eq. (V.21) we used the FLRW EM tensor $T_{\mu\nu} = \mathrm{diag}(\rho, -p, -p, -p)$ and that $\omega \equiv p/\rho$, where p and ρ denotes pressure and energy density, respectively. To find $\dot{\mathcal{R}}$, we need $\dot{\rho}$, which is obtained from the covariant conservation equation

$$\nabla_\mu T^\mu_{\ \nu} = \partial_\mu T^\mu_{\ \nu} + \Gamma^\mu_{\mu\lambda} T^\lambda_{\ \nu} - \Gamma^\lambda_{\mu\nu} T^\mu_{\ \lambda} = 0, \tag{V.22}$$

which upon setting $\nu = 0$ and using isotropy yields

$$\nabla_0 \rho = \partial_0 \rho + \Gamma^\mu_{\mu 0} \rho - \Gamma^\lambda_{\mu 0} T^\mu_{\ \lambda} = 0. \tag{V.23}$$

In FLRW geometry, one has $\Gamma^i_{0j} = H\delta_{ij}$, $\Gamma^0_{0\beta} = 0$, so the equation further simplifies to

$$\nabla_0 \rho = \partial_0 \rho + 3H\rho + 3Hp = 0, \tag{V.24}$$

or equivalently

$$\dot{\rho} = -3H(1+\omega)\rho. \tag{V.25}$$

Combining this with Eq. (V.21), we obtain Eq. (V.17).

Derivation of EoS during inflaton oscillations: Following Ref. [430], we derive the result $\omega = \frac{p-2}{p+2}$ for a universe where the inflaton field oscillates in a monomial potential $V \sim \phi^p$. The inflaton oscillation frequency is $f \sim \frac{\dot{\phi}}{\phi} \gg H$, and the equation of motion for ϕ is given by[10]

$$\dot{\rho}_\phi + (3H + \Gamma_\phi)(\rho_\phi + p_\phi) = 0. \tag{V.26}$$

As ϕ oscillates, the energy density ρ_ϕ varies slowly, decreasing on a timescale characterized by H^{-1} (for $\Gamma_\phi \ll H$, where Γ_ϕ is the decay rate of ϕ to radiation). In contrast, $\dot{\phi}^2 = \rho_\phi + p_\phi$ oscillates rapidly, changing on a timescale set by $f^{-1} \ll H^{-1}$. Averaging the equation of motion over one oscillation period yields

$$\langle \dot{\rho}_\phi \rangle = -\langle (3H + \Gamma_\phi)(\rho_\phi + p_\phi) \rangle \simeq -(3H + \Gamma_\phi)\langle (\rho_\phi + p_\phi) \rangle. \tag{V.27}$$

Next, we write

$$\langle (\rho_\phi + p_\phi) \rangle = (\gamma + \gamma_p)\langle \rho_\phi \rangle, \qquad \gamma \equiv \langle 1 + \frac{p_\phi}{\rho_\phi} \rangle = \langle \frac{\rho_\phi + p_\phi}{\rho_\phi} \rangle = \frac{1}{V_{\max}} \langle \dot{\phi}^2 \rangle, \tag{V.28}$$

where $V_{\max}$ denotes the maximal potential energy attained by the inflaton field during one oscillation. Here, $\gamma_p \sim \mathcal{O}(H/f) \ll 1$ [430], and we therefore neglect it and treat ρ_ϕ as constant on the timescale in question.[11] By definition, we have

$$\gamma = \frac{1}{V_{\max}} \frac{\int_0^t \dot{\phi}^2 dt}{\int_0^t dt}, \qquad dt = \frac{d\phi}{\dot{\phi}}, \qquad \dot{\phi}^2 = 2[\rho_\phi - V(\phi)] = 2[V_{\max} - V(\phi)], \tag{V.29}$$

[10] Note that this is nothing but the continuity equation Eq. (V.24) with the decay rate of ϕ taken into account.

[11] Note that γ_p encodes the quality of the approximation ρ =constant.

where the time runs over one oscillation. For a symmetric potential, we can integrate over a quarter of an oscillation and obtain

$$\gamma = 2\frac{\int_0^{\phi_{\max}} (1 - V(\phi)/V_{\max})^{1/2}\, d\phi}{\int_0^{\phi_{\max}} (1 - V(\phi)/V_{\max})^{-1/2}\, d\phi}. \tag{V.30}$$

Using $V(\phi) = a\,\phi^p$, where a is constant, we obtain the final result

$$\gamma = \frac{2p}{p+2}, \qquad \omega = \gamma - 1 = \frac{p-2}{p+2}. \tag{V.31}$$

CHAPTER VI

Gravitational chargegenesis

The present chapter provides a technical analysis of the chargegenesis mechanism introduced in the previous chapter. All results, arguments, and equations in this chapter were initially reported in Ref. [2] unless stated otherwise.

VI.1 Setup

As discussed in Section V.2, our analysis focuses on the gravitational charge-production mechanism during the inflationary reheating stage, where the inflaton oscillates around the minimum of its potential. In this era, the evolution of the inflaton field ϕ, the radiation energy density ρ_R, and the charge asymmetry q_C is governed by the following three equations,

$$\ddot{\phi} + (3H + \Gamma_\phi)\dot{\phi} = -\frac{dV}{d\phi}, \tag{VI.1}$$

$$\dot{\rho}_R + 4H\rho_R = \Gamma_\phi(\rho_\phi + p_\phi), \tag{VI.2}$$

$$\dot{q}_C + 3Hq_C = \Gamma_C(q_C^{\text{eq}} - q_C). \tag{VI.3}$$

Here, H denotes the Hubble parameter, V is the inflaton potential, and Γ_ϕ is the decay rate of ϕ to radiation. The inflaton energy density and pressure are given by $\rho_\phi = \frac{1}{2}\dot{\phi}^2 + V$ and $p_\phi = \frac{1}{2}\dot{\phi}^2 - V$, respectively. The rate of the charge-violating process(es) driving q_C towards its equilibrium value q_C^{eq} is denoted by Γ_C. Finally, q_C^{eq} is related to the effective chemical potential (introduced in the previous chapter), μ_A^{eff}, via a susceptibility matrix χ_{CA},

$$q_C^{\text{eq}} = \chi_{CA} T^2 \mu_A^{\text{eff}}/6, \tag{VI.4}$$

where χ_{CA} depends on the specific choices of A and C, as well as the temperature scale of chargegenesis. Typically, the non-vanishing entries of χ_{CA} are of $\mathcal{O}(1)$ [371, 431]. For simplicity, we will assume $q_C^{\text{eq}} = T^2\mu_A^{\text{eff}}/6$ in the following.

To model the reaction rate Γ_C in a model-independent manner, we parametrize it in terms of a mass scale M_C,

$$\Gamma_C = \frac{T^{2n+1}}{M_C^{2n}}, \tag{VI.5}$$

where n is a positive integer.[1] For calculational convenience, it is useful to define the

[1] This parametrization can be motivated by an effective operator with mass dimension $D = 4+n$, which would give rise to a reaction rate of this form.

charge density in a comoving volume as,

$$Q_C \equiv q_C(a/a_i)^3, \qquad Q_C^{\rm eq} \equiv q_C^{\rm eq}(a/a_i)^3, \tag{VI.6}$$

where a is the FLRW scale factor and a_i denotes its value at the first peak of the ϕ oscillations.

Inflationary potential

In the previous chapter, we argued from Eq. (V.17) that gravitational chargegenesis cannot be efficient during inflation ($\omega \approx -1$) or radiation domination ($\omega \approx 1/3$). Hence, the specifics of the inflaton potential in the slow-roll regime are unimportant for the predictions of chargegenesis, and only affects inflationary predictions. However, the generated charge, q_C, is sensitive to the shape of the potential close to its minimum, i.e. the part of $V(\phi)$ relevant for reheating. For concreteness, we adopt the following T-model potential [441]

$$V(\phi) = 6^{k/2} M_P^4 \lambda \tanh^k\left(\frac{\phi}{\sqrt{6}M_P}\right), \tag{VI.7}$$

where λ is a coupling constant and k is a positive even number. This potential scales as $V(\phi) \sim \phi^k$ near the origin. In the following, we will primarily focus on the case where $k = 2$ (unless stated otherwise), for which the potential reduces to $V(\phi) \approx \frac{1}{2} m_\phi^2 \phi^2$ with $m_\phi = \sqrt{2\lambda} M_P$ at small ϕ. The slow-roll parameters for this potential are,

$$\epsilon \equiv \frac{M_P^2}{2}\left(\frac{V'}{V}\right)^2 = \frac{4}{3}\text{csch}^2\left(\sqrt{\frac{2}{3}}\frac{\phi}{M_P}\right), \tag{VI.8}$$

$$\eta \equiv M_P^2\left(\frac{V''}{V}\right) = \frac{4}{3}\left[2 - \cosh\left(\sqrt{\frac{2}{3}}\frac{\phi}{M_P}\right)\right]\text{csch}^2\left(\sqrt{\frac{2}{3}}\frac{\phi}{M_P}\right), \tag{VI.9}$$

and the number of inflationary e-folds, N_e, is given by

$$N_e \equiv \frac{1}{\sqrt{2}M_P}\int_{\phi_e}^{\phi}\frac{d\phi'}{\sqrt{\epsilon(\phi')}} = \frac{3}{4}\cosh\left(\sqrt{\frac{2}{3}}\frac{\phi}{M_P}\right) - \frac{3}{4}\cosh\left(\sqrt{\frac{2}{3}}\frac{\phi_e}{M_P}\right), \tag{VI.10}$$

where ϕ_e denotes ϕ at the end of inflation. The constant λ is determined by $\lambda \approx 18\pi^2 A_S/(6N_e^2)$ [442], and $A_S \approx 2.1 \times 10^{-9}$ [443].

Selected example solutions

With the necessary ingredients in place, we can now examine the time evolution of Q_C. To illustrate the latter, we solve Eqs. (VI.1)–(VI.3) starting from an initial point deep within the slow-roll regime, where $\epsilon \ll 1$. More precisely, the initial point of the inflaton is set at $\phi = 6.13$, which corresponds to $N_e = 55$ e-folds of inflation, c.f. Eq. (VI.10). The system is then evolved through the end of slow-roll inflation, multiple inflaton oscillations, and eventually terminated at large times when Q_C has reached a steady state. The results are presented in Fig. VI.1 for the parameter values

$$M_*/M_P = 8.22 \times 10^{-5}, \quad \Gamma_\phi/M_P = 1.23 \times 10^{-7}, \quad n = 1, \tag{VI.11}$$

and various values of M_C, as indicated by the labels. Quantities evaluated at the end of slow-roll ($\epsilon = 1$) are denoted by a subscript "$_\star$". For the examples shown, we find $t_\star \approx 59.4\, m_\phi^{-1}$, $\phi_\star/M_P \approx 1.21$, and $H_\star/M_P \approx 3.3 \times 10^{-6}$.

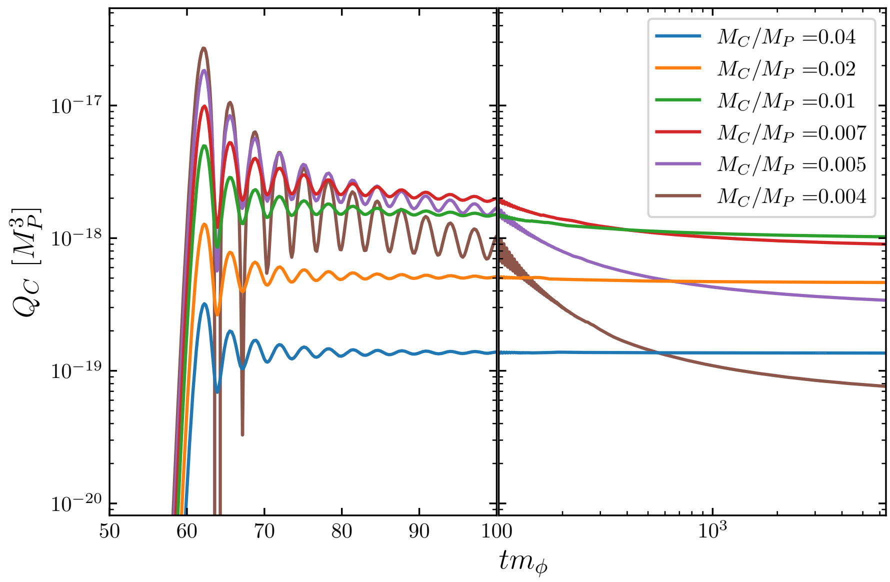

Figure VI.1: Example solutions of Eq. (VI.3) for different values of M_C specified in the top-right corner. The tm_ϕ axis is logarithmically scaled for $tm_\phi > 100$. Figure by X. X. [2].

During the initial slow-roll phase, the production of Q_C is negligible due to $\omega \approx -1$ and $Q_C^{\text{eq}} \propto \mu_A^{\text{eff}} \approx 0$, c.f. the discussion in Section V.2. As the inflaton exits the slow-roll regime, Q_C is efficiently generated until $t \sim \mathcal{O}(100)\, m_\phi^{-1}$. This time interval corresponds to the range between the initial rise in the colored curves and the vertical black line in Fig. VI.1. To the right of the black line, we switch to a logarithmic spacing for the time axis. The oscillations in Q_C arise from the inflaton oscillating around the minimum of its potential, with a frequency set by the inflaton mass. During this oscillatory (reheating) phase, the inflaton can be effectively treated as a fluid with $\omega \approx 0$, as discussed in Section V.2. At large times, Q_C approaches a constant value.

The behavior of $Q_C(t)$ for different M_C values can be broadly categorized into two regimes: freeze-in (FI) and FO. In the FI regime, Γ_C is suppressed due to large M_C values, preventing Q_C from following the rapid oscillations in Q_C^{eq} generated by the inflaton motion. This behavior is evident in the blue and orange curves in Fig. VI.1. By increasing M_C^{-1} further, the generated charge asymmetry reaches a maximum value, roughly set by the time-averaged $\langle Q_C^{\text{eq}} \rangle$ during the oscillatory stage, as seen in the green and red curves. However, further increasing M_C^{-1} enhances the coupling between Q_C and $\langle Q_C^{\text{eq}} \rangle$. As the universe transitions to radiation domination ($\omega \approx 1/3$), μ_A^{eff} and $\langle Q_C^{\text{eq}} \rangle$ drop significantly. A stronger coupling between Q_C and $\langle Q_C^{\text{eq}} \rangle$ allows Q_C to track $\langle Q_C^{\text{eq}} \rangle$ into radiation domination, eventually freezing out at a value substantially lower than the average value during reheating. This behavior is illustrated by the purple and brown curves in Fig. VI.1.

Validity of calculation

To ensure that our calculations are under theoretical control, we review some of the underlying assumptions. Our analysis implicitly assumes an FLRW universe and neglects potential backreaction effects of the current-Ricci interaction on the spacetime geometry.

Recall that the theory is described by the an action of the schematic form,

$$S = \int d^4x\sqrt{-g}\left[\frac{\mathcal{R}}{2}M_P^2\left(1 - \frac{2\partial_\mu J_C^\mu}{M_*^2 M_P^2}\right) + \mathcal{L}_M\right] + ..., \tag{VI.12}$$

where $\mathcal{L}_M$ represents non-gravitational interactions, and we have omitted a total derivative and additional gravitational operators that may appear in a more complete model. The standard Einstein-Hilbert action is recovered by neglecting the current operator and $\mathcal{L}_M$. In this limit, the standard Einstein equation (V.20) is recovered by varying Eq. (VI.12) with respect to the metric. The expansion of the universe is governed by the Friedmann equation, which is the $(0,0)$ component of Einstein's equation. The presence of the current operator modifies the Friedmann equation, but the effect is negligible if,[2]

$$\frac{\dot{q}_C}{M_*^2 M_P^2} \ll 1. \tag{VI.13}$$

Recall that q_C is negligible during inflation, and that it oscillates rapidly with a period set by the inflaton mass m_ϕ during the early stages of reheating (see Fig. VI.1). Thus, we have $\dot{q}_C(t) \sim \langle q_C\rangle(t) m_\phi$, where the time-average is taken over one oscillation. It follows that the current-operator under study has negligible impact on the expansion of the universe if

$$M_*^2 \gg \frac{q_C m_\phi}{M_P^2}. \tag{VI.14}$$

We verified that this condition is satisfied at all times in our calculations.

Additionally, if the operator (V.18) is derived from a UV-complete theory via a low-energy expansion, further constraints are necessary to ensure control over the expansion parameters. To suppress higher-dimensional operators arising from a weak-gravitational field expansion, the condition $\mathcal{R}/M_*^2 \lesssim 1$ must be satisfied. Moreover, to suppress higher-dimensional derivative operators, the condition $T\sqrt{\mathcal{R}}/M_*^2 \lesssim 1$ is required (see Refs. [432–435] and references therein for details). We have verified that our chosen parameters satisfy these constraints both during and after reheating.

VI.2 Selected analytical results

In Ref. [2], we provide a detailed time-resolved analytical analysis of various quantities, including ϕ, ρ_ϕ, ρ_R, $\mathcal{R}$, and $\dot{\mathcal{R}}$. We then utilized these analytical expressions to derive approximations for $Q_C(t)$, which is the quantity of primary interest to us. In the following, we review the derivation of these analytical approximations for $Q_C(t)$, while referencing the results for other quantities, whose derivations can be found in Ref. [2].

The starting point is Eq. (VI.3), which using the definitions in Eq. (VI.6) can be rewritten as

$$\frac{dQ_C}{dt} = \Gamma_C\left(Q_C^{\text{eq}} - Q_C\right). \tag{VI.15}$$

One can readily verify that the general solution to this equation is

$$Q_C(t) = G(t)\int_0^t \frac{\Gamma_C(t')Q_C^{\text{eq}}(t')}{G(t')}dt', \quad G(t) \equiv \exp\left[-\int_0^t \Gamma_C(t')\,dt'\right]. \tag{VI.16}$$

This general solution can be simplified significantly in certain limits, which we consider in the following.

[2] Heuristically, this can be seen by comparing the two terms proportional to $\mathcal{R}$ in Eq. (VI.12).

Freeze-in regime

The first limit we will consider is the FI regime, where $\Gamma_C \to 0$ such that $G \to 1$ and the general solution in Eq. (VI.16) reduces to

$$Q_C \approx \int \Gamma_C Q_C^{\rm eq} dt \approx \int \dot{\mathcal{R}} K dt\,, \quad K \equiv \frac{(a/a_i)^3}{6M_*^2}\frac{T^{2n+3}}{M_C^{2n}}\,. \tag{VI.17}$$

Quantities marked with "i" are evaluated at the time when the inflaton velocity reaches zero for the first time, i.e. $\dot{\phi}(t_i) = 0$. The temperature T is determined from the radiation energy density ρ_R,

$$T = \left(\frac{30}{\pi^2 g_\star}\rho_R\right)^{1/4} = c_g \rho_R^{1/4} \quad \text{with} \quad c_g \equiv \left(\frac{30}{\pi^2 g_\star}\right)^{1/4}. \tag{VI.18}$$

Evaluating Eq. (VI.17) requires expressions for $a(t)$, $\rho_R(t)$, and $\dot{\mathcal{R}}$. In Ref. [2], we show that in the limit $H \gg \Gamma_\phi$, i.e. well before the end of reheating, the quantities are well approximated as follows

$$a \approx a_i \left(1 + \frac{3}{2} h_m \theta_t\right)^{\frac{2}{3}}, \tag{VI.19}$$

$$\rho_R \approx \frac{12\Gamma_\phi M_P^2 m_\phi h_m}{5\,(3h_m\theta_t + 2)}\,, \tag{VI.20}$$

$$\dot{\mathcal{R}} \approx \frac{12 m_\phi^3 \phi_i^2}{M_P^2\,(3\theta_t h_m + 2)^2}\left[\sin 2\theta_t + \frac{h_m(1 + 3\cos 2\theta_t)}{3\theta_t h_m + 2}\right], \tag{VI.21}$$

where

$$h_m \equiv \frac{H_i}{m_\phi}\,, \quad \theta_t \equiv m_\phi(t - t_i), \quad H \approx \frac{2m_\phi h_m}{3h_m\theta_t + 2}\,. \tag{VI.22}$$

By combining these results, one can write the integrand in Eq. (VI.17) as

$$\begin{aligned}\dot{\mathcal{R}} K \approx{}& \frac{m_\phi^3 \phi_i^2}{2M_*^2 M_C^{2n} M_P^2}\left(\frac{h_m}{3h_m\theta_t + 2}\right)\left(\frac{72\,\Gamma_\phi M_P^2 m_\phi h_m}{\pi^2 g_\star (3h_m\theta_t + 2)}\right)^{\frac{2n+3}{4}} \\ &\times \left[1 + 3\cos 2\theta_t + \frac{3\theta_t h_m + 2}{h_m}\sin 2\theta_t\right].\end{aligned} \tag{VI.23}$$

As a first approximation, one can neglect the oscillatory terms and integrate from $t = t_i$, corresponding to $\theta_t = 0$, to $t = \infty$:

$$\int_{\not{s}\not{c}} \dot{\mathcal{R}} K dt \approx \frac{2}{3(2n+3)}\frac{m_\phi^2 \phi_i^2}{M_*^2 M_C^{2n} M_P^2}\left(\frac{36\,\Gamma_\phi M_P^2 m_\phi h_m}{\pi^2 g_\star}\right)^{\frac{2n+3}{4}}. \tag{VI.24}$$

Here, the notation "$\not{s}\not{c}$" indicates that the terms proportional to $\sin 2\theta_t$ and $\cos 2\theta_t$ in Eq. (VI.23) have been neglected. The deviation of this simplified result from the full result, where oscillations in $\dot{\mathcal{R}} K$ are accounted for, is parametrized by the following quantity,

$$r_h \equiv \frac{\int_{\not{s}\not{c}} \dot{\mathcal{R}} K dt}{\int \dot{\mathcal{R}} K dt} = \frac{\int_0^\infty d\theta_t\,(3h_m\theta_t + 2)^{-(2n+7)/4}}{\int_0^\infty d\theta_t\,(3h_m\theta_t + 2)^{-(2n+7)/4}\left[1 + 3\cos 2\theta_t + \frac{3\theta_t h_m + 2}{h_m}\sin 2\theta_t\right]}\,. \tag{VI.25}$$

Note that r_h only depends on h_m. Numerically, we find that r_h varies within a narrow range in the limit $h_m \ll 1$. For $n = 1$, we find that r_h typically varies between 0.34 and 0.35. Combining Eqs. (VI.17), (VI.24) and (VI.25), we obtain the final analytic result for Q_C in the FI regime

$$Q_C \approx \frac{1}{r_h} \frac{2}{3(2n+3)} \frac{m_\phi^2 \phi_i^2}{M_*^2 M_C^{2n} M_P^2} \left(\frac{36\,\Gamma_\phi M_P^2 m_\phi h_m}{\pi^2 g_\star} \right)^{\frac{2n+3}{4}} . \tag{VI.26}$$

Freeze-out regime

Next, we will consider the opposite regime where Γ_C is sufficiently strong to ensure that Q_C remains tightly coupled to $Q_C^{\rm eq}$ during the reheating phase. As the universe enters the radiation-dominated epoch, $Q_C^{\rm eq}$ quickly vanishes as ρ_ϕ decays exponentially, resulting in $\omega \approx 1/3$. In this FO regime, where Q_C tracks $Q_C^{\rm eq}$ during reheating, we are only concerned with the evolution of Q_C from the end of reheating $\rho_R = \rho_\phi$, where the latter can be approximated as

$$\rho_\phi \approx 3 \left(\frac{2 M_P m_\phi h_m}{3 h_m \theta_t + 2} \right)^2 , \tag{VI.27}$$

during reheating [2].

The end of the reheating epoch is determined by equating Eq. (VI.27) with (VI.20),

$$\theta_t \approx \frac{5 m_\phi h_m - 2\Gamma_\phi}{3\Gamma_\phi h_m} \quad (\text{for } \rho_R = \rho_\phi) . \tag{VI.28}$$

Using the definition $Q_C^{\rm eq} = q_C^{\rm eq} \left(\frac{a}{a_i} \right)^3$, where $q_C^{\rm eq} = \frac{T^2 \dot{\mathcal{R}}}{6 M_*^2}$, and Eqs. (VI.19)-(VI.21), Eq. (VI.28), and neglecting oscillating terms in $Q_C^{\rm eq}$, we obtain

$$\langle Q_C^{\rm eq} \rangle \approx \frac{\sqrt{3} c_g^2 \Gamma_\phi^2 m_\phi^2 \phi_i^2}{25 M_P M_*^2} \quad (\text{at } \rho_R = \rho_\phi) . \tag{VI.29}$$

As the radiation-density ρ_R increases and overtakes ρ_ϕ, $Q_C^{\rm eq}$ will drop dramatically as t becomes comparable to Γ_ϕ^{-1} driving $\omega \to 1/3$. Meanwhile, Q_C drops at a lower rate set by Γ_C, and the subsequent part of the evolution becomes insensitive to $Q_C^{\rm eq}$, which can safely be set to zero. The gravitationally produced charge, Q_C, will eventually reach a stable value as $\Gamma_C \ll H$. Applying these assumptions to Eq. (VI.16) results in

$$Q_C \approx \langle Q_C^{\rm eq} \rangle \exp \left[-\frac{\sqrt{3}}{2n-1} \left(\frac{2\sqrt{3}}{5} \right)^{\frac{2n-1}{2}} \frac{c_g^{2n+1} M_P^{\frac{2n+1}{2}} \Gamma_\phi^{\frac{2n-1}{2}}}{M_C^{2n}} \right] \quad (\text{for FO}) . \tag{VI.30}$$

or equivalently

$$Q_C \approx \langle Q_C^{\rm eq} \rangle \exp \left[-\frac{\sqrt{3} c_g^2 M_P T_{\rm rh}^{2n-1}}{M_C^{2n} (2n-1)} \right] \quad (\text{for FO}) , \tag{VI.31}$$

where $\langle Q_C^{\rm eq} \rangle$ is given in Eq. (VI.29), and we used $\rho_R(T_{\rm rh}) = \frac{12}{25} \Gamma_\phi^2 M_P^2$ in the last step.[3] From Eqs. (VI.30) and (VI.31), it is clear that if M_C is very small, then the resulting charge

[3]This relation follows from $\rho_R(T_{\rm rh}) = \rho_\phi(T_{\rm rh})$, see e.g. Ref. [444] for details.

produced would be exponentially suppressed. As a means of estimating the magnitude of M_C for when the exponential suppression becomes severe, we solve the following equation,

$$\frac{Q_C}{\langle Q_C^{\rm eq}\rangle} = e^{-10}\,, \tag{VI.32}$$

which yields

$$M_C = \left(\frac{\sqrt{3}}{10(2n-1)}\right)^{\frac{1}{2n}} \left(\frac{2\sqrt{3}}{5}\right)^{\frac{2n-1}{4n}} \sqrt{c_g^2 M_P \Gamma_\phi} \left(\frac{c_g^2 M_P}{\Gamma_\phi}\right)^{\frac{1}{4n}}. \tag{VI.33}$$

We refer to this value for M_C as $M_C^{\rm cut}$ (or e^{-10} cut), below which Q_C is expected to be suppressed by at least a factor of $e^{-10} \sim 10^{-5}$ compared to the value of $Q_C^{\rm eq}$ at the end of reheating $\rho_R = \rho_\phi$.

Finally, to estimate and illustrate the transition from the FI to the FO regime, we find it useful to introduce a transition value $M_C^{\rm trans}$ for which the argument of the exponential in (VI.30) equals -1. This definition implies the following relation

$$M_C^{\rm trans} = 10^{\frac{1}{2n}} M_C^{\rm cut}. \tag{VI.34}$$

Eq. (VI.34) makes it clear that the region of parameter space where FO results in significant charge production becomes narrower for increasing n.

Using the same parameters as in Sec. VI.1, we present the final gravitationally produced charge Q_C as a function of M_C in Fig. VI.2 for $n = 1$. The blue curve shows the exact numerical result, while the green and orange dashed lines represent the analytical FI and FO approximations in Eqs. (VI.26) and (VI.31), respectively. We see that the analytical approximation in the FI regime is in excellent agreement with the full numerical result. The red and purple dashed curves indicate the two cuts in Eqs. (VI.33) and (VI.34), respectively. We find that both approximations deviate significantly from the exact result around the transition region, $M_C^{\rm trans}$, where a full numerical calculation is required to obtain an accurate result.

VI.3 Parameter space

Finally, we investigate the viable parameter space for gravitational chargegenesis, focusing on $n = 1$ and $k = 2$ (we comment on $k > 2$ at the end of this section). With the inflaton potential fixed, our setup has three free parameters: Γ_ϕ, M_C, and M_*. Since the effective chemical potential is proportional to M_*^{-2}, the final Q_C is also proportional to M_*^{-2} (as seen parametrically in Eq. (V.16) and in e.g. Eqs. (VI.26) and (VI.31)), hence, we focus on the Γ_ϕ–M_C parameter space. We set $M_* = 2 \times 10^{14}$ GeV, a value respecting the constraint in and below Eq. (VI.14), throughout our analysis.

Fig. VI.3 shows the full numerical scan of q_C/s (where s is the entropy density) in the Γ_ϕ–M_C plane. The top axis indicates the reheating temperature $T_{\rm rh}$, defined by $\rho_\phi(T_{\rm rh}) = \rho_R(T_{\rm rh})$, which is extracted from our numerical solutions for ρ_ϕ and ρ_R. We find $T_{\rm rh} \approx 0.35 M_P^{1/2}\Gamma_\phi^{1/2}$ within the scanned range, and observe that the charge asymmetry yield increases with $T_{\rm rh}$ (or Γ_ϕ) for fixed M_C. However, increasing Γ_ϕ to larger and larger values would eventually lead to an inconsistency, as too large Γ_ϕ would result in inflaton decay before the slow-roll period ends, altering the slow-roll paradigm. Results from Planck constrains the Hubble parameter during inflation, $H < 2.5 \times 10^{-5}$ at 95% CL [443],

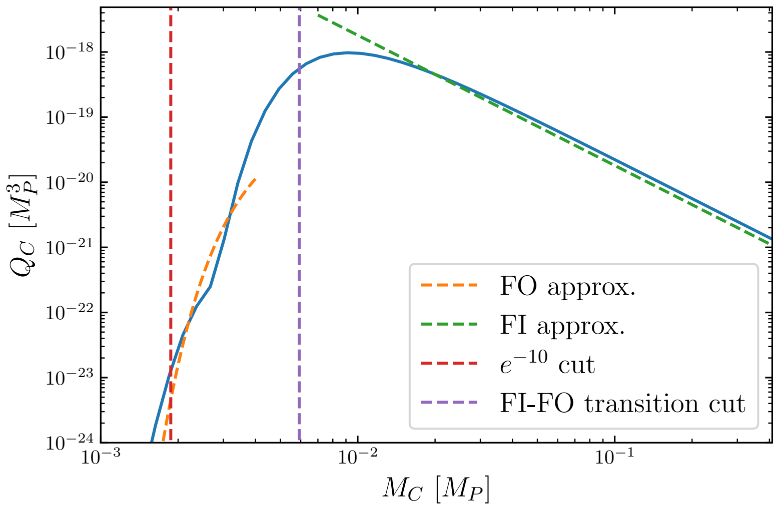

Figure VI.2: Final value for the gravitationally-produced charge, Q_C, as a function of M_C. The analytical FI and FO approximations in Eqs. (VI.26) and (VI.31) are shown by the green and orange dashed lines, respectively. The red and purple dashed curves indicate the two cuts in Eqs. (VI.33) and (VI.34), respectively. Figure by X. Xu [2].

which implies $T_{\rm rh} < 6.6\times 10^{15}$ GeV (for instantaneous reheating). By naively extrapolating $T_{\rm rh} \approx 0.35 M_P^{1/2}\Gamma_\phi^{1/2}$ to this scale, the upper limit from Planck can be interpreted as $\Gamma_\phi < 1.5\times 10^{14}$ GeV. However, such a large value for Γ_ϕ would exceed $H_\star$ and therefore significantly modify the slow-roll evolution. With this in mind, we set $\Gamma_\phi < H_\star \approx 8\times 10^{12}$ GeV as the upper bound on Γ_ϕ in Fig. VI.3.

Ultimately, we are not only interested in the gravitationally-produced charge density q_C, but also the resulting baryon asymmetry Y_B. Recall that in WILG, these two quantities are related via

$$Y_B = C_{\rm sph} x_C \frac{q_C}{s}\,, \tag{VI.35}$$

where x_C is the coefficient relating the q_C asymmetry to the $B-L$ asymmetry and $C_{\rm sph}$ is the sphaleron-conversion factor. In Chapter V, we primarily focused on the example where an electron asymmetry is produced. In the scenario considered there, where the $B-L$ asymmetry is washed in at a temperature $T\sim 10^5-10^6$ GeV, one has $x_C = -3/10$ in the strong wash-in regime [371]. Hence, to generate the BAU $Y_B \approx 8.7\times 10^{-11}$ (see e.g. [226]), one would need $|q_C|/s = |q_e|/s \approx 8.2\times 10^{-10}$ in that case. This value is shown by the black dashed line in Fig. VI.3. The interested reader is referred to Tab. II in Ref. [371] for other charge asymmetries and different temperature regimes for WILG. However, note that $|x_C|$ typically varies from 1/6 to 1. The dotted black curve corresponds to $|x_C| = 1/6$ and the dotted-dashed curve to $|x_C| = 1$.

Finally, we have checked that for T-model potentials with $k = 6, 8, 10, \ldots$,[4] it may be possible to reproduce the BAU in gravitational chargegenesis scenarios for significantly lower inflationary-reheating temperatures than those indicated in Fig. VI.3. However, a conclusive statement would call for a consistent study accounting for e.g. fragmentation of the inflaton condensate (see for example [445, 446]), which is beyond the scope of this thesis.

[4] Recall that for $k=4$, the EoS during reheating is $\omega \approx \frac{k-2}{k+2} = \frac{1}{3}$, resulting in suppressed charge production, c.f. Eqs. (V.17) and (V.19).

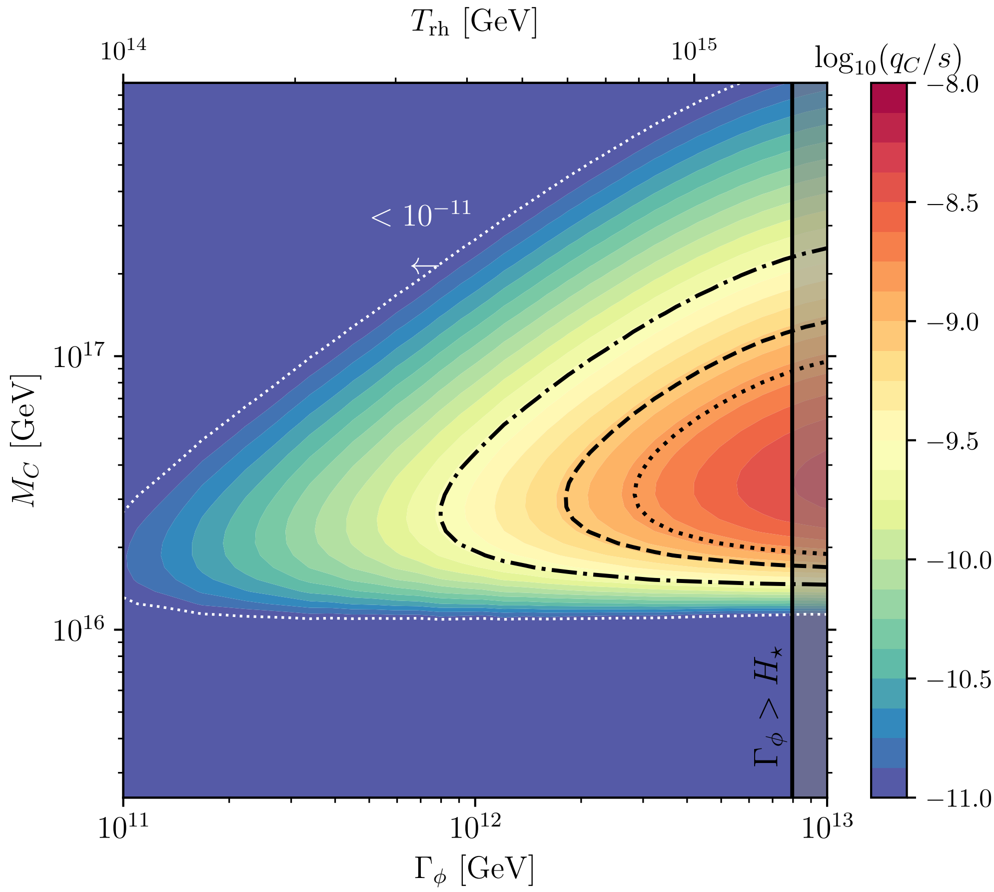

Figure VI.3: Parameter space showing the outcome of gravitational chargegenesis. The black dashed contour ($q_C/s = 8.2 \times 10^{-10}$) can generate the BAU for $|x_C| = 3/10$ (relevant for a right-handed electron charge), while the dotted and dash-dotted contours assume $|x_C| = 1/6$ and 1. Larger Γ_ϕ (or equivalently, larger $T_{\rm rh}$) generally leads to a higher yield of charge asymmetry. However, too large Γ_ϕ would spoil slow-roll predictions. To avoid this, we cut off the scan when $\Gamma_\phi > H_\star$, represented by the black solid line and the gray shaded region to the right. Figure by X. Xu [2].

VI.4 Conclusions

In this chapter, we presented a technical analysis of the gravitational chargegenesis framework proposed in Ref. [2]. This mechanism, in combination with WILG, can be viewed as an extension of the gravitational-baryogenesis framework to explain the BAU. Gravitational chargegenesis relies on a gravitational interaction that generates effective chemical potentials, a charge-violating interaction driving the plasma to a state with nonzero q_C, and RHNs washing in $B - L$ asymmetry, with the notable feature that the gravitational interaction and charge-violating interaction charges need not be identical. Our mechanism's primary advantage over previous gravitational baryogenesis mechanisms is that it allows for the generated charge to satisfy $B - L = 0$ if at least one RHN remains active when q_C is nonvanishing.

To illustrate the framework, we considered an application where gravitational chargegenesis is realized during inflationary reheating. Focusing on the most generic setup, where the inflaton potential is quadratic near the minimum, we showed both numerically and analytically how the gravitationally-produced charge evolves as a function of time, and that the mechanism can indeed be employed to explain the BAU while staying consistent with experimental and theoretical constraints.

Finally, since this mechanism generically requires a high inflation scale, its realization during reheating, as considered by us, is in principle falsifiable since a high inflation scale also implies a large primordial tensor-to-scalar ratio in the cosmic microwave background power spectrum that could be detected by upcoming experiments.

CHAPTER VII

A lower bound on the right-handed neutrino mass from wash-in leptogenesis

In the previous chapter, we considered a mechanism for producing a primordial charge asymmetry through a non-minimal gravitational interaction that could provide suitable initial conditions for WILG. This framework can be viewed as one possibility among a list of several chargegenesis mechanisms, including axion inflation [372], evaporating primordial black holes [447], the decay of heavy Higgs doublets [378], and GUT baryogenesis [371].

In the following, we will assume that a suitable chargegenesis mechanism created a primordial charge asymmetry, which includes an asymmetry in e_R.[1] We focus on e_R, as it is the last global charge to be erased by the SM interactions, c.f. the discussion in Section V.1. There, we argued that for $T_{B-L} > T_e \simeq 85\,\text{TeV}$ [373], it is possible to realize successful WILG by assuming a nonzero primordial electron charge, $q_e^{\text{ini}} \neq 0$. This observation was used in Ref. [371] to argue that WILG can be realized at temperatures as low as $T \simeq 100\,\text{TeV}$.

In the following chapter, we will improve this statement by considering WILG at $T \lesssim T_e$, where q_e/T^3 can no longer be treated as a constant due to the (partial) equilibration of the electron-yukawa interaction. In this temperature regime, the treatment in Ref. [371] must be extended by considering the Boltzmann equation for the time-dependent electron charge, q_e, in addition to the three Boltzmann equations for Δ_α. By solving this coupled set of four Boltzmann equations, we will find that WILG can account for the BAU for RHN masses slightly below 10 TeV. To put this into context, recall that in standard TLG where RHN interactions act as a source of both CP and $B-L$ violation, the RHN mass scale must satisfy the Davidson–Ibarra bound, $M_N \gtrsim 10^{9-10}\,\text{GeV}$ for hierarchical RHN mass spectrum. The bound obtained by us, which is also valid for hierarchical RHN masses, is a result of only demanding RHNs act as a source of $B-L$ violation.[2]

All significant results and/or equations presented here were first presented in Ref. [3].

[1] We stress that this is not a fine-tuned assumption: One of the charge asymmetries produced during axion inflation is in fact e_R [372], and all the references listed above considered realizations where an asymmetry in e_R is generated.

[2] This is in contrast to other routes to low-scale leptogenesis that rely on CP-violation in the RHN sector and quasi-degenerate RHN masses (or additional fine-tuning in the RHN sector), such as resonant leptogenesis [236–238, 448] and leptogenesis via neutrino oscillations [239] (see also Refs. [240, 241]).

VII.1 Setup

The starting point for our analysis is the coupled system of three Boltzmann equations for Δ_α and e_R, which we review in the following, starting with the former.

Boltzmann equations for q_{Δ_α}

The relevant equations for flavored lepton asymmetries were already introduced in Eq. (V.7) and reproduced here for the reader's convenience,

$$-\left(\partial_t + 3H\right) q_{\Delta_\alpha} = \varepsilon_{1\alpha}\,\Gamma_1 \left(n_{N_1} - n_{N_1}^{\mathrm{eq}}\right) - \sum_\beta \gamma_{\alpha\beta}^{\mathrm{w}} \frac{\mu_{\ell_\beta} + \mu_\phi}{T} \,. \tag{VII.1}$$

The first term on the right-hand side is the source term for q_{Δ_α} in standard TLG. Since we will focus on the case of hierarchical RHN masses and the temperature regime $T \lesssim T_e$ in this chapter, we will assume negligible CP violation in the RHN sector, $\varepsilon_{1\alpha} \lll 1$ c.f. Eq. (II.124), and ignore this term. The second term on the right-hand side of Eq. (VII.1) is (a good approximation of)[3] the wash-out term in standard TLG. The wash-out interaction density, $\gamma_{\alpha\beta}^{\mathrm{w}}$, encodes contributions from RHN inverse decays as well as from LNV ($\Delta L = 2$) and lepton-flavor-violating (LFV) ($\Delta L = 0$) processes. Finally, the factors $\mu_{\ell_\beta} + \mu_\phi$, are obtained as explained around Eq. (V.4) and repeated here for convenience,

$$\begin{pmatrix} \mu_{\ell_e} + \mu_\phi \\ \mu_{\ell_\mu} + \mu_\phi \\ \mu_{\ell_\tau} + \mu_\phi \end{pmatrix} = \begin{pmatrix} -\frac{5}{13} \\ \frac{4}{37} \\ \frac{4}{37} \end{pmatrix} \bar{\mu}_e - \begin{pmatrix} \frac{6}{13} & 0 & 0 \\ 0 & \frac{41}{111} & \frac{4}{111} \\ 0 & \frac{4}{111} & \frac{41}{111} \end{pmatrix} \begin{pmatrix} \bar{\mu}_{\Delta_e} \\ \bar{\mu}_{\Delta_\mu} \\ \bar{\mu}_{\Delta_\tau} \end{pmatrix} . \tag{VII.2}$$

As explained in Section V.1, if q_e/T^3 can be treated as a constant, WILG in the strong wash-in regime results in $q_{B-L}^{\mathrm{win}} = -\frac{3}{10}\, q_e$.

In the temperature regime of interest to us, Eq. (VII.1) can be brought into a simpler form. We can rewrite Eq. (VII.1) in terms of charge-densities, by using $q_C = \frac{\mu_C T^2}{6}$ and Eq. (VII.2),

$$(\partial_t + 3H) \begin{pmatrix} q_{\Delta_e} \\ q_{\Delta_\mu} \\ q_{\Delta_\tau} \end{pmatrix} = \frac{6\gamma^{\mathrm{w}}}{T^3} \left[\begin{pmatrix} -\frac{5}{13} \\ \frac{4}{37} \\ \frac{4}{37} \end{pmatrix} q_e - \begin{pmatrix} \frac{6}{13} & 0 & 0 \\ 0 & \frac{41}{111} & \frac{4}{111} \\ 0 & \frac{4}{111} & \frac{41}{111} \end{pmatrix} \begin{pmatrix} q_{\Delta_e} \\ q_{\Delta_\mu} \\ q_{\Delta_\tau} \end{pmatrix} \right] , \tag{VII.3}$$

where γ^{w} is a 3×3 matrix. For $T \sim T_e$, the wash-out rate is dominated by inverse decays, such that γ^{w} is well approximated by

$$\gamma_{\alpha\beta}^{\mathrm{w}} = p_\alpha\, \delta_{\alpha\beta} \frac{T^3}{6} \Gamma_{\mathrm{w}} \,, \qquad p_\alpha = \frac{\Gamma_{1\alpha}}{\Gamma_1} \,. \tag{VII.4}$$

where p_α parametrizes the branching ratio for RHN decays into lepton flavor α, and Γ_{w} is the rate of wash-out via inverse decays,

$$\Gamma_{\mathrm{w}} = \frac{6}{T^3} \gamma^{\mathrm{w}} = \frac{6}{T^3} n_N^{\mathrm{eq}} \Gamma_N^{\mathrm{th}} \,. \tag{VII.5}$$

[3] It does not encode $\Delta L = 1$ washout-contributions with e.g. quarks or gauge bosons in the external states, which we have checked are highly suppressed compared to contributions from inverse decays in the temperature regime considered here.

Here, $n_N^{\rm eq}$ denotes the RHN equilibrium number density and $\Gamma_N^{\rm th}$ the thermally averaged RHN decay rate, which are given by (see e.g. [225] for details)

$$n_N^{\rm eq} = \frac{g_N}{2\pi^2 z} K_2\left(z\right) M_{N_1}^3 , \qquad g_N = 2, \qquad \Gamma_N^{\rm th} = \frac{K_1\left(z\right)}{K_2\left(z\right)} \Gamma_N^0 ,$$
$$\Gamma_N^0 = \frac{\widetilde{m}_1 M_{N_1}^2}{8\pi v^2} , \qquad z = \frac{M_{N_1}}{T} , \tag{VII.6}$$

such that

$$\Gamma_{\rm w} = \frac{3\, g_N z^2}{\pi^2} K_1\left(z\right) \frac{\widetilde{m}_1 M_{N_1}^2}{8\pi v^2} . \tag{VII.7}$$

Here, K_i denotes the i'th modified Bessel function, $v = 174\,\text{GeV}$ is the SM Higgs vev, and $\widetilde{m}_1$ is an effective light neutrino mass parameter defined as [227],

$$\widetilde{m}_1 = \frac{\left(m_D^\dagger m_D\right)_{11}}{M_{N_1}} , \tag{VII.8}$$

where m_D denotes the neutrino Dirac mass matrix. Combining the expressions above, Eq. (VII.3) can be written as,

$$\left(\partial_t + 3H\right) \begin{pmatrix} q_{\Delta_e} \\ q_{\Delta_\mu} \\ q_{\Delta_\tau} \end{pmatrix} = \Gamma_{\rm w} \begin{pmatrix} p_e & 0 & 0 \\ 0 & p_\mu & 0 \\ 0 & 0 & p_\tau \end{pmatrix} \left[\begin{pmatrix} -\frac{5}{13} \\ \frac{4}{37} \\ \frac{4}{37} \end{pmatrix} q_e - \begin{pmatrix} \frac{6}{13} & 0 & 0 \\ 0 & \frac{41}{111} & \frac{4}{111} \\ 0 & \frac{4}{111} & \frac{41}{111} \end{pmatrix} \begin{pmatrix} q_{\Delta_e} \\ q_{\Delta_\mu} \\ q_{\Delta_\tau} \end{pmatrix} \right] . \tag{VII.9}$$

Next, it is useful to introduce (normalized) comoving charge asymmetries as

$$Q_{\Delta_\alpha} = \left(\frac{a}{a_{\rm ini}}\right)^3 \frac{q_{\Delta_\alpha}}{q_e^{\rm ini}} , \qquad Q_e = \left(\frac{a}{a_{\rm ini}}\right)^3 \frac{q_e}{q_e^{\rm ini}} , \tag{VII.10}$$

where a is the FLRW scale factor. This allows us to recast the Boltzmann equations into a form where the left-hand sides are simply a single derivative w.r.t. z,

$$\frac{d}{dz} \begin{pmatrix} Q_{\Delta_e} \\ Q_{\Delta_\mu} \\ Q_{\Delta_\tau} \end{pmatrix} = W \begin{pmatrix} p_e & 0 & 0 \\ 0 & p_\mu & 0 \\ 0 & 0 & p_\tau \end{pmatrix} \left[\begin{pmatrix} -\frac{5}{13} \\ \frac{4}{37} \\ \frac{4}{37} \end{pmatrix} Q_e - \begin{pmatrix} \frac{6}{13} & 0 & 0 \\ 0 & \frac{41}{111} & \frac{4}{111} \\ 0 & \frac{4}{111} & \frac{41}{111} \end{pmatrix} \begin{pmatrix} Q_{\Delta_e} \\ Q_{\Delta_\mu} \\ Q_{\Delta_\tau} \end{pmatrix} \right] , \tag{VII.11}$$

which is the final form of the Boltzmann equations for Δ_α that will be used in our analysis. Note that the comoving charges in Eq. (VII.10) are in units of the initial electron asymmetry $q_e^{\rm ini}$ at $T_{\rm ini} \gg T_e$, which will make it simple to assess the effectiveness of WILG. In Eq. (VII.11), we introduced the dimensionless washout rate

$$W = \frac{\Gamma_{\rm w}}{zH} , \tag{VII.12}$$

where H denotes the Hubble rate, which we express as follows

$$H = \frac{T^2}{M_*} = \frac{M_{N_1}^2}{z^2 M_*} , \qquad M_* \equiv \left(\frac{90}{\pi^2 g_*}\right)^{1/2} M_{\rm Pl} , \tag{VII.13}$$

for a radiation-dominated universe. Combining the two equations above with Eq. (VII.7), we obtain a suitable expression for W,

$$W = \frac{6}{\pi^2}\frac{\widetilde{m}_1}{m_*} z^3 K_1(z) \,, \tag{VII.14}$$

where the mass m_* is the parameter introduced in Eq. (II.114),

$$m_* = \frac{8\pi v^2}{M_*} \simeq 1.07\,\mathrm{meV}\,. \tag{VII.15}$$

Boltzmann equation for q_e

Next, we consider the Boltzmann equation for q_e around T_e. To this end, we use the result derived in Ref. [373], which takes the form

$$(\partial_t + 3H)\, q_e = -\Gamma_e \left[\frac{711}{481}\, q_e + \frac{5}{13}\, q_{\Delta_e} - \frac{4}{37}\left(q_{\Delta_\mu} + q_{\Delta_\tau}\right)\right]. \tag{VII.16}$$

Here, Γ_e is the equilibration rate of right-handed electrons, which can be written as

$$\Gamma_e \equiv C_e\, T. \tag{VII.17}$$

The coefficient C_e receives contributions from $2 \leftrightarrow 2$ processes involving one electron Yukawa vertex (c.f. Fig. 3 in [373]) and from $1 \leftrightarrow 2$ decays and inverse decays of the SM Higgs bosons, right-handed electrons, and left-handed leptons.[4] A comprehensive calculation incorporating these processes was performed in Ref. [373], yielding

$$C_e = \frac{3Y_e^2}{1024\pi}\left[Y_t^2 c_t + \left(3g_2^2 + g^2\right)\left(c_\ell + \ln\frac{1}{3g_2^2+g^2}\right)\right. \tag{VII.18}$$

$$\left. + 4g^2\left(c_e + \ln\frac{1}{4g^2}\right)\right]. \tag{VII.19}$$

The coefficients c_t, c_ℓ, and c_e read,

$$c_t = 2.82 + 1.48\,, \tag{VII.20}$$
$$c_\ell = 3.52 + 0.776\,, \tag{VII.21}$$
$$c_e = 2.69 + 2.03\,, \tag{VII.22}$$

where the first (second) number in each coefficient corresponds to the contribution from $2 \leftrightarrow 2$ (LPM-resummed $1n \leftrightarrow 2n$) processes. The couplings, Y_e and Y_t in Eq. (VII.18) denote the electron and top-quark Yukawa couplings, while g_2 and g denote the $SU(2)_L$ and $U(1)_Y$ gauge couplings, respectively. In our numerical analysis, we start from the SM values of the four couplings at the Z pole and evolve them to the scale $\mu = \pi T$ using their one-loop SM RGEs.[5]

Finally, by introducing a normalized co-moving charge asymmetry, analogous to Eq. (VII.10), for e_R

$$Q_e = \left(\frac{a}{a_{\rm ini}}\right)^3 \frac{q_e}{q_e^{\rm ini}}, \tag{VII.23}$$

[4] The decays/ inverse decays also receive corrections from $1n \leftrightarrow 2n$ scatterings with soft gauge boson exchanges, which are accounted for by Landau–Pomeranchuk–Migdal (LPM) resummation [449–451].

[5] The one-loop RGEs for Y_t, g, and g_2 can be extracted from Appendix A of Chapter III, while the one-loop RGE for the electron Yukawa can be found for example in [452]: $16\pi^2\frac{dY_e}{dt} = Y_e\left[3Y_t^2 - \frac{9}{4}(g^2+g_2^2)\right]$.

we can rewrite the Boltzmann equation (VII.16) as,

$$Q_e' = -E\left[\frac{711}{481}Q_e + \frac{5}{13}Q_{\Delta_e} - \frac{4}{37}\left(Q_{\Delta_\mu} + Q_{\Delta_\tau}\right)\right], \tag{VII.24}$$

where the prime denotes a derivative w.r.t. z and E is the dimensionless electron equilibration rate,

$$E = \frac{\Gamma_e}{zH} = C_e\,\frac{M_*}{M}\,. \tag{VII.25}$$

Summary

We have now arrived at the set of four Bolztmann equations relevant for our calculation,

$$Q_{\Delta_e}' = p_e W\left[-\frac{5}{13}Q_e - \frac{6}{13}Q_{\Delta_e}\right], \tag{VII.26}$$

$$Q_{\Delta_\mu}' = p_\mu W\left[\frac{4}{37}Q_e - \frac{41}{111}Q_{\Delta_\mu} - \frac{4}{111}Q_{\Delta_\tau}\right], \tag{VII.27}$$

$$Q_{\Delta_\tau}' = p_\tau W\left[\frac{4}{37}Q_e - \frac{4}{111}Q_{\Delta_\mu} - \frac{41}{111}Q_{\Delta_\tau}\right], \tag{VII.28}$$

$$Q_e' = -E\left[\frac{711}{481}Q_e + \frac{5}{13}Q_{\Delta_e} - \frac{4}{37}\left(Q_{\Delta_\mu} + Q_{\Delta_\tau}\right)\right]. \tag{VII.29}$$

From the equations presented in this section, one can see that our description of WILG at $T \sim T_e$ depends on four parameters:

1. The effective neutrino-mass parameter $\widetilde{m}_1$, which in standard leptogenesis controls the strength of asymmetry wash out, but in the context of our work controls the strength of asymmetry wash-in.
2. The RHN mass M_{N_1}. This parameter determines the temperature scale of WILG and, consequently, the relevance of q_e washout.
3. The branching ratio p_e.
4. The branching ratio p_μ.

Recall that the third branching ratio, p_τ, follows from $p_e + p_\mu + p_\tau = 1$.

VII.2 Numerical analysis

In the following, we numerically solve the Boltzmann equations (VII.26)-(VII.29), assuming vanishing initial lepton flavor asymmetries and a nonzero primordial electron asymmetry generated by an unspecified chargegenesis mechanism,

$$Q_{\Delta_\alpha}(z \ll 1) = 0\,, \qquad Q_e(z \ll 1) = 1\,. \tag{VII.30}$$

Four example solutions of our set of Boltzmann equations with these initial conditions are shown in Fig. VII.1, for RHN branching ratios $p_{e,\mu,\tau}$ that maximize the efficiency of WILG for given neutrino masses $\widetilde{m}_1$ and M_{N_1}. Here, $Q_{\Delta_e}, Q_{\Delta_\mu}, Q_{\Delta_\tau}, Q_e, Q_{B-L}$ are shown with orange, red, green, blue, black curves, respectively. The two upper panels show examples of the weak wash-in regime, where we have fixed $M_{N_1} = 10$ TeV, and $\widetilde{m}_1 = 0.1$ meV, corresponding to a decay parameter $K = \frac{\widetilde{m}_1}{m_*} \approx 0.09$. In the panel to the left, asymmetries in Δ_μ and Δ_τ are generated, while in the panel to the right, an asymmetry in Δ_e is generated. The two lower panels show example solutions in the strong wash-in regime

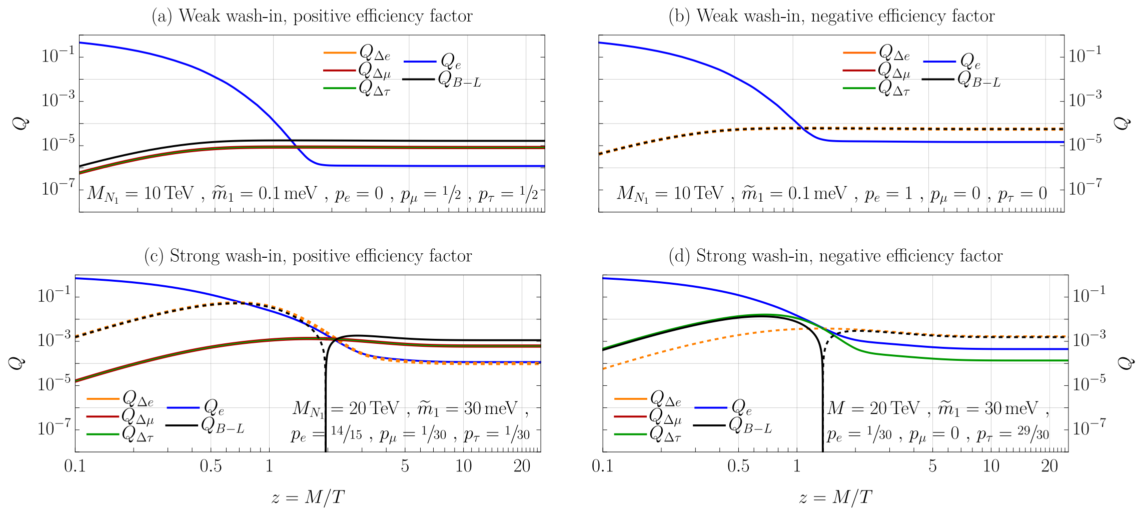

Figure VII.1: Four different example solutions of the set of Boltzmann equations in Eqs. (VII.26)-(VII.29) in the weak (strong) wash-in regime to (bottom) row. Solid (dashed) lines denote positive (negative) comoving charge asymmetries Q. The efficiency factor defined in Eq. (VII.31), $Q_{B-L}\,(z \gg 1) = C_{\rm win}\,\kappa$, can be read off from the black curves at $z \gg 1$. The solutions in the first (second) column correspond to positive (negative) κ values. In all four plots, the RHN branching ratios $p_{e,\mu,\tau}$ are set to the values that maximize $|\kappa|$ for the given values for $\widetilde{m}_1$ and M_{N_1}. Adapted from Ref. [3].

with $\widetilde{m}_1 = 30$ meV, corresponding to a decay parameter $K = \frac{\widetilde{m}_1}{m_*} \approx 28$, and $M_{N_1} = 20$ TeV. The sharp drop in the $B-L$ curve in the middle of these panels is due to a change of sign in $B-L$ as the asymmetry in Δ_e becomes either smaller or larger than the asymmetry in $\Delta_\mu + \Delta_\tau$.

To quantify how efficient WILG is in the regime under study, it is useful to introduce an efficiency factor κ,

$$\kappa = \frac{1}{3/10}\left[Q_{\Delta_e}\,(z \gg 1) + Q_{\Delta_\mu}\,(z \gg 1) + Q_{\Delta_\tau}\,(z \gg 1)\right] . \tag{VII.31}$$

This parameter encodes the deviation of WILG from the optimal outcome, $q_{B-L} = -\frac{3}{10}\,q_e$ (c.f. Eq. (V.5)), in the temperature regime under consideration. This allows us to conveniently express the resulting baryon-asymmetry that would be observed today as a result of WILG in terms of $q_e^{\rm ini} \equiv \frac{1}{6}\,\bar{\mu}_e^{\rm ini} T^2$ as,

$$\eta_B^0 = \frac{n_B}{n_\gamma}\bigg|_{\rm today} = C_{\rm sph}\,C_{\rm win}\,\frac{g_{*,s}^0}{g_{*,s}^{\rm SM}}\,\kappa\left(\widetilde{m}_1, M, p_e, p_\mu, q_e^{\rm ini}\right)\frac{q_e^{\rm ini}}{n_\gamma}\bigg|_{\rm ini} , \tag{VII.32}$$

where $C_{\rm sph} = \frac{12}{37}$ [355, 453] and $C_{\rm win} = \frac{3}{10}$ denote sphaleron and WILG conversion factors, respectively. The SM entropy DOFs today and at high temperatures are given by, $g_{*,s}^0 = \frac{43}{11}$ and $g_{*,s}^{\rm SM} = \frac{427}{4}$, and the photon number density $n_\gamma = \zeta(3)\,g_\gamma T^3/\pi^2$, where $g_\gamma = 2$.

Recall from our discussion in Section V.1, that avoiding a scenario where the initial asymmetry in q_e triggers an efficient SM chiral plasma instability that converts the chiral charge stored in q_e into helical hypermagnetic fields can be translated into an upper bound on $\bar{\mu}_e^{\rm ini}$, c.f. Eq. (V.9). Combining this upper bound with the requirement of successfully accounting for the BAU, $\eta_B^0 = \eta_B^{\rm obs}$, implies a lower bound on the efficiency factor κ as

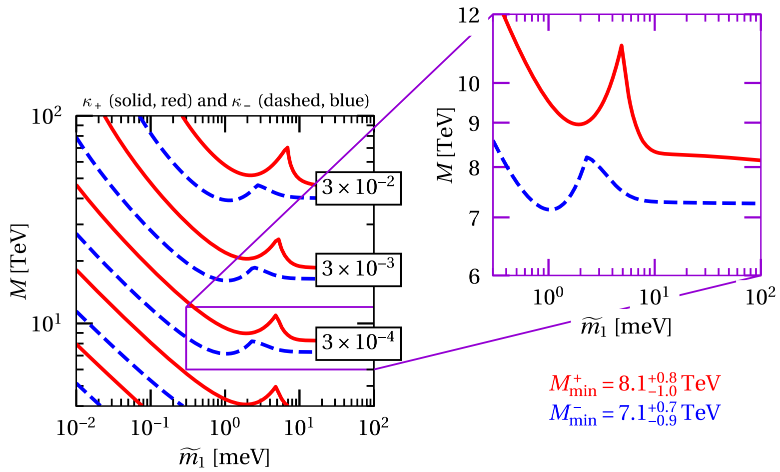

Figure VII.2: Solutions for the efficiency factor, $\kappa_+ > 0$ (solid red contours) and $\kappa_- < 0$ (dashed blue contours), which assume optimal RHN branching ratios $p_{e,\mu,\tau}$, across the $\widetilde{m}_1 - M_{N_1}$ plane (M_{N_1} is denoted by M in the figure). The colored bands in the magnified portion shown in the upper-right part of the plot indicate the ranges $|\kappa_\pm| = 2 \cdots 4 \times 10^{-4}$, with the central lines corresponding to the $|\kappa_\pm| = 3 \times 10^{-4}$ contours. Figure by D.W. [3].

seen clearly from the following relation,

$$\eta_B^0 \simeq \eta_B^{\rm obs} \left(\frac{\kappa}{2.6 \times 10^{-4}}\right) \left(\frac{\bar{\mu}_e/T}{9.6 \times 10^{-4}}\right)_{\rm ini} . \tag{VII.33}$$

Eq. (VII.33) shows that $\kappa \gtrsim 2.6 \times 10^{-4}$ is required for successful WILG, and we therefore focus on identifying the region of parameter space where this is satisfied. To achieve this, we carried out a numerical scan over the two-dimensional parameter space spanned by $\widetilde{m}_1$, M_{N_1}. At each point in the $\widetilde{m}_1 - M_{N_1}$ plane, we then scan over the two remaining free parameters in our setup, $p_e \in [0,1]$ and $p_\mu \in [0, 1-p_e]$ and identify the branching ratios that maximize the values of κ and $-\kappa$. The result of the scan are extremal solutions $\kappa_+ > 0$ and $\kappa_- < 0$ across the $\widetilde{m}_1 - M_{N_1}$ plane. We stress that both $\kappa > 0$ and $\kappa < 0$ are viable solutions, if the sign of the initial asymmetry $q_e^{\rm ini}$ can be chosen freely.

The results of our numerical scans are shown in Fig. VII.2 and in Fig. VII.3. The former is a high-resolution scan with $\widetilde{m}_1 \in [10^{-2}, 10^2]$, while the latter is a scan with lower resolution covering $\widetilde{m}_1 \in [10^{-2}, 10^3]$. Starting with Fig. VII.2, it is clear that the optimal $\kappa_\pm$ contours change as a function of $\widetilde{m}_1$. This is a reflection of the fact that the optimal branching ratios change as a function of $\widetilde{m}_1$. For $\widetilde{m}_1 \ll 5\,$meV, maximal values $|\kappa_+|$ ($|\kappa_-|$) are achieved for $p_e = 0$ and $p_{\mu,\tau} = \frac{1}{2}$ ($p_e = 1$ and $p_{\mu,\tau} = 0$). In the top row of Fig. VII.1, we have included representative solutions of the Boltzmann equations in this regime of parameter space. Meanwhile, for $\widetilde{m}_1 \gg 5\,$meV, maximal values $|\kappa_+|$ ($|\kappa_-|$) are achieved for $p_e \simeq 1 - 2.0\,{\rm meV}/\widetilde{m}_1$ ($p_e \simeq 1.1\,{\rm meV}/\widetilde{m}_1$) in combination with $p_{\mu,\tau} = (1-p_e)/2$ ($p_\mu = 0$ and $p_\tau = 1 - p_e$). In the bottom row of Fig. VII.1, we have included representative solutions of the Boltzmann equations in this regime of parameter space. The optimal values for branching ratios for $\widetilde{m}_1 \ll 5\,$meV and $\widetilde{m}_1 \gg 5\,$meV, are summarized in Table VII.1.

We now have all the ingredients to discuss a lower bound on M_{N_1} from (successful) WILG. The $|\kappa_\pm| = 3 \times 10^{-4}$ contours in Fig. VII.2 show the minimum value of M_{N_1} as a function of $\widetilde{m}_1$ for optimal branching ratios. In the case of $\kappa > 0$, an effective neutrino

	$\widetilde{m}_1 \ll 5\,\mathrm{meV}$	$\widetilde{m}_1 \gg 5\,\mathrm{meV}$
p_e^-	1	$\sim \frac{1.1\,\mathrm{meV}}{\widetilde{m}_1}$
p_μ^-	0	
p_e^+	0	$\sim 1 - \frac{2\,\mathrm{meV}}{\widetilde{m}_1}$
p_μ^+	$(1-p_e^+)/2$	

Table VII.1: Branching ratios for optimal κ_- (top) and κ_+ (bottom) in the regimes $\widetilde{m}_1 \ll 5$ meV and $\widetilde{m}_1 \gg 5\,\mathrm{meV}$. Table adapted from D.W.

mass around $\widetilde{m}_1 \sim 100\,\mathrm{meV}$ combined with an input charge saturating the upper bound in Eq. (V.9), would make it possible for WILG to account for the BAU down to $M_{N_1} \approx 8$ TeV. Meanwhile, in the case of $\kappa < 0$, an effective neutrino mass around $\widetilde{m}_1 \sim 1\,\mathrm{meV}$ and input charge saturating the upper bound in Eq. (V.9), would make it possible for WILG to account for the BAU down to $M_{N_1} \approx 7$ TeV. Since we expect the CPI to become increasingly important for q_e^{ini} around the bound in Eq. (V.9), we provide an estimate of the RHN mass bound by varying from $\kappa = 2 \cdots 4 \times 10^{-4}$. Note that this is equivalent to varying the upper bound on q_e^{ini}, c.f. Eq. (VII.33), and hence parametrizes our ignorance about the efficiency of the CPI for values of q_e^{ini} around $\sim 10^{-3}$. By doing so, we obtain the following lower bounds on M_{N_1},

$$M^+_{\mathrm{min}} = 8.1^{+0.8}_{-1.0}\,\mathrm{TeV}\,, \qquad M^-_{\mathrm{min}} = 7.1^{+0.9}_{-0.7}\,\mathrm{TeV}\,, \tag{VII.34}$$

where $M^\pm_{\mathrm{min}}$ refer to the $\kappa_\pm$ solutions in Fig. VII.2, respectively.

Figure VII.3 presents a lower-resolution parameter scan extending $\widetilde{m}_1$ up to 10^3 meV. For $\kappa_+ = 3 \times 10^{-4}$, the lower bound on M_{N_1} is now slightly below 8 TeV, and is located at $\widetilde{m}_1 = 10^3$ meV (red star). The lower bound on M_{N_1} for $|\kappa_-| = 3 \times 10^{-4}$ remains unchanged (blue star). We note that for large values of $\widetilde{m}_1$, p_e^+ (p_e^-) asymptotes towards 1 (0), c.f. Tab. VII.1.

VII.3 Conclusion

In this chapter, we obtained a lower bound on M_{N_1} from the requirement of successful WILG. Our analysis presents a significant step in the development of the WILG framework, as it establishes its range of applicability. The main result, Eq. (VII.34), shows that M_{N_1} can be significantly lower than the right-handed electron Yukawa equilibration temperature $T_e \approx 85$ TeV, and is one order of magnitude lower than the initial estimate of $M_{\mathrm{min}} \sim 100\,\mathrm{TeV}$ stated in the original paper on WILG [371]. Notably, it is also roughly five orders of magnitude below the Davidson–Ibarra bound on M_{N_1} in TLG with hierarchical RHN masses. This highlights that WILG can open up a vast region of the neutrino mass parameter space by relieving RHNs from satisfying Sakharov's condition on CP violation. However, the relaxed bound on M_{N_1} comes at the cost of requiring a chargegenesis mechanism at higher energies to account for CP violation. Exploration of chargegenesis mechanisms, and in the context of our work; chargegenesis mechanisms capable of producing a large primordial charge asymmetry in right-handed electrons, is therefore an important topic to pursue in future work.

Finally, it is worth repeating that the lower bounds on M_{N_1} presented in Eq. (VII.34) are subject to theory uncertainties, primarily due to our treatment of the CPI. Future refine-

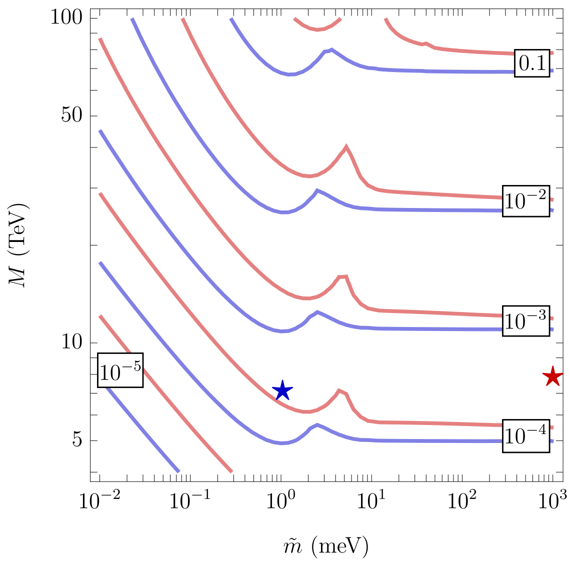

Figure VII.3: $\kappa_+ > 0$ (red contours) and $\kappa_- < 0$ (blue contours) solutions for the efficiency factor, which assume optimal RHN branching ratios $p_{e,\mu,\tau}$, as functions of the neutrino masses $\widetilde{m}_1$ and M_{N_1}. The two stars represent the lowest values of M_{N_1} for which successful WILG can take place.

ments could involve incorporating anomalous q_e violation into the Boltzmann equation for q_e and tracking hypermagnetic helicity evolution. Additionally, a detailed understanding of CPI at large chiral charge would benefit from magnetohydrodynamical simulations of the SM plasma at $T \sim T_e$. It remains to be seen whether future refinements of CPI-effects in the context of WILG will significantly impact the lower bound $M_{N_1} \sim 7\,\text{TeV}$ obtained here.

Part III

New physics in rare semileptonic B and K decays

CHAPTER VIII

Motivation and background

The first two parts of this thesis have focused on early-universe cosmology, leptogenesis, and neutrinos. These studies highlight the potential implications of LNV NP for the neutrino mass puzzle and the matter-antimatter asymmetry of the universe, which emphasizes the importance of searching for LNV NP. Traditionally, LNV searches have relied on $0\nu\beta\beta$ experiments and collider searches (see, e.g., Ref. [454] and references therein). In this part of the thesis, we explore rare semileptonic Kaon and B-decays as complementary probes of LNV NP. In fact, the scope of the following chapters will extend beyond LNV, as we develop general strategies to disentangle NP contributions parametrized by effective operators, with a particular emphasis on LNV operators. We begin by motivating the relevance of flavor physics and its thematic connection to the preceding parts, followed by an outline of the remainder of this chapter.

Flavor physics is a branch of particle physics that investigates the properties of the different generations of leptons and quarks, and the various transitions among them. Historically, it played a major role in the theoretical development of the SM by e.g. predicting the charm quark and the third generation of quarks [455, 456]. Today, flavor physics continues to be an important field in the search for BSM physics: By comparing theoretical SM predictions with experimental results, one can search for and constrain new physics models.

More precisely, by comparing SM predictions for flavor transitions with experimental measurements or bounds, one obtains predictions or constraints, respectively, on new sources of flavor violation. Flavor constraints restrict the size of couplings in BSM models that induce flavor-changing interactions. Meanwhile, any observed discrepancies between SM predictions and experimental results provide, if taken at face value, evidence for NP. Determining the magnitude of such potential discrepancies can be used to predict the scale at which the UV physics responsible is expected to emerge. Moreover, searches based on flavor observables should be seen as complementary to direct searches at colliders. While flavor experiments cannot directly produce new particles, they are not limited by the center-of-mass energy of colliding particles, and can motivate directions for new direct searches.

To sharpen the connections between flavor physics and the topics from previous chapters, note that the recurring theme has been neutrinos in the early universe. In this part, we will consider neutrinos in the context of flavor-physics searches for NP rather than the early universe. Specifically, we will study rare semileptonic B-meson and Kaon decays with either neutrinos or light dark particles in the final state, and explore how to disentangle NP contributions to such decays. The following decay channels $K \to \pi + \text{invisible}$, $B \to K(K^*) + \text{invisible}$, and inclusive decays $B \to X_s + \text{invisible}$ will be considered. Key heuristic motivational points for studying the invisible final states in these processes are summarized below.

- Evidence for new light dark particles hiding in the invisible final state would present a potential breakthrough in our understanding of dark matter and particle physics beyond the SM.
- Evidence for sterile neutrinos in the invisible final state could shed light on the neutrino mass puzzle, and leptogenesis.
- The rare semileptonic decays in question can be used to search for LNV, as will be argued in this chapter and the next. Observing NP consistent with a LNV hypothesis in these systems could have dramatic implications not only for the neutrino-mass puzzle, but also for the viability of (high-scale) leptogenesis.

A detailed explanation of the last point will be given in Section VIII.4, while the rest of the chapter is organized as follows. In Section VIII.1, we will review theoretical considerations motivating $B \to K(K^*)\nu\bar{\nu}$ and $K \to \pi\nu\bar{\nu}$ as systems to search for NP. Section VIII.2 provides an overview of current experimental limits and comparisons with SM predictions. In Section VIII.3, we introduce the effective-operator bases that will be used in the next chapter. Expressions for form factors and additional technicalities are summarized in Section VIII.5. In Section VIII.6, we summarize, contextualize our work, and provide a detailed outline of the next chapter.

VIII.1 Rare semileptonic decays

Flavor-changing neutral currents (FCNCs) are not present at tree level in the SM, but are induced by loop diagrams involving at least two $W^{\pm}$ vertices. This is illustrated in Fig. VIII.1, which shows representative one-loop Feynman diagrams contributing to $b \to s\nu\bar{\nu}$ in the SM.[1] FCNCs are highly suppressed in the SM as a result of the generic one-loop suppression factor $1/16\pi^2$, suppression from at least one off-diagonal element of the Cabibbo–Kobayashi–Maskawa (CKM) matrix [457, 458], and so-called GIM suppression [455]. The latter is a consequence of the unitarity of the CKM matrix, and can be understood as follows [459]: The amplitude for a $b \to s$ transition takes the following generic form

$$\mathcal{M}_{b\to s} = \sum_i V_{ib}^* V_{is} f\left(\frac{m_i^2}{m_W^2}\right), \tag{VIII.1}$$

where f depends on the process under consideration [460]. Assuming $m_i^2 \ll m_W^2$, which is a good approximation for all quarks except the top, one can Taylor expand the function f to first order

$$\mathcal{M}_{b\to s} \approx \sum_i V_{ib}^* V_{is} f(0) + \sum_i V_{ib}^* V_{is} \frac{m_i^2}{m_W^2} f'(0)\,. \tag{VIII.2}$$

The first term vanishes identically, due to the unitarity of the CKM matrix, $\sum_i V_{ib}^* V_{is} = 0$. In fact, if all quark masses were identical, then $\mathcal{M}_{b\to s}$ would be proportional to $\sum_i V_{ib}^* V_{is}$ and identically vanish. For non-degenerate quark masses, the second term in Eq. (VIII.2) is still suppressed by $\frac{m_i^2}{m_W^2}$, which is the core of the GIM mechanism. However, the argument

[1] For concreteness, we will consider $b \to s$ transitions (relevant for B-decays) in this section, but similar considerations apply to $s \to d$ transitions (relevant for Kaon decays).

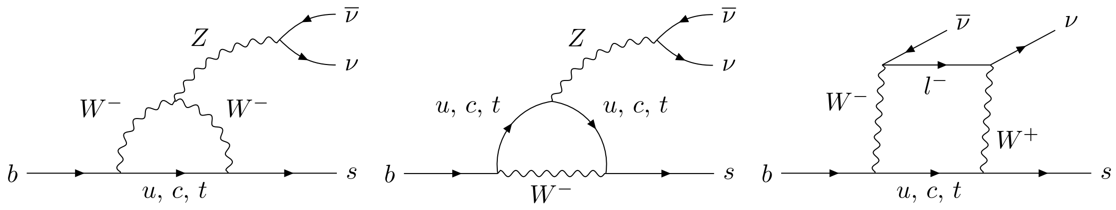

Figure VIII.1: Feynman diagrams contributing to $b \to s\nu\bar{\nu}$ in the SM.

presented above is not valid for $m_i \gtrsim m_W$, and the top quark contribution is therefore not suppressed by GIM. Still, the relevant entries in the CKM matrix involving the top are small, so top contributions to $b \to s$ receive significant suppression from V_{ts}.[2]

In practice, it is useful to calculate FCNC transitions using effective-field theory (EFT) methods. Specifically, we will be making extensive use of Low-Energy Effective Field Theory below the electroweak scale (LEFT) [461, 462], where FCNC interactions are encoded in WCs of higher-dimension operators composed of the SM fields that are lighter than $W^\pm$. For the case of $b \to s\nu\bar{\nu}$, the leading operators are current-current interactions of the schematic form $\mathcal{O} = j_\nu \cdot j_q$. Here j_ν denotes a neutrino current, and j_q denotes a quark current with appropriate flavor-quantum numbers. The contribution of such an operator to a $b \to s\nu\bar{\nu}$ transition of the form $B \to M\nu\bar{\nu}$ where B and M can be written as,[3]

$$\langle \nu\bar{\nu}M|\, \mathcal{O}\, |B\rangle = \langle \nu\bar{\nu}M|\, j_\nu \cdot j_q\, |B\rangle = \langle \nu\bar{\nu}|\, j_\nu\, |0\rangle \cdot \langle M|\, j_q\, |B\rangle \sim \langle \nu\bar{\nu}|\, j_\nu\, |0\rangle\, F(q^2), \quad \text{(VIII.3)}$$

Here, $F(q^2)$ denotes a hadronic form factor, which is a function of the dineutrino invariant mass squared, q^2, that has to be determined via nonperturbative methods.[4] The important point is that the calculation factorizes into a trivial leptonic part and a hadronic part. This should be contrasted to charged semileptonic decays, $B \to Ml^+l^-$, which receive non-factorizable contributions, as e.g. the charged leptons can arise from a photon emitted from a purely hadronic interaction. The calculation of semi-leptonic decays with a dineutrino final state is therefore theoretically clean, and SM predictions are under good theoretical control. This make them, at least from a theoretical point of view, golden channels for precision tests of the SM.

The most recent SM predictions for the branching ratios of the Kaon decays considered in this thesis reads [465],

$$\mathcal{B}(K^+ \to \pi^+\nu\bar{\nu})_{\text{SM}} = (8.60 \pm 0.42) \times 10^{-11}, \quad \text{(VIII.4)}$$
$$\mathcal{B}(K_L \to \pi^0\nu\bar{\nu})_{\text{SM}} = (2.94 \pm 0.15) \times 10^{-11}. \quad \text{(VIII.5)}$$

The most recent SM predictions for the branching ratios of the B-decays of interest to us read [466]

$$\mathcal{B}(B^+ \to K^+\nu\bar{\nu})_{\text{SM}} = (4.92 \pm 0.30) \times 10^{-6}, \quad \text{(VIII.6)}$$
$$\mathcal{B}(B^0 \to K^{0*}\nu\bar{\nu})_{\text{SM}} = (10.11 \pm 0.96) \times 10^{-6}, \quad \text{(VIII.7)}$$
$$\mathcal{B}(B \to X_s\nu\bar{\nu})_{\text{SM}} = (2.7 \pm 0.2) \cdot 10^{-5}, \quad \text{(VIII.8)}$$

[2] The top contribution in $s \to d$ transitions are even more suppressed by the smallness of both V_{ts} and V_{td}.

[3] See for instance Ref. [463] and references therein for details.

[4] In particular, the most important methods for determining form factors at present are lattice QCD (LQCD) and QCD sum rules [464].

obtained using $|V_{cb}| = 42.6(4) \times 10^{-3}$ from [467,468] and form factors from Refs. [469–471] for $B^+ \to K^+\nu\bar{\nu}$ and Ref. [472] for $B^0 \to K^{0*}\nu\bar{\nu}$. Corresponding experimental results are summarized in the following section.

VIII.2 Experimental limits

Last year, NA62 released a new result for $K^+ \to \pi^+\nu\bar{\nu}$ listed in Eq. (VIII.9) [473, 474]. The decay $K_L \to \pi^0\nu\bar{\nu}$ is constrained by KOTO [475], and the 90% confidence level (CL) upper bound is given below,

$$\mathcal{B}(K^+ \to \pi^+\nu\bar{\nu})_{\text{exp}} = \left(13.0^{+3.3}_{-2.9}\right) \times 10^{-11}, \tag{VIII.9}$$

$$\mathcal{B}(K_L \to \pi^0\nu\bar{\nu})_{\text{exp}} \leq 2.0 \times 10^{-9}\,. \tag{VIII.10}$$

Comparing these results with Eqs. (VIII.4) and (VIII.5), it is clear that the experimental data leaves room for NP in these decays.

The current experimental bounds on $b \to s\bar{\nu}\nu$, including the most recent 2023 results from Belle II [476], read [477–479]

$$\mathcal{B}(B^+ \to K^+\nu\bar{\nu}) = (13 \pm 4) \times 10^{-6}, \tag{VIII.11}$$

$$\mathcal{B}(B^0 \to K^{0*}\nu\bar{\nu}) \leq 1.8 \times 10^{-5} \quad @\ 90\%\ \text{CL}\,, \tag{VIII.12}$$

$$\mathcal{B}(B \to X_s\nu\bar{\nu}) \leq 6.4 \times 10^{-4} \quad @\ 90\%\ \text{CL}\,. \tag{VIII.13}$$

Comparing this data with the SM predictions in Eqs. (VIII.6)-(VIII.8), it is evident that there is also significant room for NP contributions in these channels.

VIII.3 Operator basis and LNV

Having established that $K \to \pi\nu\bar{\nu}$ and $B \to K(K^*)\nu\bar{\nu}$ provide promising systems to search for NP, we will now consider technical foundations for the next chapter. Here, we introduce the operator bases to be utilized and discuss lepton number.

Operator basis: LEFT

As mentioned previously, we will employ the LEFT framework [461, 462] in our study. Adopting the notation in Refs. [461, 480], the leading-order (dimension 6) operators of interest to us can be written as [461, 462]

$$\mathcal{L}_{\text{eff}} = \mathcal{L}_{\text{SM}} + \sum_{X=L,R} C^{\text{VLX}}_{\nu d}\mathcal{O}^{\text{VLX}}_{\nu d} + \left(\sum_{X=L,R} C^{\text{SLX}}_{\nu d}\mathcal{O}^{\text{SLX}}_{\nu d} + C^{\text{TLL}}_{\nu d}\mathcal{O}^{\text{TLL}}_{\nu d} + \text{h.c.}\right). \tag{VIII.14}$$

This effective description encodes operators with vector currents,

$$\mathcal{O}^{\text{VLL}}_{\nu d} = (\overline{\nu_L}\gamma^\mu\nu_L)(\overline{d_L}\gamma_\mu d_L)\,, \tag{VIII.15}$$

$$\mathcal{O}^{\text{VLR}}_{\nu d} = (\overline{\nu_L}\gamma^\mu\nu_L)(\overline{d_R}\gamma_\mu d_R)\,, \tag{VIII.16}$$

scalar currents,

$$\mathcal{O}^{\text{SLL}}_{\nu d} = (\overline{\nu^c_L}\nu_L)(\overline{d_R}d_L)\,, \tag{VIII.17}$$

$$\mathcal{O}^{\text{SLR}}_{\nu d} = (\overline{\nu^c_L}\nu_L)(\overline{d_L}d_R)\,, \tag{VIII.18}$$

and tensor currents

$$\mathcal{O}_{\nu d}^{\rm TLL} = (\overline{\nu_L^c}\sigma_{\mu\nu}\nu_L)(\overline{d_R}\sigma^{\mu\nu}d_L) \; . \tag{VIII.19}$$

The dimension 5 neutrino dipole operator, $\overline{\nu_L^c}\sigma^{\mu\nu}\nu_L F_{\mu\nu}$, along with the down-type quark dipole operator, $\overline{d_L}\sigma^{\mu\nu}d_R F_{\mu\nu}$, would formally contribute to the same order in the LEFT expansion as the operators above. However, the neutrino dipole moment operator is tightly constrained by searches for magnetic dipole moments of neutrinos and therefore not considered further here [480–482].

In writing down the equations, we have employed the following notation [1]: $d_{L(R)}$ and ν_L are Weyl fermions, where the subscript denotes their chirality. Applying the charge-conjugation operator, $C = i\gamma^2\gamma^0$, makes the charge-conjugated left-handed neutrino field $\nu_L^c \equiv C\overline{\nu_L}$ right-handed. We will be working in the limit of massless neutrinos, so flavor and mass eigenstates coincide. There is an implicit sum over all possible flavor combinations in the Lagrangian (VIII.14). The scalar operators $\mathcal{O}_{\nu d}^{\rm SLL}$ and $\mathcal{O}_{\nu d}^{\rm SLR}$ are symmetric in the neutrino flavors, the tensor operator $\mathcal{O}_{\nu d}^{\rm TLL}$ is antisymmetric in the neutrino flavors, while the vector operators $\mathcal{O}_{\nu d}^{\rm VLL}$ and $\mathcal{O}_{\nu d}^{\rm VLR}$ do not exhibit a manifest (anti)symmetry in the neutrino flavors [480]. Finally, note that Eq.(VIII.14) is written in a general form suited for both K and B decays. In fact, this operator basis can also encompass light sterile neutrinos [480, 483].

Operator basis: DLEFT

In experimental searches, neutrinos in the final state are not directly detected; as a result, it is logically possible that rare meson decays could produce other, undetected invisible particles. Thus, the final state in the NP contribution could consist of a single boson, or two or more dark-sector particles. In this work, we will focus on scenarios involving two dark-sector particles in the final state.

We do not consider scenarios featuring a single dark boson in the final state, for the following reason. Our analysis is primarily concerned with disentangling NP contributions through detailed studies of kinematic distributions. If the final state contains a single boson, the resulting kinematic distributions would closely resemble those predicted by the SM, with the key distinction being a sharp peak at a specific value of the invisible invariant mass squared—corresponding to the mass of the dark boson. Thus, NP scenarios involving a single dark boson in the final state are, in principle, straightforward to distinguish from cases with two neutrinos, where the invariant mass-squared distribution is nonzero across the entire kinematically-allowed range. By contrast, distinguishing NP with two dark-sector particles from contributions from the (SM)LEFT operators Eqs. (VIII.15)-(VIII.19) is more subtle, making it the main subject of our study.

To account for the possibility of NP contributions with two dark-sector particles in the final state, we adapt the results in Ref. [484]. There, the authors extended the LEFT setup with an additional light dark-sector particle with either spin 0, spin 1/2, or spin 1, and established operator bases relevant for rare meson decays with two dark-sector particles in the final state. In the case of a spin-1 dark-sector particle, two scenarios are considered: (A) The dark field is represented by the vector potential X_μ, and (B) by the field strength tensor $X_{\mu\nu} = \partial_\mu A_\nu - \partial_\nu A_\mu$ [484]. Scenario A leads to divergences in the differential decay widths in the limit where the dark mass vanishes, $m \to 0$, caused by the longitudinal polarization component in the polarization sum. This well-known issue can be cured operationally by redefining the WCs to contain an explicit factor of m to the minimum power necessary to regularize the divergences in the $m \to 0$ limit (see [484] for examples and details). At first sight, it may seem reasonable to circumvent this issue by considering an exactly massless vector field (which would only have transverse polarization). However, it is a fundamental result in QFT [485] that theories of massless vector fields must be gauge theories. Assuming that SM quarks are not charged under the dark gauge group, the effective operators can then only include the dark vector boson through its field strength tensor, which is covered by Scenario B.

For clarity, we will henceforth refer to the operators in Eq. (VIII.14) as (SM)LEFT operators and operators involving dark-sector particles as (D)LEFT operators. The (D)LEFT operators from Ref. [484], are listed in the following.

Dark scalar basis:

$$\mathcal{O}^S_{ab\phi} = (\overline{q_a} q_b)(\phi^\dagger \phi), \tag{VIII.20}$$
$$\mathcal{O}^P_{ab\phi} = (\overline{q_a} i\gamma_5 q_b)(\phi^\dagger \phi), \tag{VIII.21}$$
$$\mathcal{O}^V_{ab\phi} = (\overline{q_a} \gamma^\mu q_b)(\phi^\dagger i\overleftrightarrow{\partial_\mu} \phi), \quad \times_{\rm rs} \tag{VIII.22}$$
$$\mathcal{O}^A_{ab\phi} = (\overline{q_a} \gamma^\mu \gamma_5 q_b)(\phi^\dagger i\overleftrightarrow{\partial_\mu} \phi), \quad \times_{\rm rs}. \tag{VIII.23}$$

The $\times_{\rm rs}$ indicates that the operator vanishes for a real scalar field [484].

Dark fermion basis:

$$\mathcal{O}^S_{ab\chi 1} = (\overline{q_a} q_b)(\overline{\chi}\chi), \qquad \mathcal{O}^S_{ab\chi 2} = (\overline{q_a} q_b)(\overline{\chi} i\gamma_5 \chi), \tag{VIII.24}$$
$$\mathcal{O}^P_{ab\chi 1} = (\overline{q_a} i\gamma_5 q_b)(\overline{\chi}\chi), \qquad \mathcal{O}^P_{ab\chi 2} = (\overline{q_a} \gamma_5 q_b)(\overline{\chi}\gamma_5\chi), \tag{VIII.25}$$
$$\mathcal{O}^V_{ab\chi 1} = (\overline{q_a} \gamma^\mu q_b)(\overline{\chi}\gamma_\mu\chi), \quad \times_{\rm M} \qquad \mathcal{O}^V_{ab\chi 2} = (\overline{q_a} \gamma^\mu q_b)(\overline{\chi}\gamma_\mu\gamma_5\chi), \tag{VIII.26}$$
$$\mathcal{O}^A_{ab\chi 1} = (\overline{q_a} \gamma^\mu \gamma_5 q_b)(\overline{\chi}\gamma_\mu\chi), \quad \times_{\rm M} \qquad \mathcal{O}^A_{ab\chi 2} = (\overline{q_a} \gamma^\mu \gamma_5 q_b)(\overline{\chi}\gamma_\mu\gamma_5\chi), \tag{VIII.27}$$
$$\mathcal{O}^T_{ab\chi 1} = (\overline{q_a} \sigma^{\mu\nu} q_b)(\overline{\chi}\sigma_{\mu\nu}\chi), \quad \times_{\rm M} \qquad \mathcal{O}^T_{ab\chi 2} = (\overline{q_a} \sigma^{\mu\nu} q_b)(\overline{\chi}\sigma_{\mu\nu}\gamma_5\chi), \quad \times_{\rm M} \tag{VIII.28}$$

The $\times_{\rm M}$ indicates that the operator vanishes if χ is Majorana [484].

Dark vector basis case A:

$$\mathcal{O}^S_{abA} = (\overline{q_a} q_b)(X^\dagger_\mu X^\mu), \tag{VIII.29}$$
$$\mathcal{O}^P_{abA} = (\overline{q_a} i\gamma_5 q_b)(X^\dagger_\mu X^\mu), \tag{VIII.30}$$
$$\mathcal{O}^T_{abA1} = \frac{i}{2}(\overline{q_a} \sigma^{\mu\nu} q_b)(X^\dagger_\mu X_\nu - X^\dagger_\nu X_\mu), \quad \times_{\rm rv} \tag{VIII.31}$$
$$\mathcal{O}^T_{abA2} = \frac{1}{2}(\overline{q_a} \sigma^{\mu\nu}\gamma_5 q_b)(X^\dagger_\mu X_\nu - X^\dagger_\nu X_\mu), \quad \times_{\rm rv} \tag{VIII.32}$$
$$\mathcal{O}^V_{abA1} = \frac{1}{2}[\overline{q_a} \gamma_{(\mu} i\overleftrightarrow{D_{\nu)}} q_b](X^{\mu\dagger} X^\nu + X^{\nu\dagger} X^\mu), \tag{VIII.33}$$
$$\mathcal{O}^V_{abA2} = (\overline{q_a} \gamma_\mu q_b)\partial_\nu(X^{\mu\dagger} X^\nu + X^{\nu\dagger} X^\mu), \tag{VIII.34}$$
$$\mathcal{O}^V_{abA3} = (\overline{q_a} \gamma_\mu q_b)(X^\dagger_\rho \overleftrightarrow{\partial_\nu} X_\sigma)\epsilon^{\mu\nu\rho\sigma}, \tag{VIII.35}$$
$$\mathcal{O}^V_{abA4} = (\overline{q_a} \gamma^\mu q_b)(X^\dagger_\nu i\overleftrightarrow{\partial_\mu} X^\nu), \quad \times_{\rm rv} \tag{VIII.36}$$
$$\mathcal{O}^V_{abA5} = (\overline{q_a} \gamma_\mu q_b) i\partial_\nu(X^{\mu\dagger} X^\nu - X^{\nu\dagger} X^\mu), \quad \times_{\rm rv} \tag{VIII.37}$$
$$\mathcal{O}^V_{abA6} = (\overline{q_a} \gamma_\mu q_b) i\partial_\nu(X^\dagger_\rho X_\sigma)\epsilon^{\mu\nu\rho\sigma}, \quad \times_{\rm rv} \tag{VIII.38}$$

$$\mathcal{O}^{A}_{abA1} = \frac{1}{2}[\overline{q_a}\gamma_{(\mu}\gamma_5 i\overleftrightarrow{D}_{\nu)}q_b](X^{\mu\dagger}X^{\nu} + X^{\nu\dagger}X^{\mu}), \tag{VIII.39}$$
$$\mathcal{O}^{A}_{abA2} = (\overline{q_a}\gamma_\mu\gamma_5 q_b)\partial_\nu(X^{\mu\dagger}X^{\nu} + X^{\nu\dagger}X^{\mu}), \tag{VIII.40}$$
$$\mathcal{O}^{A}_{abA3} = (\overline{q_a}\gamma_\mu\gamma_5 q_b)(X^{\dagger}_{\rho}\overleftrightarrow{\partial}_{\nu}X_{\sigma})\epsilon^{\mu\nu\rho\sigma}, \tag{VIII.41}$$
$$\mathcal{O}^{A}_{abA4} = (\overline{q_a}\gamma^\mu\gamma_5 q_b)(X^{\dagger}_{\nu}i\overleftrightarrow{\partial}_{\mu}X^{\nu}), \quad \times_{\rm rv} \tag{VIII.42}$$
$$\mathcal{O}^{A}_{abA5} = (\overline{q_a}\gamma_\mu\gamma_5 q_b)i\partial_\nu(X^{\mu\dagger}X^{\nu} - X^{\nu\dagger}X^{\mu}), \quad \times_{\rm rv} \tag{VIII.43}$$
$$\mathcal{O}^{A}_{abA6} = (\overline{q_a}\gamma_\mu\gamma_5 q_b)i\partial_\nu(X^{\dagger}_{\rho}X_{\sigma})\epsilon^{\mu\nu\rho\sigma}, \quad \times_{\rm rv} \tag{VIII.44}$$

The $\times_{\rm rv}$ indicates that the operator vanishes for a real vector field [484].

Vector case B:

$$\mathcal{O}^{S}_{abB1} = (\overline{q_a}q_b)X^{\dagger}_{\mu\nu}X^{\mu\nu}, \tag{VIII.45}$$
$$\mathcal{O}^{S}_{abB2} = (\overline{q_a}q_b)X^{\dagger}_{\mu\nu}\tilde{X}^{\mu\nu}, \tag{VIII.46}$$
$$\mathcal{O}^{P}_{abB1} = (\overline{q_a}i\gamma_5 q_b)X^{\dagger}_{\mu\nu}X^{\mu\nu}, \tag{VIII.47}$$
$$\mathcal{O}^{P}_{abB2} = (\overline{q_a}i\gamma_5 q_b)X^{\dagger}_{\mu\nu}\tilde{X}^{\mu\nu}, \tag{VIII.48}$$
$$\mathcal{O}^{T}_{abB1} = \frac{i}{2}(\overline{q_a}\sigma^{\mu\nu}q_b)(X^{\dagger}_{\mu\rho}X^{\rho}_{\nu} - X^{\dagger}_{\nu\rho}X^{\rho}_{\mu}), \quad \times_{\rm rv} \tag{VIII.49}$$
$$\mathcal{O}^{T}_{abB2} = \frac{1}{2}(\overline{q_a}\sigma^{\mu\nu}\gamma_5 q_b)(X^{\dagger}_{\mu\rho}X^{\rho}_{\nu} - X^{\dagger}_{\nu\rho}X^{\rho}_{\mu}). \quad \times_{\rm rv} \tag{VIII.50}$$

The $\times_{\rm rv}$ indicates that the operator vanishes for a real vector field [484].

Sterile neutrinos and LNV

The operator basis in Eq. (VIII.14) includes the three active neutrinos ν_{Li}, $i = 1, 2, 3$, and can be straightforwardly extended to accommodate any number of sterile neutrinos, $N_{Ri} = \nu^c_{Li}$, $i = 4, ..$ [486]. Both ν_{Li} and N_{Ri} carry lepton number +1. Consequently, the operators in (VIII.14) could be either LNV or lepton-number conserving (LNC) [486], depending on whether the neutrinos are sterile and/ or active. The following discussion aims to clarify under which conditions these operators violate lepton number [1]. We will use indices $i, j \in \{1, 2, 3\}$ for active neutrino generations and $i, j \geq 4$ for sterile neutrinos. The outcome of the discussion is summarized in Table VIII.1.

For $i, j \leq 3$,, corresponding to two active neutrinos in the final state, the vector-current operators $\mathcal{O}^{\rm VLL}_{\nu d}$ and $\mathcal{O}^{\rm VLR}_{\nu d}$ are LNC. In contrast, the scalar-current operators $\mathcal{O}^{\rm SLL}_{\nu d}$ and $\mathcal{O}^{\rm SLR}_{\nu d}$, and the tensor-current operator $\mathcal{O}^{\rm TLL}_{\nu d}$ violate lepton number. Therefore, in the absence of light sterile neutrinos, measuring a nonzero WC for any of the scalar or tensor-current operators would constitute direct evidence for LNV.

For $i, j \geq 4$, corresponding to two sterile neutrinos in the final state, the vector-current operators are LNC while the scalar- and tensor-current operators are LNV. This result is the same as that for two active neutrinos in the final state.

For $1 \leq i \leq 3 < j$ and $1 \leq j \leq 3 < i$, the vector-current operators violate lepton number while the scalar- and tensor-current operators conserve lepton number. An important consequence of this observation is that a nonzero measurement of a WC corresponding to a scalar-current or tensor-current operator is *not* a proof of LNV, unless the pair of associated neutrinos can be identified as either both active or both sterile. A similar arguments holds for vector currents: measuring a nonzero WC for $\mathcal{O}^{\rm VLR}_{\nu d}$ or a WC differing from the SM value for $\mathcal{O}^{\rm VLL}_{\nu d}$ does *not* automatically imply LNC NP.

$\mathcal{O}$	$1 \leq i, j \leq 3$	$1 \leq i \leq 3 < j$	$1 \leq j \leq 3 < i$	$i, j \geq 4$
$\mathcal{O}_{\nu d}^{\mathrm{SLL}}$ & $\mathcal{O}_{\nu d}^{\mathrm{SLR}}$	LNV	LNC	LNC	LNV
$\mathcal{O}_{\nu d}^{\mathrm{VLL}}$ & $\mathcal{O}_{\nu d}^{\mathrm{VLR}}$	LNC	LNV	LNV	LNC
$\mathcal{O}_{\nu d}^{\mathrm{TLL}}$	LNV	LNC	LNC	LNV

Table VIII.1: Classification of the (SM)LEFT operators according to LNV/LNC for all possible combinations of neutrino-generation indices i, j [1].

For the sake of completeness, we mention in the case of Majorana neutrinos, the basis in Eq. (VIII.14) has been explicitly matched to the standard S, P, V, A, T operator basis, and used to calculate finite mass corrections to B meson processes considered in this thesis [480]. Finite neutrino mass effects may become significant if there exists at least one (light) sterile neutrino with mass comparable to the experimental sensitivity or other mass scales in the processes of interest [480, 483, 487].

VIII.4 LNV and leptogenesis

Rare meson decays offer a new avenue for searching for LNV NP, which can serve as a complementary probe to $0\nu\beta\beta$ experiments and collider searches [454]. Notably, while $0\nu\beta\beta$ can only probe LNV physics in the first generation of SM fermions, rare meson decays probe LNV involving at least one quark beyond the first generation.

Observation of new LNV physics could have important implications for our understanding of leptogenesis. In particular, it has been shown that a discovery of LNV events at the LHC could put leptogenesis under serious tension, since the production cross section of LNV events is related to a $\Delta L = 2$ washout term that could erase asymmetry in the early universe [488, 489]. Similarly, an observation of LNV in rare meson decays would put high-scale leptogenesis under tension as the LNV operator(s) contribute to washout, and thereby diminish preexisting asymmetry. Following the steps detailed in Refs. [490, 491], it is possible to formulate a Boltzmann equation governing the evolution of a lepton-asymmetry (generated at a high scale) in the presence of washout induced by an effective LNV operator of mass dimension D with associated mass-scale Λ as,[5]

$$zHn_\gamma \frac{d\eta_{\Delta L}}{dz} = -c_D \frac{T^{2D-4}}{\Lambda^{2D-8}} \eta_{\Delta L}. \tag{VIII.51}$$

Here $n_\gamma \approx 2T^3/\pi^2$ denotes the equilibrium density of photons, and $\eta_{\Delta L}(T)$ is the lepton-asymmetry density normalized to the number density of photons at temperature T. The equation is obtained by estimating the equilibrium reaction densities of the processes induced by the LNV operator and applying chemical equilibrium conditions to relate SM chemical potentials. The coefficient c_D encodes the parametrization of the equilibrium reaction densities, summed over all relevant permutations of processes generated by the LNV operator. Its value can be determined following the procedure outlined in Ref. [491]

[5] It is understood that this equation is only valid for $T \lesssim \Lambda$, where the effective-operator description can be applied.

for a specific operator. Finally, the parametric dependence $\frac{T^{2D-4}}{\Lambda^{2D-8}}$ is dictated by dimensional analysis, as any squared matrix element derived from the effective operator scales as $\frac{1}{\Lambda^{2D-8}}$.

Assuming a radiation-dominated universe, i.e. $H = \sqrt{\frac{\pi^2 g_*}{90}}\frac{T^2}{M_P}$, Eq. (VIII.51) can be straightforwardly integrated from an initial temperature $T_i \lesssim \Lambda$ down to the electroweak scale $T_f = v$, which gives

$$T_i = \left[v^{2D-9} + (2D-9)\frac{2}{c_D \pi}\sqrt{\frac{g_*}{90}}\frac{\Lambda^{2D-8}}{M_P}\log\left(\frac{\eta_{\Delta L}(T_i)}{\eta_{\Delta L}(T_f)}\right)\right]^{\frac{1}{2D-9}} . \tag{VIII.52}$$

To connect with observations, we relate the observed baryon asymmetry η_B^{obs} to the lepton asymmetry at T_f via $\eta_B^{\text{obs}} = -\frac{3}{4}\frac{C_{\text{sph}}}{f}\eta_{\Delta L}(T_f)$, where f accounts for the dilution of the photon number density between T_f and recombination [228]. With $\frac{3}{4}\frac{C_{\text{sph}}}{f} \approx 10^{-2}$, it follows that an initial asymmetry of order unity would be washed out to below the observed value if generated at a temperature T_{LG} satisfying

$$T_{\text{LG}} \gtrsim \left[v^{2D-9} + (2D-9)\frac{2}{c_D \pi}\sqrt{\frac{g_*}{90}}\frac{\Lambda^{2D-8}}{M_P}\log\left(\frac{10^{-2}}{\eta_B^{\text{obs}}}\right)\right]^{\frac{1}{2D-9}} . \tag{VIII.53}$$

However, a definitive falsification of high-scale leptogenesis through low-scale washout processes is contingent upon verifying equilibration among all lepton flavors, e.g., by observing LNV in all flavors. In the absence of such equilibration, the lepton asymmetry may remain safely hidden in a single flavor [397]. A general discussion of caveats and loopholes can be found in Refs. [489, 491].

VIII.5 Form factors

Calculating the contributions of effective operators to rare meson decay rates, requires evaluating hadronic matrix elements of the form $\langle M|\, j_q \,|B\rangle$, as introduced in Eq. (VIII.3). The hadronic matrix elements are commonly parametrized in terms of scalar form factors associated with each allowed Lorentz structure in the matrix element. In the following, we review their precise definitions (following the parametrization in Ref. [492]) and the numerical fits used by us.

Let M_1 denote the initial meson and M_2 a final state pseudoscalar meson. In our case, if M_1 is a B-meson (Kaon), then M_2 is a Kaon (pion). The non-vanishing hadronic matrix elements from M_1 to M_2 via the scalar, vector, and tensor quark currents are parametrized by the form factors f_0, f_+, and f_T,

$$\langle M_2(k)|\, \bar{q}_2 q_1 \,|M_1(p)\rangle = \frac{m_{M_1}^2 - m_{M_2}^2}{m_{q_1} - m_{q_2}} f_0(q^2), \tag{VIII.54}$$

$$\begin{aligned}\langle M_2(k)|\, \bar{q}_2 \gamma^\mu q_1 \,|M_1(p)\rangle &= \left[(p+k)^\mu - \frac{m_{M_1}^2 - m_{M_2}^2}{q^2} q^\mu\right] f_+(q^2) \\ &\quad + \frac{m_{M_1}^2 - m_{M_2}^2}{q^2} q^\mu f_0(q^2),\end{aligned} \tag{VIII.55}$$

$$\langle M_2(k)|\, \bar{q}_2 \sigma^{\mu\nu} q_1 \,|M_1(p)\rangle = \frac{2i}{m_{M_1} + m_{M_2}}(p^\mu q^\nu - p^\nu q^\mu) f_T(q^2). \tag{VIII.56}$$

Here, m_{q_j} denotes the mass of q_j appearing in the scalar current, and m_{M_i} denotes the mass of the meson of type $i = 1, 2$. The momentum transfer between the initial and final state is denoted by $q^\mu = p^\mu - k^\mu$, where k and p are the 4-momenta of the M_2 pseudoscalar meson and the M_1 meson, respectively.

For the transition of a B-meson to K^*, the non-vanishing form factors V_0, $A_{0,1,2,3}$, and $T_{1,2,3}$ read

$$\langle K^*(k)|\,\bar{q}\gamma_5 b\,|B(p)\rangle = -i\epsilon_{K^*,\nu}q^\nu \frac{2m_{K^*}}{m_b+m_q}A_0, \tag{VIII.57}$$

$$\langle K^*(k)|\,\bar{q}\gamma^\mu b\,|B(p)\rangle = \epsilon^{\mu\nu\rho\sigma}\epsilon_{K^*,\nu}p_\rho k_\sigma \frac{2}{m_B+m_{K^*}}V_0, \tag{VIII.58}$$

$$\begin{aligned}\langle K^*(k)|\,\bar{q}\gamma^\mu\gamma_5 b\,|B(p)\rangle = i\epsilon_{K^*,\nu}\Bigg[&g^{\mu\nu}(m_B+m_{K^*})A_1 - \frac{(p+k)^\mu q^\nu}{m_B+m_{K^*}}A_2 \\ &-q^\mu q^\nu \frac{2m_{K^*}}{q^2}(A_3-A_0)\Bigg],\end{aligned} \tag{VIII.59}$$

$$\begin{aligned}\langle K^*(k)|\,\bar{q}\sigma_{\mu\nu} b\,|B(p)\rangle = i\epsilon_{\mu\nu\rho\sigma}\epsilon_{K^*,\alpha}\Bigg\{&g^{\alpha\rho}(p+k)^\sigma T_1 - g^{\alpha\rho}q^\sigma\frac{m_B^2-m_{K^*}^2}{q^2}(T_1-T_2) \\ &+ 2q^\alpha p^\rho k^\sigma\left[\frac{1}{m_B^2-m_{K^*}^2}T_3 - \frac{1}{q^2}(T_1-T_2)\right]\Bigg\},\end{aligned} \tag{VIII.60}$$

where ϵ_{K^*} is the polarization vector of K^*, m_{K^*} its mass, and m_B the mass of the B-meson. The form factor A_3 is redundant and can be expressed in terms of A_1 and A_2,

$$A_3 \equiv \frac{m_B+m_{K^*}}{2m_{K^*}}A_1 - \frac{m_B-m_{K^*}}{2m_{K^*}}A_2. \tag{VIII.61}$$

Furthermore, it is common practice in the literature to replace A_2 and T_3 by

$$A_{12} \equiv \frac{(m_B+m_{K^*})^2(m_B^2-m_{K^*}^2-q^2)A_1 - \lambda(m_B^2,m_{K^*}^2,q^2)A_2}{16m_B m_{K^*}^2(m_B+m_{K^*})}, \tag{VIII.62}$$

$$T_{23} \equiv \frac{(m_B^2-m_{K^*}^2)(m_B^2+3m_{K^*}^2-q^2)T_2 - \lambda(m_B^2,m_{K^*}^2,q^2)T_3}{8m_B m_{K^*}^2(m_B-m_{K^*})}. \tag{VIII.63}$$

Kaons: Numerical values

In the following, we list the numerical functions used in the Kaon form factors. The scalar-current form factors $f_0^{K^+}(s)$ and $f_0^{K^0}(s)$ are given by [493–495]

$$f_0^{K^+}(s) = f_+^{K^+}(0)\left(1+\lambda_0\frac{s}{m_\pi^2}\right), \quad f_0^{K^0}(s) = f_+^{K^0}(0)\left(1+\lambda_0\frac{s}{m_\pi^2}\right), \tag{VIII.64}$$

where,

$$\lambda_0 = 13.38\times10^{-3}, \qquad f_+^{K^+}(0) = 0.9778, \qquad f_+^{K^0}(0) = 0.9544. \tag{VIII.65}$$

The form factor for the vector current reads

$$f_+^K(s) = f_+^K(0)\left(1+\lambda'_+\frac{s}{m_\pi^2}+\lambda''_+\frac{s^2}{2m_\pi^4}\right), \tag{VIII.66}$$

where,

$$\lambda'_+ = 24.82\times10^{-3}, \qquad \lambda''_+ = 1.64\times10^{-3} \tag{VIII.67}$$

The form factor for the tensor current reads [496]

$$f_T^{K^+}(s) = \frac{f_T^{K^+}(0)}{1-\lambda_T s}, \quad f_T^{K^0}(s) = \frac{f_T^{K^0}(0)}{1-\lambda_T s}, \tag{VIII.68}$$

where

$$\frac{1}{\sqrt{2}} f_T^{K^+}(0) = f_T^{K^0}(0) = \frac{0.417}{\sqrt{2}}, \quad \lambda_T = 1.1\,\mathrm{GeV}^{-2}. \tag{VIII.69}$$

Note that the factor $\frac{1}{\sqrt{2}}$ after the second equality appears as a result of the difference in normalization used in [497] compared to [496].

B-mesons: Numerical values

To obtain numerical results for the form factors used in B-meson calculations, we adopted the following parametrization template inspired by Ref. [498],

$$F(s) = \frac{r_1}{(1-a_1 s/m_B^2)} + \frac{r_2}{(1-a_2 s/m_B^2)}. \tag{VIII.70}$$

The values of r_1, r_2, a_1 and a_2 were then extracted from [472,492,498], see also [499–501], by taking simple averages of the results obtained in these papers and making a numerical fit. The results of our fit for the ten form factors presented in Eqs. (VIII.54)-(VIII.63) are collected in Table VIII.2.

F(s)	r_1	a_1	r_2	a_2
$f_0^B(s)$	13.84	0.80	−13.52	0.80
$f_+^B(s)$	0.18	1.08	0.22	1.08
$f_T^B(s)$	1.19	0.98	−0.87	0.79
$A_0(s)$	0.20	1.15	0.19	1.15
$A_1(s)$	0.66	0.74	−0.39	0.74
$A_{12}(s)$	0.59	0.58	−0.35	0.58
$V_0(s)$	0.07	1.15	0.33	1.15
$T_1(s)$	0.25	1.14	0.11	1.14
$T_2(s)$	0.70	0.73	−0.40	0.73
$T_{23}(s)$	0.22	−0.11	0.41	0.86

Table VIII.2: Fitted form factors for B-meson decays.

VIII.6 Summary and detailed outline

In this chapter, we have established FCNC transitions as a promising avenue for probing potential NP, including LNV. We reviewed SM predictions and experimental limits for selected rare semileptonic decays, and the numerical values of relevant form factors. We also presented the operator bases that will be used in calculations, with special emphasis on LNV operators, and discussed how observing LNV in rare meson decays can be used to constrain high-scale leptogenesis. As a final preparation for the next chapter, we provide a brief overview of its outline and comment on some related work.

Kinematic distributions will play an important role in much of our analysis. Schematically, the shape of kinematic distributions $d\Gamma(\text{Meson}_1 \to \text{Meson}_2 + \text{invisible})/ds$, where s is the invariant mass squared of the invisible state, can vary significantly when different effective operators are induced. This suggests that kinematic distributions can be a useful tool for distinguishing between NP scenarios with different underlying operators. Prior to our work, a systematic study of how to quantitatively extract NP contributions from kinematic distributions in rare meson decays was lacking. Specifically, previous analyses were limited to scenarios with only one or two non-zero WCs [480, 484, 487, 502, 503]. These papers represented the state-of-the-art on searching for and disentangling (LNV) NP in rare semi-leptonic meson decays using kinematic distributions, before our work. Our paper, Ref. [1], addressed a gap in the literature by developing a systematic (algebraic) approach to quantifying NP contributions in rare meson decays, allowing for the possibility of multiple higher-dimensional operators contributing to the experimental data. Moreover, the analysis presented in the next chapter does not rely on any assumptions about flavor structure in the UV unless stated explicitly in the text.

In Section IX.1, we explore strategies to probe effective operators contributing to rare Kaon decays. We begin by considering the (SM)LEFT framework only, with a special emphasis on scalar currents, which have received significantly less attention than vector currents in the literature. In this context, we examine the correlation between the branching ratios of $K_L \to \pi^0 \nu\bar{\nu}$ and $K^+ \to \pi^+ \nu\bar{\nu}$ in scenarios where scalar-current operators dominate the NP contribution, and compare this to the correlation found in NP scenarios where vector currents dominate. We then investigate the kinematic distributions of $K^+ \to \pi^+ \nu\bar{\nu}$ and $K_L \to \pi^0 \nu\bar{\nu}$, and demonstrate how dedicated measurements of these distributions can be used to disentangle contributions from the different operators listed in Eqs. (VIII.15)-(VIII.19). In the last part of the section, we go beyond (SM)LEFT by exploring prospects of disentangling (SM)LEFT operators from light NP originating from a dark sector. This discussion provides a foundation for Section IX.2, where we present a more comprehensive analysis of disentangling NP with neutrinos in the final state from dark-sector interactions.

In Section IX.2, we explore strategies to probe effective operators contributing to rare semi-leptonic B-meson decays. Here, the decay channel $B \to K^* + \not{E}$ provides even better opportunities for disentangling NP compared to Kaon decays [466]. This section provides a comprehensive discussion on distinguishing between contributions from (SM)LEFT and (D)LEFT when multiple operators can have non-zero WCs. We also discuss strategies that are less involved from an experimental point of view, such as correlations between different observables. In addition, we revisit and extend previous sum-rule results from Ref. [504], providing new interpretations that arise when (D)LEFT is considered and not only (SM)LEFT. Altogether, this section aims at providing strategies of various sophistication that can be used to examine which effective operators beyond the SM contribute to rare $b \to s\nu\bar{\nu}$ transitions.

In Section IX.4, we discuss implications that an observation of LNV in rare meson decays could have for our understanding of leptogenesis. We also provide a perspective on what observation of LNV in rare meson decays in combination with non-observation of $0\nu\beta\beta$ could imply for the flavor structure in the UV.

CHAPTER IX

Disentangling new physics contributions to $K \to \pi\nu\bar{\nu}$, $B \to K(K^*)\nu\bar{\nu}$, and $B \to X_s\nu\bar{\nu}$

In the previous chapter, we motivated semileptonic meson decays as interesting systems to search for NP, and in particular, LNV NP. We established that LNV searches are interesting from the perspective of leptogenesis and neutrino physics, and presented some technical details about operator bases and form factors. A detailed outline of the rest of this chapter was provided in Section VIII.6, along with a concise discussion of how our work addressed a gap in the literature, and we are now ready to present the detailed results of our work. The following discussion is based on our publication [1], where these results were first presented.

IX.1 Kaon analysis

IX.1.1 Branching ratios for $K^+ \to \pi^+\nu\bar{\nu}$ and $K_L \to \pi^0\nu\bar{\nu}$

As a first step, we present the contributions of the operators in Eqs. (VIII.15))-(VIII.19) to the branching ratios $K_L \to \pi^0\nu\widehat{\nu}$ and $K^+ \to \pi^+\nu\widehat{\nu}$. The results read [502]

$$\begin{aligned}\mathcal{B}(K_L \to \pi^0\nu\widehat{\nu}) = J_S^{K_L} &\sum_{\alpha\leq\beta}\left(1-\frac{1}{2}\delta_{\alpha\beta}\right)\left|C^{\rm SLL}_{\nu d,\alpha\beta sd}+C^{\rm SLR}_{\nu d,\alpha\beta sd}+C^{\rm SLL}_{\nu d,\alpha\beta ds}+C^{\rm SLR}_{\nu d,\alpha\beta ds}\right|^2\\ &+J_T^{K_L}\sum_{\alpha<\beta}\left(\left|C^{\rm TLL}_{\nu d,\alpha\beta ds}+C^{\rm TLL}_{\nu d,\alpha\beta sd}\right|^2\right)\\ &+J_V^{K_L}\sum_{\alpha,\beta}\left(1-\frac{1}{2}\delta_{\alpha\beta}\right)\left|C^{\rm VLL}_{\nu d,\alpha\beta sd}+C^{\rm VLR}_{\nu d,\alpha\beta sd}-C^{\rm VLL}_{\nu d,\alpha\beta ds}-C^{\rm VLR}_{\nu d,\alpha\beta ds}\right|^2,\end{aligned} \tag{IX.1}$$

and

$$\begin{aligned}\mathcal{B}(K^+ \to \pi^+\nu\widehat{\nu}) = J_S^{K^+}&\sum_{\alpha\leq\beta}\left(1-\frac{1}{2}\delta_{\alpha\beta}\right)\left(\left|C^{\rm SLL}_{\nu d,\alpha\beta sd}+C^{\rm SLR}_{\nu d,\alpha\beta sd}\right|^2+\left|C^{\rm SLL}_{\nu d,\alpha\beta ds}+C^{\rm SLR}_{\nu d,\alpha\beta ds}\right|^2\right)\\ +J_T^{K^+}\sum_{\alpha<\beta}\left(\left|C^{\rm TLL}_{\nu d,\alpha\beta sd}\right|^2+\left|C^{\rm TLL}_{\nu d,\alpha\beta ds}\right|^2\right)&+J_V^{K^+}\sum_{\alpha,\beta}\left(1-\frac{1}{2}\delta_{\alpha\beta}\right)\left|C^{\rm VLL}_{\nu d,\alpha\beta sd}+C^{\rm VLR}_{\nu d,\alpha\beta sd}\right|^2,\end{aligned} \tag{IX.2}$$

with

$$J_S^{K_L} = \frac{1}{\Gamma_{K_L}^{\rm Exp}} \frac{B_L^2}{2^9\pi^3 m_{K^0}^3} \int ds\, s\lambda^{1/2}(s, m_{K^0}^2, m_{\pi^0}^2) \left| f_0^{K^0}(s) \right|^2 = 34.6\, G_F^{-2}, \tag{IX.3}$$

$$\begin{aligned} J_T^{K_L} &= \frac{1}{\Gamma_{K_L}^{\rm Exp}} \frac{1}{3 \cdot 2^5 \pi^3 m_{K^0}^3 (m_{K^0} + m_{\pi^0})^2} \int ds\, s\, \lambda^{3/2}(s, m_{K^0}^2, m_{\pi^0}^2) \left| f_T^{K^0}(s) \right|^2 \\ &= 0.13\, G_F^{-2}, \end{aligned} \tag{IX.4}$$

$$J_V^{K_L} = \frac{1}{\Gamma_{K_L}^{\rm Exp}} \frac{1}{3 \cdot 2^{11} \pi^3 m_{K^0}^3} \int ds \lambda^{3/2}(s, m_{K^0}^2, m_{\pi^0}^2) \left| f_+^{K^0}(s) \right|^2 = 0.25\, G_F^{-2}, \tag{IX.5}$$

$$J_S^{K^+} = \frac{1}{\Gamma_{K^+}^{\rm Exp}} \frac{B_+^2}{2^8\pi^3 m_{K^+}^3} \int ds\, s\lambda^{1/2}(s, m_{K^+}^2, m_{\pi^+}^2) \left| f_0^{K^+}(s) \right|^2 = 15.2\, G_F^{-2}, \tag{IX.6}$$

$$\begin{aligned} J_T^{K^+} &= \frac{1}{\Gamma_{K^+}^{\rm Exp}} \frac{1}{3 \cdot 2^4 \pi^3 m_{K^+}^3 (m_{K^+} + m_{\pi^+})^2} \int ds\, s\, \lambda^{3/2}(s, m_{K^+}^2, m_{\pi^+}^2) \left| f_T^{K^+}(s) \right|^2 \\ &= 0.11\, G_F^{-2}, \end{aligned} \tag{IX.7}$$

$$J_V^{K^+} = \frac{1}{\Gamma_{K^+}^{\rm Exp}} \frac{1}{3 \cdot 2^9 \pi^3 m_{K^+}^3} \int ds \lambda^{3/2}(s, m_{K^+}^2, m_{\pi^+}^2) \left| f_+^{K^+}(s) \right|^2 = 0.23\, G_F^{-2}\,, \tag{IX.8}$$

where

$$B_L(\mu) = \frac{m_{K^0}^2 - m_{\pi^0}^2}{m_s(\mu) - m_d(\mu)}, \qquad B_+(\mu) = \frac{m_{K^+}^2 - m_{\pi^+}^2}{m_s(\mu) - m_d(\mu)}\,, \tag{IX.9}$$

and G_F denotes the Fermi constant. The notation $\nu\hat{\nu}$ indicates that $\nu\bar{\nu}$, $\bar{\nu}\bar{\nu}$, and $\nu\nu$ final states are taken into account. Here, $\Gamma_{K_L}^{\rm Exp}$ ($\Gamma_{K^+}^{\rm Exp}$) is the width of K_L (K^+), respectively, and $\lambda(a,b,c) = a^2+b^2+c^2-2(ab+bc+ac)$ is the Källén function. The invariant mass-squared of the dineutrino state is given by $s = (k+k')^2$, and is experimentally measured as missing energy in the decays. Finally, m_s and m_d denotes the mass of the s-quark and d-quark, respectively, and the numerical values reported in Eqs. (IX.3)-(IX.8) were obtained using

$$\begin{aligned} &m_{K^0} = 497.61 \text{ MeV}, \quad m_{K^+} = 493.67 \text{ MeV} \quad m_{\pi^+} = 139.57 \text{ MeV}, \\ &m_{\pi^0} = 134.977 \text{ MeV}, \quad m_s = 93.8 \text{ MeV}, \quad m_d = 4.68 \text{ MeV}, \\ &G_F = 1.16637 \cdot 10^{-5} \text{ GeV}^{-2}. \end{aligned} \tag{IX.10}$$

To the best of our knowledge, the expression for $J_T^{K_L}$ appeared in our work for the first time [1], while the results for the vector and scalar currents are consistent with those reported in Ref. [502]. Additionally, the result for $J_T^{K^+}$ is in agreement with the result for B-decays presented in [480]. The expressions in Eqs. (IX.3), (IX.5), (IX.6), and (IX.8) represent refined versions of the results in [502], with our calculations utilizing form factors that incorporate additional s-dependence and isospin-breaking effects [493]. Furthermore, the factors $B_L = 2.57$ GeV and $B_+ = 2.52$ GeV also differ from the factor B used in [502].

For completeness, we provide some details of the calculation leading to the result for $J_T^{K^+}$ and the new result for $J_T^{K_L}$. The other results were obtained using similar techniques, although the calculations were less involved due to the simpler Dirac structure of the scalar-current and vector-current operators.

Details on $J_T^{K^+}$

We need to evaluate the contributions from the tensor operator in Eq. (VIII.19) to $K^+ \to \pi^+\overline{\nu_\alpha\nu_\beta}$ and $K^+ \to \pi^+\nu_\alpha\nu_\beta$. For the first process, we have

$$\mathcal{M}(K^+ \to \pi^+\overline{\nu_\alpha\nu_\beta}) = \frac{C^T_{\alpha\beta sd}}{2} v_\alpha^T C\sigma_{\mu\nu}P_L v_\beta \left[\langle\pi^+|\,\overline{s}\sigma^{\mu\nu}d\,|K^+\rangle - \langle\pi^+|\,\overline{s}\sigma^{\mu\nu}\gamma^5 d\,|K^+\rangle\right]$$
$$+ \frac{C^T_{\beta\alpha sd}}{2} v_\beta^T C\sigma_{\mu\nu}P_L v_\alpha \left[\langle\pi^+|\,\overline{s}\sigma^{\mu\nu}d\,|K^+\rangle - \langle\pi^+|\,\overline{s}\sigma^{\mu\nu}\gamma^5 d\,|K^+\rangle\right], \tag{IX.11}$$

where the amplitude has been factorized into a hadronic and a leptonic part, as sketched in Eq. (VIII.3). By applying

$$\sigma^{\mu\nu}\gamma^5 = \frac{i}{2}\epsilon^{\alpha\beta\mu\nu}\sigma_{\alpha\beta}, \tag{IX.12}$$

the amplitude can be written as

$$\mathcal{M}(K^+ \to \pi^+\overline{\nu_\alpha\nu_\beta}) = \frac{C^T_{\alpha\beta sd}}{2} v_\alpha^T C\sigma_{\mu\nu}P_L v_\beta \left[\langle\pi^+|\,\overline{s}\sigma^{\mu\nu}d\,|K^+\rangle - \frac{i}{2}\epsilon^{\rho\sigma\mu\nu}\langle\pi^+|\,\overline{s}\sigma_{\rho\sigma}d\,|K^+\rangle\right]$$
$$+ \frac{C^T_{\beta\alpha sd}}{2} v_\beta^T C\sigma_{\mu\nu}P_L v_\alpha \left[\langle\pi^+|\,\overline{s}\sigma^{\mu\nu}d\,|K^+\rangle - \frac{i}{2}\epsilon^{\rho\sigma\mu\nu}\langle\pi^+|\,\overline{s}\sigma_{\rho\sigma}d\,|K^+\rangle\right]. \tag{IX.13}$$

Using the tensor form factor in Eq. (VIII.56) and $v^T = -\overline{u}C$, we first calculate the matrix-element squared with the aid of Feyncalc [505] and implement the result in the standard formula for the decay rate in three-body decays, c.f. Eq. (47.22) in Ref. [506]. The result reads,

$$\frac{\Gamma(K^+ \to \pi^+\overline{\nu_\alpha\nu_\beta})}{ds} = \frac{\left|f_T^{K^+}(s)\right|^2 s\,\lambda^{3/2}(s, m^2_{K^+}, m^2_{\pi^+})}{192\pi^2 m^3_{K^+}(m_{K^+}+m_{\pi^+})^2}\left(\left|C^T_{\alpha\beta sd}\right|^2 + \left|C^T_{\beta\alpha sd}\right|^2\right). \tag{IX.14}$$

Following the same procedure for $K^+ \to \pi^+\nu_\alpha\nu_\beta$ yields an identical result. Adding the two contributions, and using $\left|C^T_{\alpha\beta sd}\right| = \left|C^T_{\beta\alpha sd}\right|$, we obtain

$$\frac{d\Gamma(K^+ \to \pi^+\nu_\alpha\nu_\beta)}{ds} = \frac{\left|f_T^{K^+}(s)\right|^2 s\,\lambda^{3/2}(s, m^2_{K^+}, m^2_{\pi^+})}{96\pi^2 m^3_{K^+}(m_{K^+}+m_{\pi^+})^2}\left(\left|C^T_{\alpha\beta sd}\right|^2 + \left|C^T_{\alpha\beta ds}\right|^2\right), \tag{IX.15}$$

and finally

$$\frac{d\Gamma(K^+ \to \pi^+\nu\widehat{\nu})}{ds} = \frac{\left|f_T^{K^+}(s)\right|^2 s\,\lambda^{3/2}(s, m^2_{K^+}, m^2_{\pi^+})}{96\pi^2 m^3_{K^+}(m_{K^+}+m_{\pi^+})^2}\sum_{\alpha\neq\beta}\left(\left|C^T_{\alpha\beta sd}\right|^2 + \left|C^T_{\alpha\beta ds}\right|^2\right)$$
$$= \frac{\left|f_T^{K^+}(s)\right|^2 s\,\lambda^{3/2}(s, m^2_{K^+}, m^2_{\pi^+})}{48\pi^2 m^3_{K^+}(m_{K^+}+m_{\pi^+})^2}\sum_{\alpha<\beta}\left(\left|C^T_{\alpha\beta sd}\right|^2 + \left|C^T_{\alpha\beta ds}\right|^2\right). \tag{IX.16}$$

Details on $J_T^{K_L}$

To derive $J_T^{K_L}$ we need to consider the four processes $K^0/\overline{K^0} \to \pi^0\overline{\nu_\alpha\nu_\beta}/\nu_\alpha\nu_\beta$. The result for the processes with $\overline{\nu_\alpha\nu_\beta}$ in the final state is the same as for $\nu_\alpha\nu_\beta$, so we will only spell out the derivation of the former. The first amplitude reads,

$$\mathcal{M}(K^0 \to \pi^0\overline{\nu_\alpha\nu_\beta}) = \frac{C^T_{\alpha\beta sd}}{2} v_\alpha^T C\sigma_{\mu\nu}P_L v_\beta \left[\langle\pi^0|\,\overline{s}\sigma^{\mu\nu}d\,|K^0\rangle - \frac{i}{2}\epsilon^{\rho\sigma\mu\nu}\langle\pi^0|\,\overline{s}\sigma_{\rho\sigma}d\,|K^0\rangle\right]$$

$$+\frac{C^T_{\beta\alpha sd}}{2} v^T_\beta C\sigma_{\mu\nu}P_L v_\alpha \left[\left\langle \pi^0\right| \bar{s}\sigma^{\mu\nu}d\left|K^0\right\rangle - \frac{i}{2}\epsilon^{\rho\sigma\mu\nu}\left\langle \pi^0\right| \bar{s}\sigma_{\rho\sigma}d\left|K^0\right\rangle\right]. \tag{IX.17}$$

Using

$$\left\langle \pi^0\right| (CPT)^{-1}(CPT)\bar{d}\sigma^{\mu\nu}P_L s(CPT)^{-1}(CPT)\left|\overline{K^0}\right\rangle = \left\langle \pi^0\right| \bar{s}\sigma^{\mu\nu}P_L d\left|K^0\right\rangle, \tag{IX.18}$$

and Eq. (IX.12), we obtain the analogous result for $\overline{K^0}$,

$$\mathcal{M}(\overline{K^0} \to \pi^0\overline{\nu_\alpha\nu_\beta}) = \frac{C^T_{\alpha\beta ds}}{2} v^T_\alpha C\sigma_{\mu\nu}P_L v_\beta \left[\left\langle \pi^0\right| \bar{s}\sigma^{\mu\nu}d\left|K^0\right\rangle - \frac{i}{2}\epsilon^{\rho\sigma\mu\nu}\left\langle \pi^0\right| \bar{s}\sigma_{\rho\sigma}d\left|K^0\right\rangle\right]$$
$$+\frac{C^T_{\beta\alpha ds}}{2} v^T_\beta C\sigma_{\mu\nu}P_L v_\alpha \left[\left\langle \pi^0\right| \bar{s}\sigma^{\mu\nu}d\left|K^0\right\rangle - \frac{i}{2}\epsilon^{\rho\sigma\mu\nu}\left\langle \pi^0\right| \bar{s}\sigma_{\rho\sigma}d\left|K^0\right\rangle\right]. \tag{IX.19}$$

From Eq. (IX.17) and Eq. (IX.19), it follows that

$$\mathcal{M}(K_L \to \pi^0\overline{\nu_\alpha\nu_\beta}) = \frac{C^T_{\alpha\beta ds} + C^T_{\alpha\beta sd}}{2\sqrt{2}} v^T_\alpha C\sigma_{\mu\nu}P_L v_\beta \left[\left\langle \pi^0\right| \bar{s}\sigma^{\mu\nu}d\left|K^0\right\rangle - \frac{i}{2}\epsilon^{\rho\sigma\mu\nu}\left\langle \pi^0\right| \bar{s}\sigma_{\rho\sigma}d\left|K^0\right\rangle\right]$$
$$+\frac{C^T_{\beta\alpha ds} + C^T_{\beta\alpha sd}}{2\sqrt{2}} v^T_\beta C\sigma_{\mu\nu}P_L v_\alpha \left[\left\langle \pi^0\right| \bar{s}\sigma^{\mu\nu}d\left|K^0\right\rangle - \frac{i}{2}\epsilon^{\rho\sigma\mu\nu}\left\langle \pi^0\right| \bar{s}\sigma_{\rho\sigma}d\left|K^0\right\rangle\right]. \tag{IX.20}$$

By comparing this result with Eqs. (IX.13) and (IX.14), one can readily verify that

$$\frac{\Gamma(K_L \to \pi^0\overline{\nu_\alpha\nu_\beta})}{ds} = \frac{\left|f_T^{K^0}(s)\right|^2 s\,\lambda^{3/2}(s, m^2_{K^0}, m^2_{\pi^0})}{384\pi^2 m^3_{K^0}(m^2_{K^0} + m^2_{\pi^0})^2}\left(\left|C^T_{\alpha\beta ds} + C^T_{\alpha\beta sd}\right|^2 + \left|C^T_{\beta\alpha ds} + C^T_{\beta\alpha sd}\right|^2\right)$$
$$= \frac{\left|f_T^{K^0}(s)\right|^2 s\,\lambda^{3/2}(s, m^2_{K^0}, m^2_{\pi^0})}{192\pi^2 m^3_{K^0}(m_{K^0} + m^2_{\pi^0})^2}\left(\left|C^T_{\alpha\beta ds} + C^T_{\alpha\beta sd}\right|^2\right), \tag{IX.21}$$

where we again used $\left|C^T_{\alpha\beta q_1q_2}\right| = \left|C^T_{\beta\alpha q_1q_2}\right|$ in the final step. The result for $K_L \to \pi^0\overline{\nu_\alpha\nu_\beta}$ is identical. Adding the two results and summing over neutrino flavors, we obtain the final result

$$\frac{d\Gamma(K_L \to \pi^0\nu\hat{\nu})}{ds} = \frac{\left|f_T^{K^0}(s)\right|^2 s\,\lambda^{3/2}(s, m^2_{K^0}, m^2_{\pi^0})}{96\pi^2 m^3_{K^0}(m_{K^0} + m_{\pi^0})^2}\sum_{\alpha\neq\beta}\left(\left|C^T_{\alpha\beta ds} + C^T_{\alpha\beta sd}\right|^2\right)$$
$$= \frac{\left|f_T^{K^0}(s)\right|^2 s\,\lambda^{3/2}(s, m^2_{K^0}, m^2_{\pi^0})}{48\pi^2 m^3_{K^0}(m_{K^0} + m_{\pi^0})^2}\sum_{\alpha<\beta}\left(\left|C^T_{\alpha\beta ds} + C^T_{\alpha\beta sd}\right|^2\right). \tag{IX.22}$$

IX.1.2 Correlation of $K_L \to \pi^0\nu\bar{\nu}$ and $K^+ \to \pi^+\nu\bar{\nu}$

The primary objective of our analysis is to develop methods for disentangling NP contributions in rare meson decays. As an initial step towards this goal, we investigate the correlations between the branching ratios of $K_L \to \pi^0\nu\bar{\nu}$ and $K^+ \to \pi^+\nu\bar{\nu}$ decays. It is well established that the nature of these correlations depends on the specific NP model. While previous studies have primarily focused on the impact of vector currents on the correlation between $\mathcal{B}(K_L \to \pi^0\nu\bar{\nu})$ and $\mathcal{B}(K^+ \to \pi^+\nu\bar{\nu})$ [507–509], we extend this analysis by also examining the effects of scalar currents.[1]

[1] Preliminary steps in this direction were taken in Refs. [502, 503].

To illustrate the correlation between the branching ratios, we adopt a simplified approach by making two assumptions in this section: lepton-flavor universality (LFU) and identical flavors for the final-state neutrinos. The latter assumption implies the absence of tensor-current operators, which are antisymmetric in lepton-flavor indices. We propose a strategy for testing the validity of this assumption and searching for tensor currents at future experiments in Section IX.1.3.

The total branching ratios for $K_L \to \pi^0\nu\bar{\nu}$ and $K^+ \to \pi^+\nu\bar{\nu}$ decays can be expressed as the sum of vector and scalar contributions, as they do not interfere with each other,

$$\mathcal{B}(K_L \to \pi^0\nu\bar{\nu}) = \mathcal{B}^V(K_L \to \pi^0\nu\bar{\nu}) + \mathcal{B}^S(K_L \to \pi^0\nu\bar{\nu}), \tag{IX.23}$$
$$\mathcal{B}(K^+ \to \pi^+\nu\bar{\nu}) = \mathcal{B}^V(K^+ \to \pi^+\nu\bar{\nu}) + \mathcal{B}^S(K^+ \to \pi^+\nu\bar{\nu}), \tag{IX.24}$$

where $\mathcal{B}^{V(S)}$ represents the contribution from vector (scalar) current operators. The assumption of LFU allows us to parameterize the WCs associated with vector-current operators as

$$C^{\rm VLL}_{\nu d,\alpha\beta sd} + C^{\rm VLR}_{\nu d,\alpha\beta sd} = (|C_{\rm SM}|e^{i\phi_{\rm SM}} + |C_V|e^{i\phi_V})\delta_{\alpha\beta}, \tag{IX.25}$$
$$C^{\rm VLL}_{\nu d,\alpha\beta ds} + C^{\rm VLR}_{\nu d,\alpha\beta ds} = (|C_{\rm SM}|e^{-i\phi_{\rm SM}} + |C_V|e^{-i\phi_V})\delta_{\alpha\beta}, \tag{IX.26}$$

where the SM contribution $(C_{\rm SM}, \phi_{\rm SM})$ is manifestly separated from the NP contribution (C_V, ϕ_V). Similarly, we express the WCs associated with scalar-current operators as

$$C^{\rm SLL}_{\nu d,sd\alpha\beta} + C^{\rm SLR}_{\nu d,sd\alpha\beta} = |C_S|e^{i\phi_S}\delta_{\alpha\beta}, \tag{IX.27}$$
$$C^{\rm SLL}_{\nu d,ds\alpha\beta} + C^{\rm SLR}_{\nu d,ds\alpha\beta} = |C_S|e^{-i\phi_S}\delta_{\alpha\beta}. \tag{IX.28}$$

In this notation, the vector and scalar contributions to the branching ratios, including SM contributions, are given by

$$\mathcal{B}^V(K_L \to \pi^0\nu\bar{\nu}) = 12J_V^{K_L}T_1, \qquad \mathcal{B}^V(K^+ \to \pi^+\nu\bar{\nu}) = 3J_V^{K^+}(T_1 + T_2), \tag{IX.29}$$
$$\mathcal{B}^S(K_L \to \pi^0\nu\bar{\nu}) = 6J_S^{K_L}|C_S|^2\cos^2\phi_S, \quad \mathcal{B}^S(K^+ \to \pi^+\nu\bar{\nu}) = 3J_S^{K^+}|C_S|^2, \tag{IX.30}$$

where

$$T_1 = (|C_{\rm SM}|\sin\phi_{\rm SM} + |C_V|\sin\phi_V)^2, \tag{IX.31}$$
$$T_2 = (|C_{\rm SM}|\cos\phi_{\rm SM} + |C_V|\cos\phi_V)^2. \tag{IX.32}$$

Comparing these expressions with Eqs. (VIII.4)-(VIII.5), we obtain the following SM values,

$$\begin{aligned}\mathcal{B}_{\rm SM}(K_L \to \pi^0\nu\bar{\nu}) &= 12J_V^{K_L}|C_{\rm SM}|^2\sin^2\phi_{\rm SM}, \qquad \mathcal{B}_{\rm SM}(K^+ \to \pi^+\nu\bar{\nu}) = 3J_V^{K^+}|C_{\rm SM}|^2,\\ |C_{\rm SM}| &= 1.30\times 10^{-10}\ \text{GeV}^{-2}, \qquad \phi_{\rm SM} = 0.09\,\pi.\end{aligned} \tag{IX.33}$$

From the equations above, we can now establish two equations relating the branching ratios for K^+ and K_L decays. The first equation involves only vector contributions,

$$\mathcal{B}^V(K_L \to \pi^0\nu\bar{\nu}) = 4\frac{J_V^{K_L}}{J_V^{K^+}}\mathcal{B}^V(K^+ \to \pi^+\nu\bar{\nu}) - 12J_V^{K_L}T_2. \tag{IX.34}$$

The second equation relates both scalar and vector contributions,

$$\mathcal{B}(K_L \to \pi^0\nu\bar{\nu}) = 4\frac{J_V^{K_L}}{J_V^{K^+}}\left[\mathcal{B}^V(K^+ \to \pi^+\nu\bar{\nu}) + \mathcal{B}^S(K^+ \to \pi^+\nu\bar{\nu})\cos^2\phi_S\right]$$

$$- 12 J_V^{K_L} T_2, \tag{IX.35}$$

derived using the approximation

$$\frac{J_S^{K_L}}{J_S^{K^+}} \approx 2 \frac{J_V^{K_L}}{J_V^{K^+}}, \tag{IX.36}$$

which is justified by the numerical values

$$2\frac{J_S^{K_L}}{J_S^{K^+}} = 4.55 \qquad \text{and} \qquad 4\frac{J_V^{K_L}}{J_V^{K^+}} = 4.35. \tag{IX.37}$$

The latter ratio is known as the Grossmann-Nir (GN) bound [510].

In Fig. IX.1, we show the relations in Eq. (IX.34) and (IX.35) in the $\mathcal{B}(K^+ \to \pi^+\nu\bar{\nu})$-$\mathcal{B}(K_L \to \pi^0\nu\bar{\nu})$ plane. The upper panel illustrates the effect of a pure NP vector contribution, achieved by setting $C_S = 0$ and varying C_V. Conversely, the lower panel displays the results for a pure NP scalar contribution, obtained by setting $C_V = 0$ and varying C_S. In both panels, the SM contribution given in Eq. (IX.33) is denoted by a black point, the central experimental value of $\mathcal{B}(K^+ \to \pi^+\nu\bar{\nu})$ is represented by a thin vertical black line, and the GN bound is indicated by a red line. In the following, we summarize key observations derived from these relations and the corresponding plots.

New vector currents

Eq. (IX.34) describes a class of scenarios that have been explored previously in the literature [507–509]. Notably, when $\phi_V = 0$, the NP contribution to the $K_L \to \pi^0\nu\bar{\nu}$ branching ratio vanishes, and the right-hand side of Eq. (IX.34) reduces to the SM contribution. This scenario is represented by the horizontal green line in the upper panel of Fig. IX.1. In contrast, when $\phi_V = \pi/2$, the correlation between the branching ratios is parallel to the GN bound, as illustrated by the brown line in the same figure. The first term in Eq. (IX.34) corresponds to the GN bound, and the correlation between the two branching ratios occurs along a line parallel to the GN bound due to a negative shift from the SM contribution.

For $0 < \phi_V < \pi/2$, the correlation between the branching ratios is represented by curves that lie between the two extreme cases discussed above, with slopes becoming increasingly steep as ϕ_V approaches $\pi/2$, as shown in the upper panel of Fig. IX.1. For $\phi_V > \pi/2$, the curves fall between the GN line and the branch parallel to it. The black line, representing models with Minimal Flavor Violation (MFV),[2] extends on both sides of the $\phi_V = \pi/2$ curve. Our results are consistent with the findings reported in Refs. [507–509].

NP beyond vector currents

The novel feature, presented in Ref. [1] for the first time, is the impact of pure scalar contributions on the correlation relation in Eq. (IX.35), as illustrated in the lower panel of Fig. IX.1. In contrast to the NP vector contribution, which vanishes for $\phi_V = 0$, the NP scalar contribution is maximal for $\phi_S = 0$, resulting in a straight line parallel to the GN bound. For non-zero ϕ_S, the correlation between the branching ratios follows straight lines with slopes that decrease as ϕ_S increases from 0 to $\frac{\pi}{2}$.

[2] MFV is the assumption that all flavor and CP violation in a BSM extension arise solely from the SM Yukawa couplings.

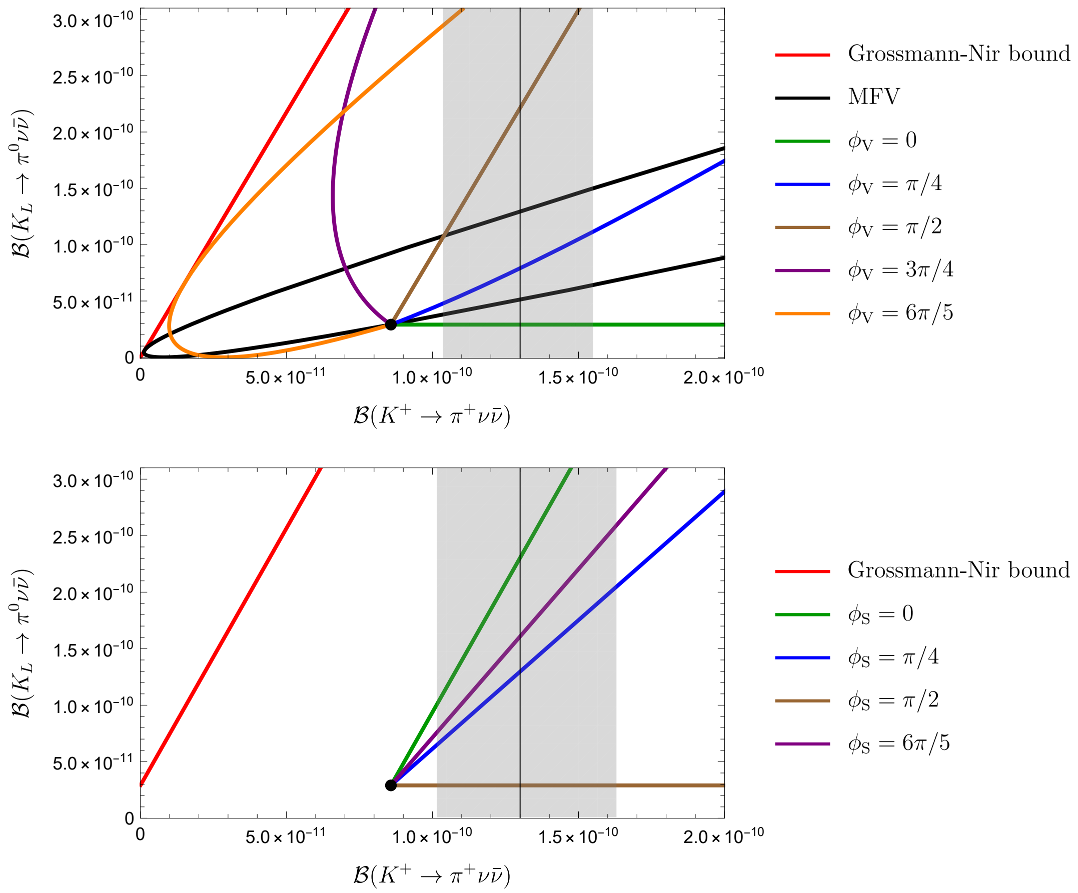

Figure IX.1: $\mathcal{B}(K^+ \to \pi^+ \nu\bar{\nu}) - \mathcal{B}(K_L \to \pi^0 \nu\bar{\nu})$-plane for vector-current contributions with $C_S = 0$ (top) and scalar-current contributions with $C_V = 0$ (bottom) assuming LFU. The different curves correspond to different values for ϕ_V (ϕ_S), as indicated in the legend, and C_V (C_S) is varied. The red line shows the GN bound. The SM contribution in Eq. (IX.33) is shown by a black point. The grey region represents the present experimental 1σ range [1].

A comparative analysis of the two plots in Fig. IX.1 reveals distinct characteristics of scalar and vector contributions. Specifically, scalar contributions can only enhance the branching ratios relative to their SM predictions, whereas a vector contribution can both increase and decrease the values relative to the SM predictions. When all four NP parameters ($|C_V|$, ϕ_V, $|C_S|$, and ϕ_S) are allowed to be non-zero simultaneously, the entire $\mathcal{B}(K^+ \to \pi^+ \nu\bar{\nu})$-$\mathcal{B}(K_L \to \pi^0 \nu\bar{\nu})$ plane below the GN bound (red solid line) becomes accessible. In contrast, a pure scalar NP contribution is restricted to the region between the green ($\phi_S = 0$) and brown ($\phi_S = \pi/2$) lines in the lower panel of Fig. IX.1. Consequently, if experimental measurements indicate a deviation from the SM to lower values in either $\mathcal{B}(K^+ \to \pi^+ \nu\bar{\nu})$ or $\mathcal{B}(K_L \to \pi^0 \nu\bar{\nu})$, a scalar current can only be present in conjunction with a vector contribution.

The above results highlight the distinct signatures that vector and scalar contributions can imprint on the $\mathcal{B}(K^+ \to \pi^+ \nu\bar{\nu})$-$\mathcal{B}(K_L \to \pi^0 \nu\bar{\nu})$ plane. However, relying solely on branching ratios is insufficient to identify the underlying nature of the NP contribution. Fortunately, previous studies [502, 503] have suggested that kinematic distributions for $K^+ \to \pi^+ \nu\bar{\nu}$ and $K_L \to \pi^0 \nu\bar{\nu}$ can provide valuable insights. As a first step in this

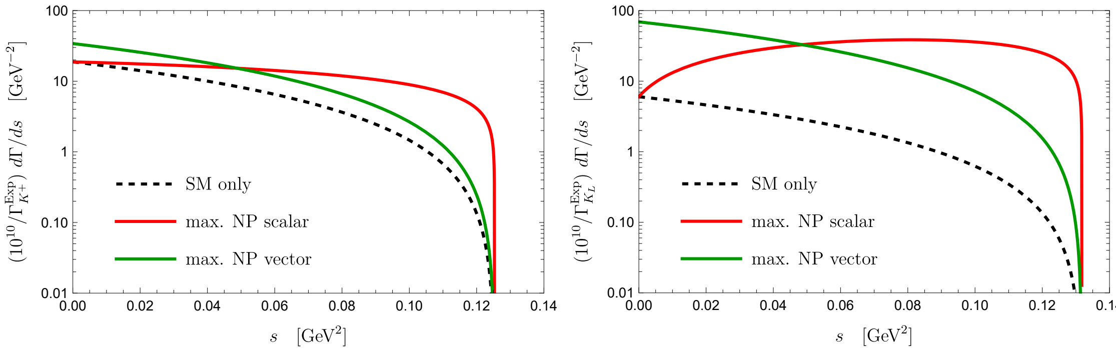

Figure IX.2: Differential distribution of $d\Gamma(K^+ \to \pi^+\nu\bar{\nu})/ds$ (left) and $d\Gamma(K_L \to \pi^0\nu\bar{\nu})/ds$ (right) normalized to the total experimental decay width $\Gamma^{\rm Exp}_{K^+}$ and $\Gamma^{\rm Exp}_{K_L}$, respectively. The black dashed curves show the SM contributions. For the red (green) curve, we have assumed a NP scalar (vector) contribution, leading to a signal close to the current experimental upper limit $\mathcal{B}(K^+ \to \pi^+\nu\bar{\nu}) = 1.63 \times 10^{-10}$. For the vector (scalar) contribution, a phase of $\phi_V = \pi/2$ ($\phi_S = 0$) was chosen. LFU is assumed [1].

direction, we show how it may be possible to probe complex phases with differential distributions.

Probing complex phases with differential distributions

Fig. IX.2 shows the normalized differential decay widths $d\Gamma(K^+ \to \pi^+\nu\bar{\nu})/ds$ and $d\Gamma(K_L \to \pi^0\nu\bar{\nu})/ds$, scaled to the experimental total decay widths $\Gamma^{\rm Exp}_{K^+}$ and $\Gamma^{\rm Exp}_{K_L}$, respectively. The black dashed curve represents the SM expectation, while the red and green lines illustrate the effects of adding scalar and vector contributions, respectively, on top of the SM. The NP signal is adjusted to be close to the current experimental upper limit $\mathcal{B}(K^+ \to \pi^+\nu\bar{\nu}) = 1.63 \times 10^{-10}$.[3] A key observation is that the vector contribution closely follows the shape of the SM distribution, whereas the scalar contribution exhibits a distinct distribution, clearly distinguishable from the vector contribution.

It is noteworthy that the NP vector distribution for K_L decays exhibits a significant difference in magnitude compared to the SM distribution, particularly for the chosen phase $\phi_V = \pi/2$. In contrast, the difference between the NP vector distribution and the SM distribution is less pronounced in K^+ decays. Similarly, the scalar contribution has a more substantial impact on K_L decays than on K^+ decays for the chosen scalar phase $\phi_S = 0$.

While the scalar differential distribution, $d\Gamma(K^+ \to \pi^+\nu\bar{\nu})/ds$, is insensitive to ϕ_S, $d\Gamma(K_L \to \pi^0\nu\bar{\nu})/ds$ depends on it, as evident from Eq. (IX.30). Consequently, a combined analysis of the differential distributions for $d\Gamma(K^+ \to \pi^+\nu\bar{\nu})/ds$ and $d\Gamma(K_L \to \pi^0\nu\bar{\nu})/ds$ offers a powerful tool for investigating ϕ_S. In a scenario with evidence for new scalar contributions, a comparative analysis of $d\Gamma(K^+ \to \pi^+\nu\bar{\nu})/ds$ and $d\Gamma(K_L \to \pi^0\nu\bar{\nu})/ds$ can reveal whether it is accompanied by a non-zero scalar phase ϕ_S. Thus, a non-zero ϕ_S can be probed not only at the level of branching ratios, as illustrated in Fig. IX.1, but also through differential distributions.

As demonstrated above, a detailed analysis of kinematic distributions can, in principle,

[3] For the vector contribution, a phase of $\phi_V = \pi/2$ is chosen. Notably, $d\Gamma(K^+ \to \pi^+\nu\bar{\nu})/ds$ is independent of the scalar phase ϕ_S, whereas $\mathcal{B}(K_L \to \pi^0\nu\bar{\nu})$ depends on ϕ_S. For the scalar contribution (red), we fix $\phi_S = 0$, resulting in the maximum contribution to $\mathcal{B}(K_L \to \pi^0\nu\bar{\nu})$.

distinguish between vector and scalar current contributions without requiring a specific NP model. While Refs. [502, 503] have made initial steps in this direction, they were limited in scope. In particular, Ref. [503] focused exclusively on the possibility of a LNV scalar current and its potential to be distinguished from the SM current. In the following, we significantly extend previous ideas by proposing a systematic method to discriminate and quantify different NP contributions. Using purely analytical methods, we start by demonstrating that kinematic distributions can be used to separate vector, scalar, and tensor contributions in the following.

IX.1.3 Extracting different contributions with neutrino final states only

In Section IX.1.2, we employed simplifying assumptions to facilitate an illustrative study. Here, we relax all simplifying assumptions and provide a completely model-independent analysis. In particular, this opens up the possibility of having tensor-current contributions in addition to vector and scalar currents. To streamline the notation in the subsequent equations, we introduce the following representation for the differential partial decay widths,

$$\mathcal{D}_L^{\rm exp}(s) \equiv \frac{d\Gamma(K_L \to \pi^0 \nu\widehat{\nu})}{ds}, \qquad \mathcal{D}_+^{\rm exp}(s) \equiv \frac{d\Gamma(K^+ \to \pi^+ \nu\widehat{\nu})}{ds}. \tag{IX.38}$$

The absence of interference between vector, scalar, and tensor contributions in (IX.1) and (IX.2), allows us to parametrize the differential partial widths as

$$\mathcal{D}_L^{\rm exp}(s) = C_S^L f_S^L(s) + C_T^L f_T^L(s) + C_V^L f_V^L(s), \tag{IX.39}$$
$$\mathcal{D}_+^{\rm exp}(s) = C_S^+ f_S^+(s) + C_T^+ f_T^+(s) + C_V^+ f_V^+(s)\,. \tag{IX.40}$$

The right-hand sides of Eqs. (IX.39) and (IX.40) comprise terms that are products of effective WCs, C, and kinematic functions $f(s)$. The effective WCs are simply sums over WCs (squared), whereas the kinematic functions depend solely on particle masses and the invariant-mass squared of the dineutrino state s. The effective WCs in Eqs. (IX.39) and (IX.40) are given by,

$$C_S^L = \sum_{\alpha\leq\beta}\left(1-\frac{1}{2}\delta_{\alpha\beta}\right)\left|C^{\rm SLL}_{\nu d,sd\alpha\beta} + C^{\rm SLR}_{\nu d,sd\alpha\beta} + C^{\rm SLL}_{\nu d,ds\alpha\beta} + C^{\rm SLR}_{\nu d,ds\alpha\beta}\right|^2, \tag{IX.41}$$
$$C_T^L = \sum_{\alpha<\beta}\left|C^{\rm TLL}_{\nu d,\alpha\beta ds} + C^{\rm TLL}_{\nu d,\alpha\beta sd}\right|^2, \tag{IX.42}$$
$$C_V^L = \sum_{\alpha,\beta}\left(1-\frac{1}{2}\delta_{\alpha\beta}\right)\left|C^{\rm VLL}_{\nu d,sd\alpha\beta} + C^{\rm VLR}_{\nu d,sd\alpha\beta} - C^{\rm VLL}_{\nu d,ds\alpha\beta} - C^{\rm VLR}_{\nu d,ds\alpha\beta}\right|^2, \tag{IX.43}$$
$$C_S^+ = \sum_{\alpha\leq\beta}\left(1-\frac{1}{2}\delta_{\alpha\beta}\right)\left(\left|C^{\rm SLL}_{\nu d,sd\alpha\beta} + C^{\rm SLR}_{\nu d,sd\alpha\beta}\right|^2 + \left|C^{\rm SLL}_{\nu d,ds\alpha\beta} + C^{\rm SLR}_{\nu d,ds\alpha\beta}\right|^2\right), \tag{IX.44}$$
$$C_T^+ = \sum_{\alpha<\beta}\left(\left|C^{\rm TLL}_{\nu d,\alpha\beta sd}\right|^2 + \left|C^{\rm TLL}_{\nu d,\alpha\beta ds}\right|^2\right) \tag{IX.45}$$
$$C_V^+ = \sum_{\alpha,\beta}\left(1-\frac{1}{2}\delta_{\alpha\beta}\right)\left|C^{\rm VLL}_{\nu d,sd\alpha\beta} + C^{\rm VLR}_{\nu d,sd\alpha\beta}\right|^2. \tag{IX.46}$$

Explicit expressions for the kinematic functions can be read out from Eqs. (IX.1)-(IX.8), and are listed below,

$$f_S^L(s) = \frac{B_L^2}{2^9\pi^3 m_{K^0}^3}\cdot s\,\lambda^{1/2}(s, m_{K^0}^2, m_{\pi^0}^2)\left|f_0^{K^0}(s)\right|^2, \tag{IX.47}$$

$$f_S^+(s) = \frac{B_+^2}{2^8\pi^3 m_{K^+}^3} \cdot s\,\lambda^{1/2}(s, m_{K^+}^2, m_{\pi^+}^2)\,\left|f_0^{K^+}(s)\right|^2, \tag{IX.48}$$

$$f_V^L(s) = \frac{1}{3\cdot 2^{11}\pi^3 m_{K^0}^3} \cdot \lambda^{3/2}(s, m_{K^0}^2, m_{\pi^0}^2)\,\left|f_+^{K^0}(s)\right|^2, \tag{IX.49}$$

$$f_V^+(s) = \frac{1}{3\cdot 2^{9}\pi^3 m_{K^+}^3} \cdot \lambda^{3/2}(s, m_{K^+}^2, m_{\pi^+}^2)\,\left|f_+^{K^+}(s)\right|^2, \tag{IX.50}$$

$$f_T^L(s) = \frac{1}{3\cdot 2^{5}\pi^3 m_{K^0}^3(m_{K^0}+m_{\pi^0})^2} \cdot s\,\lambda^{3/2}(s, m_{K^0}^2, m_{\pi^0}^2)\,\left|f_T^{K^0}(s)\right|^2, \tag{IX.51}$$

$$f_T^+(s) = \frac{1}{3\cdot 2^{4}\pi^3 m_{K^+}^3(m_{K^+}+m_{\pi^+})^2} \cdot s\,\lambda^{3/2}(s, m_{K^+}^2, m_{\pi^+}^2)\,\left|f_T^{K^+}(s)\right|^2. \tag{IX.52}$$

The preceding expressions indicate that the number of independent, real parameters is limited to three for both $K_L \to \pi^0\nu\bar{\nu}$ and $K^+ \to \pi^+\nu\bar{\nu}$ decays, namely C_S^L, C_T^L, C_V^L and C_S^+, C_T^+, C_V^+, respectively. Note that these parameters are kinematic-independent. Consequently, measuring the s-distribution at three distinct values, s_1, s_2, and s_3, yields a system of three linear equations with three unknowns. For $K_L \to \pi^0\nu\bar{\nu}$ and $K^+ \to \pi^+\nu\bar{\nu}$ decays, the unknowns are C_S^L, C_V^L, C_T^L and C_S^+, C_V^+, C_T^+, respectively. By solving this system, we can determine the magnitude of the scalar, vector, and tensor contributions,

$$C_S^+ = \frac{D_+^{\exp}(s_1)\left[f_V^+(s_2)f_T^+(s_3) - f_V^+(s_3)f_T^+(s_2)\right] + \text{cyclic}}{f_S^+(s_1)\left[f_V^+(s_2)f_T^+(s_3) - f_V^+(s_3)f_T^+(s_2)\right] + \text{cyclic}}, \tag{IX.53}$$

$$C_V^+ = \frac{D_+^{\exp}(s_1)\left[f_S^+(s_2)f_T^+(s_3) - f_S^+(s_3)f_T^+(s_2)\right] + \text{cyclic}}{f_V^+(s_1)\left[f_S^+(s_2)f_T^+(s_3) - f_S^+(s_3)f_T^+(s_2)\right] + \text{cyclic}}, \tag{IX.54}$$

$$C_T^+ = \frac{D_+^{\exp}(s_1)\left[f_S^+(s_2)f_V^+(s_3) - f_S^+(s_3)f_V^+(s_2)\right] + \text{cyclic}}{f_T^+(s_1)\left[f_S^+(s_2)f_V^+(s_3) - f_S^+(s_3)f_V^+(s_2)\right] + \text{cyclic}}, \tag{IX.55}$$

where *cyclic* refers to the remaining two terms obtained by one and two applications of $s_1 \to s_2$, $s_2 \to s_3$, $s_3 \to s_1$, respectively. Similarly, we obtain

$$C_S^L = \frac{D_L^{\exp}(s_1)\left[f_V^L(s_2)f_T^L(s_3) - f_V^L(s_3)f_T^L(s_2)\right] + \text{cyclic}}{f_S^L(s_1)\left[f_V^L(s_2)f_T^L(s_3) - f_V^L(s_3)f_T^L(s_2)\right] + \text{cyclic}}, \tag{IX.56}$$

$$C_V^L = \frac{D_L^{\exp}(s_1)\left[f_S^L(s_2)f_T^L(s_3) - f_S^L(s_3)f_T^L(s_2)\right] + \text{cyclic}}{f_V^L(s_1)\left[f_S^L(s_2)f_T^L(s_3) - f_S^L(s_3)f_T^L(s_2)\right] + \text{cyclic}}, \tag{IX.57}$$

$$C_T^L = \frac{D_L^{\exp}(s_1)\left[f_S^L(s_2)f_V^L(s_3) - f_S^L(s_3)f_V^L(s_2)\right] + \text{cyclic}}{f_T^L(s_1)\left[f_S^L(s_2)f_V^L(s_3) - f_S^L(s_3)f_V^L(s_2)\right] + \text{cyclic}}. \tag{IX.58}$$

In the absence of tensor contributions, the relations simplify to

$$C_S^+ = \frac{D_+^{\exp}(s_1)f_V^+(s_2) - D_+^{\exp}(s_2)f_V^+(s_1)}{f_S^+(s_1)f_V^+(s_2) - f_S^+(s_2)f_V^+(s_1)}\,, \tag{IX.59}$$

$$C_V^+ = \frac{D_+^{\exp}(s_1)f_S^+(s_2) - D_+^{\exp}(s_2)f_S^+(s_1)}{f_V^+(s_1)f_S^+(s_2) - f_V^+(s_2)f_S^+(s_1)}\,. \tag{IX.60}$$

and

$$C_S^L = \frac{D_L^{\exp}(s_1)f_V^L(s_2) - D_L^{\exp}(s_2)f_V^L(s_1)}{f_S^L(s_1)f_V^L(s_2) - f_S^L(s_2)f_V^L(s_1)}\,, \tag{IX.61}$$

$$C_V^L = \frac{D_L^{\exp}(s_1)f_S^L(s_2) - D_L^{\exp}(s_2)f_S^L(s_1)}{f_V^L(s_1)f_S^L(s_2) - f_V^L(s_2)f_S^L(s_1)}\,. \tag{IX.62}$$

Let us now interpret these results. A non-zero value for C_S^L or C_S^+ indicates the presence of scalar currents, while a non-zero C_T^L or C_T^+ signals tensor currents. As discussed in the previous chapter, this could be a strong indication of LNV. In this case, complementary probes of LNV interactions, such as neutrinoless double beta decay or collider experiments, are essential to confirm the underlying NP. Furthermore, if any tensor operators have non-zero WCs, C_T^+ must be non-zero, as there is no possibility for destructive interference between different WCs in Eq. (IX.45).

A deviation of C_V^L and/or C_V^+ from their SM values would signify the presence of new vector currents. However, the proposed strategy cannot distinguish between new left-handed and right-handed currents. In contrast, we will show in Section IX.2 that this distinction is possible in the context of B decays.

The key point is that, under the assumption that vector, scalar, and tensor (SM)LEFT currents are the only contributions present, they can be disentangled from experimental data. To achieve good statistics, multiple values of s may be required, and suitable values of s must be chosen to optimize sensitivity to NP dynamics. A crucial cross-check will be the s-independence of the determined values of the effective WCs.

IX.1.4 Disentangling LEFT from dark-sector physics

So far, we have assumed that all invisible final states are neutrinos. However, as discussed in Section VIII.3, there could *a priori* also be light dark physics hiding in the final states. This raises the question of how to distinguish light dark physics from neutrinos. In the following, we investigate the possibility of disentangling (SM)LEFT from (D)LEFT in rare meson decays using kinematic distributions.

The contributions to $K_L \to \pi^0\nu\bar{\nu}$ and $K^+ \to \pi^+\nu\bar{\nu}$ from (D)LEFT operators were first reported in Ref. [484]. We have verified and further refined the existing results by incorporating additional s-dependence and isospin-breaking effects. A detailed account of these results is presented in Appendix A, where we provide a list of the relevant differential decay widths. Here, we will utilize these results to investigate the differences between (SM)LEFT NP and (D)LEFT NP. It is worth noting that all of our results are obtained in the limit of negligible DM mass, which leads to non-zero contributions to kinematic distributions at small s values, similar to the case of active neutrinos.

Our idea for distinguishing between (SM)LEFT and (D)LEFT in rare meson decays hinges on the ability to disentangle distinct kinematic structures arising from different operators contributing to the relevant differential decay widths. For instance, Eqs. (IX.3) and (IX.6) reveal that the kinematic functions induced by scalar-current operators in $d\Gamma(K_L \to \pi^0\nu\bar{\nu})/ds$ and $d\Gamma(K^+ \to \pi^+\nu\bar{\nu})/ds$ are proportional to

$$s\,\lambda^{1/2}(s, m_{K_L}^2, m_{\pi^0}^2)\,\left|f_0^{K^0}(s)\right|^2, \qquad s\,\lambda^{1/2}(s, m_{K^+}^2, m_{\pi^+}^2)\,\left|f_0^{K^+}(s)\right|^2, \tag{IX.63}$$

respectively. At this point, it is useful to introduce a new notion, *kinematic structures*. We will use this notion to refer to kinematic functions with an overall s-independent prefactor removed, as illustrated in Eq. (IX.63). This allows us to write down compact expressions that encode all the s-dependent information of kinematic functions. Table IX.1 provides a comprehensive list of the kinematic structures present in $d\Gamma(K_L \to \pi^0\nu\bar{\nu})/ds$ and $d\Gamma(K^+ \to \pi^+\nu\bar{\nu})/ds$ for all (SM)LEFT and (D)LEFT operators. The results were obtained from the expressions for the differential decay widths provided in Appendix A.

By examining Table IX.1, it is clear that unlike massless dark scalars and vectors, only very light or massless dark fermions can produce the same kinematic structure as the

Type	Operator	Kinematic structure in $K \to \pi + \not{E}$
(SM)LEFT	$\mathcal{O}_{\nu d}^{\rm SLL}$, $\mathcal{O}_{\nu d}^{\rm SLR}$	$s\,\lambda^{1/2}\,\lvert f_0^K\rvert^2$
	$\mathcal{O}_{\nu d}^{\rm VLL}$, $\mathcal{O}_{\nu d}^{\rm VLR}$	$\lambda^{3/2}\,\lvert f_+^K\rvert^2$
	$\mathcal{O}_{\nu d}^{\rm TLL}$	$s\,\lambda^{3/2}\,\lvert f_T^K\rvert^2$
Scalar DM	$\mathcal{O}_{sd\phi}^{S}$	$\lambda^{1/2}\,\lvert f_0^K\rvert^2$
	$\mathcal{O}_{sd\phi}^{V}$	$\lambda^{3/2}\,\lvert f_+^K\rvert^2$
Fermion DM	$\mathcal{O}_{sd\chi1}^{S}, \mathcal{O}_{sd\chi2}^{S}$	$s\,\lambda^{1/2}\,\lvert f_0^K\rvert^2$
	$\mathcal{O}_{sd\chi1}^{V}, \mathcal{O}_{sd\chi2}^{V}$	$\lambda^{3/2}\,\lvert f_+^K\rvert^2$
	$\mathcal{O}_{sd\chi1}^{T}, \mathcal{O}_{sd\chi2}^{T}$	$s\,\lambda^{3/2}\,\lvert f_T^K\rvert^2$
Vector DM: A	$\mathcal{O}_{sdA}^{S}$	$s^2\,\lambda^{1/2}\,\lvert f_0^K\rvert^2$
	$\mathcal{O}_{sdA2}^{V}$	$s^2\,\lambda^{1/2}\,\lvert f_0^K\rvert^2$
	$\mathcal{O}_{sdA3}^{V}, \mathcal{O}_{sdA6}^{V}$	$s\,\lambda^{3/2}\,\lvert f_+^K\rvert^2$
	$\mathcal{O}_{sdA4}^{V}, \mathcal{O}_{sdA5}^{V}$	$s^2\,\lambda^{3/2}\,\lvert f_+^K\rvert^2$
	$\mathcal{O}_{sdA1}^{T}$	$s^2\,\lambda^{3/2}\,\lvert f_T^K\rvert^2$
Vector DM: B	$\mathcal{O}_{sdB1}^{S}, \mathcal{O}_{sdB2}^{S}$	$s^2\,\lambda^{1/2}\,\lvert f_0^K\rvert^2$
	$\mathcal{O}_{sdB1}^{T}, \mathcal{O}_{sdB2}^{T}$	$s^2\,\lambda^{3/2}\,\lvert f_T^K\rvert^2$

Table IX.1: List of operators contributing to $K^{+(L)} \to \pi^{+(0)} + \not{E}$ along with the kinematic structure they induce in $d\Gamma(K^{+(L)} \to \pi^{+(0)} + \not{E})/ds$. Here, λ is shorthand notation for $\lambda(m_K^2, m_\pi^2, s)$, and f_0^K is short for $f_0^K(s)$, etc. Only operators contributing to $K^{+(L)} \to \pi^{+(0)} + \not{E}$ have been listed (see text for details) [1].

operators $\mathcal{O}_{\nu d}^{\rm SLL}$ and $\mathcal{O}_{\nu d}^{\rm SLR}$, which are highlighted in blue. Thus, under the assumption that only one operator is non-zero at a time, it is possible to distinguish these operators from any (D)LEFT operator involving a dark scalar or a dark vector. For $\mathcal{O}_{\nu d}^{\rm TLL}$, we find that only a dark fermion can replicate its kinematic structure, as highlighted in green. Furthermore, we observe that both dark-fermion operators with vector currents and dark-scalar operators with vector currents generate a kinematic structure identical to that of $\mathcal{O}_{\nu d}^{\rm VLL}$ and $\mathcal{O}_{\nu d}^{\rm VLR}$, as highlighted in red.[4]

[4]Only for type A dark vectors do the differential decay widths $d\Gamma(K^{+(L)} \to \pi^{+(0)} + \not{E})/ds$ receive contributions from interference terms between different WCs. The full expressions for these decay widths

Having investigated the kinematic structures arising from individual operators, it is natural to consider how our findings are modified when multiple operators are present simultaneously. We will address this question in the context of B-mesons in the next section.

IX.2 B-meson analysis: Kinematic distributions

In this section, we will apply and further develop our strategy of disentangling NP with kinematic distributions in the context of B-meson decays. We will start by considering (SM)LEFT in Section IX.2.1, where the story extends beyond that of Kaons due to angular distributions in $B \to K^*\nu\bar{\nu}$. In Section IX.2.2, we consider the general case where both (D)LEFT and (SM)LEFT operators may contribute to NP. Some benchmark examples are provided in Section IX.2.3.

IX.2.1 Disentangling NP with neutrino final states only

In the following, we consider NP induced by the (SM)LEFT operators in Eqs. (VIII.15)-(VIII.19).

Disentangling different contributions in $B \to K^*\widehat{\nu}\nu$

The first channel we consider is B decaying to an intermediate K^*, which subsequently decays into $K\pi$. By performing an angular analysis of the K^* decay products, it is possible to extract the differential decay widths for longitudinally and transversely polarized K^*, denoted as $d\Gamma_L/ds$ and $d\Gamma_T/ds$, respectively. Since it is possible to distinguish between longitudinally and transversely polarized K^*, it is meaningful to introduce the following two observables,

$$P_L^{\text{exp}}(s) \equiv \frac{d\Gamma_L}{ds}, \qquad P_T^{\text{exp}}(s) \equiv \frac{d\Gamma_T}{ds}, \tag{IX.64}$$

which measure the differential decay width for a given K^* polarization. We can parameterize these quantities as follows,

$$\begin{aligned} P_T^{\text{exp}}(s) &= f_{V+}^T(s) \times \sum_{\alpha,\beta} \left(1 - \frac{1}{2}\delta_{\alpha\beta}\right) |C^{\text{VLL}}_{\nu d,\alpha\beta sb} + C^{\text{VLR}}_{\nu d,\alpha\beta sb}|^2 \\ &+ f_{V-}^T(s) \times \sum_{\alpha,\beta} \left(1 - \frac{1}{2}\delta_{\alpha\beta}\right) |C^{\text{VLL}}_{\nu d,\alpha\beta sb} - C^{\text{VLR}}_{\nu d,\alpha\beta sb}|^2 \\ &+ f_T^T(s) \times \sum_{\alpha<\beta} \left(|C^{\text{TLL}}_{\nu d,\alpha\beta bs}|^2 + |C^{\text{TLL}}_{\nu d,\alpha\beta sb}|^2\right), \\ &\equiv f_{V+}^T(s) C_{V+}^T + f_{V-}^T(s) C_{V-}^T + f_T^T(s) C_T^T, \end{aligned} \tag{IX.65}$$

and

$$\begin{aligned} P_L^{\text{exp}}(s) = f_{V-}^L(s) &\times \sum_{\alpha,\beta} \left(1 - \frac{1}{2}\delta_{\alpha\beta}\right) |C^{\text{VLL}}_{\nu d,\alpha\beta sb} - C^{\text{VLR}}_{\nu d,\alpha\beta sb}|^2 \\ + f_T^L(s) &\times \sum_{\alpha<\beta} \left(|C^{\text{TLL}}_{\nu d,\alpha\beta bs}|^2 + |C^{\text{TLL}}_{\nu d,\alpha\beta sb}|^2\right) \end{aligned}$$

are provided in Section A, and it is noted that none of the interference terms have a kinematic structure similar to that of any (SM)LEFT operator.

$$
\begin{aligned}
&+ f_S^L(s) \times \sum_{\alpha \le \beta} \left(1 - \frac{1}{2}\delta_{\alpha\beta}\right) \left[|C^{\rm SLR}_{\nu d,\alpha\beta sb} - C^{\rm SLL}_{\nu d,\alpha\beta sb}|^2 + |C^{\rm SLR}_{\nu d,\alpha\beta bs} - C^{\rm SLL}_{\nu d,\alpha\beta bs}|^2\right] \\
&\equiv f^L_{V-}(s) C^L_{V-} + f^L_T(s) C^L_T + f^L_S(s) C^L_S, \qquad \text{(IX.66)}
\end{aligned}
$$

where the notation was explained in Section IX.1.3. To calculate the kinematic functions, f, we first obtained the matrix elements using the form factors listed in Section VIII.5. After squaring the matrix elements, we found it useful to work in the rest frame of the B-meson and assign appropriate values for polarization vectors and momenta for the decay products and evaluate all resulting inner products explicitly in this way. After ecalculating the squared matrix elements, we computed the differential decay rate using [506]

$$
\frac{d\Gamma}{ds} = \frac{1}{(2\pi)^5} \frac{|\mathcal{M}|^2}{128 m_B^3} \lambda^{1/2}(s, m_B^2, m_{K^*}^2) d\Omega_1^* d\Omega_{K^*}, \qquad \text{(IX.67)}
$$

where Ω_1^* denotes the direction of the momentum of the first neutrino in the rest frame of the dineutrino system, and Ω_{K^*} is the angle of K^* in the rest frame of the decaying B meson. The results of our calculations are listed below [1, 480]

$$
\begin{aligned}
\frac{1}{\Gamma^{\rm exp}_{B^0}} \int ds\, f^T_{V+}(s) &= \frac{1}{\Gamma^{\rm exp}_{B^0}} \frac{1}{768\pi^3 m_B^3 (m_B + m_{K^*})^2} \int ds\, s\, \lambda^{3/2}(m_B^2, m_{K^*}^2, s)\, |V_0(s)|^2 \\
&= 0.6\, G_F^{-2}, \qquad \text{(IX.68)} \\
\frac{1}{\Gamma^{\rm exp}_{B^0}} \int ds\, f^T_{V-}(s) &= \frac{1}{\Gamma^{\rm exp}_{B^0}} \frac{(m_B + m_{K^*})^2}{768\pi^3 m_B^3} \int ds\, s\, \lambda^{1/2}(m_B^2, m_{K^*}^2, s)\, |A_1(s)|^2 \\
&= 1.2\, G_F^{-2}, \qquad \text{(IX.69)} \\
\frac{1}{\Gamma^{\rm exp}_{B^0}} \int ds\, f^T_T(s) &= \frac{1}{\Gamma^{\rm exp}_{B^0}} \frac{1}{24\pi^3 m_B^3} \int ds\, \lambda^{1/2}(m_B^2, m_{K^*}^2, s) \Big[\lambda(m_B^2, m_{K^*}^2, s)\, |T_1(s)|^2 \\
&\quad + (m_B^2 - m_{K^*}^2)^2\, |T_2(s)|^2\Big] = 178\, G_F^{-2}, \qquad \text{(IX.70)} \\
\frac{1}{\Gamma^{\rm exp}_{B^0}} \int ds\, f^L_{V-}(s) &= \frac{1}{\Gamma^{\rm exp}_{B^0}} \frac{m_B^2 m_{K^*}^2}{24\pi^3 m_B^3} \int ds\, \lambda^{1/2}(m_B^2, m_{K^*}^2, s)\, |A_{12}(s)|^2 = 1.7\, G_F^{-2}, \qquad \text{(IX.71)} \\
\frac{1}{\Gamma^{\rm exp}_{B^0}} \int ds\, f^L_T(s) &= \frac{1}{\Gamma^{\rm exp}_{B^0}} \frac{m_B^2 m_{K^*}^2}{3\pi^3 m_B^3 (m_B + m_{K^*})^2} \int ds\, s\, \lambda^{1/2}(m_B^2, m_{K^*}^2, s)\, |T_{23}(s)|^2 \\
&= 22.6\, G_F^{-2}, \qquad \text{(IX.72)} \\
\frac{1}{\Gamma^{\rm exp}_{B^0}} \int ds\, f^L_S(s) &= \frac{1}{\Gamma^{\rm exp}_{B^0}} \frac{1}{256\pi^3 m_B^3 (m_b + m_s)^2} \int ds\, s\, \lambda^{3/2}(m_B^2, m_{K^*}^2, s)\, |A_0(s)|^2 \\
&= \left(\frac{4.19\,\mathrm{GeV}}{m_b}\right)^2 3.5\, G_F^{-2}, \qquad \text{(IX.73)}
\end{aligned}
$$

where m_b is the mass of the b-quark and all form factors can be found in Section VIII.5. The numerical values used to obtain the quoted numerical results are [18],

$$
\begin{aligned}
&m_B = 5.279 \text{ GeV}, \quad m_{K^*} = 895.8 \text{ MeV} \quad m_K = 493.67 \text{ MeV}, \\
&m_s = 93.8 \text{ MeV}, \quad G_F = 1.16637 \cdot 10^{-5} \text{ GeV}^{-2}. \qquad \text{(IX.74)}
\end{aligned}
$$

The combination of WCs in Eq. (IX.65) is determined in a similar way as was done for the Kaons, c.f. the text between Eq. (IX.52) and (IX.53), and the result reads,

$$
C^T_{V+} = \frac{P_T^{\rm exp}(s_1)\left[f^T_{V-}(s_2) f^T_T(s_3) - f^T_{V-}(s_3) f^T_T(s_2)\right] + \text{cyclic}}{f^T_{V+}(s_1)\left[f^T_{V-}(s_2) f^T_T(s_3) - f^T_{V-}(s_3) f^T_T(s_2)\right] + \text{cyclic}}, \qquad \text{(IX.75)}
$$

$$C^T_{V-} = \frac{P^{\rm exp}_T(s_1)\left[f^T_{V+}(s_2)f^T_T(s_3) - f^T_{V+}(s_3)f^T_T(s_2)\right] + \text{cyclic}}{f^T_{V-}(s_1)\left[f^T_{V+}(s_2)f^T_T(s_3) - f^T_{V+}(s_3)f^T_T(s_2)\right] + \text{cyclic}}, \tag{IX.76}$$

$$C^T_{T} = \frac{P^{\rm exp}_T(s_1)\left[f^T_{V+}(s_2)f^T_{V-}(s_3) - f^T_{V+}(s_3)f^T_{V-}(s_2)\right] + \text{cyclic}}{f^T_{T}(s_1)\left[f^T_{V+}(s_2)f^T_{V-}(s_3) - f^T_{V+}(s_3)f^T_{V-}(s_2)\right] + \text{cyclic}}. \tag{IX.77}$$

Here, *cyclic* again refers to the remaining two terms obtained by one and two applications of $s_1 \to s_2$, $s_2 \to s_3$, $s_3 \to s_1$, respectively. The combination of WCs in (IX.66) are obtained in a similar way,

$$C^L_{S} = \frac{P^{\rm exp}_L(s_1)\left[f^L_{V-}(s_2)f^L_T(s_3) - f^L_{V-}(s_3)f^L_T(s_2)\right] + \text{cyclic}}{f^L_{S}(s_1)\left[f^L_{V-}(s_2)f^L_T(s_3) - f^L_{V-}(s_3)f^L_T(s_2)\right] + \text{cyclic}}, \tag{IX.78}$$

$$C^L_{V-} = \frac{P^{\rm exp}_L(s_1)\left[f^L_{S}(s_2)f^L_T(s_3) - f^L_{S}(s_3)f^L_T(s_2)\right] + \text{cyclic}}{f^L_{V-}(s_1)\left[f^L_{S}(s_2)f^L_T(s_3) - f^L_{S}(s_3)f^L_T(s_2)\right] + \text{cyclic}}, \tag{IX.79}$$

$$C^L_{T} = \frac{P^{\rm exp}_L(s_1)\left[f^L_{S}(s_2)f^L_{V-}(s_3) - f^L_{S}(s_3)f^L_{V-}(s_2)\right] + \text{cyclic}}{f^L_{T}(s_1)\left[f^L_{S}(s_2)f^L_{V-}(s_3) - f^L_{S}(s_3)f^L_{V-}(s_2)\right] + \text{cyclic}}. \tag{IX.80}$$

In the simplifying limit where all tensor-current contributions vanish, the relations above simplify to give

$$C^T_{V+} = \frac{P^{\rm exp}_T(s_1)f^T_{V-}(s_2) - P^{\rm exp}_T(s_2)f^T_{V-}(s_1)}{f^T_{V+}(s_1)f^T_{V-}(s_2) - f^T_{V+}(s_2)f^T_{V-}(s_1)}\,, \tag{IX.81}$$

$$C^T_{V-} = \frac{P^{\rm exp}_T(s_1)f^T_{V+}(s_2) - P^{\rm exp}_T(s_2)f^T_{V+}(s_1)}{f^T_{V-}(s_1)f^T_{V+}(s_2) - f^T_{V-}(s_2)f^T_{V+}(s_1)}\,, \tag{IX.82}$$

$$C^L_{S} = \frac{P^{\rm exp}_L(s_1)f^L_{V-}(s_2) - P^{\rm exp}_L(s_2)f^L_{V-}(s_1)}{f^L_{S}(s_1)f^L_{V-}(s_2) - f^L_{V+}(s_2)f^L_{V-}(s_1)}\,, \tag{IX.83}$$

$$C^L_{V-} = \frac{P^{\rm exp}_L(s_1)f^L_{S}(s_2) - P^{\rm exp}_L(s_2)f^L_{S}(s_1)}{f^L_{V-}(s_1)f^L_{S}(s_2) - f^L_{V-}(s_2)f^L_{S}(s_1)}\,. \tag{IX.84}$$

Note that the information encoded in Eq. (IX.75)-(IX.80) can also be extracted from dedicated measurements of the differential decay width of $B \to K^*\nu\widehat{\nu}$, which is simply the sum of P_T and P_L introduced above. The calculation of $\frac{d\Gamma(B\to K^*\nu\widehat{\nu})}{ds}$ proceeds along the lines described in Section IX.1.1. The notable differences are that the expressions for the relevant form factors are slightly more involved, c.f. Section VIII.5, and that we now need to perform a sum over polarizations of K^*. For completeness, we have included the relevant equations below,

$$\begin{aligned}\frac{d\Gamma(B\to K^*\nu\widehat{\nu})}{ds} &= J^{BK^*}_S \sum_{\alpha\le\beta}\left(1-\frac{\delta_{\alpha\beta}}{2}\right)\left(\left|C^{\rm SLL}_{\nu d,\alpha\beta bs} - C^{\rm SLR}_{\nu d,\alpha\beta bs}\right|^2 + \left|C^{\rm SLL}_{\nu d,\alpha\beta sb} - C^{\rm SLR}_{\nu d,\alpha\beta sb}\right|^2\right)\\ &+ J^{BK^*}_T \sum_{\alpha<\beta}\left(\left|C^{\rm TLL}_{\nu d,\alpha\beta sb}\right|^2 + \left|C^{\rm TLL}_{\nu d,\alpha\beta bs}\right|^2\right)\\ &+ \sum_{\alpha,\beta}\left(1-\frac{1}{2}\delta_{\alpha\beta}\right)\left(J^{BK^*}_{V1}\left|C^{\rm VLL}_{\nu d,\alpha\beta bs} - C^{\rm VLR}_{\nu d,\alpha\beta bs}\right|^2 + J^{BK^*}_{V2}\left|C^{\rm VLL}_{\nu d,\alpha\beta bs} + C^{\rm VLR}_{\nu d,\alpha\beta bs}\right|^2\right),\end{aligned} \tag{IX.85}$$

where

$$J^{BK^*}_S = f^L_S = \frac{s\,\lambda^{3/2}(m_B^2, m_{K^*}^2, s)}{256\pi^3 m_B^3(m_b+m_s)^2}\left|A_0(s)\right|^2, \tag{IX.86}$$

$$J_T^{BK^*} = f_T^T + f_T^L = \frac{\lambda^{1/2}(m_B^2, m_{K^*}^2, s)}{24\pi^3 m_B^3}\left[\frac{8m_B^2 m_{K^*}^2\, s}{(m_B+m_{K^*})^2}\left|T_{23}(s)\right|^2 + \lambda(m_B^2, m_{K^*}^2, s)\left|T_1(s)\right|^2 \right.$$
$$\left. +(m_B^2 - m_{K^*}^2)^2\left|T_2(s)\right|^2\right], \tag{IX.87}$$
$$J_{V1}^{BK^*} = f_{V-}^T + f_{V-}^L = \frac{\lambda^{1/2}(m_B^2, m_{K^*}^2, s)}{768\pi^3 m_B^3}\left(\left|A_1(s)\right|^2 s(m_B+m_{K^*})^2\right.$$
$$\left. +32\left|A_{12}(s)\right|^2 m_B^2 m_{K^*}^2\right), \tag{IX.88}$$
$$J_{V2}^{BK^*} = f_{V+}^T = \frac{s\,\lambda^{3/2}(m_B^2, m_{K^*}^2, s)}{768\pi^3 m_B^3(m_B+m_{K^*})^2}\left|V_0(s)\right|^2, \tag{IX.89}$$

which is in agreement with [466,480]. Note that analyzing P_T and P_L separately provides an additional layer of consistency checks. Specifically, the measured values of C_T^L and C_T^T, as well as C_{V-}^L and C_{V-}^T, should be equal, as evident from Eqs. (IX.65) and (IX.66).

To summarize, through our analysis of $B \to K^*\hat{\nu}\nu$ we have demonstrated that scalar, tensor, left-handed vector, and right-handed vector currents can be distinguished. This is worth emphasizing: In contrast to Kaon decays (and $B \to K\hat{\nu}\nu$, as discussed below), the contributions from left-handed and right-handed quark currents can be differentiated by comparing $C_{V-}^{L/T}$ and C_{V+}^L, as seen in Eqs. (IX.65) and (IX.66). A similar statement does not hold for scalar currents, as we only gain access to the combination

$$\sum_{\alpha\le\beta}\left(1-\frac{1}{2}\delta_{\alpha\beta}\right)\left[|C^{\rm SLR}_{\nu d,\alpha\beta sb} - C^{\rm SLL}_{\nu d,\alpha\beta sb}|^2 + |C^{\rm SLR}_{\nu d,\alpha\beta bs} - C^{\rm SLL}_{\nu d,\alpha\beta bs}|^2\right], \tag{IX.90}$$

through $B \to K^*\hat{\nu}\nu$. To make progress on distinguishing scalar currents, it turns out to be very useful to consider the decay channel $B \to K\nu\hat{\nu}$, as shown below.

Complementarity between different decay channels: $B \to K\nu\hat{\nu}$

The next decay channel that we will consider is $B \to K\nu\hat{\nu}$. For notational simplicity, it is useful to make the following definition,

$$\mathcal{D}^{\rm exp}_{BK}(s) \equiv \frac{d\Gamma(B\to K\nu\hat{\nu})}{ds}. \tag{IX.91}$$

The calculation of $B \to K\nu\hat{\nu}$ is structurally identical to $K^+ \to \pi^+\nu\hat{\nu}$: The matrix elements take the exact same mathematical form in both cases. We can therefore immediately recycle our results from Eq. (IX.40) and Eqs. (IX.44)-(IX.55) upon making appropriate replacements of form factors and quark flavors. It follows that the partial differential decay width of $B \to K\nu\hat{\nu}$ can be parametrized as,

$$\mathcal{D}^{\rm exp}_{BK}(s) = C_S^{BK} f_S^{BK}(s) + C_T^{BK} f_T^{BK}(s) + C_V^{BK} f_V^{BK}(s), \tag{IX.92}$$

where

$$C_S^{BK} = \sum_{\alpha\le\beta}\left(1-\frac{1}{2}\delta_{\alpha\beta}\right)\left(\left|C^{\rm SLL}_{\nu d,\alpha\beta bs} + C^{\rm SLR}_{\nu d,\alpha\beta bs}\right|^2 + \left|C^{\rm SLL}_{\nu d,\alpha\beta sb} + C^{\rm SLR}_{\nu d,\alpha\beta sb}\right|^2\right), \tag{IX.93}$$
$$C_T^{BK} = \sum_{\alpha<\beta}\left(\left|C^{\rm TLL}_{\nu d,\alpha\beta bs}\right|^2 + \left|C^{\rm TLL}_{\nu d,\alpha\beta sb}\right|^2\right), \tag{IX.94}$$
$$C_V^{BK} = \sum_{\alpha,\beta}\left(1-\frac{1}{2}\delta_{\alpha\beta}\right)\left|C^{\rm VLL}_{\nu d,\alpha\beta sb} + C^{\rm VLR}_{\nu d,\alpha\beta sb}\right|^2, \tag{IX.95}$$

and the integrated currents read

$$\frac{1}{\Gamma^{\rm exp}_{B^+}}\int ds\, f_S^{BK}(s) = 10.4\, G_F^{-2}, \tag{IX.96}$$
$$\frac{1}{\Gamma^{\rm exp}_{B^+}}\int ds\, f_T^{BK}(s) = 17.7\, G_F^{-2}, \tag{IX.97}$$
$$\frac{1}{\Gamma^{\rm exp}_{B^+}}\int ds\, f_V^{BK}(s) = 2.2\, G_F^{-2}. \tag{IX.98}$$

The numerical values were obtained using the values in Eq. (IX.74). The combinations C_S^{BK}, C_T^{BK}, C_V^{BK} of WCs can then be extracted as[5]

$$C_S^{BK} = \frac{D^{\rm exp}_{BK}(s_1)\left[f_V^{BK}(s_2)f_T^{BK}(s_3) - f_V^{BK}(s_3)f_T^{BK}(s_2)\right] + \text{cyclic}}{f_S^{BK}(s_1)\left[f_V^{BK}(s_2)f_T^{BK}(s_3) - f_V^{BK}(s_3)f_T^{BK}(s_2)\right] + \text{cyclic}}, \tag{IX.99}$$
$$C_V^{BK} = \frac{D^{\rm exp}_{BK}(s_1)\left[f_S^{BK}(s_2)f_T^{BK}(s_3) - f_S^{BK}(s_3)f_T^{BK}(s_2)\right] + \text{cyclic}}{f_V^{BK}(s_1)\left[f_S^{BK}(s_2)f_T^{BK}(s_3) - f_S^{BK}(s_3)f_T^{BK}(s_2)\right] + \text{cyclic}}, \tag{IX.100}$$
$$C_T^{BK} = \frac{D^{\rm exp}_{BK}(s_1)\left[f_S^{BK}(s_2)f_V^{BK}(s_3) - f_S^{BK}(s_3)f_V^{BK}(s_2)\right] + \text{cyclic}}{f_T^{BK}(s_1)\left[f_S^{BK}(s_2)f_V^{BK}(s_3) - f_S^{BK}(s_3)f_V^{BK}(s_2)\right] + \text{cyclic}}. \tag{IX.101}$$

Let us summarize what we have gained through the analysis above: By extracting the coefficients C_S^L from $B \to K^*\nu\widehat{\nu}$ and C_S^{BK} from $B \to K\nu\widehat{\nu}$, it is possible to determine whether left-handed and right-handed scalar currents are present or only currents of a single handedness, as evident from Eqs. (IX.66) and (IX.93). If the latter is the case, kinematic distributions alone cannot distinguish between left-handed and right-handed scalar NP. However, a measurement of $C_S^L = 0$ would imply that $C^{\rm SLL}_{\nu d,\alpha\beta bs} = C^{\rm SLR}_{\nu d,\alpha\beta bs}$, indicating purely scalar quark currents (i.e., parity-symmetric quark currents). Conversely, measuring $C_S^{BK} = 0$, and consequently $C^{\rm SLL}_{\nu d,\alpha\beta bs} = -C^{\rm SLR}_{\nu d,\alpha\beta bs}$, would suggest purely pseudoscalar quark currents (i.e., parity-antisymmetric quark currents).

Complementarity between different decay channels: $B \to X_s\nu\widehat{\nu}$

As our third and final example of decay channels for the B-meson, we have considered inclusive decays, $B \to X_s\nu\widehat{\nu}$, where the hadronic part of the final state is summed over. Here, a heavy quark expansion [511, 512] allows one to write the decay rate in terms of the quark-level transition as

$$\frac{d\Gamma(B \to X_s\nu\widehat{\nu})}{ds} = \frac{d\Gamma(b \to s\nu\widehat{\nu})}{ds} + \mathcal{O}\left(\frac{\Lambda_{\rm QCD}}{m_b}\right). \tag{IX.102}$$

TEq. (IX.102) turns calculating $\Gamma(B \to X_s\nu\widehat{\nu})$ into a straightforward task that, unlike the decays considered above, does not involve hadronic form factors. The final result can be expressed as,

$$\frac{d\Gamma(B \to X_s\nu\widehat{\nu})}{ds} = C_1^S J_1^S(s) + C_2^S J_2^S(s) + C_1^V J_1^V(s) + C_2^V J_2^V(s) + C^T J^T(s), \tag{IX.103}$$

where the effective WCs read

$$C_1^S = \sum_{\alpha\leq\beta}\left(1 - \frac{\delta_{\alpha\beta}}{2}\right)\left(\left|C^{\rm SLL}_{\nu d,\alpha\beta bs}\right|^2 + \left|C^{\rm SLL}_{\nu d,\alpha\beta sb}\right|^2 + \left|C^{\rm SLR}_{\nu d,\alpha\beta bs}\right|^2 + \left|C^{\rm SLR}_{\nu d,\alpha\beta sb}\right|^2\right), \tag{IX.104}$$

[5] It is worth noting that measuring both $B \to K^*\nu\widehat{\nu}$ and $B \to K\nu\widehat{\nu}$ would offer the following consistency checks, $C_V^{BK} = C_{V+}^T$ and $C_T^{BK} = C_T^T = C_T^L$.

$$C_2^S = \sum_{\alpha\leq\beta}\left(1-\frac{\delta_{\alpha\beta}}{2}\right)\mathrm{Re}\left(C^{\rm SLL}_{\nu d,\alpha\beta bs}C^{\rm SLR*}_{\nu d,\alpha\beta bs}+C^{\rm SLL}_{\nu d,\alpha\beta sb}C^{\rm SLR*}_{\nu d,\alpha\beta sb}\right), \tag{IX.105}$$

$$C_1^V = \sum_{\alpha,\beta}\left(1-\frac{1}{2}\delta_{\alpha\beta}\right)\left(\left|C^{\rm VLL}_{\nu d,\alpha\beta sb}\right|^2+\left|C^{\rm VLR}_{\nu d,\alpha\beta sb}\right|^2\right), \tag{IX.106}$$

$$C_2^V = \sum_{\alpha,\beta}\left(1-\frac{1}{2}\delta_{\alpha\beta}\right)\mathrm{Re}\left(C^{\rm VLL}_{\nu d,\alpha\beta sb}C^{\rm VLR*}_{\nu d,\alpha\beta sb}\right), \tag{IX.107}$$

$$C^T = \sum_{\alpha<\beta}\left(\left|C^{\rm TLL}_{\nu d,\alpha\beta bs}\right|^2+\left|C^{\rm TLL}_{\nu d,\alpha\beta sb}\right|^2\right), \tag{IX.108}$$

and the integrated kinematic functions are given by,

$$\frac{1}{\Gamma^{\rm exp}_{B^+}}\int ds\, J_1^S(s) = \frac{1}{\Gamma^{\rm exp}_{B^+}}\frac{\kappa(0)}{128\pi^3 m_b^3}\int ds\,(m_b^2+m_s^2-s)s\,\lambda^{1/2}(m_b^2,m_s^2,s)$$
$$= 7.6\left(\frac{m_b}{4.19\,\mathrm{GeV}}\right)^5 G_F^{-2}, \tag{IX.109}$$

$$\frac{1}{\Gamma^{\rm exp}_{B^+}}\int ds\, J_2^S(s) = \frac{1}{\Gamma^{\rm exp}_{B^+}}\frac{\kappa(0)m_s m_b}{32\pi^3 m_b^3}\int ds\, s\,\lambda^{1/2}(m_b^2,m_s^2,s) = 1.3\left(\frac{m_b}{4.19\,\mathrm{GeV}}\right)^5 G_F^{-2}, \tag{IX.110}$$

$$\frac{1}{\Gamma^{\rm exp}_{B^+}}\int ds\, J_1^V(s) = \frac{1}{\Gamma^{\rm exp}_{B^+}}\frac{\kappa(0)}{768\pi^3 m_b^3}\int ds\,\lambda^{1/2}(m_b^2,m_s^2,s)\left[\lambda(m_b^2,m_s^2,s)+3s(m_b^2+m_s^2-s)\right]$$
$$= 7.6\left(\frac{m_b}{4.19\,\mathrm{GeV}}\right)^5 G_F^{-2}, \tag{IX.111}$$

$$\frac{1}{\Gamma^{\rm exp}_{B^+}}\int ds\, J_2^V(s) = -\frac{1}{\Gamma^{\rm exp}_{B^+}}\frac{\kappa(0)m_s m_b}{64\pi^3 m_b^3}\int ds\,\lambda^{1/2}(m_b^2,m_s^2,s)\,s$$
$$= -0.7\left(\frac{m_b}{4.19\,\mathrm{GeV}}\right)^5 G_F^{-2}, \tag{IX.112}$$

$$\frac{1}{\Gamma^{\rm exp}_{B^+}}\int ds\, J^T(s) = \frac{1}{\Gamma^{\rm exp}_{B^+}}\frac{\kappa(0)}{24\pi^3 m_b^3}\int ds\,\lambda^{1/2}(m_b^2,m_s^2,s)\left[2\lambda(m_b^2,m_s^2,s)+3s\left(m_s^2+m_b^2-s\right)\right]$$
$$= 365\left(\frac{m_b}{4.19\,\mathrm{GeV}}\right)^5 G_F^{-2}. \tag{IX.113}$$

The factor $\kappa(0) = 0.83$ represents the QCD correction to the $b \to s\nu\bar{\nu}$ matrix element [513–515], and the numerical values in the equations above were obtained using the values in Eq. (IX.74).

It is noteworthy that the number of linearly independent kinematic structures in Eqs. (IX.109)-(IX.113) is smaller than the number of effective WCs in Eqs. (IX.104)-(IX.108). All of the kinematic functions in Eqs. (IX.109)-(IX.113) can be expressed as linear combinations of the following three independent kinematic structures,

$$s\,\lambda^{1/2}(m_b^2,m_s^2,s), \qquad s^2\,\lambda^{1/2}(m_b^2,m_s^2,s), \qquad \lambda^{3/2}(m_b^2,m_s^2,s), \tag{IX.114}$$

with their associated combinations of WCs given by

$$C_1^V + 2C_1^S + 32C^T + \frac{4m_s m_b}{m_b^2+m_s^2}\left(2C_2^S - C_2^V\right), \tag{IX.115}$$

$$C_1^V + 2C_1^S + 32C^T, \tag{IX.116}$$

$$C_1^V + 64C^T, \tag{IX.117}$$

respectively. These combinations of WCs can, in principle, be determined through dedicated measurements of $B \to X_s \nu\hat{\nu}$.

At this point, it is useful to recapitulate the main points of this section: Detailed measurements of the kinematic distributions for $B \to K^* \nu\hat{\nu}$ and $B \to K\nu\hat{\nu}$ enable the determination of the effective coefficients in Eqs. (IX.75)-(IX.80) and (IX.93)-(IX.95), respectively. Subsequently, simple algebraic manipulations can be used to determine the coefficients in Eqs. (IX.104)-(IX.108), which can also be experimentally determined through careful measurements of $B \to X_s\nu\hat{\nu}$. This highlights that measuring $B \to X_s\nu\hat{\nu}$ and extracting the values of Eqs. (IX.115)-(IX.117) offers three consistency checks on the results obtained from measurements of $B \to K\nu\hat{\nu}$ and $B \to K^*\nu\hat{\nu}$.

IX.2.2 Disentangling LEFT from dark-sector physics

So far in our treatment of B-decays, we have assumed that only neutrinos hide in the invisible part of the final state. In the following section, we relax the assumption about missing energy in the $B \to K + \not{E}$, $B \to K^* + \not{E}$, and $B \to X_s + \not{E}$ channels being attributed solely to neutrinos. As an initial step, we will expand on the discussion in Section IX.1.4 regarding the prospects of distinguishing between (SM)LEFT and (D)LEFT, under the simplifying assumption that NP is encoded primarily in a single effective operator. Subsequently, we will go beyond this (simplified) treatment and investigate the extent to which it is possible to distinguish between (SM)LEFT and (D)LEFT in full generality using kinematic distributions.

Single operator analysis

$B \to K + \not{E}$: As argued below Eq. (IX.91), it is possible to derive analytical expressions for $d\Gamma(B \to K + \not{E})/ds$ by appropriately modifying the result for $d\Gamma(K^+ \to \pi^+ + \not{E})/ds$ presented in Section IX.1.1, through appropriate replacements of meson masses, quark masses, and form factors. Consequently, the kinematic distributions in the single-operator analysis of $B \to K + \not{E}$ are identical in form to those presented for $K^+ \to \pi^+ + \not{E}$ in Table IX.1. For the reader's convenience, we summarize the main findings:

- The only operators that generate the same kinematic distribution as $\mathcal{O}_{\nu d}^{\mathrm{SLL}}$ or $\mathcal{O}_{\nu d}^{\mathrm{SLR}}$ are two (D)LEFT operators with fermionic dark-sector particles $\mathcal{O}_{sb\chi1}^{\mathrm{S}}$ and $\mathcal{O}_{sb\chi2}^{\mathrm{S}}$ as highlighted in blue in Table IX.1.[6]
- Two (D)LEFT operators, $\mathcal{O}_{sb\chi1}^{\mathrm{T}}$ and $\mathcal{O}_{sb\chi2}^{\mathrm{T}}$, yield the same kinematic distribution as $\mathcal{O}_{\nu d}^{\mathrm{TLL}}$, as highlighted in green in Table IX.1.
- Both dark-fermion operators with vector currents ($\mathcal{O}_{sd\chi1}^{V}$ and $\mathcal{O}_{sd\chi2}^{V}$) and a dark-scalar operator with vector currents ($\mathcal{O}_{sd\phi}^{V}$) generate a kinematic structure identical to that of $\mathcal{O}_{\nu d}^{\mathrm{VLL}}$ and $\mathcal{O}_{\nu d}^{\mathrm{VLR}}$, as highlighted in red in Table IX.1.

$B \to K^* + \not{E}$: We have performed a similar analysis for $B \to K^* + \not{E}$, and the results are summarized in Table IX.2. Among all (D)LEFT operators, only those with vector dark matter (DM) of type A yield interference terms between different WCs in this decay. The full expressions for the differential decay distributions are provided in Section B. Notably, none of the interference terms exhibit a kinematic structure similar to any (SM)LEFT operator.[7] The highlights of this analysis is summarized below:

[6] The two corresponding dark pseudoscalar (D)LEFT operators $\mathcal{O}_{sb\chi1}^{\mathrm{P}}$ and $\mathcal{O}_{sb\chi2}^{\mathrm{P}}$ do not contribute to $B \to K + \not{E}$ due to parity conservation.

[7] Similar observations also apply to $B \to X_s + \not{E}$.

Type	Operator	Kinematic structure in $B \to K^* + \not{E}$
(SM)LEFT	$\mathcal{O}_{\nu d}^{\rm SLL}$, $\mathcal{O}_{\nu d}^{\rm SLR}$	$s\lambda^{3/2}\,|A_0|^2$
	$\mathcal{O}_{\nu d}^{\rm VLL}$, $\mathcal{O}_{\nu d}^{\rm VLR}$	$\lambda^{1/2}\big[\frac{s\lambda}{(m_B+m_{K^*})^2}\,|V_0|^2 + s(m_B+m_{K^*})^2\,|A_1|^2 + 32m_B^2m_{K^*}^2\,|A_{12}|^2\big]$
	$\mathcal{O}_{\nu d}^{\rm TLL}$	$\lambda^{1/2}\Big[\lambda\,|T_1|^2 + (m_B^2-m_{K^*}^2)^2\,|T_2|^2 + \frac{8m_B^2m_{K^*}^2s}{(m_B+m_{K^*})^2}\,|T_{23}|^2\Big]$
Scalar DM	$\mathcal{O}_{sb\phi}^{P}$	$\lambda^{3/2}\,|A_0|^2$
	$\mathcal{O}_{sb\phi}^{A}$	$\lambda^{1/2}\Big[s(m_B+m_{K^*})^2\,|A_1|^2 + 32m_B^2m_{K^*}^2\,|A_{12}|^2\Big]$
	$\mathcal{O}_{sb\phi}^{V}$	$s\lambda^{3/2}\,|V_0|^2$
Fermion DM	$\mathcal{O}_{sb\chi1}^{P}, \mathcal{O}_{sb\chi2}^{P}$	$s\lambda^{3/2}\,|A_0|^2$
	$\mathcal{O}_{sb\chi1}^{A}, \mathcal{O}_{sb\chi2}^{A}$	$\lambda^{1/2}\Big[s(m_B+m_{K^*})^2\,|A_1|^2 + 32m_B^2m_{K^*}^2\,|A_{12}|^2\Big]$
	$\mathcal{O}_{sb\chi1}^{V}, \mathcal{O}_{sb\chi2}^{V}$	$s\lambda^{3/2}\,|V_0|^2$
	$\mathcal{O}_{sb\chi1}^{T}, \mathcal{O}_{sb\chi2}^{T}$	$\lambda^{1/2}\Big[\lambda\,|T_1|^2 + (m_B^2-m_{K^*}^2)^2\,|T_2|^2 + \frac{8m_B^2m_{K^*}^2s}{(m_B+m_{K^*})^2}\,|T_{23}|^2\Big]$
Vector DM: A	$\mathcal{O}_{sbA}^{P}$	$s^2\lambda^{3/2}\,|A_0|^2$
	$\mathcal{O}_{sbA1}^{T}$	$s\lambda^{3/2}\,|T_1|^2$
	$\mathcal{O}_{sbA2}^{T}$	$s\lambda^{1/2}\Big[(m_B^2-m_{K^*}^2)^2\,|T_2|^2 + \frac{8m_B^2m_{K^*}^2s}{(m_B+m_{K^*})^2}\,|T_{23}|^2\Big]$
	$\mathcal{O}_{sbA3}^{V}, \mathcal{O}_{sbA6}^{V}$	$s^2\lambda^{3/2}\,|V_0|^2$
	$\mathcal{O}_{sbA4}^{V}, \mathcal{O}_{sbA5}^{V}$	$s^3\lambda^{3/2}\,|V_0|^2$
	$\mathcal{O}_{sbA2}^{A}$	$s^2\lambda^{3/2}\,|A_0|^2$
	$\mathcal{O}_{sbA3}^{A}, \mathcal{O}_{sbA6}^{A}$	$s\lambda^{1/2}\Big[s(m_B+m_{K^*})^2\,|A_1|^2 + 32m_B^2m_{K^*}^2\,|A_{12}|^2\Big]$
	$\mathcal{O}_{sbA4}^{A}, \mathcal{O}_{sbA5}^{A}$	$s^2\lambda^{1/2}\Big[s(m_B+m_{K^*})^2\,|A_1|^2 + 32m_B^2m_{K^*}^2\,|A_{12}|^2\Big]$
Vector DM: B	$\mathcal{O}_{sbB1}^{P}, \mathcal{O}_{sbB2}^{P}$	$s^2\lambda^{3/2}\,|A_0|^2$
	$\mathcal{O}_{sbB1}^{T}, \mathcal{O}_{sbB2}^{T}$	$s\lambda^{1/2}\Big[\lambda\,|T_1|^2 + (m_B^2-m_{K^*}^2)^2\,|T_2|^2 + \frac{8m_B^2m_{K^*}^2s}{(m_B+m_{K^*})^2}\,|T_{23}|^2\Big]$

Table IX.2: List of operators contributing to $B \to K^* + \not{E}$ along with the kinematic structure they induce in $d\Gamma(B \to K^* + \not{E})/ds$. Here λ is short for $\lambda(m_B^2, m_{K^*}^2, s)$, and V_0 for $V_0(s)$, etc. We have only listed operators that contribute to $B \to K^* + \not{E}$, and interference terms are neglected under the assumption that only one operator is active (see text for details) [1].

- Our results show that only the dark pseudoscalar (D)LEFT operators $\mathcal{O}_{sb\chi1}^{\rm P}$ and $\mathcal{O}_{sb\chi2}^{\rm P}$ produce the same kinematic distribution as the (SM)LEFT operators $\mathcal{O}_{\nu d}^{\rm SLL}$ and $\mathcal{O}_{\nu d}^{\rm SLR}$, respectively, which are highlighted in blue. In contrast, the dark scalar (D)LEFT operators $\mathcal{O}_{sb\chi1}^{\rm S}$ and $\mathcal{O}_{sb\chi2}^{\rm S}$, which yield the same kinematic distribution

Type	Operator	Kinematic structure in $B \to X_s + \not{E}$
(SM)LEFT	$\mathcal{O}_{\nu d}^{\rm SLL}$, $\mathcal{O}_{\nu d}^{\rm SLR}$	$s\lambda^{1/2}(m_b^2 + m_s^2 - s)$
	$\mathcal{O}_{\nu d}^{\rm VLL}$, $\mathcal{O}_{\nu d}^{\rm VLR}$	$\lambda^{1/2}\big[\lambda + 3s(m_b^2 + m_s^2 - s)\big]$
	$\mathcal{O}_{\nu d}^{\rm TLL}$	$\lambda^{1/2}\big[2\lambda + 3s(m_b^2 + m_s^2 - s)\big]$
Scalar DM	$\mathcal{O}_{sb\phi}^{S}$	$\lambda^{1/2}\big[(m_b + m_s)^2 - s\big]$
	$\mathcal{O}_{sb\phi}^{P}$	$\lambda^{1/2}\big[(m_b - m_s)^2 - s\big]$
	$\mathcal{O}_{sb\phi}^{V}$	$\lambda^{1/2}\big[\lambda + 3s\big((m_b - m_s)^2 - s\big)\big]$
	$\mathcal{O}_{sb\phi}^{A}$	$\lambda^{1/2}\big[\lambda + 3s\big((m_b + m_s)^2 - s\big)\big]$
Fermion DM	$\mathcal{O}_{sb\chi 1}^{S}, \mathcal{O}_{sb\chi 2}^{S}$	$s\lambda^{1/2}\big[\big((m_b + m_s)^2 - s\big)\big]$
	$\mathcal{O}_{sb\chi 1}^{P}, \mathcal{O}_{sb\chi 2}^{P}$	$s\lambda^{1/2}\big[\big((m_b - m_s)^2 - s\big)\big]$
	$\mathcal{O}_{sb\chi 1}^{A}, \mathcal{O}_{sb\chi 2}^{A}$	$\lambda^{1/2}\big[\lambda + 3s\big((m_b + m_s)^2 - s\big)\big]$
	$\mathcal{O}_{sb\chi 1}^{V}, \mathcal{O}_{sb\chi 2}^{V}$	$\lambda^{1/2}\big[\lambda + 3s\big((m_b - m_s)^2 - s\big)\big]$
	$\mathcal{O}_{sb\chi 1}^{T}, \mathcal{O}_{sb\chi 2}^{T}$	$\lambda^{1/2}\big[2\lambda + 3s(m_b^2 + m_s^2 - s)\big]$
Vector DM: A	$\mathcal{O}_{sbA}^{S}$	$s^2\lambda^{1/2}\big[(m_b + m_s)^2 - s\big]$
	$\mathcal{O}_{sbA}^{P}$	$s^2\lambda^{1/2}\big[(m_b - m_s)^2 - s\big]$
	$\mathcal{O}_{sbA1}^{T}$	$s\lambda^{1/2}\big[2\lambda + 3s\big((m_b - m_s)^2 - s\big)\big]$
	$\mathcal{O}_{sbA2}^{T}$	$s\lambda^{1/2}\big[2\lambda + 3s\big((m_b + m_s)^2 - s\big)\big]$
	$\mathcal{O}_{sbA2}^{V}$	$s^2\lambda^{1/2}\big[(m_b + m_s)^2 - s\big]$
	$\mathcal{O}_{sbA3}^{V}, \mathcal{O}_{sbA6}^{V}$	$s\lambda^{1/2}\big[\lambda + 3s\big((m_b - m_s)^2 - s\big)\big]$
	$\mathcal{O}_{sbA4}^{V}, \mathcal{O}_{sbA5}^{V}$	$s^2\lambda^{1/2}\big[\lambda + 3s\big((m_b - m_s)^2 - s\big)\big]$
	$\mathcal{O}_{sbA2}^{A}$	$s^2\lambda^{1/2}\big[(m_b - m_s)^2 - s\big]$
	$\mathcal{O}_{sbA3}^{A}, \mathcal{O}_{sbA6}^{A}$	$s\lambda^{1/2}\big[\lambda + 3s\big((m_b + m_s)^2 - s\big)\big]$
	$\mathcal{O}_{sbA4}^{A}, \mathcal{O}_{sbA5}^{A}$	$s^2\lambda^{1/2}\big[\lambda + 3s\big((m_b + m_s)^2 - s\big)\big]$
Vector DM: B	$\mathcal{O}_{sbB1}^{S}, \mathcal{O}_{sbB2}^{S}$	$s^2\lambda^{1/2}\big[(m_b + m_s)^2 - s\big]$
	$\mathcal{O}_{sbB1}^{P}, \mathcal{O}_{sbB2}^{P}$	$s^2\lambda^{1/2}\big[(m_b - m_s)^2 - s\big]$
	$\mathcal{O}_{sbB1}^{T}, \mathcal{O}_{sbB2}^{T}$	$s^2\lambda^{1/2}\big[2\lambda + 3s(m_b^2 + m_s^2 - s)\big]$

Table IX.3: List of operators contributing to $B \to X_s + \not{E}$ and the kinematic structure they induce in $d\Gamma(B \to X_s + \not{E})/ds$. λ is a shor for $\lambda(m_b^2, m_s^2, s)$. Interference terms are neglected under the assumption that only one operator is active (see text for details) [1].

as $\mathcal{O}_{\nu d}^{\rm SLL}$ and $\mathcal{O}_{\nu d}^{\rm SLR}$ in $B \to K + \not{E}$, do not contribute to $B \to K^* + \not{E}$ due to parity conservation.

- The operators $\mathcal{O}_{sb\chi 1}^{\rm T}$ and $\mathcal{O}_{sb\chi 2}^{\rm T}$, highlighted in green, are the only operators that produce the same kinematic distribution as $\mathcal{O}_{\nu d}^{\rm TLL}$.
- For the (SM)LEFT vector-current operators $\mathcal{O}_{\nu d}^{\rm VLL}$ and $\mathcal{O}_{\nu d}^{\rm VLR}$, highlighted in red, we find that no single (D)LEFT operator yields a similar kinematic structure within the considered operator basis. Nevertheless, the (SM)LEFT vector-current kinematic structure can be replicated by considering suitable linear combinations of dark-fermion or dark-scalar operators, going beyond a single-operator analysis. We elaborate on this statement in the multiple-operator analysis below.

$B \to X_s + \not{E}$: Our results for the inclusive decay $B \to X_s + \not{E}$ are summarized in Table IX.3, and the important points are summarized below. The results for (D)LEFT were, to the best of our knowledge, presented in Ref. [1] for the first time.

- The kinematic distributions of $\mathcal{O}_{\nu d}^{\rm SLL}$ and $\mathcal{O}_{\nu d}^{\rm SLR}$, highlighted in dark blue, are distinct in this decay channel. However, in practice, they are challenging to differentiate from $\mathcal{O}_{sb\chi 1,2}^{\rm P}$ and $\mathcal{O}_{sb\chi 1,2}^{\rm S}$, highlighted in light blue.
- The (SM)LEFT tensor operator $\mathcal{O}_{\nu d}^{\rm TLL}$ induces the same kinematic distribution as the (D)LEFT operators $\mathcal{O}_{sb\chi 1}^{\rm T}$ and $\mathcal{O}_{sb\chi 2}^{\rm T}$. Consequently, $\mathcal{O}_{\nu d}^{\rm TLL}$ is indistinguishable from these operators across all three decay channels. To differentiate $\mathcal{O}_{\nu d}^{\rm TLL}$ from the fermionic tensorial operators in (D)LEFT, additional analysis is necessary.
- The kinematic distributions of $\mathcal{O}_{\nu d}^{\rm VLL}$ and $\mathcal{O}_{\nu d}^{\rm VLR}$, highlighted in red, are distinct within this decay channel. However, in practice, they are challenging to differentiate from $\mathcal{O}_{sb\phi}^{\rm V/A}$ and $\mathcal{O}_{sb\chi 1,2}^{\rm V/A}$, highlighted in light red.

The discussion above may leave the impression that $\mathcal{O}_{\nu d}^{\rm SLL}$ and $\mathcal{O}_{\nu d}^{\rm SLR}$ can be distinguished from (D)LEFT operators by analyzing the kinematic distributions of $B \to K + \not{E}$ and $B \to K^* + \not{E}$, assuming a single (SM)LEFT or (D)LEFT operator dominance. However, while this is true in the basis considered above, the statement does not hold in a (D)LEFT basis where the four operators $\mathcal{O}_{sb\chi 1,2}^{\rm S}$ and $\mathcal{O}_{sb\chi 1,2}^{\rm P}$ are combined into four basis operators with similar Dirac structure as $\mathcal{O}_{\nu d}^{\rm SLL}$ and $\mathcal{O}_{\nu d}^{\rm SLR}$. Consequently, distinguishing $\mathcal{O}_{\nu d}^{\rm SLL}$ and $\mathcal{O}_{\nu d}^{\rm SLR}$ from all (D)LEFT operators is not always possible. This makes intuitive sense, since distinguishing operators based on kinematic structures only works if operators have different Dirac structures. For further insights into the (in)distinguishability of dark fermions from (SM)LEFT scalar currents, we refer the reader to Appendix F in Ref. [1]. We will instead move on to consider multiple-operator analyses, where (in)distinguishability of operators in different bases becomes manifest.

Multiple operator analysis

Before proceeding, it is worth noting that the strategy outlined in Sections IX.1.3 and IX.2.1 for disentangling different operator contributions to meson decays in the context of (SM)LEFT is universally applicable to any operator set. After identifying the kinematic structures induced by the operator set, the disentanglement procedure simplifies to solving a system of linear equations, as illustrated in the discussion following Eq. (IX.52). The primary effect of considering a larger number of operators is that more measurements of s may be required to distinguish between different contributions, provided the new operators introduce new kinematic structures, thereby enlarging the system of linear equations in s_i. Notably, for a given decay channel, the number of linear equations is determined by the number of linearly independent kinematic structures contributing to the differential decay distribution.

As a most general case, it is possible to combine the (SM)LEFT basis with the four (D)LEFT bases listed in Section VIII.3 into a unified operator set. A straightforward extension of the procedure outlined in Sections IX.1.3 and IX.2.1 would yield a large system of linear equations, whose solution would constrain various combinations of WCs within the set. For a more tractable scenario, we examine a basis comprising the (SM)LEFT operators in Eqs. (VIII.15)-(VIII.19) and the dark scalar and dark fermion operators in Eqs. (VIII.20)-(VIII.28). The inclusion of vector operators, while straightforward, is less compelling. As evident from Tables IX.1, IX.2, and IX.3, no linear combination of vector operators can replicate the kinematic structures of (SM)LEFT operators in $B \to K + \not{E}$, $B \to K^* + \not{E}$, and $B \to X_s + \not{E}$, respectively. Thus, detailed measurements of kinematic distributions in these decay channels enable a complete disentanglement of (SM)LEFT from dark vectors. Consequently, the expressions below involving (SM)LEFT WCs remain unmodified.

In the following, the working assumption will be that the invisible final states can be comprised of two neutrinos, two dark-sector scalars, or two dark-sector fermions. We will go through the considered B-decay channels in turn, identifying the combinations of WCs that can be determined along with their corresponding kinematic structures [1].

For $B \to K + \not{E}$, it is evident from Table IX.1[8] that the following four combinations can be determined:

- Kinematic structure:

$$\lambda^{1/2} \left| f_0^K \right|^2 . \tag{IX.118}$$

  Associated WC:

$$\left| C_{sb\phi}^S \right|^2 . \tag{IX.119}$$

- Kinematic structure:

$$s\, \lambda^{1/2} \left| f_0^K \right|^2 . \tag{IX.120}$$

  Associated combination of WCs:

$$\begin{aligned} &\sum_{\alpha \le \beta} \left(1 - \frac{1}{2}\delta_{\alpha\beta}\right) \left(\left| C_{\nu d,\alpha\beta bs}^{\rm SLL} + C_{\nu d,\alpha\beta bs}^{\rm SLR} \right|^2 + \left| C_{\nu d,\alpha\beta sb}^{\rm SLL} + C_{\nu d,\alpha\beta sb}^{\rm SLR} \right|^2 \right) \\ &+ 2 \left(\left| C_{sb\chi 1}^S \right|^2 + \left| C_{sb\chi 2}^S \right|^2 \right) . \end{aligned} \tag{IX.121}$$

- Kinematic structure:

$$\lambda^{3/2} \left| f_+^K \right|^2 . \tag{IX.122}$$

  Associated combination of WCs:

$$2 \left| C_{sb\phi}^V \right|^2 + 8 \left(\left| C_{sb\chi 1}^V \right|^2 + \left| C_{sb\chi 2}^V \right|^2 \right) + \sum_{\alpha,\beta} \left(1 - \frac{1}{2}\delta_{\alpha\beta}\right) \left| C_{\nu d,\alpha\beta bs}^{\rm VLL} + C_{\nu d,\alpha\beta bs}^{\rm VLR} \right|^2 . \tag{IX.123}$$

[8] Recall that the kinematic structures for $B \to K + \not{E}$ can be obtained from $K \to \pi + \not{E}$ by appropriately substituting masses and form factors.

- Kinematic structure:

$$s\lambda^{3/2}\left|f_T^K\right|^2 . \tag{IX.124}$$

Associated combination of WCs:

$$\left(\left|C^T_{sb\chi 1}\right|^2+\left|C^T_{sb\chi 2}\right|^2\right)+2\sum_{\alpha<\beta}\left(\left|C^{\text{TLL}}_{\nu d,\alpha\beta bs}\right|^2+\left|C^{\text{TLL}}_{\nu d,\alpha\beta sb}\right|^2\right). \tag{IX.125}$$

In the case of $B \to K^* + \not{E}$, it is deducible from Table IX.2 that there are five independent kinematic structures. Hence, dedicated measurements of kinematic distributions can determine the value of the five combinations of WCs, which we list below. Note that (SM)LEFT vector currents enter two of the combinations in this case.

- Kinematic structure:

$$\lambda^{3/2}\left|A_0\right|^2 . \tag{IX.126}$$

Associated WC:

$$\left|C^P_{sb\phi}\right|^2 . \tag{IX.127}$$

- Kinematic structure:

$$s\,\lambda^{3/2}\left|A_0\right|^2 . \tag{IX.128}$$

Associated combination of WCs:

$$\sum_{\alpha\leq\beta}\left(1-\frac{\delta_{\alpha\beta}}{2}\right)\left(\left|C^{\text{SLL}}_{\nu d,\alpha\beta bs}-C^{\text{SLR}}_{\nu d,\alpha\beta bs}\right|^2+\left|C^{\text{SLL}}_{\nu d,\alpha\beta sb}-C^{\text{SLR}}_{\nu d,\alpha\beta sb}\right|^2\right)$$
$$+\,2\left(\left|C^P_{sb\chi 1}\right|^2+\left|C^P_{sb\chi 2}\right|^2\right). \tag{IX.129}$$

- Kinematic structure:

$$\lambda^{1/2}\Big[s(m_B+m_{K^*})^2\left|A_1\right|^2+32m_B^2m_{K^*}^2\left|A_{12}\right|^2\Big]. \tag{IX.130}$$

Associated combination of WCs:

$$2\left|C^A_{sb\phi}\right|^2+8\left(\left|C^A_{sb\chi 1}\right|^2+\left|C^A_{sb\chi 2}\right|^2\right)+\sum_{\alpha,\beta}\left(1-\frac{1}{2}\delta_{\alpha\beta}\right)\left|C^{\text{VLL}}_{\nu d,\alpha\beta bs}-C^{\text{VLR}}_{\nu d,\alpha\beta bs}\right|^2 . \tag{IX.131}$$

- Kinematic structure:

$$s\,\lambda^{3/2}\left|V_0\right|^2 . \tag{IX.132}$$

Associated combination of WCs:

$$2\left|C^V_{sb\phi}\right|^2+8\left(\left|C^V_{sb\chi 1}\right|^2+\left|C^V_{sb\chi 2}\right|^2\right)+\sum_{\alpha,\beta}\left(1-\frac{1}{2}\delta_{\alpha\beta}\right)\left|C^{\text{VLL}}_{\nu d,\alpha\beta bs}+C^{\text{VLR}}_{\nu d,\alpha\beta bs}\right|^2 . \tag{IX.133}$$

- Kinematic structure:
$$\lambda^{1/2}\Big[\lambda\,|T_1|^2 + (m_B^2 - m_{K^*}^2)^2\,|T_2|^2 + \frac{8m_B^2 m_{K^*}^2 s}{(m_B+m_{K^*})^2}\,|T_{23}|^2\Big]. \tag{IX.134}$$
Associated combination of WCs:
$$\Big(\big|C^T_{sb\chi1}\big|^2 + \big|C^T_{sb\chi2}\big|^2\Big) + 2\sum_{\alpha<\beta}\Big(\big|C^{\mathrm{TLL}}_{\nu d,\alpha\beta sb}\big|^2 + \big|C^{\mathrm{TLL}}_{\nu d,\alpha\beta bs}\big|^2\Big). \tag{IX.135}$$

In the case of $B \to X_s + \not{E}$, one can readily verify from Table IX.3 that there are only four linearly independent kinematic structures,
$$\begin{aligned}&\lambda^{1/2}(m_b^2, m_s^2, s), \qquad s\,\lambda^{1/2}(m_b^2, m_s^2, s), \qquad s^2\,\lambda^{1/2}(m_b^2, m_s^2, s),\\ &\lambda^{3/2}(m_b^2, m_s^2, s).\end{aligned} \tag{IX.136}$$
The combination of WCs associated with the first kinematic structure reads
$$\big|C^S_{sb\phi}\big|^2 + \frac{(m_b-m_s)^2}{(m_b+m_s)^2}\big|C^P_{sb\phi}\big|^2. \tag{IX.137}$$
The remaining three expressions are more lengthy and generalize the results in Eqs. (IX.115)-(IX.117). However, they do not yield information beyond what can be extracted from measurements of Eqs. (IX.119)-(IX.135). Therefore, we omit discussing them further and instead summarize key aspects of Eqs. (IX.119)-(IX.135) below [1].

- Eqs. (IX.119) and (IX.127) demonstrate that the magnitudes of the WCs associated with scalar dark matter operators with (pseudo)scalar currents can be determined.
- Eqs. (IX.121) and (IX.129) reveal that scalar currents in (SM)LEFT can be distinguished from all considered operators, with the exception of fermionic operators in (D)LEFT featuring both scalar and pseudoscalar currents. Notably, the operator combinations in Eqs. (IX.121) and (IX.129) share a similar Dirac structure.
- We observe that vector currents in (SM)LEFT are always distinguishable from dark vectors and dark scalars with (pseudo)scalar currents. However, Eqs. (IX.123), (IX.131), and (IX.133) indicate that distinguishing vector currents in (SM)LEFT from dark scalars and dark fermions with (axial)vector currents is not always feasible. The operator combinations appearing in these equations exhibit a similar Dirac structure.
- Eqs. (IX.125) and (IX.135) demonstrate that tensor currents in (SM)LEFT can be distinguished from all considered operators, except for dark fermions with tensor currents, through analysis of kinematic distributions alone.

Using purely analytical methods, we have now demonstrated that detailed measurements of kinematic distributions in $B \to K^* + \not{E}$ and $B \to K + \not{E}$ can distinguish contributions from various operators in (SM)LEFT and (D)LEFT. Note that our method, by construction, cannot distinguish a given (SM)LEFT operator from a fermionic (D)LEFT operator with a similar Dirac structure. This would require methods beyond kinematic distributions, which is beyond the scope of our analysis.

IX.2.3 Benchmark illustrations

In this section, we will showcase kinematic distributions for selected examples. The primary purpose is to graphically illustrate differences in kinematic distributions for different operators. Following the Belle II measurement from 2023 [476], we set
$$\mathcal{B}(B \to K + \not{E}) = (1.3 \pm 0.4) \times 10^{-5}, \tag{IX.138}$$

for the $B \to K + \not{E}$ branching fraction in our examples. We emphasize that our goal is not to analyze the recent Belle II data, but rather to utilize the combined inclusive and hadronic tagging results for the $B \to K + \not{E}$ branching fraction as a reference value for our numerical illustrations.[9] A comprehensive analysis would treat the measured branching ratio as a function of BSM parameters, as detailed in Ref. [527]. For simplicity, we analyze a single operator at a time, reserving more complex scenarios with multiple contributing operators for future studies. We focus on the two scalar-current (SM)LEFT operators $\mathcal{O}_{\nu d}^{\rm SLL}$ and $\mathcal{O}_{\nu d}^{\rm SLR}$. The results depend on the chiral structure of the NP inducing the (SM)LEFT operators. We consider two scenarios: a left-right symmetric (LRs) case where $C^{\rm SLR}_{\alpha\beta bs(sb)} = C^{\rm SLL}_{\alpha\beta bs(sb)}$, and a maximally left-right violating (LoR) scenario where only one of the scalar (SM)LEFT operators is present. For clarity, we use central values of branching ratios when calculating WCs.

In the following examples, the discrepancy between the measured $B \to K + \not{E}$ branching fraction and the SM prediction is ascribed to a single new operator. This implies that the operator must account for a NP branching ratio of approximately,

$$\begin{aligned}\mathcal{B}(B \to K + \not{E})_{\rm NP} &= \mathcal{B}(B \to K + \not{E})_{\rm Exp} - \mathcal{B}(B \to K + \not{E})_{\rm SM} \\ &= (0.8 \pm 0.4) \times 10^{-5},\end{aligned} \tag{IX.139}$$

where we have used the SM prediction in (VIII.6). In our effective description, the SM prediction corresponds to a central value of

$$\sum_{\alpha,\beta} \left(1 - \frac{1}{2}\delta_{\alpha\beta}\right) \left|C^{\rm VLL}_{\nu d,\alpha\beta bs} + C^{\rm VLR}_{\nu d,\alpha\beta bs}\right|^2 = 3.0 \times 10^{-16} ({\rm GeV})^{-4}. \tag{IX.140}$$

If the LNV operators $\mathcal{O}_{\nu d}^{\rm SLL}$ and $\mathcal{O}_{\nu d}^{\rm SLR}$ are responsible for the entire NP contribution to $B \to K + \not{E}$, the central value of the WC is

$$\sum_{\alpha\leq\beta} \left(1 - \frac{1}{2}\delta_{\alpha\beta}\right) \left[\left|C^{\rm SLR}_{\alpha\beta sb} + C^{\rm SLL}_{\alpha\beta sb}\right|^2 + \left|C^{\rm SLR}_{\alpha\beta bs} + C^{\rm SLL}_{\alpha\beta bs}\right|^2\right] = 1.4 \times 10^{-16} ({\rm GeV})^{-4}. \tag{IX.141}$$

The corresponding effective scale of NP is

$$\Lambda_{\rm LNV} \approx 9.3\,{\rm TeV}, \tag{IX.142}$$

where the approximate equality reflects the dependence of the effective scale on the flavor structure, i.e. the dependence on α and β, of the induced scalar-current operators.

In the following, we will consider three examples, corresponding to scalar DM, vector (type A) DM, and vector (type B) DM. The examples are structured in the same way: We first list the operators that contribute to $B^+ \to K^+ + \not{E}$. For example, for scalar DM, only the operators $\mathcal{O}^S_{sb\phi}$ and $\mathcal{O}^V_{sb\phi}$ will be considered, c.f. Tab. IX.1. We then list the central values of the WCs obtained by assuming that each of the considered operators account for the full NP contribution to $\mathcal{B}(B^+ \to K^+ + \not{E})$ in Eq. (IX.139). The WCs are also translated into effective operator scales Λ for the readers convenience. With the obtained values for the WCs, we then display kinematic distributions for the various effective operators along with the kinematic distributions of the two (SM)LEFT scalar-current scenarios discussed above.

[9] For some analyses and NP explanations following the Belle II result for $B \to K + \not{E}$, see e.g. [516–526].

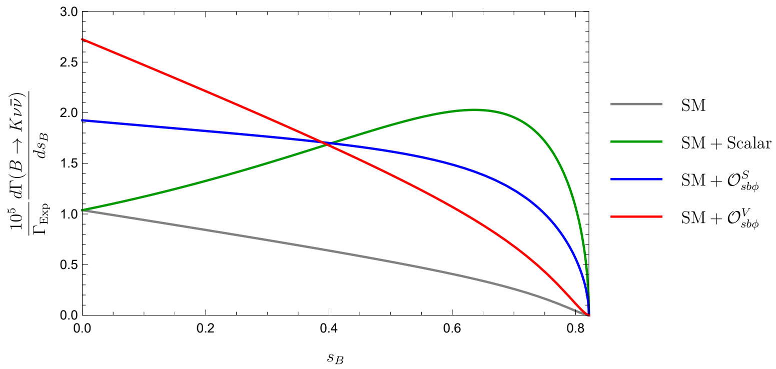

Figure IX.3: **Scalar DM.** Differential decay width of $B \to K + \not{E}$ for the SM (gray), scalar-current (SM)LEFT operators (green), and scalar (D)LEFT operators (blue and red) [1].

Example 1: scalar DM

Out of the four (D)LEFT operators listed in (VIII.20)-(VIII.23), only the following two yield non-vanishing contributions to $B^+ \to K^+ + \not{E}$,

$$\mathcal{O}^S_{sb\phi}, \qquad \mathcal{O}^V_{sb\phi}. \tag{IX.143}$$

When each of these operators is required to account for the entire NP contribution to $\mathcal{B}(B^+ \to K^+ + \not{E})$, the resulting central values for their WCs are

$$\left|C^S_{sb\phi}\right|^2 = 1.5 \times 10^{-15} (\text{GeV})^{-2}, \qquad \left|C^V_{sb\phi}\right|^2 = 2.4 \times 10^{-16} (\text{GeV})^{-4}, \tag{IX.144}$$

which correspond to the following effective scales

$$\Lambda_S \equiv \left|C^S_{sb\phi}\right|^{-1} = 2.6 \times 10^4 \text{ TeV}, \qquad \Lambda_V \equiv |C^V_{sb\phi}\Big|^{-1/2} = 8.0 \text{ TeV}, \tag{IX.145}$$

respectively. With these values for the WCs, we show

$$d\Gamma(B \to K + \not{E})_{\text{SM+NP}}/ds_B, \tag{IX.146}$$

in Fig. IX.3. Here $s_B = s/m_B^2$. The kinematic distributions associated with the (SM)LEFT operators $\mathcal{O}^{\text{SLL}}_{\nu d}$ and $\mathcal{O}^{\text{SLR}}_{\nu d}$, represented by the green curve, differ significantly from those associated with $\mathcal{O}^S_{sb\phi}$ and $\mathcal{O}^V_{sb\phi}$, shown in blue and red, respectively. Consequently, the scenarios are easily distinguishable.

Example 2: Vector DM (A)

The full operator basis for this scenario is listed in Eqs. (VIII.29)-(VIII.44). Ref. [528] demonstrated that the following subset of operators can account for the Belle II excess without conflicting with experimental constraints on $B \to K^*\nu\bar{\nu}$,

$$\mathcal{O}^S_{sbA}, \qquad \mathcal{O}^V_{sbA2}, \qquad \mathcal{O}^V_{sbA3}, \qquad \mathcal{O}^V_{sbA4}, \qquad \mathcal{O}^V_{sbA5}, \qquad \mathcal{O}^V_{sbA6}. \tag{IX.147}$$

Using the contributions of these operators to $d\Gamma(B \to K + \not{E})/ds_B$, as listed in Appendix B.1, we obtain the following central values for their corresponding WCs and associated effective mass scales,

$$\left|C^S_{sbA}\right|^2 = 3.7 \times 10^{-17} (\text{GeV})^{-6}, \qquad \Lambda^S_{sbA} = 550\,\text{GeV}, \tag{IX.148}$$

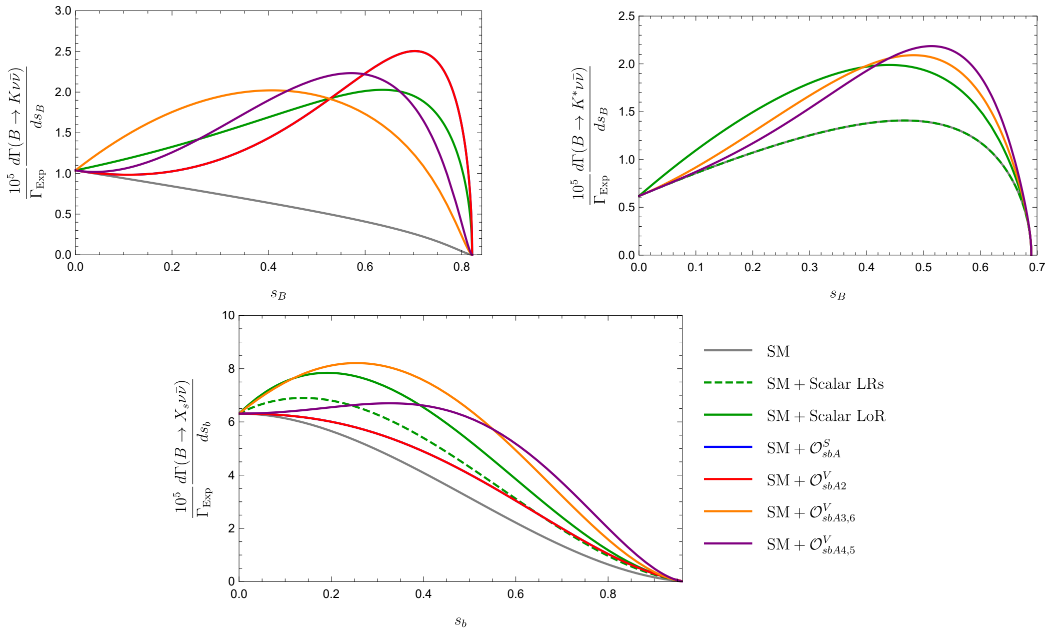

Figure IX.4: **Vector DM (A).** Differential decay width of $B \to K + \not{E}$ (top left), $B \to K^* + \not{E}$ (top right), and $B \to X_s + \not{E}$ (bottom) for the SM (gray), scalar-current (SM)LEFT operators (green), and (D)LEFT operators of type A (blue, red, orange, and purple) [1].

$$\left|C^V_{sbA2}\right|^2 = 5.0 \times 10^{-17}(\text{GeV})^{-8}, \qquad \Lambda^V_{sbA2} = 110\,\text{GeV}, \tag{IX.149}$$
$$\left|C^V_{sbA3}\right|^2 = 2.9 \times 10^{-17}(\text{GeV})^{-6}, \qquad \Lambda^V_{sbA3} = 570\,\text{GeV}, \tag{IX.150}$$
$$\left|C^V_{sbA4}\right|^2 = 9.6 \times 10^{-18}(\text{GeV})^{-8}, \qquad \Lambda^V_{sbA4} = 130\,\text{GeV}, \tag{IX.151}$$
$$\left|C^V_{sbA5}\right|^2 = 9.6 \times 10^{-18}(\text{GeV})^{-8}, \qquad \Lambda^V_{sbA5} = 130\,\text{GeV}, \tag{IX.152}$$
$$\left|C^V_{sbA6}\right|^2 = 2.9 \times 10^{-17}(\text{GeV})^{-6}, \qquad \Lambda^V_{sbA6} = 570\,\text{GeV}. \tag{IX.153}$$

With these values for the WCs, we show

$$d\Gamma(B \to K + \not{E})_{\text{SM+NP}}/ds_B, \tag{IX.154}$$
$$d\Gamma(B \to K^* + \not{E})_{\text{SM+NP}}/ds_B, \tag{IX.155}$$
$$d\Gamma(B \to X_s + \not{E})_{\text{SM+NP}}/ds_b, \tag{IX.156}$$

in Fig. (IX.4). Here $s_b = s/m_b^2$, and we employ the 1S quark-mass value $m_b^{1S} = 4.75$ GeV [529]. The blue and red curves overlap, and equal the SM contribution in $B \to K^* + \not{E}$.

Fig. IX.4 demonstrates the complementarity of different decay channels in identifying the source of NP. Specifically, it shows that the differences between the (SM)LEFT operators and the $\mathcal{O}^V_{sbA2,3,4,5,6}$ operators can be most pronounced for certain values of $s_{B(b)}$ in one decay channel and for different values of $s_{B(b)}$ in another decay channel. This is evident when comparing, for example, the green and purple curves in the three plots.

Example 3: Vector DM (B)

For the final example, the full operator basis is listed in Eqs. (VIII.45)-(VIII.50). The following four operators contribute to $B \to K\nu\widehat{\nu}$,

$$\mathcal{O}^S_{sbB1}, \qquad \mathcal{O}^S_{sbB2}, \qquad \mathcal{O}^T_{sbB1}, \qquad \mathcal{O}^T_{sbB2}. \tag{IX.157}$$

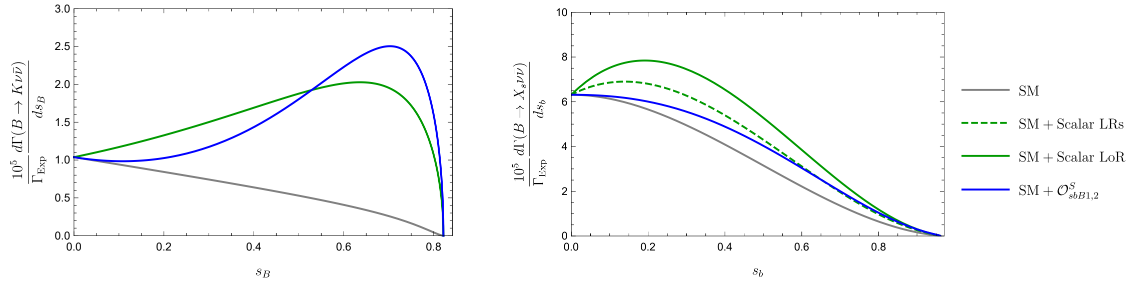

Figure IX.5: **Vector DM (B).** Differential decay width of $B \to K + \not{E}$ (left), and $B \to X_s + \not{E}$ (right) for the SM (gray), scalar-current (SM)LEFT operators (green), and (D)LEFT operators of type B (blue) [1].

The central values for their corresponding WCs and associated effective mass scale are listed below,

$$\left|C^S_{sbB1,2}\right|^2 = 4.6 \times 10^{-18} (\text{GeV})^{-6}, \qquad \Lambda^S_{sbB1,2} = 780\,\text{GeV}, \tag{IX.158}$$

$$\left|C^T_{sbB1,2}\right|^2 = 1.5 \times 10^{-16} (\text{GeV})^{-6}, \qquad \Lambda^T_{sbB1,2} = 430\,\text{GeV}. \tag{IX.159}$$

We found that $\mathcal{O}^T_{sbB1,2}$ are excluded by experimental constraints on $B \to K^*\nu\bar{\nu}$. Using the obtained WCs, we present $d\Gamma(B \to K + \not{E})_{\text{SM+NP}}/ds_B$ and $d\Gamma(B \to X_s + \not{E})_{\text{SM+NP}}/ds_b$ in the left and right panels of Fig. IX.5, respectively. In this scenario, the low $s_{B(b)}$ region is particularly sensitive to distinguishing between the scalar-current (SM)LEFT operators and the (D)LEFT operators $\mathcal{O}^S_{sbB1,2}$.

IX.3 B-meson analysis: Correlations and sum rules

In the previous sections, we have developed theoretical strategies to disentangle NP contributions by studying s-distributions in $b \to s\nu\widehat{\nu}$ transitions. The following discussion aims to highlight alternative strategies that are less involved from the experimental side. First, we will examine correlations between different observables, similar to the analysis performed for Kaons in Section IX.1.2. As a second step, we will investigate the utility of sum rules. Although the majority of this section focuses on NP with neutrinos in the final state, we also provide several comments on (D)LEFT.

IX.3.1 Correlations between branching ratios

In the following, we examine correlations in the $\mathcal{B}(B \to K\nu\widehat{\nu}) - \mathcal{B}(B \to K^*\nu\widehat{\nu})$ and $\mathcal{B}(B \to K^*_T\nu\widehat{\nu}) - \mathcal{B}(B \to K^*_L\nu\widehat{\nu})$ planes, as shown in the upper and lower parts of Fig. IX.6, respectively.[10] Our analysis considers various benchmark scenarios, where only one type of current is present, i.e. only tensor (blue), scalar (green), or vector (red) (SM)LEFT currents.

Tensor currents: Any NP scenario where only tensor currents are present is restricted to the blue lines in Fig. (IX.6). The upper plot reveals that the blue line is incompatible with the light-gray region allowed by Belle II [476] without violating the experimental constraint on $B \to K^*\nu\widehat{\nu}$. This finding is consistent with the results reported in Ref. [483].

Scalar currents: The green lines represent different scenarios where only scalar currents are present. The solid line (Scalar LoR) corresponds to the case where only left-

[10] For a recent analysis of similar ideas, see Ref. [530].

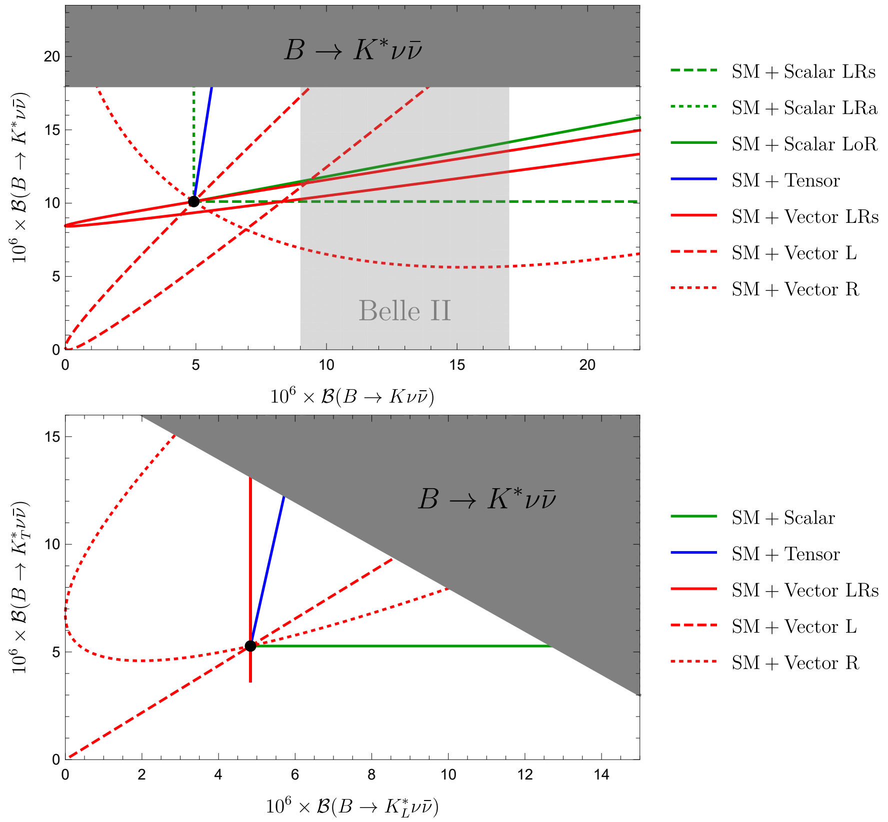

Figure IX.6: $\mathcal{B}(B^+ \to K^+\nu\hat{\nu}) - \mathcal{B}(B \to K^*\nu\hat{\nu})$-plane (top) and $\mathcal{B}(B \to K_L^*\nu\hat{\nu}) - \mathcal{B}(B \to K_T^*\nu\hat{\nu})$-plane (bottom) for different NP scenarios. SM predictions are shown by black points. The light gray region in the upper plot shows the present experimentally allowed range from Belle II [476]. Dark gray regions are excluded by the experimental bound on $B \to K^*\hat{\nu}\nu$ in (VIII.12). Green curves show NP scenarios with scalar currents, blue curves NP scenarios with tensor currents, and red curves NP scenarios with vector currents (see text for details) [1].

handed or only right-handed currents are generated. The dashed line (Scalar LRs) represents the symmetric scenario where $C^{\text{SLL}}_{\nu d,\alpha\beta q_1 q_2} = C^{\text{SLR}}_{\nu d,\alpha\beta q_1 q_2}$, while the dotted line (Scalar LRa) corresponds to the antisymmetric scenario where $C^{\text{SLL}}_{\nu d,\alpha\beta q_1 q_2} = -C^{\text{SLR}}_{\nu d,\alpha\beta q_1 q_2}$. All NP scenarios with only scalar currents are bounded by the dashed and dotted lines in the upper plot and lie on the green line in the lower plot. This is a direct consequence of the fact that scalar currents cannot reduce the theoretical prediction of any B-decay below its SM prediction.

Vector currents: Finally, the red curves illustrate various scenarios where only vector currents are present. Here, we assume LFU, LFC, and that only three SM neutrinos contribute.[11]

The solid curve (Vector LRs) corresponds to the symmetric scenario $C^{\text{VLL}}_{\nu d,\alpha\beta q_1 q_2} - \left(C^{\text{VLL}}_{\nu d,\alpha\beta q_1 q_2}\right)_{\text{SM}} = C^{\text{VLR}}_{\nu d,\alpha\beta q_1 q_2}$, while the dashed curve (Vector L) represents the case with only left-handed currents, and the dotted curve (Vector R) represents the case with only

[11] In the presence of vector currents, interference between SM WCs and NP WCs is possible. The absence of LFV implies maximal interference (as there is no LFV in the SM), and LFU fixes the WCs associated with each generation to be equal (by definition). Relaxing either assumption can generate curves differing from those in Fig. IX.6.

right-handed currents. These curves cover a larger region of the two planes in Fig. IX.6 due to possible interference between NP WCs and SM WCs, allowing for observable values below their SM predictions. If future measurements indicate NP outside the region bounded by the green dashed and dot-dashed curves in the upper plot, and the region bounded by the blue and green lines in the lower plot, it implies the presence of vector currents generated by NP. Notably, only vector currents in (SM)LEFT can access these regions, whereas dark operators with vector currents cannot, as their WCs do not interfere with SM WCs. As discussed in Section IX.2.2, distinguishing vector currents in (SM)LEFT from certain operators in (D)LEFT based on kinematic distributions is not feasible. However, if future measurements reveal observable values lower than SM predictions, it would confirm the presence of vector currents in (SM)LEFT.

IX.3.2 Sum-rule analysis

In the following, we consider a second type of analysis that is readily accessible to experimentalists, namely sum rules. In the seminal paper, Ref. [531], it was shown that under the assumption of LFU, LFC, new vector currents only, and no NP lighter than the B-meson, one can describe the four observables R^ν_K, $\mathcal{R}^\nu_{K^*}$, $\mathcal{R}^\nu_{\rm incl}$, and $\mathcal{R}^\nu_{F_L}$ (to be defined below) in terms of two real parameters, ϵ and η. These results were derived under the assumptions LFU and no LFV. Here, we refine these results and generalize them to scenarios with LFV and violation of LFU, and comment on light dark physics contributions.

If we assume that only the vector-current (SM)LEFT operators (VIII.15) and (VIII.16) contribute to rare B-decays, then the quantities $\mathcal{R}^\nu_K$, $\mathcal{R}^\nu_{K^*}$, $\mathcal{R}^\nu_{\rm incl}$, and $\mathcal{R}^\nu_{F_L}$ can be expressed in terms of real parameters $\epsilon_{\alpha\beta} > 0$ and $\eta_{\alpha\beta} \in [-1/2, 1/2]$ as follows [531],[12]

$$\mathcal{R}^\nu_K \equiv \frac{\mathcal{B}(B\to K\nu\bar\nu)}{\mathcal{B}_{\rm SM}(B\to K\nu\bar\nu)} = \sum_{\alpha\beta}\frac{1}{3}(1-2\eta_{\alpha\beta})\epsilon^2_{\alpha\beta}\,, \tag{IX.160}$$

$$\mathcal{R}^\nu_{K^*} \equiv \frac{\mathcal{B}(B\to K^*\nu\bar\nu)}{\mathcal{B}_{\rm SM}(B\to K^*\nu\bar\nu)} = \sum_{\alpha\beta}\frac{1}{3}(1+\kappa_\eta\eta_{\alpha\beta})\epsilon^2_{\alpha\beta}\,, \tag{IX.161}$$

$$\mathcal{R}^\nu_{\rm incl} \equiv \frac{\mathcal{B}(B\to X_s\nu\bar\nu)}{\mathcal{B}(B\to X_s\nu\bar\nu)_{\rm SM}} = \sum_{\alpha\beta}\frac{1}{3}(1+\kappa_X\eta_{\alpha\beta})\epsilon^2_{\alpha\beta}\,, \tag{IX.162}$$

$$\mathcal{R}^\nu_{F_L} \equiv \frac{F_L}{F_L^{\rm SM}} = \frac{1}{\mathcal{R}^\nu_{K^*}}\sum_{\alpha\beta}\frac{1}{3}(1+2\eta_{\alpha\beta})\epsilon^2_{\alpha\beta}\,, \tag{IX.163}$$

with

$$\epsilon_{\alpha\beta} = \frac{\sqrt{|C^{\rm VLL,SM}_{\nu d,\alpha\beta bs}\delta_{\alpha\beta} + C^{\rm VLL}_{\nu d,\alpha\beta bs}|^2 + |C^{\rm VLR}_{\nu d,\alpha\beta bs}|^2}}{|C^{\rm VLL,SM}_{\nu d,\alpha\beta bs}|}\,, \tag{IX.164}$$

$$\eta_{\alpha\beta} = -\frac{{\rm Re}\left[\left(C^{\rm VLL,SM}_{\nu d,\alpha\beta bs}\delta_{\alpha\beta} + C^{\rm VLL}_{\nu d,\alpha\beta bs}\right)C^{\rm VLR*}_{\nu d,\alpha\beta bs}\right]}{|C^{\rm VLL,SM}_{\nu d,\alpha\beta bs}\delta_{\alpha\beta} + C^{\rm VLL}_{\nu d,\alpha\beta bs}|^2 + |C^{\rm VLR}_{\nu d,\alpha\beta bs}|^2}\,. \tag{IX.165}$$

In the SM, one has $\epsilon_{\alpha\beta} = \delta_{\alpha\beta}$. Note from Eq. (IX.165) that $\eta_{\alpha\beta} \neq 0$ signals the presence of right-handed currents. The parameter κ_η in Eq. (IX.161) depends on the form factors relevant for $B \to K^*$, and its explicit form can be found in Appendix A in Ref. [531].

[12] It is straightforward to verify/ reproduce these results using explicit expressions for branching ratios presented in Section IX.2.

Currently, $\kappa_\eta = 1.33 \pm 0.05$. The parameter κ_X, entering Eq. (IX.162) was introduced for the first time in Ref. [1], and is given by

$$\kappa_X = \frac{12 m_b m_s \int_0^{s_{\max}} ds\, \lambda^{1/2}(s, m_b^2, m_s^2) \cdot s}{\int_0^{s_{\max}} ds\, \lambda^{1/2}(s, m_b^2, m_s^2) \left[\lambda(s, m_b^2, m_s^2) + 3s(m_b^2 + m_s^2 - s)\right]} \approx 0.08. \tag{IX.166}$$

From the relations presented in Eqs. (IX.160)-(IX.163), it is possible to deduce two model-independent relations, as first pointed out in [531] for the case of LFU and LFC. The first relation is

$$\langle F_L \rangle = \langle F_L^{\rm SM} \rangle \left[\left(\frac{(\kappa_\eta - 2)\mathcal{R}_K + 4\,\mathcal{R}_{K^*}}{(\kappa_\eta + 2)\mathcal{R}_{K^*}} \right) + X_1 \right], \tag{IX.167}$$

where X_1 parametrizes NP that is not described by vector-current (SM)LEFT operators. The second relation is

$$\mathcal{B}(B \to X_s\nu\bar{\nu}) = \mathcal{B}(B \to X_s\nu\bar{\nu})_{\rm SM} \left[\left(\frac{\kappa_\eta \mathcal{R}_K + 2\,\mathcal{R}_{K^*} + \kappa_X(\mathcal{R}_{K^*} - \mathcal{R}_K)}{\kappa_\eta + 2} \right) + X_2 \right], \tag{IX.168}$$

where X_2 parametrizes NP that is *not* encoded in vector-current (SM)LEFT operators. We note that this relation is a refinement of the result presented in [531], where the term involving κ_X was neglected. Some important comments regarding Eqs. (IX.167) and (IX.168) are provided below [1].

- Experimental results indicating $X_1 = X_2 = 0$ do not uniquely imply that the vector-current (SM)LEFT operators in Eqs. (VIII.15)–(VIII.16) are the source of NP. Eqs. (IX.167) and (IX.168) with $X_1 = X_2 = 0$ are also satisfied if the NP is scalar Dark Matter (DM) with $\left|C^A_{sb\phi}\right|^2 = \left|C^V_{sb\phi}\right|^2 \neq 0$, with all other NP WCs set to zero. Similarly, this holds if the NP is fermionic DM with $\left|C^A_{sb\chi 1}\right|^2 + \left|C^A_{sb\chi 2}\right|^2 = \left|C^V_{sb\chi 1}\right|^2 + \left|C^V_{sb\chi 2}\right|^2$, with all other NP WCs set to zero. For completeness, we provide derivations of these two statements below. This result is consistent with the analysis in Section IX.2.2, where we demonstrated that vector-current interactions in (SM)LEFT cannot always be disentangled from dark fermions or dark scalars by solely studying $B \to K + \not{E}$, $B \to K^* + \not{E}$, and inclusive decays.
- The relations Eqs. (IX.167) and (IX.168) with $X_1 = X_2 = 0$ hold even in the presence of lepton flavor non-universality and LFV, provided the NP is attributed to either the vector-current (SM)LEFT operators in Eqs. (VIII.15)–(VIII.16) or the aforementioned scenarios involving dark particles. Consequently, measuring a nonzero value for X_1 or X_2 would unambiguously indicate the presence of either particles other than neutrinos in the invisible final state or (SM)LEFT scalar/tensor currents. In other words, a nonzero measurement of X_1 or X_2 could be interpreted as a potential sign of LNV, although a conclusive statement would require additional evidence. This evidence could be strengthened through dedicated studies of s-distributions in $b \to s\nu\bar{\nu}$ transitions, which have the potential to rule out dark scalars and dark fermions as the invisible final states, as demonstrated in Section IX.2.2.

Below, we derive some of the claims above. The sum-rule analysis is continued below Eq. (IX.178).

Derivation of sum-rule claim for scalar DM: In the following, we show that the two sum rules (IX.167) and (IX.168) are satisfied by scalar DM with

$$\left|C^{A}_{sb\phi}\right|^2 = \left|C^{V}_{sb\phi}\right|^2 \tag{IX.169}$$

assuming that all other NP WCs are zero.

From Eqs (IX.2), (IX.8), and (A.1), it follows that

$$\mathcal{R}^{\nu}_{K} \equiv \frac{\mathcal{B}(B\to K+\not{E})}{\mathcal{B}_{\rm SM}(B\to K\nu\bar{\nu})} = 1+\frac{2}{3}\left(\frac{\left|C^{V}_{sb\phi}\right|^2}{\left|C^{\rm VLL(SM)}_{\nu d,\alpha\beta bs}\delta_{\alpha\beta}\right|^2}\right). \tag{IX.170}$$

It follows from Eqs. (IX.85), (IX.88), (IX.89), (B.9), and the assumption in (IX.169), that

$$\mathcal{R}^{\nu}_{K^*} \equiv \frac{\mathcal{B}(B\to K^*+\not{E})}{\mathcal{B}_{\rm SM}(B\to K^*\nu\bar{\nu})} = 1+\frac{2}{3}\left(\frac{\left|C^{V}_{sb\phi}\right|^2}{\left|C^{\rm VLL(SM)}_{\nu d,\alpha\beta bs}\delta_{\alpha\beta}\right|^2}\right) = \mathcal{R}^{\nu}_{K}. \tag{IX.171}$$

It follows from Eqs. (IX.103), (IX.106), (IX.111), (B.13) and the assumption in (IX.169), that

$$\mathcal{R}^{\nu}_{\rm incl} \equiv \frac{\mathcal{B}(B\to X_s+\not{E})}{\mathcal{B}(B\to X_s\nu\bar{\nu})_{\rm SM}} = 1+\frac{2}{3}\left(\frac{\left|C^{V}_{sb\phi}\right|^2}{\left|C^{\rm VLL(SM)}_{\nu d,\alpha\beta bs}\delta_{\alpha\beta}\right|^2}\right) = \mathcal{R}^{\nu}_{K}. \tag{IX.172}$$

The terms proportional to A_{12} in Eq. (B.9) contribute to the longitudinal polarization fraction. This fact, along with Eqs. (IX.66), (IX.71), and the assumption in (IX.169) gives

$$\mathcal{R}^{\nu}_{F_L} \equiv \frac{F_L}{F_L^{\rm SM}} = \frac{1}{\mathcal{R}^{\nu}_{K^*}}\frac{P_L}{P_L^{\rm SM}} = \frac{1}{\mathcal{R}^{\nu}_{K^*}}\left(1+\frac{2}{3}\left(\frac{\left|C^{V}_{sb\phi}\right|^2}{\left|C^{\rm VLL(SM)}_{\nu d,\alpha\beta bs}\delta_{\alpha\beta}\right|^2}\right)\right) = 1. \tag{IX.173}$$

With these results at hand, it is now trivial to verify that Eqs. (IX.167) and (IX.168) are satisfied by (IX.170)-(IX.173), which proves the claim.

Derivation of sum-rule claim for fermion DM: In the following, we show that the two sum rules (IX.167) and (IX.168) are satisfied by fermionic DM with

$$\left|C^{A}_{sb\chi1}\right|^2 + \left|C^{A}_{sb\chi2}\right|^2 = \left|C^{V}_{sb\chi1}\right|^2 + \left|C^{V}_{sb\chi2}\right|^2, \tag{IX.174}$$

assuming that all other NP WCs are zero.

From Eqs (IX.2), (IX.8), and (A.2), it follows that

$$\mathcal{R}^{\nu}_{K} \equiv \frac{\mathcal{B}(B\to K+\not{E})}{\mathcal{B}_{\rm SM}(B\to K\nu\bar{\nu})} = 1+\frac{8}{3}\left(\frac{\left|C^{V}_{sb\chi1}\right|^2+\left|C^{V}_{sb\chi2}\right|^2}{\left|C^{\rm VLL(SM)}_{\nu d,\alpha\beta bs}\delta_{\alpha\beta}\right|^2}\right). \tag{IX.175}$$

It follows from Eqs. (IX.85), (IX.88), (IX.89), (B.10), and the assumption in (IX.174), that

$$\mathcal{R}^{\nu}_{K^*} \equiv \frac{\mathcal{B}(B\to K^*+\not{E})}{\mathcal{B}_{\rm SM}(B\to K^*\nu\bar{\nu})} = 1+\frac{8}{3}\left(\frac{\left|C^{V}_{sb\chi1}\right|^2+\left|C^{V}_{sb\chi2}\right|^2}{\left|C^{\rm VLL(SM)}_{\nu d,\alpha\beta bs}\delta_{\alpha\beta}\right|^2}\right) = \mathcal{R}^{\nu}_{K}. \tag{IX.176}$$

It follows from Eqs. (IX.103), (IX.106), (IX.111), (B.14) and the assumption in (IX.174), that

$$\mathcal{R}^{\nu}_{\text{incl}} \equiv \frac{\mathcal{B}(B \to X_s + \not{E})}{\mathcal{B}(B \to X_s\nu\bar{\nu})_{\text{SM}}} = 1 + \frac{8}{3}\left(\frac{\left|C^V_{sb\chi 1}\right|^2 + \left|C^V_{sb\chi 2}\right|^2}{\left|C^{\text{VLL(SM)}}_{\nu d,\alpha\beta bs}\delta_{\alpha\beta}\right|^2}\right) = \mathcal{R}^{\nu}_K. \tag{IX.177}$$

The terms proportional to A_{12} in Eq. (B.10) along with Eqs. (IX.66), (IX.71), and the assumption in (IX.174) gives

$$\mathcal{R}^{\nu}_{F_L} \equiv \frac{F_L}{F_L^{\text{SM}}} = \frac{1}{\mathcal{R}^{\nu}_{K^*}}\frac{P_L}{P_L^{\text{SM}}} = \frac{1}{\mathcal{R}^{\nu}_{K^*}}\left(1 + \frac{8}{3}\left(\frac{\left|C^V_{sb\chi 1}\right|^2 + \left|C^V_{sb\chi 2}\right|^2}{\left|C^{\text{VLL(SM)}}_{\nu d,\alpha\beta bs}\delta_{\alpha\beta}\right|^2}\right)\right) = 1. \tag{IX.178}$$

It is trivial to verify that Eqs. (IX.167) and (IX.168) are satisfied by (IX.175)-(IX.178), which proves the claim.

Limit of LFU and LFC

Finally, we will comment on the simplifying limit of LFU and LFC, where $\epsilon_{\alpha\beta} = \epsilon$, $\eta_{\alpha\beta} = \eta$ and

$$\epsilon = \frac{\sqrt{|C^{\text{VLL,SM}}_{\nu d,bs} + C^{\text{VLL}}_{\nu d,bs}|^2 + |C^{\text{VLR}}_{\nu d,bs}|^2}}{|C^{\text{VLL,SM}}_{\nu d,bs}|}\,, \qquad \eta = \frac{-\text{Re}\left[\left(C^{\text{VLL,SM}}_{\nu d,bs} + C^{\text{VLL}}_{\nu d,bs}\right)C^{\text{VLR}*}_{\nu d,bs}\right]}{|C^{\text{VLL,SM}}_{\nu d,bs} + C^{\text{VLL}}_{\nu d,bs}|^2 + |C^{\text{VLR}}_{\nu d,bs}|^2}\,. \tag{IX.179}$$

Under these assumptions, the relations above simplify to the results obtained in Ref. [531]:

$$\mathcal{R}^{\nu}_K = (1 - 2\,\eta)\epsilon^2\,, \qquad \mathcal{R}^{\nu}_{K^*} = (1 + \kappa_\eta\eta)\epsilon^2\,, \qquad \mathcal{R}^{\nu}_{F_L} \equiv \frac{F_L}{F_L^{\text{SM}}} = \frac{1+2\eta}{1+\kappa_\eta\eta}\,, \tag{IX.180}$$

$$\mathcal{R}^{\nu}_{\text{incl}} = \frac{\mathcal{B}(B \to X_s\nu\bar{\nu})}{\mathcal{B}(B \to X_s\nu\bar{\nu})_{\text{SM}}} = (1 + \kappa_X\eta)\epsilon^2\,, \tag{IX.181}$$

which leads to very simple correlations between $\mathcal{R}^{\nu}_K$, $\mathcal{R}^{\nu}_{K^*}$, and $\mathcal{R}^{\nu}_{\text{incl}}$,

$$\mathcal{R}^{\nu}_K = \frac{1-2\eta}{1+\kappa_\eta\eta}\mathcal{R}^{\nu}_{K^*} = \frac{1-2\eta}{1+\kappa_X\eta}\mathcal{R}^{\nu}_{\text{incl}}. \tag{IX.182}$$

Notably, the presence of right-handed currents, i.e., $\eta \neq 0$, introduces non-trivial correlations between $\mathcal{R}^{\nu}_K$, $\mathcal{R}^{\nu}_{K^*}$, and $\mathcal{R}^{\nu}_{\text{incl}}$ through Eq. (IX.182). This is in contrast with the dark NP scenarios mentioned above, where either $\left|C^A_{sb\phi}\right|^2 = \left|C^V_{sb\phi}\right|^2$ (scalar DM) or $\left|C^A_{sb\chi 1}\right|^2 + \left|C^A_{sb\chi 2}\right|^2 = \left|C^V_{sb\chi 1}\right|^2 + \left|C^V_{sb\chi 2}\right|^2$ (fermionic DM), resulting in a trivial correlation,

$$\mathcal{R}^{\nu}_K = \mathcal{R}^{\nu}_{K^*} = \mathcal{R}^{\nu}_{\text{incl}}. \tag{IX.183}$$

Thus, while NP scenarios involving only (SM)LEFT vector currents are indistinguishable from the aforementioned (D)LEFT NP scenarios at the level of the sum rules in Eqs. (IX.167) and (IX.168), these (SM)LEFT and (D)LEFT NP scenarios can be discriminated in certain cases by examining the correlations among $\mathcal{R}^{\nu}_K$, $\mathcal{R}^{\nu}_{K^*}$, and $\mathcal{R}^{\nu}_{\text{incl}}$, as summarized below:

- A (SM)LEFT NP scenario where only left-handed vector currents are present cannot be distinguished from the aforementioned dark scalar and dark fermion NP scenarios by measuring correlations among $\mathcal{R}^{\nu}_{K}$, $\mathcal{R}^{\nu}_{K^*}$, and $\mathcal{R}^{\nu}_{\text{incl}}$.
- All other (SM)LEFT NP scenarios involving only vector currents can be distinguished from the aforementioned dark scalar and dark fermion NP scenarios by measuring correlations among $\mathcal{R}^{\nu}_{K}$, $\mathcal{R}^{\nu}_{K^*}$, and $\mathcal{R}^{\nu}_{\text{incl}}$.

The argument straightforwardly extends to the general case described by Eqs. (IX.160)–(IX.163), where no assumptions regarding LFV and LFU are made; however, the correlations between $\mathcal{R}^{\nu}_{K}$, $\mathcal{R}^{\nu}_{K^*}$, and $\mathcal{R}^{\nu}_{\text{incl}}$ are generally more involved.

This section concludes our discussion on strategies for disentangling NP contributions in rare meson decays. In the following section, we expand upon the discussion presented in Chapter VIII regarding LNV in (SM)LEFT and the potential consequences of observing LNV in rare meson decays.

IX.4 Implications of observing LNV in B decays

Next, we consider LNV in rare meson decays. LNV (SM)LEFT operators relevant to rare meson decays were discussed in Chapter VIII, c.f. the summary Table VIII.1. A key observation is that scalar and tensor current operators in (SM)LEFT are generally expected to violate lepton number, whereas vector current operators are expected to conserve lepton number. This distinction has significant implications for interpreting future measurements. Specifically, a non-zero contribution from (SM)LEFT operators with scalar or tensor currents would be a strong indication of LNV NP, while a non-zero contribution from vector current operators would point to LNC NP.

However, this general expectation is not met when the operator involves one active neutrino and one sterile neutrino. In such cases, the vector current operators $\mathcal{O}^{\text{VLL}}_{\nu d}$ and $\mathcal{O}^{\text{VLR}}_{\nu d}$ are LNV, while the scalar and tensor current operators $\mathcal{O}^{\text{SLL}}_{\nu d}$, $\mathcal{O}^{\text{SLR}}_{\nu d}$, and $\mathcal{O}^{\text{TLL}}_{\nu d}$ are LNC. From an experimental standpoint, making definitive statements about the lepton number of operators contributing to rare meson decays is typically challenging due to the difficulty in identifying the invisible final states. Nevertheless, certain inferences regarding LNV/LNC can be drawn based on mass considerations, as discussed below.

The contribution of a single operator $\mathcal{O}$ to the kinematic distribution $d\Gamma/ds$ vanishes for $s < s_{\text{min}} \equiv (m_1 + m_2)^2$, where m_1 and m_2 denote the masses of the two particles in the invisible final state. For the case of two active neutrinos in the final state, the expected range for s_{min} is $0 \lesssim s_{\text{min}} \lesssim (0.2\,\text{eV})^2$.[13] This observation leads to the following two statements:

- If future measurements of NP contributions to kinematic distributions indicate a value of s_{min} that exceeds the upper limit compatible with active neutrino masses, it suggests that NP contributions from active neutrinos alone are unlikely.[14] A potential realization of this scenario is when the lower momentum bins remain consistent with SM predictions, while an experimental excess is observed in bins corresponding to higher s values.

[13]The lower bound is implied by neutrino oscillations [506], which indicate that at least two active neutrinos have non-zero mass, while one neutrino could still be massless. The upper bound is derived from upper limits on absolute neutrino masses obtained from cosmological observations [17] and Tritium decay experiments [532, 533].

[14]This assertion relies on the assumption that the contribution from active neutrinos to the bin containing s_{min} is not significantly suppressed relative to contributions to bins at larger s values.

- If future measurements disfavor NP contributions with $s_{\rm min}$ above a certain threshold $s_{\rm min}^{\rm max}$, they would also disfavor contributions involving one active neutrino and one sterile neutrino with a mass $m_N > \sqrt{s_{\rm min}^{\rm max}}$. Similarly, contributions involving two sterile neutrinos with a mass $m_N > \frac{1}{2}\sqrt{s_{\rm min}^{\rm max}}$ would also be disfavored.

Analogous considerations apply to processes described by (D)LEFT. Specifically, an experimental excess characterized by $s_{\rm min}^{\rm exp}$ consistent with the smallness of active neutrino masses, and a distribution compatible with scalar, tensor, or vector currents in (SM)LEFT, could potentially be attributed to various scenarios, including very light or massless dark scalars, dark fermions, or different combinations of active and sterile neutrinos, see Eqs. (IX.121)–(IX.135). This highlights the need for complementary probes beyond kinematic distributions to determine the exact nature of the final states. However, exploring such probes lies beyond the scope of this work. In the following, we will instead discuss implications that an observation consistent with an LNV hypothesis could have on our understanding of leptogenesis and flavor structure in the UV.

IX.4.1 Implications for LNV physics and UV completions

To make our discussion concrete, we will focus on the compatibility of neutrinoless double beta decay ($0\nu\beta\beta$) and radiative neutrino mass corrections with the observation of LNV in rare meson decays. This will enable us to speculate about the flavor structures in the UV completion. Building upon the discussion in Section VIII.4, we will also examine the viability of leptogenesis scenarios if LNV is observed in rare meson decays. Our arguments rely on the assumption of a natural UV completion, where the NP contribution to the WCs is determined by the mass scale at which NP emerges. However, a caveat to our discussion arises if different contributions are canceled in the UV completion, which could potentially relax the NP-scale estimates presented below. The following discussion follows that in Ref. [1] very closely.

To estimate the scale of NP, we first need to match LEFT to SMEFT (for NP above the electroweak scale). The results of relevance to us, derived under the assumption that only active neutrinos contribute to NP, can be found in Ref. [486],

$$C^{\rm SLL}_{\nu d,\alpha\beta pr} = -\frac{v}{4\sqrt{2}}\left(C^{p\alpha r\beta}_{\bar{d}LQLH1} + C^{p\beta r\alpha}_{\bar{d}LQLH1}\right), \qquad C^{\rm SLR}_{\nu d,\alpha\beta pr} = 0, \tag{IX.184}$$

$$C^{\rm TLL}_{\nu d,\alpha\beta pr} = \frac{v}{16\sqrt{2}}\left(C^{p\alpha r\beta}_{\bar{d}LQLH1} - C^{p\beta r\alpha}_{\bar{d}LQLH1}\right), \tag{IX.185}$$

where the dimension-7 SMEFT operator $\mathcal{O}_{\bar{d}LQLH1}$ is given by,

$$\mathcal{O}_{\bar{d}LQLH1} = \epsilon_{ij}\epsilon_{mn}\left(\bar{d}L^i\right)\left(\overline{Q^{Cj}}L^m\right)H^n. \tag{IX.186}$$

This SMEFT operator also contributes to $0\nu\beta\beta$ decay, as shown by the Feynman diagram to the left in Fig. IX.7. The current best constraints from non-observation of $0\nu\beta\beta$ decay reads [454],

$$C_{\bar{d}LQLH1} \lesssim 7.06\cdot 10^{-8}({\rm TeV})^{-3}, \qquad \Lambda_{\rm NP} \approx 242\,{\rm TeV}. \tag{IX.187}$$

It is instructive to compare this bound with the constraints on NP derived from rare meson decays. By utilizing the effective WC obtained in Eq. (IX.141) and the matching relation in Eq. (IX.184), we derive the following bound from rare B-meson decays at Belle II,

$$C_{\bar{d}LQLH1} \lesssim 0.039\,({\rm TeV})^{-3}, \qquad \Lambda_{\rm NP} \approx 3.0\,{\rm TeV}. \tag{IX.188}$$

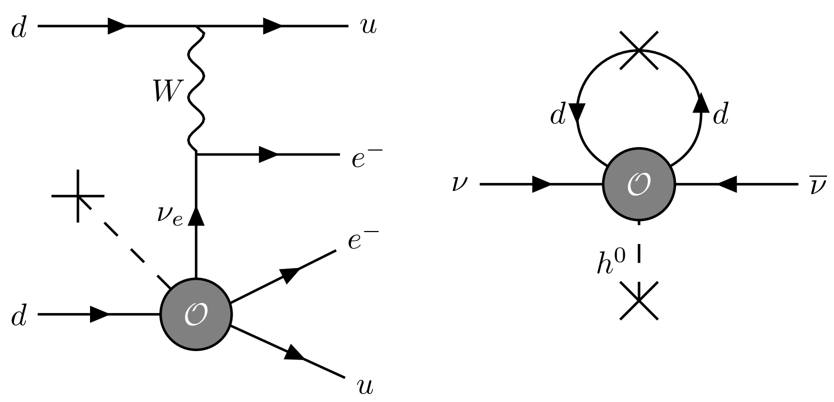

Figure IX.7: Contribution to $0\nu\beta\beta$ decay (left) and radiative neutrino-mass diagram (right) from $\mathcal{O}_{\bar{d}LQLH1}$ [1].

The numerical values in Eq. (IX.188) correspond to a scenario where the underlying couplings are flavor-conserving and flavor universal. This NP bound on $C_{\bar{d}LQLH1}$ is orders of magnitude lower than the corresponding constraint from $0\nu\beta\beta$ in Eq. (IX.187). The crucial observation is that in $0\nu\beta\beta$ decay, only a single flavor combination is tested and the bound (IX.187) only applies to $\mathcal{O}_{\bar{d}LQLH1}$ with quarks in the first generation and the leptons realized as electron and an electron neutrino. In light of this, we conclude that observing LNV in rare-meson decays would provide evidence for the UV physics being flavor non-democratic.

Next, we consider how LNV in rare meson decays could relate to (the origin of) neutrino masses. Higher-dimensional LNV operators induce radiative corrections to Majorana neutrino masses [74, 534], as shown for $\mathcal{O}_{\bar{d}LQLH1}$ to the right in Fig. IX.7. The radiative-mass contribution from $\mathcal{O}_{\bar{d}LQLH1}$ can be estimated as

$$\delta m_\nu \approx \frac{y_d v^2}{16\pi^2 \Lambda_{\rm NP}}. \tag{IX.189}$$

Assuming the radiative contribution to the neutrino mass in Eq. (IX.189) does not exceed ~ 0.1 eV, we obtain a lower bound on the NP scale, $\Lambda_{\rm NP} \gtrsim 5\times 10^4$ TeV (10^9 GeV), for the first (second) generation down-type quark Yukawa coupling, $y_d = m_d/v$. Hence, the NP scale associated with observation of LNV in rare meson decays remains orders of magnitude lower than the lower bound on the NP scale set by neutrino-mass considerations. However, note that the contribution in Eq. (IX.189) arises from the flavor-diagonal component of $\mathcal{O}_{\bar{d}LQLH1}$, whereas the contributions to rare meson decays stem from the off-diagonal elements. This observation constitutes a second argument for why we would expect non-trivial flavor structures in the UV, if we observe LNV in rare meson decays.[15]

Finally, recall from our discussion in Section VIII.4 that an observation of LNV in rare-meson decays could put (high-scale) leptogenesis models under tension. There, we considered washout effects of a general LNV operator with associated scale Λ. Under certain assumptions, we obtained a lower bound on the asymmetry-generation temperature, $T_{\rm LG}$, for which an asymmetry of order one would be washed out by the LNV operator to give a BAU below the observed value, c.f. Eq. (VIII.53) and the surrounding discussion. Following the approach outlined in Ref. [535], we compute the coefficient c_D that enters

[15] See Ref. [503] for an example of a UV setup with leptoquarks yielding sufficiently suppressed neutrino-mass contributions in the context of LNV in rare meson decays.

Eq. (VIII.53) for the dimension-seven SMEFT operator $\mathcal{O}_{\bar{d}LQLH1}$, which is relevant to our analysis, and obtain

$$c_D = \frac{11\sqrt{195}}{7\pi^7}. \tag{IX.190}$$

With this value of c_D and the cutoff scale in Eq. (IX.188), we find

$$T_{\rm LG} \gtrsim v. \tag{IX.191}$$

Hence, observing rare meson decays induced by $\mathcal{O}_{\bar{d}LQLH1}$ would imply a new $\Delta L = 2$ washout contribution that is highly efficient down to the electroweak phase transition.

IX.5 Summary

In this chapter, we considered the rare meson decays, $K \to \pi + \not{E}$, $B \to K + \not{E}$, $B \to K^* + \not{E}$, and $B \to X + \not{E}$, which impose significant constraints on NP beyond the SM. Still, a considerable gap remains between SM predictions and current experimental data, leaving room for potential NP. In anticipation of forthcoming analysis that may reveal further discrepancies with SM expectations [473,476], we have proposed a quantitative approach to distinguish the origin of NP by analyzing kinematic distributions, focusing on disentangling processes within (SM)LEFT [536] and (D)LEFT [484] in the limit of massless neutrinos and dark-sector particles. In the following we summarize some highlights.

In the context of NP fully described by (SM)LEFT, we showed that it is possible to:

- Separate contributions from (SM)LEFT operators with scalar, vector, and tensor currents in rare meson decays.
- Disentangle left-handed vector currents from right-handed vector currents.
- Determine if scalar currents have a definite handedness, or if both left-handed and right-handed scalar currents are present.

In the context of NP described fully by (SM)LEFT and (D)LEFT, we demonstrated that it is in principle possible to:

- Disentangle scalar-current (SM)LEFT operators from all (D)LEFT operators with dark scalars and all (D)LEFT operators with dark vectors.
- Disentangle operators with vector currents in (SM)LEFT from all (D)LEFT operators with spin-1 fields, and all (D)LEFT operators with dark scalars involving (pseudo)scalar currents.
- Disentangle tensor-current (SM)LEFT operators from all (D)LEFT operators with dark scalars and all (D)LEFT operators with dark vectors.
- Not possible to distinguish operators with similar Dirac structure, as summarized in Eqs. (IX.119)-(IX.125) for $B \to K + \not{E}$ and (IX.127)-(IX.135) for $B \to K^* + \not{E}$.

The main topic of this chapter, disentangling NP in rare meson decays using kinematic distributions. We acknowledge that this may be experimentally challenging to execute in the near future. For this reason, we also outlined more experimentally-accessible strategies:

- A novel correlations in the $\mathcal{B}(K^+ \to \pi^+\nu\bar{\nu}) - \mathcal{B}(K_L \to \pi^0\nu\bar{\nu})$-plane for pure scalar-current contributions, under the simplifying assumption of lepton-flavor conservation and universality, see Section IX.1.2.
- We demonstrated that the complex phase in the scalar-current WC can be probed in a combined analysis of $d\Gamma(K^+ \to \pi^+\nu\bar{\nu})/ds$ and $d\Gamma(K_L \to \pi^0\nu\bar{\nu})/ds$, see Section IX.1.3.

- We showed new correlations in the $\mathcal{B}(B^+ \to K^+\nu\bar{\nu}) - \mathcal{B}(B \to K^*\nu\bar{\nu})$-plane and the $\mathcal{B}(B \to K_L^*\nu\bar{\nu}) - \mathcal{B}(B \to K_T^*\nu\bar{\nu})$-plane for different (SM)LEFT NP scenarios where only scalar currents, tensor currents, or vector currents are generated, see Section IX.3.1.
- We revisited, refined, and extended two previously known model-independent sum rules that are valid in the presence of LFU violation and LFV [531]. The first result relates $\langle F_L \rangle$ to $\mathcal{R}_K$ and $\mathcal{R}_{K^*}$, and the second relates $\mathcal{B}(B \to X_s\nu\bar{\nu})$ to $\mathcal{R}_K$ and $\mathcal{R}_{K^*}$. We found that these relations only hold for (SM)LEFT operators with vector currents, as was previously known, and for two additional scenarios involving dark scalars and dark fermions. By considering correlations between $\mathcal{R}_K$, $\mathcal{R}_{K^*}$, and $\mathcal{R}^\nu_{\text{incl}}$, we showed that these dark-sector scenarios are distinguishable from (SM)LEFT scenarios where right-handed vector currents are generated, see Section IX.3.2.
- The violation of either of the model-independent sum rules mentioned above would unambiguously signal either the presence of new particles in the invisible final state or scalar/tensor currents in the neutrino sector.

Finally, we discussed prospects of observing LNV in rare meson decays, and compared bounds with those from (non-observation of) $0\nu\beta\beta$ decay and radiative neutrino-mass generation. We found that an experimental excess consistent with (SM)LEFT scalar-currents, would either point to highly flavor non-democratic LNV UV physics or LNC physics involving sterile neutrinos or dark-sector fermions. We also showed how an observation of LNV in rare meson decays would point to a new washout contribution in leptogenesis that is highly efficient down to the electroweak phase transition, and has the potential to put (high-scale) leptogenesis models under severe tension.

A Differential decay widths for Kaons

This Appendix provides explicit expressions for differential decay widths that were not given explicitly in the main sections. All results are given in the limit of vanishing masses for the invisible final-state particles. The calculations were performed using FeynCalc [505].

A.1 $K^+ \to \pi^+$+inv

Scalar DM final state

The result for a *complex* scalar is,

$$\frac{d\Gamma}{ds} = \frac{B_+^2 \lambda^{1/2}(m_{K^+}^2, m_{\pi^+}^2, s)}{256\pi^3 m_{K^+}^3} \left| f_0^{K^+}(s) \right|^2 \left| C_{ds\phi}^S \right|^2 + \frac{\lambda^{3/2}(m_{K^+}^2, m_{\pi^+}^2, s)}{768\pi^3 m_{K^+}^3} \left| f_+^{K^+}(s) \right|^2 \left| C_{ds\phi}^V \right|^2 , \tag{A.1}$$

while for *real* scalars the term in the second line vanishes, and the term in the first line is a factor 2 larger. The form factors are found in Section VIII.5 and B_+ is given in Eq. IX.9. This result is in agreement with (15) in [484].

Fermion DM final state

$$\frac{d\Gamma}{ds} = \frac{B_+^2 \, s \, \lambda^{1/2}(m_{K^+}^2, m_{\pi^+}^2, s)}{128\pi^3 m_{K^+}^3} \left| f_0^{K^+}(s) \right|^2 \left(\left| C_{ds\chi1}^S \right|^2 + \left| C_{ds\chi2}^S \right|^2 \right)$$

$$+ \frac{\lambda^{3/2}(m_{K^+}^2, m_{\pi^+}^2, s)}{192\pi^3 m_{K^+}^3} \left|f_+^{K^+}(s)\right|^2 \left(\left|C_{ds\chi1}^V\right|^2 + \left|C_{ds\chi2}^V\right|^2\right)$$
$$+ \frac{s\,\lambda^{3/2}(m_{K^+}^2, m_{\pi^+}^2, s)}{96\pi^3 m_{K^+}^3 (m_{K^+} + m_{\pi^+})^2} \left|f_T^{K^+}(s)\right|^2 \left(\left|C_{ds\chi1}^T\right|^2 + \left|C_{ds\chi2}^T\right|^2\right). \tag{A.2}$$

This result is consistent with the result presented in Appendix A in [528].

Vector DM final state (case A)

The result in the massless limit, $m \to 0$, reads,

$$\begin{aligned}
\frac{d\Gamma}{ds} &= \frac{B_+^2\, s^2\, \lambda^{1/2}(m_{K^+}^2, m_{\pi^+}^2, s)}{1024\pi^3 m_{K^+}^3} \left|f_0^{K^+}(s)\right|^2 \left|\tilde{C}_{dsA}^S\right|^2 \\
&+ \frac{s^2 (m_{K^+}^2 - m_{\pi^+}^2)^2\, \lambda^{1/2}(m_{K^+}^2, m_{\pi^+}^2, s)}{1024\pi^3 m_{K^+}^3} \left|f_0^{K^+}(s)\right|^2 \left|\tilde{C}_{dsA2}^V\right|^2 \\
&+ \frac{s\,\lambda^{3/2}(m_{K^+}^2, m_{\pi^+}^2, s)}{768\pi^3 m_{K^+}^3} \left|f_+^{K^+}(s)\right|^2 \left(\left|\tilde{C}_{dsA3}^V\right|^2 + \left|\tilde{C}_{dsA6}^V\right|^2\right) \\
&+ \frac{s^2\,\lambda^{3/2}(m_{K^+}^2, m_{\pi^+}^2, s)}{3072\pi^3 m_{K^+}^3} \left|f_+^{K^+}(s)\right|^2 \left(\left|\tilde{C}_{dsA4}^V\right|^2 + \left|\tilde{C}_{dsA5}^V\right|^2\right) \\
&+ \frac{s^2\,\lambda^{3/2}(m_{K^+}^2, m_{\pi^+}^2, s)}{3072\pi^3 m_{K^+}^3 (m_{K^+} + m_{\pi^+})^2} \left|f_T^{K^+}(s)\right|^2 \left|\tilde{C}_{dsA1}^T\right|^2 \\
&+ \mathcal{O}(m^2) \left|\tilde{C}_{dsA2}^T\right|^2 \\
&+ \frac{(m_{K^+}^2 - m_{\pi^+}^2)^2 s^2\, \lambda^{1/2}(m_{K^+}^2, m_{\pi^+}^2, s)}{512\pi^3 m_{K^+}^3 (m_s - m_d)} \left|f_0^{K^+}(s)\right|^2 \mathrm{Im}\left(\tilde{C}_{dsA}^{S*}\tilde{C}_{dsA2}^V\right) \\
&+ \frac{s^2 \lambda^{3/2}(m_{K^+}^2, m_{\pi^+}^2, s)}{1536\pi^3 m_{K^+}^3 (m_{K^+} + m_{\pi^+})} f_+^{K^+} f_T^{K^+} \mathrm{Re}\left[\tilde{C}_{dsA1}^T \left(\tilde{C}_{dsA5}^V - \tilde{C}_{dsA4}^V\right)^*\right] \\
&- \frac{s^2 \lambda^{3/2}(m_{K^+}^2, m_{\pi^+}^2, s)}{1536\pi^3 m_{K^+}^3} \left|f_+^{K^+}(s)\right|^2 \mathrm{Re}\left(\tilde{C}_{dsA4}^V \tilde{C}_{dsA5}^{V*}\right) + \mathcal{O}(m)\mathrm{Re}\left(\tilde{C}_{dsA2}^T \tilde{C}_{dsA6}^{V*}\right),
\end{aligned} \tag{A.3}$$

where the WCs with a tilde are formally defined as

$$\begin{aligned}
C_{dsA}^{S,P} &\equiv m^2 \tilde{C}_{dsA}^{S,P}, \quad C_{dsA2,4,5}^{V,A} \equiv m^2 \tilde{C}_{dsA2,4,5}^{V,A}, \quad C_{dsA3,6}^{V,A} \equiv m \tilde{C}_{dsA3,6}^{V,A}, \\
C_{dsA1,2}^T &\equiv m^2 \tilde{C}_{dsA1}^T,
\end{aligned} \tag{A.4}$$

to retain non-diverging results for the decay widths $\Gamma(B \to K + \not{E})$ and $\Gamma(B \to K^* + \not{E})$ in the limit $m \to 0$ [484]. These results agree with (21) and (23) in [484], up to the interference terms, which were presented in Ref. [1] for the first time.

Vector DM final state (case B)

$$\begin{aligned}
\frac{d\Gamma}{ds} &= \frac{B_+^2\, s^2\, \lambda^{1/2}(m_{K^+}^2, m_{\pi^+}^2, s)}{128\pi^3 m_{K^+}^3} \left|f_0^{K^+}(s)\right|^2 \left(\left|C_{dsB1}^S\right|^2 + \left|C_{dsB2}^S\right|^2\right) \\
&+ \frac{s^2\,\lambda^{3/2}(m_{K^+}^2, m_{\pi^+}^2, s)}{1536\pi^3 m_{K^+}^3 (m_{K^+} + m_{\pi^+})^2} \left|f_T^{K^+}(s)\right|^2 \left(\left|C_{dsB1}^T\right|^2 + \left|C_{dsB2}^T\right|^2\right).
\end{aligned} \tag{A.5}$$

This result is in agreement with (25) in [484].

A.2 $K_L \to \pi^0$+inv

Scalar DM final state

The result can be obtained from (A.1) by making the following replacements [484]: $K^+ \to K^0$, $C^S_{ds\phi} \to \mathrm{Re}\left(C^S_{ds\phi}\right)$, and $C^V_{ds\phi} \to \mathrm{Im}\left(C^V_{ds\phi}\right)$.

Fermion DM final state

The result can be obtained by replacing $K^+ \to K^0$ and

$$\begin{aligned} \left|C^S_{ds\chi1,2}\right|^2 &\to \left|\mathrm{Re}\left(C^S_{ds\chi1,2}\right)\right|, \qquad & \left|C^V_{ds\chi1,2}\right|^2 &\to \left|\mathrm{Im}\left(C^V_{ds\chi1,2}\right)\right|^2 \\ \left|C^T_{ds\chi1}\right|^2 &\to \left|\mathrm{Re}\left(C^T_{ds\chi1}\right)\right|, \qquad & \left|C^V_{ds\chi2}\right|^2 &\to \left|\mathrm{Im}\left(C^V_{ds\chi2}\right)\right|^2 \end{aligned} \tag{A.6}$$

in (A.2).

Vector DM final state (case A)

The result is in this case obtained by replacing $K^+ \to K^0$ and

$$\begin{aligned} \left|\tilde{C}^S_{dsA}\right|^2 &\to \left|\mathrm{Re}\left(\tilde{C}^S_{dsA}\right)\right|^2, \qquad & \left|\tilde{C}^V_{dsA2-6}\right|^2 &\to \left|\mathrm{Im}\left(\tilde{C}^V_{dsA2-6}\right)\right|^2, \\ \left|\tilde{C}^T_{dsA1}\right|^2 &\to \left|\mathrm{Re}\left(\tilde{C}^T_{dsA1}\right)\right|^2, \qquad & \left|\tilde{C}^T_{dsA2}\right|^2 &\to \left|\mathrm{Im}\left(\tilde{C}^T_{dsA2}\right)\right|^2, \end{aligned} \tag{A.7}$$

in (A.3).

Vector DM final state (case B)

The result is obtained by replacing $K^+ \to K^0$ and

$$\begin{aligned} \left|C^S_{dsB1,2}\right|^2 &\to \left|\mathrm{Re}\left(C^S_{dsB1,2}\right)\right|^2, \qquad & \left|C^T_{dsB1}\right|^2 &\to \left|\mathrm{Re}\left(C^T_{dsB1}\right)\right|^2, \\ \left|C^T_{dsB2}\right|^2 &\to \left|\mathrm{Im}\left(C^T_{dsB2}\right)\right|^2, \end{aligned} \tag{A.8}$$

in (A.5).

B Differential decay widths for B-mesons

B.1 $B \to K$+inv

All results for $B \to K$+inv can be extracted from Sections IX.1.1 and A.1, by replacing $K \to B$, $\pi \to K$, $m_s \to m_b$, $m_d \to m_s$, and form factors appropriately.

B.2 $B \to K^*$+inv

Scalar DM final state

$$\begin{aligned} \frac{d\Gamma}{ds} &= \frac{\lambda^{3/2}(m_B^2, m_{K^*}^2, s)A_0^2(s)}{256\pi^3 m_B^3 (m_b+m_s)^2}\left|C^P_{sb\phi}\right|^2 \\ &+ \frac{\lambda^{1/2}(m_B^2, m_{K^*}^2, s)}{384\pi^3 m_B^3}\left[s\,(m_B+m_{K^*})^2 A_1^2(s) + 32 m_B^2 m_{K^*}^2 A_{12}^2(s)\right]\left|C^A_{sb\phi}\right|^2 \\ &+ \frac{s\,\lambda^{3/2}(m_B^2, m_{K^*}^2, s)V_0^2(s)}{384\pi^3 m_B^3 (m_B+m_{K^*})^2}\left|C^V_{sb\phi}\right|^2 . \end{aligned} \tag{B.9}$$

This result was first obtained in [484].

Fermion DM final state

$$
\begin{aligned}
\frac{d\Gamma}{ds} &= \frac{s\,\lambda^{3/2}(m_B^2, m_{K^*}^2, s) A_0^2(s)}{128\pi^3 m_B^3 (m_b+m_s)^2} \left(\left|C^P_{sb\chi 1}\right|^2 + \left|C^P_{sb\chi 2}\right|^2 \right) \\
&+ \frac{\lambda^{1/2}(m_B^2, m_{K^*}^2, s)}{96\pi^3 m_B^3} \left[A_1^2(s)\, s\,(m_B+m_{K^*})^2 + 32 A_{12}^2(s) m_B^2 m_{K^*}^2 \right] \left(\left|C^A_{sb\chi 1}\right|^2 + \left|C^A_{sb\chi 2}\right|^2 \right) \\
&+ \frac{s\,\lambda^{3/2}(m_B^2, m_{K^*}^2, s) V_0^2(s)}{96\pi^3 m_B^3 (m_B+m_{K^*})^2} \left(\left|C^V_{sb\chi 1}\right|^2 + \left|C^V_{sb\chi 2}\right|^2 \right) \\
&+ \frac{\lambda^{1/2}(m_B^2, m_{K^*}^2, s)}{48\pi^3 m_B^3} \left[T_1^2(s)\,\lambda(m_B^2, m_{K^*}^2, s) + T_2^2(s)\,(m_B^2 - m_{K^*}^2)^2 + T_{23}^2 \frac{8 m_B^2 m_{K^*}^2\, s}{(m_B+m_{K^*})^2} \right] \\
&\times \left(\left|C^T_{sb\chi 1}\right|^2 + \left|C^T_{sb\chi 2}\right|^2 \right). \qquad \text{(B.10)}
\end{aligned}
$$

The first two lines were first reported in Ref. [1], while the rest was first obtained in [528].

Vector DM final state (case A)

$$
\begin{aligned}
\frac{d\Gamma}{ds} &= \frac{s^2 \lambda^{3/2}(m_B^2, m_{K^*}^2, s)\, |A_0(s)|^2}{1024\pi^3 m_B^3 (m_b+m_s)^2} \left|\tilde{C}^P_{sbA}\right|^2 \\
&+ \frac{s \lambda^{3/2}(m_B^2, m_{K^*}^2, s)\, |T_1(s)|^2}{1536\pi^3 m_B^3} \left|\tilde{C}^T_{sbA1}\right|^2 \\
&+ \frac{s \lambda^{1/2}(m_B^2, m_{K^*}^2, s)}{1536\pi^3 m_B^3} \left[\left(m_B^2 - m_{K^*}^2\right)^2 |T_2(s)|^2 + \frac{8 m_B^2 m_{K^*}^2 s}{(m_B+m_{K^*})^2} |T_{23}(s)|^2 \right] \left|\tilde{C}^T_{sbA2}\right|^2 \\
&+ \mathcal{O}(m^2) \left|\tilde{C}^V_{sbA2}\right|^2 \\
&+ \frac{s^2 \lambda^{3/2}(m_B^2, m_{K^*}^2, s)\, |V_0(s)|^2}{384\pi^3 m_B^3 (m_B+m_{K^*})^2} \left(\left|\tilde{C}^V_{sbA3}\right|^2 + \left|\tilde{C}^V_{sbA6}\right|^2 \right) \\
&+ \frac{s^3 \lambda^{3/2}(m_B^2, m_{K^*}^2, s)\, |V_0(s)|^2}{1536\pi^3 m_B^3 (m_B+m_{K^*})^2} \left(\left|\tilde{C}^V_{sbA4}\right|^2 + \left|\tilde{C}^V_{sbA5}\right|^2 \right) \\
&+ \frac{s^2 \lambda^{3/2}(m_B^2, m_{K^*}^2, s)\, |A_0(s)|^2}{1028\pi^3 m_B^3} \left|\tilde{C}^A_{sbA2}\right|^2 \\
&+ \frac{s\, \lambda^{1/2}(m_B^2, m_{K^*}^2, s)}{384\pi^3 m_B^3} \left[(m_B+m_{K^*})^2 s\, |A_1(s)|^2 + 32 m_B^2 m_{K^*}^2 |A_{12}(s)|^2 \right] \left(\left|\tilde{C}^A_{sbA3}\right|^2 + \left|\tilde{C}^A_{sbA6}\right|^2 \right) \\
&+ \frac{s^2 \lambda^{1/2}(m_B^2, m_{K^*}^2, s)}{1536\pi^3 m_B^3} \left[(m_B+m_{K^*})^2 s\, |A_1(s)|^2 + 32 m_B^2 m_{K^*}^2 |A_{12}(s)|^2 \right] \left(\left|\tilde{C}^A_{sbA4}\right|^2 + \left|\tilde{C}^A_{sbA5}\right|^2 \right) \\
&+ \frac{s^2 \lambda^{3/2}(m_B^2, m_{K^*}^2, s)\, |A_0(s)|^2}{512\pi^3 m_B^3 (m_b+m_s)} \mathrm{Im}\left(\tilde{C}^{P*}_{sbA} \tilde{C}^A_{sbA2} \right) - \frac{s^3 \lambda^{3/2}(m_B^2, m_{K^*}^2, s)\, |V_0(s)|^2}{768\pi^3 m_B^3 (m_B+m_{K^*})^2} \mathrm{Re}\left(\tilde{C}^{V*}_{sbA4} \tilde{C}^V_{sbA5} \right) \\
&- \frac{s^2 \lambda^{1/2}(m_B^2, m_{K^*}^2, s)}{768\pi^3 m_B^3} \left[(m_B+m_{K^*})^2 s\, |A_1(s)|^2 + 32 m_B^2 m_{K^*}^2 |A_{12}(s)|^2 \right] \mathrm{Re}\left(\tilde{C}^{A*}_{sbA4} \tilde{C}^A_{sbA5} \right) \\
&+ \frac{s^2 \lambda^{3/2}(m_B^2, m_{K^*}^2, s) T_1(s) V_0(s)}{768\pi^3 m_B^3 (m_B+m_{K^*})} \mathrm{Re}\left[\left(\tilde{C}^V_{sbA4} - \tilde{C}^V_{sbA5} \right)^* \tilde{C}^T_{sbA1} \right] \\
&+ \frac{s^2 \lambda^{1/2}(m_B^2, m_{K^*}^2, s)}{768\pi^3 m_B^3 (m_B+m_{K^*})} \left[(m_B^2 - m_{K^*}^2)(m_B+m_{K^*})^2 A_1(s) T_2(s) + 16 m_B^2 m_{K^*}^2 A_{12}(s) T_{23}(s) \right]
\end{aligned}
$$

$$\times\,\mathrm{Im}\left[\left(\tilde{C}^{A}_{sbA4}-\tilde{C}^{A}_{sbA5}\right)^{*}\tilde{C}^{T}_{sbA2}\right]+\mathcal{O}(m)\mathrm{Re}\left(\tilde{C}^{V*}_{sbA6}\tilde{C}^{T}_{sbA2}\right)+\mathcal{O}(m)\mathrm{Im}\left(\tilde{C}^{A*}_{sbA6}\tilde{C}^{T}_{sbA1}\right). \tag{B.11}$$

The WCs with tilde are defined as in Eq. (A.4). The result for the non-interference terms agrees with results reported in Ref. [484], while the interference terms were presented in Ref. [1] for the first time.

Vector DM final state (case B)

$$\begin{aligned}\frac{d\Gamma}{ds} &= \frac{s^2\,\lambda^{3/2}(m_B^2,m_{K^*}^2,s)}{128\pi^3 m_B^3(m_b+m_s)^2}\,|A_0(s)|^2\left(\left|C^P_{sbB1}\right|^2+\left|C^P_{sbB2}\right|^2\right)\\ &+\frac{s\,\lambda^{1/2}(m_B^2,m_{K^*}^2,s)}{768\pi^3 m_B^3}\Big[\lambda(m_B^2,m_{K^*}^2,s)\,|T_1(s)|^2+(m_B^2-m_{K^*}^2)^2\,|T_2(s)|^2\\ &+\frac{8m_B^2m_{K^*}^2\,s}{(m_B+m_{K^*})^2}\,|T_{23}(s)|^2\Big]\times\left(\left|C^T_{sbB1}\right|^2+\left|C^T_{sbB2}\right|^2\right).\end{aligned} \tag{B.12}$$

This result is in agreement with the findings in Ref. [484].

B.3 $B\to X_s$+inv

The following results were, to the best of our knowledge, presented in Ref. [1] for the first time.

Scalar DM final state

$$\begin{aligned}\frac{d\Gamma}{ds} &= \frac{\kappa(0)\lambda^{1/2}(m_b^2,m_s^2,s)}{256\pi^3 m_b^3}\left[(m_b+m_s)^2-s\right]\left|C^S_{sb\phi}\right|^2\\ &+\frac{\kappa(0)\lambda^{1/2}(m_b^2,m_s^2,s)}{256\pi^3 m_b^3}\left[(m_b-m_s)^2-s\right]\left|C^P_{sb\phi}\right|^2\\ &+\frac{\kappa(0)\lambda^{1/2}(m_b^2,m_s^2,s)}{756\pi^3 m_b^3}\left[\lambda(m_b^2,m_s^2,s)+3s\left((m_b-m_s)^2-s\right)\right]\left|C^V_{sb\phi}\right|^2\\ &+\frac{\kappa(0)\lambda^{1/2}(m_b^2,m_s^2,s)}{756\pi^3 m_b^3}\left[\lambda(m_b^2,m_s^2,s)+3s\left((m_b+m_s)^2-s\right)\right]\left|C^A_{sb\phi}\right|^2.\end{aligned} \tag{B.13}$$

Fermion DM final state

$$\begin{aligned}\frac{d\Gamma}{ds} &= \frac{\kappa(0)\lambda^{1/2}(m_b^2,m_s^2,s)}{384\pi^3 m_b^3}\left[3s\left((m_b+m_s)^2-s\right)\right]\left(\left|C^S_{sb\chi1}\right|^2+\left|C^S_{sb\chi2}\right|^2\right)\\ &+\frac{\kappa(0)\lambda^{1/2}(m_b^2,m_s^2,s)}{384\pi^3 m_b^3}\left[3s\left((m_b-m_s)^2-s\right)\right]\left(\left|C^P_{sb\chi1}\right|^2+\left|C^P_{sb\chi2}\right|^2\right)\\ &+\frac{\kappa(0)\lambda^{1/2}(m_b^2,m_s^2,s)}{192\pi^3 m_b^3}\left[\lambda(m_b^2,m_s^2,s)+3s\left((m_b-m_s)^2-s\right)\right]\left(\left|C^V_{sb\chi1}\right|^2+\left|C^V_{sb\chi2}\right|^2\right)\\ &+\frac{\kappa(0)\lambda^{1/2}(m_b^2,m_s^2,s)}{192\pi^3 m_b^3}\left[\lambda(m_b^2,m_s^2,s)+3s\left((m_b+m_s)^2-s\right)\right]\left(\left|C^A_{sb\chi1}\right|^2+\left|C^A_{sb\chi2}\right|^2\right)\\ &+\frac{\kappa(0)\lambda^{1/2}(m_b^2,m_s^2,s)}{48\pi^3 m_b^3}\left[2\lambda(m_b^2,m_s^2,s)+3s(m_b^2+m_s^2-s)\right]\left(\left|C^T_{sb\chi1}\right|^2+\left|C^T_{sb\chi2}\right|^2\right).\end{aligned} \tag{B.14}$$

Vector DM final state (case A)

$$\begin{aligned}
\frac{d\Gamma}{ds} &= \frac{\kappa(0)\, s^2\, \lambda^{1/2}(m_b^2, m_s^2, s)}{1024\pi^3 m_b^3} \left[(m_b + m_s)^2 - s\right] \left|\tilde{C}^S_{sbA}\right|^2 \\
&+ \frac{\kappa(0)\, s^2\, \lambda^{1/2}(m_b^2, m_s^2, s)}{1024\pi^3 m_b^3} \left[(m_b - m_s)^2 - s\right] \left|\tilde{C}^P_{sbA}\right|^2 \\
&+ \frac{\kappa(0)\, s\, \lambda^{1/2}(m_b^2, m_s^2, s)}{3072\pi^3 m_b^3} \left[2\lambda(m_b^2, m_s^2, s) + 3s\left((m_b - m_s)^2 - s\right)\right] \left|\tilde{C}^T_{sbA1}\right|^2 \\
&+ \frac{\kappa(0)\, s\, \lambda^{1/2}(m_b^2, m_s^2, s)}{3072\pi^3 m_b^3} \left[2\lambda(m_b^2, m_s^2, s) + 3s\left((m_b + m_s)^2 - s\right)\right] \left|\tilde{C}^T_{sbA2}\right|^2 \\
&+ \frac{\kappa(0)\, s^2\, \lambda^{1/2}(m_b^2, m_s^2, s)}{1024\pi^3 m_b^3} (m_b - m_s)^2 \left[(m_b + m_s)^2 - s\right] \left|\tilde{C}^V_{sbA2}\right|^2 \\
&+ \frac{\kappa(0)\, s\, \lambda^{1/2}(m_b^2, m_s^2, s)}{756\pi^3 m_b^3} \left[\lambda(m_b^2, m_s^2, s) + 3s\left((m_b - m_s)^2 - s\right)\right] \left(\left|\tilde{C}^V_{sbA3}\right|^2 + \left|\tilde{C}^V_{sbA6}\right|^2\right) \\
&+ \frac{\kappa(0)\, s^2\, \lambda^{1/2}(m_b^2, m_s^2, s)}{3072\pi^3 m_b^3} \left[\lambda(m_b^2, m_s^2, s) + 3s\left((m_b - m_s)^2 - s\right)\right] \left(\left|\tilde{C}^V_{sbA4}\right|^2 + \left|\tilde{C}^V_{sbA5}\right|^2\right) \\
&+ \frac{\kappa(0)\, s^2\, \lambda^{1/2}(m_b^2, m_s^2, s)}{1024\pi^3 m_b^3} (m_b + m_s)^2 \left[(m_b - m_s)^2 - s\right] \left|\tilde{C}^A_{sbA2}\right|^2 \\
&+ \frac{\kappa(0)\, s\, \lambda^{1/2}(m_b^2, m_s^2, s)}{756\pi^3 m_b^3} \left[\lambda(m_b^2, m_s^2, s) + 3s\left((m_b + m_s)^2 - s\right)\right] \left(\left|\tilde{C}^A_{sbA3}\right|^2 + \left|\tilde{C}^A_{sbA6}\right|^2\right) \\
&+ \frac{\kappa(0)\, s^2\, \lambda^{1/2}(m_b^2, m_s^2, s)}{3072\pi^3 m_b^3} \left[\lambda(m_b^2, m_s^2, s) + 3s\left((m_b + m_s)^2 - s\right)\right] \left(\left|\tilde{C}^A_{sbA4}\right|^2 + \left|\tilde{C}^A_{sbA5}\right|^2\right) \\
&- \frac{\kappa(0)\, s^2\, \lambda^{1/2}(m_b^2, m_s^2, s)}{1536\pi^3 m_b^3} \left[\lambda(m_b^2, m_s^2, s) + 3s\left((m_b - m_s)^2 - s\right)\right] \mathrm{Re}\left(\tilde{C}^{V*}_{sbA4}\tilde{C}^V_{sbA5}\right) \\
&- \frac{\kappa(0)\, s^2\, \lambda^{1/2}(m_b^2, m_s^2, s)}{1536\pi^3 m_b^3} \left[\lambda(m_b^2, m_s^2, s) + 3s\left((m_b + m_s)^2 - s\right)\right] \mathrm{Re}\left(\tilde{C}^{A*}_{sbA4}\tilde{C}^A_{sbA5}\right) \\
&- \frac{\kappa(0)\, s^2\, \lambda^{1/2}(m_b^2, m_s^2, s)}{512\pi^3 m_b^3} (m_b - m_s)\left((m_b + m_s)^2 - s\right) \mathrm{Im}\left(\tilde{C}^{V*}_{sbA2}\tilde{C}^S_{sbA}\right) \\
&- \frac{\kappa(0)\, s^2\, \lambda^{1/2}(m_b^2, m_s^2, s)}{512\pi^3 m_b^3} (m_b + m_s)\left((m_b - m_s)^2 - s\right) \mathrm{Re}\left(\tilde{C}^{A*}_{sbA2}\tilde{C}^P_{sbA}\right) \\
&+ \frac{\kappa(0)\, s^2\, \lambda^{1/2}(m_b^2, m_s^2, s)}{512\pi^3 m_b^3} (m_b + m_s)\left((m_b - m_s)^2 - s\right) \mathrm{Im}\left[\left(\tilde{C}^V_{sbA5} - \tilde{C}^V_{sbA4}\right)^* \tilde{C}^T_{sbA1}\right] \\
&+ \frac{\kappa(0)\, s^2\, \lambda^{1/2}(m_b^2, m_s^2, s)}{512\pi^3 m_b^3} (m_b - m_s)\left((m_b + m_s)^2 - s\right) \mathrm{Im}\left[\left(\tilde{C}^A_{sbA5} - \tilde{C}^A_{sbA4}\right)^* \tilde{C}^T_{sbA2}\right] \\
&+ \mathcal{O}(m)\mathrm{Im}\left(\tilde{C}^{V*}_{sbA6}\tilde{C}^T_{sbA2}\right) + +\mathcal{O}(m)\mathrm{Re}\left(\tilde{C}^{A*}_{sbA6}\tilde{C}^T_{sbA1}\right). \qquad \text{(B.15)}
\end{aligned}$$

Vector DM final state (case B)

$$\begin{aligned}
\frac{d\Gamma}{ds} &= \frac{\kappa(0)\, s^2\, \lambda^{1/2}(m_b^2, m_s^2, s)}{128\pi^3 m_b^3} \left[(m_b + m_s)^2 - s\right] \left(\left|C^S_{sbB2}\right|^2 + \left|C^S_{sbB1}\right|^2\right) \\
&+ \frac{\kappa(0)\, s^2\, \lambda^{1/2}(m_b^2, m_s^2, s)}{128\pi^3 m_b^3} \left[(m_b - m_s)^2 - s\right] \left(\left|C^P_{sbB2}\right|^2 + \left|C^P_{sbB1}\right|^2\right)
\end{aligned}$$

$$+\frac{\kappa(0)\,s^2\,\lambda^{1/2}(m_b^2,m_s^2,s)}{756\pi^3 m_b^3}\left[2\lambda(m_b^2,m_s^2,s)+3s\left(m_b^2+m_s^2-s\right)\right]\left(\left|C_{sbB2}^T\right|^2+\left|C_{sbB1}^T\right|^2\right). \tag{B.16}$$

Epilogue

CHAPTER X

Summary and conclusion

The origin of the matter-antimatter asymmetry of our universe remains one of the most pressing open problems in high-energy physics, with profound implications for cosmology and particle physics. Addressing this question is crucial, requiring both the exploration of theoretical frameworks that can explain the origin of the BAU and the development of strategies to test models of baryogenesis. This thesis contributes to both endeavors in the context of leptogenesis, a leading paradigm that connects the BAU to the observed neutrino masses.

In the first part of the thesis, we considered BSM models where the SM gauge group is extended by $U(1)_{B-L}$. In Chapter III, we considered a minimal and predictive model realization, which provides a framework for leptogenesis, and generates sizable GWs from a cosmological FOPT. The latter will allow large regions of parameter space in this model to be tested at future GW observatories. We critically examined various aspects of the model, with particular attention on dynamics related to the FOPT, thereby extending and improving on previous studies in several directions. In particular, we mapped out the region of parameter space compatible with leptogenesis and determined the associated GW predictions. We also showed that the combination of GW production sourced by bubble dynamics and the SGWB sourced by cosmic strings leads to a characteristic spectrum that could be probed at upcoming experiments. In Chapter IV, we continued our study of gauged $B-L$ extensions of the SM, this time focusing on $B-L$ cosmic strings as a non-thermal source for leptogenesis. By carefully estimating the RHN-production rate from cosmic strings, taking the evolution of the string network properly into account, we showed that previous treatments in the literature were too optimistic. Indeed, we concluded that if $U(1)_{B-L}$ is spontaneously broken after the end of inflationary reheating, then the impact of RHNs sourced by cosmic strings is always negligible compared to the standard TLG contribution. In closing, we pointed out some generic conditions under which RHN production from cosmic strings may potentially play a significant role in the generation of the BAU.

In the second part of the thesis, we considered the WILG paradigm. Unlike standard leptogenesis mechanisms, WILG does not require CP violation in the RHN sector. Instead, a source of CP violation in the UV is required to create initial conditions suitable for WILG through a process we refer to as chargegenesis. In Chapter VI, we considered a new chargegenesis mechanism relying on non-minimal gravitational interactions. The construction represents a generalization of the gravitational baryogenesis framework [403], and we demonstrated its compatibility with standard inflationary reheating in high-scale inflation. In Chapter VII, we redirected our focus to WILG from a bottom-up perspective, without specifying a chargegenesis mechanism. In that context, we obtained a lower bound on the mass of the lightest RHN from the requirements of successful WILG, showing that $M_{N_1} \gtrsim 7-8$ TeV. Notably, this is many orders of magnitude below the famous Davidson-Ibarra bound [234] on the mass of the lightest RHN obtained in the context of standard TLG.

In the final part of the thesis, we considered strategies to disentangle NP contributions to rare semileptonic Kaon and B-meson decays with invisible leptonic final state. A driving motivation was to explore these decays as potential laboratories to search for LNV, as its observation could have major implications for our understanding of neutrino masses and leptogenesis. Our primary proposal was a systematic strategy to disentangle NP contributions to rare semileptonic decays through careful measurements of kinematic distributions of the invariant mass squared of the invisible final state. The investigation was carried out using effective-field theory methods, and included the possibility that, in addition to neutrinos, light dark scalars, fermions, or vectors may be hiding in the invisible final state. Notably, we showed that a NP signal compatible with a LNV hypothesis can be disentangled from dark scalars and dark vectors through careful measurements of kinematic distributions. In addition to our main proposal, we also presented strategies that are more easily accessible to experimentalists, including new correlations of branching ratios and refinements of previous sum-rule results.

Resolving the longstanding open problems in high-energy phenomenology is an immense task, that undoubtedly will require great efforts from both theorists and experimentalists. I hope that the results presented in this thesis can be of use to the community on our epic path to the next breakthrough discoveries in hep phenomenology.

Acknowledgements

All names and personal references were removed from the acknowledgements in the electronic publication of this dissertation.

I would like to thank my Ph.D. supervisor for the opportunity to pursue a Ph.D. in her group and for the privilege of completing the initial part of my degree in Munich and the subsequent part in Mainz. I also want to thank all committee members who took the time to read and evaluate my Ph.D. thesis.

I am grateful to all my collaborators, from whom I have learned a great deal over the years. I am particularly indebted to my mentor in Stavanger, who has been a great source of both inspiration and knowledge for me. I also extend my sincere gratitude to a collaborator in Munster for his enthusiastic collaboration, support, and guidance on our projects. Furthermore, I would like to express my thanks to a collaborator at TUM IAS for the fruitful collaboration and for sharing his infectious enthusiasm for physics.

I would like to thank the high-energy physics groups at TUM and JGU for providing a stimulating environment to pursue research. I also appreciate the support of the administrative staff at both institutions, who assisted me with various administrative tasks.

The THEP community in Mainz has provided a unique work atmosphere. I am thankful to a number of staff members, postdocs, and Ph.D. students for patiently answering many of my random physics questions. Moreover, I am thankful to all the postdocs, Ph.D. students, and masters students for making life in Mainz so enjoyable. I also want to thank the friends that I made at TUM for all the fun we had.

Finally, I am grateful to my friends outside of physics. Thanks to my flatmates in Munich, for making everyday life so fun. I also appreciate the support and encouragement from my friends in Norway, as well as the wonderful vacations we have shared. An extra heartfelt thanks to my partner for her love and support.

Last but not least, I am deeply grateful to my family for their unwavering support and love. Takk for alt.

List of Figures

Chapter II

Chapter III

Chapter V

Chapter VI

Chapter VII

Chapter VIII

Chapter IX

List of Tables

Use of AI tools

AI tool	Used for	Why	When / Where
ChatGPT	Improving sentences	Better readability	Throughout the thesis
Llama 4 Maverick	Improving sentences	Better readability	Throughout the thesis

Bibliography

[1] A. J. Buras, J. Harz and M. A. Mojahed, *Disentangling new physics in $K \to \pi\nu\overline{\nu}$ and $B \to K\,(K^*)\,\nu\overline{\nu}$ observables*, JHEP **10** (2024) 087 [2405.06742].

[2] M. A. Mojahed, K. Schmitz and X.-J. Xu, *Gravitational charge production*, Phys. Rev. D **111** (2025) 055005 [2409.10605].

[3] M. A. Mojahed, K. Schmitz and D. Wilken, *A lower bound on the right-handed neutrino mass from wash-in leptogenesis*, 2501.07634.

[4] J. Harz and M. A. Mojahed, *in preparation*, .

[5] K. Fridell, J. Harz, C. Hati and M. A. Mojahed, *in preparation*, .

[6] N. Bernal, J. Harz, M. A. Mojahed and Y. Xu, *Graviton- and inflaton-mediated dark matter production after large field polynomial inflation*, Phys. Rev. D **111** (2025) 043517 [2406.19447].

[7] M. A. Mojahed and T. Brauner, *Nonrelativistic effective field theories with enhanced symmetries and soft behavior*, JHEP **03** (2022) 086 [2201.01393].

[8] S. L. Glashow, *Partial Symmetries of Weak Interactions*, Nucl. Phys. **22** (1961) 579.

[9] S. Weinberg, *A Model of Leptons*, Phys. Rev. Lett. **19** (1967) 1264.

[10] A. Salam, *Weak and Electromagnetic Interactions*, Conf. Proc. C **680519** (1968) 367.

[11] G. R. Blumenthal, S. M. Faber, J. R. Primack and M. J. Rees, *Formation of Galaxies and Large Scale Structure with Cold Dark Matter*, Nature **311** (1984) 517.

[12] M. Davis, G. Efstathiou, C. S. Frenk and S. D. M. White, *The Evolution of Large Scale Structure in a Universe Dominated by Cold Dark Matter*, Astrophys. J. **292** (1985) 371.

[13] Supernova Search Team collaboration, *Observational evidence from supernovae for an accelerating universe and a cosmological constant*, Astron. J. **116** (1998) 1009 [astro-ph/9805201].

[14] Supernova Cosmology Project collaboration, *Measurements of Ω and Λ from 42 High Redshift Supernovae*, Astrophys. J. **517** (1999) 565 [astro-ph/9812133].

[15] WMAP collaboration, *First year Wilkinson Microwave Anisotropy Probe (WMAP) observations: Determination of cosmological parameters*, Astrophys. J. Suppl. **148** (2003) 175 [astro-ph/0302209].

[16] WMAP collaboration, *First year Wilkinson Microwave Anisotropy Probe (WMAP) observations: Preliminary maps and basic results*, Astrophys. J. Suppl. **148** (2003) 1 [astro-ph/0302207].

[17] Planck collaboration, *Planck 2018 results. VI. Cosmological parameters*, Astron. Astrophys. **641** (2020) A6 [1807.06209].

[18] Particle Data Group collaboration, *Review of particle physics*, Phys. Rev. D **110** (2024) 030001.

[19] S. Laporta, *High-precision calculation of the 4-loop contribution to the electron g-2 in QED*, Phys. Lett. B **772** (2017) 232 [1704.06996].

[20] R. Bouchendira, P. Clade, S. Guellati-Khelifa, F. Nez and F. Biraben, *New determination of the fine structure constant and test of the quantum electrodynamics*, Phys. Rev. Lett. **106** (2011) 080801 [1012.3627].

[21] ATLAS collaboration, *Observation of a new particle in the search for the Standard Model Higgs boson with the ATLAS detector at the LHC*, Phys. Lett. B **716** (2012) 1 [1207.7214].

[22] CMS collaboration, *Observation of a New Boson at a Mass of 125 GeV with the CMS Experiment at the LHC*, Phys. Lett. B **716** (2012) 30 [1207.7235].

[23] M. Fukugita and T. Yanagida, *Baryogenesis Without Grand Unification*, Phys. Lett. B **174** (1986) 45.

[24] LIGO Scientific, Virgo collaboration, *Observation of Gravitational Waves from a Binary Black Hole Merger*, Phys. Rev. Lett. **116** (2016) 061102 [1602.03837].

[25] NANOGrav collaboration, *The NANOGrav 15 yr Data Set: Evidence for a Gravitational-wave Background*, Astrophys. J. Lett. **951** (2023) L8 [2306.16213].

[26] NANOGrav collaboration, *The NANOGrav 15 yr Data Set: Search for Signals from New Physics*, Astrophys. J. Lett. **951** (2023) L11 [2306.16219].

[27] D. J. Reardon et al., *Search for an Isotropic Gravitational-wave Background with the Parkes Pulsar Timing Array*, Astrophys. J. Lett. **951** (2023) L6 [2306.16215].

[28] EPTA, InPTA: collaboration, *The second data release from the European Pulsar Timing Array - III. Search for gravitational wave signals*, Astron. Astrophys. **678** (2023) A50 [2306.16214].

[29] H. Xu et al., *Searching for the Nano-Hertz Stochastic Gravitational Wave Background with the Chinese Pulsar Timing Array Data Release I*, Res. Astron. Astrophys. **23** (2023) 075024 [2306.16216].

[30] A. D. Sakharov, *Violation of CP Invariance, C asymmetry, and baryon asymmetry of the universe*, Pisma Zh. Eksp. Teor. Fiz. **5** (1967) 32.

[31] P. J. E. Peebles and B. Ratra, *The Cosmological Constant and Dark Energy*, Rev. Mod. Phys. **75** (2003) 559 [astro-ph/0207347].

[32] J.-P. Hu and F.-Y. Wang, *Hubble Tension: The Evidence of New Physics*, Universe **9** (2023) 94 [2302.05709].

[33] M. Cirelli, A. Strumia and J. Zupan, *Dark Matter*, 2406.01705.

[34] S. Weinberg, *The Cosmological Constant Problem*, Rev. Mod. Phys. **61** (1989) 1.

[35] A. Padilla, *Lectures on the Cosmological Constant Problem*, 1502.05296.

[36] A. H. Guth, *The inflationary universe: A possible solution to the horizon and flatness problems*, Phys. Rev. D **23** (1981) 347.

[37] A. D. Linde, *A new inflationary universe scenario: A possible solution of the horizon, flatness, momogeneity, isotropy and primordial monopole problems*, Phys. Lett. B **108** (1982) 389.

[38] A. Albrecht and P. J. Steinhardt, *Cosmology for Grand Unified Theories with Radiatively Induced Symmetry Breaking*, Phys. Rev. Lett. **48** (1982) 1220.

[39] A. D. Linde, *Chaotic inflation*, Phys. Lett. B **129** (1983) 177.

[40] V. F. Mukhanov and G. V. Chibisov, *Quantum fluctuations and a nonsingular universe*, *JETP Lett.* **33** (1981) 532.
[41] A. A. Starobinsky, *Dynamics of phase transition in the new inflationary universe scenario and generation of perturbations*, *Phys. Lett. B* **117** (1982) 175.
[42] S. W. Hawking, *The development of irregularities in a single bubble inflationary universe*, *Phys. Lett. B* **115** (1982) 295.
[43] A. Achúcarro et al., *Inflation: Theory and Observations*, 2203.08128.
[44] J. C. Pati and A. Salam, *Lepton Number as the Fourth Color*, *Phys. Rev. D* **10** (1974) 275.
[45] H. Georgi and S. L. Glashow, *Unity of All Elementary Particle Forces*, *Phys. Rev. Lett.* **32** (1974) 438.
[46] H. Georgi, H. R. Quinn and S. Weinberg, *Hierarchy of Interactions in Unified Gauge Theories*, *Phys. Rev. Lett.* **33** (1974) 451.
[47] S. Dimopoulos and H. Georgi, *Softly Broken Supersymmetry and SU(5)*, *Nucl. Phys. B* **193** (1981) 150.
[48] N. Craig, *Naturalness: past, present, and future*, *Eur. Phys. J. C* **83** (2023) 825 [2205.05708].
[49] C. Abel et al., *Measurement of the Permanent Electric Dipole Moment of the Neutron*, *Phys. Rev. Lett.* **124** (2020) 081803 [2001.11966].
[50] G. Degrassi, S. Di Vita, J. Elias-Miro, J. R. Espinosa, G. F. Giudice, G. Isidori et al., *Higgs mass and vacuum stability in the Standard Model at NNLO*, *JHEP* **08** (2012) 098 [1205.6497].
[51] F. Bezrukov, M. Y. Kalmykov, B. A. Kniehl and M. Shaposhnikov, *Higgs Boson Mass and New Physics*, *JHEP* **10** (2012) 140 [1205.2893].
[52] S. Alekhin, A. Djouadi and S. Moch, *The top quark and Higgs boson masses and the stability of the electroweak vacuum*, *Phys. Lett. B* **716** (2012) 214 [1207.0980].
[53] D. Buttazzo, G. Degrassi, P. P. Giardino, G. F. Giudice, F. Sala, A. Salvio et al., *Investigating the near-criticality of the Higgs boson*, *JHEP* **12** (2013) 089 [1307.3536].
[54] G. Hiller, T. Höhne, D. F. Litim and T. Steudtner, *Vacuum stability in the Standard Model and beyond*, *Phys. Rev. D* **110** (2024) 115017 [2401.08811].
[55] Super-Kamiokande collaboration, *Evidence for oscillation of atmospheric neutrinos*, *Phys. Rev. Lett.* **81** (1998) 1562 [hep-ex/9807003].
[56] Super-Kamiokande collaboration, *Tau neutrinos favored over sterile neutrinos in atmospheric muon-neutrino oscillations*, *Phys. Rev. Lett.* **85** (2000) 3999 [hep-ex/0009001].
[57] SNO collaboration, *Measurement of the rate of $\nu_e + d \to p + p + e^-$ interactions produced by ^8B solar neutrinos at the Sudbury Neutrino Observatory*, *Phys. Rev. Lett.* **87** (2001) 071301 [nucl-ex/0106015].
[58] KamLAND collaboration, *First results from KamLAND: Evidence for reactor anti-neutrino disappearance*, *Phys. Rev. Lett.* **90** (2003) 021802 [hep-ex/0212021].
[59] K2K collaboration, *Measurement of Neutrino Oscillation by the K2K Experiment*, *Phys. Rev. D* **74** (2006) 072003 [hep-ex/0606032].
[60] Daya Bay collaboration, *Observation of electron-antineutrino disappearance at Daya Bay*, *Phys. Rev. Lett.* **108** (2012) 171803 [1203.1669].
[61] RENO collaboration, *Observation of Reactor Electron Antineutrino Disappearance in the RENO Experiment*, *Phys. Rev. Lett.* **108** (2012) 191802 [1204.0626].

[62] T2K collaboration, *Indication of Electron Neutrino Appearance from an Accelerator-produced Off-axis Muon Neutrino Beam*, *Phys. Rev. Lett.* **107** (2011) 041801 [1106.2822].
[63] P. Minkowski, *$\mu \to e\gamma$ at a Rate of One Out of 10^9 Muon Decays?*, *Phys. Lett. B* **67** (1977) 421.
[64] T. Yanagida, *Horizontal gauge symmetry and masses of neutrinos*, *Conf. Proc. C* **7902131** (1979) 95.
[65] T. Yanagida, *Horizontal Symmetry and Masses of Neutrinos*, *Prog. Theor. Phys.* **64** (1980) 1103.
[66] M. Gell-Mann, P. Ramond and R. Slansky, *Complex Spinors and Unified Theories*, *Conf. Proc. C* **790927** (1979) 315 [1306.4669].
[67] R. N. Mohapatra and G. Senjanovic, *Neutrino Mass and Spontaneous Parity Nonconservation*, *Phys. Rev. Lett.* **44** (1980) 912.
[68] M. Magg and C. Wetterich, *Neutrino Mass Problem and Gauge Hierarchy*, *Phys. Lett. B* **94** (1980) 61.
[69] J. Schechter and J. W. F. Valle, *Neutrino Masses in SU(2) x U(1) Theories*, *Phys. Rev. D* **22** (1980) 2227.
[70] T. P. Cheng and L.-F. Li, *Neutrino Masses, Mixings and Oscillations in SU(2) x U(1) Models of Electroweak Interactions*, *Phys. Rev. D* **22** (1980) 2860.
[71] G. Lazarides, Q. Shafi and C. Wetterich, *Proton Lifetime and Fermion Masses in an SO(10) Model*, *Nucl. Phys. B* **181** (1981) 287.
[72] R. N. Mohapatra and G. Senjanovic, *Neutrino Masses and Mixings in Gauge Models with Spontaneous Parity Violation*, *Phys. Rev. D* **23** (1981) 165.
[73] R. Foot, H. Lew, X. G. He and G. C. Joshi, *Seesaw Neutrino Masses Induced by a Triplet of Leptons*, *Z. Phys. C* **44** (1989) 441.
[74] Y. Cai, J. Herrero-García, M. A. Schmidt, A. Vicente and R. R. Volkas, *From the trees to the forest: a review of radiative neutrino mass models*, *Front. in Phys.* **5** (2017) 63 [1706.08524].
[75] S. Weinberg, *Baryon and Lepton Nonconserving Processes*, *Phys. Rev. Lett.* **43** (1979) 1566.
[76] R. N. Mohapatra and A. Y. Smirnov, *Neutrino Mass and New Physics*, *Ann. Rev. Nucl. Part. Sci.* **56** (2006) 569 [hep-ph/0603118].
[77] G. Steigman, *When Clusters Collide: Constraints On Antimatter On The Largest Scales*, *JCAP* **10** (2008) 001 [0808.1122].
[78] G. Steigman, *Observational tests of antimatter cosmologies*, *Ann. Rev. Astron. Astrophys.* **14** (1976) 339.
[79] S. Dupourqué, L. Tibaldo and P. Von Ballmoos, *Constraints on the antistar fraction in the Solar System neighborhood from the 10-year Fermi Large Area Telescope gamma-ray source catalog*, *Phys. Rev. D* **103** (2021) 083016 [2103.10073].
[80] A. G. Cohen, A. De Rujula and S. L. Glashow, *A Matter - antimatter universe?*, *Astrophys. J.* **495** (1998) 539 [astro-ph/9707087].
[81] L. Canetti, M. Drewes and M. Shaposhnikov, *Matter and Antimatter in the Universe*, *New J. Phys.* **14** (2012) 095012 [1204.4186].
[82] R. J. Cooke, M. Pettini and C. C. Steidel, *One Percent Determination of the Primordial Deuterium Abundance*, *Astrophys. J.* **855** (2018) 102 [1710.11129].
[83] T.-H. Yeh, J. Shelton, K. A. Olive and B. D. Fields, *Probing physics beyond the standard model: limits from BBN and the CMB independently and combined*, *JCAP* **10** (2022) 046 [2207.13133].

[84] W. Hu and S. Dodelson, *Cosmic Microwave Background Anisotropies*, *Ann. Rev. Astron. Astrophys.* **40** (2002) 171 [astro-ph/0110414].
[85] Planck collaboration, *Planck 2018 results. I. Overview and the cosmological legacy of Planck*, *Astron. Astrophys.* **641** (2020) A1 [1807.06205].
[86] E. W. Kolb and M. S. Turner, *The Early Universe*, vol. 69. Taylor and Francis, 5, 2019, 10.1201/9780429492860.
[87] J. L. Barrow et al., *Theories and Experiments for Testable Baryogenesis Mechanisms: A Snowmass White Paper*, 2203.07059.
[88] G. Elor et al., *New Ideas in Baryogenesis: A Snowmass White Paper*, in *Snowmass 2021*, 3, 2022, 2203.05010.
[89] V. A. Kuzmin, V. A. Rubakov and M. E. Shaposhnikov, *On the Anomalous Electroweak Baryon Number Nonconservation in the Early Universe*, *Phys. Lett. B* **155** (1985) 36.
[90] S. Iso, N. Okada and Y. Orikasa, *Classically conformal B^- L extended Standard Model*, *Phys. Lett. B* **676** (2009) 81 [0902.4050].
[91] M. Laine and A. Vuorinen, *Basics of Thermal Field Theory*, vol. 925. Springer, 2016, 10.1007/978-3-319-31933-9, [1701.01554].
[92] M. D'Onofrio and K. Rummukainen, *Standard model cross-over on the lattice*, *Phys. Rev. D* **93** (2016) 025003 [1508.07161].
[93] Y. Aoki, S. Borsanyi, S. Durr, Z. Fodor, S. D. Katz, S. Krieg et al., *The QCD transition temperature: results with physical masses in the continuum limit II.*, *JHEP* **06** (2009) 088 [0903.4155].
[94] A. Bazavov et al., *The chiral and deconfinement aspects of the QCD transition*, *Phys. Rev. D* **85** (2012) 054503 [1111.1710].
[95] K. Kajantie, M. Laine, K. Rummukainen and M. E. Shaposhnikov, *Is there a hot electroweak phase transition at $m_H \gtrsim m_W$?*, *Phys. Rev. Lett.* **77** (1996) 2887 [hep-ph/9605288].
[96] M. D'Onofrio, K. Rummukainen and A. Tranberg, *Sphaleron Rate in the Minimal Standard Model*, *Phys. Rev. Lett.* **113** (2014) 141602 [1404.3565].
[97] Y. Aoki, G. Endrodi, Z. Fodor, S. D. Katz and K. K. Szabo, *The Order of the quantum chromodynamics transition predicted by the standard model of particle physics*, *Nature* **443** (2006) 675 [hep-lat/0611014].
[98] M. Carena, M. Quiros and C. E. M. Wagner, *Opening the window for electroweak baryogenesis*, *Phys. Lett. B* **380** (1996) 81 [hep-ph/9603420].
[99] C. Grojean, G. Servant and J. D. Wells, *First-order electroweak phase transition in the standard model with a low cutoff*, *Phys. Rev. D* **71** (2005) 036001 [hep-ph/0407019].
[100] T. Boeckel and J. Schaffner-Bielich, *A little inflation in the early universe at the QCD phase transition*, *Phys. Rev. Lett.* **105** (2010) 041301 [0906.4520].
[101] J. R. Espinosa, T. Konstandin and F. Riva, *Strong Electroweak Phase Transitions in the Standard Model with a Singlet*, *Nucl. Phys. B* **854** (2012) 592 [1107.5441].
[102] G. C. Dorsch, S. J. Huber and J. M. No, *A strong electroweak phase transition in the 2HDM after LHC8*, *JHEP* **10** (2013) 029 [1305.6610].
[103] Y. Bai, T.-K. Chen and M. Korwar, *QCD-collapsed domain walls: QCD phase transition and gravitational wave spectroscopy*, *JHEP* **12** (2023) 194 [2306.17160].
[104] M. E. Shaposhnikov, *Possible Appearance of the Baryon Asymmetry of the Universe in an Electroweak Theory*, *JETP Lett.* **44** (1986) 465.

[105] M. E. Shaposhnikov, *Baryon Asymmetry of the Universe in Standard Electroweak Theory*, *Nucl. Phys. B* **287** (1987) 757.

[106] E. Witten, *Cosmic Separation of Phases*, *Phys. Rev. D* **30** (1984) 272.

[107] A. Vilenkin and E. P. S. Shellard, *Cosmic Strings and Other Topological Defects*. Cambridge University Press, 7, 2000.

[108] T. W. B. Kibble, *Topology of Cosmic Domains and Strings*, *J. Phys. A* **9** (1976) 1387.

[109] S. Weinberg, *The quantum theory of fields. Vol. 2: Modern applications*. Cambridge University Press, 8, 2013, 10.1017/CBO9781139644174.

[110] K. Symanzik, *Small distance behavior in field theory and power counting*, *Commun. Math. Phys.* **18** (1970) 227.

[111] S. Coleman, *Aspects of Symmetry: Selected Erice Lectures*. Cambridge University Press, Cambridge, U.K., 1985, 10.1017/CBO9780511565045.

[112] S. R. Coleman and E. J. Weinberg, *Radiative Corrections as the Origin of Spontaneous Symmetry Breaking*, *Phys. Rev. D* **7** (1973) 1888.

[113] M. E. Peskin and D. V. Schroeder, *An Introduction to quantum field theory*. Addison-Wesley, Reading, USA, 1995, 10.1201/9780429503559.

[114] M. Quiros, *Finite temperature field theory and phase transitions*, in *ICTP Summer School in High-Energy Physics and Cosmology*, pp. 187–259, 1, 1999, hep-ph/9901312.

[115] R. Jackiw, *Functional evaluation of the effective potential*, *Phys. Rev. D* **9** (1974) 1686.

[116] G. 't Hooft and M. J. G. Veltman, *Regularization and Renormalization of Gauge Fields*, *Nucl. Phys. B* **44** (1972) 189.

[117] C. Delaunay, C. Grojean and J. D. Wells, *Dynamics of Non-renormalizable Electroweak Symmetry Breaking*, *JHEP* **04** (2008) 029 [0711.2511].

[118] D. A. Kirzhnits, *Weinberg model in the hot universe*, *JETP Lett.* **15** (1972) 529.

[119] S. Weinberg, *Gauge and Global Symmetries at High Temperature*, *Phys. Rev. D* **9** (1974) 3357.

[120] L. Dolan and R. Jackiw, *Symmetry Behavior at Finite Temperature*, *Phys. Rev. D* **9** (1974) 3320.

[121] D. A. Kirzhnits and A. D. Linde, *Symmetry Behavior in Gauge Theories*, *Annals Phys.* **101** (1976) 195.

[122] J. I. Kapusta and C. Gale, *Finite-temperature field theory: Principles and applications*, Cambridge Monographs on Mathematical Physics. Cambridge University Press, 2011, 10.1017/CBO9780511535130.

[123] T. Matsubara, *A New approach to quantum statistical mechanics*, *Prog. Theor. Phys.* **14** (1955) 351.

[124] A. D. Linde, *Infrared Problem in Thermodynamics of the Yang-Mills Gas*, *Phys. Lett. B* **96** (1980) 289.

[125] D. J. Gross, R. D. Pisarski and L. G. Yaffe, *QCD and Instantons at Finite Temperature*, *Rev. Mod. Phys.* **53** (1981) 43.

[126] E. Braaten and A. Nieto, *Free energy of QCD at high temperature*, *Phys. Rev. D* **53** (1996) 3421 [hep-ph/9510408].

[127] R. R. Parwani, *Resummation in a hot scalar field theory*, *Phys. Rev. D* **45** (1992) 4695 [hep-ph/9204216].

[128] P. B. Arnold and O. Espinosa, *The Effective potential and first order phase transitions: Beyond leading-order*, *Phys. Rev. D* **47** (1993) 3546 [hep-ph/9212235].

[129] D. A. Kirzhnits and A. D. Linde, *Macroscopic Consequences of the Weinberg Model*, Phys. Lett. B **42** (1972) 471.
[130] S. R. Coleman, *The Fate of the False Vacuum. 1. Semiclassical Theory*, Phys. Rev. D **15** (1977) 2929.
[131] C. G. Callan, Jr. and S. R. Coleman, *The Fate of the False Vacuum. 2. First Quantum Corrections*, Phys. Rev. D **16** (1977) 1762.
[132] A. D. Linde, *Fate of the False Vacuum at Finite Temperature: Theory and Applications*, Phys. Lett. B **100** (1981) 37.
[133] A. D. Linde, *Decay of the False Vacuum at Finite Temperature*, Nucl. Phys. B **216** (1983) 421.
[134] V. Guada, M. Nemevšek and M. Pintar, *FindBounce: Package for multi-field bounce actions*, Comput. Phys. Commun. **256** (2020) 107480 [2002.00881].
[135] A. H. Guth and S. H. H. Tye, *Phase Transitions and Magnetic Monopole Production in the Very Early Universe*, Phys. Rev. Lett. **44** (1980) 631.
[136] A. H. Guth and E. J. Weinberg, *Cosmological Consequences of a First Order Phase Transition in the SU(5) Grand Unified Model*, Phys. Rev. D **23** (1981) 876.
[137] P. Athron, C. Balázs, A. Fowlie, L. Morris and L. Wu, *Cosmological phase transitions: From perturbative particle physics to gravitational waves*, Prog. Part. Nucl. Phys. **135** (2024) 104094 [2305.02357].
[138] J. Ellis, M. Lewicki and J. M. No, *On the Maximal Strength of a First-Order Electroweak Phase Transition and its Gravitational Wave Signal*, JCAP **04** (2019) 003 [1809.08242].
[139] A. H. Guth and E. J. Weinberg, *Could the Universe Have Recovered from a Slow First Order Phase Transition?*, Nucl. Phys. B **212** (1983) 321.
[140] P. Athron, C. Balázs and L. Morris, *Supercool subtleties of cosmological phase transitions*, JCAP **03** (2023) 006 [2212.07559].
[141] M. S. Turner, E. J. Weinberg and L. M. Widrow, *Bubble nucleation in first order inflation and other cosmological phase transitions*, Phys. Rev. D **46** (1992) 2384.
[142] K. Enqvist, J. Ignatius, K. Kajantie and K. Rummukainen, *Nucleation and bubble growth in a first order cosmological electroweak phase transition*, Phys. Rev. D **45** (1992) 3415.
[143] C. Caprini et al., *Detecting gravitational waves from cosmological phase transitions with LISA: an update*, JCAP **03** (2020) 024 [1910.13125].
[144] M. Lewicki and V. Vaskonen, *Gravitational waves from bubble collisions and fluid motion in strongly supercooled phase transitions*, Eur. Phys. J. C **83** (2023) 109 [2208.11697].
[145] J. Ellis, M. Lewicki, J. M. No and V. Vaskonen, *Gravitational wave energy budget in strongly supercooled phase transitions*, JCAP **06** (2019) 024 [1903.09642].
[146] D. Bodeker and G. D. Moore, *Can electroweak bubble walls run away?*, JCAP **05** (2009) 009 [0903.4099].
[147] S. Höche, J. Kozaczuk, A. J. Long, J. Turner and Y. Wang, *Towards an all-orders calculation of the electroweak bubble wall velocity*, JCAP **03** (2021) 009 [2007.10343].
[148] A. Azatov and M. Vanvlasselaer, *Bubble wall velocity: heavy physics effects*, JCAP **01** (2021) 058 [2010.02590].
[149] Y. Gouttenoire, R. Jinno and F. Sala, *Friction pressure on relativistic bubble walls*, JHEP **05** (2022) 004 [2112.07686].
[150] D. Bodeker and G. D. Moore, *Electroweak Bubble Wall Speed Limit*, JCAP **05** (2017) 025 [1703.08215].

[151] W.-Y. Ai, M. Carosi, B. Garbrecht, C. Tamarit and M. Vanvlasselaer, *Bubble wall dynamics from nonequilibrium quantum field theory*, 2504.13725.
[152] J. Ellis, M. Lewicki and V. Vaskonen, *Updated predictions for gravitational waves produced in a strongly supercooled phase transition*, *JCAP* **11** (2020) 020 [2007.15586].
[153] A. Ekstedt, O. Gould, J. Hirvonen, B. Laurent, L. Niemi, P. Schicho et al., *How fast does the WallGo? A package for computing wall velocities in first-order phase transitions*, 2411.04970.
[154] P. J. Steinhardt, *Relativistic Detonation Waves and Bubble Growth in False Vacuum Decay*, *Phys. Rev. D* **25** (1982) 2074.
[155] C. Caprini and D. G. Figueroa, *Cosmological Backgrounds of Gravitational Waves*, *Class. Quant. Grav.* **35** (2018) 163001 [1801.04268].
[156] M. Lewicki and V. Vaskonen, *Gravitational wave spectra from strongly supercooled phase transitions*, *Eur. Phys. J. C* **80** (2020) 1003 [2007.04967].
[157] M. Hindmarsh, S. J. Huber, K. Rummukainen and D. J. Weir, *Numerical simulations of acoustically generated gravitational waves at a first order phase transition*, *Phys. Rev. D* **92** (2015) 123009 [1504.03291].
[158] J. R. Espinosa, T. Konstandin, J. M. No and G. Servant, *Energy Budget of Cosmological First-order Phase Transitions*, *JCAP* **06** (2010) 028 [1004.4187].
[159] LISA Cosmology Working Group collaboration, *Gravitational waves from first-order phase transitions in LISA: reconstruction pipeline and physics interpretation*, *JCAP* **10** (2024) 020 [2403.03723].
[160] G. Barenboim and W.-I. Park, *Gravitational waves from first order phase transitions as a probe of an early matter domination era and its inverse problem*, *Phys. Lett. B* **759** (2016) 430 [1605.03781].
[161] K. Schmitz, *New Sensitivity Curves for Gravitational-Wave Signals from Cosmological Phase Transitions*, *JHEP* **01** (2021) 097 [2002.04615].
[162] LISA collaboration, *Laser Interferometer Space Antenna*, 1702.00786.
[163] J. Crowder and N. J. Cornish, *Beyond LISA: Exploring future gravitational wave missions*, *Phys. Rev. D* **72** (2005) 083005 [gr-qc/0506015].
[164] K. Yagi and N. Seto, *Detector configuration of DECIGO/BBO and identification of cosmological neutron-star binaries*, *Phys. Rev. D* **83** (2011) 044011 [1101.3940].
[165] LIGO Scientific collaboration, *Advanced LIGO*, *Class. Quant. Grav.* **32** (2015) 074001 [1411.4547].
[166] VIRGO collaboration, *Advanced Virgo: a second-generation interferometric gravitational wave detector*, *Class. Quant. Grav.* **32** (2015) 024001 [1408.3978].
[167] KAGRA, LIGO Scientific, Virgo collaboration, *Prospects for observing and localizing gravitational-wave transients with Advanced LIGO, Advanced Virgo and KAGRA*, *Living Rev. Rel.* **19** (2016) 1 [1304.0670].
[168] M. Punturo et al., *The Einstein Telescope: A third-generation gravitational wave observatory*, *Class. Quant. Grav.* **27** (2010) 194002.
[169] LIGO Scientific collaboration, *Exploring the Sensitivity of Next Generation Gravitational Wave Detectors*, *Class. Quant. Grav.* **34** (2017) 044001 [1607.08697].
[170] D. Reitze et al., *Cosmic Explorer: The U.S. Contribution to Gravitational-Wave Astronomy beyond LIGO*, *Bull. Am. Astron. Soc.* **51** (2019) 035 [1907.04833].
[171] D. Croon, O. Gould, P. Schicho, T. V. I. Tenkanen and G. White, *Theoretical uncertainties for cosmological first-order phase transitions*, *JHEP* **04** (2021) 055 [2009.10080].

[172] M. Lewicki, M. Merchand, L. Sagunski, P. Schicho and D. Schmitt, *Impact of theoretical uncertainties on model parameter reconstruction from GW signals sourced by cosmological phase transitions*, Phys. Rev. D **110** (2024) 023538 [2403.03769].

[173] M. Kierkla, B. Swiezewska, T. V. I. Tenkanen and J. van de Vis, *Gravitational waves from supercooled phase transitions: dimensional transmutation meets dimensional reduction*, JHEP **02** (2024) 234 [2312.12413].

[174] O. Gould and J. Hirvonen, *Effective field theory approach to thermal bubble nucleation*, Phys. Rev. D **104** (2021) 096015 [2108.04377].

[175] J. Hirvonen, J. Löfgren, M. J. Ramsey-Musolf, P. Schicho and T. V. I. Tenkanen, *Computing the gauge-invariant bubble nucleation rate in finite temperature effective field theory*, JHEP **07** (2022) 135 [2112.08912].

[176] D. Marfatia, P.-Y. Tseng and Y.-M. Yeh, *Phenomenology of bubble size distributions in a first-order phase transition*, 2407.15419.

[177] M. B. Hindmarsh and T. W. B. Kibble, *Cosmic strings*, Rept. Prog. Phys. **58** (1995) 477 [hep-ph/9411342].

[178] A. A. Abrikosov, *On the Magnetic properties of superconductors of the second group*, Sov. Phys. JETP **5** (1957) 1174.

[179] H. B. Nielsen and P. Olesen, *Vortex Line Models for Dual Strings*, Nucl. Phys. B **61** (1973) 45.

[180] A. Vilenkin, *Cosmic string dynamics with friction*, Phys. Rev. D **43** (1991) 1060.

[181] M. G. Alford and F. Wilczek, *Aharonov-Bohm Interaction of Cosmic Strings with Matter*, Phys. Rev. Lett. **62** (1989) 1071.

[182] T. W. B. Kibble, *Evolution of a system of cosmic strings*, Nucl. Phys. B **252** (1985) 227.

[183] D. P. Bennett and F. R. Bouchet, *Evidence for a Scaling Solution in Cosmic String Evolution*, Phys. Rev. Lett. **60** (1988) 257.

[184] D. P. Bennett and F. R. Bouchet, *Cosmic string evolution*, Phys. Rev. Lett. **63** (1989) 2776.

[185] A. Albrecht and N. Turok, *Evolution of Cosmic String Networks*, Phys. Rev. D **40** (1989) 973.

[186] B. Allen and E. P. S. Shellard, *Cosmic string evolution: a numerical simulation*, Phys. Rev. Lett. **64** (1990) 119.

[187] C. Ringeval, M. Sakellariadou and F. Bouchet, *Cosmological evolution of cosmic string loops*, JCAP **02** (2007) 023 [astro-ph/0511646].

[188] V. Vanchurin, K. D. Olum and A. Vilenkin, *Scaling of cosmic string loops*, Phys. Rev. D **74** (2006) 063527 [gr-qc/0511159].

[189] C. J. A. P. Martins and E. P. S. Shellard, *Fractal properties and small-scale structure of cosmic string networks*, Phys. Rev. D **73** (2006) 043515 [astro-ph/0511792].

[190] J. J. Blanco-Pillado, K. D. Olum and B. Shlaer, *Large parallel cosmic string simulations: New results on loop production*, Phys. Rev. D **83** (2011) 083514 [1101.5173].

[191] Y. Cui, M. Lewicki, D. E. Morrissey and J. D. Wells, *Probing the pre-BBN universe with gravitational waves from cosmic strings*, JHEP **01** (2019) 081 [1808.08968].

[192] Y. Gouttenoire, G. Servant and P. Simakachorn, *Beyond the Standard Models with Cosmic Strings*, JCAP **07** (2020) 032 [1912.02569].

[193] J. J. Blanco-Pillado, K. D. Olum and B. Shlaer, *The number of cosmic string*

loops, Phys. Rev. D **89** (2014) 023512 [1309.6637].
[194] J. J. Blanco-Pillado, K. D. Olum and X. Siemens, *New limits on cosmic strings from gravitational wave observation*, Phys. Lett. B **778** (2018) 392 [1709.02434].
[195] G. Vincent, N. D. Antunes and M. Hindmarsh, *Numerical simulations of string networks in the Abelian Higgs model*, Phys. Rev. Lett. **80** (1998) 2277 [hep-ph/9708427].
[196] M. Hindmarsh, S. Stuckey and N. Bevis, *Abelian Higgs Cosmic Strings: Small Scale Structure and Loops*, Phys. Rev. D **79** (2009) 123504 [0812.1929].
[197] M. Hindmarsh, J. Lizarraga, J. Urrestilla, D. Daverio and M. Kunz, *Scaling from gauge and scalar radiation in Abelian Higgs string networks*, Phys. Rev. D **96** (2017) 023525 [1703.06696].
[198] M. Hindmarsh, J. Lizarraga, A. Urio and J. Urrestilla, *Loop decay in Abelian-Higgs string networks*, Phys. Rev. D **104** (2021) 043519 [2103.16248].
[199] J. Baeza-Ballesteros, E. J. Copeland, D. G. Figueroa and J. Lizarraga, *Gravitational Wave Emission from Cosmic String Loops, II: Local Case*, 2408.02364.
[200] K. D. Olum and J. J. Blanco-Pillado, *Radiation from cosmic string standing waves*, Phys. Rev. Lett. **84** (2000) 4288 [astro-ph/9910354].
[201] J. N. Moore, E. P. S. Shellard and C. J. A. P. Martins, *On the evolution of Abelian-Higgs string networks*, Phys. Rev. D **65** (2002) 023503 [hep-ph/0107171].
[202] D. Matsunami, L. Pogosian, A. Saurabh and T. Vachaspati, *Decay of Cosmic String Loops Due to Particle Radiation*, Phys. Rev. Lett. **122** (2019) 201301 [1903.05102].
[203] P. Auclair, D. A. Steer and T. Vachaspati, *Particle emission and gravitational radiation from cosmic strings: observational constraints*, Phys. Rev. D **101** (2020) 083511 [1911.12066].
[204] G. Servant and P. Simakachorn, *Ultrahigh frequency primordial gravitational waves beyond the kHz: The case of cosmic strings*, Phys. Rev. D **109** (2024) 103538 [2312.09281].
[205] C.-F. Chang and Y. Cui, *Gravitational waves from global cosmic strings and cosmic archaeology*, JHEP **03** (2022) 114 [2106.09746].
[206] Y. Gouttenoire, G. Servant and P. Simakachorn, *Kination cosmology from scalar fields and gravitational-wave signatures*, 2111.01150.
[207] A. Ghoshal, Y. Gouttenoire, L. Heurtier and P. Simakachorn, *Primordial black hole archaeology with gravitational waves from cosmic strings*, JHEP **08** (2023) 196 [2304.04793].
[208] R. Roshan and G. White, *Using gravitational waves to see the first second of the Universe*, Rev. Mod. Phys. **97** (2025) 015001 [2401.04388].
[209] J. J. Blanco-Pillado, K. D. Olum and B. Shlaer, *Cosmic string loop shapes*, Phys. Rev. D **92** (2015) 063528 [1508.02693].
[210] Planck collaboration, *Planck 2015 results. XIII. Cosmological parameters*, Astron. Astrophys. **594** (2016) A13 [1502.01589].
[211] T. Charnock, A. Avgoustidis, E. J. Copeland and A. Moss, *CMB constraints on cosmic strings and superstrings*, Phys. Rev. D **93** (2016) 123503 [1603.01275].
[212] J. Lizarraga, J. Urrestilla, D. Daverio, M. Hindmarsh and M. Kunz, *New CMB constraints for Abelian Higgs cosmic strings*, JCAP **10** (2016) 042 [1609.03386].

[213] S. A. Sanidas, R. A. Battye and B. W. Stappers, *Constraints on cosmic string tension imposed by the limit on the stochastic gravitational wave background from the European Pulsar Timing Array*, Phys. Rev. D **85** (2012) 122003 [1201.2419].
[214] J. J. Blanco-Pillado, K. D. Olum and X. Siemens, *New limits on cosmic strings from gravitational wave observation*, Phys. Lett. B **778** (2018) 392 [1709.02434].
[215] C. Ringeval and T. Suyama, *Stochastic gravitational waves from cosmic string loops in scaling*, JCAP **12** (2017) 027 [1709.03845].
[216] J. Kume and M. Hindmarsh, *Revised bounds on local cosmic strings from NANOGrav observations*, JCAP **12** (2024) 001 [2404.02705].
[217] R. Barbieri, P. Creminelli, A. Strumia and N. Tetradis, *Baryogenesis through leptogenesis*, Nucl. Phys. B **575** (2000) 61 [hep-ph/9911315].
[218] T. Endoh, T. Morozumi and Z.-h. Xiong, *Primordial lepton family asymmetries in seesaw model*, Prog. Theor. Phys. **111** (2004) 123 [hep-ph/0308276].
[219] A. Abada, S. Davidson, F.-X. Josse-Michaux, M. Losada and A. Riotto, *Flavor issues in leptogenesis*, JCAP **04** (2006) 004 [hep-ph/0601083].
[220] A. Abada, S. Davidson, A. Ibarra, F. X. Josse-Michaux, M. Losada and A. Riotto, *Flavour Matters in Leptogenesis*, JHEP **09** (2006) 010 [hep-ph/0605281].
[221] E. Nardi, Y. Nir, E. Roulet and J. Racker, *The Importance of flavor in leptogenesis*, JHEP **01** (2006) 164 [hep-ph/0601084].
[222] S. Blanchet and P. Di Bari, *Flavor effects on leptogenesis predictions*, JCAP **03** (2007) 018 [hep-ph/0607330].
[223] M. A. Luty, *Baryogenesis via leptogenesis*, Phys. Rev. D **45** (1992) 455.
[224] G. F. Giudice, A. Notari, M. Raidal, A. Riotto and A. Strumia, *Towards a complete theory of thermal leptogenesis in the SM and MSSM*, Nucl. Phys. B **685** (2004) 89 [hep-ph/0310123].
[225] W. Buchmuller, P. Di Bari and M. Plumacher, *Leptogenesis for pedestrians*, Annals Phys. **315** (2005) 305 [hep-ph/0401240].
[226] S. Davidson, E. Nardi and Y. Nir, *Leptogenesis*, Phys. Rept. **466** (2008) 105 [0802.2962].
[227] M. Plumacher, *Baryogenesis and lepton number violation*, Z. Phys. C **74** (1997) 549 [hep-ph/9604229].
[228] D. Bodeker and W. Buchmuller, *Baryogenesis from the weak scale to the grand unification scale*, Rev. Mod. Phys. **93** (2021) 035004 [2009.07294].
[229] DESI collaboration, *DESI 2024 VI: cosmological constraints from the measurements of baryon acoustic oscillations*, JCAP **02** (2025) 021 [2404.03002].
[230] M. C. Gonzalez-Garcia, M. Maltoni and T. Schwetz, *NuFIT: Three-Flavour Global Analyses of Neutrino Oscillation Experiments*, Universe **7** (2021) 459 [2111.03086].
[231] N. Bernal, C. S. Fong, Y. F. Perez-Gonzalez and J. Turner, *Rescuing high-scale leptogenesis using primordial black holes*, Phys. Rev. D **106** (2022) 035019 [2203.08823].
[232] E. W. Kolb and A. J. Long, *Cosmological gravitational particle production and its implications for cosmological relics*, Rev. Mod. Phys. **96** (2024) 045005 [2312.09042].
[233] K. Hamaguchi, H. Murayama and T. Yanagida, *Leptogenesis from N dominated early universe*, Phys. Rev. D **65** (2002) 043512 [hep-ph/0109030].

[234] S. Davidson and A. Ibarra, *A Lower bound on the right-handed neutrino mass from leptogenesis*, Phys. Lett. B **535** (2002) 25 [hep-ph/0202239].
[235] L. Covi, E. Roulet and F. Vissani, *CP violating decays in leptogenesis scenarios*, Phys. Lett. B **384** (1996) 169 [hep-ph/9605319].
[236] A. Pilaftsis, *Resonant CP violation induced by particle mixing in transition amplitudes*, Nucl. Phys. B **504** (1997) 61 [hep-ph/9702393].
[237] A. Pilaftsis and T. E. J. Underwood, *Resonant leptogenesis*, Nucl. Phys. B **692** (2004) 303 [hep-ph/0309342].
[238] A. Pilaftsis and T. E. J. Underwood, *Electroweak-scale resonant leptogenesis*, Phys. Rev. D **72** (2005) 113001 [hep-ph/0506107].
[239] E. K. Akhmedov, V. A. Rubakov and A. Y. Smirnov, *Baryogenesis via neutrino oscillations*, Phys. Rev. Lett. **81** (1998) 1359 [hep-ph/9803255].
[240] J. Klarić, M. Shaposhnikov and I. Timiryasov, *Uniting Low-Scale Leptogenesis Mechanisms*, Phys. Rev. Lett. **127** (2021) 111802 [2008.13771].
[241] J. Klarić, M. Shaposhnikov and I. Timiryasov, *Reconciling resonant leptogenesis and baryogenesis via neutrino oscillations*, Phys. Rev. D **104** (2021) 055010 [2103.16545].
[242] N. Okada and O. Seto, *Higgs portal dark matter in the minimal gauged $U(1)_{B-L}$ model*, Phys. Rev. D **82** (2010) 023507 [1002.2525].
[243] N. Okada and Y. Orikasa, *Dark matter in the classically conformal B-L model*, Phys. Rev. D **85** (2012) 115006 [1202.1405].
[244] S. Iso, N. Okada and Y. Orikasa, *The minimal B-L model naturally realized at TeV scale*, Phys. Rev. D **80** (2009) 115007 [0909.0128].
[245] S. Iso and Y. Orikasa, *TeV Scale B-L model with a flat Higgs potential at the Planck scale: In view of the hierarchy problem*, PTEP **2013** (2013) 023B08 [1210.2848].
[246] H. Okada and Y. Orikasa, *Classically conformal radiative neutrino model with gauged $B-L$ symmetry*, Phys. Lett. B **760** (2016) 558 [1412.3616].
[247] J. Guo, Z. Kang, P. Ko and Y. Orikasa, *Accidental dark matter: Case in the scale invariant local B-L model*, Phys. Rev. D **91** (2015) 115017 [1502.00508].
[248] A. Das, N. Okada and N. Papapietro, *Electroweak vacuum stability in classically conformal B-L extension of the Standard Model*, Eur. Phys. J. C **77** (2017) 122 [1509.01466].
[249] C. G. Callan, Jr., S. R. Coleman and R. Jackiw, *A New improved energy - momentum tensor*, Annals Phys. **59** (1970) 42.
[250] D. J. Gross and J. Wess, *Scale invariance, conformal invariance, and the high-energy behavior of scattering amplitudes*, Phys. Rev. D **2** (1970) 753.
[251] L. Randall and G. Servant, *Gravitational waves from warped spacetime*, JHEP **05** (2007) 054 [hep-ph/0607158].
[252] T. Konstandin and G. Servant, *Cosmological Consequences of Nearly Conformal Dynamics at the TeV scale*, JCAP **12** (2011) 009 [1104.4791].
[253] T. Hambye and A. Strumia, *Dynamical generation of the weak and Dark Matter scale*, Phys. Rev. D **88** (2013) 055022 [1306.2329].
[254] J. Kubo and M. Yamada, *Scale genesis and gravitational wave in a classically scale invariant extension of the standard model*, JCAP **12** (2016) 001 [1610.02241].
[255] J. Jaeckel, V. V. Khoze and M. Spannowsky, *Hearing the signal of dark sectors with gravitational wave detectors*, Phys. Rev. D **94** (2016) 103519 [1602.03901].
[256] R. Jinno and M. Takimoto, *Probing a classically conformal B-L model with gravitational waves*, Phys. Rev. D **95** (2017) 015020 [1604.05035].

[257] L. Marzola, A. Racioppi and V. Vaskonen, *Phase transition and gravitational wave phenomenology of scalar conformal extensions of the Standard Model*, Eur. Phys. J. C **77** (2017) 484 [1704.01034].
[258] C. Marzo, L. Marzola and V. Vaskonen, *Phase transition and vacuum stability in the classically conformal B–L model*, Eur. Phys. J. C **79** (2019) 601 [1811.11169].
[259] I. Baldes and C. Garcia-Cely, *Strong gravitational radiation from a simple dark matter model*, JHEP **05** (2019) 190 [1809.01198].
[260] S. Bruggisser, B. Von Harling, O. Matsedonskyi and G. Servant, *Electroweak Phase Transition and Baryogenesis in Composite Higgs Models*, JHEP **12** (2018) 099 [1804.07314].
[261] I. Baldes and C. Garcia-Cely, *Strong gravitational radiation from a simple dark matter model*, JHEP **05** (2019) 190 [1809.01198].
[262] T. Prokopec, J. Rezacek and B. Świeżewska, *Gravitational waves from conformal symmetry breaking*, JCAP **02** (2019) 009 [1809.11129].
[263] A. Mohamadnejad, *Gravitational waves from scale-invariant vector dark matter model: Probing below the neutrino-floor*, Eur. Phys. J. C **80** (2020) 197 [1907.08899].
[264] A. Dasgupta, P. S. B. Dev, A. Ghoshal and A. Mazumdar, *Gravitational wave pathway to testable leptogenesis*, Phys. Rev. D **106** (2022) 075027 [2206.07032].
[265] M. Kierkla, A. Karam and B. Swiezewska, *Conformal model for gravitational waves and dark matter: a status update*, JHEP **03** (2023) 007 [2210.07075].
[266] L. Sagunski, P. Schicho and D. Schmitt, *Supercool exit: Gravitational waves from QCD-triggered conformal symmetry breaking*, Phys. Rev. D **107** (2023) 123512 [2303.02450].
[267] A. Salvio, *Supercooling in radiative symmetry breaking: theory extensions, gravitational wave detection and primordial black holes*, JCAP **12** (2023) 046 [2307.04694].
[268] J. a. Gonçalves, D. Marfatia, A. P. Morais and R. Pasechnik, *Gravitational waves from supercooled phase transitions in conformal Majoron models of neutrino mass*, 2412.02645.
[269] S. Balan, T. Bringmann, F. Kahlhoefer, J. Matuszak and C. Tasillo, *Sub-GeV dark matter and nano-Hertz gravitational waves from a classically conformal dark sector*, 2502.19478.
[270] A. Gonstal, M. Lewicki and B. Swiezewska, *Reconstructing early universe evolution with gravitational waves from supercooled phase transitions*, 2502.18436.
[271] M. Kierkla, P. Schicho, B. Swiezewska, T. V. I. Tenkanen and J. van de Vis, *Finite-temperature bubble nucleation with shifting scale hierarchies*, 2503.13597.
[272] W. Chao, W.-F. Cui, H.-K. Guo and J. Shu, *Gravitational wave imprint of new symmetry breaking*, Chin. Phys. C **44** (2020) 123102 [1707.09759].
[273] N. Okada and O. Seto, *Probing the seesaw scale with gravitational waves*, Phys. Rev. D **98** (2018) 063532 [1807.00336].
[274] L. Bian, W. Cheng, H.-K. Guo and Y. Zhang, *Cosmological implications of a $B-L$ charged hidden scalar: leptogenesis and gravitational waves*, Chin. Phys. C **45** (2021) 113104 [1907.13589].
[275] T. Hasegawa, N. Okada and O. Seto, *Gravitational waves from the minimal gauged $U(1)_{B-L}$ model*, Phys. Rev. D **99** (2019) 095039 [1904.03020].
[276] KAGRA collaboration, *Detector configuration of KAGRA: The Japanese*

cryogenic gravitational-wave detector, Class. Quant. Grav. **29** (2012) 124007 [1111.7185].

[277] KAGRA collaboration, *KAGRA: 2.5 Generation Interferometric Gravitational Wave Detector*, Nature Astron. **3** (2019) 35 [1811.08079].

[278] KAGRA collaboration, *Interferometer design of the KAGRA gravitational wave detector*, Phys. Rev. D **88** (2013) 043007 [1306.6747].

[279] S. Hild et al., *Sensitivity Studies for Third-Generation Gravitational Wave Observatories*, Class. Quant. Grav. **28** (2011) 094013 [1012.0908].

[280] ET collaboration, *Science Case for the Einstein Telescope*, JCAP **03** (2020) 050 [1912.02622].

[281] M. A. McLaughlin, *The North American Nanohertz Observatory for Gravitational Waves*, Class. Quant. Grav. **30** (2013) 224008 [1310.0758].

[282] R. N. Manchester et al., *The Parkes Pulsar Timing Array Project*, Publ. Astron. Soc. Austral. **30** (2013) 17 [1210.6130].

[283] EPTA collaboration, *European Pulsar Timing Array Limits On An Isotropic Stochastic Gravitational-Wave Background*, Mon. Not. Roy. Astron. Soc. **453** (2015) 2576 [1504.03692].

[284] G. Hobbs et al., *The international pulsar timing array project: using pulsars as a gravitational wave detector*, Class. Quant. Grav. **27** (2010) 084013 [0911.5206].

[285] I. Baldes, Y. Gouttenoire, F. Sala and G. Servant, *Supercool composite Dark Matter beyond 100 TeV*, JHEP **07** (2022) 084 [2110.13926].

[286] P. Huang and K.-P. Xie, *Leptogenesis triggered by a first-order phase transition*, JHEP **09** (2022) 052 [2206.04691].

[287] I. Baldes, M. Dichtl, Y. Gouttenoire and F. Sala, *Ultrahigh-Energy Particle Collisions and Heavy Dark Matter at Phase Transitions*, Phys. Rev. Lett. **134** (2025) 061001 [2306.15555].

[288] Y. Gouttenoire, *Primordial black holes from conformal Higgs*, Phys. Lett. B **855** (2024) 138800 [2311.13640].

[289] Y. Gouttenoire and T. Volansky, *Primordial black holes from supercooled phase transitions*, Phys. Rev. D **110** (2024) 043514 [2305.04942].

[290] X.-R. Wong and K.-P. Xie, *Freeze-in of WIMP dark matter*, Phys. Rev. D **108** (2023) 055035 [2304.00908].

[291] E. J. Chun, T. P. Dutka, T. H. Jung, X. Nagels and M. Vanvlasselaer, *Bubble-assisted leptogenesis*, JHEP **09** (2023) 164 [2305.10759].

[292] T. Bringmann, T. E. Gonzalo, F. Kahlhoefer, J. Matuszak and C. Tasillo, *Hunting WIMPs with LISA: correlating dark matter and gravitational wave signals*, JCAP **05** (2024) 065 [2311.06346].

[293] M. Cataldi and B. Shakya, *Leptogenesis via bubble collisions*, JCAP **11** (2024) 047 [2407.16747].

[294] I. Baldes, S. Blasi, A. Mariotti, A. Sevrin and K. Turbang, *Baryogenesis via relativistic bubble expansion*, Phys. Rev. D **104** (2021) 115029 [2106.15602].

[295] A. Azatov, M. Vanvlasselaer and W. Yin, *Baryogenesis via relativistic bubble walls*, JHEP **10** (2021) 043 [2106.14913].

[296] A. Azatov, G. Barni, S. Chakraborty, M. Vanvlasselaer and W. Yin, *Ultra-relativistic bubbles from the simplest Higgs portal and their cosmological consequences*, JHEP **10** (2022) 017 [2207.02230].

[297] D. Schmitt and L. Sagunski, *QCD-sourced tachyonic phase transition in a supercooled Universe*, 2409.05851.

[298] F. Ferrer, A. Ghoshal and M. Lewicki, *Imprints of a supercooled phase transition in*

the gravitational wave spectrum from a cosmic string network, JHEP **09** (2023) 036 [2304.02636].
[299] B. Fornal and B. Shams Es Haghi, *Baryon and Lepton Number Violation from Gravitational Waves*, Phys. Rev. D **102** (2020) 115037 [2008.05111].
[300] J. Bosch, Z. Delgado, B. Fornal and A. Leon, *Gravitational wave signatures of gauged baryon and lepton number*, Phys. Rev. D **108** (2023) 095014 [2306.00332].
[301] C. Coriano, L. Delle Rose and C. Marzo, *Constraints on abelian extensions of the Standard Model from two-loop vacuum stability and $U(1)_{B-L}$*, JHEP **02** (2016) 135 [1510.02379].
[302] M. Sher, *Electroweak Higgs Potentials and Vacuum Stability*, Phys. Rept. **179** (1989) 273.
[303] K. A. Meissner and H. Nicolai, *Renormalization Group and Effective Potential in Classically Conformal Theories*, Acta Phys. Polon. B **40** (2009) 2737 [0809.1338].
[304] L. Basso, S. Moretti and G. M. Pruna, *A Renormalisation Group Equation Study of the Scalar Sector of the Minimal B-L Extension of the Standard Model*, Phys. Rev. D **82** (2010) 055018 [1004.3039].
[305] G.-y. Huang and S. Zhou, *Precise Values of Running Quark and Lepton Masses in the Standard Model*, Phys. Rev. D **103** (2021) 016010 [2009.04851].
[306] M. E. Carrington, *The Effective potential at finite temperature in the Standard Model*, Phys. Rev. D **45** (1992) 2933.
[307] D. Comelli and J. R. Espinosa, *Bosonic thermal masses in supersymmetry*, Phys. Rev. D **55** (1997) 6253 [hep-ph/9606438].
[308] E. Witten, *Cosmological Consequences of a Light Higgs Boson*, Nucl. Phys. B **177** (1981) 477.
[309] S. Iso, P. D. Serpico and K. Shimada, *QCD-Electroweak First-Order Phase Transition in a Supercooled Universe*, Phys. Rev. Lett. **119** (2017) 141301 [1704.04955].
[310] B. von Harling and G. Servant, *QCD-induced Electroweak Phase Transition*, JHEP **01** (2018) 159 [1711.11554].
[311] S. Ipek and T. M. P. Tait, *Early Cosmological Period of QCD Confinement*, Phys. Rev. Lett. **122** (2019) 112001 [1811.00559].
[312] Y. Guan and S. Matsuzaki, *Ladder top-quark condensation imprints in supercooled electroweak phase transition*, JHEP **09** (2024) 140 [2405.03265].
[313] W. Liu and K.-P. Xie, *Probing radiative electroweak symmetry breaking with colliders and gravitational waves*, Phys. Rev. D **110** (2024) 115001 [2408.03649].
[314] M. Lewicki, O. Pujolàs and V. Vaskonen, *Escape from supercooling with or without bubbles: gravitational wave signatures*, Eur. Phys. J. C **81** (2021) 857 [2106.09706].
[315] Y. Cui, M. Lewicki, D. E. Morrissey and J. D. Wells, *Cosmic Archaeology with Gravitational Waves from Cosmic Strings*, Phys. Rev. D **97** (2018) 123505 [1711.03104].
[316] N. Bernal and F. Hajkarim, *Primordial Gravitational Waves in Nonstandard Cosmologies*, Phys. Rev. D **100** (2019) 063502 [1905.10410].
[317] S. Blasi, V. Brdar and K. Schmitz, *Fingerprint of low-scale leptogenesis in the primordial gravitational-wave spectrum*, Phys. Rev. Res. **2** (2020) 043321 [2004.02889].

[318] M. Pearce, L. Pearce, G. White and C. Balázs, *Using Gravitational Wave Signals to Disentangle Early Matter Dominated Epochs*, 2503.03101.

[319] F. Hahn-Woernle and M. Plumacher, *Effects of reheating on leptogenesis*, Nucl. Phys. B **806** (2009) 68 [0801.3972].

[320] X. Zhang, *Towards a systematic study of non-thermal leptogenesis from inflaton decays*, JHEP **05** (2024) 147 [2311.05824].

[321] J.-Y. Tong, Z.-H. Yu and H.-H. Zhang, *Leptogenesis assisted by scalar decays*, 2406.13468.

[322] M. Cataldi, A. Mariotti, F. Sala and M. Vanvlasselaer, *ALP leptogenesis*, 2407.01667.

[323] F. Lyonnet and I. Schienbein, *PyR@TE 2: A Python tool for computing RGEs at two-loop*, Comput. Phys. Commun. **213** (2017) 181 [1608.07274].

[324] P. Bhattacharjee, T. W. B. Kibble and N. Turok, *Baryon Number From Collapsing Cosmic Strings*, Phys. Lett. B **119** (1982) 95.

[325] R. H. Brandenberger, A.-C. Davis and M. Hindmarsh, *Baryogenesis from collapsing topological defects*, Phys. Lett. B **263** (1991) 239.

[326] A.-C. Davis and M. A. Earnshaw, *Baryogenesis from collapsing cosmic string loops*, Nucl. Phys. B **394** (1993) 21.

[327] H. Lew and A. Riotto, *Baryogenesis through collapsing string loops in gauged baryon and lepton models*, Phys. Rev. D **49** (1994) 3837 [hep-ph/9306336].

[328] M. Mohazzab, *Baryogenesis from long cosmic strings*, Phys. Lett. B **350** (1995) 13 [hep-ph/9409274].

[329] R. Jeannerot, *A New mechanism for leptogenesis*, Phys. Rev. Lett. **77** (1996) 3292 [hep-ph/9609442].

[330] P. Bhattacharjee and G. Sigl, *Origin and propagation of extremely high-energy cosmic rays*, Phys. Rept. **327** (2000) 109 [astro-ph/9811011].

[331] N. Sahu, P. Bhattacharjee and U. A. Yajnik, *B - L cosmic strings and baryogenesis*, Phys. Rev. D **70** (2004) 083534 [hep-ph/0406054].

[332] P.-H. Gu and H. Mao, *Constraint on B - L cosmic string from leptogenesis with degenerate neutrinos*, Phys. Lett. B **619** (2005) 226 [hep-ph/0503126].

[333] N. Sahu, P. Bhattacharjee and U. A. Yajnik, *Baryogenesis via leptogenesis in presence of cosmic strings*, Nucl. Phys. B **752** (2006) 280 [hep-ph/0512350].

[334] R. Jeannerot and M. Postma, *Leptogenesis from reheating after inflation and cosmic string decay*, JCAP **12** (2005) 006 [hep-ph/0507162].

[335] C. J. A. P. Martins and E. P. S. Shellard, *String evolution with friction*, Phys. Rev. D **53** (1996) 575 [hep-ph/9507335].

[336] C. J. A. P. Martins and E. P. S. Shellard, *Quantitative string evolution*, Phys. Rev. D **54** (1996) 2535 [hep-ph/9602271].

[337] C. J. A. P. Martins and E. P. S. Shellard, *Extending the velocity dependent one scale string evolution model*, Phys. Rev. D **65** (2002) 043514 [hep-ph/0003298].

[338] C. J. A. P. Martins, *Defect Evolution in Cosmology and Condensed Matter: Quantitative Analysis with the Velocity-Dependent One-Scale Model*, SpringerBriefs in Physics. Springer, Cham, 2016, 10.1007/978-3-319-44553-3.

[339] R. Jackiw and P. Rossi, *Zero Modes of the Vortex - Fermion System*, Nucl. Phys. B **190** (1981) 681.

[340] E. J. Weinberg, *Index Calculations for the Fermion-Vortex System*, Phys. Rev. D **24** (1981) 2669.

[341] E. Witten, *Superconducting Strings*, Nucl. Phys. B **249** (1985) 557.

[342] H. Chavez and L. Masperi, *A Possible origin of superconducting currents in cosmic*

strings, New J. Phys. **4** (2002) 65 [hep-ph/0206275].
[343] R. H. Brandenberger, A.-C. Davis and A. M. Matheson, *Callan-rubakov Effect for Strings*, Nucl. Phys. B **307** (1988) 909.
[344] Y.-Z. Chu and T. Vachaspati, *Fermions on one or fewer kinks*, Phys. Rev. D **77** (2008) 025006 [0709.3668].
[345] C. J. A. P. Martins, P. Peter, I. Y. Rybak and E. P. S. Shellard, *Generalized velocity-dependent one-scale model for current-carrying strings*, Phys. Rev. D **103** (2021) 043538 [2011.09700].
[346] C. J. A. P. Martins, P. Peter, I. Y. Rybak and E. P. S. Shellard, *Charge-velocity-dependent one-scale linear model*, Phys. Rev. D **104** (2021) 103506 [2108.03147].
[347] P. Auclair, S. Blasi, V. Brdar and K. Schmitz, *Gravitational Waves from Current-Carrying Cosmic Strings*, 2207.03510.
[348] I. Y. Rybak and L. Sousa, *Emission of gravitational waves by superconducting cosmic strings*, 2209.01068.
[349] I. Y. Rybak, C. J. A. P. Martins, P. Peter and E. P. S. Shellard, *Cosmic microwave background signatures from current-carrying cosmic strings*, Phys. Rev. D **110** (2024) 023534 [2403.16332].
[350] J. R. C. C. C. Correia, C. J. A. P. Martins and F. C. N. Q. Pimenta, *Evolution of current-carrying string networks*, Phys. Lett. B **855** (2024) 138788 [2406.03931].
[351] K. Harigaya, X. Niu, W. Xue and F. Yang, *Stability of Superconducting Strings*, 2412.12259.
[352] T. Binder, T. Bringmann, M. Gustafsson and A. Hryczuk, *Early kinetic decoupling of dark matter: when the standard way of calculating the thermal relic density fails*, Phys. Rev. D **96** (2017) 115010 [1706.07433].
[353] T. Binder, T. Bringmann, M. Gustafsson and A. Hryczuk, *Dark matter relic abundance beyond kinetic equilibrium*, Eur. Phys. J. C **81** (2021) 577 [2103.01944].
[354] J. Heeck and D. Teresi, *Leptogenesis and neutral gauge bosons*, Phys. Rev. D **94** (2016) 095024 [1609.03594].
[355] J. A. Harvey and M. S. Turner, *Cosmological baryon and lepton number in the presence of electroweak fermion number violation*, Phys. Rev. D **42** (1990) 3344.
[356] J. Garriga and M. Sakellariadou, *Effects of friction on cosmic strings*, Phys. Rev. D **48** (1993) 2502 [hep-th/9303024].
[357] M. Hindmarsh, J. Lizarraga, J. Urrestilla, D. Daverio and M. Kunz, *Scaling from gauge and scalar radiation in Abelian Higgs string networks*, Phys. Rev. D **96** (2017) 023525 [1703.06696].
[358] J. N. Moore, E. P. S. Shellard and C. J. A. P. Martins, *On the evolution of Abelian-Higgs string networks*, Phys. Rev. D **65** (2002) 023503 [hep-ph/0107171].
[359] C. J. A. P. Martins, J. N. Moore and E. P. S. Shellard, *A Unified model for vortex string network evolution*, Phys. Rev. Lett. **92** (2004) 251601 [hep-ph/0310255].
[360] D. Baumann, *Cosmology*. Cambridge University Press, 7, 2022, 10.1017/9781108937092.
[361] A. D. Linde, *Hybrid inflation*, Phys. Rev. D **49** (1994) 748 [astro-ph/9307002].
[362] E. J. Copeland, A. R. Liddle, D. H. Lyth, E. D. Stewart and D. Wands, *False vacuum inflation with Einstein gravity*, Phys. Rev. D **49** (1994) 6410 [astro-ph/9401011].

[363] G. R. Dvali, Q. Shafi and R. K. Schaefer, *Large scale structure and supersymmetric inflation without fine tuning*, Phys. Rev. Lett. **73** (1994) 1886 [hep-ph/9406319].
[364] W. Buchmuller, K. Schmitz and G. Vertongen, *Matter and Dark Matter from False Vacuum Decay*, Phys. Lett. B **693** (2010) 421 [1008.2355].
[365] W. Buchmuller, K. Schmitz and G. Vertongen, *Entropy, Baryon Asymmetry and Dark Matter from Heavy Neutrino Decays*, Nucl. Phys. B **851** (2011) 481 [1104.2750].
[366] W. Buchmuller, V. Domcke and K. Schmitz, *Spontaneous B-L Breaking as the Origin of the Hot Early Universe*, Nucl. Phys. B **862** (2012) 587 [1202.6679].
[367] F. Hahn-Woernle, M. Plumacher and Y. Y. Y. Wong, *Full Boltzmann equations for leptogenesis including scattering*, JCAP **08** (2009) 028 [0907.0205].
[368] P. Bhattacharjee and G. Sigl, *Origin and propagation of extremely high-energy cosmic rays*, Phys. Rept. **327** (2000) 109 [astro-ph/9811011].
[369] A. J. Gill and T. W. B. Kibble, *Cosmic rays from cosmic strings*, Phys. Rev. D **50** (1994) 3660 [hep-ph/9403395].
[370] J. J. Blanco-Pillado and K. D. Olum, *Form of cosmic string cusps*, Phys. Rev. D **59** (1999) 063508 [gr-qc/9810005].
[371] V. Domcke, K. Kamada, K. Mukaida, K. Schmitz and M. Yamada, *Wash-In Leptogenesis*, Phys. Rev. Lett. **126** (2021) 201802 [2011.09347].
[372] V. Domcke, K. Kamada, K. Mukaida, K. Schmitz and M. Yamada, *Wash-in leptogenesis after axion inflation*, JHEP **01** (2023) 053 [2210.06412].
[373] D. Bödeker and D. Schröder, *Equilibration of right-handed electrons*, JCAP **05** (2019) 010 [1902.07220].
[374] S. Antusch, S. F. King and A. Riotto, *Flavour-Dependent Leptogenesis with Sequential Dominance*, JCAP **11** (2006) 011 [hep-ph/0609038].
[375] W. Buchmuller and M. Plumacher, *Spectator processes and baryogenesis*, Phys. Lett. B **511** (2001) 74 [hep-ph/0104189].
[376] B. Garbrecht and P. Schwaller, *Spectator Effects during Leptogenesis in the Strong Washout Regime*, JCAP **10** (2014) 012 [1404.2915].
[377] B. Garbrecht, P. Klose and C. Tamarit, *Relativistic and spectator effects in leptogenesis with heavy sterile neutrinos*, JHEP **02** (2020) 117 [1904.09956].
[378] K. Mukaida, H. Watanabe and M. Yamada, *Thermal wash-in leptogenesis via heavy Higgs decay*, JCAP **09** (2024) 063 [2405.14332].
[379] M. Joyce and M. E. Shaposhnikov, *Primordial magnetic fields, right-handed electrons, and the Abelian anomaly*, Phys. Rev. Lett. **79** (1997) 1193 [astro-ph/9703005].
[380] A. Boyarsky, J. Frohlich and O. Ruchayskiy, *Self-consistent evolution of magnetic fields and chiral asymmetry in the early Universe*, Phys. Rev. Lett. **108** (2012) 031301 [1109.3350].
[381] Y. Akamatsu and N. Yamamoto, *Chiral Plasma Instabilities*, Phys. Rev. Lett. **111** (2013) 052002 [1302.2125].
[382] Y. Hirono, D. Kharzeev and Y. Yin, *Self-similar inverse cascade of magnetic helicity driven by the chiral anomaly*, Phys. Rev. D **92** (2015) 125031 [1509.07790].
[383] N. Yamamoto, *Scaling laws in chiral hydrodynamic turbulence*, Phys. Rev. D **93** (2016) 125016 [1603.08864].
[384] I. Rogachevskii, O. Ruchayskiy, A. Boyarsky, J. Fröhlich, N. Kleeorin, A. Brandenburg et al., *Laminar and turbulent dynamos in chiral*

magnetohydrodynamics-I: Theory, Astrophys. J. **846** (2017) 153 [1705.00378].
[385] K. Kamada, *Return of grand unified theory baryogenesis: Source of helical hypermagnetic fields for the baryon asymmetry of the universe*, Phys. Rev. D **97** (2018) 103506 [1802.03055].
[386] V. Domcke, K. Kamada, K. Mukaida, K. Schmitz and M. Yamada, *New Constraint on Primordial Lepton Flavor Asymmetries*, Phys. Rev. Lett. **130** (2023) 261803 [2208.03237].
[387] M. Giovannini and M. E. Shaposhnikov, *Primordial hypermagnetic fields and triangle anomaly*, Phys. Rev. D **57** (1998) 2186 [hep-ph/9710234].
[388] M. Giovannini and M. E. Shaposhnikov, *Primordial magnetic fields, anomalous isocurvature fluctuations and big bang nucleosynthesis*, Phys. Rev. Lett. **80** (1998) 22 [hep-ph/9708303].
[389] M. Giovannini, *Primordial hypermagnetic knots*, Phys. Rev. D **61** (2000) 063004 [hep-ph/9905358].
[390] M. Giovannini, *Hypermagnetic knots, Chern-Simons waves and the baryon asymmetry*, Phys. Rev. D **61** (2000) 063502 [hep-ph/9906241].
[391] K. Bamba, *Baryon asymmetry from hypermagnetic helicity in dilaton hypercharge electromagnetism*, Phys. Rev. D **74** (2006) 123504 [hep-ph/0611152].
[392] K. Bamba, C. Q. Geng and S. H. Ho, *Hypermagnetic Baryogenesis*, Phys. Lett. B **664** (2008) 154 [0712.1523].
[393] T. Fujita and K. Kamada, *Large-scale magnetic fields can explain the baryon asymmetry of the Universe*, Phys. Rev. D **93** (2016) 083520 [1602.02109].
[394] K. Kamada and A. J. Long, *Baryogenesis from decaying magnetic helicity*, Phys. Rev. D **94** (2016) 063501 [1606.08891].
[395] K. Kamada and A. J. Long, *Evolution of the Baryon Asymmetry through the Electroweak Crossover in the Presence of a Helical Magnetic Field*, Phys. Rev. D **94** (2016) 123509 [1610.03074].
[396] B. A. Campbell, S. Davidson, J. R. Ellis and K. A. Olive, *On the baryon, lepton flavor and right-handed electron asymmetries of the universe*, Phys. Lett. B **297** (1992) 118 [hep-ph/9302221].
[397] J. M. Cline, K. Kainulainen and K. A. Olive, *On the erasure and regeneration of the primordial baryon asymmetry by sphalerons*, Phys. Rev. Lett. **71** (1993) 2372 [hep-ph/9304321].
[398] J. M. Cline, K. Kainulainen and K. A. Olive, *Protecting the primordial baryon asymmetry from erasure by sphalerons*, Phys. Rev. D **49** (1994) 6394 [hep-ph/9401208].
[399] H. Davoudiasl, D. E. Morrissey, K. Sigurdson and S. Tulin, *Hylogenesis: A Unified Origin for Baryonic Visible Matter and Antibaryonic Dark Matter*, Phys. Rev. Lett. **105** (2010) 211304 [1008.2399].
[400] G. R. Farrar and G. Zaharijas, *Dark matter and the baryon asymmetry*, Phys. Rev. Lett. **96** (2006) 041302 [hep-ph/0510079].
[401] R. Kitano and I. Low, *Dark matter from baryon asymmetry*, Phys. Rev. D **71** (2005) 023510 [hep-ph/0411133].
[402] K. Dick, M. Lindner, M. Ratz and D. Wright, *Leptogenesis with Dirac neutrinos*, Phys. Rev. Lett. **84** (2000) 4039 [hep-ph/9907562].
[403] H. Davoudiasl, R. Kitano, G. D. Kribs, H. Murayama and P. J. Steinhardt, *Gravitational baryogenesis*, Phys. Rev. Lett. **93** (2004) 201301 [hep-ph/0403019].
[404] A. G. Cohen and D. B. Kaplan, *Thermodynamic Generation of the Baryon*

Asymmetry, Phys. Lett. B **199** (1987) 251.
[405] A. G. Cohen and D. B. Kaplan, *SPONTANEOUS BARYOGENESIS*, Nucl. Phys. B **308** (1988) 913.
[406] A. G. Cohen, D. B. Kaplan and A. E. Nelson, *Spontaneous baryogenesis at the weak phase transition*, Phys. Lett. B **263** (1991) 86.
[407] A. Dolgov and K. Freese, *Calculation of particle production by Nambu Goldstone bosons with application to inflation reheating and baryogenesis*, Phys. Rev. D **51** (1995) 2693 [hep-ph/9410346].
[408] A. Dolgov, K. Freese, R. Rangarajan and M. Srednicki, *Baryogenesis during reheating in natural inflation and comments on spontaneous baryogenesis*, Phys. Rev. D **56** (1997) 6155 [hep-ph/9610405].
[409] M.-z. Li, X.-l. Wang, B. Feng and X.-m. Zhang, *Quintessence and spontaneous leptogenesis*, Phys. Rev. D **65** (2002) 103511 [hep-ph/0112069].
[410] T. Chiba, F. Takahashi and M. Yamaguchi, *Baryogenesis in a flat direction with neither baryon nor lepton charge*, Phys. Rev. Lett. **92** (2004) 011301 [hep-ph/0304102].
[411] S. M. Carroll and J. Shu, *Models of baryogenesis via spontaneous Lorentz violation*, Phys. Rev. D **73** (2006) 103515 [hep-ph/0510081].
[412] A. De Simone and T. Kobayashi, *Cosmological Aspects of Spontaneous Baryogenesis*, JCAP **08** (2016) 052 [1605.00670].
[413] H. M. Sadjadi, *A Note on Gravitational Baryogenesis*, Phys. Rev. D **76** (2007) 123507 [0709.0697].
[414] H. Li, M.-z. Li and X.-m. Zhang, *Gravitational leptogenesis and neutrino mass limit*, Phys. Rev. D **70** (2004) 047302 [hep-ph/0403281].
[415] B. Feng, H. Li, M.-z. Li and X.-m. Zhang, *Gravitational leptogenesis and its signatures in CMB*, Phys. Lett. B **620** (2005) 27 [hep-ph/0406269].
[416] G. Lambiase and G. Scarpetta, *Baryogenesis in f(R): Theories of Gravity*, Phys. Rev. D **74** (2006) 087504 [astro-ph/0610367].
[417] G. Lambiase, S. Mohanty and A. R. Prasanna, *Neutrino coupling to cosmological background: A review on gravitational Baryo/Leptogenesis*, Int. J. Mod. Phys. D **22** (2013) 1330030 [1310.8459].
[418] V. K. Oikonomou and E. N. Saridakis, *$f(T)$ gravitational baryogenesis*, Phys. Rev. D **94** (2016) 124005 [1607.08561].
[419] S. D. Odintsov and V. K. Oikonomou, *Gauss–Bonnet gravitational baryogenesis*, Phys. Lett. B **760** (2016) 259 [1607.00545].
[420] M. P. L. P. Ramos and J. Páramos, *Baryogenesis in Nonminimally Coupled $f(R)$ Theories*, Phys. Rev. D **96** (2017) 104024 [1709.04442].
[421] S. Bhattacharjee and P. K. Sahoo, *Baryogenesis in $f(Q,\mathcal{T})$ gravity*, Eur. Phys. J. C **80** (2020) 289 [2002.11483].
[422] D. S. Pereira, *Scalar-tensor Baryogenesis*, 2412.06984.
[423] D. S. Pereira, F. S. N. Lobo and J. P. Mimoso, *Gravitational baryogenesis in energy-momentum squared gravity*, 2409.04623.
[424] A. De Simone, T. Kobayashi and S. Liberati, *Geometric Baryogenesis from Shift Symmetry*, Phys. Rev. Lett. **118** (2017) 131101 [1612.04824].
[425] Q. Liang, J. Sakstein and M. Trodden, *Baryogenesis via gravitational spontaneous symmetry breaking*, Phys. Rev. D **100** (2019) 063518 [1904.10510].
[426] L. Kofman, A. D. Linde and A. A. Starobinsky, *Reheating after inflation*, Phys. Rev. Lett. **73** (1994) 3195 [hep-th/9405187].
[427] L. Kofman, A. D. Linde and A. A. Starobinsky, *Towards the theory of reheating*

after inflation, Phys. Rev. D **56** (1997) 3258 [hep-ph/9704452].
[428] B. A. Bassett, S. Tsujikawa and D. Wands, *Inflation dynamics and reheating*, Rev. Mod. Phys. **78** (2006) 537 [astro-ph/0507632].
[429] R. Allahverdi, R. Brandenberger, F.-Y. Cyr-Racine and A. Mazumdar, *Reheating in Inflationary Cosmology: Theory and Applications*, Ann. Rev. Nucl. Part. Sci. **60** (2010) 27 [1001.2600].
[430] M. S. Turner, *Coherent Scalar Field Oscillations in an Expanding Universe*, Phys. Rev. D **28** (1983) 1243.
[431] V. Domcke, Y. Ema, K. Mukaida and M. Yamada, *Spontaneous Baryogenesis from Axions with Generic Couplings*, JHEP **08** (2020) 096 [2006.03148].
[432] J. I. McDonald and G. M. Shore, *Gravitational leptogenesis, C, CP and strong equivalence*, JHEP **02** (2015) 076 [1411.3669].
[433] J. I. McDonald and G. M. Shore, *Leptogenesis from loop effects in curved spacetime*, JHEP **04** (2016) 030 [1512.02238].
[434] J. I. McDonald and G. M. Shore, *Leptogenesis and gravity: baryon asymmetry without decays*, Phys. Lett. B **766** (2017) 162 [1604.08213].
[435] J. I. McDonald and G. M. Shore, *Dynamical Evolution of Gravitational Leptogenesis*, JHEP **10** (2020) 025 [2006.09425].
[436] R. Samanta and S. Datta, *Gravitational wave complementarity and impact of NANOGrav data on gravitational leptogenesis*, JHEP **05** (2021) 211 [2009.13452].
[437] R. Samanta and S. Datta, *Flavour effects in gravitational leptogenesis*, JHEP **12** (2020) 067 [2007.11725].
[438] R. Samanta and S. Datta, *Probing leptogenesis and pre-BBN universe with gravitational waves spectral shapes*, JHEP **11** (2021) 017 [2108.08359].
[439] R. M. Wald, *General Relativity*. Chicago Univ. Pr., Chicago, USA, 1984, 10.7208/chicago/9780226870373.001.0001.
[440] S. M. Carroll, *Spacetime and Geometry: An Introduction to General Relativity*. Cambridge University Press, 7, 2019, 10.1017/9781108770385.
[441] R. Kallosh and A. Linde, *Universality Class in Conformal Inflation*, JCAP **07** (2013) 002 [1306.5220].
[442] B. Barman, S. Cléry, R. T. Co, Y. Mambrini and K. A. Olive, *Gravity as a portal to reheating, leptogenesis and dark matter*, JHEP **12** (2022) 072 [2210.05716].
[443] Planck collaboration, *Planck 2018 results. X. Constraints on inflation*, Astron. Astrophys. **641** (2020) A10 [1807.06211].
[444] Y. Mambrini and K. A. Olive, *Gravitational Production of Dark Matter during Reheating*, Phys. Rev. D **103** (2021) 115009 [2102.06214].
[445] K. D. Lozanov and M. A. Amin, *Equation of State and Duration to Radiation Domination after Inflation*, Phys. Rev. Lett. **119** (2017) 061301 [1608.01213].
[446] K. D. Lozanov and M. A. Amin, *Self-resonance after inflation: oscillons, transients and radiation domination*, Phys. Rev. D **97** (2018) 023533 [1710.06851].
[447] K. Schmitz and X.-J. Xu, *Wash-in leptogenesis after the evaporation of primordial black holes*, Phys. Lett. B **849** (2024) 138473 [2311.01089].
[448] L. Covi and E. Roulet, *Baryogenesis from mixed particle decays*, Phys. Lett. B **399** (1997) 113 [hep-ph/9611425].
[449] L. D. Landau and I. Pomeranchuk, *Limits of applicability of the theory of bremsstrahlung electrons and pair production at high-energies*, *Dokl. Akad. Nauk Ser. Fiz.* **92** (1953) 535.
[450] L. D. Landau and I. Pomeranchuk, *Electron cascade process at very high-energies*,

Dokl. Akad. Nauk Ser. Fiz. **92** (1953) 735.

[451] A. B. Migdal, *Bremsstrahlung and pair production in condensed media at high-energies*, Phys. Rev. **103** (1956) 1811.

[452] P. Ramond, *Journeys beyond the standard model*, vol. 101. 1999.

[453] M. Laine and M. E. Shaposhnikov, *A Remark on sphaleron erasure of baryon asymmetry*, Phys. Rev. D **61** (2000) 117302 [hep-ph/9911473].

[454] K. Fridell, L. Gráf, J. Harz and C. Hati, *Probing Lepton Number Violation: A Comprehensive Survey of Dimension-7 SMEFT*, 2306.08709.

[455] S. L. Glashow, J. Iliopoulos and L. Maiani, *Weak Interactions with Lepton-Hadron Symmetry*, Phys. Rev. D **2** (1970) 1285.

[456] M. K. Gaillard, B. W. Lee and J. L. Rosner, *Search for Charm*, Rev. Mod. Phys. **47** (1975) 277.

[457] N. Cabibbo, *Unitary Symmetry and Leptonic Decays*, Phys. Rev. Lett. **10** (1963) 531.

[458] M. Kobayashi and T. Maskawa, *CP Violation in the Renormalizable Theory of Weak Interaction*, Prog. Theor. Phys. **49** (1973) 652.

[459] Y. Grossman and P. Tanedo, *Just a taste: lectures on flavor physics.*, in *Theoretical Advanced Study Institute in Elementary Particle Physics: Anticipating the Next Discoveries in Particle Physics*, pp. 109–295, 2018, 1711.03624, DOI.

[460] T. Inami and C. S. Lim, *Effects of Superheavy Quarks and Leptons in Low-Energy Weak Processes k(L) —> mu anti-mu, K+ —> pi+ Neutrino anti-neutrino and K0 <—> anti-K0*, Prog. Theor. Phys. **65** (1981) 297.

[461] E. E. Jenkins, A. V. Manohar and P. Stoffer, *Low-Energy Effective Field Theory below the Electroweak Scale: Anomalous Dimensions*, JHEP **01** (2018) 084 [1711.05270].

[462] J. Aebischer, M. Fael, C. Greub and J. Virto, *B physics Beyond the Standard Model at One Loop: Complete Renormalization Group Evolution below the Electroweak Scale*, JHEP **09** (2017) 158 [1704.06639].

[463] T. Blake, G. Lanfranchi and D. M. Straub, *Rare B Decays as Tests of the Standard Model*, Prog. Part. Nucl. Phys. **92** (2017) 50 [1606.00916].

[464] P. Colangelo and A. Khodjamirian, *QCD sum rules, a modern perspective*, hep-ph/0010175.

[465] A. J. Buras and E. Venturini, *Searching for New Physics in Rare K and B Decays without $|V_{cb}|$ and $|V_{ub}|$ Uncertainties*, 2109.11032.

[466] W. Altmannshofer, A. J. Buras, D. M. Straub and M. Wick, *New strategies for New Physics search in $B \to K^* \nu \bar{\nu}$, $B \to K \nu \bar{\nu}$ and $B \to X_s \nu \bar{\nu}$ decays*, JHEP **04** (2009) 022 [0902.0160].

[467] A. J. Buras and E. Venturini, *The exclusive vision of rare K and B decays and of the quark mixing in the standard model*, Eur. Phys. J. C **82** (2022) 615 [2203.11960].

[468] A. J. Buras, *Standard Model predictions for rare K and B decays without new physics infection*, Eur. Phys. J. C **83** (2023) 66 [2209.03968].

[469] HPQCD collaboration, *Standard Model predictions for $B \to K \ell^+ \ell^-$, $B \to K \ell_1^- \ell_2^+$ and $B \to K \nu \bar{\nu}$ using form factors from $N_f = 2+1+1$ lattice QCD*, Phys. Rev. D **107** (2023) 014511 [2207.13371].

[470] W. G. Parrott, C. Bouchard and C. T. H. Davies, *$B \to K$ and $D \to K$ form factors from fully relativistic lattice QCD*, 2207.12468.

[471] W. G. Parrott, C. Bouchard and C. T. H. Davies, *The search for new physics in $B \to K \ell^+ \ell^-$ and $B \to K \nu \bar{\nu}$ using precise lattice QCD form factors*, in *39th*

International Symposium on Lattice Field Theory, 10, 2022, 2210.10898.
[472] A. Bharucha, D. M. Straub and R. Zwicky, *$B \to V\ell^+\ell^-$ in the Standard Model from light-cone sum rules*, *JHEP* **08** (2016) 098 [1503.05534].
[473] NA62 collaboration, *Measurement of the very rare $K^+ \to \pi^+\nu\bar{\nu}$ decay*, *JHEP* **06** (2021) 093 [2103.15389].
[474] NA62 collaboration, *New measurement of the $K^+ \to \pi^+\nu\bar{\nu}$ decay by the NA62 Experiment*, EP seminar, 2024, https://indico.cern.ch/event/1447422/.
[475] KOTO collaboration, *Search for the $K_L \to \pi^0\nu\bar{\nu}$ and $K_L \to \pi^0 X^0$ decays at the J-PARC KOTO experiment*, *Phys. Rev. Lett.* **122** (2019) 021802 [1810.09655].
[476] Belle-II collaboration, *Evidence for $B^+ \to K^+\nu\bar{\nu}$ Decays*, 2311.14647.
[477] Particle Data Group collaboration, *Review of Particle Physics*, *Chin. Phys.* **C40** (2016 and 2017 update) 100001.
[478] Belle collaboration, *Search for $B \to h\nu\bar{\nu}$ decays with semileptonic tagging at Belle*, *Phys. Rev.* **D96** (2017) 091101 [1702.03224].
[479] ALEPH collaboration, *Measurements of BR (b —> tau- anti-nu(tau) X) and BR (b —> tau- anti-nu(tau) D*+- X) and upper limits on BR (B- —> tau- anti-nu(tau)) and BR (b—> s nu anti-nu)*, *Eur. Phys. J. C* **19** (2001) 213 [hep-ex/0010022].
[480] T. Felkl, S. L. Li and M. A. Schmidt, *A tale of invisibility: constraints on new physics in $b \to s\nu\nu$*, *JHEP* **12** (2021) 118 [2111.04327].
[481] A. G. Beda, V. B. Brudanin, V. G. Egorov, D. V. Medvedev, V. S. Pogosov, M. V. Shirchenko et al., *The results of search for the neutrino magnetic moment in GEMMA experiment*, *Adv. High Energy Phys.* **2012** (2012) 350150.
[482] Borexino collaboration, *Limiting neutrino magnetic moments with Borexino Phase-II solar neutrino data*, *Phys. Rev. D* **96** (2017) 091103 [1707.09355].
[483] T. Felkl, A. Giri, R. Mohanta and M. A. Schmidt, *When Energy Goes Missing: New Physics in $b \to s\nu\nu$ with Sterile Neutrinos*, 2309.02940.
[484] X.-G. He, X.-D. Ma and G. Valencia, *FCNC B and K meson decays with light bosonic Dark Matter*, *JHEP* **03** (2023) 037 [2209.05223].
[485] S. Weinberg, *The Quantum theory of fields. Vol. 1: Foundations*. Cambridge University Press, 6, 2005, 10.1017/CBO9781139644167.
[486] T. Li, X.-D. Ma and M. A. Schmidt, *General neutrino interactions with sterile neutrinos in light of coherent neutrino-nucleus scattering and meson invisible decays*, *JHEP* **07** (2020) 152 [2005.01543].
[487] M. Gorbahn, U. Moldanazarova, K. H. Sieja, E. Stamou and M. Tabet, *The Anatomy of $K^+ \to \pi^+\nu\bar{\nu}$ Distributions*, 2312.06494.
[488] J.-M. Frere, T. Hambye and G. Vertongen, *Is leptogenesis falsifiable at LHC?*, *JHEP* **01** (2009) 051 [0806.0841].
[489] F. F. Deppisch, J. Harz and M. Hirsch, *Falsifying High-Scale Leptogenesis at the LHC*, *Phys. Rev. Lett.* **112** (2014) 221601 [1312.4447].
[490] F. F. Deppisch, J. Harz, M. Hirsch, W.-C. Huang and H. Päs, *Falsifying High-Scale Baryogenesis with Neutrinoless Double Beta Decay and Lepton Flavor Violation*, *Phys. Rev. D* **92** (2015) 036005 [1503.04825].
[491] F. F. Deppisch, L. Graf, J. Harz and W.-C. Huang, *Neutrinoless Double Beta Decay and the Baryon Asymmetry of the Universe*, *Phys. Rev. D* **98** (2018) 055029 [1711.10432].
[492] N. Gubernari, A. Kokulu and D. van Dyk, *$B \to P$ and $B \to V$ Form Factors from B-Meson Light-Cone Sum Rules beyond Leading Twist*, *JHEP* **01** (2019) 150 [1811.00983].

[493] F. Mescia and C. Smith, *Improved estimates of rare K decay matrix-elements from $K_{\ell 3}$ decays*, *Phys. Rev.* **D76** (2007) 034017 [0705.2025].

[494] R.-X. Shi, L.-S. Geng, B. Grinstein, S. Jäger and J. Martin Camalich, *Revisiting the new-physics interpretation of the $b \to c\tau\nu$ data*, *JHEP* **12** (2019) 065 [1905.08498].

[495] P. Colangelo, F. De Fazio and F. Loparco, *Probing New Physics with $\bar{B} \to \rho(770)\,\ell^-\bar{\nu}_\ell$ and $\bar{B} \to a_1(1260)\,\ell^-\bar{\nu}_\ell$*, *Phys. Rev. D* **100** (2019) 075037 [1906.07068].

[496] I. Baum, V. Lubicz, G. Martinelli, L. Orifici and S. Simula, *Matrix elements of the electromagnetic operator between kaon and pion states*, *Phys. Rev. D* **84** (2011) 074503 [1108.1021].

[497] M. Bordone, M. Jung and D. van Dyk, *Theory determination of $\bar{B} \to D^{(*)}\ell^-\bar{\nu}$ form factors at $\mathcal{O}(1/m_c^2)$*, *Eur. Phys. J. C* **80** (2020) 74 [1908.09398].

[498] P. Ball and R. Zwicky, *New results on $B \to \pi, K, \eta$ decay formfactors from light-cone sum rules*, *Phys. Rev.* **D71** (2005) 014015 [hep-ph/0406232].

[499] C. Bouchard, G. P. Lepage, C. Monahan, H. Na and J. Shigemitsu, *Rare decay $B \to Kll$ form factors from lattice QCD*, *Phys. Rev. D 88,* **054509** (2013) 054509 [1306.2384].

[500] R. R. Horgan, Z. Liu, S. Meinel and M. Wingate, *Lattice QCD calculation of form factors describing the rare decays $B \to K^*\ell^+\ell^-$ and $B_s \to \phi\ell^+\ell^-$*, *Phys. Rev.* **D89** (2014) 094501 [1310.3722].

[501] R. R. Horgan, Z. Liu, S. Meinel and M. Wingate, *Rare B decays using lattice QCD form factors*, *PoS* **LATTICE2014** (2015) 372 [1501.00367].

[502] T. Li, X.-D. Ma and M. A. Schmidt, *Implication of $K \to \pi\nu\bar{\nu}$ for generic neutrino interactions in effective field theories*, *Phys. Rev. D* **101** (2020) 055019 [1912.10433].

[503] F. F. Deppisch, K. Fridell and J. Harz, *Constraining lepton number violating interactions in rare kaon decays*, *JHEP* **12** (2020) 186 [2009.04494].

[504] A. J. Buras, J. Girrbach-Noe, C. Niehoff and D. M. Straub, *$B \to K^{(*)}\nu\bar{\nu}$ decays in the Standard Model and beyond*, *JHEP* **02** (2015) 184 [1409.4557].

[505] V. Shtabovenko, R. Mertig and F. Orellana, *FeynCalc 9.3: New features and improvements*, *Comput. Phys. Commun.* **256** (2020) 107478 [2001.04407].

[506] Particle Data Group collaboration, *Review of Particle Physics*, *Phys. Rev. D* **98** (2018) 030001.

[507] M. Blanke, *Insights from the Interplay of $K \to \pi\nu\bar{\nu}$ and ϵ_K on the New Physics Flavour Structure*, *Acta Phys.Polon.* **B41** (2010) 127 [0904.2528].

[508] A. J. Buras, D. Buttazzo and R. Knegjens, *$K \to \pi\nu\bar{\nu}$ and ϵ'/ϵ in Simplified New Physics Models*, *JHEP* **11** (2015) 166 [1507.08672].

[509] J. Aebischer, A. J. Buras and J. Kumar, *Another SMEFT story: Z' facing new results on ϵ'/ϵ, ΔM_K and $K \to \pi\nu\bar{\nu}$*, *JHEP* **12** (2020) 097 [2006.01138].

[510] Y. Grossman and Y. Nir, *$K_L \to \pi^0\nu\bar{\nu}$ beyond the standard model*, *Phys. Lett.* **B398** (1997) 163 [hep-ph/9701313].

[511] H. Georgi, *An Effective Field Theory for Heavy Quarks at Low-energies*, *Phys. Lett. B* **240** (1990) 447.

[512] M. Neubert, *Heavy quark symmetry*, *Phys. Rept.* **245** (1994) 259 [hep-ph/9306320].

[513] Y. Grossman, Z. Ligeti and E. Nardi, *First limit on inclusive $b \to x_s\nu\bar{\nu}$ decay and constraints on new physics*, *Nucl. Phys.* **B465** (1996) 369 [hep-ph/9510378].

[514] G. Buchalla, A. J. Buras and M. E. Lautenbacher, *Weak decays beyond leading*

logarithms, Rev. Mod. Phys. **68** (1996) 1125 [hep-ph/9512380].
[515] C. Bobeth, A. J. Buras, F. Kruger and J. Urban, *Qcd corrections to $\bar{b} \to x_{d,s}\nu\bar{\nu}$, $\bar{b}_{d,s} \to \ell^+\ell^-$, $k \to \pi\nu\bar{\nu}$ and $k_l \to \mu^+\mu^-$ in the mssm*, Nucl. Phys. **B630** (2002) 87 [hep-ph/0112305].
[516] R. Bause, H. Gisbert and G. Hiller, *Implications of an enhanced $B \to K\nu\bar{\nu}$ branching ratio*, 2309.00075.
[517] L. Allwicher, D. Becirevic, G. Piazza, S. Rosauro-Alcaraz and O. Sumensari, *Understanding the first measurement of $\mathcal{B}(B \to K\nu\bar{\nu})$*, 2309.02246.
[518] H. K. Dreiner, J. Y. Günther and Z. S. Wang, *The Decay $B \to K\nu\bar{\nu}$ at Belle II and a Massless Bino in R-parity-violating Supersymmetry*, 2309.03727.
[519] W. Altmannshofer, A. Crivellin, H. Haigh, G. Inguglia and J. Martin Camalich, *Light New Physics in $B \to K^{(*)}\nu\bar{\nu}$?*, 2311.14629.
[520] E. Gabrielli, L. Marzola, K. Müürsepp and M. Raidal, *Explaining the $B^+ \to K^+\nu\bar{\nu}$ excess via a massless dark photon*, 2402.05901.
[521] B.-F. Hou, X.-Q. Li, M. Shen, Y.-D. Yang and X.-B. Yuan, *Deciphering the Belle II data on $B \to K\nu\bar{\nu}$ decay in the (dark) SMEFT with minimal flavour violation*, 2402.19208.
[522] X.-G. He, X.-D. Ma, M. A. Schmidt, G. Valencia and R. R. Volkas, *Scalar dark matter explanation of the excess in the Belle II $B^+ \to K^+ +$ invisible measurement*, 2403.12485.
[523] P. D. Bolton, S. Fajfer, J. F. Kamenik and M. Novoa-Brunet, *Signatures of Light New Particles in $B \to K^{(*)}E_{\rm miss}$*, 2403.13887.
[524] D. Marzocca, M. Nardecchia, A. Stanzione and C. Toni, *Implications of $B \to K\nu\bar{\nu}$ under Rank-One Flavor Violation hypothesis*, 2404.06533.
[525] S.-Y. Ho, J. Kim and P. Ko, *Recent $B^+ \to K^+\nu\bar{\nu}$ Excess and Muon $g-2$ Illuminating Light Dark Sector with Higgs Portal*, 2401.10112.
[526] D. McKeen, J. N. Ng and D. Tuckler, *Higgs portal interpretation of the Belle II B+→K+νν measurement*, Phys. Rev. D **109** (2024) 075006 [2312.00982].
[527] L. Gärtner, N. Hartmann, L. Heinrich, M. Horstmann, T. Kuhr, M. Reboud et al., *Constructing model-agnostic likelihoods, a method for the reinterpretation of particle physics results*, 2402.08417.
[528] X.-G. He, X.-D. Ma and G. Valencia, *Revisiting models that enhance $B^+ \to K^+\nu\bar{\nu}$ in light of the new Belle II measurement*, 2309.12741.
[529] SIMBA collaboration, *Precision Global Determination of the B→Xsγ Decay Rate*, Phys. Rev. Lett. **127** (2021) 102001 [2007.04320].
[530] S. Rosauro-Alcaraz and L. P. S. Leal, *Disentangling left and right-handed neutrino effects in $B \to K^{(*)}\nu\nu$*, 2404.17440.
[531] A. J. Buras, J. Girrbach-Noe, C. Niehoff and D. M. Straub, *$B \to K^{(*)}\nu\bar{\nu}$ decays in the Standard Model and beyond*, JHEP **02** (2015) 184 [1409.4557].
[532] KATRIN collaboration, *Improved Upper Limit on the Neutrino Mass from a Direct Kinematic Method by KATRIN*, Phys. Rev. Lett. **123** (2019) 221802 [1909.06048].
[533] KATRIN collaboration, *Direct neutrino-mass measurement with sub-electronvolt sensitivity*, Nature Phys. **18** (2022) 160 [2105.08533].
[534] R. Cepedello, M. Hirsch and J. C. Helo, *Lepton number violating phenomenology of $d = 7$ neutrino mass models*, JHEP **01** (2018) 009 [1709.03397].
[535] F. F. Deppisch, L. Graf, J. Harz and W.-C. Huang, *Neutrinoless Double Beta Decay and the Baryon Asymmetry of the Universe*, Phys. Rev. D **98** (2018) 055029 [1711.10432].

[536] E. E. Jenkins, A. V. Manohar and P. Stoffer, *Low-Energy Effective Field Theory below the Electroweak Scale: Operators and Matching*, *JHEP* **03** (2018) 016 [1709.04486].

Martin Aria Mojahed

Personal Data

Date of Birth:	12 September 1996 in Stavanger, Norway
Countries of citizenship:	Norway, (Iran)
Email:	martinmoja96@gmail.com
Address:	Christofsstrasse 11, 55116 Mainz, Germany

Education

Dec 2021 - Present	**Ph.D. in theoretical particle physics and cosmology**, TUM/ JGU Currently focusing on early universe physics. Supervisor: Professor Julia Harz. Expected completion: September 2025.
Fall 2015 - Summer 2020	**M.Sc. in Applied Physics and Mathematics**, NTNU Combined undergraduate and master's program. Thesis: Two-flavor chiral perturbation theory at finite isospin density beyond leading order. Supervisor: Professor Jens O. Andersen.
2018 - 2019	**Fulbright exchange student**, UC Berkeley Exchange student doing graduate school coursework in high-energy physics.

Scholarships and Awards

2021	**Best Technology Student at Faculty of Natural Sciences** Award for being the best M.Sc. student among the graduating students in technology programs at the NTNU Faculty of Natural Sciences in 2020.
2018 - 2019	**Fulbright Scholarship** Fulbright Scholarship for studying in the US in the academic year of 2018/2019.
2015	**Best Student Award** Award for being the best student in my high school among the approximately 250 graduating students.
2015	**International Physics Olympiad (IPhO) Participant** I was ranked among the top five best high school physics students in the country after three rounds of national qualifying tests.

Publications and preprints

Prabal Adhikari, Jens O. Andersen, and Martin A. Mojahed: "Condensates and pressure of two-flavor chiral perturbation theory at nonzero isospin and temperature".
arXiv: 2010.13655 [hep-ph].
In: Eur. Phys. J. C (2021) 81:173.

Prabal Adhikari, Jens O. Andersen, and Martin A. Mojahed: "Quark, pion and axial condensates in three-flavor finite isospin chiral perturbation theory".
arXiv: 2012.04339 [hep-ph].
In: Eur. Phys. J. C (2021) 81:449.

Martin A. Mojahed, and Tomas Brauner: "On-Shell Recursion Relations for Nonrelativistic Effective Field Theories".
arXiv: 2108.03189 [hep-th].
In: Physics Letters B 822, 136705.

Martin A. Mojahed, and Tomas Brauner ”Nonrelativistic effective field theories with enhanced symmetries and soft behavior”.
arXiv: 2201.01393 [hep-th].
In: JHEP 03 (2022) 086.

Andrzej J. Buras, Julia Harz, and Martin A. Mojahed ”Disentangling new physics in $K \to \pi\nu\bar{\nu}$ and $B \to K(K^*)\nu\bar{\nu}$ observables”.
arXiv: 2405.06742 [hep-ph].
In: JHEP 10 (2024) 087.

Nicolás Bernal, Julia Harz, Martin A. Mojahed, and Yong Xu ”Graviton- and Inflaton-mediated Dark Matter Production after Large Field Polynomial Inflation”.
arXiv: 2406.19447 [hep-ph].
In: Phys. Rev. D. (2025) 111, 043517.

Martin A. Mojahed, Kai Schmitz, and Xun-Jie Xu ”Gravitational chargegenesis”.
arXiv: 2409.10605 [hep-ph].
In: Phys. Rev. D. (2025) 111 055005.

Martin A. Mojahed, Kai Schmitz, and Dominik Wilken ”A lower bound on the right-handed neutrino mass from wash-in leptogenesis”.
arXiv: 2501.07634 [hep-ph].
In: Under review in Physical Letters B.

Link to Inspire HEP page: Inspire Link

Teaching Experience

Fall 2023- Present | **Teaching Assistant**, JGU
Exercise instructor in the following courses:
- Early Universe Cosmology.
- Relativistic quantum field theory (once as the head tutor, once as a regular tutor).

Spring 2022 - Spring 2023 | **Teaching Assistant**, TUM
Exercise instructor in the following courses:
- PH 1005 Theoretical Particle Physics.
- PH 2041 Quantum Field Theory.

Spring 2017 - Winter 2021 | **Teaching Assistant**, NTNU
Exercise instructor in the following courses:
- TFY 4345 Classical Mechanics.
- FY 2045 Quantum Mechanics 1.
- TFY 4215 Introduction to Quantum Physics.
- FY 1003 Electricity and Magnetism.
- TFY 4104 Physics.
- FY 0001 Physics.

2016 - 2018 | **Science Mentor**, ENT3R Trondheim
Weekly mentoring of a group of high school students majoring in physics and mathematics.

Languages

Norwegian:	Mother tongue.
English:	Fluent.
Farsi:	Good.